
Electronic Thesis and Dissertation Repository

11-8-2017 12:30 PM

Geochemistry of the Dome Mine Ankerite Veins: Insights into the Multi-Stage Enrichment of a World-Class Orogenic Gold Deposit

Jessica M. Stromberg
The University of Western Ontario

Supervisor

Dr. Neil Banerjee
The University of Western Ontario Co-Supervisor

Dr. Ed Cloutis
The University of Western Ontario Co-Supervisor

Dr. Gordon Southam
The University of Western Ontario

Graduate Program in Geology

A thesis submitted in partial fulfillment of the requirements for the degree in Doctor of Philosophy

© Jessica M. Stromberg 2017

Follow this and additional works at: <https://ir.lib.uwo.ca/etd>



Part of the [Geochemistry Commons](#), and the [Geology Commons](#)

Recommended Citation

Stromberg, Jessica M., "Geochemistry of the Dome Mine Ankerite Veins: Insights into the Multi-Stage Enrichment of a World-Class Orogenic Gold Deposit" (2017). *Electronic Thesis and Dissertation Repository*. 5090.

<https://ir.lib.uwo.ca/etd/5090>

This Dissertation/Thesis is brought to you for free and open access by Scholarship@Western. It has been accepted for inclusion in Electronic Thesis and Dissertation Repository by an authorized administrator of Scholarship@Western. For more information, please contact wlsadmin@uwo.ca.

Abstract

The Dome Mine in the world-class Timmins camp has produced over 16 Moz of gold during its 108 year production history. This gold endowment is the result of multistage enrichment of which the first stage is a set of ankerite veins that extend over 5,400 m in strike and 1,500 m vertically. A deposit wide geochemical study of the Dome ankerite veins was undertaken to characterize their genesis, geochemistry, and role in the deposit mineralization history. Samples and mapping from new and historic mine workings, bulk rock geochemistry, and stable isotope geochemistry were used to constrain the depositional context of the ankerite veins as forming syntectonically from auriferous metamorphic fluids, and provide insights into geochemical controls on vein formation. The $\delta^{18}\text{O}$ values for dolomite from the ankerite veins show a trend of increasing $\delta^{18}\text{O}_{\text{VSMOW}}$ values from 10.8 to 14.9‰ downdip of the ankerite veins and to the northwest away from the Dome Fault Deformation Zone (DFDZ), which is likely a long-lived fluid conduit. Gold is intimately related to pyrite mineralization with contributions from multiple sources. This was investigated by a suite of high-resolution geochemical techniques including synchrotron-radiation X-ray fluorescence (SR-XRF). Three stages of pyrite growth were identified, each with a distinct gold and trace element fingerprint. These stages of pyrite growth and gold endowment are related to deposit wide fluid events. The application of high-resolution synchrotron techniques to ore deposit studies was developed and evaluated on a number of different types of auriferous samples from across the Timmins gold camp. These applications address the present challenges of today's global minerals industry by quickly and effectively answering key questions regarding deposit formation and informing exploration strategies and extractive geometallurgy. This body of work addresses several key questions in the field of orogenic gold regarding fluid sources and key components of multi-stage deposit formation. It reveals the integral role of early carbonate veining and alteration at the Dome mine and that the ore system was fertile for a period of over 20 Ma with variability in gold tenor, trace element contents and redox throughout the deposit history.

Keywords: Orogenic Gold, Geochemistry, Pyrite, Timmins, Synchrotron

Co-Authorship Statement

This thesis consists of five chapters, three of which are in manuscript format. Chapter 2 has been submitted to Ore Geology Reviews and is authored by J.M. Stromberg, E. Barr and N.R. Banerjee, Chapter 3 has been submitted to Economic Geology and is authored by J.M. Stromberg, E. Barr, L.L. VanLoon, R.A. Gordon and N.R. Banerjee, and Chapter 4 is in preparation for submission and is authored by J.M. Stromberg, L.L. Van Loon, R.A. Gordon, A. Woll, D. Schumann, and N.R. Banerjee. Dr. Banerjee provided funding, access to and training in the operation of laboratory equipment and guidance on the conduct of the research. Goldcorp provided funding for analytical costs, access to samples, support in sample collection, and training. They also provided an internal geochemical dataset for the local host rocks, which was used in Chapter 2. The co-authors of the publications associated with the chapters of this thesis have provided their expertise in the parts of the experimental design for the relevant work and guidance on the proper presentation of the material. All data collection and processing apart from the EMPA maps and TEM work in Chapter 4, and the D-SIMS analysis in Chapter 3 was performed by me. The SIMS data was collected at Surface Science Western by Dr. Stamen Dimov, the TEM analysis was performed by Dr. Dirk Schumann, and the EMPA maps were collected by Marc Beauchamp. The intellectual development of the ideas is mine, with guidance and input from my supervisors and collaborators.

Dedication

This thesis dedicated to my grandfather, Jarmo Juhani Sinisalo, who taught me sisu and to stay curious.

Acknowledgements

I would like to thank my supervisor Dr. Neil Banerjee, as well as my unofficial supervisors Erik Barr and Dr. Lisa Van Loon for their support and guidance through the evolution of this thesis. It was Erik's curiosity and willingness to look beyond ore and waste that initially propelled this project into existence. Erik has continued to be a strong mentor and enthusiastic collaborator for the last 6 years and without his support a former biochemist certainly would not have taken on the role of beat geologist. Neil has encouraged and supported me to take the project in an entirely different direction than planned and Lisa reigned us in when the geologist in us was overzealous with our spectral interpretations. I would also like to acknowledge my two satellite supervisors, Dr. Ed Cloutis and Dr. Gordon Southam, who were integral to my decision to pursue graduate school and introduced me to spectroscopy.

I would like to acknowledge all the research associates and support staff from the following institutions who played an integral role in ensuring the success of this research by sharing their expertise and often their troubleshooting skills. This includes, but is not limited to the following groups: The Banerjee Research Group, Resource Geoscience Western, Western LSIS (Laboratory for Stable Isotope Science), Western Powder and Micro X-Ray Diffraction Laboratory, Western EPMA (Earth and Planetary Materials Analysis) Laboratory, Western Nanofabrication Facility, SSW (Surface Science Western), CLS (Canadian Light Sources) beam line 07B2-1, APS (Advanced Photon Source) Sector 20, CHESS (Cornell High Energy Synchrotron Source) F3 beam line, and the technical services group at Goldcorp Porcupine Gold Mines. I would also like to acknowledge Bob Hodder and Dick Hutchinson, two titans of this field whose body of work provided the base on which this work and our interest in the Dome mine was built. They provided me with a wealth of knowledge, a healthy dose of skepticism, and instilled an appreciation for the importance of primary observations.

This project would not have come to fruition without the support of Goldcorp Porcupine Gold Mines. They provided support for analytical costs and took me on for 10 months over the course of two summers as a student production geologist. The training and

experiences provided during this time shaped my perspective on geology and ore deposit research. In addition to Goldcorp, this research was financially supported by the National Science and Engineering Research Council of Canada (NSERC), the Ontario Centers of Excellence, the Society of Economic Geologists (SEG) Canada Foundation, NSERC Post graduate scholarship program, NSERC CREATE (Collaborative Research and Training Experience) fellowship program, Ontario graduate scholarship, Western Graduate Research Scholarship, R.W. Hodder travel award, Canadian Light Source Travel Support program, the SEG, CSA (Canadian Space Agency) ASTRO (Astromaterials Training and Research Opportunities) graduate research grant program, and the GAC-MDD (Geologic Association of Canada- Mineral Deposits Division).

To all the classmates, colleagues, officemates, and lifelong friends that I acquired during my tenure at Western, this would not have been possible without your support and many laughs, tears, and words of advice and encouragement over hours spent at the grad club. I would like to acknowledge my peer mentors Dr. Andrea Prentice, Dr. Rachel Schwartz-Narbonne and Dr. Matt Izawa, who have provided much needed perspective, especially in the last two years. A special thank you to Dave Edey, Dr. Laura Sanchez and Dr. Tim Officer, with whom I shared many late nights, afternoons at the grad club, and discussions of variable relevance to this project.

Thank you to my family (Äiti, Isi, Justine, Jasmine, Mummi, Ukki) for their unwavering support over the last 6 years of this endeavor and throughout my life. They have tolerated me bringing rocks home for almost 25 years now and could I not have come this far without their support. I would also like to thank my future in-laws who graciously gave up their kitchen table and provided encouragement and a bottomless pot of coffee for my final four-month writing “retreat” on beautiful Vancouver Island.

And lastly, I want to thank my fiancé Nicole who has endured the hardest part of this endeavor by my side, the final two years, and especially the last 6 months. Without her support, encouragement, and patience the completion of this work would not have been possible. Kiitos.

Table of Contents

Abstract	ii
Co-Authorship Statement	iii
Dedication	iv
Acknowledgments	v
Table of Contents	vi
List of Tables	xi
List of Figures	xii
List of Appendices	xv
List of Abbreviations	xvii
Chapter 1. Introduction and Research Objectives	1
1.1.0 Archean Orogenic Gold	1
1.1.1 Timmins Gold Camp	3
1.1.2 Dome Mine	4
1.1.3 Dome Ankerite Veins	5
1.2.0 Ore Deposit Geochemistry	5
1.2.1 Pyrite Geochemistry	7
1.3.0 Synchrotron X-ray Spectroscopy	7
1.3.1 X-Ray Fluorescence	10
1.3.2 X-Ray Absorption Fine Structure Spectroscopy	11
1.3.3 Geoscience Applications of Synchrotron Techniques	12
1.4.0 Research Objectives	12
1.5.0 References	13
Chapter 2. Early Carbonate Veining and Gold Mineralization in the Timmins Camp: Depositional Context of the Dome Mine Ankerite Veins	19
2.1.0 Introduction	19
2.2.0 Geologic Setting	20

2.2.1 Timmins Gold Camp	21
2.2.2 Dome Mine	25
2.3.0 Dome Ankerite Veins	28
2.4.0 Analytical Methods	31
2.5.0 Field Observations	34
2.6.0 Mineralogy and Gold Mineralization	38
2.7.0 Geochemistry Results	41
2.7.1 Major Element Geochemistry	42
2.7.2 Rare Earth Element Geochemistry	47
2.7.3 Metal and Trace Element Geochemistry	50
2.7.4 Stable Isotope Geochemistry	53
2.8.0 Discussion	59
2.9.0 Regional Implications and Conclusions	66
2.10.0 References	68
Chapter 3. Fingerprinting Multiple Gold Mineralization Events at the Dome Mine: Trace Element and Gold Content of Pyrite	75
3.1.0 Introduction	75
3.2.0 Regional Geology	76
3.2.1 Abitibi Greenstone Belt	76
3.2.2 Timmins Gold Camp	78
3.3.0 Mine Geology and Mineralization History	80
3.4.0 Sample Suite and Analytical Methods	85
3.4.1 Sample Suite	85
3.4.2 Sample Preparation	85
3.4.3 Scanning Electron Microscopy	86
3.4.4 Dynamic Secondary Ion Mass Spectrometry	87
3.4.5 Synchrotron Radiation X-Ray Fluorescence	87
3.4.6 SR-XRF Data Analysis	88
3.5.0 Results	89

3.5.1 Vein Mineralogy	89
3.5.2 Gold Mineralization	91
3.5.3 Electron Dispersive Spectroscopy	94
3.5.4 Pyrite Textures	96
3.5.5 Dynamic Secondary Ion Mass Spectrometry	99
3.5.6 SR-XRF	100
3.6.0 Discussion	110
3.7.0 Conclusions	116
3.8.0 References	118
 Chapter 4. Applications of Synchrotron X-ray Technology to Improving Mineral Exploration and Production: Examples from Orogenic Gold Deposits of the Timmins Camp, Canada	 128
4.1.0 Introduction	128
4.2.0 Methods	135
4.2.1 Sample Preparation	135
4.2.2 Synchrotron Radiation – X-Ray Fluorescence Maps	135
4.2.3 X-Ray Absorption Near Edge Spectroscopy	137
4.2.4 Electron Microprobe Analysis (EMPA)	138
4.2.5 High-Resolution Transmission Electron Microscopy	138
4.3.0 Data Analysis	139
4.3.1 Peakaboo	139
4.3.2 2D-Scan Plot	140
4.3.3 Athena	140
4.3.4 GeoPIXE	140
4.4.0 Results	141
4.4.1 Conventional Grain Scale Mapping	141
4.4.2 Multi-Scale Mapping	142
4.4.3 Point SR-XRF and XANES	147
4.4.4 Transmission Electron Microscopy	151
4.4.5 Multi-Scale Thin Section vs. Billet Analysis	154

4.4.6 Whole Rock Mapping	159
4.5.0 Discussion	163
4.6.0 Conclusion	164
4.7.0 References	165
Chapter 5. Summary and Conclusions	171
5.1.0 Summary	171
5.1.1 Mine Scale Geochemistry	171
5.1.2 Fingerprinting Fluids and Gold	172
5.1.3 Mine to Micron Studies on the Time-Scale of Mining	173
5.2.0 Future Work	173
5.3.0 Conclusions	175
Appendices	176
Curriculum Vitae	317

List of Tables

2-1	Average bulk rock geochemistry	43
2-2	Bulk carbonate stable isotopes	55
3-1	Summary of gold mineralization styles observed in the Dome ankerite veins	92
3-2	Summary of pyrite generations observed in the Dome ankerite veins	96
3-3	Summary of calculated As and Au values by D-SIMS	101
3-4	Summary of mineralization events in the Dome mine ankerite veins, their pyrite content and gold mineralization.	112
4-1	Sample Information	135

List of Figures

1-1	Geologic map of the Abitibi Greenstone Belt	2
1-2	Summary of gold deposits around the world with at least 30 tonnes of gold in combined production and reserves.	4
1-3	General schematic of a 3 rd generation synchrotron	8
1-4	Schematic of the VESPERS beamline at the CLS	8
1-5	Schematic layout of the microprobe station at the APS	9
1-6	X-Ray fluorescence spectra of an arsenian pyrite	10
1-7	Arsenic K-edge XANES spectra	11
2-1	Geologic map of the Abitibi Greenstone Belt	21
2-2	Regional map of the Timmins Gold Camp	23
2-3	Stratigraphic column of the Central Timmins Gold Camp	25
2-4	Plan view of the Dome mine geology	27
2.5	Composite section of the Dome mine stratigraphy	30
2.6	Dome mine ankerite vein field relationships	36
2.7	Curts ankerite vein field relationships	37
2-8	Representative photomicrography	40
2-9	Bulk rock geochemistry of the Vipond Formation	45
2-10	Box and whisker plots for major elements	46
2-11	Chondrite normalized REE patterns	49
2-12	Box and whisker plots for trace metals	51
2-13	Plots of trace metal associations in the ankerite veins	52
2-14	Plot of Dome ankerite vein dolomite $\delta^{13}\text{C}_{\text{PDB}}$ vs. $\delta^{18}\text{O}_{\text{VSMOW}}$ values	54
2-15	Plot of Dome ankerite vein dolomite $\delta^{13}\text{C}_{\text{PDB}}$ vs. $\delta^{18}\text{O}_{\text{VSMOW}}$ compared to values from across the Timmins camp and Archean Dolomites	56
2-16	Carbonate stable isotope vs. gold, Sr/Ca and Fe/Sr	57
2-17	General geology map of the Dome mine showing the relative positions of ankerite veins samples and their carbonate $\delta^{18}\text{O}_{\text{VSMOW}}$ values	59

2-18	Paragenetic sequence of deformation and alteration vs. time in the Timmins gold camp, and gold mineralization at the Dome mine	66
3-1	Geologic map of the Abitibi Greenstone Belt	77
3-2	Regional map of the Timmins Gold Camp	79
3-3	The Dome mine geology at the 12 level of the mine	81
3-4	Veining styles observed at the Dome mine	84
3-5	Typical ankerite vein mineralogy	90
3-6	Gold mineralization styles observed in the Dome ankerite veins	93
3-7	Gold EDS results	95
3-8	BSE-SEM photomicrographs of the three generations of pyrite growth observed in the Dome ankerite veins	98
3-9	Plot of As and Au content of the three pyrite types determined by D-SIMS	100
3-10	Depth profiled by D-SIMS	102
3-11	SR-XRF maps of Py08 (Py ₁ growth)	104
3-12	SR-XRF map of an inclusion rich Py ₁ grain	105
3-13	SR-XRF map of a Ni rich Py ₂ grain with a Py ₁ core	106
3-14	SR-XRF maps of a Py ₁ grain overgrown by Ni enriched Py ₂ growth	107
3-15	SR-XRF maps of Py ₃ grains	108
3-16	SR-XRF spectra showing the variability in trace element content of the three pyrite types	109
3-17	SR-XRF Spectra showing the variability in trace element content between gold inclusions (Inclusion I) in Py ₁ , free gold II (FGII) associated with tourmaline stringers, and free gold (FGI) associated with Py ₃	110
4-1	Comparison of the spatial resolution and detection range of microanalytical trace element mapping techniques	130
4-2	Comparison of EPMA and SR-XRF mapping.	142
4-3	SR-XRF maps of E885276	144
4-4	SR-XRF maps of C408780	145
4-5	SR-XRF maps of C406934	147

4-6	SR-XRF and XANES spectrum of C406934	149
4-7	SR-XRF As XANES stack of C406834	150
4-8	BSE-SEM images and EDS maps of the C406934 FIB foil	152
4-9	HAADF imaging of FIB foil C406934	153
4-10	SR-XRF mapping of C408779 thin section and billet	155
4-11	SR-XRF and XANES spectra of C408779	157
4-12	XANES As stack of C408779	158
4-13	Whole rock SR-XRF RGB maps	160
4-14	Whole rock SR-XRF maps of BA	161
4-15	Whole rock SR-XRF maps of C409403	162

List of Appendices

Appendix A Sample Information and Mineralogy	176
A.1 Sample List	176
A.3 Dome Mine Sample Location Map	179
A.3 Sample Descriptions	180
A.4 X-Ray Diffraction	224
Appendix B Bulk Rock Geochemistry	253
B.1 Major and Trace Elements	253
B.1.1 Dome Ankerite Samples	253
B.1.2 Other Samples	262
B.2 Map of Geochemically Distinguished Vipond Formation Flows	268
B.3 Carbonate Stable Isotopes	269
B.3.1 Raw Data	269
B.3.1 Standards	271
B.3.3 Average Plotted Values	272
Appendix C Trace Element Geochemistry	274
C.1 Electron Dispersive Spectroscopy	274
C.1.1 Electrum	274
C.1.2 Tellurides	275
C.2 Dynamic Secondary Ion Mass Spectrometry	276
C.2.1 Samples for D-SIMS	276
C.2.2 Raw Data Table	276
C.2.3 Depth Profiles and Petrography	277
Appendix D Trace Element Mapping	290
D.1 X-Ray Fluorescence Parameters	290
D.1.1 Beamline Specs	290
D.1.2 Regions of Interest for APS 20-ID Mapping	290
D.1.3 Mapping Parameters	291
D.1.4 XANES Parameters	294
D.2 SR-XRF Maps	295

List of Abbreviations

AGB	Abitibi Greenstone Belt
Ank	Ankerite
approx.	Approximately
APS	Advanced Photon Source
Apy	Arsenopyrite
Assem.	Assemblage
BSE	Back Scatter Electron
Ccp	Chalcopyrite
CHESS	Cornell High Energy Synchrotron Source
CLLDZ	Cadillac Larder-Lake Deformation Zone
CLS	Canadian Light Source
cg	conglomerate
cm	Centimeter
DA	Dynamic Analysis
DFDZ	Dome Fault Deformation Zone
D-SIMS	Dynamic- Secondary Ion Mass Spectrometry
EDS	Electron Dispersive Spectroscopy
e.g.	for example
EMPA	Electron Microprobe Analysis
eV	Electron Volt
et al.,	and others
EXAFS	Extended X-Ray Absorption Fine-Structure
Fm	Formation
Fsp	Feldspar
GeV	Giga electron volt
gw	Greywacke
HAADF	High-Angle Annular Dark Field
HREE	Heavy Rare Earth Elements
HR-TEM	High-Resolution Transmission Electron Microscopy

ICP-AES	Inductively Coupled Plasma Atomic Emission Spectroscopy
ICP-MS	Inductively Coupled Plasma Mass Spectroscopy
KB	Kirkpatrick-Baez
keV	kilo electron volt
LOI	Loss on Ignition
LREE	Light Rare Earth Elements
m	Meter
mm	Millimeter
Mol	Molybdenite
Mon	Monazite
mrad	Milliradian
mv	mafic volcanic
PDB	Pee Dee Belemnite
PDDZ	Porcupine Destor Deformation Zone
PGC	Porcupine Gold Camp
Por	Porphyry
Ppb	Parts per billion
PPL	Plain Polarized Light
Ppm	Parts per million
Py	Pyrite
QFP	Quartz-Feldspar Porphyry
QFV	Quartz-Fuchsite Vein
Qtz	Quartz
REE	Rare Earth Elements
RFL	Reflected Light
Rt	Rutile
Seds	Sediments
SEM	Scanning Electron Microscopy
Ser	Sericite
SD	Standard Deviation
SDD	Silicon drift detector

Sp	Sphalerite
SP	Sodic Porphyry
SR-XRF	Synchrotron Radiation X-Ray Fluorescence
Tel	Tellurides
Tur	Tourmaline
um	ultramafic
VG	Visible Gold
VSMOW	Vienna Standard Mean Ocean Water
Wt%	Weight percent
XAFS	X-ray Absorption Fine-Structure
XANES	X-ray Absorption Near Edge Structure
XPL	Cross Polarized Light
XRD	X-Ray Diffraction
μm	micron

Chapter 1

Introduction and Research Objectives

1.1.0 Archean Orogenic Gold

Archean orogenic gold deposits represent almost 30% of global gold endowment and are distinctive worldwide, sharing common tectonic environments, fluid compositions, and alteration patterns (Kerrich & Fyfe, 1981; Hutchinson, 1993; Groves et al., 1998, 2003; Ridley and Diamond, 2000; Goldfarb et al., 2001; Bateman and Bierlan, 2006; Dube and Gosselin, 2007; Lispon et al., 2014 Goldfarb and Groves, 2015). Orogenic gold deposits are generally hosted in deformed and variably metamorphosed terranes, commonly greenschist facies, and are spatially related to large scale fault zones (Figure 1-1; Robert & Poulson, 1997; Groves et al., 1998, 2003). Alteration assemblages are dominated by gold bearing quartz-carbonate veins and carbonate-sulfide-sericite-chlorite alteration from low salinity, near-neutral, 250-700°C, CO₂-rich ore fluids (e.g., Ridley and Diamond, 2000; Mikucki, 2000; Groves et al., 2003). Economic mineralization is generally the result of a multi-stage, multi-process mineralization history (Hutchinson, 1993; Goldfarb et al., 2001; Bateman and Bierlan, 2006, Dube & Gosselin, 2007; Meffre et al., 2016). The largest orogenic gold camps in the world are the Timmins gold camp in Canada's Abitibi Province of the Superior craton and Australia's Golden Mile deposits of Kalgoorlie in the Yilgarn craton with 63.7 and 46 Moz Au respectively (Figure 1-1,2; Bateman and Bierlan, 2006).

Despite the large body of work on this deposit type, there are still some outstanding questions and knowledge gaps in this field and the classification of distinctive deposit types is ongoing (e.g., Groves et al., 2003; Phillips and Powell, 2015). The source of orogenic fluids and metal endowment, as well as depositional mechanisms, continue to be contentious points (e.g., Jia and Kerrich 2000; Phillips and Powell, 2010; Large et al., 2011, 2017; Goldfarb and Groves, 2015; Fougereuse et al., 2016). On a deposit scale, the timing of complex mineralization histories and overprinting events is often poorly defined and the relative metal and gold endowment of those events is not well understood (Groves et al., 2003).

In addition to questions regarding deposit formation (genetic models), there are several practical challenges presently facing the minerals industry on a global scale. The number of gold deposits being discovered each year is steadily decreasing, and the number of years between deposit discovery and production is increasing (Holmes, 2016). This is in large part because all the low hanging fruit have been picked over the past 100 years of exploration for orogenic gold. The result is that new discoveries are increasingly deeper, have lower grades (gold concentrations), and have more complex ores making them harder to discover and to mine (Holmes, 2016). Exploring and mining in this climate requires improved genetic models as well as innovation and greater efficiency across the mining cycle. There is a need for improved exploration techniques and vectors to discover new deposits and the value of characterizing ores early in the mining cycle (exploration stage) to identify and mitigate potential metallurgical and environmental issues is being recognized by the minerals industry. This provides a unique niche for the development and application of novel techniques.

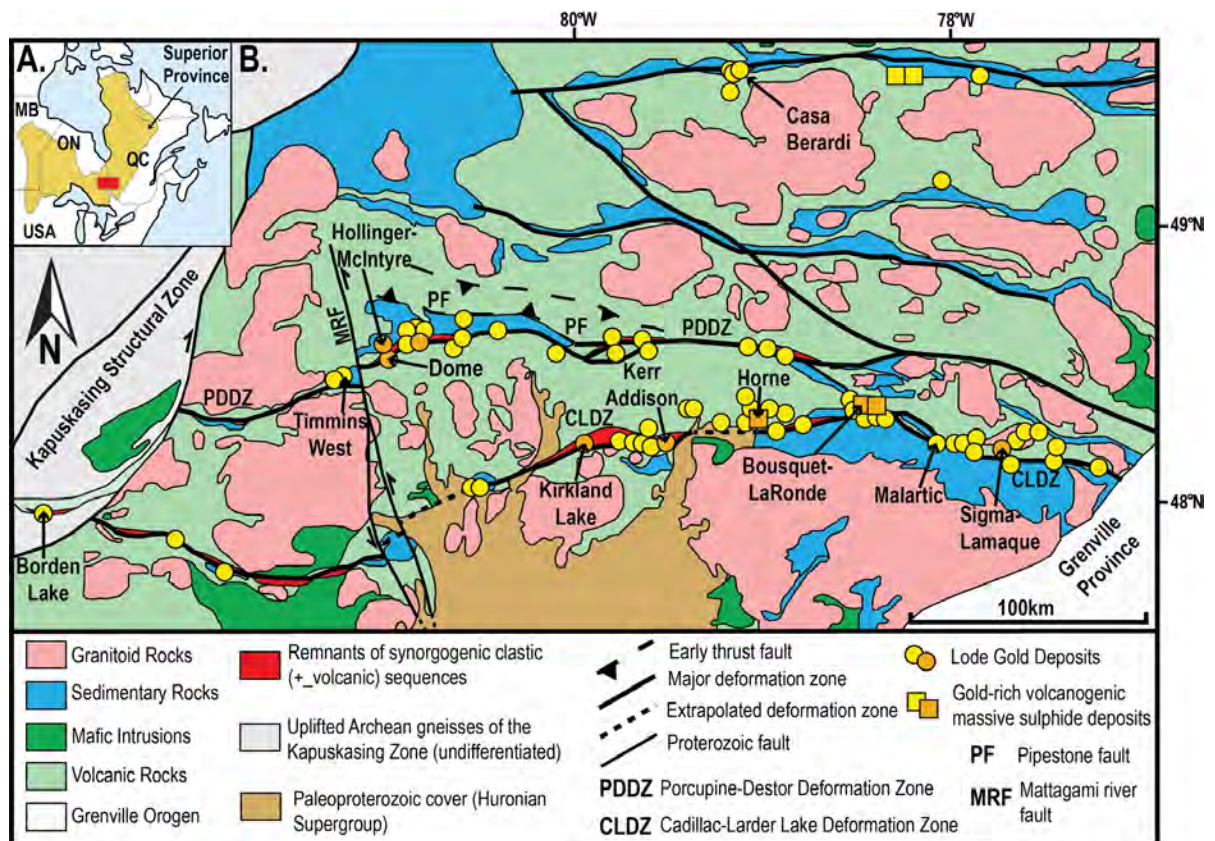


Figure 1-1. Geologic map of the Abitibi Greenstone Belt showing multiple world class orogenic (lode gold deposits) and the Timmins Gold Camp to the West hosting multiple deposits including the Hollinger-McIntyre, Dome and Timmins West mines. A. Simplified map showing the Superior Province (the red box signifies the regions shown in B). B. Simplified geologic map of the central and southern Abitibi greenstone belt, highlighting major faults, deformation zones, and the distribution of gold deposits (world-class deposits are in orange) (modified after Poulson et al., 2000; Dube and Gosselin, 2007; Bleeker, 2016).

1.1.1 Timmins Gold Camp

The Timmins gold camp was discovered in 1898 and is the world's largest known Archean orogenic lode gold camp having produced over 67 million ounces to date (Figure 1-1, 2). This prolific camp is located in the Abitibi greenstone belt (AGB) in Canada's Superior Province. It occurs along the northern margin of the Porcupine Deformation Zone (PDDZ), a major E to W crustal scale structural zone that stretches several hundred kilometers and is associated with mineral deposits across the AGB (Figure 1-1; Bleeker, 2015). The Timmins area is host to multiple world class deposits across an over 35 km strike length (e.g., Dome, Hollinger-McIntyre; Figure 1-1, 2). Like most orogenic gold camps, it has a complicated structural and metamorphic history, having undergone multiple deformation events (D_{1-7}), lower to middle greenschist facies metamorphism, and multiple stages of gold enrichment (e.g., Fryer et al., 1979; Gray & Hutchinson, 2001; Groves et al., 2003; Thompson et al., 2003; Bateman et al., 2008). The complex deformation history of the camp and the implications for gold mineralization are described in detail by Bateman et al., 2008. While the mineralization history of the region has been a contentious issue, Gray and Hutchinson (2001) identified three distinct regional mineralization events over the course of 7-17 Ma. Along with its complex mineralization history, the camp has a complicated structural history which controlled much of the mineralization. The dominant structural features are the PDDZ and the Porcupine syncline (Ferguson, 1968; Davies, 1977). These structures play an integral role in the formation of fluid conduits and camp scale pervasive carbonate alteration that is correlated with the gold mineralization (Davies et al., 1982).

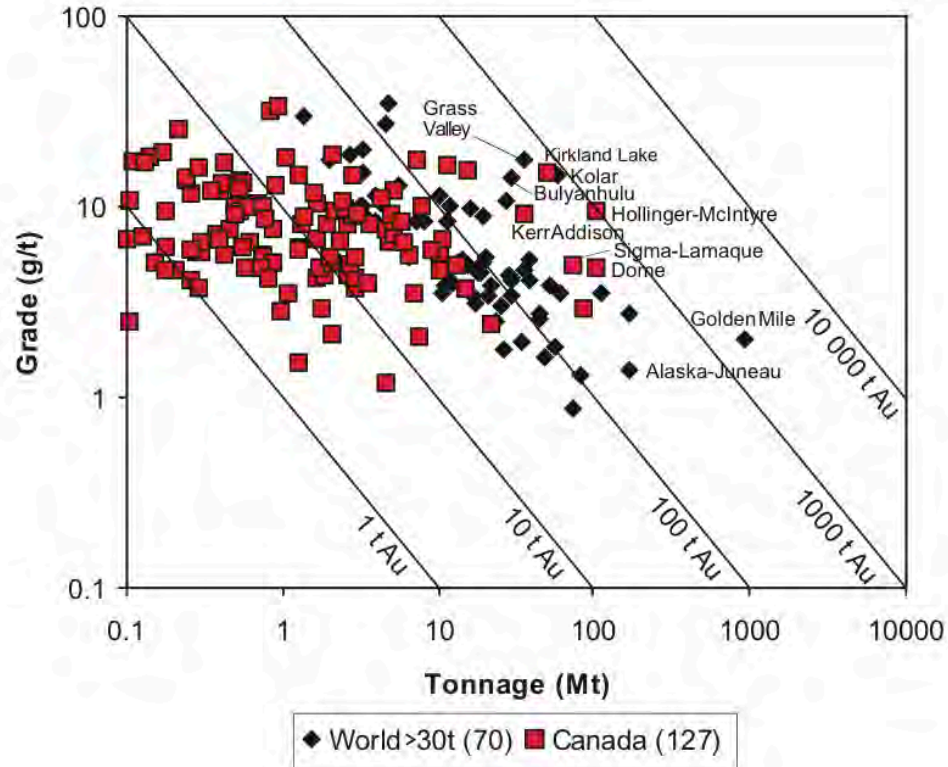


Figure 1-2. Summary of gold deposits around the world and in Canada with at least 30 tonnes of gold in combined production and reserves. Many of these deposits occur in the AGB (e.g, Kirkland Lake, Kerr-Addison and Sigma-Lamaque) and the Dome mine and Hollinger-McIntyre are in the Timmins gold camp (Dube and Gosselin, 2007).

1.1.2 Dome Mine

The Dome mine is the longest continually operating underground mine in the world, and has produced over 16 Moz over its 108 year history (Figure 1-2). It sits at the intersection of the dominant structural features in the Timmins gold camp; on the southern limb of the Porcupine Syncline and a splay of the PDDZ referred to as the Dome Fault Deformation Zone (DFDZ). The Dome mine is host to multiple styles and stages of gold mineralization and nearly all of the lithologies in the mine are mineralized (Holmes, 1968; Ferguson, 1968; Pressacco, 1999). It is a classic orogenic gold system in that it is characterized by multiple generations of syn-orogenic veining accompanied by intense carbonate and sericite alteration. Despite this lengthy mining history, questions remain regarding the

timing and nature of early veining and its role in the deposit history. These questions are integral to an improved genetic model for the formation of this world class gold deposit with implications for our understanding of orogenic gold deposits world-wide.

1.1.3 Dome Ankerite Veins

The earliest stage of veining at the Dome mine is an enigmatic set of ankerite veins which have contributed almost 20% of the 16 Moz of gold mined to date. They are restricted to a narrow region of the stratigraphy, but have been historically mined for over 2,000 m strike length. The ankerite veins were first studied in detail in 1979 and were interpreted to be synvolcanic exhalatives based on their conformity within the volcanic stratigraphy (Kerrick and Fryer, 1979; Fryer et al., 1979). The multi-phase mineralization history of these veins was recognized (Proudlove et al., 1989), but the syn-volcanic formation model remained. The ankerite veins are overprinted by later stages of veining and are the most laterally extensive ore type in the mine. While the ankerite veins have been extensively mined, grade is very irregular and notoriously difficult to predict. As a result, there are regions of up to 500 m strike length in the middle of the deposit where the ankerite veins were historically considered barren. On the mine scale, the highest ankerite vein grades are associated with quartz and quartz-tourmaline veining; however, overprinting veining does not ensure ore grade. In hand samples, gold is most commonly related to pyrite mineralization. However, the relative gold content of each mineralizing event is not well constrained and the role of the early ankerite vein forming event in the history of the deposit is not well understood.

1.2.0 Ore Deposit Geochemistry

The unravelling of complex mineralization histories of orogenic systems requires a multi-disciplinary, multi-scale approach. Mapping, bulk rock geochemistry, and stable isotope geochemistry (C and O) have historically been the foundation of ore deposit studies and are still integral to our understanding of fluid source, alteration, and fluid flow pathways (e.g., Fryer et al., 1979; McCuaig and Kerrich 1998; Jia and Kerrich, 2000; Swain et al., 2015). However, with the increasing complexity of deposit types and discoveries of deeper and lower grade deposits it has become necessary to improve models of

orogenesis, investigate source rocks, and develop new exploration vectors. This need has brought high-resolution geochemical techniques, such as secondary ion mass spectrometry (SIMS), laser-ablation inductively-coupled mass spectrometry (LA-ICP-MS) and electron probe micro analysis (EPMA) and the characterization of pyrite to the forefront of research on gold deposits (e.g., Deditius et al., 2009, 2014; Large et al., 2011, 2017; Steadman et al., 2015; Gregory et al., 2016; Reich et al., 2017).

1.2.1 Pyrite Geochemistry

Pyrite is ubiquitous in multiple gold deposit types (e.g., Carlin-type, Au-rich VMS, epithermal, orogenic) and is often intimately associated with gold mineralization in orogenic gold deposits (e.g., Proudlove et al., 2000; Cabri et al., 2000; Large et al., 2007, Deditius et al., 2014; Fougereuse et al., 2016). This is in part due to the fluid conditions under which these deposits form. Most commonly, orogenic fluids are between 300-350°C, slightly reducing, and gold is primarily carried as gold bisulfide complexes ($\text{Au}(\text{HS})_2^-$, $\text{HAu}(\text{HS})_2$ and $\text{Au}(\text{HS})$) (e.g., Seward, 1973, 1991; Mikucki, 1998). A common interaction of gold bisulfide-fluids in orogenic systems is with iron-bearing wall rock, which results in pyrite formation, removal of sulfur from the fluid, and the subsequent reduction of Au solubility in the fluid (Bolke, 1988; Seward, 1993; Phillips and Powell., 2010).

This relationship between pyrite and gold deposition, and the refractory nature of pyrite, make the characterization of pyrite trace element content a powerful tool for understanding the geochemistry of depositional environments and in exploration for multiple deposit types (e.g., Deditius et al., 2008; Large et al., 2014; Tardani et al., 2017; Mukherjee and Large, 2017). Pyrite typically contains a wide range of trace elements (e.g., Ag, Bi, Cd, Hg, Mo, Pb, Pd, Ru, Sb, Se, Sn, Te, Tl, Zn) in variable amounts and minor elements are often present up to several percent in the crystal lattice (e.g., As, Co, Ni, Sb, Cu, Ag, Au). This is enhanced in arsenian pyrites, which may contain up to 10% As and are typically rich in other minor and trace elements, including Au (Cook and Chryssoulis, 1990; Abratis et al., 2004; Reich et al., 2005; Deditius et al., 2014). The advance of high-resolution analytical techniques has shown that the geochemical

signatures of diagenetic sedimentary pyrites can be preserved in the cores of metamorphic and hydrothermal pyrite (e.g., Large et al., 2007, 2011, 2017; Steadman et al., 2015; Gregory et al., 2016;). Due to pyrite preserving changes in fluid chemistry in its trace element contents, it provides an effective proxy for the mineralization and metamorphic history of an ore deposit and can also provide insights into source rock (e.g., Large et al., 2017)

1.3.0 Synchrotron X-Ray Spectroscopy

Synchrotron radiation spectroscopy is a powerful technique for investigating complex materials at high spatial resolutions, although its application to ore deposit studies has been limited. Synchrotron radiation is produced by the acceleration of charged particles (electrons, proton, positrons) in a ring when a magnetic field is applied by bending magnets, which form the circular orbit of a synchrotron (Figure 1-3), or by insertion devices which apply an alternating magnetic field. When the charged particles near the speed of light with energies on the order of GeV, they emit synchrotron radiation tangentially to their orbit on a circular path (Figure 1-3). With the development of insertion devices (wigglers and undulators), third generation synchrotron sources such as the Canadian Light Source (CLS), Advanced Photon Source (APS), and Cornell High Energy Synchrotron Source (CHESS) were developed and operate at 3, 7, and 6 GeV respectively. Acceleration occurs in the booster ring and the particles are then injected into the storage ring where bending magnets maintain their circular orbit. The radiation produced by the synchrotron is directed into the beam line where it can be used and tuned to desired energies by monochromators to be used for experiments (Figure 1-4).

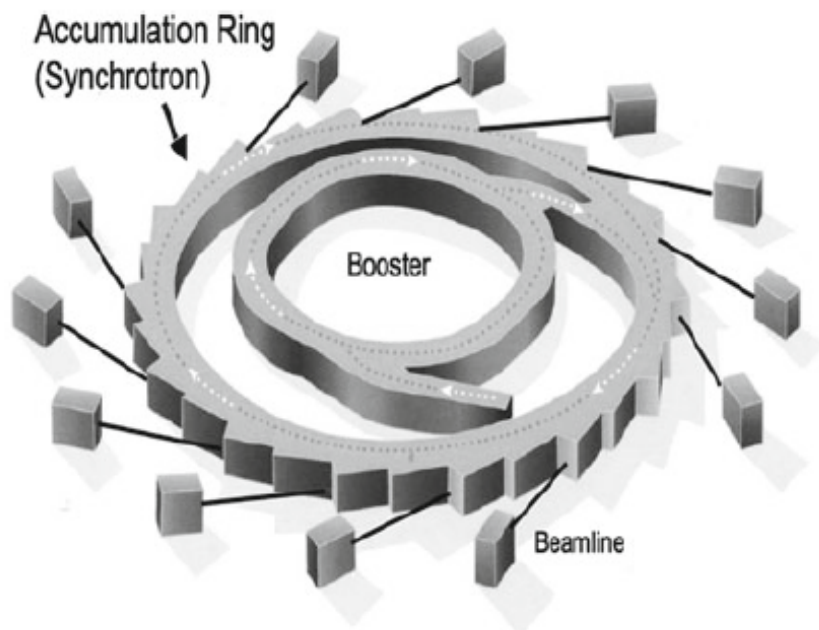


Figure 1-3. General schematic of a 3rd generation synchrotron (Aquilanti et al., 2015).

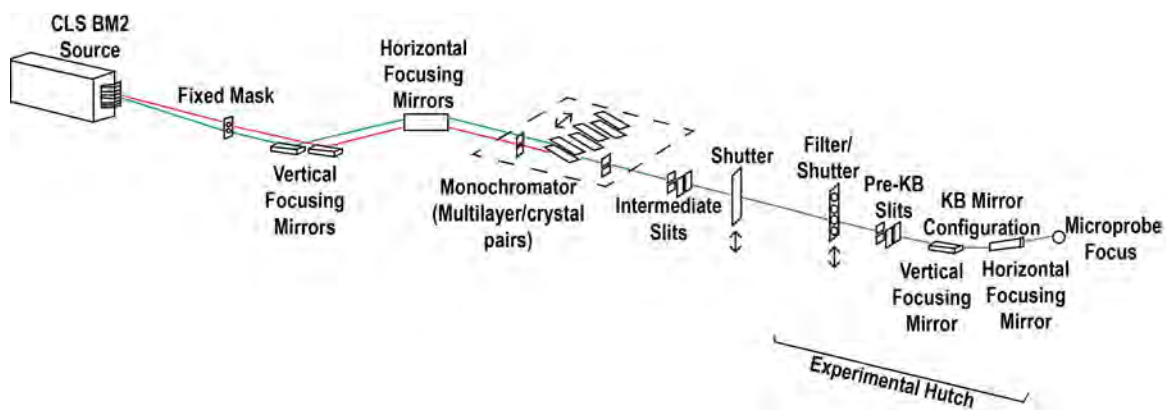


Figure 1-4. Schematic of the VESPERS beamline at the CLS. VESPERS (Very Sensitive Elemental and Structural Probe Employing Radiation from a Synchrotron Source) is a bending magnet beam line with a tunable energy range of 6-30 keV and spatial resolution of 2-4 μm . (KB – Kirkpatrick-Baez) (Modified from the Canadian Light Source)

There are several advantages to using a synchrotron X-ray source over a conventional X-ray source other than the high photon flux (up to 10^{12} greater). These include: intense brightness, tunability, the fact that it is highly focused, and its pulsed and ultra-stable time structure (Sham, 2002). This means that synchrotron radiation can be applied to a number of different types of experiment and conditions depending on the setup of the beam line and the end station into which it is directed (e.g., Figure 1-4, 5).

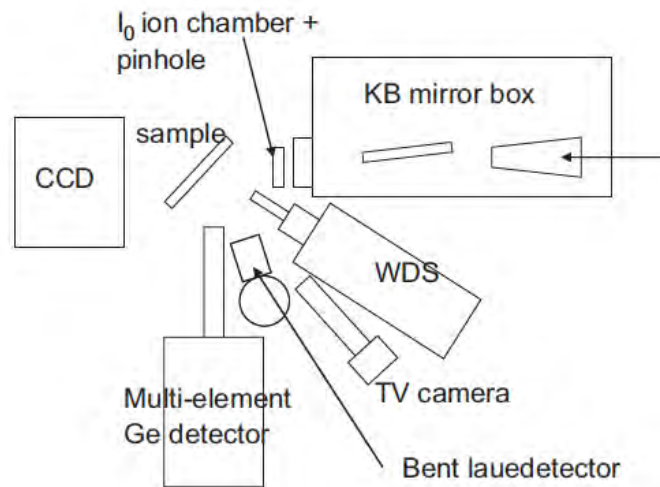


Figure 1-5. Schematic layout of the hard X-ray microprobe station at the APS (Advanced Photon Source) Sector 20-ID beamline. This end station on an insertion device beamline is optimized for high resolution ($<10 \mu\text{m}$) analysis for material science, environmental science and chemistry applications (Heald et al., 2007).

Beamline and end station configurations are specifically designed to maximize different capabilities of a given synchrotron, including storage ring-generated beam brightness and X-ray flux. X-rays are defined as electromagnetic radiation within the energy range of $\sim 500 \text{ eV}$ to 500 keV and are classified as either hard or soft depending on their energy. Hard X-rays have photon energies which penetrate air ($> \sim 5 \text{ keV}$), therefore experiments are not limited to vacuum conditions. X-rays interact with matter through the photoelectric effect and can either be totally or partially absorbed. If an incident X-ray photon has an energy greater than the binding energy of an electron in a tightly bound quantum

core level of an atom it encounters (e.g., 1s or 2p level), the electron is excited and ejected and the photon is absorbed.

1.3.1 X-Ray Fluorescence

Following excitation of a core-level electron, there is relaxation of the excited state through radiative and non-radiative de-excitation processes. The radiative form of decay is X-ray fluorescence (XRF), a process in which a shallower core-level electron fills the core-hole created by the X-ray induced photoionization process. This results in the release of energy in the form of a fluorescent X-ray, which can be detected using an XRF detector. The energy of the released X-ray is diagnostic of the excited core-level of the absorbing atom (Figure 1-6). While conventional XRF is commonly used in geochemical studies, the highly collimated and intense radiation emitted from a synchrotron source results in orders of magnitude more flux than a conventional XRF source, allowing for faster analysis and lower detection limits. This, in combination with the highly-focused nature of synchrotron X-rays, beam line optics and end station set up, makes it possible to do spatially resolved XRF mapping where each pixel contains an entire XRF spectrum (e.g., Figure 1-6).

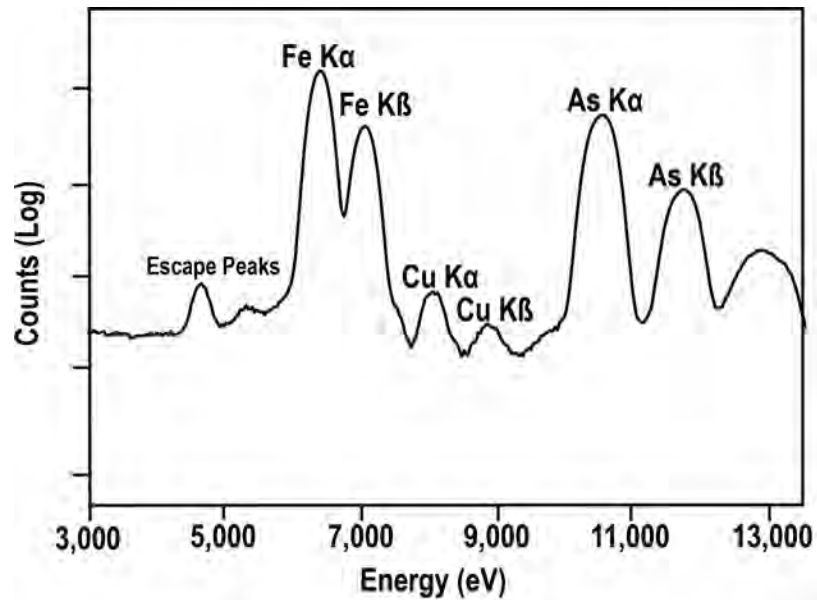


Figure 1-6. X-Ray fluorescence spectra of an arsenian pyrite grain.

1.3.2 X-Ray Absorption Fine-Structure Spectroscopy

X-Ray Absorption Fine-Structure (XAFS) spectroscopy allows for investigation of the local electronic structure of matter. When the X-ray incident energy is equal to that of the binding energy of a core-level electron, there is sharp increase in absorption referred to as the absorption edge. By tuning the incident photon energy using a monochromator across the absorption edge of a particular atom of interest, an XAFS spectrum is produced. The XANES (X-ray absorption near edge spectroscopy) energy region is sensitive to the oxidation state and coordination chemistry of the absorbing atom (Figure 1-7). Every atom has core-level electrons with well-defined binding energies, and changes in the shape and position of the absorption edge can provide information on the speciation of trace elements. XANES is an element specific technique capable of detecting minor species of trace elements, such as As in a variety of sample types (e.g., Figure 1-7). For example, the most common arsenic species observed in geologic materials (arsenate (As^{5+}), arsenite (As^{3+}) and arsenide (As^{1-})) are easily distinguished by their XANES edge position (e.g., Figure 1-7; Blanchard et al., 2017)

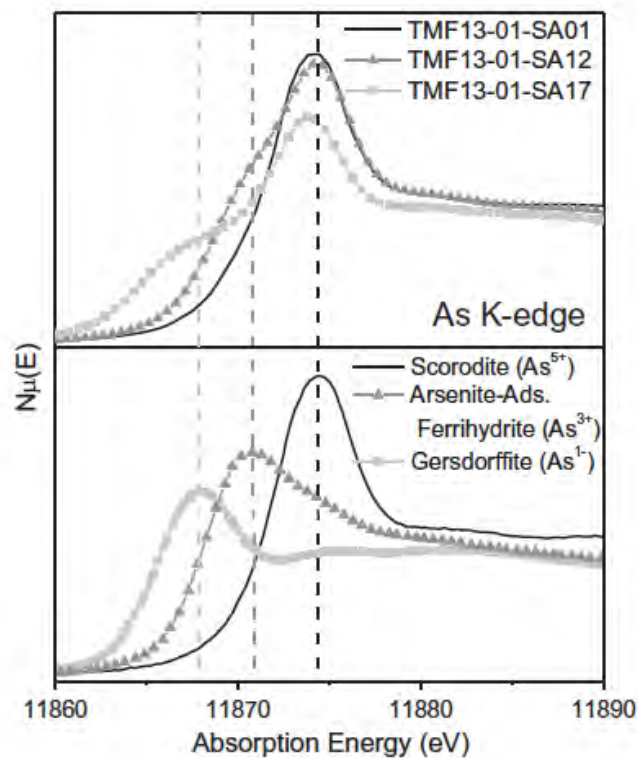


Figure 1-7. Arsenic K-edge XANES spectra of selected tailings samples from AREVAS JEB tailings management facility and arsenic standards (Blanchard et al., 2017)

1.3.3 Geoscience Applications of Synchrotron Techniques

There are applications for synchrotron techniques throughout the mining cycle, including exploration, remediation and ore processing (geometallurgy). SR-XRF mapping and XANES analysis are well established in the remediation and environmental side of the mining industry, with applications for mobility of deleterious elements such as As, Se, Cr. (e.g., Blanchard et al., 2017). The bulk of the work beyond this involves the characterization of trace metals in pyrite and other ore minerals (e.g., Cabri et al., 2000), as well as metal complexing in hydrothermal fluids (e.g., Brugger et al., 2010). The application of these techniques to deposit scale studies throughout the mine cycle is beginning to be explored and has great potential (e.g., Fischer et al., 2014), but has yet to be put forward in a workflow that integrates multiple techniques to answer industry relevant questions.

1.4.0 Research Objectives

The over 100 year mining history and body of research on the Dome mine makes it an ideal model for studying orogenic processes and for the development of applications of novel techniques. The mineralization history of the deposit is relatively well constrained, with in-depth studies of the main mineralizing events and exposed stratigraphy in the open pit and in extensive underground workings (e.g., Kerrich and Fryer, 1979; Fryer et al., 1979; Moritz, 1988; Proudlove et al., 1989). Despite their massive strike length and long mining history, the Dome ankerite veins have been understudied with respect to main stage mineralization due to their lower grade (gold content). Gold is intimately associated with pyrite mineralization, and as the earliest veining event at the mine, the ankerite veins are overprinted by multiple mineralizing events. Characterizing this vein set is also relevant beyond the Dome mine as the presence of early carbonate veining is not limited to the Dome mine or the Timmins camp. This type of veining is observed at the Aunor, Hollinger, and Buffalo Ankerite mines (e.g., Van Hees, 1979), and has also been described in other world class orogenic gold camps including Red Lake (e.g., Dube et al., 2003).

This body of work is centered on three main objectives which are outlined in the subsequent three chapters. The first objective is to constrain the depositional context of the Dome mine ankerite veins, characterize ankerite vein forming fluid source and pathways, and to explore their role in the world-class gold endowment at the Dome mine. This was undertaken through a deposit wide geochemical study combined with observations from new and old underground mapping. The second objective of this work is to fingerprint the multiple fluid events which contributed to the gold endowment of the Dome ankerite veins and elucidate the contribution of these events to ankerite vein metal and gold content. To do so, the trace element geochemistry of multiple generations of pyrite was characterized using a suite of high-resolution geochemical techniques. The final objective is to evaluate the application of synchrotron based X-ray techniques to ore deposit studies and their potential to quickly and effectively answer key questions regarding deposit formation and inform exploration strategies, extractive geometallurgy, and potential environmental issues. This was tested in a number of different, well constrained sample types from across the Dome mine and the Timmins camp by integrating and comparing synchrotron based XRF and XANES datasets with conventional techniques. These three objectives address the challenges of the minerals industry in an increasingly difficult climate, including the need for improved genetic models for deposit formation to improve exploration efficiency and role of innovation to improve efficiency throughout the mining cycle.

1.5.0 References

Abratis, P.K., Patrick, R.A.D. and Vaughan, D.J., 2004. Variations in the compositional, textural and electrical properties of natural pyrite: a review. *International Journal of Mineral Processing*, 74(1), pp.41-59.

Aquilanti, G., Vaccari, L., Plaisier, J.R. and Goldoni, A., 2015. Instrumentation at Synchrotron Radiation Beamlines. In *Synchrotron Radiation* (pp. 65-104). Springer Berlin Heidelberg.

Ayer, J.A., Thurston, P.C., Bateman, R., Dubé, B., Gibson, H.L., Hamilton, M.A., Hathway, B., Hocker, S., Houlié, M., Hudak, G., Ispolatov, V., Lafrance, B., Leshner, C.M., MacDonald, P.J., Peloquin, A.S., Piercey, S.J., Reed, L.E., and Thompson, P.H., 2005, Overview of results from the Greenstone Architecture Project: Discover Abitibi Initiative. Ontario Geological Survey Open File Report 6154, 146 p.

Bateman, R. and Bierlein, F.P., 2007. On Kalgoorlie (Australia), Timmins–Porcupine (Canada), and factors in intense gold mineralisation. *Ore Geology Reviews*, 32(1), pp.187-206.

Bateman, R., Ayer, J.A. and Dubé, B., 2008. The Timmins-Porcupine gold camp, Ontario: anatomy of an Archean greenstone belt and ontogeny of gold mineralization. *Economic Geology*, 103(6), pp.1285-1308.

Blanchard, P.E., Van Loon, L.L., Reid, J.W., Cutler, J.N., Rowson, J., Hughes, K.A., Brown, C.B., Mahoney, J.J., Xu, L., Bohan, M. and Demopoulos, G.P., 2017. Investigating arsenic speciation in the JEB Tailings Management Facility at McClean Lake, Saskatchewan using X-ray absorption spectroscopy. *Chemical Geology*, 466(5), pp. 617-626.

Bleeker, W., 2015. Synorogenic gold mineralization in granite-greenstone terranes: the deep connection between extension, major faults, synorogenic clastic basins, magmatism, thrust inversion, and long-term preservation, In: *Targeted Geoscience Initiative 4: Contributions to the Understanding of Precambrian Lode Gold Deposits and Implications for Exploration*, (ed.) B. Dubé and P. Mercier-Langevin. Geological Survey of Canada, Open File 7852, pp. 25–47.

Bohlke, J.K., 1989. Comparison of metasomatic reactions between a common CO₂-rich vein fluid and diverse wall rocks; intensive variables, mass transfers, and Au mineralization at Alleghany, California. *Economic Geology*, 84(2), pp.291-327.

Brugger, J., Pring, A., Reith, F., Ryan, C., Etschmann, B., Liu, W., O'Neill, B. and Ngothai, Y., 2010. Probing ore deposits formation: New insights and challenges from synchrotron and neutron studies. *Radiation Physics and Chemistry*, 79(2), pp.151-161.

Cabri, L.J., Newville, M., Gordon, R.A., Crozier, E.D., Sutton, S.R., McMahon, G. and Jiang, D.T., 2000. Chemical speciation of gold in arsenopyrite. *The Canadian Mineralogist*, 38(5), pp.1265-1281.

Cook, N.J. and Chryssoulis, S.L., 1990. Concentrations of invisible gold in the common sulfides. *The Canadian Mineralogist*, 28(1), pp.1-16.

Dube, B., Williamson, K., Malo, M., 2003. Gold mineralization within the Red Lake mine trend: example from the Cochenour-Willans mine area, Red Lake, Ontario, with new key information from the Red Lake mine and potential analogy with the Timmins camp. *Geologic Survey of Canada, Current Research 2003-C21*, 15 p.

Deditius, A.P., Utsunomiya, S., Ewing, R.C., Chryssoulis, S.L., Venter, D. and Kesler, S.E., 2009. Decoupled geochemical behavior of As and Cu in hydrothermal systems. *Geology*, 37(8), pp.707-710.

Deditius, A.P., Reich, M., Kesler, S.E., Utsunomiya, S., Chryssoulis, S.L., Walshe, J. and Ewing, R.C., 2014. The coupled geochemistry of Au and As in pyrite from hydrothermal ore deposits. *Geochimica et Cosmochimica Acta*, 140, pp.644-670

Dubé, B., and Gosselin, P., 2007, Greenstone-hosted quartz-carbonate vein deposits, in Goodfellow, W.D., ed., *Mineral Deposits of Canada: A Synthesis of Major Deposit-Types, District Metallogeny, the Evolution of Geological Provinces, and Exploration Methods*: Geological Association of Canada, Mineral Deposits Division, Special Publication No. 5, pp. 49-73.

Ferguson, S.A., 1968, *Geology and ore deposits of Tisdale township*. Ontario Department of Mines Geological Report 58, 177 p.

Fougerouse, D., Micklethwaite, S., Tomkins, A.G., Mei, Y., Kilburn, M., Guagliardo, P., Fisher, L.A., Halfpenny, A., Gee, M., Paterson, D. and Howard, D.L., 2016. Gold remobilisation and formation of high grade ore shoots driven by dissolution-reprecipitation replacement and Ni substitution into auriferous arsenopyrite. *Geochimica et Cosmochimica Acta*, 178, pp.143-159.

Fryer, B.J., Kerrich, R., Hutchinson, R.W., Peirce, M.G. and Rogers, D.S., 1979. Archaean precious-metal hydrothermal systems, Dome Mine, Abitibi Greenstone Belt. I. Patterns of alteration and metal distribution. *Canadian Journal of Earth Sciences*, 16(3), pp.421-439.

Goldfarb, R.J., Groves, D.I., Gardoll, D., 2001. Orogenic gold and geologic time: A global synthesis: *Ore Geology Reviews*, 18(1), pp.1-75.

Goldfarb, R.J. and Groves, D.I., 2015. Orogenic gold: Common or evolving fluid and metal sources through time. *Lithos*, 233, pp.2-26.

Gray, M.W., Hutchinson, R.W., 2001, New Evidence for Multiple Periods of Gold Emplacement in the Porcupine Mining District, Timmins Area, Ontario, Canada. *Economic Geology*, 96(3), pp. 453-475

Gregory, D.D., Large, R.R., Bath, A.B., Steadman, J.A., Wu, S., Danyushevsky, L., Bull, S.W., Holden, P. and Ireland, T.R., 2016. Trace element content of pyrite from the kapai slate, St. Ives Gold District, Western Australia. *Economic Geology*, 111(6), pp.1297-1320.

Groves, D.I., Goldfarb, R.J., Gebre-Mariam, H., Hagemann, S.G., Robert, F., 1998. Orogenic gold deposits—a proposed classification in the context of their crustal distribution and relationship to other gold deposit type. *Ore Geology Reviews*. 13(1), pp.7–27

Groves, D.I., Goldfarb, R.J., Robert, F., Hart, C.J.R., 2003. Gold Deposits in Metamorphic belts: Overview of Current Understanding, Outstanding Problems, Future Research, and Exploration Significance. *Economic Geology*, 98(1), p.1-29.

- Heald, S.M., Cross, J.O., Brewster, D.L. and Gordon, R.A., 2007. The PNC/XOR X-ray microprobe station at APS sector 20. *Nuclear Instruments and Methods in Physics Research Section A: Accelerators, Spectrometers, Detectors and Associated Equipment*, 582(1), pp.215-217.
- Holmes, T.C., 1968, Dome Mines Limited: in *Geology and Ore Deposits of the Tisdale Township*. Ontario Department of Mines Geological Report 58, 172p.
- Holmes, F., 2016. *The Last Known Gold Deposit*. US Global Investors. August 8.
- Hutchinson, R.W, 1993, A Multi-stage, multi-process genetic hypothesis for greenstone hosted gold lodes. *Ore Geology Reviews*, 8, pp. 349-382
- Jia, Y. and Kerrich, R., 2000. Giant quartz vein systems in accretionary orogenic belts: the evidence for a metamorphic fluid origin from $\delta^{15}\text{N}$ and $\delta^{13}\text{C}$ studies. *Earth and Planetary Science Letters*, 184(1), pp.211-224.
- Kerrich, R. and Fyfe, W.S., 1981. The gold--carbonate association: source of CO_2 , and CO_2 fixation reactions in Archaean lode deposits. *Chemical Geology*(1-4), 33, pp. 265-294.
- Kerrich, R. and Fryer, B.J., 1979. Archaean precious-metal hydrothermal systems, Dome Mine, Abitibi Greenstone Belt. II. REE and oxygen isotope relations. *Canadian Journal of Earth Sciences*, 16(3), pp.440-458.
- Large, R.R., Maslennikov, V.V., Robert, F., Danyushevsky, L.V. and Chang, Z., 2007. Multistage sedimentary and metamorphic origin of pyrite and gold in the giant Sukhoi Log deposit, Lena gold province, Russia. *Economic Geology*, 102(7), pp.1233-1267.
- Large, R.R., Bull, S.W. and Maslennikov, V.V., 2011. A carbonaceous sedimentary source-rock model for Carlin-type and orogenic gold deposits. *Economic Geology*, 106(3), pp.331-358.
- Large, R.R., Mukherjee, I., Gregory, D.D., Steadman, J.A., Maslennikov, V.V. and Meffre, S., 2017. Ocean and Atmosphere Geochemical Proxies Derived from Trace Elements in Marine Pyrite: Implications for Ore Genesis in Sedimentary Basins. *Economic Geology*, 112(2), pp.423-450.
- Lipson, R., 2014. *The Promise and Perils of Porphyry Deposits in the Future of Gold Production*. SEG Newsletter., 98
- McCuaig, T.C. and Kerrich, R., 1998. P—T—t—deformation—fluid characteristics of lode gold deposits: evidence from alteration systematics. *Ore Geology Reviews*, 12(6), pp.381-453.

- Meffre, S., Large, R.R., Steadman, J.A., Gregory, D.D., Stepanov, A.S., Kamenetsky, V.S., Ehrig, K. and Scott, R.J., 2016. Multi-stage enrichment processes for large gold-bearing ore deposits. *Ore Geology Reviews*, 76, pp.268-279.
- Moritz, R.P., 1988. Geological and Geochemical Studies of the Gold-Bearing Quartz-Fuchsite Vein at the Dome Mine, Timmins Area. PhD Dissertation, McMaster University, 341p.
- Mikucki, E.J., 1998. Hydrothermal transport and depositional processes in Archean lode-gold systems: A review. *Ore Geology Reviews*, 13(1), pp.307-321.
- Mukherjee, I. and Large, R., 2017. Application of pyrite trace element chemistry to exploration for SEDEX style Zn-Pb deposits: McArthur Basin, Northern Territory, Australia. *Ore Geology Reviews*, 81, pp.1249-1270.
- Newville, M., 2014. Fundamentals of XAFS. *Reviews in Mineralogy and Geochemistry*, 78(1), pp.33-74.
- Phillips, G.N. and Powell, R., 2010. Formation of gold deposits: a metamorphic devolatilization model. *Journal of Metamorphic Geology*, 28(6), pp.689-718.
- Phillips, G.N. and Powell, R., 2015. A practical classification of gold deposits, with a theoretical basis. *Ore Geology Reviews*, 65, pp.568-573.
- Proudlove, D.C., Hutchinson, R.W., Rogers, D.S., 1989. Multiphase Mineralization in Concordant and Discordant Gold Veins, Dome Mine, South Porcupine, Ontario, Canada. *Economic Geology Monograph*, 6, pp.112-123.
- Pressacco, R., 1999. Economic Geology and Mineralization of the Dome Mine. Ontario Geologic Survey, Open File Report 598, pp.1-32.
- Reich, M., Kesler, S.E., Utsunomiya, S., Palenik, C.S., Chryssoulis, S.L. and Ewing, R.C., 2005. Solubility of gold in arsenian pyrite. *Geochimica et Cosmochimica Acta*, 69(11), pp.2781-2796.
- Reich, M., Large, R. and Deditius, A.P., 2017. New advances in trace element geochemistry of ore minerals and accessory phases. *Ore Geology Reviews*, 81, pp. 1215-1217.
- Ridley, J.R. and Diamond, L.W., 2000. Fluid chemistry of orogenic lode gold deposits and implications for genetic models. *Reviews in Economic Geology*, 13, pp.141-162.
- Robert, F., Poulson, K.H., 1997. World-class Archean gold deposits in Canada: an overview. *Australian Journal of Earth Sciences*, 44, pp.329-351.
- Sham, T.K., 2002. Synchrotron Radiation: Earth, Environmental and Materials Sciences Applications, edited by G. S. Henderson, D. R. Baker

Seward, T.M., 1973. Thio complexes of gold and the transport of gold in hydrothermal ore solutions. *Geochimica et Cosmochimica Acta*, 37(3), pp.379-399.

Seward, T.M., 1993. The hydrothermal geochemistry of gold. In *Gold Metallogeny and Exploration* (pp. 37-62). Springer Netherlands.

Swain, S.K., Sarangi, S., Srinivasan, R., Sarkar, A., Bhattacharya, S., Patel, S.C., Pasayat, R.M. and Sawkar, R.H., 2015. Isotope (C and O) composition of auriferous quartz carbonate veins, central lode system, Gadag Gold Field, Dharwar Craton, India: Implications to source of ore fluids. *Ore Geology Reviews*, 70, pp.305-320.

Steadman, J.A., Large, R.R., Meffre, S., Olin, P.H., Danyushevsky, L.V., Gregory, D.D., Belousov, I., Lounejeva, E., Ireland, T.R. and Holden, P., 2015. Synsedimentary to early diagenetic gold in black shale-hosted pyrite nodules at the Golden Mile Deposit, Kalgoorlie, Western Australia. *Economic Geology*, 110(5), pp.1157-1191

Tardani, D., Reich, M., Deditius, A.P., Chryssoulis, S., Sánchez-Alfaro, P., Wrage, J. and Roberts, M.P., 2017. Copper–arsenic decoupling in an active geothermal system: A link between pyrite and fluid composition. *Geochimica et Cosmochimica Acta*, 204, pp.179-204.

Thompson, P.H., 2003, Discover Abitibi. Metamorphic subproject. Metamorphism and its relationships to gold deposits in the Timmins-Kirkland Lake area, western Abitibi greenstone belt, Ontario: Report 1: Ontario Geological Survey Open File Report 6120, p. 37–1 - 37–8.

VanHees, E.H., 1979. Auriferous ankerite vein genesis in the Aunor Mine, Timmins, Ontario. Unpublished MSc. thesis, University of Western Ontario, London, Ontario.

Chapter 2

Early Carbonate Veining and Gold Mineralization in the Timmins Camp: Depositional Context of the Dome Mine Ankerite Veins

2.1.0 Introduction

The world class Timmins gold camp in Canada's Abitibi Greenstone Belt has produced more than 67 million ounces of gold over the last 109 years. The Dome mine has produced more than 16.5 million ounces of gold since beginning operations in 1910. Like other deposits in the camp, the gold endowment at the Dome mine is the result of multi-stage, multi-process mineralization where main stage mineralization occurred towards the end of a period of deformation and magmatism (Hutchinson, 1993; Goldfarb et al., 2001; Dube & Gosselin, 2007). The earliest mined stage of gold mineralization identified at the Dome mine is a unique set of 2,690–2,679 Ma (Corfu et al., 1989; Ayer et al., 2005) ankerite veins. The genesis of these laterally extensive veins and their role in the world class gold endowment at the Dome mine has been contentious throughout the 100-year history of the mine (e.g., Gibson, 1912; Fryer and Hutchinson, 1976; Roberts et al., 1978; Kerrich and Fryer, 1979; Roberts and Reading, 1981; Proudlove et al., 1989). They were historically interpreted as sedimentary ankerite horizons deposited on the seafloor as an exhalative (e.g., Fryer et al., 1979). However, despite representing ~20% of the resource at the Dome mine, no comprehensive, deposit wide study of their depositional context has been undertaken. Early ankerite-hosted gold mineralization is not restricted to the Dome mine, but has been observed in other deposits of the camp where it has also been attributed to sedimentary exhalative processes (e.g., Aunor, Delnite, Buffalo-Ankerite deposits), as well in other Archean quartz-carbonate vein deposits (e.g., the Red Lake camp; Van Hees, 1979; Kerrich et al., 1981; Dube et al., 2003). This chapter presents observations from new underground mapping and mineralogical and geochemical data from the most comprehensive deposit wide sampling program to date to constrain the depositional context of the Dome ankerite veins and their role in the mineralization history of the Dome mine.

2.2.0 Geologic Setting

Hosted in Canada's Superior Province, the Abitibi Greenstone Belt (AGB) is the world's largest and best-preserved Archean greenstone terrain. Its vast mineral deposits (orogenic gold, intrusion related gold, volcanogenic massive sulfide (VMS), gold-rich VMS, magmatic Ni-Cu-PGE) are hosted in an 18-km thick succession of Archean metavolcanic and metasedimentary rocks which contains Canada's primary gold resources (Figure 2-1; Poulson et al., 2000; Dube & Gosselin, 2007). The AGB has a complex and contentious evolutionary and tectonic history which has been studied in detail (e.g., Mueller et al., 1996, 2009; Ayer et al., 2002a; Thurston et al., 2002, 2008; Bleeker, 2012). Its history includes oceanic arc formation, collision, and fragmentation with numerous types of volcanic edifices and sedimentary basins controlled by oblique subduction, extension, and mantle plumes (Thurston et al., 2008). The regional scale structural geology is dominated by two major East-West trending crustal scale structural features; the Porcupine-Destor deformation zone (PDDZ) and Larder Lake-Cadillac deformation zone (Figure 1). These two features are considered the most important deformation zones in the AGB in terms of structural effects and gold mineralization (Daigneault et al., 2002; Bateman et al., 2008).

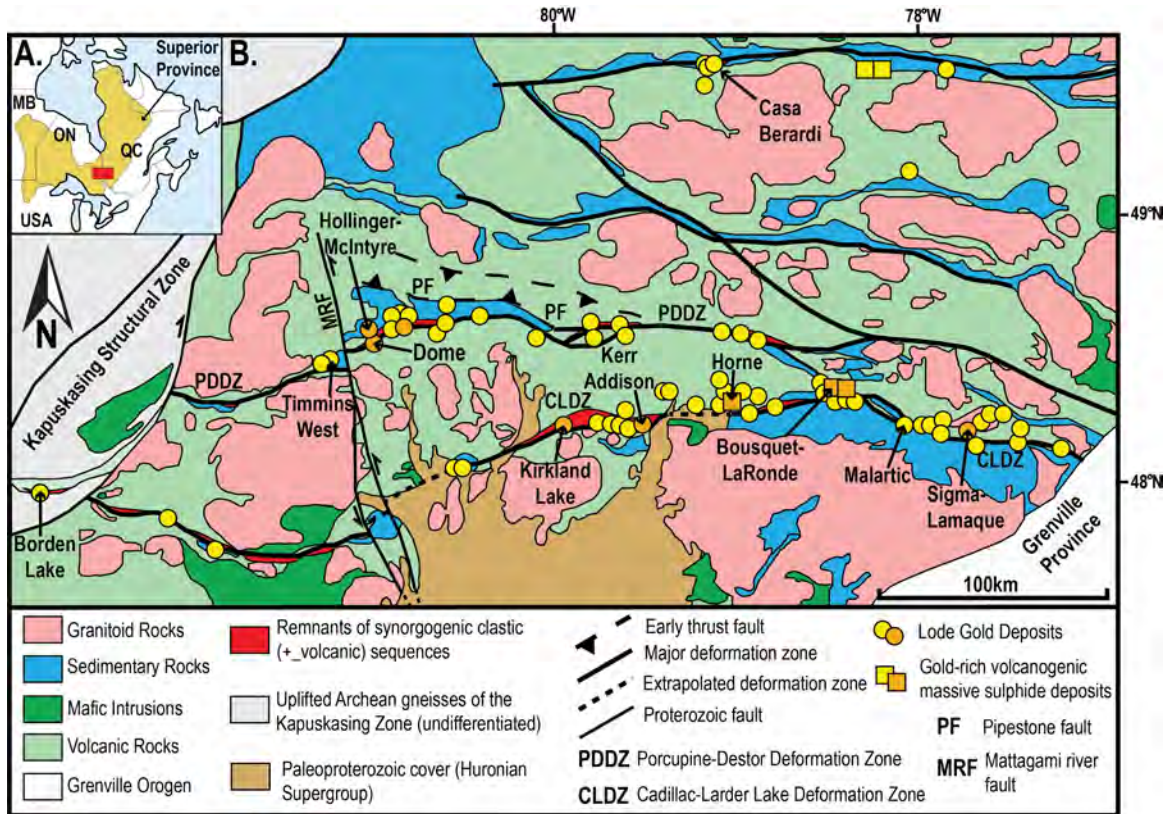


Figure 2-1. Geologic map of the Abitibi Greenstone Belt. A. Simplified map showing the Superior Province. The red box signifies the regions shown in B. B. Simplified geologic map of the central and southern Abitibi greenstone belt, highlighting major faults, deformation zones, and the distribution of gold deposits (world-class deposits are in orange) (modified after Poulson et al., 2000; Dube and Gosselin, 2007; Bleeker, 2016).

2.2.1 Timmins Gold Camp

The Timmins gold camp is the world's largest Archean orogenic lode gold camp, and as such, its geologic history has been extensively studied (see Bateman et al., 2008 for a review). Gold was discovered in 1896 with the first claims being staked in 1906 at the Hunter Mine area on the eastern shore of Porcupine Lake (Bureau of Mines, 1912 Report). It is on the northern margin of the PDDZ and encompasses multiple world class gold deposits including the Dome, Hollinger, McIntyre and Pamour (Figures 2-1, 2; Bateman et al., 2008). The region represents an oceanic back-arc setting which can be stratigraphically divided into four assemblages; the Deloro (2730-2724 Ma) and Tisdale

(2720-2695 Ma) volcanic assemblages, and the Porcupine (2690-2685 Ma) and Timiskaming (2681-2668 Ma) sedimentary assemblages; each representing a phase of basin development (Corfu et al., 1991; Brisbin, 1997; Kerrich et al., 1999; Ayer et al., 2005; Bateman et al., 2008; Figure 2-2). Additionally, the Timmins camp is characterized by the emplacement of multiple Porcupine age (2691-2687 Ma) quartz-feldspar porphyry intrusions, most notably the Paymaster, Dome, Pearl Lake and Preston (Corfu et al., 1991; Gray and Hutchinson, 2001; Ayer et al., 2003, 2005; MacDonald et al., 2005). Figure 2-3 shows the type stratigraphy for the central portion of the camp which hosts most of the region's gold mineralization.

The oldest assemblage in the camp; the Deloro assemblage (2730-2724 Ma), is found south of the PDDZ and is characterized by pillowed calc-alkaline mafic volcanics with minor local intermediate to felsic volcanics and iron formations (Ayer et al., 2005; Figure 2-2 and 2-3). The Deloro assemblage is disconformably overlain by the volcanics of the Tisdale assemblage which is divided into 4 formations; Hersey Lake, Central, Vipond and Gold Center (Ferguson, 1968; Bateman et al., 2008). The Tisdale assemblage is disconformably overlain by the sediments of the Porcupine and Timiskaming assemblages. The lowermost unit of the Porcupine assemblage is the Krist formation, a calc-alkaline pyroclastic deposit with zircon ages ranging from 2690-2688 Ma, that has an organic carbon rich basal graphitic argillite (Corfu et al., 1989; Ayer et al., 2002b, 2003, 2005). This is overlain by the greywackes, mudstones and shales of the Beatty-Hoyle formation. The Timiskaming assemblage unconformably overlies the Porcupine assemblage, and consists of the Dome formation and the Three Nations formation. The Dome formation has a basal conglomerate containing ultramafic clasts of the underlying Tisdale volcanics as well as auriferous massive sulfide clasts and clasts of ankerite vein material (Gray and Hutchinson, 2001). It is overlain by alternating greywacke beds of shale and sandstone, representing a turbiditic fan sequence (Born, 1995). The Three Nations formation consists of deltaic-fluvial deposits and is the youngest unit of the Timiskaming assemblage (Born, 1995). While most of the gold mineralization in the region is hosted in the volcanic sequences, it is also present in the Timiskaming conglomerates and to a lesser extent the argillites and Porcupine age porphyries where

they are cross-cut by gold bearing quartz-carbonate vein systems (Ferguson, 1968; Gray and Hutchinson, 2001).

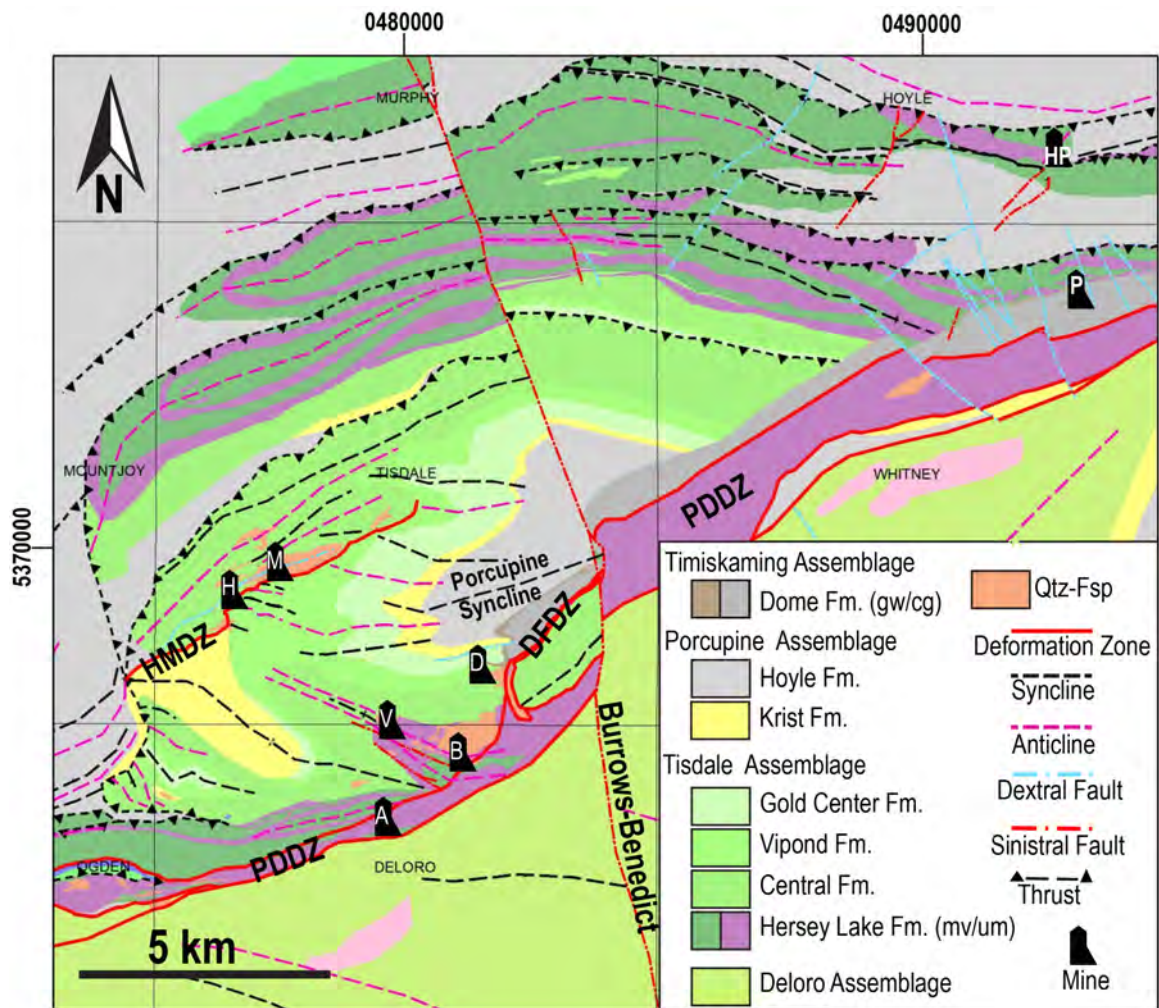


Figure 2-2. Regional map of the Timmins Gold Camp showing lithological contacts, major structures, mines (D – Dome, H – Hollinger, M – McIntyre, HP – Hoyle Pond, B- Buffalo-Ankerite, V-Vedron, A-Aunor, P-Pamour) and townships. Abbreviations: HMDZ – Hollinger-McIntyre Deformation Zone (99 shear), DFDZ – Dome Fault Deformation Zone, PDDZ – Porcupine Destor Deformation Zone, Fm – Formation, gw- greywacke, cg – conglomerate, mv – mafic volcanic, um - ultramafic, Qtz-Fsp – Quartz-Feldspar Porphyry. (Modified from E. Barr, Goldcorp Porcupine Gold Mines internal report, 2015)

The region has undergone multiple deformation events (D_{1-6}), and lower to middle greenschist facies metamorphism during which multiple stages of lode gold emplacement are recognized (Fryer et al., 1979; Proudlove et al., 1989; Gray & Hutchinson, 2001; Thompson et al., 2003; Bateman et al., 2008). Along with its complex mineralization history, the camp has a complicated structural history which controlled much of the mineralization (Bateman et al., 2008; Bleeker, 2015). The dominant structural features associated with the camp are the PDDZ and the Porcupine syncline, both of which play an integral role in the formation of fluid conduits (Davies et al., 1976). Within the central portion of the camp, the Dome Fault Deformation Zone (DFDZ) also plays an integral role in mineralization and has been interpreted as a thrust fault (Bleeker, 2015). Most of the region's gold resource is concentrated in large structurally controlled quartz-carbonate-sericite veins, and can be correlated with pervasive camp scale carbonatization of the volcanics (Davies et al., 1982; Gray & Hutchinson, 2001). The camp is host to at least two broad stages of gold mineralization, prior to and postdating formation of the Timiskaming unconformity surface (Gray and Hutchinson, 2001).

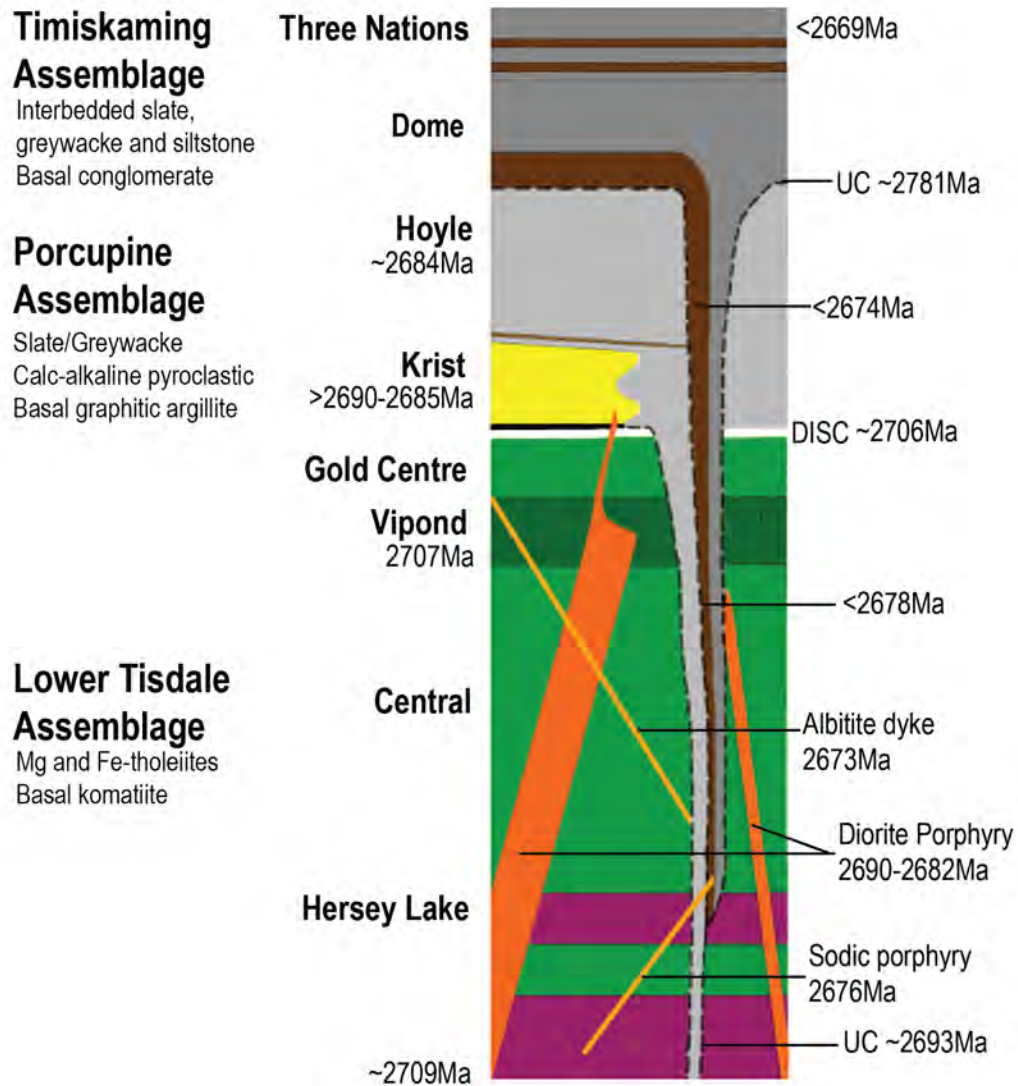


Figure 2-3. Stratigraphic column of the central Timmins Gold Camp (north of the PDDZ), showing ages of the units, the unconformities between the volcanics and sediments, and the cross-cutting relationships between the intrusive units (orange units) and the regional stratigraphy (UC – unconformity). (Modified from E. Barr, Goldcorp Porcupine Gold Mines internal report, 2014)

2.2.2 Dome Mine

The Dome mine is located ~6 km southeast of the town of Timmins. The mine consists of open pit and underground workings hosted in the volcanics of the Tisdale assemblage, the

intrusives and metasediments of the Porcupine assemblage and the metasediments of the Timiskaming assemblage, which represent the type stratigraphy of the Timmins Gold Camp (Figures 2-3 and 2-4). Production started at the Dome mine in 1910 and reached full production in 1912 (Bureau of Mines, 1912 Report). Open pit mining began in 1988 and was centered on what is locally referred to as the “sedimentary trough” region of the deposit where the Timiskaming sediments have eroded off the Tisdale volcanics (Figure 2-4). The underground mine is accessed via No. 8 Shaft which extends to -1650 meters. The Dome mine is located on the southeast limb of the Porcupine syncline and the structural footwall of the PDDZ at the unconformity of the Vipond formation volcanics and the Timiskaming sediments locally known as the “greenstone nose” (Figures 2-2 and 2-4). Another major structural feature associated with the mine is the Dome fault deformation zone (DFDZ), a northeast striking ~100 m wide unit of highly carbonatized porphyry and ultramafic rocks locally referred to as “carb rock” (or “highly altered” rock where fuchsite is present) which is the southern boundary of the Timiskaming sediments on the Dome property. The DFDZ has a complex structural history and may have originated as early as Pre-Timiskaming as a synvolcanic normal fault which was then activated as a thrust fault during D2 folding and rotated into a subvertical orientation during later deformation (Brisban, 1997). The rocks at the Dome mine have undergone lower greenschist facies metamorphism with the dominant alteration being ankeritization and sericitization with local silification/albitization. The earliest mineralization event is hosted in massive ankerite veins, which were historically interpreted as carbonate-chert chemical sediments within the lower mafic volcanics (Fryer and Hutchinson, 1976; Roberts et al., 1978; Kerrich and Fryer, 1979; Roberts and Reading, 1981). Later, main-stage gold mineralization is hosted by hydrothermal quartz veins proposed to be controlled by movement along the DFDZ, PDDZ and other minor faults subsidiary to them during D3/D4 deformation (Kerrich & Fryer, 1979; Moritz, 1988; Bateman et al., 2008).

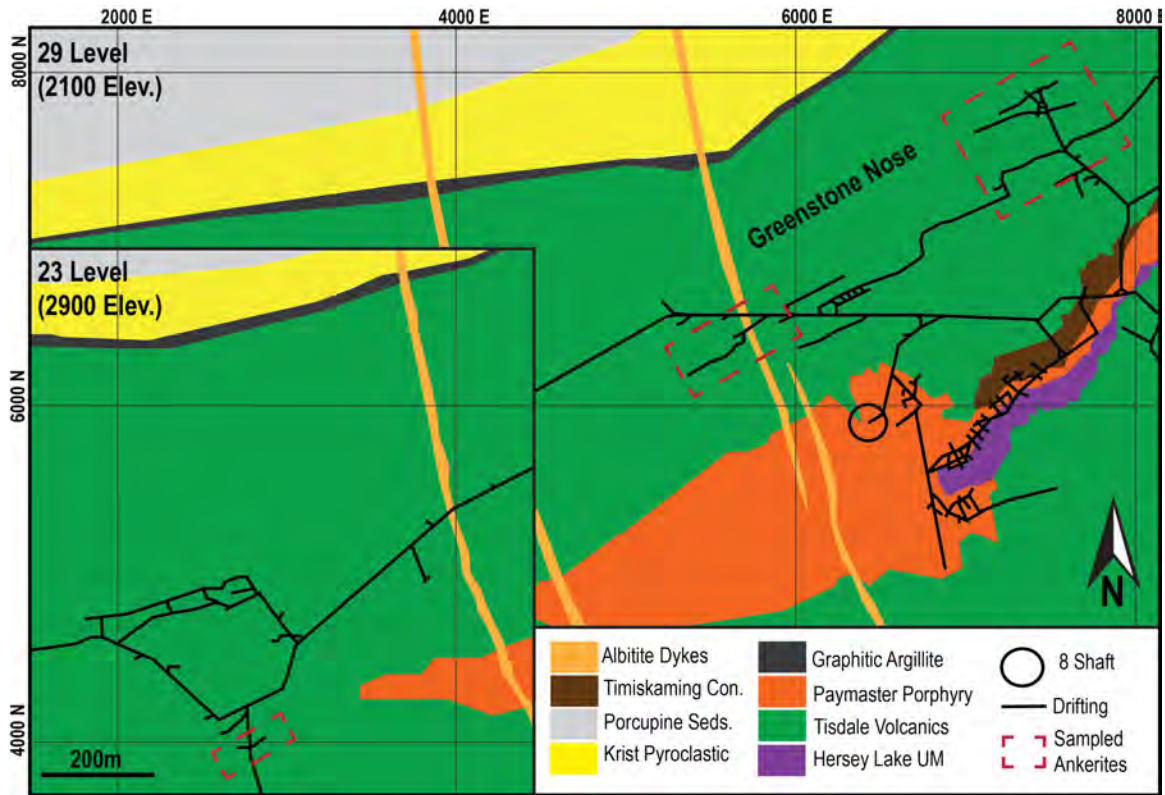


Figure 2-4. Plan view map of the Dome mine geology showing drifting (near horizontal excavated tunnels) in the 23 and 21 levels of the mine. The west section of the 23 level of the mine is inlayed over the east section of 29 level of the mine to show the position and orientation of ankerite veining within the mine stratigraphy. Sampled ankerite vein drifts are boxed in red, and most drifting in the same orientation in the Tisdale volcanics is also along ankerite veins. The east ankerite veins (concordant and discordant) have been extensively mined in on 29L and the lower levels of the mine. The west ankerites were historically mines and their crosscutting of the Paymaster porphyry can be seen on 23L where grade dies off as you approach the Paymaster. (Easting, Northing and Elevation (Elev.) are in historical Dome mine coordinates). Abbreviations: Con. – conglomerate, Seds. – sediments, UM – ultramafic. (Modified from Goldcorp Porcupine Gold Mines, internal report, 2012)

Gold occurs mainly as quartz vein hosted free gold and the most prolific gold producing zone at the Dome mine is locally called “dacite ore”. This is a region of the G1 flow of the Gold Center formation in the “greenstone nose” region of the mine which is intensely carbonate altered and was originally misidentified as a dacite. The “dacite ore” mineralization occurs as sets of en-echelon, sigmoidal quartz vein arrays (Holmes, 1968; Pressaco, 1999). The richest single structure at the mine is a steeply dipping on ~4-meter-wide massive banded quartz-fuchsite vein (QFV) which extends up to 550 m along strike, occurring close to the contact of a slate unit and the highly carbonatized ultramafic unit locally referred to as “carb rock” in the DFDZ region of the mine (Holmes, 1968; Rogers, 1982; Moritz and Crockett, 1990, 1991). Gold in the QFV occurs as free gold confined to the vein and is associated with galena (Moritz, 1988). The bulk of the ore at the Dome mine is from quartz vein stockworks in the greenstone nose and sedimentary trough regions of the mine and quartz-tourmaline veins in the “highly altered” rock (Holmes, 1968). Vein gold is found predominately as native gold associated with sulfides, with minor amounts found as tellurides (Holmes, 1968; Fryer et al., 1979; Proudlove et al., 1989; Pressaco, 1999; Harris, 2012). Mineralization at the Dome mine is not genetically related to the Porcupine intrusive suites as the main Dome ore postdates the emplacement of these porphyries by ~15 Ma (Ayer et al., 2004; McDonald et al., 2005; MacDonald, 2010).

2.3.0 Dome Ankerite Veins

The earliest stage of veining at the Dome mine is found in a series of extensive ankerite veins hosted in the Fe-tholeiitic basalts of the Vipond formation. These veins are generally conformable with flows, commonly dipping 50-65° to the north in the region of the mine referred to as the “greenstone nose” (Figures 2-4 and 2-5). Over the history of the mine, it is estimated that more than 3 million ounces of gold with an average grade of ~6 g/t have been produced from these veins. They were first studied in detail by Fryer et al. (1979) who identified 14 “ankerite layers” 1 cm to 1 m in width and up to 700 m in lateral extent within the Tisdale metabasalts. Based on their apparent conformity with volcanic layers and perceived sedimentary structures they were interpreted to be

synvolcanic chemical exhalative sediments (Gibson, 1912; Fryer and Hutchinson, 1976; Roberts et al., 1978; Kerrich and Fryer, 1979; Roberts and Reading, 1981; Proudlove et al., 1989). Fryer et al., (1979) proposed that deposition of the ankerite, chert, sulfides and graphite “chemical sediments” was the first of two stages of gold emplacement. While discordance of some of the veins was recognized (Holmes, 1968), this was interpreted to be the result of either localized interruption of sedimentation by impersistent volcanic units (Roberts and Reading, 1981), or due to later deformation and unconformities within the volcanic sequence (Fryer et al., 1979).

This interpretation has since been refuted by a more detailed study of patterns of wall rock alteration associated with the “#1 south quartz-ankerite vein” (Crick, 1991), and interpretations of banding as sedimentary have been revisited and re-interpreted as “crack-seal” structures formed during successive movements along the host shear (Pressacco, 1999). The age of the ankerite veining has also been better constrained by cross-cutting relationships. They cross-cut the ~ 2,690 Ma (Corfu et al, 1989) Paymaster porphyry intrusion in the region of the Dome pit, and are found as clasts in the overlying <2,679 Ma (Ayer et al., 2003) Timiskaming conglomerate at the 21 level of the mine (Figure 2-6). These cross-cutting relationships can be observed both underground on 26 level, and in the walls of the Dome pit (Figure 6). Historically, the ankerite vein ore has been classified as either East, Center or West, where there is a 500 m gap underground between the Center and the West Ankerite Zone which was not mined because grade was lost (Figure 2-4).

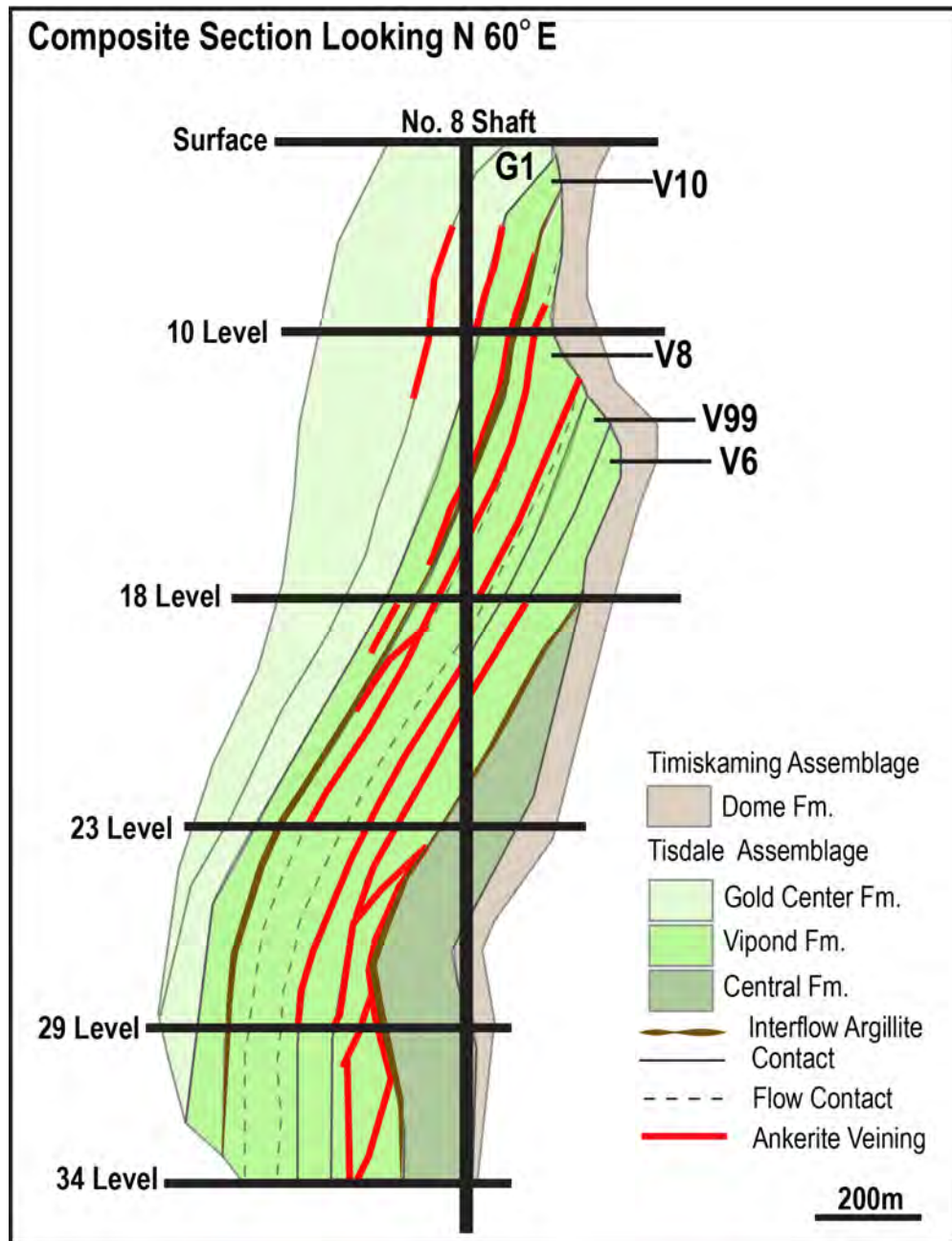


Figure 2-5. Composite section of the Dome mine stratigraphy perpendicular to the trend of the Porcupine Syncline, showing the major mined, mapped, and sampled ankerite veins relative to individual flows in the Vipond Formation (Modified from Crick, 1991 and Ferguson, 1968). Flows are labelled and the historical flow boundaries interpreted by Crick, 1991 are also shown (G1 – dacite, V10 - andesite, V8 –spherulitic, key, broken spherulitic, V99- 99, V6- lower spherulitic), as are interflow argillites identified by Ferguson, 1968.

In addition to their underground expression, the Dome ankerite veins in the “greenstone nose” can be correlated over 1000 meters west to surface at the Paymaster property as the Curts vein, a massive network of east-trending anastomosing ankerite veins that can be traced for over 300 m on surface (Figure 2-7). The Curts vein was first described by Gibson, 1912, as having an origin which is difficult to explain, with distinct banding suggesting a vein or bed origin rather than replacement. Historically, the Curts vein contains erratic gold values and has only produced ore where thick, irregular masses (or veins) of quartz-tourmaline-sulfide veins developed in the ankerite vein (Ferguson, 1968).

The Vipond formation which hosts the ankerite veins is made up of a series of high Fe-tholeiitic spherulitic pillowed mafic volcanic flows, variolitic hyaloclastic mafic flows, massive mafic flows and interflow carbonaceous argillite (Figure 5; Brisbin, 1997). The base of the Vipond formation across the camp is marked by the V99 flow (Graton et al., 1933), a massive flow which is intensely ankeritized, and weakly to moderately sericitized and pyritized (Figure 5). At the Dome Mine, the V99 flow is underlain by a basal “Spherulitic” flow (V6 flow). Historically, the Vipond stratigraphy at the Dome mine has been described as 7 units; the basal “Lower Spherulitic”, “99”, “Broken Spherulitic”, “Key”, “Spherulitic”, “Andesite”, and “Dacite” flows (Mason and Brisbin, 1987; Rogers, 1988; Crick, 1991) which are correlative to the V6, V99, V8, V10 and G1 flows described by Ferguson, 1968 across the camp (Figure 2-5). The V8 and V10 flows are important hosts for mineralization across the camp, and for the Dome ankerite veins. They are characterized by their spherulitic nature, hyaloclastite units, flow top breccias and interflow sediment units (Holmes, 1968; Crick, 1991; Brisbin, 1997).

2.4.0 Analytical Methods

A suite of 50 samples were collected underground at the Dome Mine. This suite includes samples of ankerite veins and surrounding lithologies. Multiple veins (concordant and discordant) were sampled and mapped on multiple levels of the mine. Sampling in older regions of the mine was limited by ground conditions, however, newly exposed ankerite veins were sampled and mapped as development in the greenstone nose region of the mine occurred in the summers of 2014 and 2015. Ten complementary surface samples

were collected on a transect along strike of the Curts vein, including carbonate vein samples from the Hollinger open pit, Buffalo-Ankerite open pit, and an outcrop across from Pearl Lake (See Appendix A for full sample list).

All samples were subsampled for subsequent geochemical analysis and polished thin sections of selected samples were prepared and characterized using transmitted and reflected light microscopy at the *Western University High Resolution Earth and Planetary Materials Imaging Facility*. Representative polished thin sections were coated with 5nm amorphous osmium using a Vacuum Desk II sputter coater to reduce charging, and imaged using Backscatter Scanning Electron Microscopy on a LEO (Zeiss) 1540 XB field emission gun – scanning electron microscope (FEG-SEM). The SEM was operated between 10 to 18 kV to examine samples using a quadrant-backscattered electron detector for better contrast at the *Western University Nanofabrication Facility*.

X-ray diffraction was carried out on bulk powdered samples by wet-mounting into custom sample holders using ethanol. Patterns were collected with a Rigaku Giegerflex powder diffractometer at the *Western University Powder X-ray Diffraction and Micro X-Ray Diffraction Laboratory* with a step-scan method from 5 to 120° 2 θ with 0.02° per step, and a 2 second dwell time per step. The Rigaku diffractometer uses Cu K α radiation with an emission tube voltage of 40 kV and 35 mA. The diffractometer was configured with a stationary emission tube, a horizontal goniometer with a radius of 173 mm and diverging and receiving slits of 0.5 mm and 0.3 by 12 mm respectively. Crystalline mineral phases were identified using the International Center for Diffraction Data Powder Diffraction File (ICDD PDF-4) and the Bruker AXS Eva software package.

Whole-rock major and trace elements were determined by inductively coupled plasma atomic-emission spectrometry (ME-ICP06 -Whole Rock Package ICP-AES) and inductively coupled plasma – mass spectrometry (ME-MS81 – Lithium Borate Fusion ICP-MS) respectively, following pulverization at ALS Minerals in Sudbury, Canada (Appendix B.1). The sample set was complemented with a dataset from Porcupine Joint Venture (PJV) (now Goldcorp Porcupine Gold Mines) of whole rock geochemistry for samples of the Vipond formation from the Dome mine (n=99) which hosts the ankerite veins. These samples were taken in 2001 and 2002 and analyzed for major oxides and

trace elements by XRF (x-ray fluorescence) and ICP-MS at ALS Chemex and XRAL laboratories. Reflex ioGAS™ software was used to analyze and plot the datasets.

For carbon and oxygen stable isotope analysis, carbonate separates were extracted from the bulk rock samples using a rock saw followed by crushing, and handpicking of grains. The resulting carbonate fraction was powdered and composition (carbonate abundance and mineralogy) was determined by XRD at the *Laboratory for Stable Isotope Science* at Western University. Powders were analyzed on a Rigaku rotating-anode X-Ray diffractometer employing a $\text{CoK}\alpha$ radiation source with monochromation using a curved crystal, diffracted beam and graphite monochromator with a voltage of 45 kV and 160 mA. Samples were scanned from 10θ to 75θ using a normal scan rate of $10^\circ 2\theta$ per minute, equivalent to $0.5^\circ 2\theta$ on conventional diffractometers. X-rays were collimated using 1° divergent and scatter slits and a 0.15mm receiving slit. Peaks were manually picked and relative abundances were determined from 100 peak heights.

Approximately 0.8 mg of ankerite sample was reacted with 100% orthophosphoric acid (H_3PO_4) under vacuum for 25 min at $90 \pm 1^\circ \text{C}$ in an adaptation of the method described by McCrea (1950) using a Micromass MultiPrep automated sampling device coupled with a VG Optima dual-inlet isotope ratio mass spectrometer. Stable isotope results are reported in standard delta ($\delta\text{‰}$) notation relative to Vienna-Standard Mean Ocean Water (V-SMOW) for oxygen and Vienna-PeeDee Belemnite (V-PDB) for carbon. A minimum of one duplicate was run for every ten samples analyzed. The average reproducibility for the 7 duplicate samples was $\pm 0.35 \text{‰}$ for $\delta^{13}\text{C}$ VPDB and $\pm 0.20 \text{‰}$ for $\delta^{18}\text{O}$ VSMOW. International standards (NBS-18, NBS-19) and four internal standards were analyzed concurrently with one standard every five samples and average values fall within accepted values. Over the course of the analysis, NBS-19 (n=6) had an average value of $1.92 \pm 0.12 \text{‰}$ for $\delta^{13}\text{C}$ VPDB (expected 1.95) and $28.01 \pm 0.77 \text{‰}$ (expected 28.60) for $\delta^{18}\text{O}$ VSMOW and NBS-18 (n=6) had an average of $-5.08 \pm 0.09 \text{‰}$ for $\delta^{13}\text{C}$ VPDB (expected -5) and $6.88 \pm 0.4 \text{‰}$ (expected 7.2) for $\delta^{18}\text{O}$ VSMOW.

2.5.0 Field Observations

The advance of further mine workings and a compilation of historical and new mapping from the Paymaster and Dome mines indicates that the ankerite veins extend over 5,400 m in strike length and 1,500 m vertically. The veins are eroded off at the Timiskaming unconformity to the east in the sedimentary trough, and continue west to become the Curts vein until they disappear from the stratigraphy towards the hinge of the Porcupine syncline. At the Timiskaming contact, auriferous pyritic clasts like those described by Gray and Hutchinson, 2001 were observed. The ankerite veins occur at flow contacts as well as trending at shallow angles ($\sim 20^\circ$) across the flow and are most common in the V6, V8, and V10 flows of the Vipond formation (Figure 2-5). They are generally boudinaged, and on occasion closely associated with interflow sediment units at flow contacts, some with auriferous massive sulfide lenses (Figures 2-6 and 2-7). Sets of multiple anastomosing veins with discontinuous and discordant splays are commonly observed in both historic and new mapping from 29 and 35 levels of the mine. The ankerite veins are weathered to a brownish red, and dark to light grey when fresh. They are cross cut at a high angle by two phases of veining; quartz-tourmaline veins and quartz veins, and have highly foliated schistose (often laminated) sericite and sulfide rich vein envelopes a few cm wide. The schistosity is parallel to the vein margins and follows the boudinaging of the vein (Figures 2-6 and 2-7).

The initial overprinting veining is dominated by stringers of black tourmaline (schorl) which gives way to quartz-tourmaline veins dominated by quartz with ribbons or clots of dravite (Figure 2-8). This is overprinted by later white quartz rich veins (Figure 2-6). Quartz veining occurs primarily within the ankerite vein margins as tension veins, but also occasionally overprints the veins entirely, or runs parallel to ankerite veining in the same structures (flow contacts; Figures 2-6 and 2-7). In some regions of the mine (e.g., 24 level), the ankerite vein structures have been reactivated by later quartz and quartz-tourmaline veining resulting in quartz-tourmaline veining with ankerite clasts, or quartz veins with ankerite cores. These differ from quartz-ankerite vein arrays seen throughout the mine, where quartz veins contain dog-toothed ankerite concentrated at vein margins.

Main stage quartz, quartz-tourmaline, and quartz-ankerite veins do not have prominent laminated sulfide rich and schistose vein envelopes.

Ankerite veining at the far east region of the deposit has been eroded by the Timiskaming conglomerate contact but is overprinted by later quartz veining which extends into both units in the underground, carrying with it clasts of ankerite, some of which are as large as 50 cm. In the West, the ankerite veins are drifted along in the sheared V99 flow until the contact with the Paymaster porphyry where grade is lost. New development along the ankerite veins in the lower levels of the mine (34/35 level) has exposed a region of ankerite veining within a massive (up to 3 meters wide) highly sericitized, and in some cases silicified and sulfide rich alteration zone which is interpreted to be an early shear zone (Figure 6). This early shear occurs in the spherulitic pillow basalts of the Lower Spherulitic, or V6 flow of the Vipond formation (Figure 5). The ankerite veining in this region occurs as multiple anastomosing 10 cm to 1 m wide boudinaged veins within the shear zone, and on its margins. This vein set can be correlated between the 34 and 35 levels of the mine (a vertical extent of over 70 m), and were mapped and sampled over a strike length of over 300 m on two sub-levels of the mine. Like other ankerite veins across the mine, the veining in this region dips at 55-65° degrees to the north, has laminated sulfide rich cm scale haloes, and contains later quartz extension veining. In this development, a ~50 cm wide discordant vein as well as several minor concordant veins were observed in addition to the main concordant vein. Chip sampling of the development face indicated that the alteration halo was auriferous (~1 g/t Au), however the bulk of the gold was concentrated in regions of ankerite veining with grades ranging from 2-15 g/t Au.

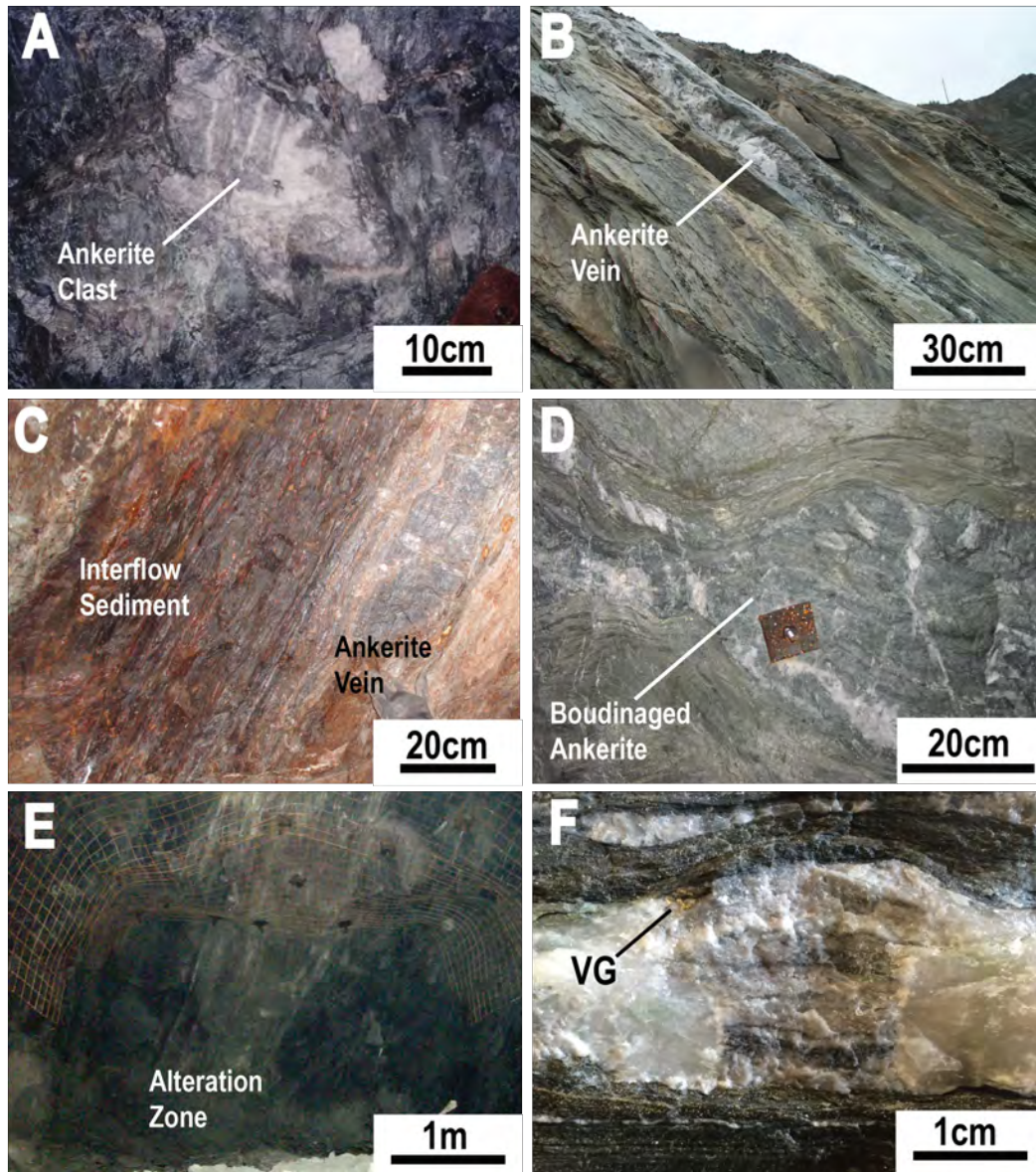


Figure 2-6. Dome mine ankerite vein field relationships on multiple scales. A. Ankerite clast in the Timiskaming age (>2679 Ma) Dome formation basal conglomerate (26 level) B. Ankerite vein crosscutting the Paymaster porphyry (~2890 Ma) in the wall of the open pit C. Ankerite vein at a flow contact associated with an interflow sediment unit (1605 X/C) D. Boudinaged ankerite in 2125DR with well-developed sulfide banded shear envelope E. Alteration zone (3509W DR) from an early shear which is associated with the 34/3509 ankerite veins F. Quartz tension veins in a banded ankerite veinlet with visible gold (VG) at the quartz/ankerite margin from 3509W DR.

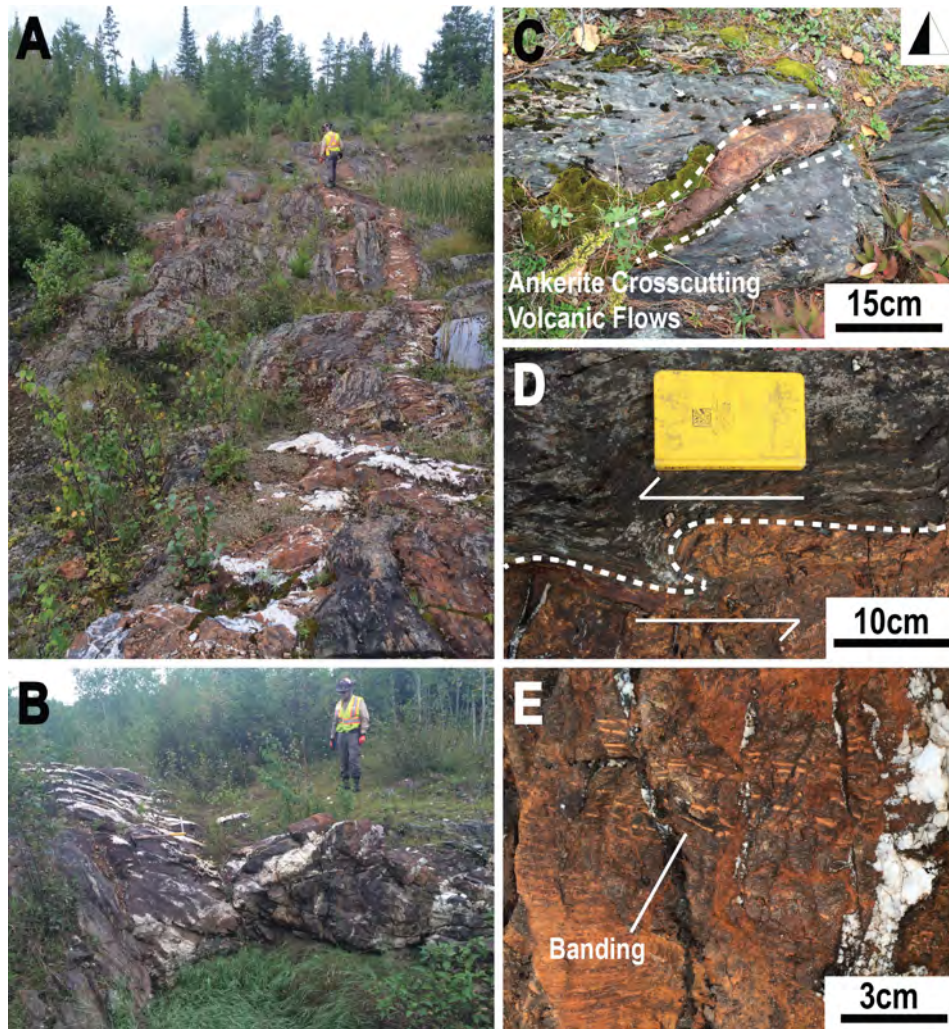


Figure 2-7. Curts ankerite vein field relationships on the Paymaster property. A. The vein anastomoses and can be traced over 300 m. B. At its widest it is 5 m, and in regions where quartz veining is abundant, test pits have been blasted. C. Local branches of veining cross-cut the volcanic stratigraphy which strikes E-W D. Evidence of sinistral shearing can be seen at the vein margins E. Banding in the vein is well preserved and accentuated by weathering.

The Curts vein extends over 300 m almost due E-W (260-275° relative to grid north) on surface, and the main vein is up to 5 m wide at some points, splaying into multiple smaller veins ranging from 10-50 cm in width (Figure 2-7). The Curts vein has been projected at depth to the historic Paymaster mine ankerite vein underground workings, and with Dome mine underground east ankerite stopes. In general, the Curts vein dips 70-85 degrees to the North at surface and shallows at depth to 50-70 degrees. At depth, the strike changes to more NE-SW due to its position closer to the Porcupine Syncline which has rotated the volcanic package (Figure 2-2). Like the Dome ankerite veins, the Curts ankerite veins are heavily cut by two generations of crosscutting extensional veining which are orthogonal to one another. However, tourmaline is less common than in the ankerite veins hosted at the Dome mine; both in the ankerite vein itself and in the overprinting quartz veining. Boudinaging is ubiquitous and the veins have intensely foliated, schistose, and sericitized wall rock haloes. Banding is well preserved, and pieces of wall rock are found in the vein material (Figure 2-7). Based on a compilation of regional lithogeochemistry, the Curts veins are not hosted in the Vipond formation, but at the bottom of the Gold Center formation, the massive G1 flow (Figure 2-2).

2.6.0 Mineralogy and Gold Mineralization

The bulk mineralogy of the ankerite veins is consistent across the deposit, in different vein sets and variable depths of the mine. X-ray diffraction shows that mineralogy is dominated by ankerite/ferroan dolomite, quartz, and muscovite (sericite). Calcite is found in minor amounts in some samples, and secondary phases include sulfides (pyrite, chalcopyrite, arsenopyrite and minor galena), as well as tourmaline (dravite) concentrated at the vein margin and in later quartz tourmaline shear veins (Figure 2-8).

In thin section, the central portion of the ankerite veins are dominated by coarse-grained ankerite intergrown with quartz (Figure 2-8). Banding observed in ankerite vein hand samples is the result of differences in grain size and ankerite content. Pyrite in the central portion of the ankerite veins occurs as disseminated, euhedral, sieve textured pyrite grains which are commonly associated with sericite and chalcopyrite. Stringers of tourmaline occur near vein margins and are commonly associated with fine-grained quartz, sericite

and pyrite. Ankerite becomes increasingly fine-grained and shows evidence of recrystallization closer to the highly schistose vein margin which is dominated by fine-grained sericite, tourmaline and pyrite. Other minor phases include sphalerite, monazite, and rutile, rare molybdenite and apatite. These accessory phases are concentrated at the vein margins (Figure 2-8). Arsenopyrite occurs commonly as inclusions in pyrite grains, and is often associated with gold inclusions and chalcopyrite.

Gold mineralization is concentrated at the ankerite vein margins and is intimately associated with pyrite mineralization. In high-grade samples, this gold mineralization can commonly be observed with a hand lens. However, gold is most commonly observed as inclusions (up to 50 μm) in pyrite grains, at grain margins and in fractures (Figure 2-8). Visible gold (VG) is uncommon in the vein material, and generally occurs as free gold at the margins of crosscutting quartz veins or associated with tourmaline stringers (Figures 2-6 and 2-8). Gold occurs primarily as electrum, and occasionally as small (<10 μm) inclusions of Au-Ag-tellurides in pyrite grains or along fractures.

The mineralogy of the Vipond formation metavolcanics, which host the ankerite veins, is dominated by chlorite, albite, quartz, and Mg-rich calcite with minor ankerite and biotite observed in hyaloclastite units. There are two main types of interflow sediment units observed in the Vipond formation; carbonaceous (argillic) and sulfide rich. Their mineralogy is dominated by quartz, chlorite, muscovite, ankerite and calcite, with occasional tourmaline observed only in the carbonaceous sediments. The sulfide content of the carbonaceous interflow varies from <1% -10% and is concentrated in laminated layers dominated by pyrite, with sphalerite, chalcopyrite and arsenopyrite being common accessory phases. The “sulfide rich” interflow units have sulfide contents exceeding 40% and are dominated by laminated pyrite, pyrrhotite, arsenopyrite, and sphalerite, with significant interstitial chalcopyrite observed in thin section. The sulfide rich interflow units are auriferous, and free gold (10-60 μm in size) is observed in pyrite fractures associated with sphalerite (Figure 2-8).

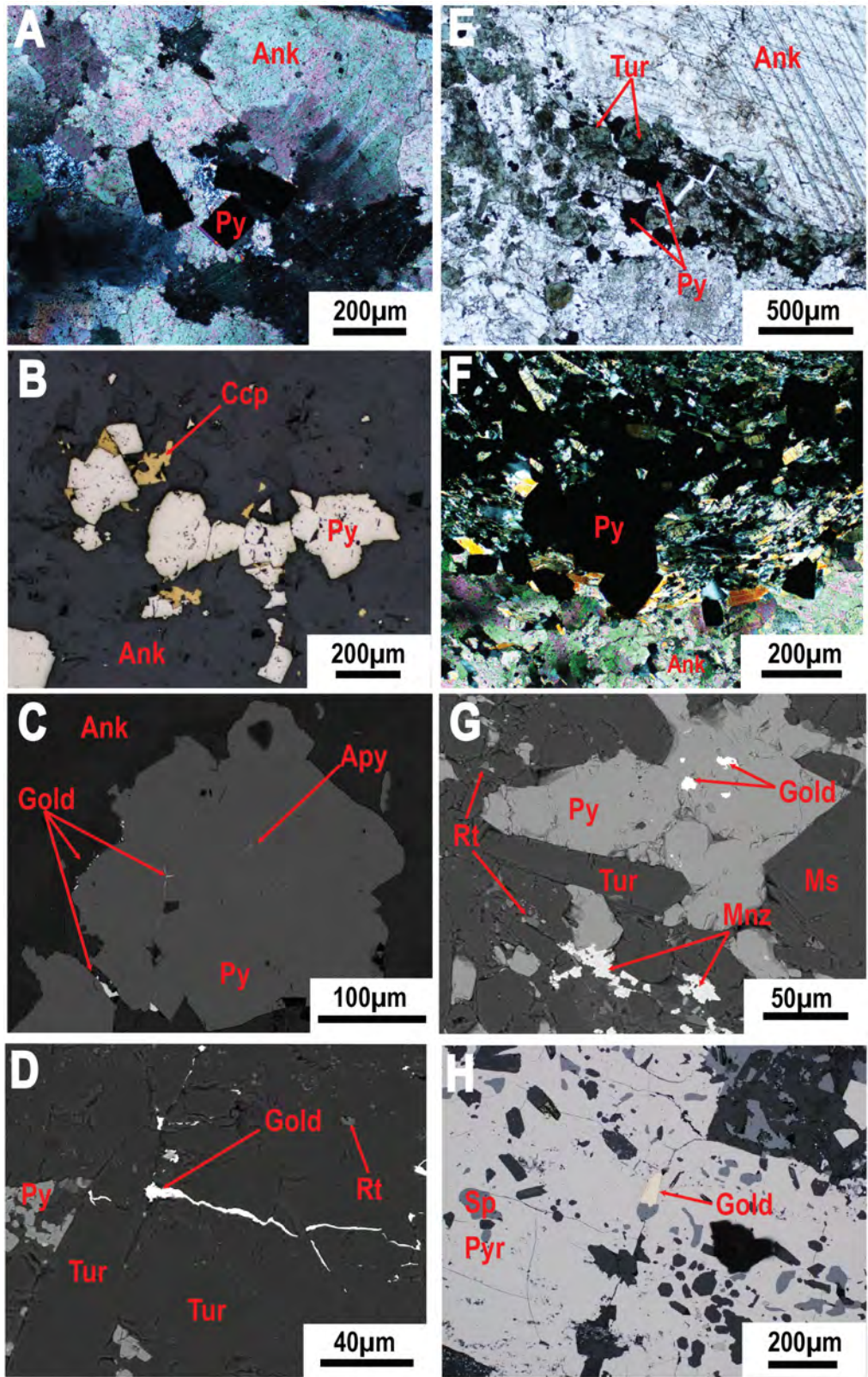


Figure 2-8. Representative photomicrographs showing typical mineralization in the central ankerite portion of the ankerite veins (A-C) and in the ankerite vein margin (D-G) and a spatially related interflow sediment (H). A. Euhedral pyrite grains in a coarse-grained ankerite ground mass (10x XPL). B. AnhedraI chalcopyrite associated with subhedral pyrites in medium-grained ankerite groundmass (5x RFL). C. Subhedral pyrite grain with a central arsenopyrite halo and gold in fractures and at its grain margins (198x 15kV QBSD). D. Tourmaline stringer with interstitial free gold (495x 15kV QBSD) E. Seam of tourmaline and pyrite cutting through coarse-grained ankerite (5x PPL) F. Ankerite vein margin with abundant pyrite, sericite and tourmaline with a preferred orientation parallel to the vein margin (10x XPL). G. Subhedral pyrite grain with gold inclusions in a groundmass of tourmaline and muscovite with fine-grained anhedraI monazite and rutile (376x 15kV QBSD) H. Auriferous sulfide rich interflow sediment with gold at pyrite grain margins associated with sphalerite (10x RFL).

2.7.0 Geochemistry Results

2.7.1 Major Element Geochemistry

The Vipond formation samples are classified as primarily Fe-rich and tholeiitic in nature by their major element geochemistry, with some samples from the V99 flow plotting in the tholeiitic andesite and basaltic fields of the Jensen cation plot (Figure 2-9). Different flows within the Vipond formation can be distinguished by comparing immobile element ratios (Figure 2-9), a classification proposed by Barret et al., 1991. This has been applied to samples lower in the Vipond formation stratigraphy as protolith Al, Ti and REE signatures are retained even with alteration (Kerrick et al., 1999; Wyman, 2003; Bateman et al., 2005; DinéI et al., 2008a,b). Based on this classification, a group of samples initially interpreted to be from the V99 flow in the PJV dataset have been reinterpreted as belonging to the V6 flow (Figure 2-9). This is also supported by the relative position of the V6 samples in the mine stratigraphy below those classified as V99 (Appendix B.2). The general trend of increasing Ti/Al₂O₃ and Zr/Al₂O₃ ratios up stratigraphy in the Tisdale assemblage, from the Central to the Vipond formation (Mg-tholeiites to Fe-

tholeiites) follows what is observed by Dinel et al., (2008b) and proposed by Kerrich et al., (1999) for evolution of Fe-tholeiitic basalt during greenstone belt genesis. There is a bimodal pattern in the total Fe and Ti contents as well as Ti/Al₂O₃ ratio observed in the Vipond flows in which the V6 and V8 flows are enriched and plot above the V99, V10 flows respectively, which sit above them in the mine stratigraphy (Figure 2-9). This bimodal behavior is also observed in SiO₂, Al₂O₂, Fe₂O₃, CaO, MgO, K₂O, P₂O₅, and Y contents (Table 2-1, Figure 2-9) and has also been reported for V and TiO₂ in the Hersey Lake and Gold Center formations (Bateman et al., 2005). Despite this, Zr increases consistently up the stratigraphy from the V6 to the V10 flow (Figure 2-9), and the Vipond series appears to be a true volcanic stratigraphic sequence based on litho-geochemistry. The Vipond formation has undergone greenschist facies metamorphism and variable degrees of both sodic and potassic alteration. Alteration patterns are not uniform between volcanic flows, but range from moderate sericite and chlorite alteration to weak albite alteration (Figure 2-9).

The major element content of the Vipond formation interflow sediments resembles that of its host volcanic flows apart from depletions in Al₂O₃, Na₂O, TiO₂, and P₂O₅ (Table 2-1, Figure 2-10). The sediments have a wide range of SiO₂, Fe₂O₃, Al₂O₃, and Zr contents, reflecting differences in the mineralogy between carbonaceous and sulfide rich interflow units.

Table 2-1. Average bulk rock geochemistry for major element and trace metals of the ankerite veins and their host Vipond Formation volcanic flows, interflow sediments, and other early carbonate veining from across the camp (major elements are in weight %, and metals in ppm).

	Ankerite (n=40)	Sediments (n=6)	V6 (n=37)	V99 (n=42)	V8 (n=8)	V10 (n=11)	Carbonate Vein (n=3)
Au	12.30 ± 19.67	16.95 ± 39.76	0.167 ± 0.645	0.176 ± 0.532	0.008 ± 0.020	*0.516 ± 1.686	0.32 ± 0.20
SiO₂	27.72 ± 12.13	43.51 ± 15.69	48.69 ± 2.88	51.30 ± 4.43	46.53 ± 4.65	50.93 ± 1.88	31.85 ± 13.63
Al₂O₃	3.29 ± 3.46	7.36 ± 3.24	12.46 ± 1.00	12.83 ± 1.82	10.47 ± 1.21	11.20 ± 0.63	5.89 ± 3.36
Fe₂O₃	8.18 ± 2.9	17.17 ± 13.00	14.87 ± 2.12	12.16 ± 2.69	16.54 ± 2.94	14.71 ± 1.35	12.19 ± 6.52
CaO	20.26 ± 6.12	7.66 ± 2.58	6.82 ± 2.16	6.32 ± 3.23	7.13 ± 1.49	6.19 ± 1.17	15.85 ± 5.52
MgO	9.89 ± 3.47	3.44 ± 1.27	3.78 ± 0.84	3.98 ± 0.98	2.88 ± 0.97	2.63 ± 0.26	6.67 ± 2.87
Na₂O	0.14 ± 0.14	0.34 ± 0.54	1.73 ± 1.26	1.53 ± 1.33	1.40 ± 0.92	1.85 ± 0.73	0.39 ± 0.29
K₂O	0.73 ± 0.86	1.23 ± 0.70	0.81 ± 0.95	1.18 ± 1.04	0.80 ± 0.23	0.77 ± 0.61	0.73 ± 0.42
TiO₂	0.25 ± 0.27	0.47 ± 0.26	1.53 ± 0.21	1.07 ± 0.17	1.43 ± 0.19	1.42 ± 0.11	0.32 ± 0.23
MnO	0.31 ± 0.09	0.28 ± 0.05	0.22 ± 0.06	0.23 ± 0.11	0.35 ± 0.1	0.23 ± 0.07	0.64 ± 0.51
P₂O₅	0.60 ± 0.09	0.09 ± 0.05	0.22 ± 0.09	0.14 ± 0.06	0.62 ± 0.07	0.53 ± 0.07	0.11 ± 0.12
Cr₂O₃	<0.01	0.01 ± 0.01	0.02 ± 0.02	0.02 ± 0.02	<0.01	<0.01	0.02 ± 0.01
SrO	0.01 ± 0.01	0.01 ± 0.01	<0.01	<0.01	<0.01	<0.01	<0.01
BaO	<0.01	<0.01	<0.01	0.01 ± 0.02	<0.01	<0.01	<0.01
LOI	26.96 ± 8.06	11.93 ± 6.47	8.06 ± 2.42	8.62 ± 3.19	11.34 ± 2.17	9.15 ± 1.41	19.8 ± 8.62
Total	97.82 ± 3.28	93.46 ± 6.91	99.21 ± 0.59	99.32 ± 0.62	99.49 ± 0.68	99.63 ± 0.80	94.48 ± 4.54
Ag	7.69 ± 16.48	4.75 ± 6.05	0.33 ± 0.29	0.55 ± 0.72	0.37 ± 0.14	0.43 ± 0.12	<0.05
As	438.0 ± 1702.0	1786.8 ± 4026.6	24.0 ± 82.9	34.9 ± 60.5	7.0 ± 6.6	2.5 ± 4.1	80.7 ± 35.9
Cu	74.0 ± 126.0	330.3 ± 344.3	64.12 ± 34.0	102.1 ± 50.0	29.9 ± 15.8	31.1 ± 11.0	29.7 ± 25.4
Pb	13.3 ± 16.3	51.3 ± 37.6	4.4 ± 2.8	8.5 ± 11.3	3.6 ± 1.4	3.2 ± 1.3	17.0 ± 18.4
Zn	71.0 ± 24.4	2605.7 ± 3751.6	135.7 ± 59.7	110.5 ± 59.5	179 ± 82.9	122.6 ± 31.1	47.0 ± 12.3
Mo	15.1 ± 25.8	2.8 ± 3.5	0.7 ± 0.7	0.7 ± 0.4	0.8 ± 0.3	0.8 ± 0.3	<0.05
Co	9.9 ± 8.5	61.0 ± 77.7	32.4 ± 9.7	37.0 ± 13.7	18.1 ± 2.7	17.9 ± 4.6	12.7 ± 6.7
Cr	32.0 ± 26.2	105.0 ± 121.4	64.5 ± 31.2	116.7 ± 86.2	25.3 ± 12.6	53.7 ± 26.3	76.7 ± 83.2
V	206.0 ± 152.1	78.6 ± 62.5	165.0 ± 79.5	222.2 ± 59.1	14.5 ± 15.6	25.3 ± 10.2	56.0 ± 44.0
Rb	19.4 ± 2.3	32.6 ± 18.6	19.6 ± 22.6	31.2 ± 28.2	19.6 ± 10.6	18.4 ± 14.5	16.7 ± 10.4
Sr	107.5 ± 54.0	82.3 ± 56.8	92.7 ± 34.1	117.4 ± 62.4	93.4 ± 30.1	92.4 ± 63.7	85.7 ± 28.2
Y	14.0 ± 11.8	29.6 ± 22.7	38.3 ± 6.9	40.0 ± 16.0	66.2 ± 8.8	68.4 ± 7.2	22.4 ± 20.1
Zr	38.2 ± 39.0	81.0 ± 92.3	91.8 ± 16.7	119.2 ± 55.0	142.2 ± 14.9	165.4 ± 12.2	29.0 ± 31.0
Ni	15.3 ± 12.4	51.4 ± 41.8	38.6 ± 16.9	65.9 ± 26.0	8.1 ± 4.1	21.3 ± 33.2	33.3 ± 45.2
W	68.8 ± 230.2	16.7 ± 15.6	4.0 ± 7.7	6.0 ± 7.4	4.9 ± 7.7	11.5 ± 13.3	16.0 ± 16.9

For values below detection limit, half detection limit was used to calculate averages

*One 5.6ppm Au sample (without, average is 0.007 ± 0.01)

There is extensive variability in the major element content of ankerite vein samples, but no spatial trends observed across their over 5400 m strike length (Table 2-1, Figure 2-10). The largest variability is in SiO₂ content which ranges from ~ 2-50%. This reflects overprinting of the ankerite veins by later cross cutting quartz extension veins and variations in the quartz content of the primary vein material. CaO and MgO vein contents

correlate negatively with SiO₂ content with r² values of -0.8 and -0.6 respectively, and correlations in K₂O and Al₂O₃ contents (r² = 0.8) reflect their sericite content, which is also related to increased TiO₂ (Figure 2-13). In general, the ankerite veins are depleted in immobile elements (Al₂O₃, TiO₂, NaO, P₂O₅, Zr) with respect to their host rock (Figure 2-10). There are no correlations observed between major oxide content and gold, and overall, the ankerite major element values are consistent with those of previous reports (Fyer et al., 1979; Proudlove et al., 1989). The major element content is similar to that of carbonate veins from across the camp (Table 2-1), with the exception of the sample from the Buffalo-Ankerite pit, which has lower Fe₂O₃, CaO, MgO and MnO values and elevated K₂O, Na₂O and Al₂O₃ values, a result of its lower overall carbonate content.

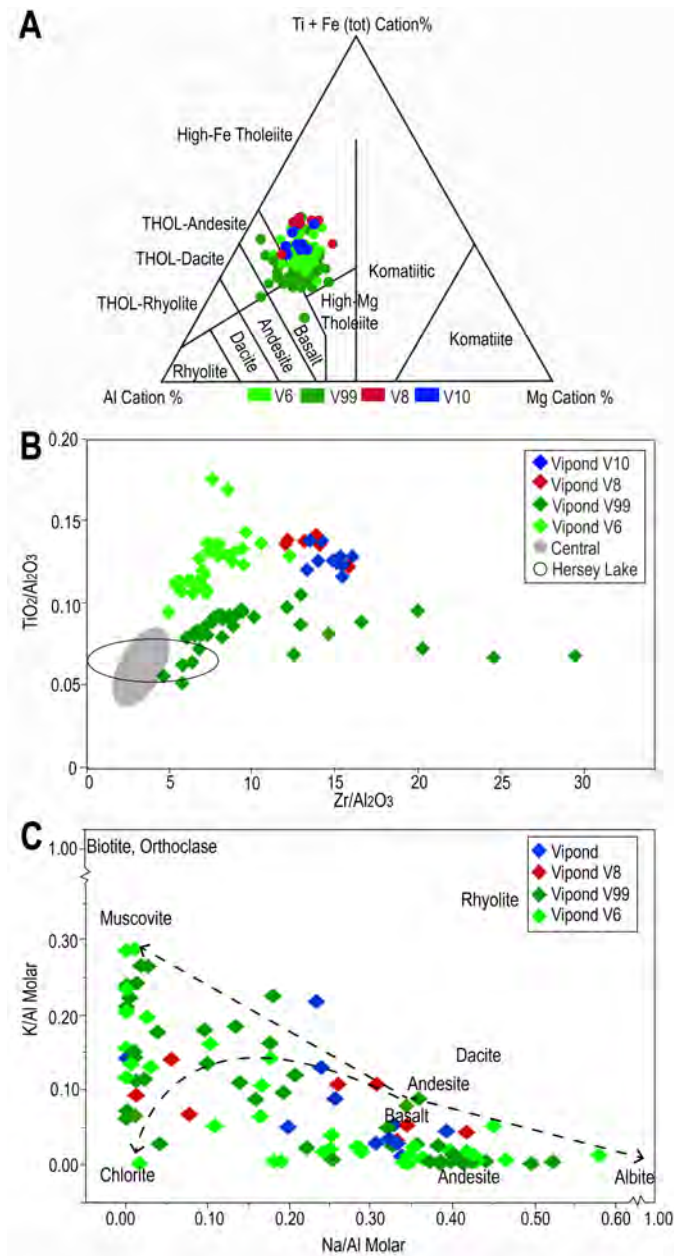


Figure 2-9. Bulk rock geochemistry of the Vipond Formation A. Jensen cation plot (Jensen, 1976) for the Vipond Formation volcanics B. Immobile elements ($\text{TiO}_2/\text{Al}_2\text{O}_3$ vs. $\text{Zr}/\text{Al}_2\text{O}_3$) vary between different flows of the Vipond Formation. Data for the Central and Hersey Lake Formations from Diné et al, 2008 is shown as zones. C. Na/Al vs K/Al molar ratios for the Vipond Formation metavolcanics displaying the degree of sodic vs potassic alteration (albite vs. sericite). Trends of sericization, chloritization and albitization from basaltic andesite composition are shown by dashed arrows. Igneous values are from Cox et al, 1979.

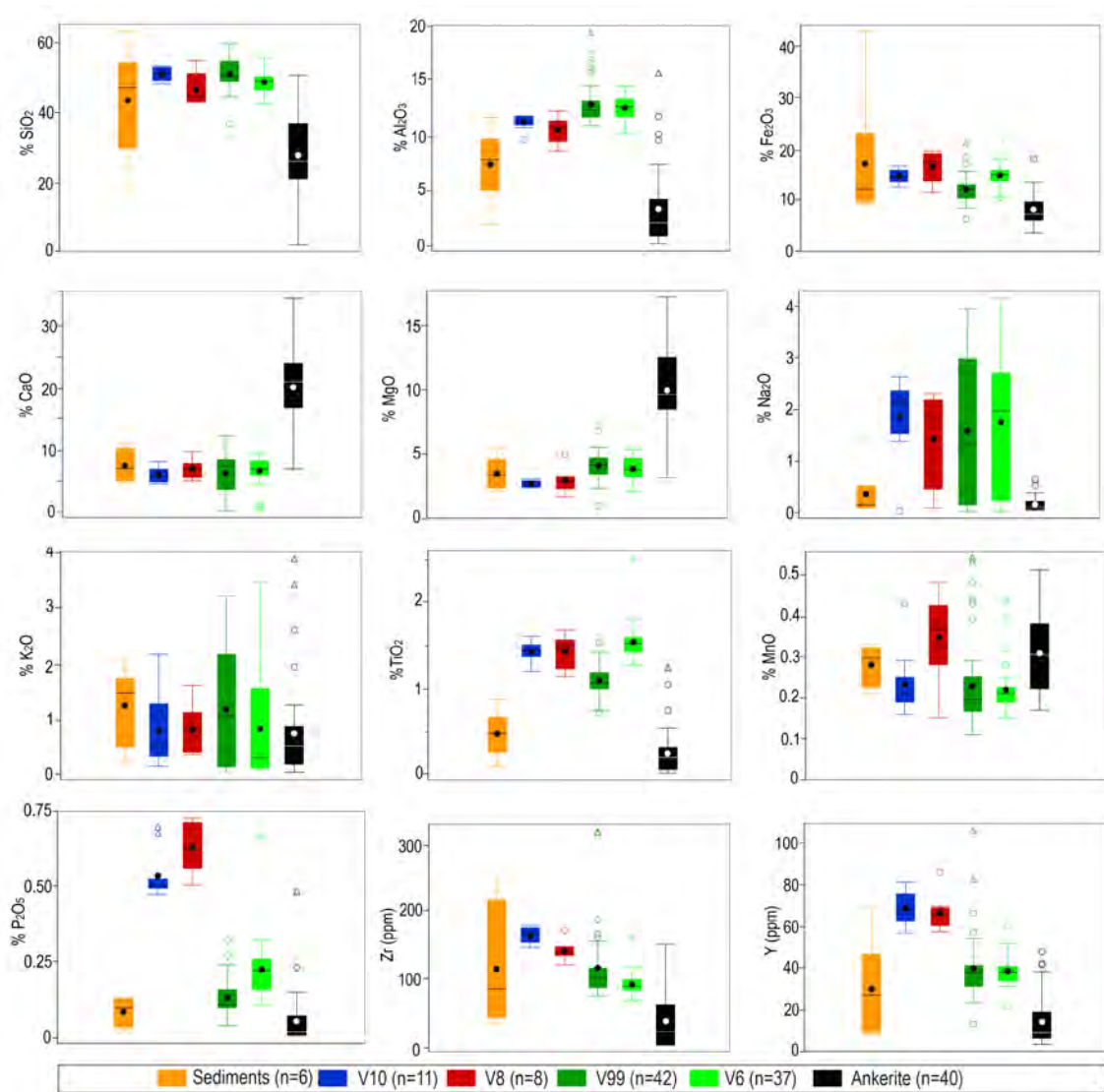


Figure 2-10. Box and whisker plots showing the variability in major elements, Zr and Y in the ankerite veins and their host rock Vipond Formation Fe-tholeiites and interflow sediments. The horizontal line represents the median, the solid black dot represents the mean and the box represents the 25th to 75th percentile of the data. Whiskers are drawn to the last data point that is 1.5 times the length of box from the maximum and minimum. Open circles are outliers (within 3 box lengths), open triangles are far outliers (beyond 3 box length)

2.7.2 Rare Earth Element Geochemistry

The Vipond formation volcanic flows are enriched 30 to 70 times chondrite values with flat profiles and some slightly negative Eu anomalies (Figure 2-11). This is consistent with previous work in the camp for the Tisdale assemblage and is expected in Archean tholeiitic basalts (Reading et al., 1982; Henderson, 1984; Bateman et al., 2005; Dinel, 2008a,b). The REE content of the Vipond formation volcanics is considered representative of primary lithochemistry as sericite, albite, and carbonate alteration have only slightly mobilized LREE in the Timmins Gold Camp volcanic assemblages, and HREE are relatively immobile with respect to this alteration (MacLean and Barret, 1993; Bateman et al., 2005; Dinel et al., 2008a). This is reflected in marked differences in the total REE content of different flows. REE content increases up the Vipond formation stratigraphy, where the V8 and V10 flows are enriched in total REE content with respect to the V6 and V99 flows (Figure 2-11). This trend follows what is observed up the Tisdale assemblage stratigraphy (Bateman et al., 2005). As REE are relatively immobile with respect to alteration, there are no correlations observed between REE content and CaO, K₂O or Na₂O, however, REE content correlates positively with higher Zr and P₂O₅ values ($r^2 = 0.8$ and 0.3), reflecting the geochemical evolution of the volcanic sequence up stratigraphy.

The Vipond interflow sediments have variable REE content (10-40 times chondrite) with flat to gently sloping patterns and slight HREE depletion. Samples with a higher REE content have a slightly negative Eu anomaly, resembling the profile of their host metavolcanics. Samples with overall lower REE content have gently sloping profiles with HREE depletion and a prominent positive Eu anomaly, more closely resembling the ankerite vein patterns, possibly reflecting a hydrothermal overprint (Figure 2-11).

The REE geochemistry of the ankerite veins are distinct from their host rock, and in general are characterized by REE contents of 2 to 30 times chondrite, with a positive Eu anomaly (Figure 2-11). Samples with a higher REE content have REE patterns which more closely resemble those of the host Vipond formation metavolcanics, flat with minimal to even slightly negative Eu anomalies. Ankerite samples with lower overall REE contents (<10 times chondrite) have prominent positive Eu anomalies. Aside from

the overall low REE content of the Curts vein ankerite samples, there are no spatial trends in REE content observed across their extensive strike. However, ankerite vein REE contents (Sum of REE) correlate with Zr, Y, P₂O₅ and Al₂O₃ contents ($r^2 = 0.8, 0.8, 0.4$ and 0.5) and are antithetic with CaO and MgO ($r^2 = 0.4$ and 0.4). The ankerite vein REE profiles resemble the profiles from carbonate vein samples collected across the camp (Figure 11), apart from a HREE enrichment in the sample from the Buffalo-Ankerite mine, and agree with previous work at the Dome mine (Kerrick and Fryer, 1979; Roberts and Reading, 1981). Across the deposit, there are no correlations between total REE contents, Eu anomalies, HREE depletions and gold.

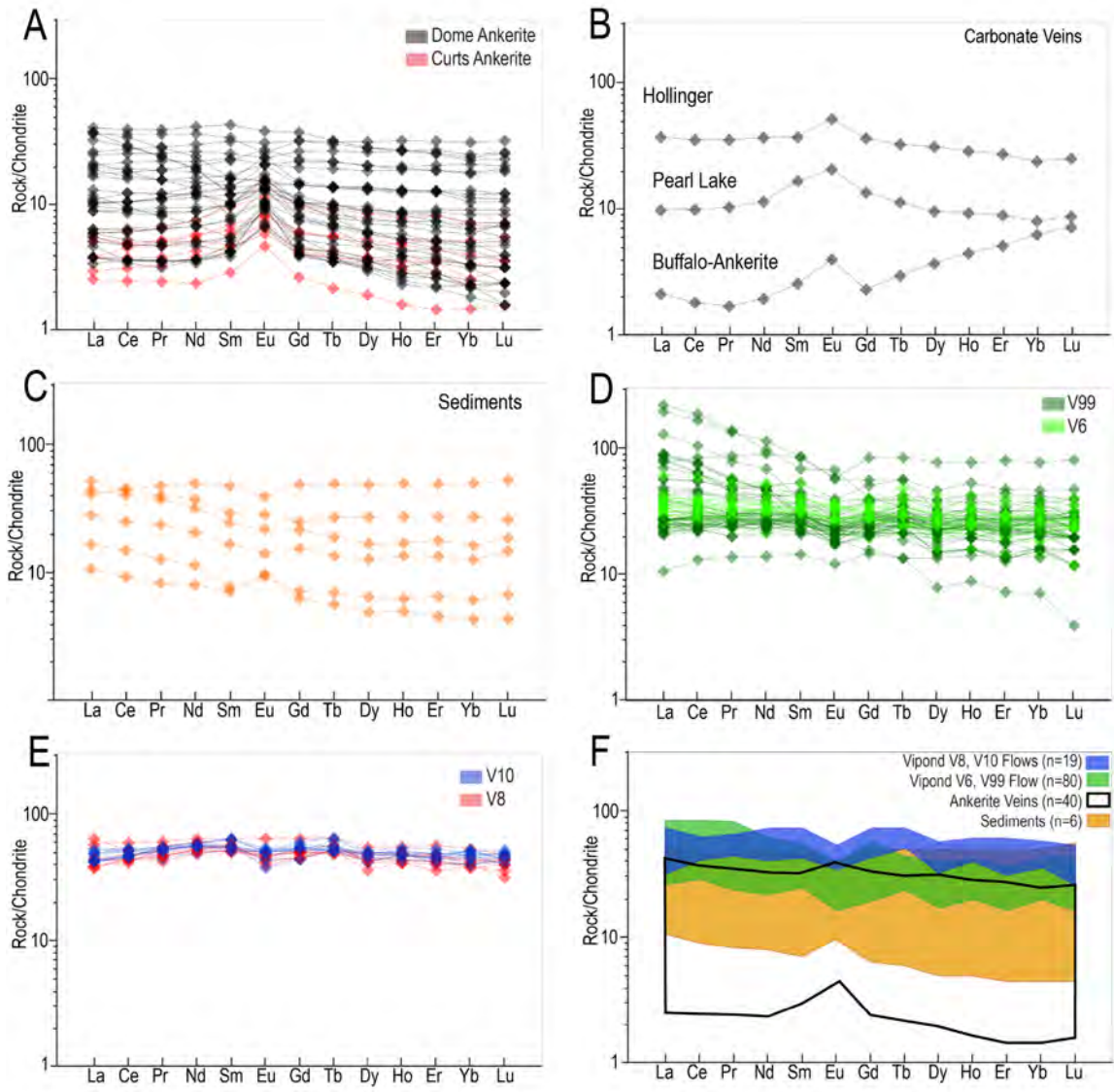


Figure 2-11. Chondrite normalized REE patterns (Sun and McDonough, 1989) for the A. Dome and Curts ankerite veins, B. Carbonate veining across the camp, C. Vipond formation interflow sediments, D. Vipond formation V6 and V99 flows, E. Vipond formation V8 and V10 flows, F. Simplified overlay of the different units.

2.7.3 Metal and Trace Element Geochemistry

In addition to variability in major and REE elements, there are marked differences in the metal content of the Vipond formation flows (Table 2-1, Figures 2-9 and 2-12). The lower V6 and V99 flows can be distinguished from the V8 and V10 flows by enrichments in Y, Zr, Co, Ni, Cr, and V. The bimodal relationship observed in major element (SiO_2 , Al_2O_3 , P_2O_5) content up stratigraphy is also observed in enrichments of Cr, V, and Ni in the V99 and V10 flows with respect to the V6 and V8 (Figure 2-12). In general, the V99 flow has the highest base and precious metal content with enrichments in Au, Cu, Pb, as well as As. The V6 and V99 flows also have slightly higher Cu, and lower Mo content, than the V8 and V10 flows. Both Zr and Y content increases up stratigraphy from the V6 to the V10 flow (Table 2-1, Figure 2-14).

The Vipond formation interflow sediments have the greatest variability in terms of metal and trace element content (Figure 2-12). They are enriched in Au, Ag, base metals and metalloids (As, Cu, Zn, Pb, Ni) with respect to the Vipond flows (Table 2-1, Figure 2-12). Au and Ag contents are variable between sediment types (16.95 ± 39.76 g/t Au, 4.75 ± 6.05 g/t Ag), with the sulfide rich sediments being the most auriferous (up to 98 g/t Au).

In general, the metal content of the ankerite veins is extremely variable (Table 2-1, Figure 2-12), and there are no single linear trends observed between any trace metals and gold (e.g., Figure 2-15). The gold content of the ankerite veins is nuggety and varies considerably across their strike length with a range from 0.02-85.40 g/t and an average grade of 12.30 g/t (± 19.67 g/t). This is higher than previously reported values of 8.1 g/t (± 8.4 g/t) (Fryer et al., 1979) but is the result of four samples with grades exceeding 50.0 g/t. Samples from the Curts ankerite vein have a uniformly lower grade than the Dome ankerite veins, with an average of 1.20 ± 1.40 g/t Au and <0.5 ppm Ag (n=6).

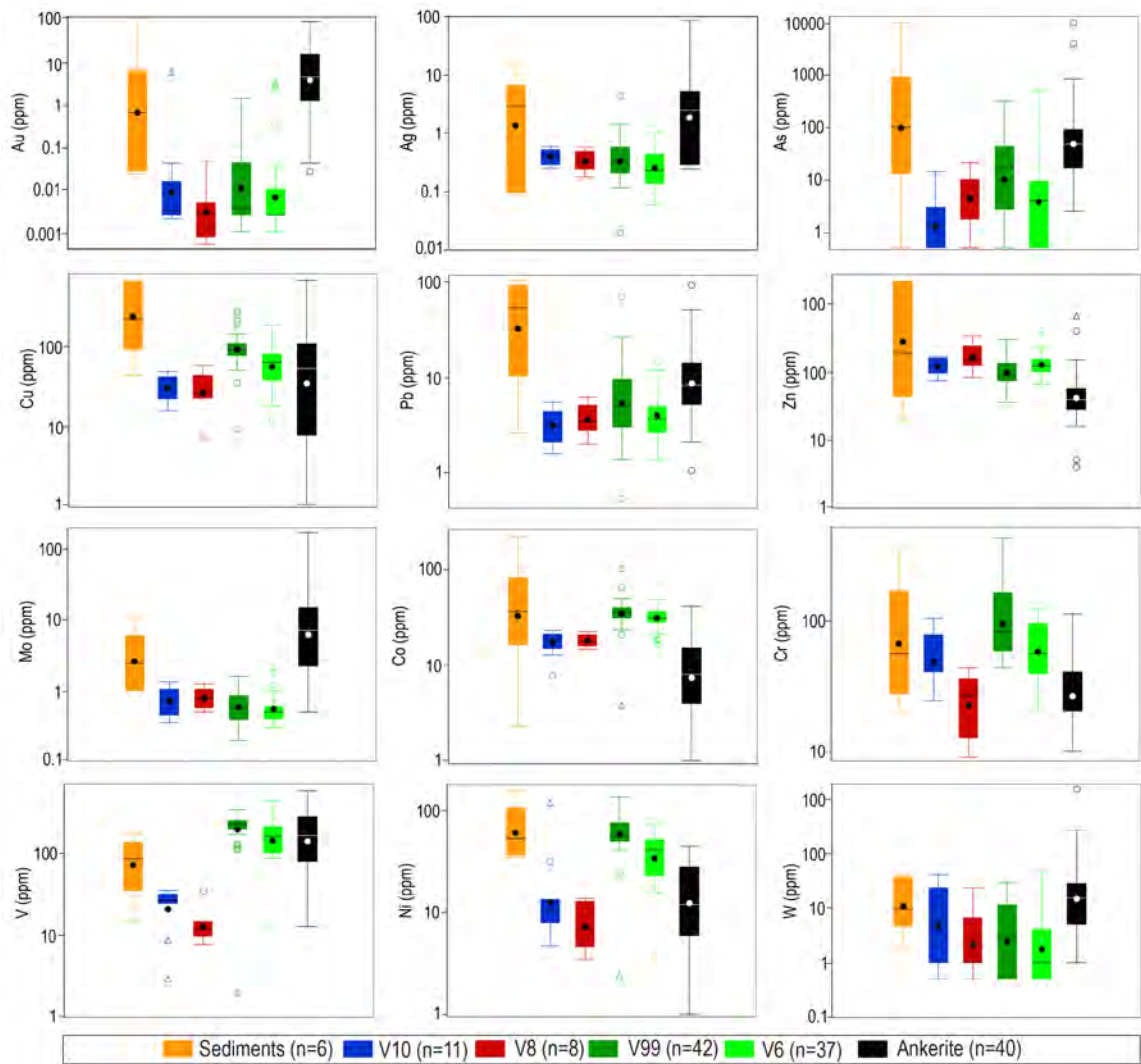


Figure 2-12. Box and whisker plots showing the variability in metals in the ankerite veins and their host rock Vipond Formation Fe-tholeiites and interflow sediments. Data has been logged to better show trends between sample types. The horizontal line represents the median, the solid black dot represents the mean of logged values, and the box represents the 25th to 75th percentile of the data. Whiskers are drawn to the last data point that is 1.5 times the length of box from the maximum and minimum. Open circles are outliers (within 3 box lengths), open triangles are far outliers (beyond 3 box length).

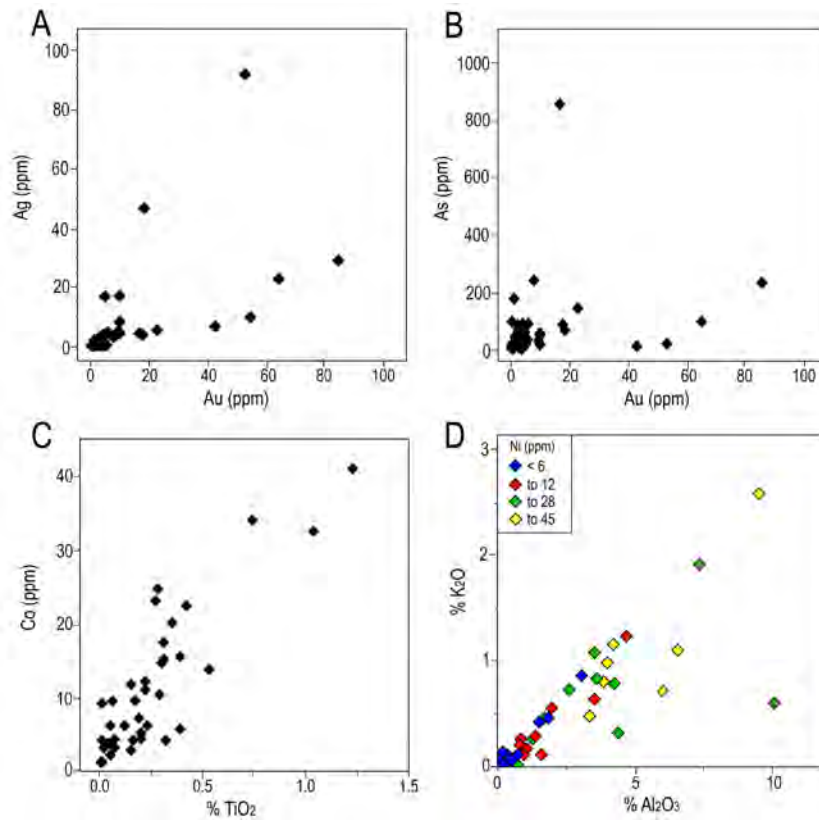


Figure 2-13. Plots of trace metal associations of the ankerite veins. A. Au vs. Ag plot ($r^2 = 0.4$) B. Au vs. As (4040 and >10,000 ppm As outliers removed) C. TiO₂ vs. Co plot ($r^2 = 0.6$) D. % Al₂O₃ vs. K₂O plot ($r^2 = 0.8$) with the data points colored by Ni content (quartiles).

The strongest correlation observed between any trace metal and gold is with Ag ($r^2 = 0.35$) in which the bulk of the data clusters below a grade of ~10 g/t Au and splits into a low and high Ag trend (Figure 2-13). However, there are no spatial correlations between high grade samples with low vs. high Ag contents. A similar lack of a singular trend is also observed between Au, trace metals, and common pathfinder elements for orogenic gold (e.g., As, Cu, Co, Cr, Mo, Ni, Pb, W) making it difficult to vector towards mineralization. While the average Au:Ag of the ankerite vein samples is 3.2 ± 3.7 in whole rock data, there is significant variability, with ratios ranging from >10 to 0.1. Previously reported Au:Ag for the ankerite veins range from 0.6-10.6 with an average of 4.6 (± 4.5) for the ankerite veins (Fryer et al., 1979). Like this study, they report that the

Au and Ag contents of the ankerite veins are heterogeneously distributed, with no systematic variation in abundance or ratio across their strike length. As well as being enriched in Au and Ag with respect to the Vipond formation flows, the ankerite veins are enriched in As, Pb, Mo, and W, and are depleted in Zn, Co, Ni and Cr (Table 2-1, Figure 2-12). Correlations are observed between Co and Ni ($r^2 = 0.5$) as well as TiO_2 and Co ($r^2 = 0.6$) in the ankerite veins. Enrichments in Co, Ni and TiO_2 are generally observed in samples with higher K_2O and Al_2O_3 contents (Figure 2-13). This trend is antithetic with vein CaO and MgO content and is likely the result of overprinting quartz-tourmaline veining.

In general, the ankerite veins are enriched in metals, especially Au and Ag, with respect to other carbonate veining across the camp (Table 2-1). However, when comparing to a low grade ankerite vein, the metal contents of the Hollinger and Pearl Lake samples are similar. The Buffalo-Ankerite sample which is hosted in Hersey Lake komatiite is enriched in Cr, Ni and Co (170 ppm, 85 ppm, 20 ppm) compared to metabasalt hosted veining.

2.7.4 Stable Isotope Geochemistry

The $\delta^{13}\text{C}$ and $\delta^{18}\text{O}$ values for dolomite from the ankerite veins range from -2.2 to 1.0 ‰ $\delta^{13}\text{C}_{\text{PDB}}$ and 10.8–14.9‰ $\delta^{18}\text{O}_{\text{VSMOW}}$, and correlate slightly with an r^2 value of 0.3 (Figure 2-14, Appendix B.3). These values are comparable to those previously reported for dolomite from the Dome ankerite veins (Table 2-2, Figure 2-15). In general, dolomite from ankerite veining have higher $\delta^{13}\text{C}$ and $\delta^{18}\text{O}$ values than dolomite from basalt hosted quartz-carbonate veining across the camp (Table 2-2; Figure 2-15). The exception is samples from the Buffalo-Ankerite mine which are closer to the composition of dolomite from quartz-carbonate veining. The data for the Porcupine Gold Camp falls within the range of values for Archean hydrothermal Fe-dolomites with a few samples of Dome ankerite vein falling in the overlapping region with Archean marine sediments (Figure 2-15).

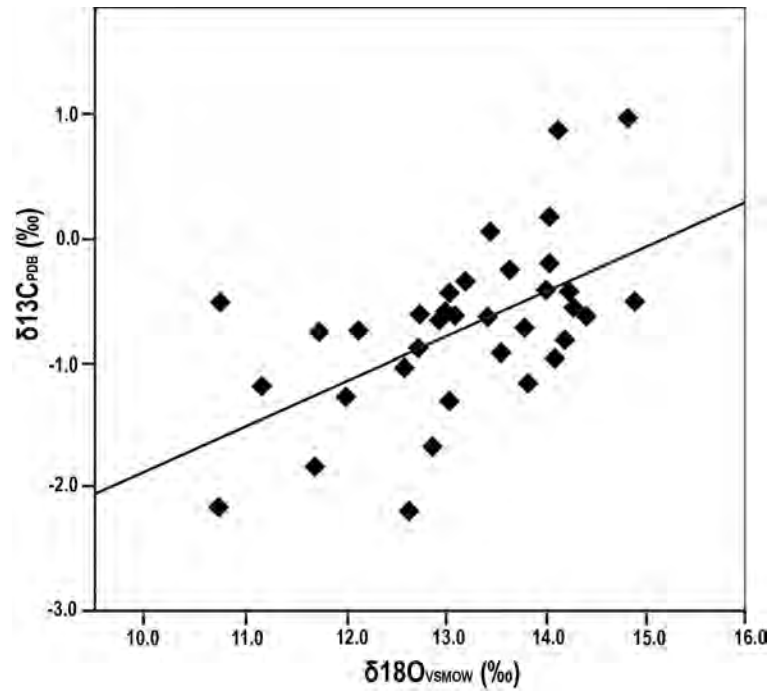


Figure 2-14. Plot of Dome ankerite vein dolomite $\delta^{13}\text{C}_{\text{PDB}}$ vs. $\delta^{18}\text{O}_{\text{VSMOW}}$ values shows a weak linear correlation (solid line, $r^2 = 0.3$).

Table 2-2. Bulk carbonate stable isotope values for ankerite vein samples as well as carbonate veins from across the camp as well as historic work in the camp. (¹Reading, 1989, ²Proudlove et al, 1989, ³Jia and Kerrich, 2000, ⁴Kerrich, 1990)

Deposit	Vein Type	$\delta^{13}\text{C}_{\text{PDB}}$	$\delta^{18}\text{O}_{\text{VSMOW}}$
Dome	Ankerite (n=36)	-0.7 ± 0.7	13.2 ± 1.1
Hollinger	Carbonate	-1.5	13.1
Pearl	Carbonate	-1.9	12.3
Buffalo Ankerite	Carbonate	-3.6	12.56
¹ Dome	Ankerite (n=16)	-1.7 ± 0.5	13.9 ± 0.8
² Dome	Ankerite (n=7)	-1.1 ± 0.7	13.9 ± 0.5
³ Dome	Quartz-Carbonate (n=4)	-3.2 ± 0.3	12.2 ± 0.5
³ Hollinger	Quartz-Carbonate (n=9)	-3.3 ± 0.5	12.1 ± 0.8
⁴ Hollinger, 11 pit	Quartz-Carbonate (n=9)	-3.4 ± 0.4	11.5 ± 0.3
⁴ Hollinger, 55 pit	Quartz-Carbonate (n=7)	-1.1 ± 0.5	11.7 ± 1.1
⁴ Hollinger, 400 pit	Quartz-Carbonate (n=4)	-2.9 ± 1.0	11.2 ± 0.3
⁴ McIntyre, 3600	Quartz-Carbonate (n=4)	-3.2 ± 0.3	10.7 ± 0.5
⁴ Dome	Quartz-Carbonate (n=4)	-1.9 ± 0.1	13.9 ± 0.8
⁴ Dome	Ankerite (n=3)	-1.2 ± 0.7	13.6 ± 0.8
⁴ Buffalo Ankerite	Ankerite (n=5)	-2.8 ± 0.6	12.3 ± 0.1

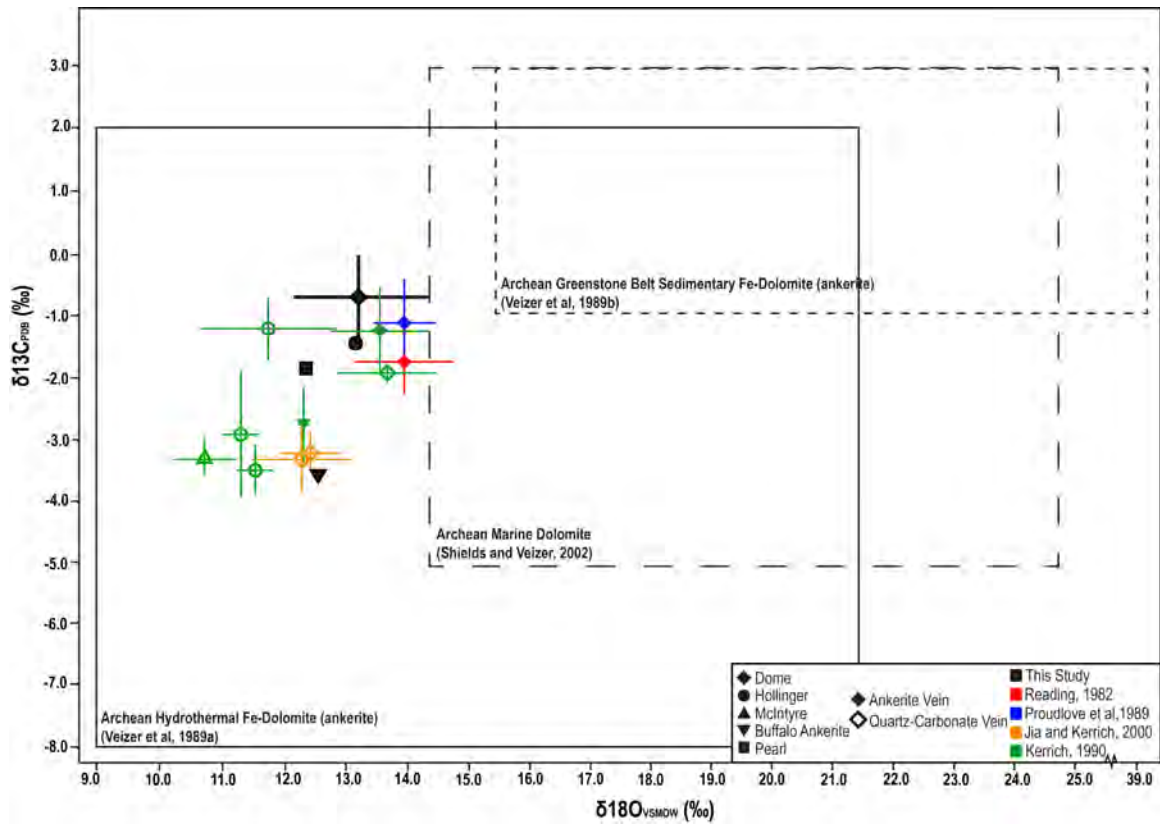


Figure 2-15. Plot of vein dolomite $\delta^{13}\text{C}_{\text{PDB}}$ vs. $\delta^{18}\text{O}_{\text{VSMOW}}$ values comparing average values (1 σ SD) of Dome mine ankerite veins with carbonate and quartz-carbonate veins from across the Timmins Gold Camp (values from Table 2-2), and Archean dolomites.

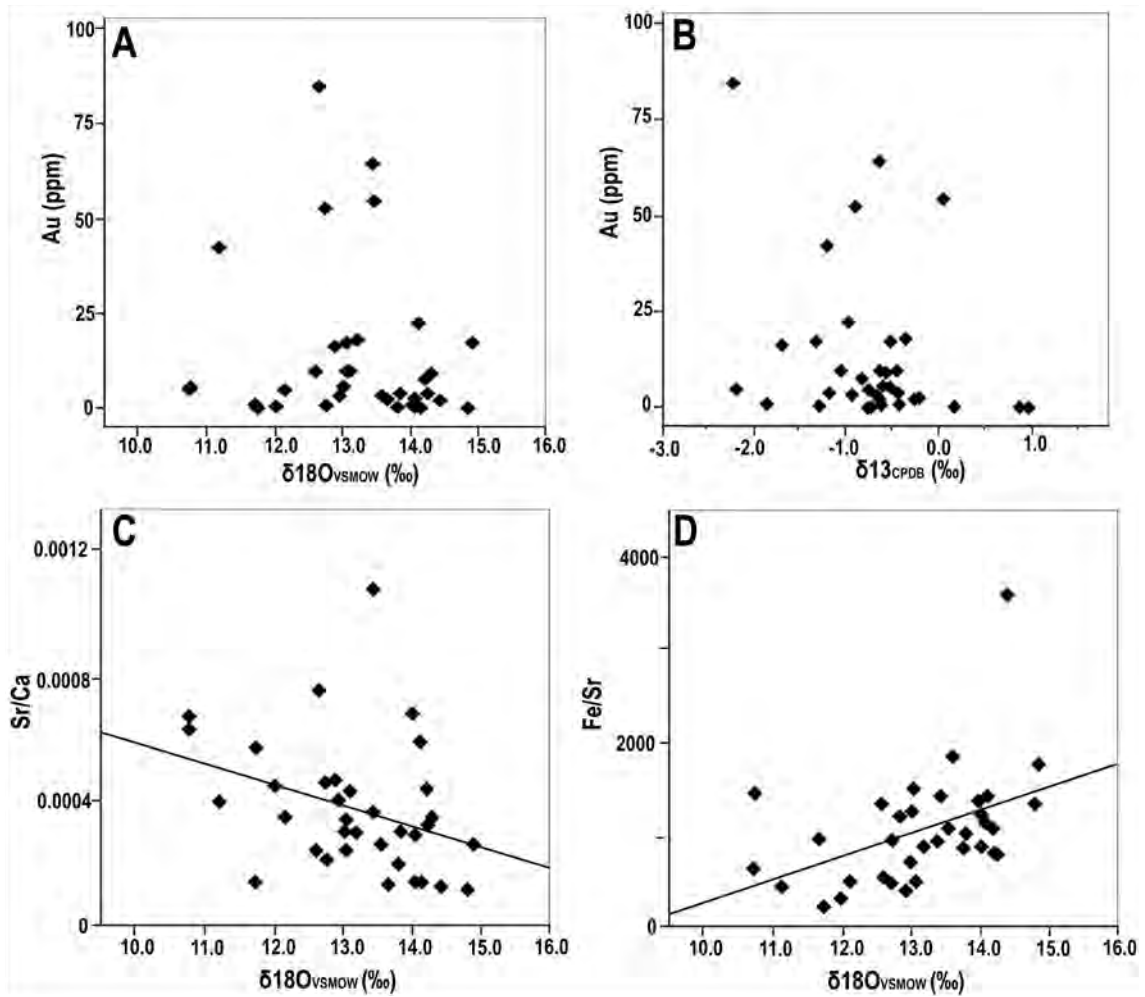


Figure 2-16. Carbonate stable isotope vs. gold, Sr/Ca and Fe/Sr. Stable isotope values do not correlate with Au, and show no evidence of influence from post-depositional processes. A. Plot of $\delta^{18}\text{O}_{\text{VSMOW}}$ vs. Au for the ankerite veins ($r^2 = 0.01$). B. Plot of $\delta^{13}\text{C}_{\text{PDB}}$ vs. Au ($r^2 = 0.08$). C. $\delta^{18}\text{O}_{\text{VSMOW}}$ values show a slight negative correlation with Sr/Ca ($r^2 = 0.1$). D. $\delta^{18}\text{O}_{\text{VSMOW}}$ values show a slight positive correlation with Sr/Ca ($r^2 = 0.2$)

There are no correlations observed between stable isotope values, gold grade, major elements, LILE or any other trace metals. $\delta^{13}\text{C}_{\text{PDB}}$ and $\delta^{18}\text{O}_{\text{VSMOW}}$ values were compared with Ca, Mg, Fe, Mn and Sr molar ratios to evaluate the influence of post depositional processes (Figure 2-16) (Veizer et al., 1983; Veizer et al., 1990; Swain et al., 2015). The expected result of post-depositional processes is a positive correlation between Sr/Ca molar ratios and isotope values, and negative correlations with Mn/Sr, Fe/Sr and Mg/Ca ratios and isotope values (Veizer et al., 1983; Veizer et al., 1990; Swain et al., 2015). Apart from Sr/Ca and Fe/Sr vs. $\delta^{18}\text{O}_{\text{VSMOW}}$, all comparisons yield r^2 values of < 0.1 , and slight correlations observed with Sr/Ca ($r^2 = 0.1$) and Fe/Sr ($r^2 = 0.2$) are antithetic to what would be expected from post depositional processes (Figure 2-16). This lack of post depositional influence has also been observed in the stable isotope systematics of other dolomite and calcite samples across the camp (Fyon et al., 1980). There are no spatial trends in $\delta^{13}\text{C}_{\text{PDB}}$ values, however, there is a spatial trend observed in $\delta^{18}\text{O}_{\text{VSMOW}}$ values (Figure 2-17). There is general trend of increasing $\delta^{18}\text{O}_{\text{VSMOW}}$ from southeast to northwest and down dip of the ankerite veins, with samples at the lowest regions toward the northwest regions of the mine and the Curts vein to the far west having the highest $\delta^{18}\text{O}_{\text{VSMOW}}$ values (Figure 2-17).

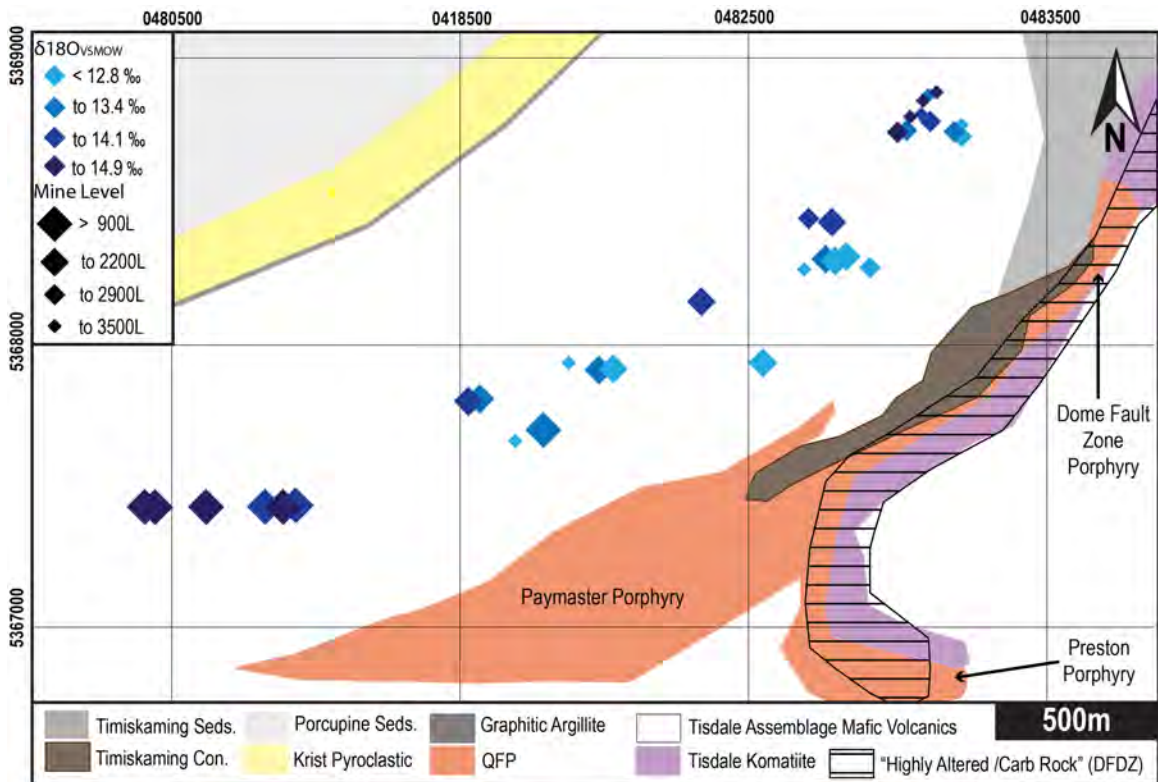


Figure 2-17. General geology map of the Dome mine showing the relative positions of ankerite veins samples and their carbonate $\delta^{18}\text{O}_{\text{VSMOW}}$ values. Carbonate $\delta^{18}\text{O}_{\text{VSMOW}}$ are split into quartiles. (Geology is after Rogers, 1982; Proudlove et al, 1989; Goldcorp Porcupine Gold Mines, internal report, 2014).

2.8.0 Discussion

The Dome ankerite veins were emplaced in the Vipond formation between 2,690 and 2,678 Ma. This coincides with Porcupine assemblage sedimentation (2693-2684 Ma), and D_2 and D_3 deformation events, concluding with Timiskaming basin formation and Timiskaming basal conglomerate emplacement which eroded the ankerite veins (Ayer et al., 2003; Bateman et al., 2008; Bleeker, 2015). Mid crustal fluids have been proposed as a source for early gold mineralization in the camp based on timing relationships with D_2 thrusting and the geometry of major faults and fracture arrays (Bateman et al., 2008). The mobilization of large volumes of mid crustal fluids requires a major conduit to focus fluids into the volcanic pile for vein formation. We suggest that the structure exploited by

the ankerite forming fluids was the Dome fault deformation zone (DFDZ). Oxygen isotopes of ankerite shows a southeast to northwest trend towards more enriched $\delta^{18}\text{O}$ values (10.8 to 14.9‰ $\delta^{18}\text{O}_{\text{VSMOW}}$) away from the DFDZ, across over 5,400 m strike, and 1,500 m down dip (Figure 2-17). More enriched $\delta^{18}\text{O}$ values are observed at the distal regions of the system; the Curts vein to the west and at the deepest levels of the mine to the east (Figure 2-17). This may correspond to increasing mineral-water fractionations at lower temperatures in more distal regions of the hydrothermal system, an interpretation which has been put forward previously by Fyon et al., (1980 and 1983) for dolomites in the Timmins camp. This interpretation is supported by the lack of post-depositional influence on the $\delta^{13}\text{C}_{\text{PDB}}$ or $\delta^{18}\text{O}_{\text{VSMOW}}$ values, and that no correlations are observed between isotope values, sample geochemistry, metal content, or overprinting quartz veining. Additionally, it has been suggested that large orogenic hydrothermal systems are highly-fluid dominated, so fluid $\delta^{18}\text{O}$ ratios are unlikely to undergo significant modification along the pathway (Goldfarb and Groves, 2015). The DFDZ was active during D_2 thrusting, formed the southern faulted margin of a D_3 transitional graben, and is overprinted by carbonate alteration and S_2 and S_3 (Bateman et al., 2008; Bleeker, 2015). It likely formed as a synvolcanic normal fault which was re-activated during subsequent deformation events (Brisbin, 1997). The DFDZ strikes northeast and is a ~100 m wide unit of highly carbonatized porphyry and ultramafic rocks. The intense carbonate alteration is proposed to result from the ascent of the CO_2 rich fluids up the Dome fault and was accompanied by gains of K, Ca, Rb, Sr, B, Au, and As, indicating that the early CO_2 rich fluids were auriferous (Moritz and Crocket, 1991).

In addition to the DFDZ, the role of porphyry emplacement and orientation is integral to the formation of long-lived fluid pathways for mineralizing fluids at the Dome mine. Quartz-feldspar porphyry emplacement is not genetically linked to gold mineralization in the main camp, however, there is a spatial association with gold and zones of deformation (MacDonald et al., 2005; MacDonald, 2010). At the Dome mine, there are multiple intrusions spatially associated with the inferred strike of the DFDZ. The ~2690 Ma (Corfu et al., 1989; Gray and Hutchinson, 2001) Preston, Paymaster and Dome Fault Zone porphyries intrude into the Central and Vipond Formations of the Tisdale assemblage,

plunge eastward and coalesce at depth (Figure 2-2, 2-4 and 2-17). The Paymaster and Dome Fault Zone porphyries are semi-conformable with the volcanic stratigraphy, and the Preston cuts it at a high angle, possibly a feeder for the sill-like Paymaster and Dome Fault Zone porphyries. On the Dome property, all three are intensely carbonate and sericite altered. The spatial relationship between porphyries, intense alteration, and gold mineralization hinges on emplacement conduits; the re-activated regional faults that facilitated porphyry emplacement, and the formation of dilational zones during deformation due to the inherent rheology contrast that porphyry emplacement creates (MacDonald, 2010). In the case of the Dome mine, both factors contributed to its world-class gold endowment. An early form of the DFDZ created a region of crustal weakness for porphyry intrusion which was re-activated during D₂ thrusting and D₃ basin formation, acting as a fluid conduit for ankerite forming fluids. The resulting intense carbonate alteration in the “highly altered zone” drastically reduced the permeability of the komatiite which, in conjunction with the presence of the less reactive porphyry intrusion, created favorable conditions during subsequent deformation events for emplacement of the quartz-fuchsite vein (Moritz et al., 1990; Moritz and Crocket, 1991). During QFV formation, auriferous fluids were channeled from depth along the porphyries where they leached lead from the porphyries and deposited it with gold (Moritz et al., 1990). The ankerite veins are also enriched in Pb with respect the Vipond formation (Table 2-1, Figure 2-12), and auriferous quartz and quartz-tourmaline veins at the Dome (Kerrick and Hodder, 1982). This Pb enrichment is not spatially associated with interflow sediments, and is most likely the result of fluid interaction with the porphyry bodies in the DFDZ.

The ankerite vein forming fluids travelled up the DFDZ into the Vipond formation, and exploited regions of competency contrast and rheological weakness in the volcanic package; primarily flow boundaries, interflow sediments, and early shear zones (Figure 6). This accounts for the conformable nature of the veins with respect to the volcanic flows and suggests that the less common cross cutting discordant veins were feeder structures between flows. The exploitation of regions of high permeability such as of flow tops and contacts by mineralizing fluids has been recognized across the camp (e.g., Hurst,

1935; Ferguson, 1968; Brisbin, 1997). The Vipond formation is ideal for channeling and reacting with gold bearing fluids due to its fragmental character and high Fe/Mg ratios, as wall rock with high Fe:Mg ratios favors the formation of pyrite from Au-thio complexes (Dunbar, 1948; Kerrich and Fyfe, 1981; Bolke, 1988; Dinel et al., 2008b). The ideal geochemistry and rheology of the Vipond formation flows for vein formation is reflected in the concentration of the bulk of the Dome ankerite veins between the base of the massive Gold Center formation G1 flow and Vipond formation V6 flow, with little to no veining in the Central or Gold Center formations. The underlying Central formation contains variolitic and pillowed flows with pillow top breccias, but it is Mg-rich (Pyke, 1982; Bateman et al., 2005). The Gold Central formation is mostly Fe-tholeiite (Brisbin, 1997; Dinel et al., 2008a), but its massive flows are not ideal for channeling of fluids. The massive nature of the G1 and 99 flow likely acted to focus fluids into the more porous variolitic and spherulitic pillowed flows and hyaloclastites of the V8, V10 and V6 flows where the ankerite veins formed as dilational fractures above and laterally away from the porphyry sills. While the G1 flow (“dacite ore”) is associated with only one ankerite vein at its upper flow contact, it is the most prolific gold producing zone at the Dome mine and hosts auriferous quartz and quartz-tourmaline veining. The dacite ore is characterized by intense ankerite alteration, which becomes less developed more distal to the DFDZ (Pressacco, 1999). In the western regions of the mine the massive V99 flow is sheared and intruded by the Paymaster porphyry and contains ankerite veining along the porphyry margins (Figures 2-4 and 2-6), however mineralization (grade) is lost as the veins approach the Fe-depleted porphyry, suggesting iron content as a key control to gold deposition. To the southeast, the erosional contact of the sedimentary trough region of the mine could represent the more proximal region of the veins, where the source fluid conduits have been eroded off during Timiskaming sedimentation. Sub-angular to rounded ankerite clasts are found in this sedimentary trough contact.

A hydrothermal system of this magnitude (5,400 m strike length) requires large volumes of fluid for formation and in this case, a single fluid source in a fluid-dominated system, with multiple pulses over a short period is proposed for ankerite vein formation. The ankerite veins crosscut sedimentary units enriched in base metals and reduced carbon

(Figure 2-12), yet there are no correlations observed between proximity to sediments and vein base metal contents, or $\delta^{13}\text{C}$. Evidence for multiple fluid pulses of a uniform fluid source is also observed in the banding of the ankerite veins, which likely results from hydraulic crack-seal style vein formation as observed in the Dome quartz fuchsite vein. Both magmatic (Burrows et al., 1986) and metamorphic (Kerrich and Hodder, 1982; Jia and Kerrich, 2000) fluid sources have been proposed for the Timmins camp based on $\delta^{13}\text{C}$ and $\delta^{18}\text{O}$ values. The bulk of the work in the Timmins gold camp has focused on the main stage quartz-carbonate veining which hosts most of the region's gold, with most authors invoking a metamorphic fluid source for mineralization in the main camp (e.g., Kerrich and Fryer, 1979; Kerrich and Hodder, 1982; Fyon et al., 1983; Moritz et al., 1990; Jia and Kerrich, 2000). Typical dolomite values for the Timmins region quartz-carbonate veins are -4 to -2‰ for $\delta^{13}\text{C}_{\text{PDB}}$, and +10.7 to +14‰ $\delta^{18}\text{O}_{\text{VSMOW}}$, which also support a metamorphic fluid hypothesis for vein formation (Jia and Kerrich, 2000). The dolomite $\delta^{18}\text{O}$ and $\delta^{13}\text{C}_{\text{PDB}}$ values for the Dome ankerite veins fall into this range (-2.2 to 1.0‰ $\delta^{13}\text{C}_{\text{PDB}}$ and 10.8 to 14.9‰ $\delta^{18}\text{O}_{\text{VSMOW}}$), and the role of post-depositional processes on these values has been shown to be negligible (Figure 2-16). These values support a CO_2 rich metamorphic fluid source for ankerite vein formation and align with previous work by Proudlove et al., (1989). However, they concluded that ankerite veins were of sedimentary origin despite $\delta^{18}\text{O}$ being lower than expected for Archean seawater and attributed this to re-equilibration of primary chemical carbonate with subsequent metamorphic fluids. Given the overwhelming field evidence against the synvolcanic emplacement of the Dome ankerite veins as chemical sediments, it is more likely that $\delta^{18}\text{O}$ values are the result of vein formation from metamorphic fluids with little to no re-equilibration with later fluids. Fluids of this nature are generally described as saline aqueous carbonic fluids with 2-5 mol% CO_2 , 0.01-0.36 mol% H_2S , near neutral pH with temperatures ranging from 250-700°C, which are produced by decarbonation and dehydration processes during regional prograde metamorphism at the greenschist-amphibolite facies transition (e.g., McCuaig and Kerrich, 1998; Mikucki, 1998; Ridley and Diamond, 2000; Goldfarb and Groves, 2015).

The behavior of Eu in hydrothermal fluids is strongly dependent on redox conditions in a fluid dominated system, and the ankerite vein REE patterns reflect a slightly reduced fluid in their prominent positive Eu anomaly (e.g., Figure 2-11; Lottermoser et al., 1992). This Eu anomaly is consistent with previous work (Kerrick and Fryer, 1979; Proudlove et al., 1989). The reduced nature of the fluids is also supported by the strong sericite alteration associated with the ankerite veins and is ideal for the stability of bisulfide complexes for metal transport (Hemley and Jones, 1964; Kerrich and Hodder, 1982; Seward, 1973, 1991). However, total REE contents range from 2 to 40 times chondrite, and the Eu anomaly is most prominent in samples with lower REE contents. There is no spatial trend in total REE contents, although, the most pronounced depletion is in the Curts vein samples. This lower REE content reflects the mineralogy of the ankerite veins, where samples with higher REE contents have been enriched in REE by overprinting quartz-tourmaline events. Proudlove et al., (1989) reported that concordant ankerite lodes which were more ankerite rich, had uniformly lower REE contents than their tourmaline rich end members due to lower apatite contents. The tourmaline content of the Curts vein material is minimal compared to the Dome ankerite vein samples where it is commonly found in the vein margins and as stringers. Additionally, the cross-cutting main stage veining at the Curts vein has a negligible tourmaline content and is dominated by barren milky-quartz veins. This later quartz-tourmaline event is associated with higher Co, Cr, Ni, TiO₂ and Al₂O₃ contents which are related to REE contents (Figure 2-13), a trend which is observed in the QFV and quartz-tourmaline veins across the mine, implying significant hydrothermal transport of those elements (Fryer et al., 1979). The bulk of the ankerite vein gold endowment is related to later quartz-tourmaline and quartz veining, however gold inclusions in pyrite are commonly observed in primary ankerite vein material. It is apparent from the bulk rock geochemistry that there is more than one population of gold mineralization, an observation also made by Proudlove et al., 1989 in which ankerite veins that were tourmaline rich had lower Au:Ag ratios than more ankerite rich samples.

Gold mineralization in the ankerite veins (pre-quartz-tourmaline overprint) is low-grade, but ubiquitous and intimately associated with pyrite; most commonly in the form of micron scale inclusions in pyrite grains. This relationship provides textural evidence for

the transport of gold as a bisulfide complex where gold has precipitated coevally with pyrite. There are multiple mechanisms for the deposition of gold in a hydrothermal system; changes in pH, Eh, temperature, pressure, fluid interaction with host rock, and fluid mixing (Mikucki, 1998). Given the conspicuous lack of spatial trends in Au grade with temperature proxies, no correlations with trace metals and redox sensitive trace metals, and the lack of free gold, fluctuations in pressure, temperature, or fluid chemistry from fluid mixing are unlikely mechanisms for gold deposition. Gold mineralization was likely facilitated through a decrease in total sulfur in the system by wall rock sulfidation and the resulting destabilization of the gold carrying bisulfide complex as pyrite was formed, a common mechanism for the precipitation of gold in hydrothermal fluids (e.g., Seward, 1973; Kerrich and Hodder, 1982; Bolke, 1988; Proudlove et al., 1989; Phillips and Powell, 2010). The high CO₂ content of the fluids may have also played a critical role in the transport of gold in the system by buffering the fluid in a pH range favoring the complexation with reduced sulfur (Phillips and Evans, 2004). This would account for the association between ankerite vein hosted gold and pyrite, as free gold is observed only with overprinting tourmaline stringers and quartz veining. The conditions for free gold deposition during the quartz-tourmaline and quartz veining events would have been significantly different than during ankerite vein formation. The ankerite forming fluids evolved earlier in the metamorphic history of the camp than main stage quartz forming fluids, which were released during D₃ and D₄ deformation events (Bateman et al., 2005; Bateman et al., 2008). Ankerite veining may have begun as early as D₁ extension (Bleeker, 2016), and likely occurred towards the end of the Porcupine assemblage sedimentation penecontemporaneously with D₂ thrusting, while the volcanic package was relatively flat. Overprinting quartz veining at the Dome occurred at 2670 ±10 Ma and was coeval with D₄ shortening and transpression (Ayer et al., 2003; Bateman et al., 2008). Gold deposition in the quartz and quartz-tourmaline veins may have occurred by a number of mechanisms; two possibilities are fluid mixing and/or pressure changes. Gold in the QFV has been attributed to pressure drops during crack-seal events (Moritz and Crocket, 1990), and may have also occurred during quartz shear vein formation as dilational fractures opened in the ankerite veins. The presence and variability of redox sensitive elements such as V and Cr requires a more oxidizing fluid for transport, which

may have interacted with more reduced Au bearing fluids, a mechanism which was active during the formation of quartz veining at Hoyle Pond (Dinel et al., 2008a). This is also supported by the lack of a prominent Eu anomaly in samples with high REE contents and overprinting quartz-tourmaline veining may signify a difference in fluid redox chemistry (less reduced) for the later veining events than the ankerite veins.

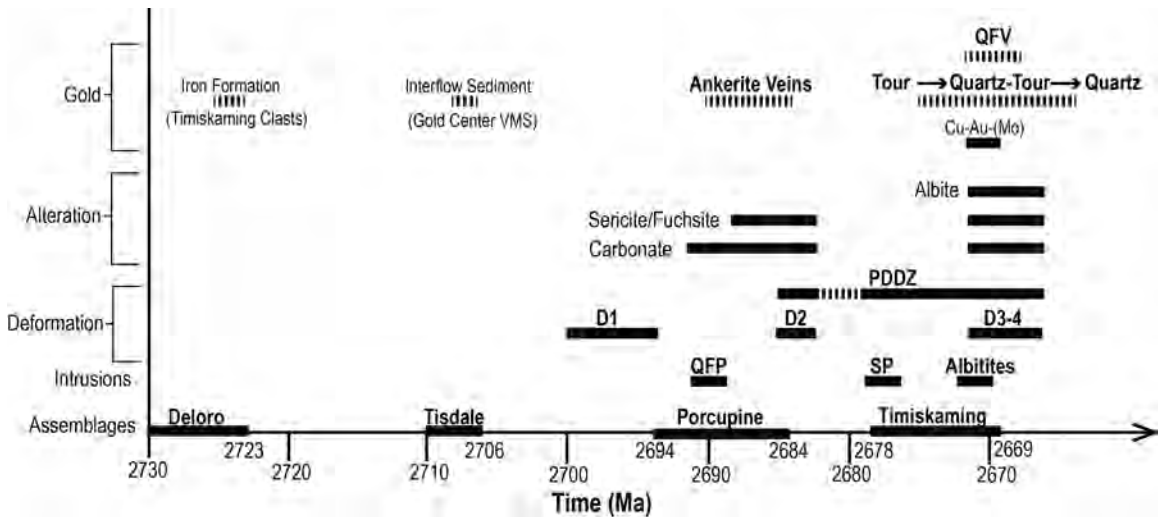


Figure 2-18. Paragenetic sequence of deformation and alteration vs. time in the Timmins gold camp, and gold mineralization at the Dome mine based on observations from across the camp, underground at the Dome mine, and E. Barr, Goldcorp Porcupine Gold Mines internal report, 2005. Geochronology is from Ayer et al, 2003, and Ayer et al., 2005. Abbreviations: QFV- quartz-fuchsite vein, PDDZ – Porcupine Distor Deformation Zone, QFP – quartz-feldspar porphyry, SP – sodic porphyry.

2.9.0 Regional Implications and Conclusions

The Dome mine ankerite veins and the intense carbonate alteration which accompanied their formation is a clear example of the role of early fluids in facilitating conditions for subsequent auriferous events. When mineralizing fluids encountered the massive G1 flow and DFDZ komatiites whose rheology was not optimal for ankerite vein formation, the CO₂ rich fluids strongly carbonatized the host rock preparing the rock for later mineralizing events resulting in two highly auriferous regions of the mine, the “dacite

ore” in the G1 flow and the quartz-fuchsite vein in the DFDZ. The fluid pathway exploited by ankerite vein forming fluids was long-lived, likely tapping the same fluid reservoir as it evolved throughout the metamorphic history of the camp. The syntectonic veining events at the Dome evolved from early ankerite veins, to ribboned quartz-fuchsite/tourmaline veins and quartz extension veining, all a part of an evolving metamorphic fluid system along common fluid channels. While enriched in Au with respect to the host rock, the ankerite veins are not economic except where they have been exploited by later auriferous fluids.

This paragenesis is also observed in the Aunor-Delnite and Buffalo-Ankerite systems where early ankerite veins are not economic except where overprinted by D₄ associated auriferous quartz and quartz-tourmaline veining (VanHees, 1979; Brisin, 1997). These deposits also formed at the intersection of a major fault (DFDZ) and porphyry intrusions (Delnite, Buffalo-Ankerite, Buffalo Ankerite #5, Aunor Porphyries) and likely originated as a linear belt, later folded in F₃ and has produced over 4.5 Moz of gold (Bateman et al., 2008; Bleeker, 2015). The formation of world class deposits and camps is a dynamic process involving multiple stages of mineralization over an extended period, so understanding the early processes, fluid conduits and sources which lead to large gold endowments is integral to the development of genetic models and future exploration. The Timmins camp has undergone three broad cycles of deformation, veining, and gold mineralization, synchronous with D₁, D₂ to D₃, and D₄; all of which are present at the Dome mine (Figure 2-18). The depositional context of the Dome ankerite veins highlights the important role of long lived fluid conduits, and the ideal combination of structural, rheological, and geochemical conditions which led to the world-class gold endowment at the Dome mine.

2.10.0 References

- Ayer, J., Amelin, Y., Corfu, F., Kamo, S., Ketchum, J., Kwok, K. and Trowell, N., 2002a. Evolution of the southern Abitibi greenstone belt based on U–Pb geochronology: autochthonous volcanic construction followed by plutonism, regional deformation and sedimentation. *Precambrian Research*, 115(1), pp.63-95.
- Ayer, J.A., Ketchum, J.W.F., and Trowell, N., 2002b, New geochronological and Nd isotopic results from the Abitibi greenstone belt, with emphasis on timing and implications of Late Archean sedimentation and volcanism: Ontario Geological Survey Open File Report 6100, pp. 5-1–5-16.
- Ayer, J.A., Barr, E., Bleeker, W., Creaser, R.A., Hall, G., Ketchum, J.W.F., Powers, D., Salier, B., Still, A., and Trowell, N., 2003, New geochronological results from the Timmins area: Implications for the timing of late-tectonic stratigraphy, magmatism and gold mineralization: Ontario Geological Survey Miscellaneous Paper, pp.33/1–33/9.
- Ayer, J.A., Thurston, P.C., Dube, B., Gibson, H.L., Hudak, G., Lafrance, B., Leshner, C.M., Piercey, S.J., Reed, L.E., Thompson, P.H., 2004, Discover Abitibi Greenstone Architecture Project: Overview of Results and Belt Scale Implication. Ontario Geologic Society Open File Report 6145, pp.37-1–37-15.
- Ayer, J.A., Thurston, P.C., Bateman, R., Dubé, B., Gibson, H.L., Hamilton, M.A., Hathway, B., Hocker, S., Houlié, M., Hudak, G., Ispolatov, V., Lafrance, B., Leshner, C.M., MacDonald, P.J., Peloquin, A.S., Piercey, S.J., Reed, L.E., and Thompson, P.H., 2005, Overview of results from the Greenstone Architecture Project: Discover Abitibi Initiative. Ontario Geological Survey Open File Report 6154, 146 p.
- Bateman, R., Ayer, J.A., Dubé, B., and Hamilton, M.A., 2005, The Timmins- Porcupine gold camp, northern Ontario: the anatomy of an Archean greenstone and its gold mineralization. Discover Abitibi initiative: Ontario Geological Survey Open File Report 6158, 90 p.
- Bateman, R., Ayer, J.A. and Dubé, B., 2008. The Timmins-Porcupine gold camp, Ontario: anatomy of an Archean greenstone belt and ontogeny of gold mineralization. *Economic Geology*, 103(6), pp.1285-1308.
- Bleeker, W., 2012. Targeted Geoscience Initiative 4. Lode Gold Deposits in Ancient Deformed and Metamorphosed Terranes: The Role of Extension in the Formation of Timiskaming Basins and Large Gold Deposits, Abitibi Greenstone Belt – A Discussion. Summary of Field Work and Other Activities 2012. Ontario Geologic Survey, Open File Report 6280, pp.47-1, 47-12.
- Bleeker, W., 2015. Synorogenic gold mineralization in granite-greenstone terranes: the deep connection between extension, major faults, synorogenic clastic basins, magmatism, thrust inversion, and long-term preservation, In: Targeted Geoscience Initiative 4: Contributions to the Understanding of Precambrian Lode Gold Deposits and Implications for Exploration, (ed.) B. Dubé and P. Mercier-Langevin. Geological Survey of Canada, Open File 7852, pp. 25–47.

- Bohlke, J.K., 1989. Comparison of metasomatic reactions between a common CO₂-rich vein fluid and diverse wall rocks; intensive variables, mass transfers, and Au mineralization at Alleghany, California. *Economic Geology*, 84(2), pp.291-327.
- Born, P., 1995, A sedimentary basin analysis of the Abitibi greenstone belt in the Timmins area, northern Ontario, Canada: Unpublished Ph.D. dissertation, Ottawa, Ontario, Carleton University, 489 p.
- Brisbin, D.I., 1997, Geological Setting of Gold Deposits in the Porcupine Gold Camp, Timmins, Ontario: Ph.D. thesis, Queens University, Kingston, Ontario, 532 p.
- Burrows, A.G., 1912. The Porcupine Gold Area. Twenty-First Annual Report of the Bureau of Mines, 1912, pp.205-249.
- Burrows, D.R., Wood, P.C., Spooner, E.T.C., 1986. Carbon isotope evidence for a magmatic origin for Archean gold-quartz vein ore deposits. *Nature*. 321(26), pp.851-854.
- Corfu, F., Krogh, T.E., Kwok, Y.Y. and Jensen, L.S., 1989. U–Pb zircon geochronology in the southwestern Abitibi greenstone belt, Superior Province. *Canadian Journal of Earth Sciences*, 26(9), pp.1747-1763.
- Crick, D.B., 1991. Evidence for epigenetic emplacement of the #1 South Quartz-Ankerite Vein, Dome Mine, South Porcupine, Ontario. Unpublished MSc. Thesis. Sudbury, Ontario, Laurentian University, 219 p.
- Daigneault, R., Mueller, W.U. and Chown, E.H., 2002. Oblique Archean subduction: accretion and exhumation of an oceanic arc during dextral transpression, Southern Volcanic Zone, Abitibi Subprovince Canada. *Precambrian Research*, 115(1), pp.261-290.
- Davies, J.F., 1977. Structural interpretation of the Timmins Mining area, Ontario. *Canadian Journal of Earth Sciences*, 14(5), pp.1046-1053.
- Davies, J.F., Whitehead, R.E.S., Cameron, R.A., Duff, D., 1982. Regional and local patterns of CO₂-K-Rb-As alteration: A guide to gold in the Timmins Area. Ontario Geologic Survey Open File Report 5376, 77 p.
- Dinel, E., Fowler, A.D., Ayer, J., Still, A., Tylee, K. and Barr, E., 2008a. Lithogeochemical and stratigraphic controls on gold mineralization within the metavolcanic rocks of the Hoyle Pond mine, Timmins, Ontario. *Economic Geology*, 103(6), pp.1341-1363.
- Dinel, E., Saumur, B.M. and Fowler, A.D., 2008b. Spherulitic aphyric pillow-lobe metatholeiitic dacite lava of the Timmins Area, Ontario, Canada: a new Archean facies formed from superheated melts. *Economic Geology*, 103(6), pp.1365-1378.
- Dube, B., Williamson, K., Malo, M., 2003. Gold mineralization within the Red Lake mine trend: example from the Cochonour-Willans mine area, Red Lake, Ontario, with new key information from the Red Lake mine and potential analogy with the Timmins camp. Geologic Survey of Canada, Current Research 2003-C21, 15 p.

- Dubé, B., and Gosselin, P., 2007, Greenstone-hosted quartz-carbonate vein deposits, in Goodfellow, W.D., ed., Mineral Deposits of Canada: A Synthesis of Major Deposit-Types, District Metallogeny, the Evolution of Geological Provinces, and Exploration Methods: Geological Association of Canada, Mineral Deposits Division, Special Publication No. 5, pp.49-73.
- Ferguson, S.A., 1968, Geology and ore deposits of Tisdale township. Ontario Department of Mines Geological Report 58, 177 p.
- Fryer, B.J. and Hutchinson, R.W., 1976. Generation of metal deposits on the sea floor. Canadian Journal of Earth Sciences, 13(1), pp.126-135.
- Fryer, B.J., Kerrich, R., Hutchinson, R.W., Peirce, M.G. and Rogers, D.S., 1979. Archaean precious-metal hydrothermal systems, Dome Mine, Abitibi Greenstone Belt. I. Patterns of alteration and metal distribution. Canadian Journal of Earth Sciences, 16(3), pp.421-439.
- Fyon, J.A., Schwarcz, H.P., Crocket, J.H., 1980 Grant 49 Carbon and Oxygen Isotope Geochemistry of Replacement Carbonates from the Timmins-Porcupine Gold Camp in Geoscience Research Grant Program, Summary of Research, 1979-1980, edited by E.G. Pye. Ontario Geological Survey, MP93, 262 p.
- Fyon, J.A., Crocket, J.H., 1981, Gold Exploration in the Timmins Area Using Field and Litho-geochemical Characteristics of Carbonate Alteration Halos. Ontario Geologic Survey Open File Report, 5339. 187 p.
- Fyon, J.A., Crocket, J.H., Schwarcz, H.P., 1983. Ontario Geoscience Research Grant Program, Grant No. 49 - Application of Stable Isotope Studies to Gold Metallogeny in the Timmins-Porcupine Camp. Ontario Geological Survey Open File Report 5464, 182 p
- Gibson, T.W., 1912. Twenty-First Annual Report of the Bureau of Mines, 1912. Vol. XXI., Part 1, 216 p.
- Goldfarb, R.J., Groves, D.I. and Gardoll, S., 2001. Orogenic gold and geologic time: a global synthesis. Ore geology reviews, 18(1), pp.1-75.
- Goldfarb, R.J. and Groves, D.I., 2015. Orogenic gold: Common or evolving fluid and metal sources through time. Lithos, 233, pp.2-26.
- Graton, L.C., McKinstry, H.E., 1933. Outstanding features of Hollinger geology. Canadian Institute of Mining and Metallurgy, Transactions, 35, pp.1-20.
- Gray, M.D. and Hutchinson, R.W., 2001. New evidence for multiple periods of gold emplacement in the Porcupine mining district, Timmins area, Ontario, Canada. Economic Geology, 96(3), pp.453-475.
- Harris, R., 2013. Telluride Associations with Gold Mineralization at Goldcorp's Dome Mine; Timmins, ON. Unpublished BSc. Thesis, University of Western Ontario.

- Hemley, J.J. and Jones, W.R., 1964. Chemical aspects of hydrothermal alteration with emphasis on hydrogen metasomatism. *Economic Geology*, 59(4), pp.538-569.
- Holmes, T.C., 1968, Dome Mines Limited: in *Geology and Ore Deposits of the Tisdale Township*. Ontario Department of Mines Geological Report 58, 172p.
- Hurst, M.E., 1935. Vein formation at Porcupine, Ontario. *Economic Geology*, 30(2), pp.103-127.
- Hutchinson, R.W., 1993. A multi-stage, multi-process genetic hypothesis for greenstone-hosted gold lodes. *Ore Geology Reviews*, 8(3-4), pp.349-382.
- Jia, Y. and Kerrich, R., 2000. Giant quartz vein systems in accretionary orogenic belts: the evidence for a metamorphic fluid origin from $\delta^{15}\text{N}$ and $\delta^{13}\text{C}$ studies. *Earth and Planetary Science Letters*, 184(1), pp.211-224.
- Karvinen, W.O., 1976. Distribution of carbonate-rich rocks, porphyries and gold deposits, Timmins area; pp. 182- 183 In *Summary of Field Work, 1976*, by the Geological Branch, V.G. Milne, W.R. Cowan, K.D. Card, and J.A. Robertson. Ontario Division of Mines, MP 67, 83p.
- Kerrich, R. and Fryer, B.J., 1979. Archaean precious-metal hydrothermal systems, Dome Mine, Abitibi Greenstone Belt. II. REE and oxygen isotope relations. *Canadian Journal of Earth Sciences*, 16(3), pp.440-458.
- Kerrich, R. and Fyfe, W.S., 1981. The gold—carbonate association: source of CO_2 , and CO_2 fixation reactions in Archaean lode deposits. *Chemical geology*, 33(1-4), pp.265-294.
- Kerrich, R., Fryer, B.J., Milner, K.J. and Peirce, M.G., 1981. The geochemistry of gold-bearing chemical sediments, Dickenson Mine, Red Lake, Ontario: a reconnaissance study. *Canadian Journal of Earth Sciences*, 18(3), pp.624-637.
- Kerrich, R. and Hodder, R.W., 1982. Archean lode gold and base metal deposits: Evidence for metal separation into independent hydrothermal systems. *Geology of Canadian gold deposits*, 24, pp.144-160.
- Kerrich, R., Polat, A., Wyman, D. and Hollings, P., 1999. Trace element systematics of Mg-, to Fe-tholeiitic basalt suites of the Superior Province: implications for Archean mantle reservoirs and greenstone belt genesis. *Lithos*, 46(1), pp.163-187.
- Lottermoser, B.G., 1992. Rare earth elements and hydrothermal ore formation processes. *Ore Geology Reviews*, 7(1), pp.25-41.
- Mason, R., Brisbin, D.I., 1987. The geological setting of gold deposits in the Porcupine mining camp. Ontario Geological Survey, MP136, pp.215-223.
- McCuaig, T.C. and Kerrich, R., 1998. P—T—t—deformation—fluid characteristics of lode gold deposits: evidence from alteration systematics. *Ore Geology Reviews*, 12(6), pp.381-453.

- McCrea, J.M., 1950. On the isotopic chemistry of carbonates and a paleotemperature scale. *The Journal of Chemical Physics*, 18(6), pp.849-857.
- MacDonald, P.J., Piercey, S.J. and Hamilton, M.A. 2005. An integrated study of intrusive rocks spatially associated with gold and base metal mineralization in the Abitibi greenstone belt, Timmins area and Clifford Township: Discover Abitibi Initiative; Ontario Geological Survey, Open File Report 6160, 190p.
- MacDonald, P.J., 2010. The geology, lithogeochemistry and petrogenesis of intrusions associated with gold mineralization in the Porcupine Gold Camp, Timmins, Canada. MSc. Dissertation, Laurentian University, 201p.
- MacLean, W.H. and Barrett, T.J., 1993. Lithogeochemical techniques using immobile elements. *Journal of geochemical exploration*, 48(2), pp.109-133.
- Mikucki, E.J., 1998. Hydrothermal transport and depositional processes in Archean lode-gold systems: A review. *Ore Geology Reviews*, 13(1), pp.307-321.
- Moritz, R.P., 1988. Geological and Geochemical Studies of the Gold-Bearing Quartz-Fuchsite Vein at the Dome Mine, Timmins Area. PhD Dissertation, McMaster University, 341p.
- Moritz, R.P. and Crocket, J.H., 1990. Mechanics of formation of the gold-bearing quartz-fuchsite vein at the Dome mine, Timmins area, Ontario. *Canadian Journal of Earth Sciences*, 27(12), pp.1609-1620.
- Moritz, R.P., Crocket, J.H. and Dickin, A.P., 1990. Source of lead in the gold-bearing quartz-fuchsite vein at the Dome mine, Timmins area, Ontario, Canada. *Mineralium Deposita*, 25(4), pp.272-280.
- Moritz, R.P. and Crocket, J.H., 1991. Hydrothermal wall-rock alteration and formation of the gold-bearing quartz-fuchsite vein at the Dome Mine, Timmins area, Ontario, Canada. *Economic Geology*, 86(3), pp.620-643.
- Mueller, W.U., Daigneault, R., Mortensen, J.K. and Chown, E.H., 1996. Archean terrane docking: upper crust collision tectonics, Abitibi greenstone belt, Quebec, Canada. *Tectonophysics*, 265(1-2), pp.127-150.
- Mueller, W.U., Stix, J., Corcoran, P.L. and Daigneault, R., 2009. Subaqueous calderas in the Archean Abitibi greenstone belt: an overview and new ideas. *Ore Geology Reviews*, 35(1), pp.4-46.
- Phillips, G.N., and Evans, K.A., 2004. Role of CO₂ in the formation of gold deposits. *Nature*. 429, pp.860-863.
- Phillips, G.N. and Powell, R., 2010. Formation of gold deposits: a metamorphic devolatilization model. *Journal of Metamorphic Geology*, 28(6), pp.689-718.
- Poulson, K.H., Robert, F., Dube, B., 2000, Geological classification of Canadian gold deposits. Geological Survey of Canada Bulletin 540, 113p.

- Pressacco, R, 1999. Economic Geology and Mineralization of the Dome Mine. Ontario Geologic Survey, Open File Report 598, pp.1-32.
- Proudlove, D.C., Hutchinson, R.W., Rogers, D.S., 1989. Multiphase Mineralization in Concordant and Discordant Gold Veins, Dome Mine, South Porcupine, Ontario, Canada. Economic Geology Monograph. 6, pp.112-123.
- Pyke, D.R., 1982, Geology of the Timmins area, district of Cochrane. Ontario Department of Mines Geological Report 219, 141 p.
- Reading, D.J., 1982. The Geology and Isotope Geochemistry of the Dome Ankerite Units. Unpublished MSc. Thesis, University of Waterloo.
- Roberts, R.G., Carnevali, J., Harris, J.D., 1978. The volcanic-tectonic setting of gold-quartz vein systems in the Timmins District. Geologic Survey of Canada, Paper 78-1B, pp.187-224.
- Roberts, R.G., Reading, D.J., 1981, Grant 32 The Volcanic-Tectonic Setting of Gold Deposits in the Timmins District – Carbonate Bearing Rocks at the Dome Mine. Ontario Geologic Survey MP098, 222p.
- Rogers, D.S., 1982. The Geology and Ore Deposits of the No.8 Shaft Area. Canadian Institute of Mining and Metallurgy Special Volume 24, pp.161-168.
- Seward, T.M., 1973. Thio complexes of gold and the transport of gold in hydrothermal ore solutions. *Geochimica et Cosmochimica Acta*, 37(3), pp.379-399.
- Seward, T.M., 1993. The hydrothermal geochemistry of gold. In *Gold Metallogeny and Exploration* (pp. 37-62). Springer Netherlands.
- Shields, G. and Veizer, J., 2002. Precambrian marine carbonate isotope database: Version 1.1. *Geochemistry, Geophysics, Geosystems*, 3(6).
- Swain, S.K., Sarangi, S., Srinivasan, R., Sarkar, A., Bhattacharya, S., Patel, S.C., Pasayat, R.M. and Sawkar, R.H., 2015. Isotope (C and O) composition of auriferous quartz carbonate veins, central lode system, Gadag Gold Field, Dharwar Craton, India: Implications to source of ore fluids. *Ore Geology Reviews*, 70, pp.305-320.
- Thompson, P.H., 2003, Discover Abitibi. Metamorphic subproject. Metamorphism and its relationships to gold deposits in the Timmins-Kirkland Lake area, western Abitibi greenstone belt, Ontario: Report 1, Ontario Geological Survey Open File Report 6120, p. 37-1 - 37-8.
- Thurston, P.C., 2002. Autochthonous development of Superior Province greenstone belts. *Precambrian Research*, 115(1), pp.11-36.
- Thurston, P.C., Ayer, J.A., Goutier, J. and Hamilton, M.A., 2008. Depositional gaps in Abitibi greenstone belt stratigraphy: A key to exploration for syngenetic mineralization. *Economic Geology*, 103(6), pp.1097-1134.

Wyman, D.A., 2003. Upper mantle processes beneath the 2.7 Ga Abitibi belt, Canada: a trace element perspective. *Precambrian Research*, 127(1), pp.143-165.

VanHees, E.H., 1979. Auriferous ankerite vein genesis in the Aunor Mine, Timmins, Ontario. Unpublished MSc. thesis, University of Western Ontario, London, Ontario.

Veizer, J., 1983. Trace elements and isotopes in sedimentary carbonates. *Reviews in Mineralogy and Geochemistry*, 11(1), pp.265-299.

Veizer, J., Hoefs, J., Ridler, R.H., Jensen, L.S. and Lowe, D.R., 1989. Geochemistry of Precambrian carbonates: I. Archean hydrothermal systems. *Geochimica et Cosmochimica Acta*, 53(4), pp.845-857.

Veizer, J., Hoefs, J., Lowe, D.R. and Thurston, P.C., 1989. Geochemistry of Precambrian carbonates: II. Archean greenstone belts and Archean sea water. *Geochimica et Cosmochimica Acta*, 53(4), pp.859-871.

Veizer, J., Clayton, R.N., Hinton, R.W., Von Brunn, V., Mason, T.R., Buck, S.G. and Hoefs, J., 1990. Geochemistry of Precambrian carbonates: 3-shelf seas and non-marine environments of the Archean. *Geochimica et Cosmochimica Acta*, 54(10), pp.2717-2729.

Chapter 3

Fingerprinting Multiple Gold Mineralization Events at the Dome Mine: Trace Element and Gold Content of Pyrite

3.1.0 Introduction

The Dome mine in Timmins Ontario has been in operation since 1910, producing over 16 million ounces of gold to date. Like most world-class orogenic systems, the over 67 million ounces of gold produced in the Timmins gold camp, is the result of multiple mineralization events over a span of 10-15 Ma years (Proudlove et al., 1989; Hutchinson, 1993; Bateman and Bierlein, 2007; Bateman et al., 2008; Meffre et al., 2016; Stromberg et al., 2017). Characterizing the timing, trace element, and gold content of these mineralization events is integral to exploration in the region, and for a better understanding of the mineralization histories that result in world-class gold deposits and camps worldwide. Historically, the bulk of the gold mined in the Timmins camp occurred as quartz vein hosted free gold, so minimal high-resolution analytical work has been undertaken to better characterize the relationship between gold, pyrite, and pyrite trace element content. Due to its refractory nature, pyrite preserves changes in fluid chemistry in its distribution of trace elements, making its growth history effective as a proxy for mineralization events, with distinct growth haloes and core/rim patterns representing different fluid events in hydrothermal ore deposit settings (e.g., Large et al., 2007, 2009, 2011; Sung et al., 2009; Thomas et al., 2011; Hazarika et al., 2013; Reich et al., 2013; Mukherjee and Large, 2017; Tardani et al., 2017).

The Dome mine is host to multiple minor stages of early sulfide rich gold mineralization, only one of which has been mined, an extensive (5,400 m in strike and 1,500 m vertically) set of ankerite veins (e.g., Gray and Hutchinson, 2001; Stromberg et al., 2017). These ankerite veins predate camp wide main stage mineralization, represent a significant portion (~20%, or 3.2 Moz) of the ore mined throughout the 108-year history of the Dome mine, and their deposition played an integral role in the mineralization history of

the Dome mine (Stromberg et al., 2017). Gold in the ankerite veins is intimately associated with sulfide mineralization. However, the association between sulfide mineralization and gold is not restricted to the ankerite veins at the Dome mine (Gray and Hutchinson, 2001; Stromberg et al., 2017), it is also observed at other deposits across the camp (e.g., Hoyle Pond, Hollinger, Timmins west; Dinel et al., 2008; Campbell, 2015). This study combines traditional petrography and scanning electron microscopy imaging with synchrotron radiation X-ray fluorescence (SR-XRF) and dynamic secondary ion mass spectrometry (D-SIMS) analysis to characterize the relationship between gold, trace elements, and pyrite mineralization at the Dome mine.

3.2.0 Regional Geology

3.2.1 Abitibi Greenstone Belt

The Abitibi Greenstone Belt (AGB), located in the southern part of Canada's Superior Province, spans over 2 million square kilometers and is host to some of the world's most prolific mineral deposits. These mineral endowments contain Canada's primary gold resource (e.g., Timmins, Kirkland Lake gold camps), world-class volcanogenic-massive sulfide base metal deposits (e.g., Kidd Creek, Noranda, LaRonde), and significant magmatic Ni-Cu-PGE deposits (e.g., Temagami, Shaw Dome) hosted in a thick succession of metavolcanics, metasediments and metagranites (Figure 3-1; Dube and Gosselin, 2007; Houle et al., 2008). The AGB is made up of 9 chronostratigraphic assemblages and has undergone multiple stages of volcanism, sedimentation, and deformation (Ayer et al., 2002b, 2005). The result is a series of steeply dipping, east-trending synclines and east-west trending bands of turbiditic wackes intruded by synvolcanic and syntectonic plutonic rocks (Figure 3-1; Poulson, Card and Franklin, 1992; Ayer et al., 2002a; Daigneault et al., 2004; Bateman et al., 2008). Regional metamorphism is constrained to 2677-2643 Ma and ranges from sub-greenschist to greenschist facies with local amphibolite facies associated with intrusions (Powell et al., 1995).

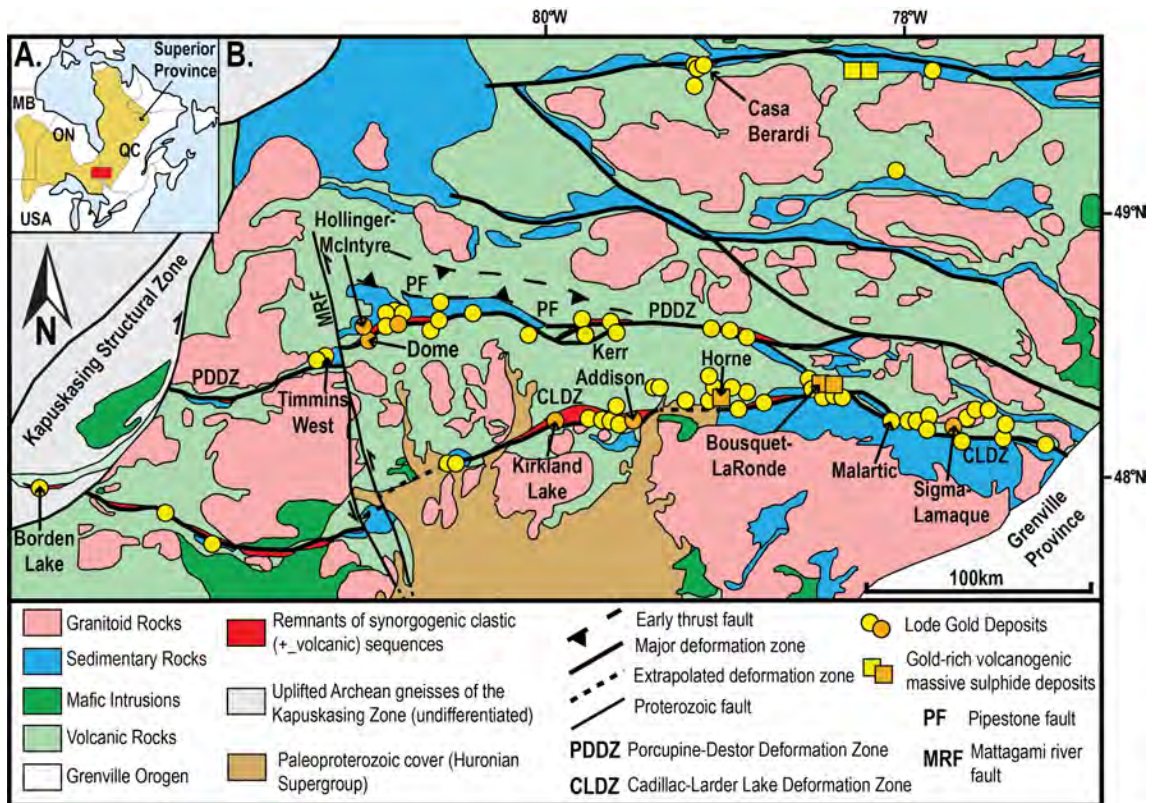


Figure 3-1. Geologic map of the Abitibi Greenstone Belt **A.** Simplified map showing the Superior Province. The red box signifies the regions shown in **B.** **B.** Simplified geologic map of the central and southern Abitibi greenstone belt, highlighting major faults, deformation zones, and the distribution of gold deposits (world-class deposits are in orange). (Stromberg et al., 2017, modified after Poulson et al, 2000; Dube and Gosselin, 2007; Bleeker, 2016).

In Ontario, the AGB is subdivided into 6 early volcanic assemblages, which are unconformably overlain by two late sedimentary assemblages (Ayer et al, 2005; Houle et al, 2008; Thurston et al, 2008). A comprehensive overview of all assemblages, depositional gaps and implications for mineralization can be found in Thurston et al., 2008. Mineralization across the AGB spans a period of almost 100 Ma from ~2740–2640 Ma and is primarily focused along two major East-West trending, over 400 km long crustal scale structural features; the Porcupine Destor Deformation Zone (PDDZ) and the Larder Lake-Cadillac Deformation Zone (Poulson et al., 1992; Bateman et al, 2005, 2008; Houle et al, 2008; Thurston et al, 2008; Bleeker, 2015). Gold across the AGB occurs in

three main deposit types; Au-rich VMS, orogenic/lode gold and syenite associated gold, with grades ranging from over 30 g/t to <1 g/t (Dube and Gosselin, 2007; Robert, 2001; Bigot and Jébrak, 2015; Bleeker, 2015)

3.2.2 Timmins Gold Camp

The Timmins gold camp, discovered in 1898, is located on the western side of the AGB and is the world's largest Archean orogenic gold camp. It is host to multiple world-class deposits some of which have been mined for over 100 years (e.g., Dome, Hollinger), with new deposits still being developed, explored, and discovered (e.g., Hoyle Pond, Timmins West, etc.). There are four distinct supracrustal units present in the Timmins camp, the Deloro, Tisdale, Porcupine and Timiskaming assemblages. All of these units host gold in variable amounts. The mineralized main portion of the camp north of the PDDZ is dominated by the 2710-2704 Ma Lower Tisdale assemblage metavolcanics, which are overlain by the 2690-2685 Ma Porcupine and 2677-2670 Ma Timiskaming metasediments, and is also host to Porcupine age intrusions (Figure 3-2; Ayer et al., 2005; Thurston et al., 2008). The stratigraphy and deformation history of the camp is described in detail in Bateman et al., 2008 and 6 stages of deformation and metamorphism up to middle greenschist facies are interpreted to have occurred (Bleeker, 1999; Thompson, 2003; Bateman et al., 2008).

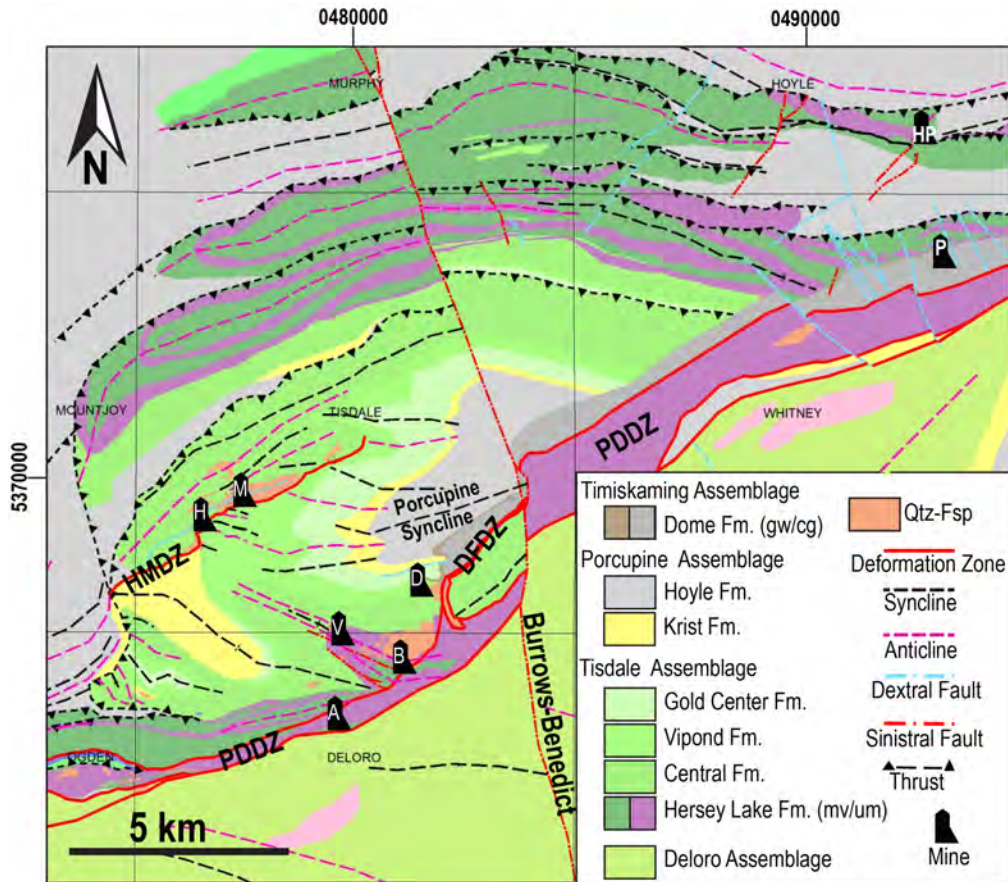


Figure 3-2. Regional map of the Timmins Gold Camp showing lithological contacts, major structures, mines (D – Dome, H – Hollinger, M – McIntyre, HP – Hoyle Pond, B- Buffalo-Ankerite, V-Vedron, A-Aunor, P-Pamour) and townships. Abbreviations: HMDZ – Hollinger-McIntyre Deformation Zone (99 shear), DFDZ – Dome Fault Deformation Zone, PDDZ – Porcupine Destor Deformation Zone, Fm – Formation, gw- greywacke, cg – conglomerate, mv – mafic volcanic, um - ultramafic, Qtz-Fsp – Quartz-Feldspar Porphyry. (Modified from E. Barr, Goldcorp Porcupine Gold Mines internal report, 2015)

This lengthy deformation history is integral to the over 67 Moz. gold endowment of the camp, as are the roles of early thrusting, extension, and synorogenic basin development (Bleeker, 2015). The bulk of the resulting mineralization is hosted in the Tisdale assemblage volcanics in close proximity to the PDDZ, its second-order shear structures, and the hanging walls of D₂ thrusts (Brisbin, 1997; Ayer et al., 2005, Bateman et al., 2008; Dinel et al., 2008a,b; Bleeker, 2015). Main stage mineralization in the camp

occurred post-Timiskaming sedimentation (<2679 Ma) and syn to post peak metamorphism (D₃, D₄; Bateman et al., 2008). Peak regional metamorphism is constrained to pre 2663.3±3 Ma by the undeformed Prosser Porphyry intrusion, indicating that the mineralization in the camp occurred over period of at least 7 Ma and for up to 25 Ma (Bleeker et al., 1999; Gray and Hutchinson, 2001; Bateman et al., 2008).

The mineralization history of the camp can be separated into two broad stages; pre- and post-Timiskaming sedimentation (Gray and Hutchinson, 2001; Bateman et al, 2008; Stromberg et al, 2017). There are two minor early, or pre-Timiskaming gold events; distally sourced auriferous detrital sulfide clasts in the Timiskaming conglomerate at the Dome and Pamour mines younger than 2679±4 Ma, and early ankerite veining described at the Dome, Buffalo-Ankerite and Aunor-Delnite mines around 2690 - 2679 Ma (VanHees, 1979; Corfu et al., 1991; Gray and Hutchinson, 2001; Ayer et al., 2003, 2005; Dube and Gosselin, 2007; Stromberg et al., 2017). There are also at least two stages of post-Timiskaming mineralization; a 2672±7 Ma (Ayer et al., 2003) Cu-Au-(Mo) mineralization event hosted in the 2688±2 Ma Pearl Lake Porphyry, and main stage quartz mineralization at around 2665 Ma. Main stage quartz veining is related to the D₃ and D₄ deformation events and occurs as a series of extensional fracture arrays and ladder veins (Gray and Hutchinson, 2001; Bateman et al., 2008).

3.3.0 Mine Geology and Mineralization History

The Dome mine is the second largest producer in the Timmins Gold Camp and is located ~6 km southeast of the Town of Timmins on the southern limb of the Porcupine Syncline where it is eroded off by the Timiskaming Assemblage disconformity (Figure 3-2). As such, the mine workings sit in a structurally complicated region of the camp, which encompasses the entire camp stratigraphy (Figure 3-3). Gold was discovered in 1909 at the Dome mine in two large visible gold bearing quartz veins, and the mine has been in continuous production since 1910 (Holmes, 1968). Like most of the deposits of the Timmins Gold Camp, it sits to the north of the PDDZ, and is associated with one of its

second order structures, the northeast striking Dome Fault Deformation Zone (DFDZ; Bateman et al., 2008).

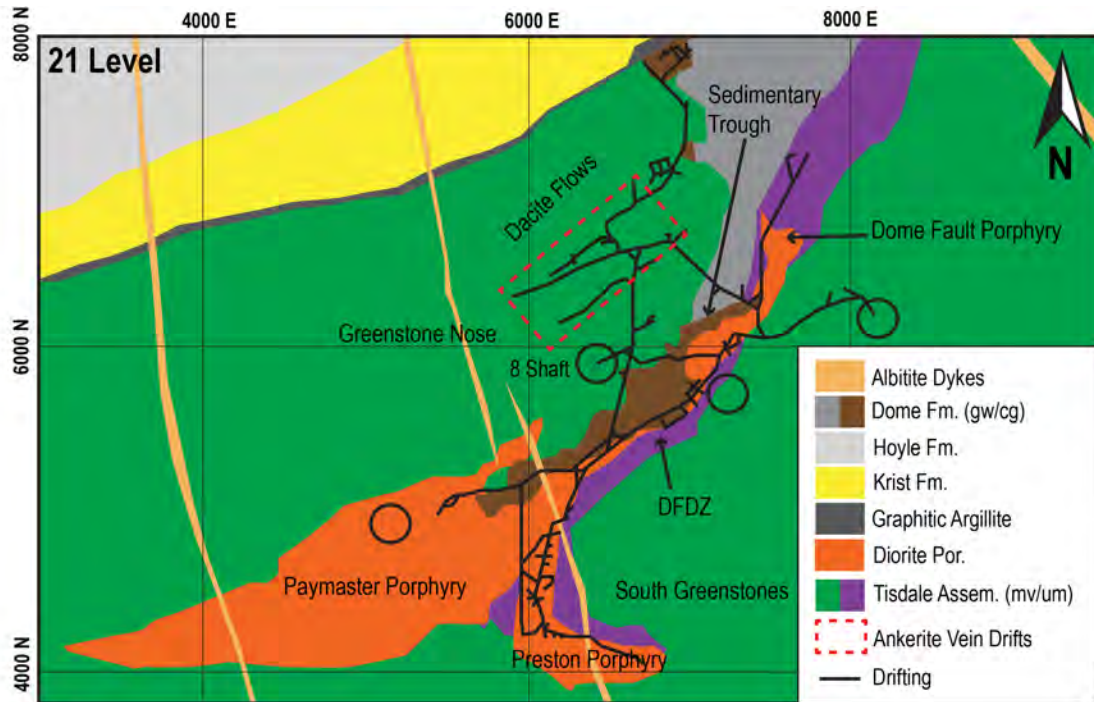


Figure 3-3. The Dome Mine geology at the 21 level of the mine. Drifting along the ankerite veins is shown in the red box. (Fm – formation, gw – greywacke, cg – conglomerate, por – porphyry, Assem – assemblage, mv – mafic volcanic, um – ultramafic) (Modified from Goldcorp Porcupine Gold mines, internal report 2014).

The DFDZ played a key role as a mineralization host, as well as a fluid conduit for mineralizing fluids at the Dome mine (Stromberg et al., 2017). On the mine property, it manifests as a ~100 m wide zone of highly carbonatized ultramafic flows and porphyry intrusions locally referred to as “carb rock”, or “highly altered” rock in regions containing fuchsite (Figure 3-3; Holmes, 1968; Stromberg et al., 2017). The DFDZ hosts quartz tourmaline veins in “highly altered” regions, as well as the highest producing structure in the mine; the quartz fuchsite vein (QFV). The QFV is a massive ribboned quartz vein, which was mined over 500 m in strike near a slate contact (Moritz, 1998). The most

prolific gold producing zone is a region of the “Greenstone Nose” locally referred to as “Dacite Ore”. The dacite flows are highly carbonatized tholeiitic flows at the base of the Gold Center formation of the Tisdale assemblage, and are heavily mineralized by quartz veining (Figure 3-3, 3-4; Holmes, 1968; Pressacco, 1999). While quartz-tourmaline and quartz veining account for the bulk of the gold endowment at the deposit, the most laterally extensive veining at the mine is a set of ankerite veins hosted primarily in the Fe-tholeiites of the Vipond formation in the greenstone nose region of the mine (Stromberg et al., 2017).

The Dome ankerite veins represent ~20% of the ore at the Dome mine, and run from surface down to the 35 level of the mine (>1500 m). They extend over 5400 m in strike and are up to 4 m wide. Timing of these veins is constrained by crosscutting relationships to between 2690 Ma (porphyry intrusion age) and 2679 Ma (Timiskaming age), making them some of the earliest veining in the camp (Corfu et al., 1989; Ayer et al., 2003; Stromberg et al., 2017). The ankerite veins are crosscut by both the tourmaline-quartz and quartz veining events (Figure 3-4). Historically the ankerite veins were interpreted to be barren sedimentary exhalatives, which were only economic where overprinted heavily by later veining (e.g., Fyer et al., 1979; Kerrich and Fyer, 1979; Proudlove et al., 1989). However, reinterpretation of the ankerite veins demonstrates they are syntectonic and formed from early auriferous fluids (Stromberg et al., 2017). Predicting gold grade in the ankerite veins is difficult as the presence of overprinting veining does not always ensure a high gold tenor, and there are large regions of the mine in which the ankerite veins are not economic despite being overprinted by later veining (Stromberg et al., 2017). Across the mine, gold most commonly occurs as free gold in quartz veins, but this is not the case with the ankerite veins. Free gold occurs rarely and when observed is related to overprinting by quartz veining. The bulk of the gold in the ankerite veins is associated with pyrite mineralization, primarily at the pyrite rich vein margins. The bulk rock gold and metal contents of the ankerite veins vary greatly across their strike with grades ranging from 0.2 to 85 g/t Au, with no trends identified between grade, region of the mine, or vein trace metal content. Additionally, there is a heterogeneous distribution of gold:silver ratios observed in the Dome ankerite veins with no systematic variation across

strike length or with vein major element and metal content (Fyer et al., 1979; Stromberg et al., 2017).

The heterogeneity in both gold content and Au:Ag ratios points towards contributions of gold from multiple sources. The intimate relationship between gold and pyrite in the ankerite veins makes this an ideal system for investigating the micron scale relationships between gold, pyrite, and pyrite trace element content to characterize the nature of the mineralization events which contributed to the 16 Moz endowment at the Dome mine.

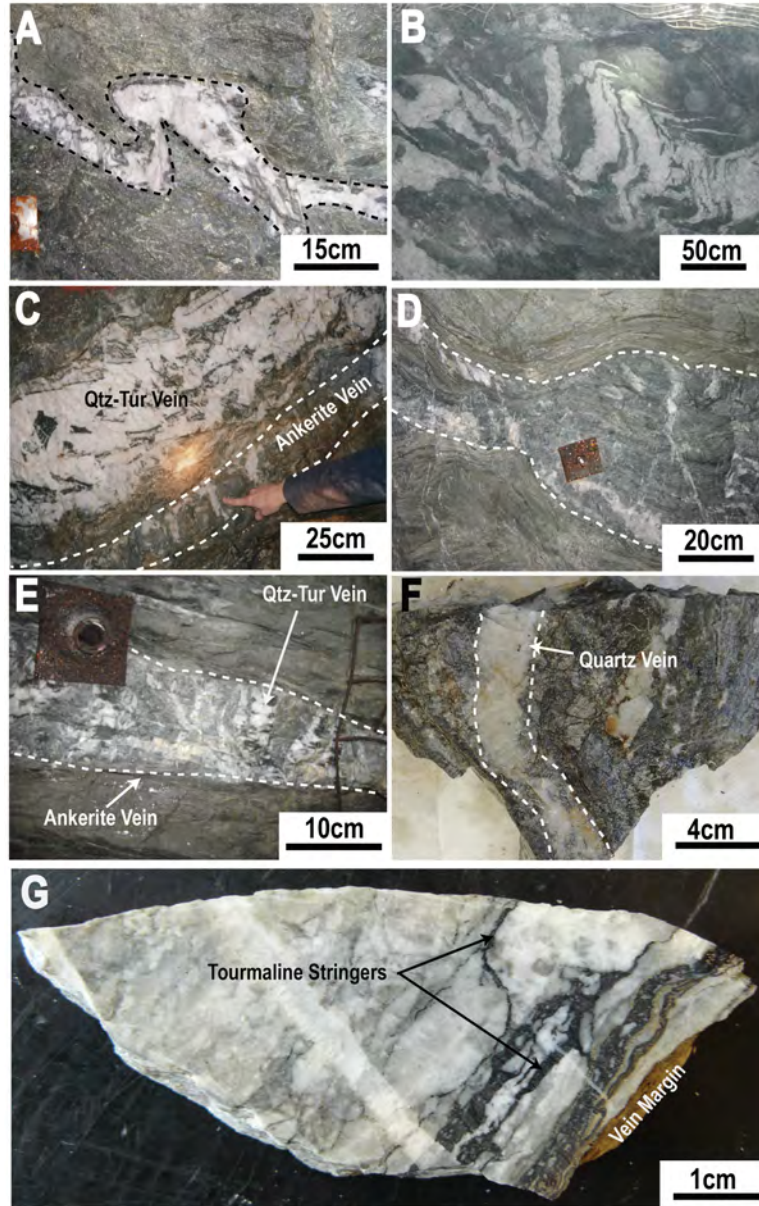


Figure 3-4. Veining styles observed at the Dome mine and their relationship to the Dome ankerite veins. A. A folded quartz-tourmaline vein in the DFDZ region of the mine with a sulfide rich halo B. En echelon quartz veining hosted in “dacite” region of the mine with sulfide halo C. Quartz tourmaline veining along a structure exploited by an earlier ankerite vein in the Paymaster Porphyry D. Boudinaged ankerite vein with overprinting quartz veining E. Ankerite vein with overprinting quartz-tourmaline veining F. Ankerite vein sample with crosscutting quartz veining G. Ankerite sample with tourmaline stringers near the vein margin. These stringers contain pyrite, galena and less commonly, visible gold.

3.4.0 Sample Suite and Analytical Methods

3.4.1 Sample Suite

Thirty-three ankerite vein samples were collected in 2012-2015 across >3,500 m lateral underground strike and 1,500 m vertical extent of the veins. These samples were selected to highlight multiple vein sets across different levels and regions of the mine as well as variable degrees of mineralization and overprinting by later veining. They were collected from newly developed and historic regions of the mine where safely accessible. Mapping of new regions of the mine was undertaken in 2014 and 2015 as development occurred along ankerite veins as well as regions of quartz and quartz-tourmaline veining.

3.4.2 Sample Preparation

All samples were subsampled for bulk rock geochemical and mineralogical (XRD) analysis. Whole-rock major and trace elements were determined by inductively coupled plasma atomic-emission spectrometry (ICP-AES; package ME-ICP06 -Whole Rock Package ICP-AES) and inductively coupled plasma – mass spectrometry (ICP-MS; package ME-MS81 – Lithium Borate Fusion ICP-MS) respectively, following pulverization at ALS Minerals in Sudbury, Canada.

Polished thin sections were prepared and examined using conventional petrographic techniques to characterize gold mineralization and associations with pyrite. Following detailed petrographic and BSE-SEM analysis, samples and pyrite grains were selected for synchrotron and SIMS analysis. Grains were selected to be representative of the mineralization observed across the deposit including auriferous and barren regions of veining. For D-SIMS, the pyrite rich vein margin regions of two thin section offcuts were cut and mounted in 1-inch diameter epoxy mounts with 15 wt% graphitic carbon to reduce charging. The mounts were polished and first characterized by reflected light microscopy. Circles were etched around regions of interest, and the mounts were carbon coated for D-SIMS analysis.

3.4.3 Scanning Electron Microscopy

At the Western University Nanofabrication Facility, thin sections were coated with 5 nm amorphous osmium to reduce charging and imaged using backscatter scanning electron microscopy (BSE-SEM) on a LEO (Zeiss) 1540 XB field emission gun – scanning electron microscope (FEG-SEM). The instrument was operated between 10 and 15 kV to examine samples using a quadrant-backscattered electron detector for better contrast. An Oxford Instruments' INCAx-sight energy dispersive spectrophotometer (EDS) was utilized for elemental analysis of gold and telluride grains at an operating voltage of 15 kV. Data was normalized and collected for 2 to 4 iterations depending on the grain size to optimize Au, Te and Ag signal.

3.4.4 Dynamic Secondary Ion Mass Spectrometry (D-SIMS)

D-SIMS analysis of the carbon coated polished epoxy mounts was undertaken at Surface Science Western using a Cameca IMS 3f with a Cs⁺ primary ion beam. The instrument was operated with a 10 kV primary ion energy and 15 nA primary current which results in a 10-15 µm beam size. A -180V offset was used to suppress molecular interferences of the 197V peak. Data was collected for 4 elements (³⁴S, ⁵⁶Fe, ⁷⁵As, ¹⁹⁷Au) and a linear calibration curve (to 5 orders of magnitude) was constructed using mineral specific ion implanted standards to account for matrix effects. To provide accurate quantification, depth profiles are produced in the corresponding mineral implant standards at the same operating conditions (Dimov and Hart, 2011).

3.4.5 Synchrotron Radiation - X-Ray Fluorescence (SR-XRF)

SR-XRF data was collected over multiple visits to the Advanced Photon Source (APS) 20-ID beamline, the Cornell High Energy Synchrotron Source (CHESS) F3 beamline, and 07B2-1 (VESPERS - Very Sensitive Elemental and Structural Probe Employing Radiation from a Synchrotron) beamline at the Canadian Light Source (CLS). All are hard X-ray beamlines with microprobe stations optimized for SR-XRF on different scales. A table of specific beam conditions and all experimental parameters for each analysis can be found in Appendix D.

The CHESS F3 station is a bend magnet station with a water cooled double crystal Si (111) monochromator which is tunable from 3-31 keV and uses a Sagittal Si (111), mirrors to focus down to 20 μm . The end station is equipped with a Maia detector (CSIRO; Kirkham et al., 2010; Ryan et al., 2010a,b), a 384-element pixel array detector (PAD) oriented at 180° to the sample. The Maia detector is optimized for rapid full spectrum data collection with high count rates (in excess of 10^7 photos/ second) allowing for high resolution large area SR-XRF mapping.

APS 20-ID is a multi-purpose insertion device beamline with a Kirkpatrick-Baez (KB) mirror microprobe set-up and Si (111) LN₂-cooled monochromator which provides a monochromatic beam that can be focused down to ~ 2 μm for energies in the range of 4.2-27 keV with a photon flux of 10^{11} at 10 keV. The end station is equipped with a Vortex-ME4 4-element silicon drift detector for SR-XRF mapping which was positioned at 90° to the source with the sample placed in a 45° geometry (Heald et al., 2001; 2007).

The CLS VESPERS beamline is a bend magnet station which has multi-bandpass and pink (polychromatic) beam capabilities with an energy range of 6-30 keV with a focus of (2-4) μm x (2-4) μm using KB mirrors. The end station is equipped with a 4 element Vortex multi-element Si drift detector located 90° to the incident beam in the direction of the polarization, and the detector is calibrated to ~30 eV per channel.

Thin sections and off-cuts were affixed onto custom sample holders and mounted on the sample translation stage. Samples were raster-scanned through the focused beam to collect full spectrum XRF data for each pixel over grains of interest. Element maps were collected with an incident X-ray energy of 13.1 keV (APS and CHESS) and with the pink beam (polychromatic) at the CLS. The spatial resolution ranged from 2-20 μm and dwell times ranged from 4 to 500 msec (Appendix D). Standard foils (Au, Mn, Fe, Sb) were used for energy calibration and the NIST standard SRM 1834 was analyzed to determine beamline parameters and yields for GeoPIXE.

3.4.6 SR-XRF Data Analysis

Large-scale maps collected at CHESS F3 were analyzed using GeoPIXE, a software suite that uses a fundamental parameters approach with spectral deconvolution and imaging using the dynamic analysis method (Ryan, 2000; Ryan et al., 2010a). This is based on fitting a representative total spectrum and detailed model of the Maia detector array efficiency, the details of which are outlined in Ryan et al., 2010. This method results in a matrix transformation which can produce real time and off-line projections of full spectrum data into elemental maps yielding both qualitative and quantitative maps and provide mineral specific trace element contents (e.g., Fischer et al., 2014). For real time mapping we created a bulk rock matrix which approximates the average composition of auriferous pyrite rich samples. This was then refined and refit using sample specific information with yields calculated using the specific matrix for that sample or region of interest with the sample.

High resolution mapping data from APS ID-20 was analyzed using in house software (2D Q-Scan Plot). 2D Q-Scan Plot collects full spectrum data and simultaneously creates intensity maps for preselected regions of interest (ROI's) within the full spectrum. Up to fifteen regions of interest were preselected based on the expected chemistry of the sample. These regions were refined prior to mapping by collecting point spectra from representative regions of the sample and adjusted to minimize the effects of peak overlap. Following mapping, the raw XRF spectra for anomalous features, hotspots, as well as growth haloes was further investigated to confirm the geochemistry observed in the map.

SR-XRF maps collected at the CLS were processed using Peakaboo, a software program developed by the University of Western Ontario as a part of the Science Studio package. Peakaboo allows for the identification of the spectral origins of an XRF spectrum by fitting the components of the K, L, or M peaks, escape and pileup peaks, and then plots their spatial intensity distribution as maps (e.g., McIntyre et al., 2010). For VESPERs data, a 90% Brukner background removal is applied to the mean averaged spectrum for the entire map to suppress background from X-ray scattering, and then the mean average spectrum is fit. The fitting of spectral peaks to a Gaussian function is used with preset

widths, and the identification of an element requires a close fit to multiple lines in the spectrum. Following peak fitting, two dimensional maps are created to show the distribution of selected element using 2 interpolation passes.

3.5.0 Results

3.5.1 Vein Mineralogy

The Dome ankerite veins are dominated by coarse-grained ankerite and quartz, fine-grained sericite, and minor pyrite (Figure 3-5). The veins commonly appear laminated, a result of variability in carbonate and quartz content, carbonate chemistry, and grain size. Pyrite is most concentrated at vein margins but also occurs along tourmaline stringers and less commonly disseminated in the main vein material (Figure 3-5). The pyrite rich vein margins are also enriched in accessory phases including galena, chalcopyrite, sphalerite, rutile, monazite, and rare molybdenite. Gold is most commonly observed in the vein margins associated with pyrite mineralization. The veins are commonly overprinted by quartz and quartz tourmaline veining (Figure 3-4). The earlier overprinting veining is tourmaline rich and grades to more quartz rich. Quartz rich overprinting veins are accompanied by sericite alteration and little to no pyrite. Tourmaline rich veinlets occur as stringers and along vein margins and are commonly accompanied by pyrite mineralization, rutile, and monazite (Figure 3-4g, 3-5c).

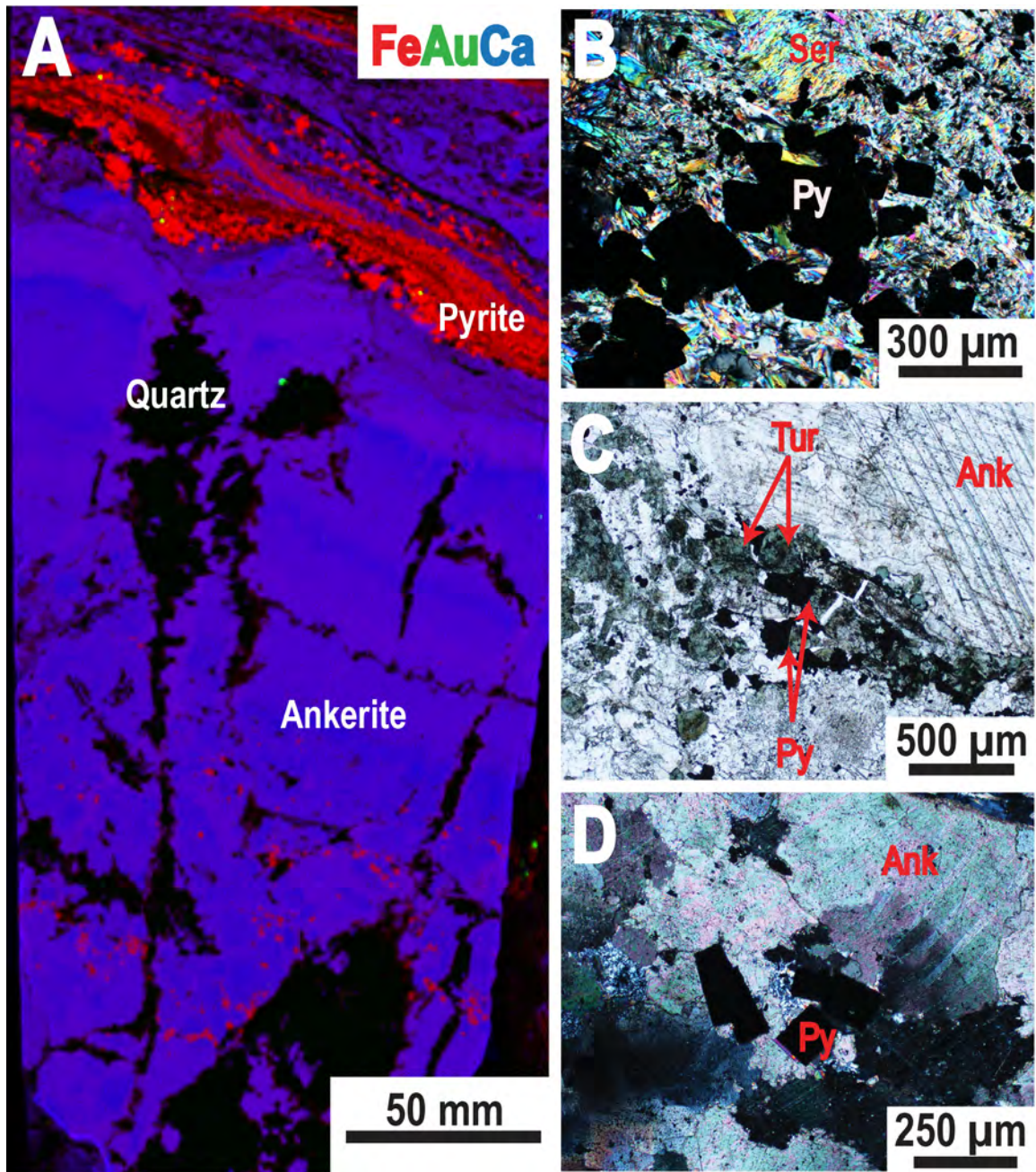


Figure 3-5. Typical ankerite vein mineralogy. A. SR-XRF RGB map (iron – red, gold-green, calcium – blue) of an ankerite vein showing the pyrite rich vein margin and the laminated nature of the ankerite veins as well as quartz, gold and pyrite in the vein material (C410280). B. Euhedral pyrite and abundant sericite in the vein margin (10x XPL) C. Tourmaline veinlet with euhedral pyrite cutting through coarse-grained ankerite (5x PPL). D. Euhedral pyrite grains in the coarse-grained ankerite ground mass that makes up much of the main vein material (10x XPL)

3.5.2 Gold Mineralization

The bulk of the gold in the Dome mine ankerite veins is intimately associated with pyrite mineralization. Five types of gold mineralization are observed and summarized in Table 3-1 with examples in Figure 3-6. Most commonly, gold is intimately associated with pyrite mineralization as either free gold in fractures and on grain margins, or as inclusions. The most commonly observed type of gold mineralization occurs as small inclusions in the cores of sieve textured, inclusion rich pyrite grains (Inclusion I) (Figure 3-6a,b). These pyrite grains are ubiquitous in the ankerite vein margins and in the primary ankerite vein material. The gold inclusions most commonly occur in the central core region of pyrite grains and are often associated with chalcopyrite and arsenopyrite mineralization (Figure 3-6a). Inclusions of this type are generally electrum, but occasional inclusions of gold and silver tellurides are also observed (Figure 3-6b). The next most common style of gold mineralization, and the one that contributes the bulk of the gold tenor of the ankerite veins is free gold at the margins of pyrite grains and in fractures (Free Gold I; Figure 3-6c). This occurs either at the inner edge of the pyrite rich vein margins where it is quartz rich or in regions of the ankerite vein which have been overprinted by later veining. It is occasionally accompanied by coarse-grained anhedral pyrite grains with large gold inclusions at their margins (Inclusion II; Figure 3-6f). Free gold also occurs in close association with tourmaline both at the vein margins, and in tourmalines stringers (Free Gold II; Figure 3-6d,g). In the pyrite rich vein margins, it occurs in association with tourmaline, rutile and euhedral pyrite growth (Figure 3-6d,e), and in the ankerite vein it occurs interstitially in tourmaline stringers (Figure 3-6g). There is fine-grained pyrite associated with these stringers, but not in contact with the gold. The rarest and most spectacular gold occurrences are associated with overprinting quartz veining and occur at the margins of the quartz veins (Figure 3-6h).

Table 3-1. Summary of gold mineralization styles observed in the Dome ankerite veins.
 Ordered from most common (Inclusion I) to very rare (Visible Gold).

Type	Description
Inclusion I.	Inclusions (typically <50 µm) in the core of sieve textured, inclusion rich pyrites
Free Gold I.	At pyrite grain margins and in fractures (sometimes VG)
Inclusion II.	Large (typically >50 µm) inclusions in coarse euhedral to subhedral pyrites (usually at margins)
Free Gold II.	Free gold associated with tourmaline, occasionally with pyrite
Visible Gold	Coarse visible gold at margins of later quartz veining (not associated with pyrite)

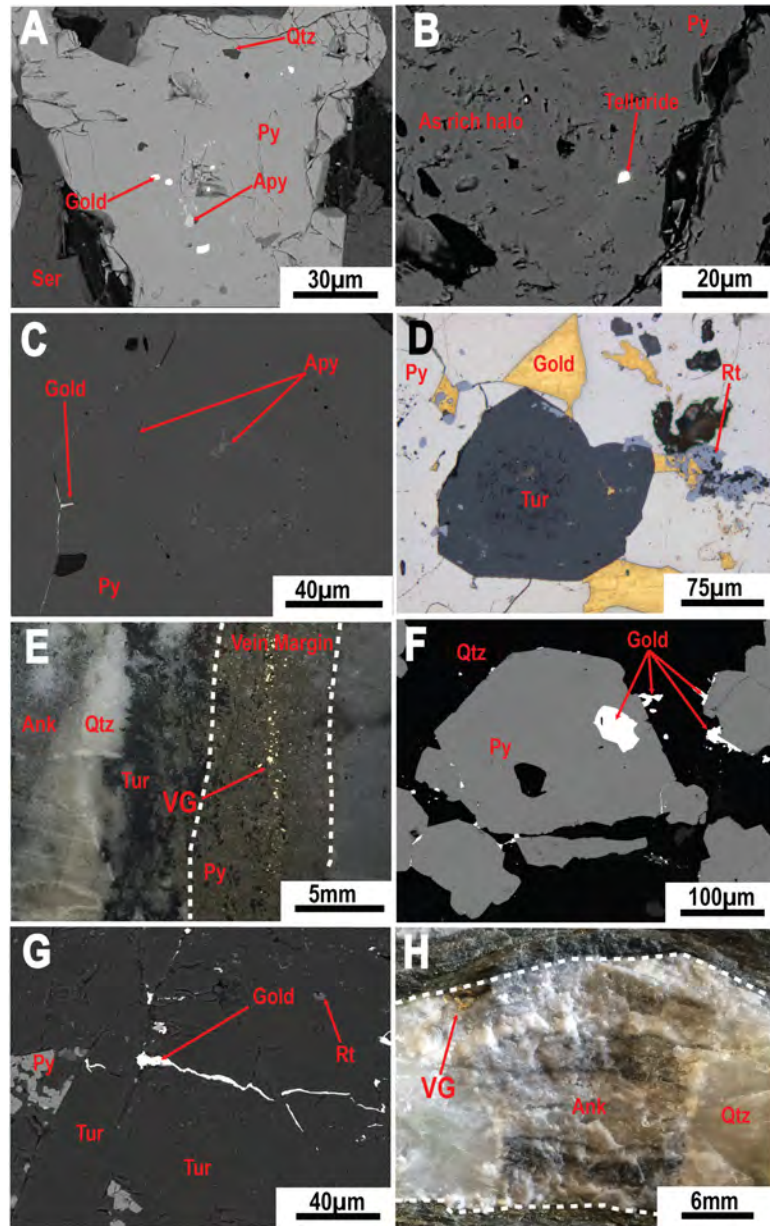


Figure 3-6. Gold mineralization styles observed in the Dome ankerite veins (Summarized in Table 3-1). A. Inclusion I in the core of a sieve textured pyrite with inclusions of arsenopyrite (615x 15 kV QBSB) B. Telluride (AgAuTe) inclusion I in a haloed pyrite grain. (1.06k x 15 kV QBSD) C. Free Gold I in fractures and at grain margins (198x 15 kV QBSD) D. Free Gold II associated with pyrite rich vein margins (thin section from C) (5x RFL) E. Free Gold II associated with pyrite in the vein margin F. Inclusions II and Free Gold I associated with pyrite grain margins (215x 8 kV QBSD). G. Free Gold II in a tourmaline stringer (495x 15 kV QBSD). H. Visible gold (VG) at the vein margin associated with quartz veining.

3.5.3 Electron Dispersive Spectroscopy (EDS)

EDS analysis of 56 gold grains shows variability of Au:Ag ratios between gold grains from the different styles of gold mineralization described in Table 1 (Figure 3-7a).

Inclusion I, the most common style of gold mineralization observed has a wide range of Au:Ag ratios with an average of 6.6 ± 2.7 (n=29) and a range from 3 to 12.8 (median = 5.4). Free Gold I is associated with grain margins and fractures, and has a narrower range of values with an average of 3.7 ± 0.7 (n=23, median = 3.3). The less common styles of gold mineralization are not as well represented and have averages of 3.8 ± 1.1 (n=2, median 3.8) for Inclusion II, and 8.1 ± 1.5 (n=4, median 7.8) for the tourmaline associated Free Gold II.

Eight telluride grains were analyzed, six were inclusions <10 μm in size (Inclusion I) and two were in pyrite grain fractures (Free Gold I). All are associated with fine-grained, inclusion-rich and haloed pyrite grains in the ankerite vein margins. The four silver tellurides plot between stutzite (Ag_7Te_4) and hessite (Ag_2Te) on a ternary diagram but are closer to the composition of stutzite. The gold-silver tellurides trend towards the composition of petzite (Ag_3AuTe_2 ; Figure 3-7b, Appendix C.1).

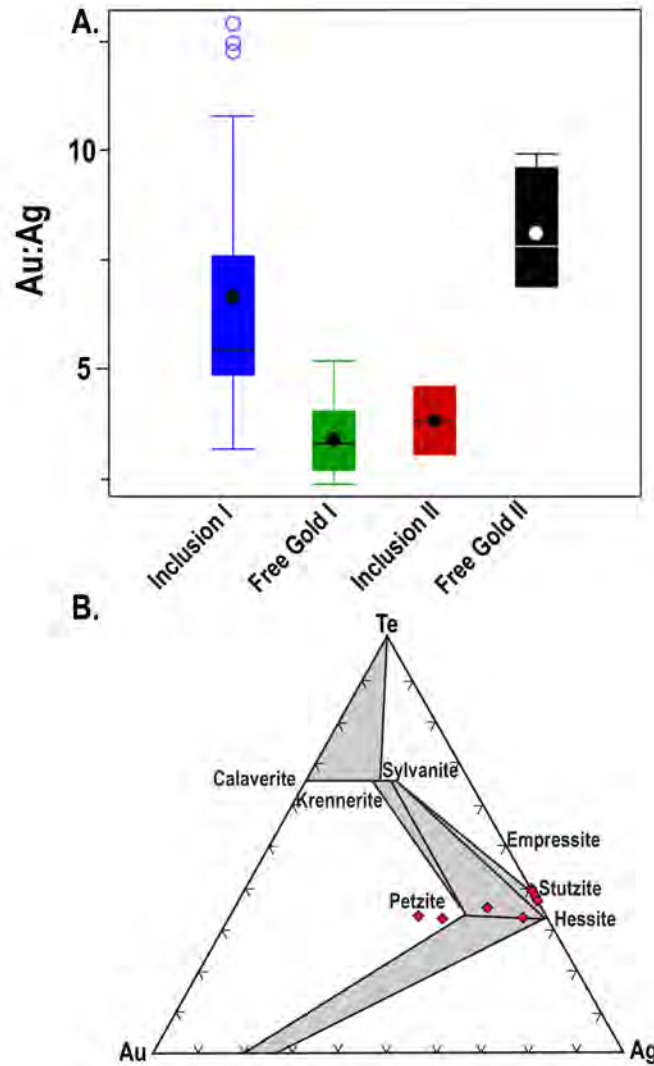


Figure 3-7. Gold EDS results. A. Boxplot showing the difference in Au:Ag ratio between different styles of gold mineralization (Inclusion I (n=29), Free Gold I (n=23), Inclusion II (n=2), Free Gold II (n=4)) (EDS analysis). B. Tellurides occur as both Au and AgAu telluride inclusions in P1 pyrite grains. Ag tellurides fall in the between Stutzite ($Ag_{5-x}Te_3$) and Hessite (Ag_2Te) while AuAg tellurides trend towards Petzite (Ag_3AuTe_3) (EDS analysis). Ternary plot adapted from Voudouris et al. (2011) and Ag, Te, and Au values were normalized to 100%. For the boxplot, the horizontal line represents the median, the solid black dot represents the mean, and the box represents the 25th to 75th percentile of the data. Whiskers are drawn to the last data point that is 1.5 times the length of box from the maximum and minimum. Open circles are outliers (within 3 box lengths), open triangles are far outliers (beyond 3 box length).

3.5.4 Pyrite Textures

Three generations of pyrite growth (Py₁₋₃) are observed in the Dome ankerite veins based on texture, gold content and context (Table 3-2). Py₁ is the earliest stage of pyrite growth and is characterized by fine-grained anhedral to subhedral pyrites, which are generally sieve textured and inclusion rich with ragged margins (Figure 3-8a, b). These grains are ubiquitous in the ankerite veins and are the only type of pyrite found in the core ankerite portion of the vein where it is not overprinted by later veining. They are commonly associated with chalcopyrite and sphalerite mineralization and occasionally molybdenite (Figure 3-8). Their inclusions generally consist of arsenopyrite, chalcopyrite, gold and ankerite, and less commonly sphalerite and rutile. Gold in Py₁ occurs as inclusions in the core of the grain (Inclusion I; Figure 3-6a, b). Py₁ in the central portions of the veins are very disseminated, generally as single grains or small bunches of grains in coarse-grained ankerite and quartz.

Table 3-2. Summary of the pyrite generations observed in the Dome ankerite veins

Type	Description	Gold Mineralization	Context
Py ₁	Fine-grained, subhedral to anhedral, sieve textured, inclusion rich	Inclusion I	Vein margins and vein center
Py ₂	Euhedral to subhedral with growth haloes and rim/core structure	Inclusions I., Free Gold I.	Vein margins and altered vein material
Py ₃	Medium to coarse-grained, anhedral to subhedral grains with no core/rim structure or halo	Inclusion II., Free Gold I.	Vein margins and later quartz veining

Py₂ is observed at vein margins as well as regions of the ankerite vein, which are overprinted by later sericitic alteration and tourmaline stringers. Py₂ are medium to coarse-grained subhedral to euhedral pyrites that commonly overprint the early Py₁ resulting in an inclusion rich central anhedral core with inclusion poor euhedral

overgrowth (Figure 3-8c, d). Py_2 is commonly associated with monazite, rutile, tourmaline, and intense sericitization. However, the sieve-textured cores of overprinted Py_1 grains overprinted by Py_2 rarely host gold inclusions, but more commonly silicate, and galena inclusions. The haloed Py_2 grains are the primary host for telluride inclusions, often spatially associated with galena mineralization. While Inclusion I gold is uncommon with Py_2 , the grain margins of Py_2 commonly are associated with Free Gold I (e.g., Figure 3-6c).

However, the most common host for Free Gold I is regions with Py_3 . Py_3 dominates at the inner edge of the ankerite vein margins and regions of vein that are overprinted by quartz veining. Py_3 grains are coarse-grained, anhedral to subhedral, inclusion free with the exception of large gold inclusions (Inclusion II) and contain no visible growth haloes (Figure 3-8e,f). They are not generally associated with other sulfide minerals like Py_1 and Py_2 but are associated with sericite and quartz. They host gold as large inclusions (Inclusion II; Figure 3-8e,f) at their grain margins and at grain boundaries (e.g., Figure 3-6f).

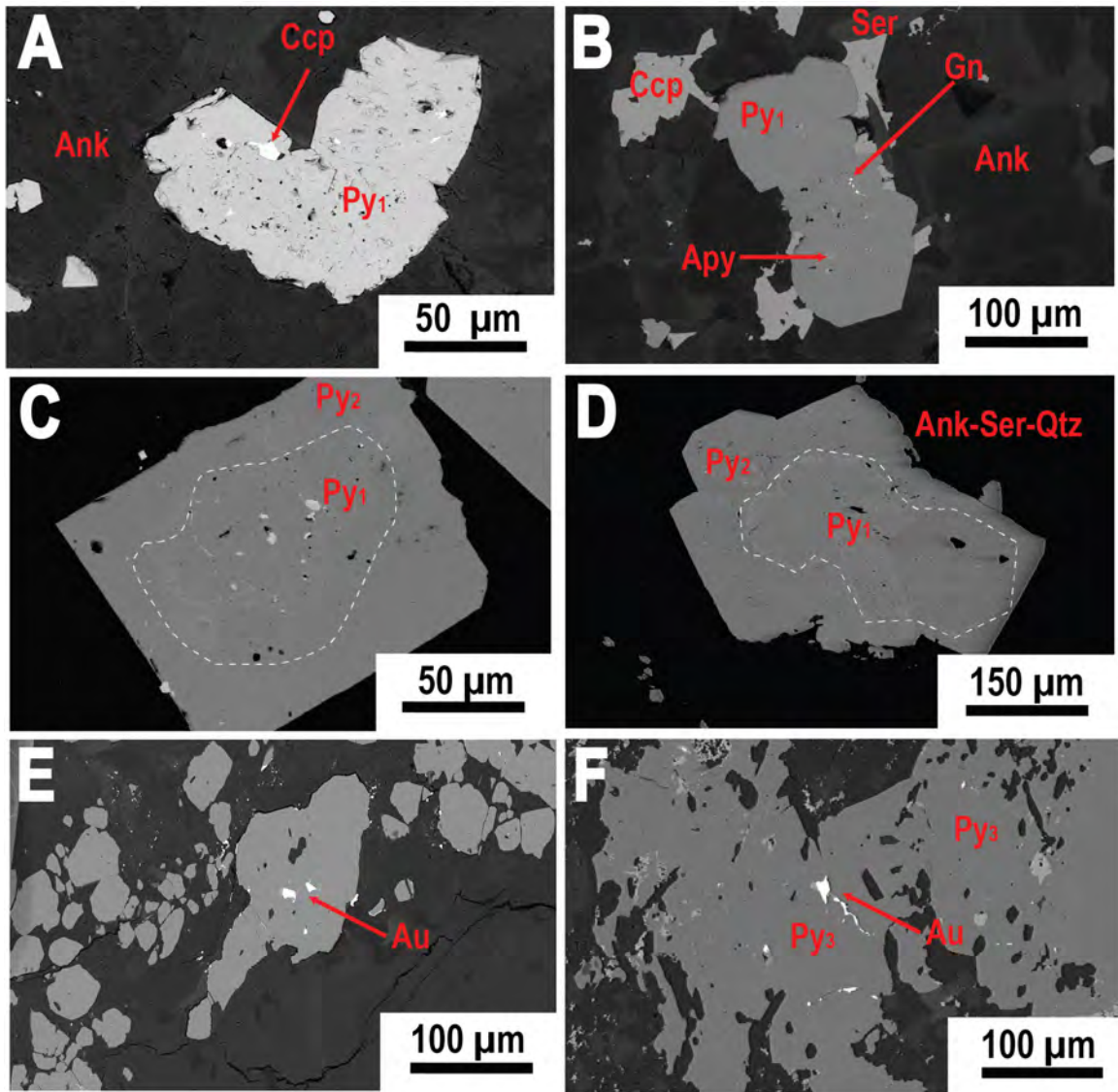


Figure 3-8. BSE-SEM photomicrographs of the three generations of pyrite growth observed in the Dome ankerite veins. A-B. Inclusion rich, sieve textured Py₁ pyrites with chalcopyrite mineralization C-D Euhedral Py₂ overgrowth on Py₁ cores. E-F. Subhedral Py₃ pyrite growth with no core-rims structure or growth haloes, associated with gold mineralization (Inclusion II).

3.5.5 Dynamic Secondary Ion Mass Spectrometry (D-SIMS)

The arsenic and gold content of 13 pyrite grains were analyzed by D-SIMS to characterize the presence and nature of refractory gold. The pyrite grains contain a wide range of As and Au values, 0.5 – 33 ppm Au and 34 – 4400 ppm As (Figure 3-9, Table 3-3). Plotting As vs Au reveals a positive correlation between them, and that As and Au content appear to be related to the type of pyrite analyzed (Py_{1,2,3}). Py₁ pyrites have the highest refractory Au and As contents (average 16.85 ppm Au and 2065 ppm As), and Py₂ and Py₃ have lower Au and As contents (Table 3-3). The molar ratio of Au to As was also calculated, and all but one Py₃ sample (py07) fall well below the ~0.02 threshold defined by Reich et al., 2005 as a solubility limit for Au in arsenian pyrites, with most falling closer to the solubility limit of 0.004 proposed by Deditius et al., 2014 for higher temperature orogenic pyrite (Table 3-3).

The dynamic mode of SIMS enables detection of submicron gold inclusions from changes in signal intensity in SIMS depth profiles (e.g., Figure 3-10; Chrysoulis, 1990). D-SIMS depth profiles were used to investigate the nature of the refractory gold; nano-particulate vs. lattice bound (solid-solution gold). Au nano-inclusions register as spikes in signal intensity where a homogeneous distribution appears as a flat profile. In general, Py₁ and Py₂ have flat profiles indicating a homogeneous distribution of gold in the pyrite (Figure 3-10, Table 3-3). Py₃ as well as two Py₁ analyses show evidence for the presence of gold nanoparticles ranging from 100 nm to 600 nm in size (Appendix C.2).

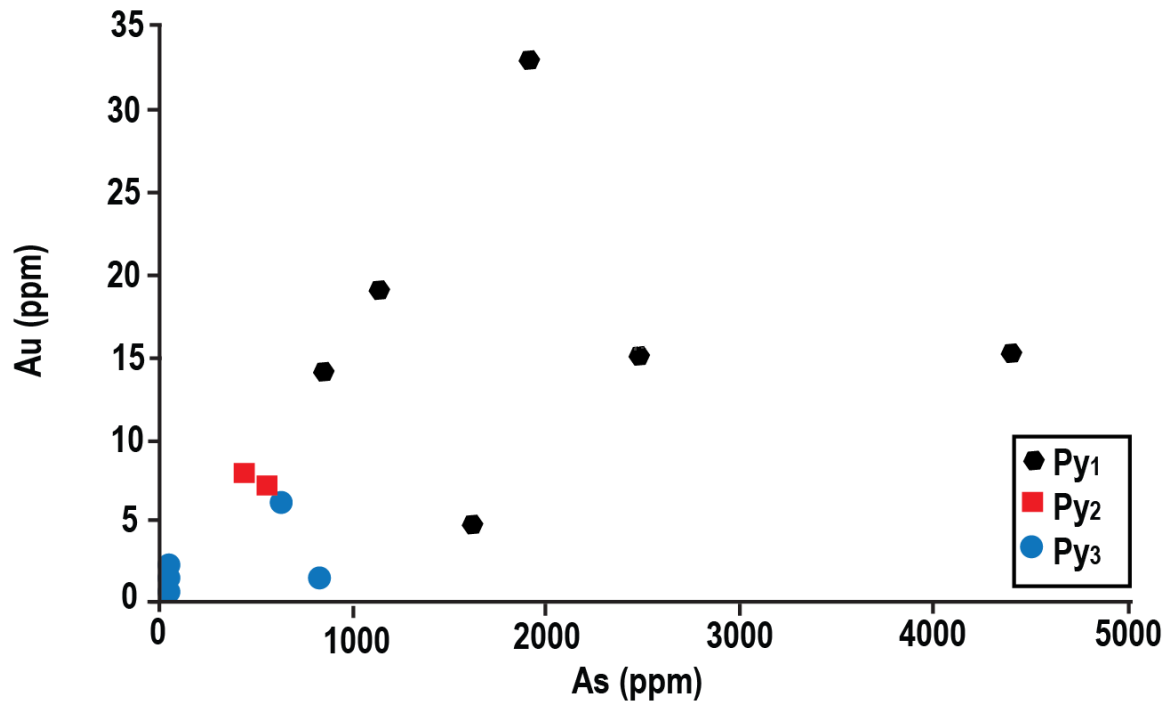


Figure 3-9. Plot of As and Au contents of the three pyrite types determined by D-SIMS. Increasing pyrite Au contents correlated with As content where fine-grained (Py₁) pyrites have the highest gold contents.

Table 3-3. Summary of calculated As and Au values by D-SIMS analysis of “barren” pyrites and the interpreted gold distribution based on the depth profiles

Texture	Grain I.D.	Au (ppm)	As (ppm)	D-SIMS Profile	Molar Au:As
Py1	py03	4.89	1614	Nanoparticle	0.001
	py04	14.91	2481	Homogeneous	0.002
	py05a	15.23	4400	Homogeneous	0.001
	py05b	18.94	1132	Nanoparticle	0.006
	py08	33.00	1914	Homogeneous	0.007
	py12	14.12	848	Homogeneous	0.006
<i>Mean (n=6)</i>		<i>16.85±9.19</i>	<i>2065±1281</i>		
Py2	py10	7.92	456	Homogeneous	0.007
	py11	6.11	644	Homogeneous	0.004
<i>Mean (n=2)</i>		<i>7.02±1.28</i>	<i>550±133</i>		
Py3	py01	1.44	843	Nanoparticle	0.001
	py02	6.95	577	Nanoparticle	0.005
	py06	1.05	24	Nanoparticle	0.017
	py07	2.35	40	Nanoparticle	0.022
	py09	0.50	34	Nanoparticle	0.006
<i>Mean (n=5)</i>		<i>2.46±2.60</i>	<i>303±383</i>		
<i>Total Mean</i>		<i>9.8±0.3</i>	<i>1154±1229</i>		

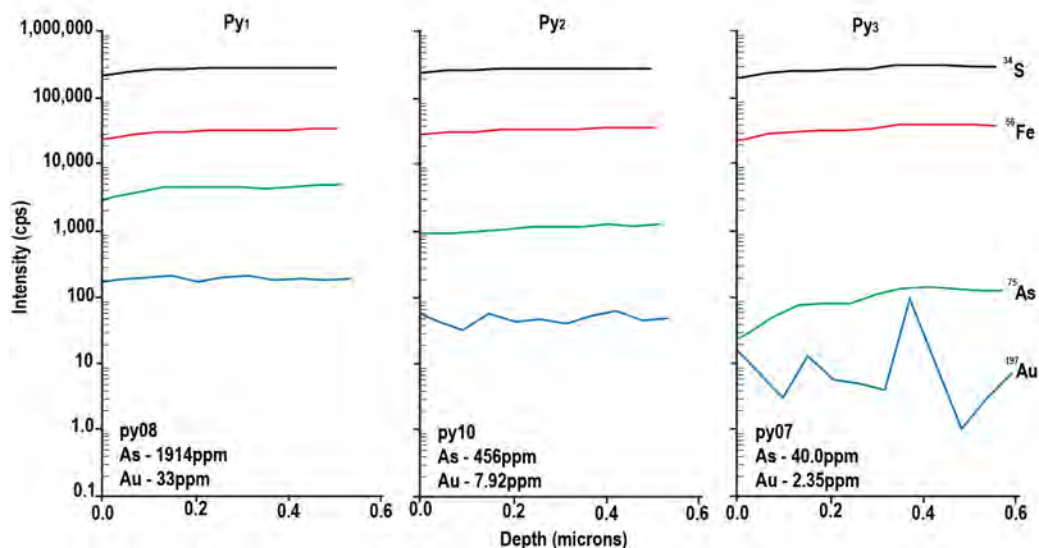


Figure 3-10. Depth profiles by D-SIMS showing the distribution of gold in the three different types of pyrite grains. A profile py07 is indicative of nano-particulate gold, while a flat profile like py08 is characteristic of gold evenly distributed in the pyrite crystal lattice.

3.5.6 SR- XRF

SR-XRF mapping at multiple scales on over 20 samples has identified significant heterogeneity in the trace element content of pyrites in the Dome ankerite veins. The distribution of trace elements in pyrite is related to the pyrite type (Py_{1,2,3}; Figure 3-11). A progressive zonation of trace elements from core to rim of pyrite grains is observed. Regions of Py₁ growth are enriched in trace metals and metalloids (Cu, Ni, Zn, Au, As) with respect to later stages of pyrite growth (Figure 3-11 to 3-16). This is observed as enrichments in As, Cu, Ni and Au, and/or inclusions that are Cu, Zn, As and Au rich in Py₁ (Figure 3-12). This trace element fingerprint is also observed in the Py₁ core of euhedral Py₂ grains (Figure 3- 13, 3-14, 3-16). In these grains, the metal (and inclusion) enriched Py₁ core is overgrown by a rim of Ni enriched pyrite, which generally does not contain any inclusions (Py₂). This Ni rich rim is depleted in other trace metals and metalloids with respect to the Py₁ core (Figure 3-13, 3-14 ,3-16). This core-rim distribution pattern is the most commonly observed distribution of trace elements in all

samples and is also confirmed in SR-XRF maps collected at the CLS (Figure 3-14). These maps are post processed using Peakaboo which fits the whole spectrum rather than creating the maps from pre-selected ROI's and in doing so reduces the effects of peak overlap (Figure 3-14B). Py₃ grains show no core-rim structures or spatial heterogeneity in their trace element contents. They have lower trace metal contents than Py₁ and Py₂ and are generally associated with free gold (Free Gold I; e.g., Figure 3-15, 3-16). Point XRF data for Py₁ associated Inclusion I gold, tourmaline stringer associated Free Gold II and Py₃ associated Free Gold I reveal that the gold also contains variable trace amounts of other trace metals such as Fe, As, and Cu (Figure 3-16). Py₁ inclusion hosted gold contains higher trace metal contents including As, Cu and Se, and tourmaline associated gold constrains Ni and (Figure 3-17).

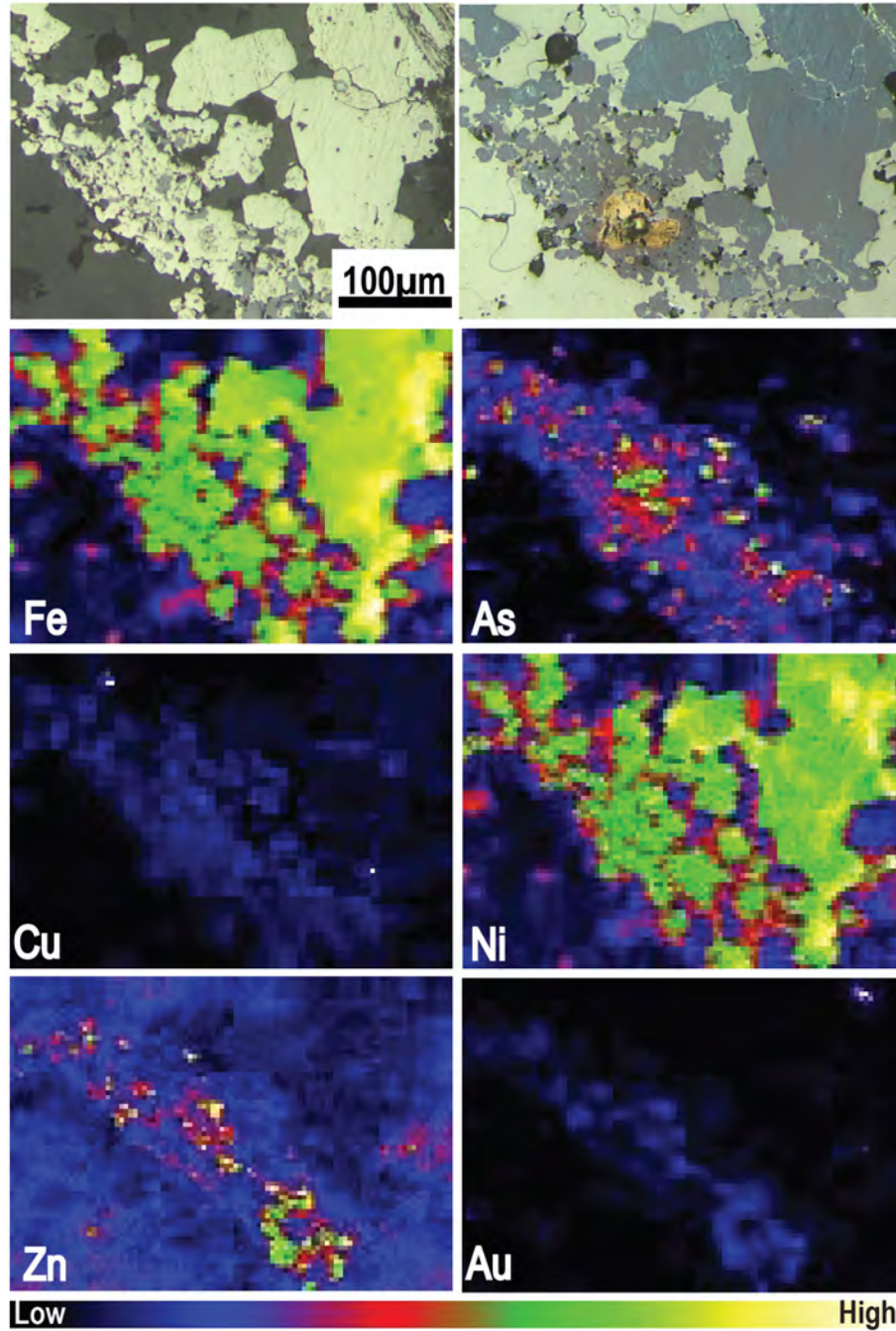


Figure 3-11. SR-XRF maps of Py08 (Py₁ growth) following SIMS analysis reveals that Py₁ pyrite growth is associated with sphalerite and is enriched in As, Cu, and Au while Py₂ growth is enriched in Ni (sample C406934, 5 μm resolution).

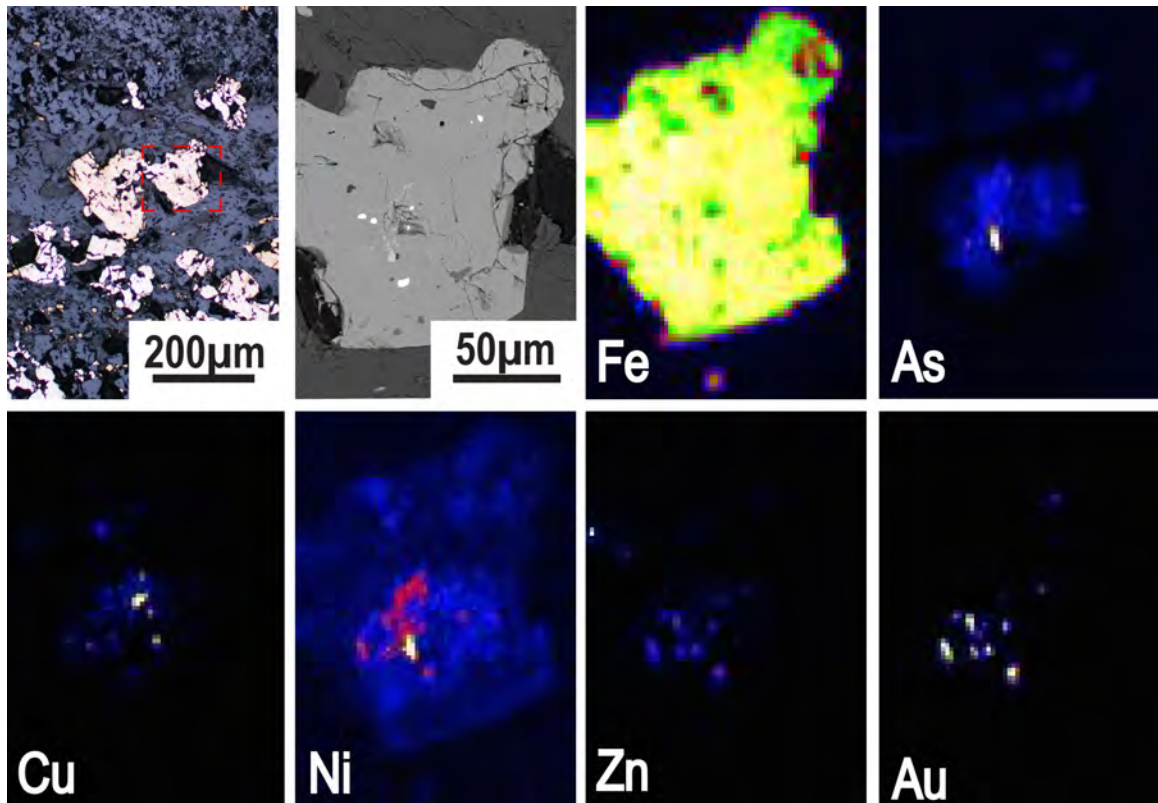


Figure 3-12. SR-XRF map of an inclusion rich Py_1 grain which is enriched in As, Ni and Au with Au, As, Zn, Ni, and Cu rich inclusions (Inclusion Gold I) (C406932, 2 μm resolution)

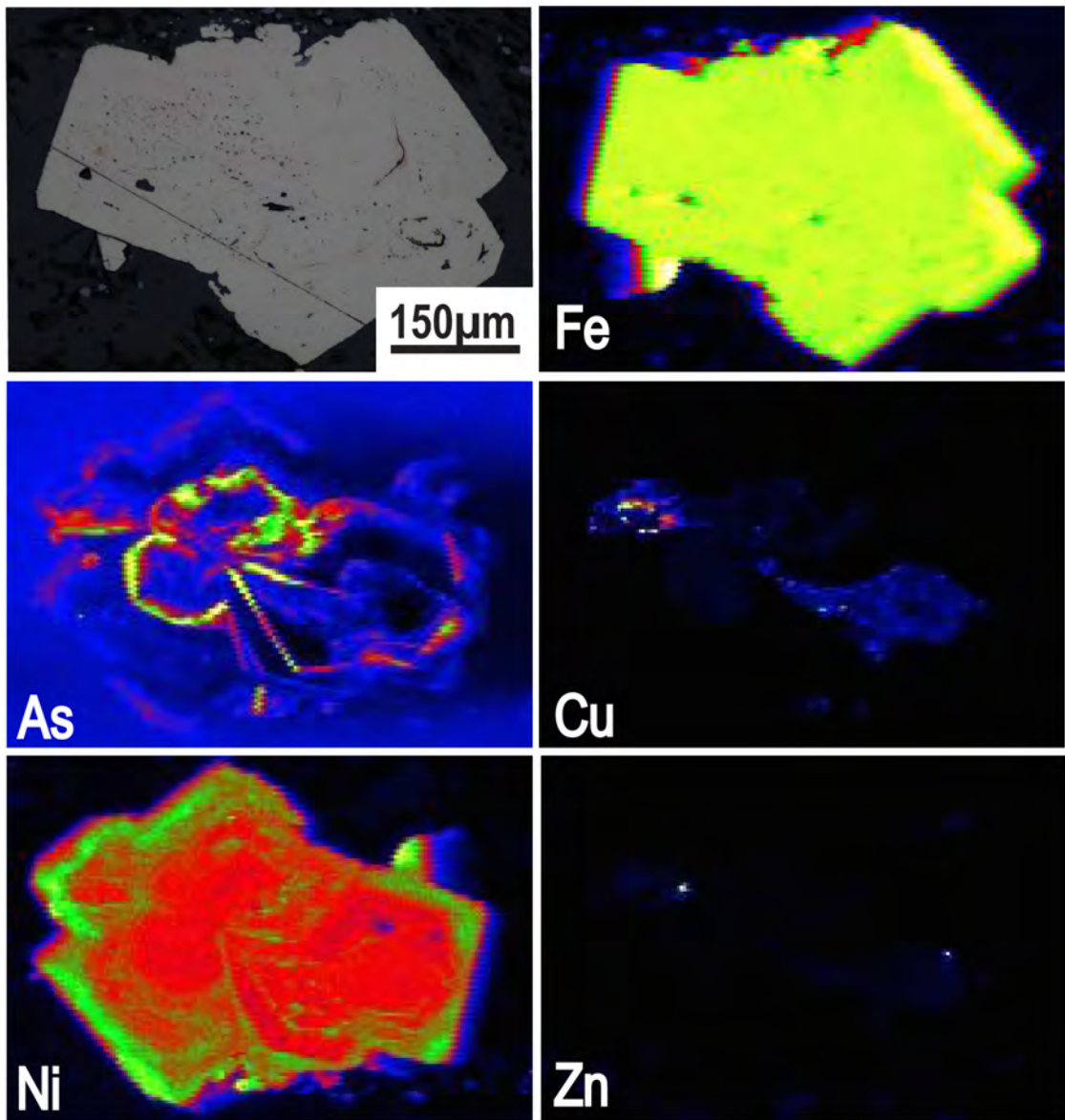


Figure 3-13. SR-XRF map of a Ni rich Py_2 grain with a Py_1 core enriched in Cu, As, and Zn (C407891A, 3 μm resolution).

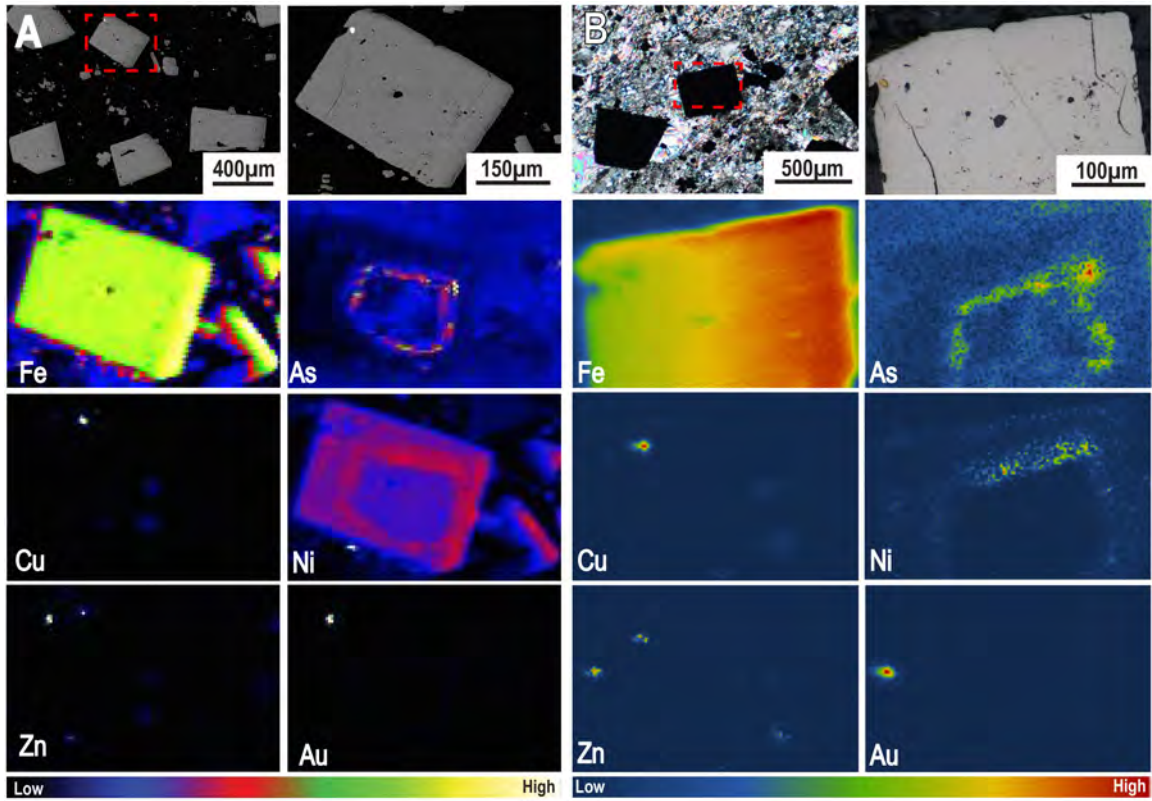


Figure 3-14. SR-XRF maps of a Py_1 grain overgrown by Ni enriched Py_2 growth confirming the trace element distribution observed in ROI based maps (A) with spectral fit based maps (B). A. 5 μm resolution ROI based maps collected at the APS. B. 3 μm resolution maps collected at the CLS and processed in Peakaboo (C407891A).

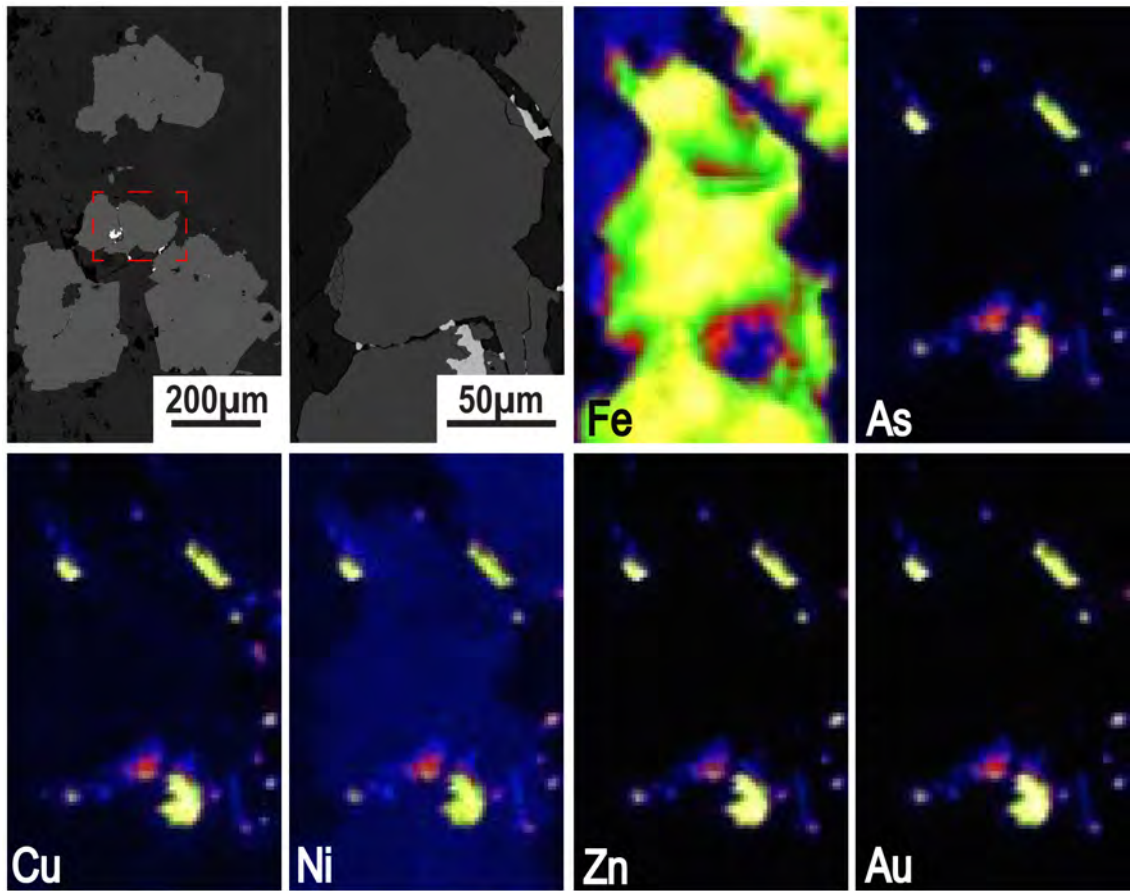


Figure 3-15. SR-XRF maps of Py₃ grains which lack rim/structures haloes, but hosts Au at the grain margins and in fractures (Free Gold I) (C406934, 3 μm resolution)

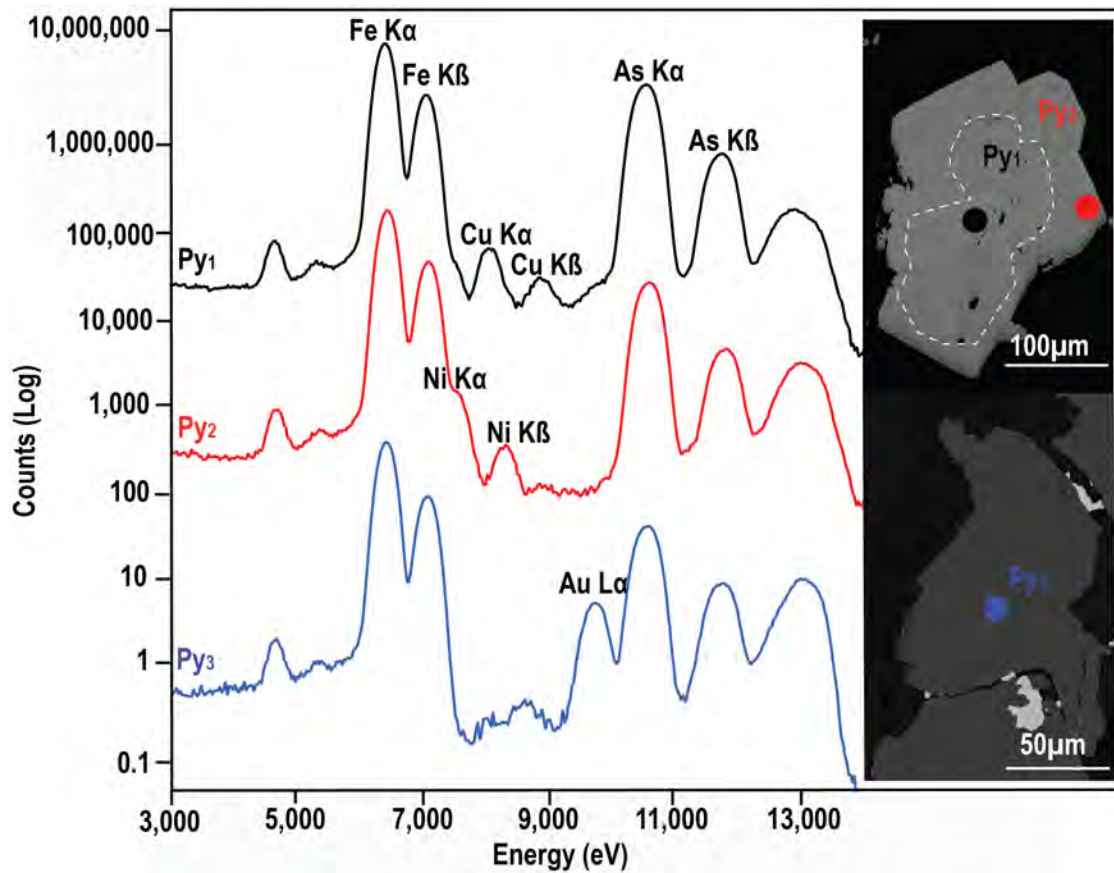


Figure 3-16. SR-XRF spectra showing the variability in trace element content of the three pyrite types. The Py₁ spectra was displaced by multiplying by 100, and the Py₃ was displaced by dividing by 100.

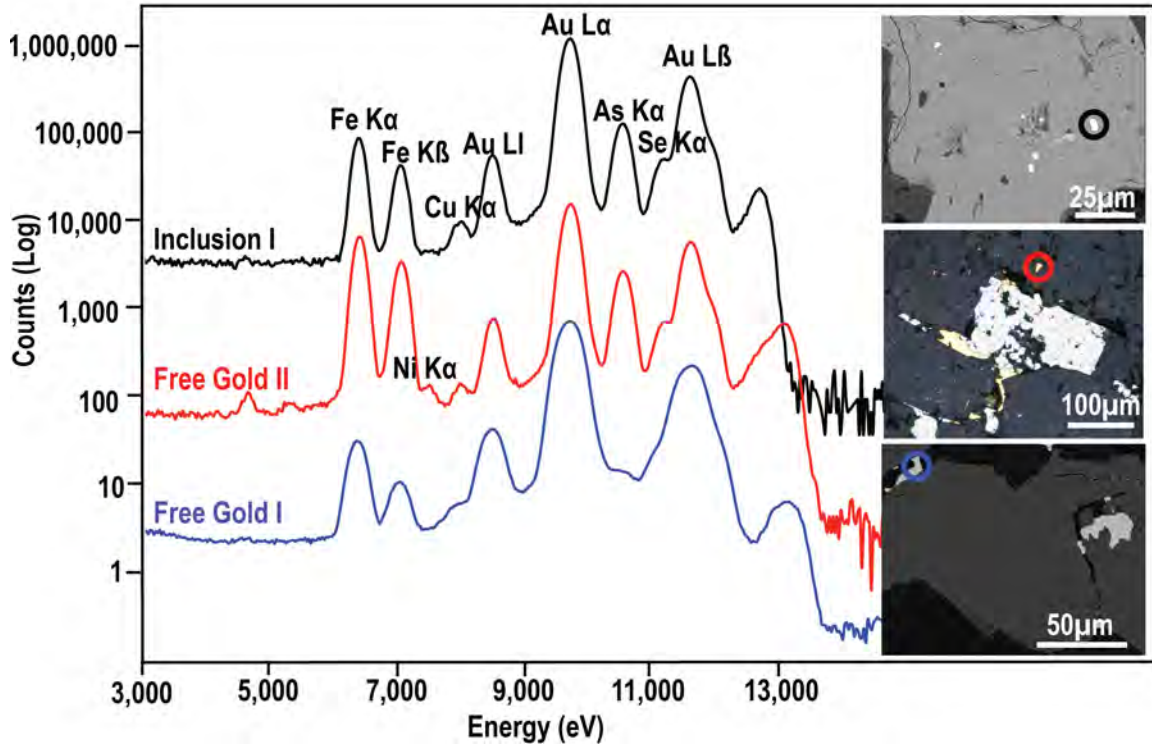


Figure 3-17. SR-XRF Spectra showing the variability in trace element content between gold inclusions (Inclusion I) in Py_1 , free gold II (FGII) associated with tourmaline stringers, and free gold (FGI) associated with Py_3 . The spectra for Free Gold I was displaced by dividing by 100 and the spectra for Inclusion 1 was displaced by was multiplying by 100.

3.6.0 Discussion

The earliest of three stages of gold mineralization observed in the Dome ankerite veins occurred with primary ankerite vein formation, and deposited the bulk of the vein sulfide content. Table 3-4 summarizes the key characteristics of each mineralizing event. This early mineralization event is characterized by extensive Py_1 growth, which is enriched in trace metals and metalloids. Py_1 growth is associated with chalcopyrite and sphalerite mineralization, and commonly hosts inclusions of chalcopyrite, arsenopyrite, and electrum. Less commonly it is associated with molybdenite and minor telluride inclusions. SR-XRF mapping and D-SIMS reveal that in addition to being inclusion rich,

Py₁ pyrites are arsenian in nature with As values ranging from 800-4400 ppm, and commonly contain regions enriched in Cu and Ni. In systems such as this, the Au and As content of arsenian pyrites is largely controlled by fluid-rock interactions (Deditius et al., 2014). Arsenic was likely introduced into the pyrite structure through a substitution of As⁻ for S⁻ to form Fe(As,S)₂, a common mechanism under reducing conditions, or as a coupled substitution with gold (e.g., Au⁺ + As³⁺ ↔ 2Fe²⁺; Simon et al., 1999; Pals et al., 2003; Reich et al., 2005; Deditius et al., 2008, 2014). It is also possible for As³⁺ to heterovalently substitute for Fe²⁺ in pyrite (Fe,As)S₂, however, this generally only occurs under acidic, oxidizing, and low temperature conditions typical of high sulfidation epithermal systems (e.g., Chouinard et al., 2005a,b; Deditius et al., 2008). The intimate relationship between Au and As in Py₁ growth is related to the transport of gold in orogenic fluids. Under a wide range of conditions, Au is transported as Au(HS)₂⁻ and deposition is thought to occur through coupled reactions during pyrite formation and fluid interaction with wall rocks. This occurs by reactions such as 'FeO'_{rock} + 2 H₂S = FeS₂ + H₂O + H₂ and Au(HS)₂⁻ + H⁺ + ½ H₂ = Au + 2 H₂S (Mikucki, 1998; Phillips and Evans, 2004; Deditius et al., 2014; Phillips and Powell, 2015). This mechanism is supported by the sulfide rich nature of the ankerite vein margins where the iron rich wall rock (Fe-tholeiite) likely contributed Fe to the system. The bulk of pyrite associated gold mineralization and Py₁ pyrite growth also occurs in this wall rock contact region.

Table 3-4. Summary of mineralization events in the Dome mine ankerite veins, their pyrite content and gold mineralization. (QFV – quartz – fuchsite vein, Ank – ankerite, Apy – arsenopyrite, Ccp- chalcopyrite, Sp- sphalerite, Tur – tourmaline, Ser – sericite, Mon – monazite, Rt – rutile, Qtz – quartz,)

Timing	~2,690 - 2,679	~2,667 Ma	~2,665 Ma
Vein Event	Ankerite Veins	Tourmaline Rich, QFV	Quartz Veining
Pyrite Type	Py ₁	Py ₂	Py ₃
Py Trace Element	Cu, As, Ni	Ni, As	As
Py As, Au (ppm)	16.85 Au, 2065 As	7.02 Au, 550 As	2.46 Au, 393 As
Gold Type	Inclusion I, refractory	Free gold II, refractory, tellurides	Visible Gold, Free Gold I, Inclusion II
Refractory Gold	Lattice	Lattice	Nano-particulate
Average Au:Ag	6.6	8.1	3.7
Accessory Minerals	Ank, Ccp, Apy, Sp, Mol	Tur, Ser, Mon, Rt, Qtz	Qtz, Ser

Sulfur was removed from the fluid during pyrite formation, lowering the solubility of gold in the fluid and facilitating gold deposition. This accounts for the textural relationships observed, where gold occurs as inclusions in Py₁ pyrite growth.

In addition to facilitating gold deposition, pyrite formation commonly scavenges trace metals and gold, incorporating them into its structure and as nano-particles, a process that is enhanced at lower temperatures (Mikucki, 1997; Deditius et al., 2011). This includes metals such as Ni and Cu that can isovalently substitute into pyrite for Fe²⁺ in up to weight percent quantities (Ortega et al., 2004; Rosua et al., 2008; Deditius et al., 2008). Au is generally heterovalently incorporated into the pyrite lattice as Au⁺ through the coupled reaction with As described earlier. The threshold for this type of solubility has been defined by Reich et al. (2005) as a molar Au:As of 0.02 and was refined for orogenic deposits to be 0.004 by Deditius et al. (2014). SIMS analysis reveals that Py₁ As and Au contents fall well below the 0.02 molar ratio and close to the 0.004 limit.

However, D-SIMS analysis indicates that refractory gold is primarily homogeneously distributed in the arsenian pyrite, not as nano-particles. Two samples have Au:As ratios above the 0.004 threshold and do not host nano-particulate gold, a likely result of the

lower formation temperature of Py₁ growth from ~ 200°C ankerite vein forming fluids (Reading, 1982). Homogeneously distributed Au in pyrite is predominantly Au⁺, indicating that the ore bearing fluids that deposited the pyrite were undersaturated with respect to native Au (Reich et al., 2005). While Py₁ is also characterized by the presence of gold inclusions, the total gold contribution to ankerite ore by Py₁ forming fluids is negligible. The ankerite vein margins are pyrite rich, however, they constitute <10% of the vein material and contain <35 ppm Au making Py₁ refractory gold a negligible source of gold to the system. Gold inclusions associated with Py₁ growth have a wide range of Au:Ag ratios, which are systematically higher than for free gold associated with later mineralizing events and the average bulk rock values (Stromberg et al., 2017). This agrees with the observation by Proudlove et al. (1989) that ankerite rich samples had higher Au:Ag ratios than regions of veining heavily overprinted by later veining.

The second stage of gold mineralization in the Dome ankerite veins is characterized by Py₂ growth. The overprinting nature of Py₂ growth and its relationship with tourmaline places its timing towards the beginning of main stage mineralization at the Dome mine, characterized by tourmaline-rich veining and coinciding with D₃ and D₄ deformation events (Pressacco et al., 1999; Stromberg et al., 2017). Gold is not commonly associated with Py₂ growth apart from minor tellurides and negligible refractory gold (<10 ppm). D-SIMS indicates that refractory gold in Py₂ growth occurs homogeneously distributed in the pyrite and Au and As content sit at or near the 0.004 Au:As molar ratio for orogenic gold systems (Deditius et al., 2014). However, free gold (Free Gold II) is observed associated with tourmaline stringers and in tourmaline rich regions of the vein margins. This type of gold mineralization has a distinctly higher Au:Ag ratio than inclusion hosted gold, as well as variable trace element contents (Fig. 17). The negligible refractory and pyrite-associated gold may be related to remobilization of gold from Py₁ as well as telluride deposition. Generally, as Au-tellurides form, the role of pyrite as a host for refractory gold becomes minor (Deditius et al., 2014). The tellurides associated with Py₂ rims geochemically resemble stutzite (Ag_{5-x}Te₃) and trend towards petzite (Ag₃AuTe₃) when gold is present. The deposition of these Ag rich tellurides may have depleted the Ag budget of the fluids resulting in more Au enriched electrum deposition. While the sample

size for tourmaline associated gold (Free Gold II) is small, a high Au:Ag ratio is also observed in the quartz fuchsite vein with values as high as ~200 reported (Harris, 2013).

The geochemical signature of Py_2 growth and gold mineralization points to a temporal relationship with the formation of the massive quartz fuchsite vein (QFV). Like the ankerite veins the QFV has anomalous Pb, Ni, and Te contents with respect to other veining in the deposit (Moritz and Crocket, 1990; Harris, 2012; Stromberg et al, 2017). The QFV formed from a Au and Pb bearing fluid that also introduced Cr, Ni, Te, As and K into the system (Moritz, 1988). Overprinting tourmaline veining in the ankerite veins is related to higher K_2O , Cr, V, TiO_2 , Ni and Co values in the bulk rock data and rutile is commonly associated with tourmaline stringers (Stromberg et al., 2017). The mobility of redox sensitive elements such as Cr, and the higher Pb, Ni and tellurium contents of this event signals a change in redox conditions from the ankerite forming fluids. Te is generally poorly soluble under reducing conditions, and a more oxidized fluid is necessary for the oxidation and mobilization of Cr in the system (Dinel et al., 2008a; Brugger et al., 2017) These metals were likely scavenged from porphyry intrusions and komatiites in the DFDZ which acted as a long-lived fluid conduit for the system and hosts the highly auriferous QFV (Stromberg et al., 2017).

While the mineralization event associated with Py_2 growth did not contribute the bulk of the gold to the Dome ankerite veins, there is evidence that it may have remobilized trace metals from inclusion and trace metal rich Py_1 growth. The porous nature of the sieve textured and inclusion rich pyrites may have acted to enhance metal remobilization from the pyrite structure and nanoparticles by hydrothermal fluids (Deditius et al., 2014). Trace metals that occur as nanoparticles or inclusions are readily expelled from pyrites during metamorphism, while trace elements that are stoichiometrically incorporated in the pyrite structure tend to remain or become more enriched (Large et al., 2007, 2009, 2011). This is evidenced by a lack of metal rich inclusions in Py_1 growth when overprinted by Py_2 growth, corroded margins of Py_1 growth, and the concentration of arsenopyrite inclusions and arsenic at the boundary between different generations of pyrite, indicating dissolution

(e.g., Figure 3-6c, 3-7e,c,d, 3-12, 3-13). This has also been observed in other orogenic systems (e.g., Sung et al., 2009; Cook et al., 2009).

The final and most significant mineralization event in terms of gold tenor was accompanied by Py₃ growth and quartz veining. SR-XRF mapping and D-SIMS analysis reveal that Py₃ growth is depleted in metals and metalloids with respect to earlier stages of pyrite growth. The low gold content of Py₃ growth is typical of vein stage coarse-grained pyrites, which generally contain less than 10 ppm Au (Deditius et al., 2014). The Au:As molar ratios are greater than the 0.004 threshold defined by Deditius et al., 2014 for orogenic systems, and D-SIMS analysis indicates that refractory gold occurs primarily as nano-particulate rather than homogeneously distributed in the pyrite. The lack of arsenopyrite mineralization related to Py₃ growth indicates that the fluids contained little As, and the presence of nanoparticulate gold reveals that the fluids may have been saturated with respect to native gold. The bulk of the gold associated with Py₃ mineralization occurs as Free Gold I (FGI) in fractures and on grain boundaries. SR-XRF maps using ROI's shows an exaggerated trace element content in FGI (e.g. Figure 3-15) due to massive concentration of gold, which results in high gold counts dominating the spectrum. When investigated further by point analysis it is apparent that FGI gold is depleted in trace metals with respect to earlier stages of gold mineralization (Figure 3-17). This style of gold mineralization has a Au:Ag of 3.7, closely resembling the average bulk rock Au:Ag of 3.1 (Stromberg et al., 2017). Less commonly, Py₃ growth hosts large inclusions (<40 µm) of electrum with an average Au:Ag ratio of 3.8, falling in the same range as Free Gold I. The intimate relationship between gold and Py₃ pyrite points towards a deposition mechanism similar to Py₁ where pyrite formation results in a loss of S from the fluid and drop in the solubility of gold. It is also possible that fluid mixing with more oxidized Py₂ fluids and/or pressure changes during shear vein formation as dilational cracks opened in the ankerite veins.

Remobilization processes in orogenic systems commonly concentrate gold and metals in recrystallized later stages of pyrite growth. This can result in enrichments in gold content of up to two orders of magnitude with no significant changes in As concentration (e.g.,

Sung et al., 2008; Large et al., 2007; Morey et al., 2008). However, this is not observed at the Dome mine, as later stages of pyrite growth are depleted in Au with respect to Py₁ growth. While Py₃ growth does contain nano-particulate gold near and below the solubility limit for Au in pyrite, this is not likely due to the extensive recrystallization of earlier pyrite and liberation of Au as is observed by Sung et al. (2009) and Cook et al. (2009). In the case of the Dome ankerite veins it appears that any metals that were remobilized from Py₁ growth did not migrate into overprinting Py₂ growth except perhaps Ni. Instead remobilized metals may have been transported with fluids to a distal location. This remobilization and removal of gold and metal inclusions in sieve textured Py₁ in addition to overprinting Py₂ and Py₃ growth and their associated gold endowments helps explain the difficulty in applying trace element vectors to gold in the ankerite veins. Input from multiple gold sources with different Au and Ag contents, telluride mineralization, and the remobilization of early gold also accounts for the heterogeneity in Au:Ag with no systematic variation across the ankerite strike length observed by Fryer et al., 1979; Proudlove et al., 1989; Stromberg et al., 2017. The similarity between the average bulk rock Au:Ag ratio and Py₃ associated gold supports that the bulk of the gold mineralization in the ankerite veins was introduced late into the system.

3.7.0 Conclusions

The Dome mine ankerite veins have remained an enigmatic ore body over the 100 year history of the Dome mine. Gold contribution by more than one mineralizing event to the ankerite veins is well documented, but the relative gold content of different events as well as trace element associations with gold was not well understood. Additionally, the initial ankerite forming event was historically considered to be non-auriferous (e.g., Kerrich and Fryer, 1979; Proudlove et al., 1989; Pressaco et al., 1999; Stromberg et al., 2017). From the overprinting textural and geochemical relationships revealed in pyrite growth in the Dome ankerite veins, the geochemical fingerprint and gold content of different fluid events can be discerned and the auriferous nature of the primary ankerite forming event is confirmed.

The range of pyrite Au and As concentrations for all three growth stages reported fall into the range of previously studied orogenic deposits (e.g., Reich et al., 2005; Deditius et al., 2014), and the variability observed between different mineralizing events is likely the result of differences in fluid temperature, metal content, and metamorphism. The increase in temperature from the ~200°C ankerite forming fluids to the 400-450°C quartz vein fluids (Reading, 1982; Kerrich and Fryer, 1979) acted to limit As and Au solubility (retrograde) in pyrite (Deditius et al., 2014). Higher temperatures also limit solubility of other trace metals such as Cu and Ni in pyrite. In the absence of post-depositional re-equilibrium or metamorphism it is suggested that pyrite can preserve the Au:As ratio of hydrothermal ore fluids (Deditius et al., 2014). This is not the case for Py₁ growth, however, Py₂ and Py₃ growth occurred penecontemporaneously with peak metamorphism and show no evidence for recrystallization and remobilization of Au and As. While the trace element content of Py₁ growth may not accurately reflect the As:As budget of the ankerite forming fluids due to remobilization, it is clear that they were more trace element rich than later mineralizing events. Py₃ growth is interpreted to represent the final fluid event to interact with the ankerite veins, and so it is likely that Py₃ Au and As contents are representative of the As budget of the ore forming fluid. Py₃ forming fluids also introduced the bulk of the gold into the system. However, the system was fertile for ~25 Ma during which gold was concentrated in the fluid over time with increasing metamorphism while trace elements such as As, Cu, Zn, and Ni were present earlier in the evolution of the metamorphic fluid.

This study demonstrates the power of characterizing pyrite trace element content for understanding complex orogenic mineralizing systems. The non-destructive, quick-scanning and full spectrum capabilities of SR-XRF mapping provide insights into the micron scale distribution of gold and trace metals in pyrite. It also allows for non-destructive geochemical fingerprinting of gold, a notoriously difficult task due to matrix effects. SR-XRF is very complementary to conventional geochemical analysis and when used together with SIMS, BSE-SEM and EDS analysis has provided insights into fluid chemistry and the multi-stage mineralization history at the Dome mine.

3.8.0 References

Abratis, P.K., Patrick, R.A.D. and Vaughan, D.J., 2004. Variations in the compositional, textural and electrical properties of natural pyrite: a review. *International Journal of Mineral Processing*, 74(1), pp.41-59.

Ayer, J., Amelin, Y., Corfu, F., Kamo, S., Ketchum, J., Kwok, K. and Trowell, N., 2002a. Evolution of the southern Abitibi greenstone belt based on U–Pb geochronology: autochthonous volcanic construction followed by plutonism, regional deformation and sedimentation. *Precambrian Research*, 115(1), pp.63-95.

Ayer, J.A., Ketchum, J.W.F., and Trowell, N., 2002b, New geochronological and Nd isotopic results from the Abitibi greenstone belt, with emphasis on timing and implications of Late Archean sedimentation and volcanism: Ontario Geological Survey Open File Report 6100, pp. 5-1–5-16.

Ayer, J.A., Barr, E., Bleeker, W., Creaser, R.A., Hall, G., Ketchum, J.W.F., Powers, D., Salier, B., Still, A., and Trowell, N., 2003, New geochronological results from the Timmins area: Implications for the timing of late-tectonic stratigraphy, magmatism and gold mineralization: Ontario Geological Survey Miscellaneous Paper, pp.33/1–33/9.

Ayer, J.A., Thurston, P.C., Bateman, R., Dubé, B., Gibson, H.L., Hamilton, M.A., Hathway, B., Hocker, S., Houlié, M., Hudak, G., Ispolatov, V., Lafrance, B., Leshner, C.M., MacDonald, P.J., Peloquin, A.S., Piercey, S.J., Reed, L.E., and Thompson, P.H., 2005, Overview of results from the Greenstone Architecture Project: Discover Abitibi Initiative. Ontario Geological Survey Open File Report 6154, 146 p.

Bateman, R., Ayer, J.A., Dubé, B., and Hamilton, M.A., 2005, The Timmins- Porcupine gold camp, northern Ontario: the anatomy of an Archean greenstone and its gold mineralization. Discover Abitibi initiative: Ontario Geological Survey Open File Report 6158, 90 p.

Bateman, R. and Bierlein, F.P., 2007. On Kalgoorlie (Australia), Timmins–Porcupine (Canada), and factors in intense gold mineralisation. *Ore Geology Reviews*, 32(1), pp.187-206.

Bateman, R., Ayer, J.A. and Dubé, B., 2008. The Timmins-Porcupine gold camp, Ontario: anatomy of an Archean greenstone belt and ontogeny of gold mineralization. *Economic Geology*, 103(6), pp.1285-1308.

Bigot, L. and Jébrak, M., 2015. Gold mineralization at the syenite-hosted Beattie gold deposit, Duparquet, Neoproterozoic Abitibi Belt, Canada. *Economic Geology*, 110(2), pp.315-335.

Bleeker, W., 1995, Surface geology of the Porcupine camp: Geological Survey of Canada Open File 3141, p. 13–47.

- Bleeker, W., Parrish, R.R. and Sager-Kinsman, A., 1999. High-precision U-Pb geochronology of the Late Archean Kidd Creek deposit and Kidd volcanic complex. *Economic Geology Monograph*, 10, pp.43-70.
- Bleeker, W., 2015. Synorogenic gold mineralization in granite-greenstone terranes: the deep connection between extension, major faults, synorogenic clastic basins, magmatism, thrust inversion, and long-term preservation, In: *Targeted Geoscience Initiative 4: Contributions to the Understanding of Precambrian Lode Gold Deposits and Implications for Exploration*, (ed.) B. Dubé and P. Mercier-Langevin. Geological Survey of Canada, Open File 7852, pp. 25–47.
- Bohlke, J.K., 1989. Comparison of metasomatic reactions between a common CO₂-rich vein fluid and diverse wall rocks; intensive variables, mass transfers, and Au mineralization at Alleghany, California. *Economic Geology*, 84(2), pp.291-327.
- Born, P., 1995, A sedimentary basin analysis of the Abitibi greenstone belt in the Timmins area, northern Ontario, Canada: Unpublished Ph.D. dissertation, Ottawa, Ontario, Carleton University, 489 p.
- Brisbin, D.I., 1997, Geological Setting of Gold Deposits in the Porcupine Gold Camp, Timmins, Ontario: Ph.D. thesis, Queens University, Kingston, Ontario, 532 p.
- Brugger, J., Liu, W., Etschmann, B., Mei, Y., Sherman, D.M. and Testemale, D., 2016. A review of the coordination chemistry of hydrothermal systems, or do coordination changes make ore deposits?. *Chemical Geology*, 447, pp.219-253.
- Cabri, L.J., Newville, M., Gordon, R.A., Crozier, E.D., Sutton, S.R., McMahon, G. and Jiang, D.T., 2000. Chemical speciation of gold in arsenopyrite. *The Canadian Mineralogist*, 38(5), pp.1265-1281.
- Campbell, Robert A., "Controls on Syenite-Hosted Gold Mineralization in the Western Timmins Camp" (2014). Electronic Thesis and Dissertation Repository. Paper 2636.
- Chouinard, A., Paquette, J. and Williams-Jones, A.E., 2005a. Crystallographic controls on trace-element incorporation in auriferous pyrite from the Pascua epithermal high-sulfidation deposit, Chile–Argentina. *The Canadian Mineralogist*, 43(3), pp.951-963.
- Chouinard, A., Williams-Jones, A.E., Leonardson, R.W., Hodgson, C.J., Silva, P., Téllez, C., Vega, J. and Rojas, F., 2005b. Geology and genesis of the multistage high-sulfidation epithermal Pascua Au-Ag-Cu deposit, Chile and Argentina. *Economic Geology*, 100(3), pp.463-490.
- Chryssoulis, S.L., Cabri, L.J. and Lennard, W., 1989. Calibration of the ion microprobe for quantitative trace precious metal analyses of ore minerals. *Economic Geology*, 84(6), pp.1684-1689.

- Chryssoulis, S.L., 1990. Detection and quantification of “invisible” gold by microprobe techniques. In *Gold* (Vol. 90, pp. 323-332).
- Cook, N.J. and Chryssoulis, S.L., 1990. Concentrations of invisible gold in the common sulfides. *The Canadian Mineralogist*, 28(1), pp.1-16.
- Cook, N.J., Ciobanu, C.L. and Mao, J., 2009. Textural control on gold distribution in As-free pyrite from the Dongping, Huangtuliang and Hougou gold deposits, North China Craton (Hebei Province, China). *Chemical Geology*, 264(1), pp.101-121.
- Cook, N.J., Ciobanu, C.L., Meria, D., Silcock, D. and Wade, B., 2013. Arsenopyrite-pyrite association in an orogenic gold ore: Tracing mineralization history from textures and trace elements. *Economic Geology*, 108(6), pp.1273-1283.
- Corfu, F., Krogh, T.E., Kwok, Y.Y. and Jensen, L.S., 1989. U–Pb zircon geochronology in the southwestern Abitibi greenstone belt, Superior Province. *Canadian Journal of Earth Sciences*, 26(9), pp.1747-1763.
- Corfu, F., Jackson, S.L. and Sutcliffe, R.H., 1991. U–Pb ages and tectonic significance of late Archean alkalic magmatism and nonmarine sedimentation: Timiskaming Group, southern Abitibi belt, Ontario. *Canadian Journal of Earth Sciences*, 28(4), pp.489-503.
- Daigneault, R., Mueller, W.U. and Chown, E.H., 2004. Abitibi greenstone belt plate tectonics: the diachronous history of arc development, accretion and collision. *Developments in Precambrian Geology*, 12, pp.88-103.
- Deditius, A.P., Utsunomiya, S., Renock, D., Ewing, R.C., Ramana, C.V., Becker, U. and Kesler, S.E., 2008. A proposed new type of arsenian pyrite: Composition, nanostructure and geological significance. *Geochimica et Cosmochimica Acta*, 72(12), pp.2919-2933.
- Deditius, A.P., Utsunomiya, S., Ewing, R.C., Chryssoulis, S.L., Venter, D. and Kesler, S.E., 2009. Decoupled geochemical behavior of As and Cu in hydrothermal systems. *Geology*, 37(8), pp.707-710.
- Deditius, A.P., Utsunomiya, S., Reich, M., Kesler, S.E., Ewing, R.C., Hough, R. and Walshe, J., 2011. Trace metal nanoparticles in pyrite. *Ore Geology Reviews*, 42(1), pp.32-46.
- Deditius, A.P., Reich, M., Kesler, S.E., Utsunomiya, S., Chryssoulis, S.L., Walshe, J. and Ewing, R.C., 2014. The coupled geochemistry of Au and As in pyrite from hydrothermal ore deposits. *Geochimica et Cosmochimica Acta*, 140, pp.644-670.
- Dimov, S.S., and Hart, B.R., 2011, Applications of Microbeam Analytical Techniques in Gold Department Studies, Proceedings of the 50th Annual Conference of Metallurgists of CIM, World Gold 2011, Edited by Deschenes, G., Dimatrikapoulis, R., Bouvhard, J., p. 17-26.

- Dinel, E., Fowler, A.D., Ayer, J., Still, A., Tylee, K. and Barr, E., 2008a. Lithogeochemical and stratigraphic controls on gold mineralization within the metavolcanic rocks of the Hoyle Pond mine, Timmins, Ontario. *Economic Geology*, 103(6), pp.1341-1363.
- Dinel, E., Saumur, B.M. and Fowler, A.D., 2008b. Spherulitic aphyric pillow-lobe metatholeiitic dacite lava of the Timmins Area, Ontario, Canada: a new Archean facies formed from superheated melts. *Economic Geology*, 103(6), pp.1365-1378.
- Dubé, B., Williamson, K., McNicoll, V., Malo, M., Skulski, T., Twomey, T. and Sanborn-Barrie, M., 2004. Timing of gold mineralization at Red Lake, northwestern Ontario, Canada: New constraints from U-Pb geochronology at the Goldcorp high-grade zone, Red Lake mine, and the Madsen mine. *Economic Geology*, 99(8), pp.1611-1641.
- Dubé, B., and Gosselin, P., 2007, Greenstone-hosted quartz-carbonate vein deposits, in Goodfellow, W.D., ed., *Mineral Deposits of Canada: A Synthesis of Major Deposit-Types, District Metallogeny, the Evolution of Geological Provinces, and Exploration Methods*: Geological Association of Canada, Mineral Deposits Division, Special Publication No. 5, pp.49-73.
- Etschmann, B.E., Liu, W., Pring, A., Grundler, P.V., Tooth, B., Borg, S., Testemale, D., Brewe, D. and Brugger, J., 2016. The role of Te (IV) and Bi (III) chloride complexes in hydrothermal mass transfer: An X-ray absorption spectroscopic study. *Chemical Geology*, 425, pp.37-51.
- Ferguson, S.A., 1968, *Geology and ore deposits of Tisdale Township. Ontario Department of Mines Geological Report 58*, 177 p.
- Fisher, L.A., Fougereuse, D., Cleverley, J.S., Ryan, C.G., Micklethwaite, S., Halfpenny, A., Hough, R.M., Gee, M., Paterson, D., Howard, D.L. and Spiers, K., 2015. Quantified, multi-scale X-ray fluorescence element mapping using the Maia detector array: Application to mineral deposit studies. *Mineralium Deposita*, 50(6), pp.665-674.
- Fougereuse, D., Micklethwaite, S., Tomkins, A.G., Mei, Y., Kilburn, M., Guagliardo, P., Fisher, L.A., Halfpenny, A., Gee, M., Paterson, D. and Howard, D.L., 2016. Gold remobilisation and formation of high grade ore shoots driven by dissolution-reprecipitation replacement and Ni substitution into auriferous arsenopyrite. *Geochimica et Cosmochimica Acta*, 178, pp.143-159.
- Fryer, B.J., Kerrich, R., Hutchinson, R.W., Peirce, M.G. and Rogers, D.S., 1979. Archaean precious-metal hydrothermal systems, Dome Mine, Abitibi Greenstone Belt. I. Patterns of alteration and metal distribution. *Canadian Journal of Earth Sciences*, 16(3), pp.421-439
- Gaboury, D., 2013. Does gold in orogenic deposits come from pyrite in deeply buried carbon-rich sediments?: Insight from volatiles in fluid inclusions. *Geology*, 41(12), pp.1207-1210.

- Goldfarb, R., Baker, T., Dube, B., Groves, D.I., Hart, C.J. and Gosselin, P., 2005. Distribution, character and genesis of gold deposits in metamorphic terranes. In: Hedenquist, J.W., Thompson, J.F.H., Goldfarb, R.G., and Richards, J.P., (eds.) Economic geology 100th Anniversary volume. Society of Economic Geologists, pp. 407-450.
- Gray, M.D. and Hutchinson, R.W., 2001. New evidence for multiple periods of gold emplacement in the Porcupine mining district, Timmins area, Ontario, Canada. *Economic Geology*, 96(3), pp.453-475.
- Gregory, D.D., Large, R.R., Halpin, J.A., Baturina, E.L., Lyons, T.W., Wu, S., Danyushevsky, L., Sack, P.J., Chappaz, A., Maslennikov, V.V. and Bull, S.W., 2015. Trace element content of sedimentary pyrite in black shales. *Economic Geology*, 110(6), pp.1389-1410.
- Gregory, D.D., Large, R.R., Bath, A.B., Steadman, J.A., Wu, S., Danyushevsky, L., Bull, S.W., Holden, P. and Ireland, T.R., 2016. Trace element content of pyrite from the kapai slate, St. Ives Gold District, Western Australia. *Economic Geology*, 111(6), pp.1297-1320.
- Harris, R., 2013. Telluride Associations with Gold Mineralization at Goldcorp's Dome Mine; Timmins, ON. Unpublished BSc. Thesis, University of Western Ontario.
- Hazarika, P., Mishra, B., Chinnasamy, S.S. and Bernhardt, H.J., 2013. Multi-stage growth and invisible gold distribution in pyrite from the Kundarkocha sediment-hosted gold deposit, eastern India. *Ore Geology Reviews*, 55, pp.134-145.
- Heald, S., Stern, E., Brewé, D., Gordon, R., Crozier, D., Jiang, D. and Cross, J., 2001. XAFS at the Pacific Northwest Consortium-Collaborative Access Team undulator beamline. *Journal of Synchrotron Radiation*, 8(2), pp.342-344.
- Heald, S.M., Cross, J.O., Brewé, D.L. and Gordon, R.A., 2007. The PNC/XOR X-ray microprobe station at APS sector 20. *Nuclear Instruments and Methods in Physics Research Section A: Accelerators, Spectrometers, Detectors and Associated Equipment*, 582(1), pp.215-217.
- Henry, S., 2000. Influence of water vapor on high-temperature oxidation of chromium and some ferritic stainless steels (Doctoral dissertation). Institut National Polytechnique de Grenoble.
- Holmes, T.C., 1968, Dome Mines Limited: in *Geology and Ore Deposits of the Tisdale Township*. Ontario Department of Mines Geological Report 58, 172p.
- Houlé, M.G., Ayer, J.A., Baldwin, G., Berger, B.R., Dinel, E., Fowler, A.D., Moulton, B., Saumur, B.--M. and Thurston, P.C. 2008. Field trip guidebook to the stratigraphy and volcanology of supracrustal assemblages hosting base metal and gold mineralization in

the Abitibi greenstone belt, Timmins, Ontario; Ontario Geological Survey, Open File Report 6225, 84p.

Hu, S.Y., Evans, K., Fisher, L., Rempel, K., Craw, D., Evans, N.J., Cumberland, S., Robert, A. and Grice, K., 2016. Associations between sulfides, carbonaceous material, gold and other trace elements in polyframboids: Implications for the source of orogenic gold deposits, Otago Schist, New Zealand. *Geochimica et Cosmochimica Acta*, 180, pp.197-213.

Hutchinson, R.W., 1993. A multi-stage, multi-process genetic hypothesis for greenstone-hosted gold lodes. *Ore Geology Reviews*, 8(3-4), pp.349-382.

Kerrick, R. and Fryer, B.J., 1979. Archaean precious-metal hydrothermal systems, Dome Mine, Abitibi Greenstone Belt. II. REE and oxygen isotope relations. *Canadian Journal of Earth Sciences*, 16(3), pp.440-458.

Kirkham, R., Dunn, P.A., Kuczewski, A.J., Siddons, D.P., Dodanwela, R., Moorhead, G.F., Ryan, C.G., De Geronimo, G., Beuttenmuller, R., Pinelli, D. and Pfeffer, M., 2010, June. The Maia Spectroscopy Detector System: Engineering for Integrated Pulse Capture, Low-Latency Scanning and Real-Time Processing. In *AIP Conference Proceedings* (Vol. 1234, No. 1, pp. 240-243). AIP.

Large, R.R., Maslennikov, V.V., Robert, F., Danyushevsky, L.V. and Chang, Z., 2007. Multistage sedimentary and metamorphic origin of pyrite and gold in the giant Sukhoi Log deposit, Lena gold province, Russia. *Economic Geology*, 102(7), pp.1233-1267.

Large, R.R., Danyushevsky, L., Hollit, C., Maslennikov, V., Meffre, S., Gilbert, S., Bull, S., Scott, R., Emsbo, P., Thomas, H. and Singh, B., 2009. Gold and trace element zonation in pyrite using a laser imaging technique: implications for the timing of gold in orogenic and Carlin-style sediment-hosted deposits. *Economic Geology*, 104(5), pp.635-668.

Large, R.R., Bull, S.W. and Maslennikov, V.V., 2011. A carbonaceous sedimentary source-rock model for Carlin-type and orogenic gold deposits. *Economic Geology*, 106(3), pp.331-358.

Large, R.R., Halpin, J.A., Danyushevsky, L.V., Maslennikov, V.V., Bull, S.W., Long, J.A., Gregory, D.D., Lounejeva, E., Lyons, T.W., Sack, P.J. and McGoldrick, P.J., 2014. Trace element content of sedimentary pyrite as a new proxy for deep-time ocean-atmosphere evolution. *Earth and Planetary Science Letters*, 389, pp.209-220.

Large, R.R., Mukherjee, I., Gregory, D.D., Steadman, J.A., Maslennikov, V.V. and Meffre, S., 2017. Ocean and Atmosphere Geochemical Proxies Derived from Trace Elements in Marine Pyrite: Implications for Ore Genesis in Sedimentary Basins. *Economic Geology*, 112(2), pp.423-450.

- Marshall, B., Vokes, F.M. and Larocque, A.C.L., 2000. Regional metamorphic remobilization: upgrading and formation of ore deposits. *Reviews in Economic Geology*, 11(1), pp.19-38.
- McIntyre, N.S., Sherry, N., Fuller, M.S., Feng, R. and Kotzer, T., 2010. X-Ray fluorescence spectroscopy and mapping using excitation from white and broad bandpass synchrotron radiation. *Journal of Analytical Atomic Spectrometry*, 25(9), pp.1381-1389.
- Meffre, S., Large, R.R., Steadman, J.A., Gregory, D.D., Stepanov, A.S., Kamenetsky, V.S., Ehrig, K. and Scott, R.J., 2016. Multi-stage enrichment processes for large gold-bearing ore deposits. *Ore Geology Reviews*, 76, pp.268-279.
- Mikucki, E.J., 1998. Hydrothermal transport and depositional processes in Archean lode-gold systems: A review. *Ore Geology Reviews*, 13(1), pp.307-321.
- Moritz, R.P., 1988. Geological and Geochemical Studies of the Gold-Bearing Quartz-Fuchsite Vein at the Dome Mine, Timmins Area. PhD Dissertation, McMaster University, 341p.
- Mukherjee, I. and Large, R., 2017. Application of pyrite trace element chemistry to exploration for SEDEX style Zn-Pb deposits: McArthur Basin, Northern Territory, Australia. *Ore Geology Reviews*, 81, pp.1249-1270.
- Ortega, L., Lunar, R., García-Palomero, F., Moreno, T., Martín-Estévez, J.R., Prichard, H.M. and Fisher, P.C., 2004. The Aguablanca Ni-Cu-PGE deposit, southwestern Iberia: magmatic ore-forming processes and retrograde evolution. *The Canadian Mineralogist*, 42(2), pp.325-350.
- Pals, D.W., Spry, P.G. and Chryssoulis, S., 2003. Invisible gold and tellurium in arsenic-rich pyrite from the Emperor gold deposit, Fiji: implications for gold distribution and deposition. *Economic Geology*, 98(3), pp.479-493.
- Phillips, G.N. and Evans, K.A., 2004. Role of CO₂ in the formation of gold deposits. *Nature*, 429(6994), p.860.
- Phillips, G.N. and Powell, R., 2015. A practical classification of gold deposits, with a theoretical basis. *Ore Geology Reviews*, 65, pp.568-573.
- Poulsen, K.H., Card, K.D. and Franklin, J.M., 1992. Archean tectonic and metallogenic evolution of the Superior Province of the Canadian Shield. *Precambrian Research*, 58(1-4), pp.25-54.
- Powell, W.G., Carmichael, D.M. and Hodgson, C.J., 1995. Conditions and timing of metamorphism in the southern Abitibi greenstone belt, Quebec. *Canadian Journal of Earth Sciences*, 32(6), pp.787-805.

Pressacco, R, 1999. Economic Geology and Mineralization of the Dome Mine. Ontario Geologic Survey, Open File Report 598, pp.1-32.

Proudlove, D.C., Hutchinson, R.W., Rogers, D.S., 1989. Multiphase Mineralization in Concordant and Discordant Gold Veins, Dome Mine, South Porcupine, Ontario, Canada. Economic Geology Monograph. 6, pp.112-123.

Reading, D.J., 1982. The Geology and Isotope Geochemistry of the Ankerite Units, Dome Mine, Timmins. Unpublished MSc Thesis, University of Waterloo.

Reich, M., Kesler, S.E., Utsunomiya, S., Palenik, C.S., Chryssoulis, S.L. and Ewing, R.C., 2005. Solubility of gold in arsenian pyrite. *Geochimica et Cosmochimica Acta*, 69(11), pp.2781-2796.

Robert, F., 2001. Syenite-associated disseminated gold deposits in the Abitibi greenstone belt, Canada. *Mineralium Deposita*, 36(6), pp.503-516.

Rosúa, F.J., Ruano, S.M. and Hach-Alí, P.F., 2003. Iron sulphides at the epithermal gold-copper deposit of Palai-Islica (Almería, SE Spain). *Mineralogical Magazine*, 67(5), pp.1059-1080.

Ryan, C.G., 2000. Quantitative trace element imaging using PIXE and the nuclear microprobe. *International Journal of Imaging Systems and Technology*, 11(4), pp.219-230.

Ryan, C.G., Kirkham, R., Hough, R.M., Moorhead, G., Siddons, D.P., De Jonge, M.D., Paterson, D.J., De Geronimo, G., Howard, D.L. and Cleverley, J.S., 2010a. Elemental X-ray imaging using the Maia detector array: The benefits and challenges of large solid-angle. *Nuclear Instruments and Methods in Physics Research Section A: Accelerators, Spectrometers, Detectors and Associated Equipment*, 619(1), pp.37-43.

Ryan, C.G., Siddons, D.P., Kirkham, R., Dunn, P.A., Kuczewski, A., Moorhead, G., De Geronimo, G., Paterson, D.J., De Jonge, M.D., Hough, R.M. and Lintern, M.J., 2010b, April. The new Maia detector system: methods for high definition trace element imaging of natural material. In *AIP Conference Proceedings* (Vol. 1221, No. 1, pp. 9-17). AIP.

Ryan, C.G., Siddons, D.P., Kirkham, R., Li, Z.Y., de Jonge, M.D., Paterson, D.J., Kuczewski, A., Howard, D.L., Dunn, P.A., Falkenberg, G. and Boesenberg, U., 2014. Maia X-ray fluorescence imaging: Capturing detail in complex natural samples. In *Journal of Physics: Conference Series* (Vol. 499, No. 1, p. 012002). IOP Publishing.

Tardani, D., Reich, M., Deditius, A.P., Chryssoulis, S., Sánchez-Alfaro, P., Wrage, J. and Roberts, M.P., 2017. Copper–arsenic decoupling in an active geothermal system: A link between pyrite and fluid composition. *Geochimica et Cosmochimica Acta*, 204, pp.179-204.

- Tauson, V.L., 1999. Gold solubility in the common gold-bearing minerals; experimental evaluation and application to pyrite. *European Journal of Mineralogy*, 11(6), pp.937-947.
- Simon, G., Huang, H., Penner-Hahn, J.E., Kesler, S.E. and Kao, L.S., 1999. Oxidation state of gold and arsenic in gold-bearing arsenian pyrite. *American Mineralogist*, 84(7-8), pp.1071-1079.
- Steadman, J.A., Large, R.R., Meffre, S., Olin, P.H., Danyushevsky, L.V., Gregory, D.D., Belousov, I., Lounejeva, E., Ireland, T.R. and Holden, P., 2015. Synsedimentary to early diagenetic gold in black shale-hosted pyrite nodules at the Golden Mile Deposit, Kalgoorlie, Western Australia. *Economic Geology*, 110(5), pp.1157-1191.
- Steadman, J.A. and Large, R.R., 2016. Synsedimentary, Diagenetic, and Metamorphic Pyrite, Pyrrhotite, and Marcasite at the Homestake BIF-Hosted Gold Deposit, South Dakota, USA: Insights on Au-As Ore Genesis from Textural and LA-ICP-MS Trace Element Studies. *Economic Geology*, 111(7), pp.1731-1752.
- Stromberg, J.M., Barr, E., Banerjee, N.R., 2017. Early Carbonate Veining and Gold Mineralization in the Timmins Camp: Depositional Context of the Dome Mine Ankerite Veins. Submitted to *Ore Geology Reviews.*, August 2017.
- Sung, Y.H., Brugger, J., Ciobanu, C.L., Pring, A., Skinner, W. and Nugus, M., 2009. Invisible gold in arsenian pyrite and arsenopyrite from a multistage Archaean gold deposit: Sunrise Dam, Eastern Goldfields Province, Western Australia. *Mineralium Deposita*, 44(7), p.765.
- Tardani, D., Reich, M., Deditius, A.P., Chryssoulis, S., Sánchez-Alfaro, P., Wrage, J. and Roberts, M.P., 2017. Copper–arsenic decoupling in an active geothermal system: A link between pyrite and fluid composition. *Geochimica et Cosmochimica Acta*, 204, pp.179-204.
- Thomas, H.V., Large, R.R., Bull, S.W., Maslennikov, V., Berry, R.F., Fraser, R., Froud, S. and Moye, R., 2011. Pyrite and pyrrhotite textures and composition in sediments, laminated quartz veins, and reefs at Bendigo gold mine, Australia: insights for ore genesis. *Economic Geology*, 106(1), pp.1-31.
- Thompson, P.H., 2003, Discover Abitibi. Metamorphic subproject. Metamorphism and its relationships to gold deposits in the Timmins-Kirkland Lake area, western Abitibi greenstone belt, Ontario: Report 1, Ontario Geological Survey Open File Report 6120, p. 37–1 - 37–8.
- Thurston, P.C., Ayer, J.A., Goutier, J. and Hamilton, M.A., 2008. Depositional gaps in Abitibi greenstone belt stratigraphy: A key to exploration for syngenetic mineralization. *Economic Geology*, 103(6), pp.1097-1134.

VanHees, E.H., 1979. Auriferous ankerite vein genesis in the Aunor Mine, Timmins, Ontario. Unpublished MSc. thesis, University of Western Ontario, London, Ontario.

Chapter 4

Applications of Synchrotron X-ray Technology to Improving Mineral Exploration and Production: Examples from Orogenic Gold Deposits of the Timmins Camp, Canada

4.1.0 Introduction

The use of synchrotron X-ray technology is well established in the remediation and environmental sectors of the mining industry for characterizing deleterious elements (e.g., Cabri et al., 2000; Walker et al., 2005; Fawcett and Jamieson, 2011; Etschmann et al., 2014; Fawcett et al., 2015; Wang et al., 2016). However, applications for exploration and production (geomettallurgy) are underdeveloped. With advances in x-ray fluorescence detector technologies, the main limiting factors for the application of this advanced technique (low availability, perceived high cost, long collection times) are mitigated, and applications to ore deposit characterization are being explored (e.g., Fischer et al., 2014; Li et al., 2016; Etschmann et al., 2017; Pearce et al., 2017). However, the integration of multiple synchrotron radiation micro-analysis tools to orogenic gold deposits has not been described previously. This study presents examples of synchrotron radiation techniques applied to the characterization of trace metals and gold in pyrite in a variety of depositional settings in the Timmins gold camp, including examples from multiple mineralization events. The relationship between Au and As is highlighted as the distribution and speciation of Au and As in gold deposits is relevant throughout the mining cycle, providing integral insights into deposit formation to guide exploration, for extractive geomettallurgy, and for assessing the potential for long term mine waste and remediation concerns (e.g., Cabri et al., 2000, Stromberg et al., 2016a, b; Van Loon et al., 2016 and Blanchard et al., 2017).

There is a large body of work on the characterization of trace elements and gold in pyrite given the ubiquitous nature of pyrite in many ore deposit types (e.g., Deditius et al., 2008; Large et al., 2014; Tardani et al., 2017; Mukherjee and Large, 2017). The refractory

nature of pyrite makes the characterization of pyrite trace element content a powerful tool for understanding the geochemistry of depositional environments, and for enhancing exploration and ore processing (e.g., Cook et al., 2013). The relationship between Au and As in pyrites has been studied in detail, primarily in the context of Carlin type deposits, and is integral for effective ore processing and remediation (e.g., Cook and Chryssoulis, 1990; Simon et al., 1999; Cabri et al., 2000; Reich et al., 2005; Deditius et al., 2008, 2011, 2014). The nature of refractory gold is well characterized, and occurs as both metallic Au⁰ nanoparticles, and Au¹⁺ in the crystal lattice of the pyrite. The As content and speciation (As¹⁻ vs. As³⁺) in arsenian pyrite plays an important role in the distribution of refractory gold mineralization and the introduction of other commonly deleterious trace elements into pyrite (Cook and Chryssoulis, 1990; Simon et al., 1999; Cabri et al., 2000; Reich et al., 2005; Deditius et al., 2008, 2011; Fougrouse et al., 2016). Understanding associations of other trace elements (e.g., Cu, Ni, Co, W) with gold in pyrite has implications for improving exploration in regions with complex mineralization histories (e.g., Feick et al., 2015 Stromberg et al., 2016a,b, Mukherjee and Large, 2017). There are multiple techniques that are commonly employed for *in situ* analysis of mineral grains applied to ore deposits, with electron probe microanalysis (EPMA), secondary ion mass spectrometry (SIMS) and laser ablation inductively coupled plasma mass spectrometry (LA-ICP-MS) being the most common. For each of these techniques there are trade-offs between image resolution, mappable area, limits of detection, and the number of elements detected (Figure 4-1; See Pearce et al., 2017 for a review).

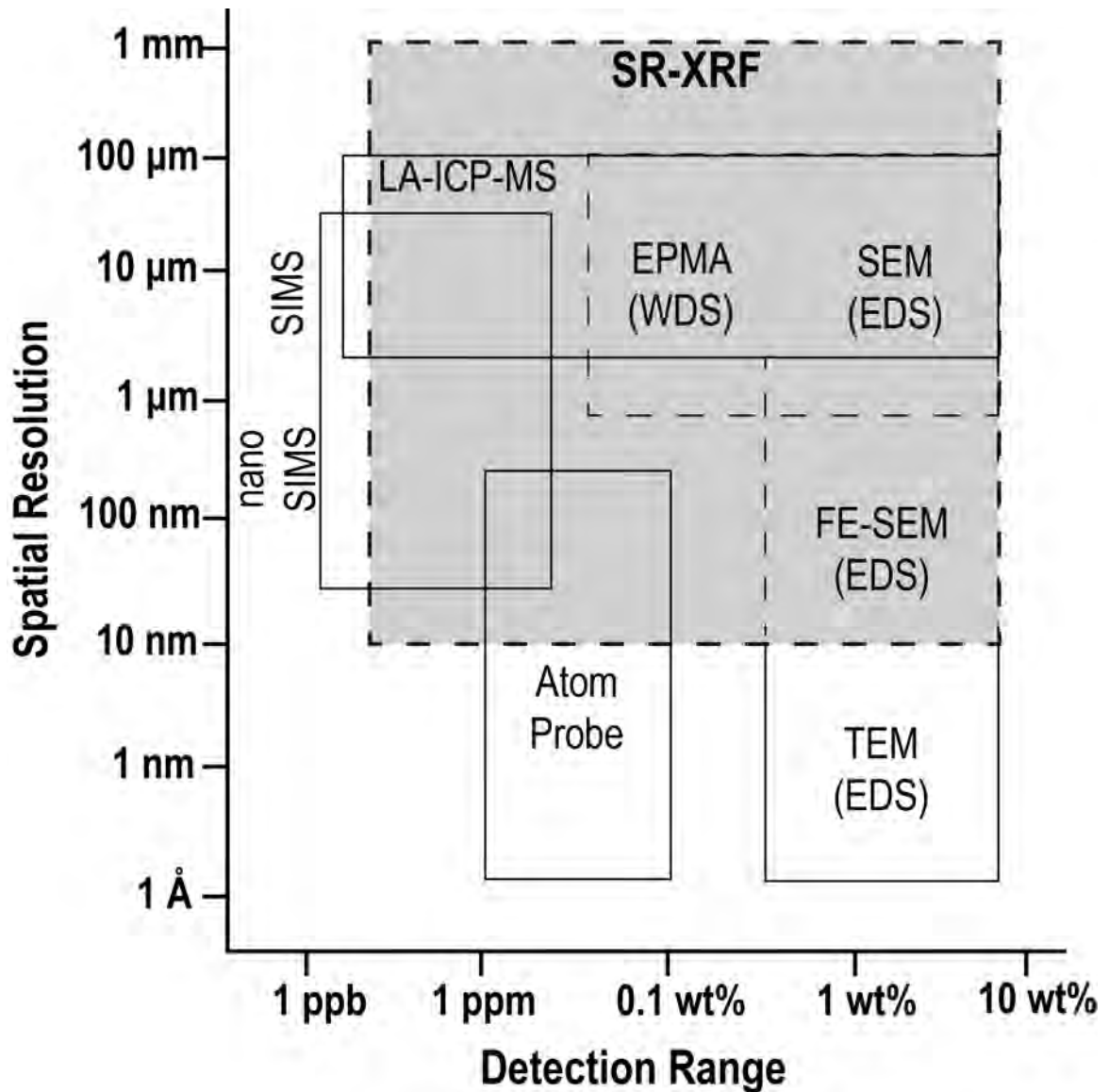


Figure 4-1. Comparison of the spatial resolution and detection range of microanalytical trace element mapping techniques. LA-ICP-MS: laser-ablation inductively-coupled plasma mass spectrometry; SR-XRF: synchrotron X-ray fluorescence; EPMA: electron microprobe analysis; WDS: wavelength dispersive X-ray spectrometry; SEM: scanning electron microscopy; EDS: energy dispersive X-ray spectrometry; (nano) SIMS: secondary ion mass spectrometry; FE-SEM: field emission scanning electron microscopy; TEM: transmission electron microscopy. Techniques with dashed outlines are non-destructive. (modified from Reich et al., 2017)

The foundation for the effective application of high-resolution ore mineral characterization is robust characterization of sample context. This is traditionally done by petrographic methods such as optical microscopy and backscatter electron scanning electron microscopy (BSE-SEM). Recently, some of these have been automated to characterize entire thin sections and may also include energy-dispersive X-ray spectrometry (EDS), which provides some chemical information (e.g., QEMSCAN, Mineralogic Mining, ZEISS Atlas 5.0). This sort of large-scale characterization is necessary given the complexity and heterogeneity of geologic samples (e.g., Schumann et al., 2014). An understanding of sample context is integral for informed sample or grain selection for these higher resolution analyses, and for making any interpretations on a deposit or ore type. As such, high-resolution techniques are generally applied at the end of a workflow, following extensive sample characterization by conventional non-destructive techniques (e.g., Large et al., 2009; Gregory et al., Fougereuse et al., 2016; Mukherjee et al., 2017). The reality in the mining sector is that key questions regarding exploration and processing need to be answered early and on short time frames. The ability to optimize the conventional workflow by bringing high-resolution analysis to the front end while also gaining key contextual information represents a paradigm shift.

LA-ICP-MS has become the technique of choice for *in situ* quantitative trace element analysis with high spatial resolution in ore deposit studies (e.g., Large et al., 2009; 2011, 2014, 2017; Mukherjee, 2017). This technique can measure both major and trace elements with 5 to 50 μm (typically 15 to 50 μm) spatial resolution, but is destructive to the sample. Historically, the standard tool in metallurgy is mineral liberation analysis (MLA), which is based on a scanning electron microscope (SEM) platform (Jones, 1987; Petruk, 2000). Electron probe micro-analysis (EPMA) also utilizes a SEM platform, but with a wavelength dispersive spectroscopy (WDS) detection system that allows for better precision in detection of minor elements, as well as elements whose emission lines are close in energy (e.g., Pt-L α and Au-L α), or have multiple line interferences (e.g., the REE). EPMA can in some cases achieve sub-micron mapping resolution, but the area that can be mapped is restricted by time and the number of elements which can be analyzed (Pearce et al., 2017). Secondary ion mass spectrometry (SIMS) is considered the

benchmark technique for quantification of submicroscopic gold and is commonly used in gold deportation studies (e.g., Dimov and Hart, 2011). SIMS analysis has lower detection limits than EMPA, however, is destructive to the sample. Samples analyzed by SIMS, EPMA and LA-ICP-MS are generally prepared as thin sections or mounted in epoxy as a polished surface is required.

Like other X-Ray fluorescence (XRF) methods, synchrotron radiation (SR) based micro-XRF is a non-destructive technique. It allows for the *in situ* mapping of major and trace elements on the nanometer to micron scale with minimal sample preparation (Figure 4-1). Both polished thin sections and whole rock samples can be analyzed, each with their own set of caveats. Float glass, which is typically used for thin section preparation, contains trace element impurities (e.g., As, Mn) that with the high flux of a synchrotron X-ray source will impact data. In addition to reduced sample preparation, the flexibility of synchrotron end stations permit for a variety of sample sizes and shapes to be analyzed under atmospheric conditions. The experimental set-up is customizable and the excitation energy is tunable, making for few limitations in terms of number of elements analyzed. The application of synchrotron SR-XRF mapping to ore deposit studies has traditionally been restricted due to availability and cost of beam time as well as long data acquisition times. However, with advances in detector technology, its application to mapping trace elements in ore minerals has been pursued (e.g., Fischer et al., 2014; Li et al., 2016). The introduction of the Maia detector (384 element Si detector) allows for very fast data collection (millisecond dwell times) with high-count rates (millions of counts; Ryan et al., 2010a,b, 2013, 2014). This makes it possible to characterize an entire thin section or rock slab at 20 μm resolution within a few hours.

The plethora of minor and trace elements found in pyrite, as well as the inherent difficulty in characterizing trace elements in gold make SR-XRF mapping a very effective technique for exploring the relationship between gold, trace elements and pyrite in orogenic systems. Unlike conventional *in situ* geochemical techniques (EPMA, SIMS, LA-ICP-MS), SR-XRF analysis produces full spectrum data sets that can identify all elements present within a complex geologic sample that are excited by the incident

energy of the beam with ppm detection limits (Figure 4-1). Additionally, the non-destructive nature of SR-XRF analysis makes it very complementary to other techniques, allowing for follow up analysis by destructive nano-scale techniques such as high-resolution transmission electron microscopy (HR-TEM), nanoSIMs, and atom probe. This includes other synchrotron X-ray techniques such as XANES (X-ray absorption near edge structure), which provides information on trace metal speciation (e.g., Cabri et al., 2000; Etschmann et al., 2017).

Synchrotron based research in ore deposit studies has primarily focused on XANES analysis to study experimentally controlled systems and processes, or using very well constrained samples (See Brugger et al., 2010 for a review). For example, metal complexing in fluid inclusions and experimental fluids (e.g., Mavrogenes et al., 2002; Etschmann et al., 2017), and speciation of Au and other trace metals in sulfides (e.g., Cabri et al., 2000; Cook et al., 2013). XANES has also been extensively applied to mining remediation studies to characterize the speciation of metals and metalloids in environmental samples (e.g., Walker et al., 2005; Fawcett and Jamieson, 2011; Blanchard et al., 2017). Advances in detector technology have also had an impact on the application of XANES analysis with the development of XRF stacking for speciation mapping (e.g., Etschmann et al., 2014). However, this technique has yet to be applied to ore samples. A well-characterized example is the Giant Mine (Northwest Territories, Canada), where the processing of ore composed of gold rich arsenopyrite resulted in a remediation cost of almost 1 billion dollars due to As contamination (Jamieson, 2014). XANES has been used extensively to better characterize and understand the mobility of deleterious elements such as As, Se, Sb, Te, and Hg in the environment to aide in the remediation efforts (e.g., Fawcett et al., 2015). Following the environmental legacy of the Giant mine, the importance of understanding the As content and distribution of different ore types early in the mining cycle is well understood and accepted. The benchmark tool for such investigations is generally SIMS analysis. However, the methods and workflow by which ores are traditionally characterized may be improved by the adoption of synchrotron radiation based techniques such as XANES and SR-XRF.

In this study, we show examples of the applications synchrotron X-ray techniques to samples of multiple styles of orogenic gold mineralization across the Timmins camp (Table 4-1). We selected thin sections on conventional and quartz slides, thin section offcuts, as well as cut slabs to highlight the versatility of SR-XRF analysis at multiple stages of deposit investigation and for multiple sample types. The use of quartz slides for thin section preparation mitigates the issue of contamination from glass trace element content in the spectra. High resolution (2 μm) SR-XRF mapping is compared with conventional EMPA analysis on a standard thin section to investigate the relationship between Au, pyrite, and trace metals. SR-XRF mapping at the whole sample/thin section scale was performed to identify regions of gold mineralization, associations with trace metals and As and inform further analysis. High-resolution mapping of individual grains in thin sections and offcuts reveal micron scale associations with trace metals, Au, and As, as well as the presence of refractory gold in pyrite. Point XRF analysis followed by XANES of individual grains was applied to better characterize the nature of refractory gold and the speciation of As. XANES mapping on thin sections revealed spatial distribution of As speciation in grains selected from multi-scale mapping. We propose that the ability to map entire samples quickly and non-destructively informs sample selection for higher resolution characterization, reducing the sample bias that is inherent in applying high-resolution geochemical techniques to describe a large mineralizing system. This is particularly relevant for orogenic deposits as gold is “nuggety” by nature on the scales that we are measuring, and is commonly the result of multiple fluid events. The complementary nature of SR-XRF to destructive nanoscale techniques such as HR-TEM for follow up analysis of enigmatic samples is also highlighted.

Table 4-1. Sample Information. Au, Ag and As values are in ppm.

Sample #	Mine	Host	Type	Sample	Au	Ag	As
C406932	Dome	Vipond Formation	Ankerite Vein	Thin Section	0.9	<0.5	177
C406934	Dome	Vipond Formation	Ankerite Vein	Thin Section	5.7	4.7	90
E885276	Hoyle Pond	Porcupine Assemblage	Greywacke	Thin Section (Qtz)	4.68		
C408781	Dome	Gold Center Formation	Interflow Sediment	Thin Section (Qtz)	98.1	16.4	>10,000
C408779	Dome	Timiskaming Conglomerate	Sulfide Clast	Thin Section and Slab	2.73	22.5	486
C410280	Dome	Vipond Formation	Ankerite Vein	Slab	16.3	4.4	856
B-A	Buffalo-Ankerite	Hersey Lake Formation	Ankerite Vein	Slab	0.5	<0.5	45

4.2.0 Methods

4.2.1 Sample Preparation

Slabs were cut from whole rock samples and standard polished thin sections were prepared from selected samples. The remaining slabs and blocks from thin section preparation were preserved. Thin sections were characterized by conventional light microscopy and backscatter emission scanning electron microscopy (BSE-SEM). BSE-SEM analysis was undertaken at the Western Nanofabrication facility where samples were coated with 5 nm amorphous osmium and imaged on a LEO (Zeiss) 1540 XB field emission gun – scanning electron microscope (FEG-SEM) that was operated at 10 kV.

4.2.2 Synchrotron Radiation – X-Ray Fluorescence (SR-XRF) Maps

SR-XRF data was collected over multiple visits at three different third generation synchrotron source facilities. All beam lines used are hard X-ray beam lines with microprobe stations optimized for SR-XRF on different spatial scales. Analyses at the Canadian Light Source (CLS) in Saskatoon, Saskatchewan, Canada, were conducted at the VESPERS (Very Sensitive Elemental and Structural Probe Employing Radiation from a Synchrotron source) beamline. The CLS operates at 3 GeV with 2 injections in a 24 hr period to a storage ring current of 250 mA. Analyses at the Advanced Photon Source (APS) in Chicago, IL, USA were conducted at the 20-ID beamline. The APS operates at 7 GeV in top up mode with a storage ring current of 100 mA. Analysis at the Cornell High

Energy Synchrotron Source (CHESS) in Ithaca, New York was undertaken at the F3 beam line. CHESS operates at 6 GeV with a storage beam current of 200 mA.

The VESPERS beamline is a bend magnet station, which has multi-bandpass and pink (polychromatic) beam capabilities with an energy range of 6-30keV and a focus of (2-4) μm x (2-4) μm using a Kirkpatrick-Baez (KB) mirror set (Feng et al., 2007). The end station is equipped with a 4 element Vortex Si drift detector calibrated to ~ 30 eV per channel and located 90° to the incident beam in the direction of the polarization and the sample at 45° . The beam line is optimized for XRF mapping at ~ 5 - $10\mu\text{m}$ resolution with simultaneous XRD (Laue x-ray diffraction) collection, and also has XANES capabilities.

The APS 20-ID beamline is a multi-purpose insertion device beam line with a KB mirror microprobe set-up and Si (111) LN₂-cooled monochromator which provides a monochromatic beam that can be focused down to $\sim 2 \times 2 \mu\text{m}^2$ for energies in the range of 4.2-27 keV with a flux of 10^{11} at 10 keV. The end station is equipped can be equipped with a Vortex-ME4 4-element silicon drift detector which was set up at 90° to the source. The sample is placed at 45° to the source and the detector calibrated to ~ 30 eV per channel (Heald et al, 2001; 2007). The beam line is optimized for high energy and high spatial resolution (2 μm) XRF and point XANES measurements.

The CHESS F3 station is a bend magnet station with a water cooled double crystal Si(111) monochromator which is tunable from 3-31 keV which is tunable from 3-31 keV and employed custom, single-bounce monocapillary optics fabricated at CHESS to focus to either 20 μm or 10 μm . The end station is equipped with a 384-element MAIA detector (Kirkham et al., 2010), a 384-element pixel array detector (PAD) oriented at 180° to the sample. With the Maia detector, the F3 beam line has large scale XRF mapping and XRF stacking capabilities which allow for XANES mapping and XRF characterization of entire cm scale samples at 20 μm resolution.

Thin sections and off-cuts were affixed onto custom designed aluminum sample holders and mounted on the sample translation stage. Samples were raster-scanned through the

focused beam to collect full spectrum XRF data for each pixel across regions of interest. Element maps were collected with an incident X-ray energy of 13.1 keV (APS and CHESS) and with the 20 eV pink (polychromatic) beam at the CLS. The spatial resolution ranged from 2-20 μm and dwell times ranged from 4 msec to 1 second (Appendix D.1.3). Standard foils (Au, Mn, Fe, Sb) were used for energy calibration and NIST standard SRM 1834 was analyzed to determine APS ID-20 beamline parameters for post processing.

4.2.3 X-Ray Absorption Near Edge Spectroscopy

Individual XANES spectra were collected at the APS on beam line 20-ID to determine the oxidation states of gold, arsenic and other trace metals (e.g., Cu, Ni, Mn, Zn). For Au and As XANES, the energy position was calibrated to the gold L3 edge (E_0 11,919 eV) using the first peak of the first derivative XANES spectrum of a metallic gold foil standard. Energy scales were referenced to the gold foil spectrum. The scan bounds of the XANES spectra were from -150 to -20 eV with 5 eV steps, -20 to 20 eV with 0.5 eV steps, and 20 eV to 9k with 0.05k steps. These values are in relation to E_0 , which is defined by the edge of interest (11919 eV for Au and 11868 eV for As). An integration time of 1 second was used. Three (3) to five (5) scans were collected for each point depending on the concentration of the element of interest.

XANES mapping was performed at the CHESS F3 beam line by collecting stacked SR-XRF elemental maps using the MAIA detector (Kirkham et al., 2010, Ryan et al., 2010a,b 2014). Regions for stacked map collection were selected from the Au and As XRF maps of entire samples. XRF maps were collected over 185 unequally spaced energies with 0.4 msec dwell as follows: 11.667-11.836 eV every 10 eV, 11.837-11.949 eV every 0.5 eV, 11.949-12.019 eV every 3 eV, and 12.019-12.119 eV every 5 eV. These parameters were chosen to step over both the As K edge (11867 eV) and the Au L3 edge (11919 eV) with high energy resolution (0.5 eV). In addition to the natural samples, stacked XRF maps were also collected of both Au and As standards (arsenopyrite, metallic gold).

4.2.4 Electron Probe Micro-Analysis

Electron probe maps were collected with a Jeol JXA-8530f field emission electron microprobe at the Earth and Planetary Materials Analysis Laboratory at the University of Western Ontario. Pyrite maps were collected for the following elements: As, Cu, Zn, Au, Ni with a wavelength dispersive x-ray spectrometer (WDS), and Fe and S with the energy dispersive spectrometer (EDS) at 0.5 and 2 μm beam diameter. Pure metal standards were used for the WDS maps (As-Gallium arsenide, gold, copper, nickel, zinc) to refine peak position for maximum counts, and for the Fe and S EDS maps the default ranges from the EDS detector were used. Maps were collected with an accelerating voltage of 15kV, 200 nA and a dwell time of 10 milliseconds. Maps were created without any manipulation to show the full spectrum of counts. For samples in which there were a few hotspots, maps were made to accentuate the counts within the pyrite grain only to better visualize variability in counts in the grain.

4.2.5 High-Resolution Transmission Electron Microscopy

An ultra-thin foil was prepared for transmission electron microscope investigation (TEM) using a focused ion beam (FIB) technique. The 5 x 10 x 0.1 μm -sized slice was extracted using a Zeiss NVision FIB-SEM system employing a Ga-ion beam accelerated to 30kV at Fibics Incorporated, Ottawa, Canada. A FEI Tecnai G² F20 Cryo-S/TEM located in the Facility for Electron Microscopy Research (FEMR) at the McGill University (Montréal, Canada) and a FEI Titan³ 80-300 S/TEM located at the National Research Council (Ottawa, Canada) were used to conduct bright-field imaging and high-angle annular dark-field (HAADF) imaging on the extracted FIB lamella.

The FEI Tecnai G² F20 200kV Cryo-S/TEM is equipped with a Gatan Ultrascan 4000 4k x 4k CCD Camera System Model 895 and EDAX Genesis EDS. The spherical aberration coefficient, C_s , of the TEM is 2.0 mm and the point-to-point resolution in bright field mode is 0.27 nm. The resolution in STEM HAADF mode is 0.24 nm. The inner and outer limits of the collection angles of the Fischione HAADF detector (model 3000) were approximately 53 mrad and 322 mrad. A 100 μm condenser aperture was used for HAADF imaging. This technique provides a signal intensity related mainly to the atomic

number (Z) and the thickness of the region analyzed. The FEI Titan³ 80-300 TEM operated at 300 keV, and equipped with a CEOS aberration corrector for the probe-forming lens and a monochromated field-emission gun was used to simultaneously acquire bright-field and HAADF images. Bright-field images were acquired with a Gatan detector, and HAADF images were collected using a Fischione detector in scanning-transmission electron microscopy (STEM) mode. The convergence angle was set at 15 mrad, and the HAADF collection angle was set at 50 mrad.

Energy dispersive spectroscopic (EDS) analyses and mapping of areas on the TEM lamellae were carried out at Fibics Incorporated on a Zeiss Crossbeam 540 equipped with a Gemini 2 electron column and an Oxford Instruments X-Max^N 80mm² EDS detector, which was controlled using Aztec 3.0 software. The operating conditions for the EDS analyses were 20 kV accelerating voltage and 2 nA probe current. For EDS analyses, the processing time parameter 5 was used and 45 to 450 s were required for the acquisition of the EDS maps. The latter were generated without quantification, and provide qualitative color-coded images of the distribution of the elements present in the sample.

4.3.0 Data Analysis

4.3.1 Peakaboo

SR-XRF maps collected at the CLS were processed using Peakaboo, a software program developed by the University of Western Ontario as a part of the Science Studio package (McIntyre et al., 2010). Peakaboo allows for the identification of peaks in the XRF spectrum such as K, L, and M fluorescence lines, escape peaks, and pileup peaks. It fits peaks using a Gaussian function with preset widths, and the identification of an element requires a close fit of multiple lines in the spectrum, each with its own shape. Fits also take into account details such as separations and relative intensities of $K\alpha$ 1 and 2, $K\beta$ 1, 2, and 3, $L\alpha$, $L\beta$ 1 and 2, $L\gamma$ 1, 2, and 3 lines. The intensity of peaks for selected elements can be plotted as a function of their spatial distribution in the sample creating a spatially resolved elemental map.

For VESPERS data, a 90% Brukner background removal is applied to the mean averaged spectrum for the entire map to suppress background from X-ray scattering, and then the mean average spectrum is fit. For the fitting of spectral peaks a Gaussian function is used with preset widths, and the identification of an element requires a close fit to multiple lines in the spectrum. Following peak fitting, two-dimensional maps are created to show the distribution of selected element using two interpolation (smoothing) passes.

4.3.2 2D-Scan Plot

High resolution mapping data from APS ID-20 was analyzed using in house software (2D Q-Scan Plot). 2D Q-Scan Plot processes full spectrum data and simultaneously creates intensity maps for preselected regions of interest (ROI's) within the full spectrum. Up to fifteen regions of interest were preselected based on the expected chemistry of the sample. In general, the peak widths are ~ 420 eV wide. However, the regions were refined prior to mapping by collecting point spectra from representative regions of the sample and adjusted to minimize the effects of peak overlap.

4.3.3 Athena

Athena 8.054 (Ravel and Newville, 2005) was used to process the XANES data. The spectra were normalized to the intensity of the incident beam measured with an ion chamber upstream of these sample. In Athena an energy calibration is performed to the gold L-edge with a gold foil measured under the same experimental conditions. Pre and post edge processing follows standard methods (e.g., Dyer et al., 2001; Fawcett et al., 2015) where the pre-edge was fit with a linear regression (-100 to -30 eV relative to edge position), and the post-edge was fit with a second order polynomial for normalization.

4.3.4 GeoPIXE

Large-scale maps collected at CHESS F3 were analyzed using GeoPIXE, a software suite that uses a fundamental parameters approach with spectral deconvolution and imaging using the dynamic analysis (DA) method (Ryan, 2000; Ryan et al., 2010a). This is based on fitting a representative total spectrum and detailed model of the Maia detector array efficiency, the details of which are outlined in Ryan et al., 2010. This method results in a

matrix transformation, which can produce real time and offline projections of full spectrum data into elemental maps yielding both qualitative and quantitative data and provide mineral specific trace element contents (e.g., Fischer et al., 2014). For real time mapping we created a bulk rock matrix, which approximates the average composition of auriferous pyrite rich samples. This was then refined and refit using sample specific information with yields calculated using the specific matrix for that sample or region of interest within the sample.

For the XRF stacks, a list of incident energies was created in GeoPIXE. The SR-XRF spectrum at the highest incident energy was fitted, and a XANES energy series DA matrix was formed. The same DA matrix was used to extract the As images from maps collected at lower incident energies. By extracting the As peak area for each pixel in all the SR-XRF images XANES spectra were formed at each pixel. Quantitative XANES stacking analysis may be achieved by methods such as PCA and linear combination fitting (e.g., Etschmann et al., 2010, 2014). This is particularly important for larger and more heterogeneous datasets. However, at present a qualitative evaluation of our dataset is sufficient to demonstrate the capability of XANES stacking analysis for identifying changes in As redox on the grain scale.

4.4.0 Results

4.4.1 Conventional Grain Scale Mapping

Grain-scale mapping of sample C406932 by EPMA and SR-XRF provided comparable spatial resolution of trace elements in pyrite (Figure 4-2). Grains for mapping were selected by detailed conventional petrographic methods to ensure that the pyrite grain is representative of the sample. This also identified the presence of gold inclusions and provided grain context. Trace element mapping by both methods confirmed the presence of gold inclusions, and identified a core-rim structure to the pyrite grain. Mapping reveals that the As-rich core of the pyrite is made up of As inclusions as well as arsenian pyrite. It also identifies the presence of Cu, and Zn rich inclusions, and zones of Ni enrichment in the pyrite which overprint the As rich core. EPMA mapping provides with slightly more detail in the As and Ni maps, showing finer structure in the enrichments as the map

resolution is 0.5 μm compared to 2 μm for the SR-XRF maps. However, SR-XRF mapping is not limited to a discrete number of preselected elements. Each pixel of the SR-XRF map contains a full XRF spectrum which can be further investigated for the presence of other trace metals.

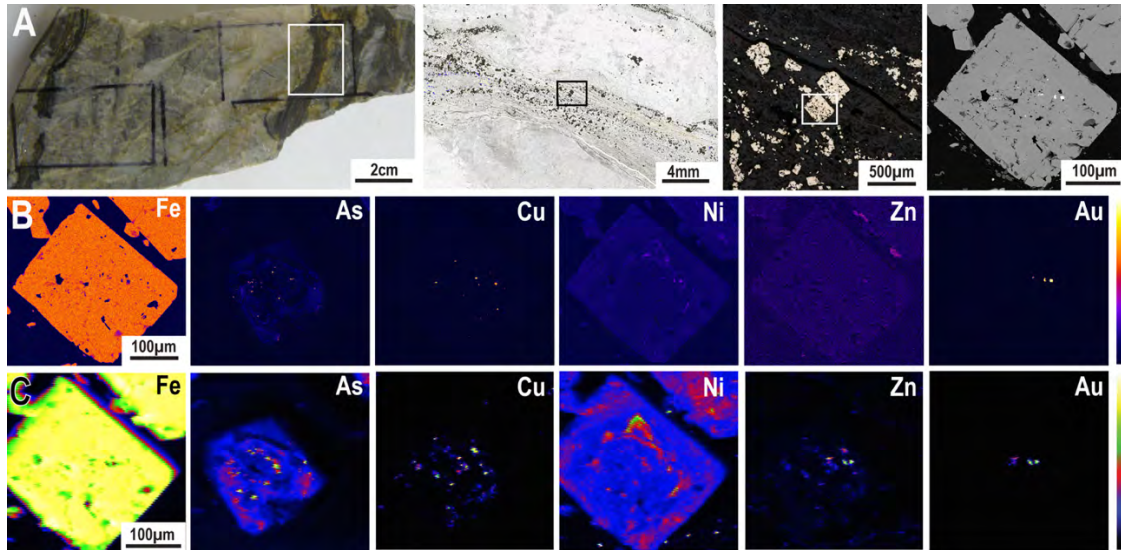


Figure 4-2. Comparison of EPMA and SR-XRF mapping of individual pyrite grains using the conventional workflow for high-resolution analysis (C406932). A. Grain selection for high-resolution analysis generally begins with selecting regions of interest from a whole rock sample (in this case a pyrite rich vein margin) for thin section preparation, followed by characterization by conventional light microscopy and BSE-SEM. B. 0.5 μm resolution EPMA trace element maps of a grain of interest C. 2 μm resolution SR-XRF maps of the same grain show comparable resolution of inclusions and trace element distributions but with full spectrum data collection.

4.4.2 Multi-Scale Mapping

SR-XRF mapping of a sample of auriferous greywacke (E885276) at multiple scales reveals multiple styles of sulfide mineralization and identifies the relationship between Au and sulfides (Figure 4-3). The thin section was prepared on a quartz slide so there is no interference from glass As content. Coarse 20 μm resolution mapping at CHESS revealed that the sample sulfide content is dominated by arsenopyrite, which occurs as

small clusters of needles at the margins of quartz-carbonate stringers, large mm scale clusters, and as elongated needles. The large clusters of arsenopyrite are associated with fine-grained chalcopyrite, sphalerite, and gold at their centers. This information guided grain selection for higher resolution mapping of auriferous regions and ensured that grain selection was representative of the samples. Fine scale mapping (8 and 2 μm resolution) reveals that the arsenopyrite needles are uniform in their geochemistry on the micron scale, with no core-rim structures or growth haloes (Figure 4-3B,C). Trace metals such as Cu, Ni, and Zn are concentrated at the center of the cluster, which does not contain arsenopyrite. Gold also occurs in the central region of the cluster, which is Ca and Mn rich (Figure 4-3B,C). Micron resolution mapping also reveals in its raw spectra that there is no refractory gold in the arsenopyrite needles and that the groundmass is carbonate rich (Figure 4-3C).

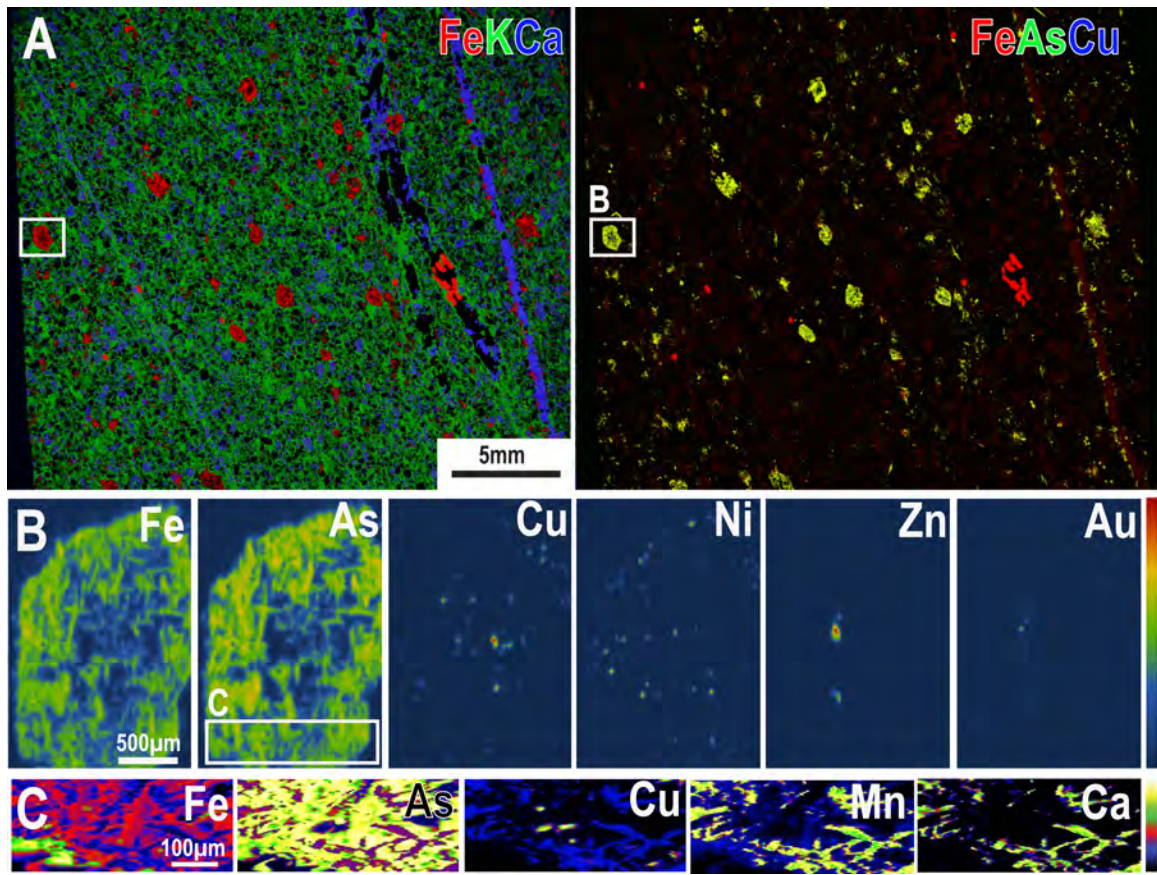


Figure 4-3. SR-XRF maps of sample E885276. A. 20 µm resolution RGB maps of a thin section mounted on a quartz slide reveal potassic and carbonate alteration as well as several styles of sulfide mineralization (apy needles, pyr). B. 8 µm resolution mapping shows that Cu and Ni are associated with arsenopyrite needles, and that Zn and Au are concentrated in the center of the apy cluster C. 3 µm resolution SR-XRF mapping shows chalcopyrite grains in the centre of the apy cluster and a Ca and Mg rich groundmass.

SR-XRF mapping of a sample of auriferous interflow sediment (C408780) at multiple scales reveals multiple styles of sulfide and gold mineralization (Figure 4-4). The thin section was prepared on a quartz slide to avoid interference from glass trace element contents. Coarse 20 µm resolution mapping reveals that there are two different associations with gold and trace metals (Au-Zn and Au-Cu-pyrite), and that gold is not related to a crosscutting ankerite veinlet in the top right of the sample (Figure 4-4A). This information guided grain selection for higher resolution analysis, which further characterized these two gold-trace metal associations (Figure 4-4B,C). The most

spectacular gold mineralization style observed is free gold associated with sphalerite, pyrite and arsenopyrite mineralization (Figure 4-4B). The second type of gold mineralization occurs as inclusions in euhedral pyrite with associated pyrrhotite and chalcopyrite mineralization. These euhedral pyrite grains contain Ni and show some zonation in their As content with As rich rims (Figure 4-4C).

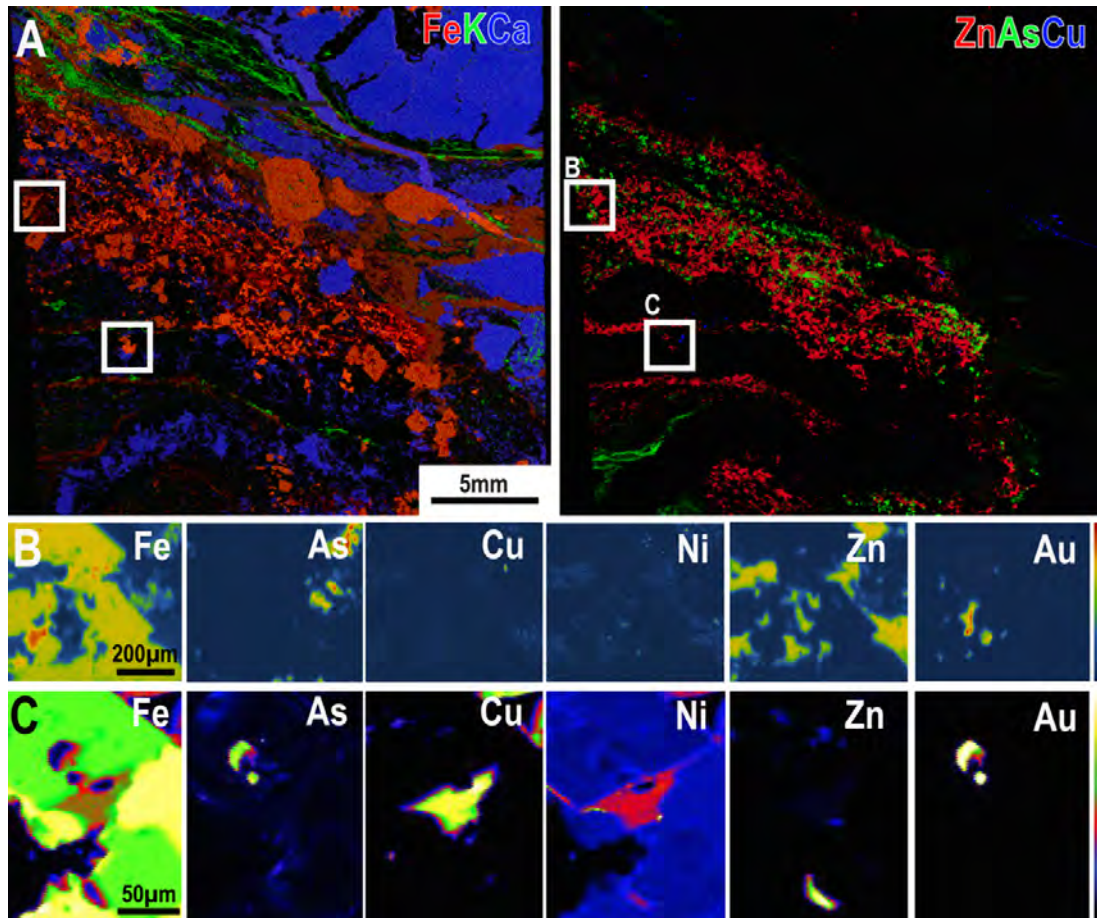


Figure 4-4. SR-XRF maps of sample C408781. A. 20 µm resolution RGB maps of a thin section mounted on a quartz slide reveal the textural and timing relationships between several styles of sulfide mineralization (sph, ccp, pyr, apy), an overprinting ankerite veinlet and two different types of gold mineralization (B,C). This provides insights in potential ore processing issues as well as mineralization history B. 8 µm resolution mapping shows an example of free gold associated with pyrite and sphalerite mineralisation at the sulfide grain margins C. 2 µm resolution SR-XRF of a euhedral pyrite grain with a gold inclusion.

SR-XRF mapping of ankerite vein sample C406934 (20 μm resolution) reveals that gold is associated with regions of pyrite mineralization in the carbonate rich vein material (Figure 4-5A). Gold in the vein material occurs in the main ankerite vein material and is not related to quartz, but it is associated with pyrite. Gold occurs with fine and coarse-grained pyrite, in pyrite stringers as well as with disseminated pyrite. The thin section is mounted on conventionally used float glass, and the As content of the glass interferes with sample scale mapping in regions which are not sulfide rich (Figure 4-5A FeAsCu map). From sample-scale mapping a grain of interest was selected based on its high Au and As content. High-resolution (3 μm) SR-XRF mapping of the selected gold bearing pyrite grain shows that gold occurs along the pyrite grain margin and in fractures (Figure 4-5B). It also reveals complex zonation of As and trace metals (Cu, Zn, Ni). This occurs both as laminations and inclusions, which are Cu and As-rich. Depletions in S are also observed in some of the As enriched haloes. At the grain-scale, the As content of the glass slide does not interfere with mapping as the density of pyrite does not allow for X-ray penetration through the ~ 30 μm thick pyrite grain to the glass, and the high As content of the arsenian pyrite overshadows any As detected in the glass through the carbonate rich groundmass (Figure 4-5B).

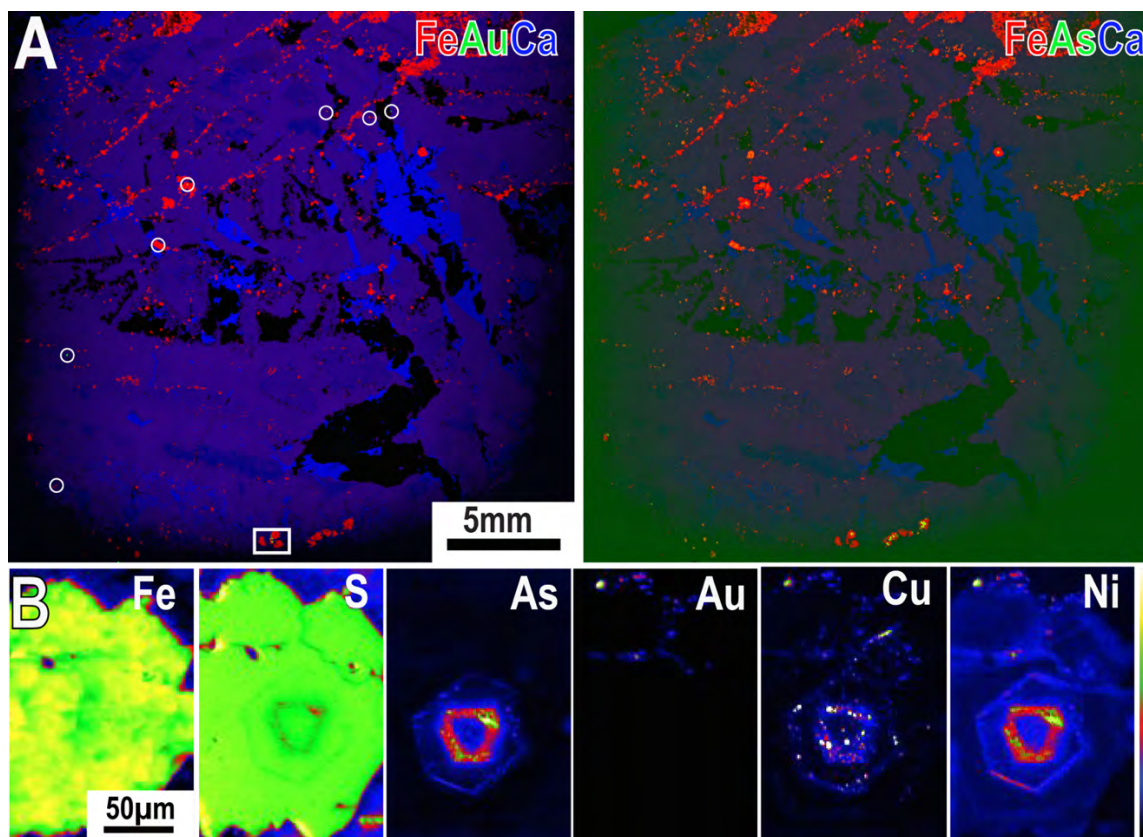


Figure 4-5. A. SR-XRF maps of C406934. A. 20 µm resolution RGB maps of a thin section of gold bearing ankerite vein show the distribution of pyrite in the ankerite rich vein material. The circles outline regions with Au mineralization, and the square is the region mapped in B. High resolution SR-XRF maps (2 µm resolution) show haloes of complex As, Cu, Zn and Ni zonation in the pyrite grain (C406934_001) as well as Au at grain margins and in fractures.

4.4.3 Point XRF and XANES

Each pixel in the SR-XRF contains a full XRF spectrum which can be investigated further for trace elements which are low in concentration and do not appear in the mapping. From this, regions of interest were interrogated by a transect of point XRF analysis with longer dwell times to increase count rates for low concentration elements. The transect reveals that even the As-poor regions of the map have substantial As contents (Figure 4-6A,B). It also reveals a negative correlation between the concentration of As and Fe in the sample from the grain center to the rim. This provides some insights into the mode of As uptake

into the pyrite lattice, and has implications for fluid redox. Most importantly, point SR-XRF identifies a minor refractory gold contribution which is highest in the outer As halo of the grain evidenced by a peak at ~9,713 eV.

XANES analysis was applied to further investigate the relationship between As and Au in the haloed pyrite grain (Figure 4-6C,D). The XANES spectra provide insights into the speciation of As in the sample, revealing a change in As speciation from the central halo to the rim of the pyrite grain (Figure 4-6C). Arsenic in the outer halo has a XANES spectrum dominated by an edge position characteristic of As^{1-} (11,867 eV) which is commonly observed in arsenopyrite and arsenian pyrite. It is clear that there is contribution of more than one As species in the inner halo and the outer rim of the grain (Figure 4-6B). The outer rim of the grain contains less As, but has a XANES spectrum characteristic of more oxidized As species with features at 11,871 eV (As^{3+}) and 11,874 eV (As^{5+}). XANES Au-edge spectra were collected from the outer halo, which showed a Au peak in the XRF spectra (Figure 4-6A). The XANES spectrum is consistent with the presence of metallic Au^0 and Au^{1+} (Figure 4-6B). SR-XRF map stacks were collected to visualize the spatial variability in As speciation across the grain. The average XANES spectra for the entire region reveals that As^{1-} as the dominant As species in the pyrite grain, with an edge position of 11,867 eV (Figure 4-7). This reflects the fact that the bulk of the As in the sample is from the As-rich core of the grain (Figure 4-6A,B). The contribution of As from the As poor regions at the edge of the grain is negligible in terms of total grain As. Another limiting factor is the 20 μm spatial resolution of the map, which is not sufficient to visualize the fine growth haloes. The map also highlights the issue of using glass slides, as the contribution of As^{3+} and As^{5+} from the glass can be detected in the 11,871 and 11,874eV maps. This is observed as the lighter blue region around the grain where the X-rays can penetrate the carbonate groundmass to sample the glass.

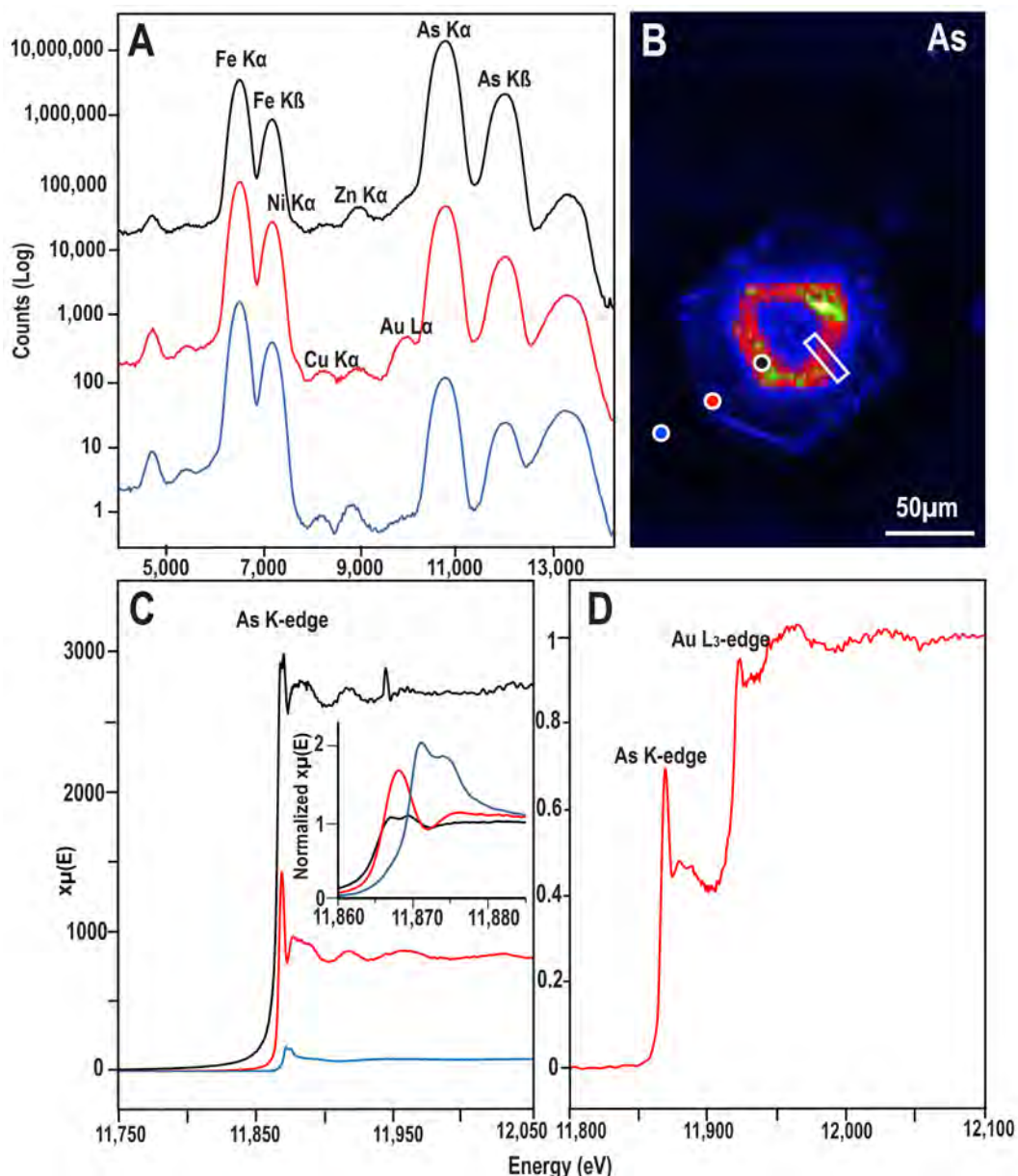


Figure 4-6. SR-XRF and XANES spectrum of C406934_001. A SR-XRF spectrum across a haloed grain (Figure 4-5, 4-6B) shows variability in As and trace metal content. The black and blue spectra are displaced for clarity. B. Map of As content (Figure 4-5) showing the positions from which point SR-XRF and XANES data was collected (spots) as well as where a TEM sample was extracted (box) C. Pre-normalization As K-edge XANES spectra from across the grain shows variability As content and in edge position. The inset normalized spectra of the edge region shows differences in edge position and shape indicating changes in As speciation across the grain. D. Au-L edge XANES spectra for the outer As halo which showed Au in the XRF spectra.

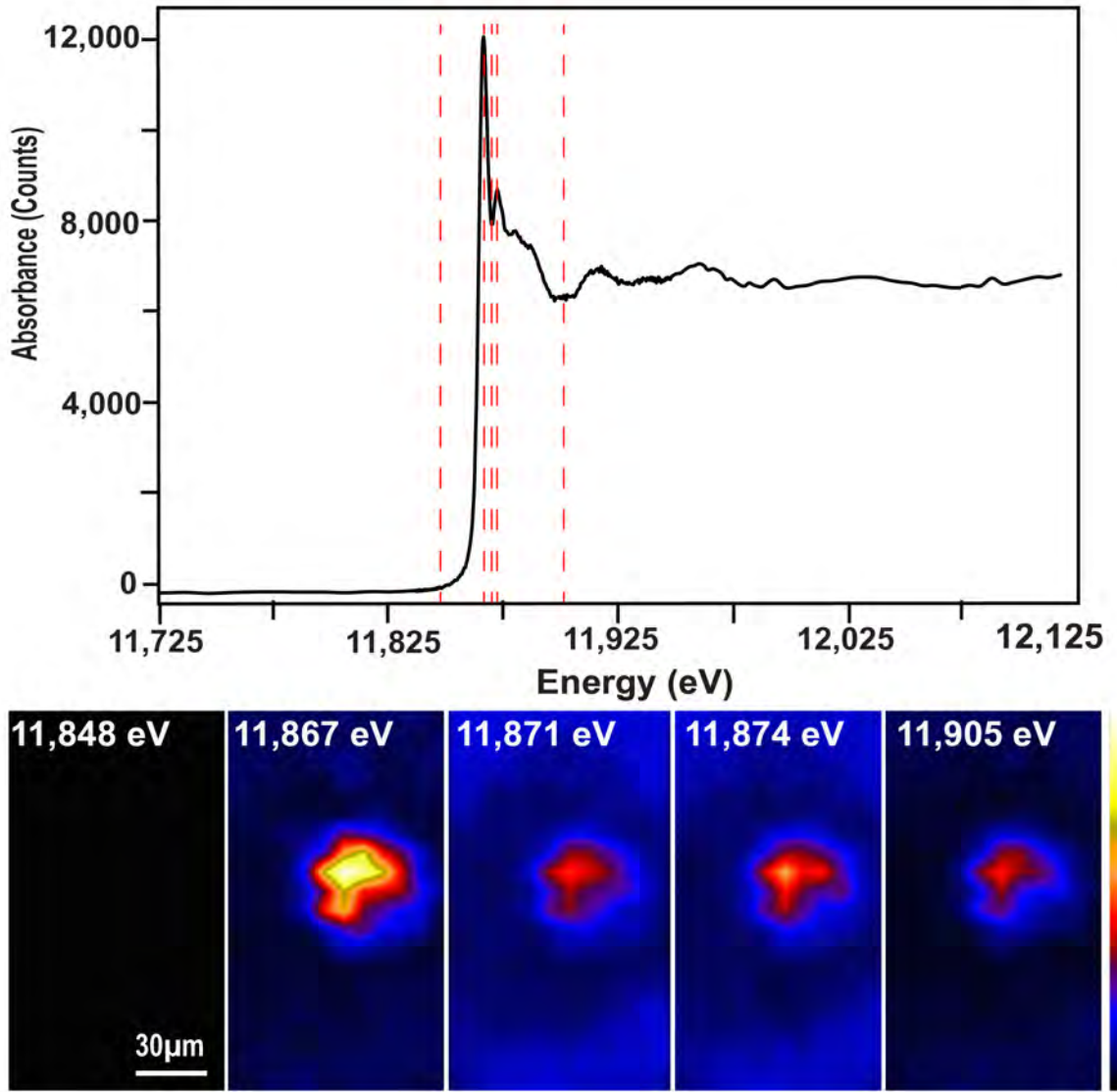


Figure 4-7. SR-XRF As XANES stacks of C406934_001 (Figure 4-5). Average As XANES spectra of a haloed pyrite grain (20 μm resolution) and As maps at multiple energies. The As K-edge is indicative of As^{1-} being the primary species of As in the pyrite grain.

4.4.4 Transmission Electron Microscopy

The non-destructive nature of SR-XRF analysis allows for further investigation of regions of interest, and so a FIB foil was extracted from the inner halo (Figure 4-6B) for TEM analysis. BSE-SEM imaging of the halo and the FIB foil reveal that the inner halo growth zone is composed both of arsenopyrite inclusions as well as irregular patches of As enriched pyrite in the vicinity of the arsenopyrite (Figure 4-8B, 9A). This supports the observation of two As contributions to the As XANES spectra of that region. The arsenopyrite crystals have anhedral to subhedral shapes and are randomly distributed in the growth zone. EDX mapping of several submicron inclusions reveals that the bulk of the inclusions are likely arsenopyrite, but that there are also Cu rich inclusions. It also shows the presence of As rich zones in the pyrite (Figure 4-8B,C). High-resolution bright field images and HAADF images reveal the {022}, {200}, and {-212} families of lattice planes of arsenopyrite (Fig. 4-9C,D).

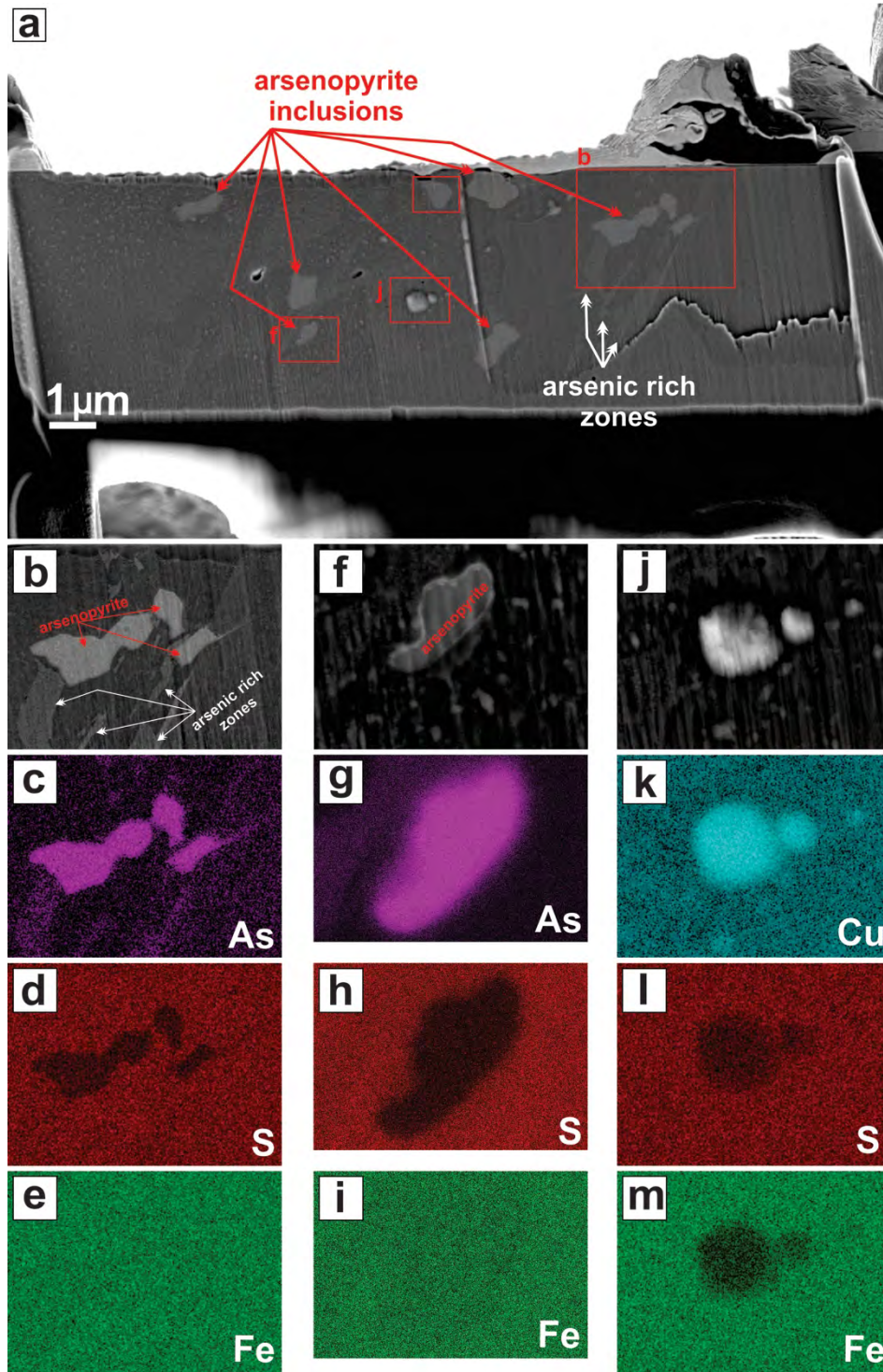


Figure 4-8. BSE-SEM images and EDS maps of the FIB foil from C406934_001 (Fig 6A). FIB milling produced a foil which shows the distribution of arsenopyrite inclusions and As rich regions in pyrite in the third dimension. B-M. EDS elemental maps showing the composition of the inclusions in the extracted ultra-thin FIB foil

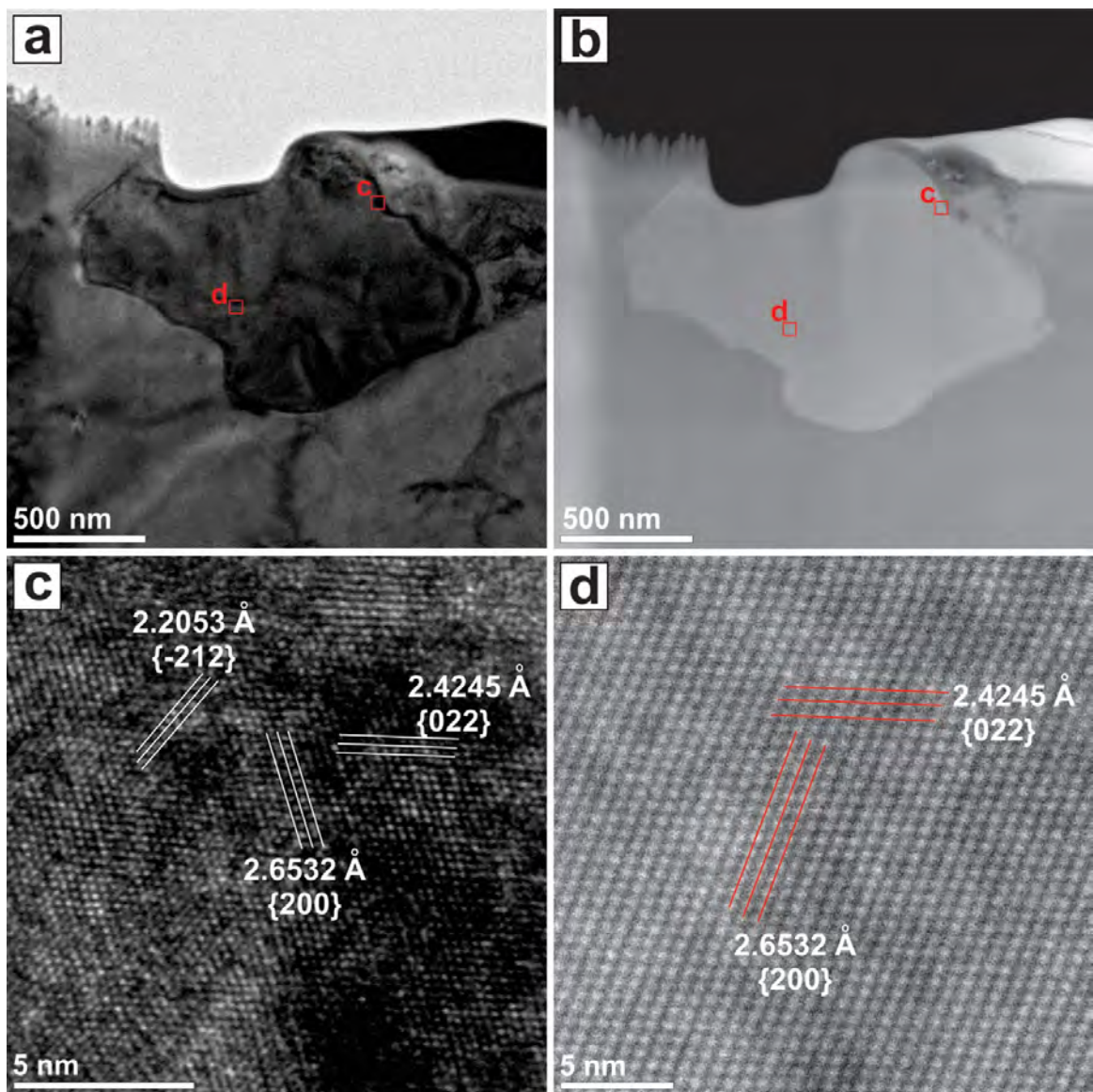


Figure 4-9. TEM analysis of FIB foil C406934_001 analysis. A. Bright-field TEM image of an arsenopyrite inclusion in the FIB foil. B. HAADF-TEM image of the same inclusion C-D. Bright-field and HAADF lattice fringe images show the {022}, {200}, and {-212} families of lattice planes of arsenopyrite

4.4.5 Multi-Scale Thin Section vs. Billet Analysis

Multi-scale mapping of thin section and off cuts of an auriferous sulfide clast (C408779) reveals that both sample types produce equivalent data sets at 20 μm mapping resolution (Figure 4-10A,D). However, because the thin section is mounted in float glass, which contains trace metals, the whole rock mapping provides better resolution for As mapping and more clearly reveals As-rich growth haloes (Figure 4-10D). The coarse sample scale mapping reveals that many of the pyrite grains contain As rich rims and inner haloes, and that gold occurs at grain margins. Higher resolution mapping (10 μm resolution) reveals euhedral Ni zonation in the pyrite grains which was not resolvable at the sample-scale, which is potentially the result of multiple stages of pyrite growth. It also reveals the textural relationships between sphalerite, chalcopyrite and pyrite mineralization which was not resolved at the sample-scale (Figure 4-10 B,E). Multi-stage pyrite growth was investigated further with 2 μm resolution mapping of a representative grain (Figure 4-10 C,F) and reveals that in addition to As and Ni zonation, the pyrite grain has a copper enriched anhedral core. This is overprinted by an arsenian euhedral overgrowth with a Ni enriched euhedral rim. In the whole rock sample, topography begins to impact mapping at the 2 μm scale, however, the trace element associations observed in thin section mapping are still resolvable (Figure 4-10C,F).

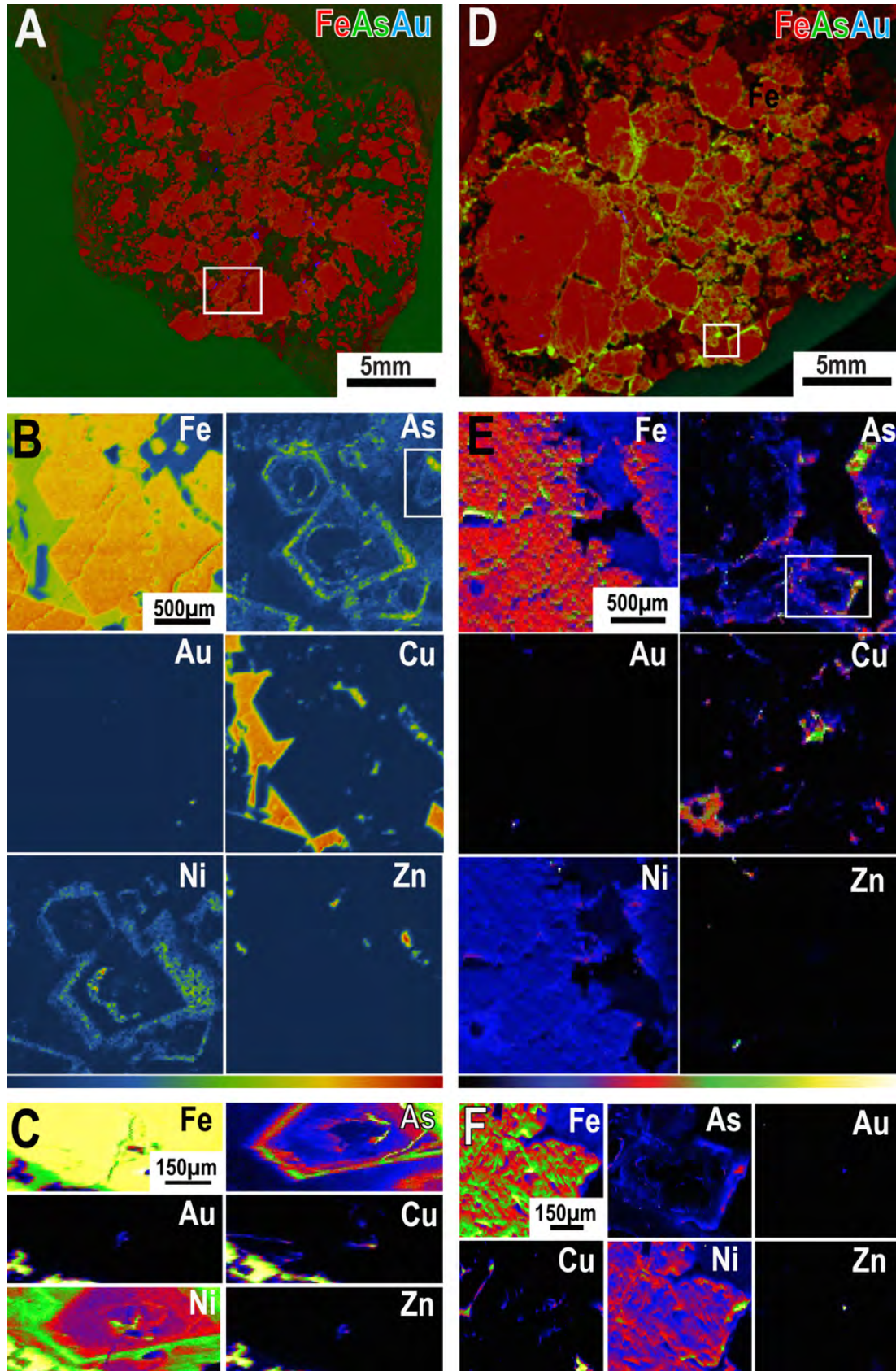


Figure 4-10. SR-XRF mapping of C408779 thin section and billet. A and D. RGB maps at 20um resolution show that there is zonation in the As contents of pyrite grains, and gold at grain margins. However, zonation in the pyrites is more pronounced in the raw rock sample due to the As content of the glass slide on which the thin section is made. B and E. At a slightly higher resolution (B-8µm resolution) and more zoomed in (E-20µm resolution) SR-XRF maps from the CLS (B) and APS (E) show that there is also a bimodal spatial relationship between As and Ni pyrite content. C. and F. At 2um resolution, the relationship between Au and Ni can be clearly seen and sample topography begins to have an influence on map quality (C- C408779_001).

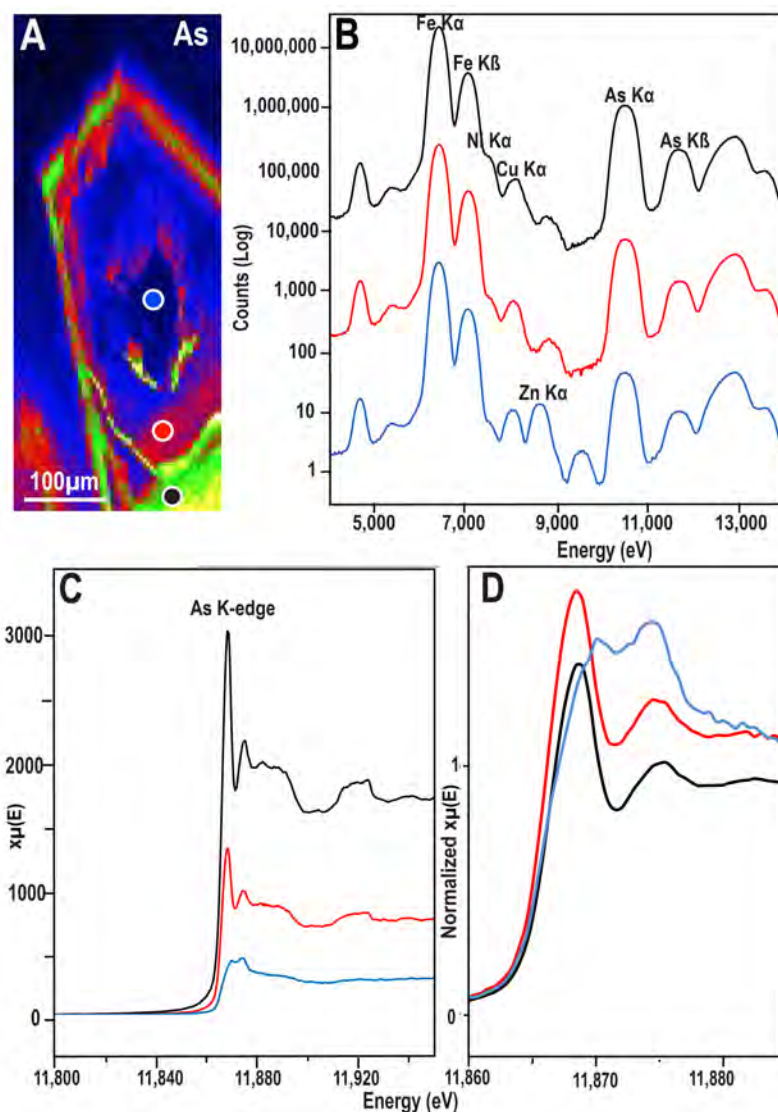


Figure 4-11. SR-XRF and XANES spectra of C408779_001. A. SR-XRF map of As in grain C408779_001 (Figure 4-10C) (color of dot in map reflects the position where the spectra in C-D were collected) B. SR-XRF spectrum show variability in As and trace metals across the growth haloes C. Pre-Normalization As K-edge XANES spectra show that there is variability in the As concentration as well as position and shape of the As edge across the grain. D. The normalized edge region of the As K-edge XANES spectra reveals that rim regions of the grain are dominated by As^{1-} and the core of the grain contain As in a higher oxidation state (As^{3+} and As^{5+}) when compared to reference spectra for those oxidation states.

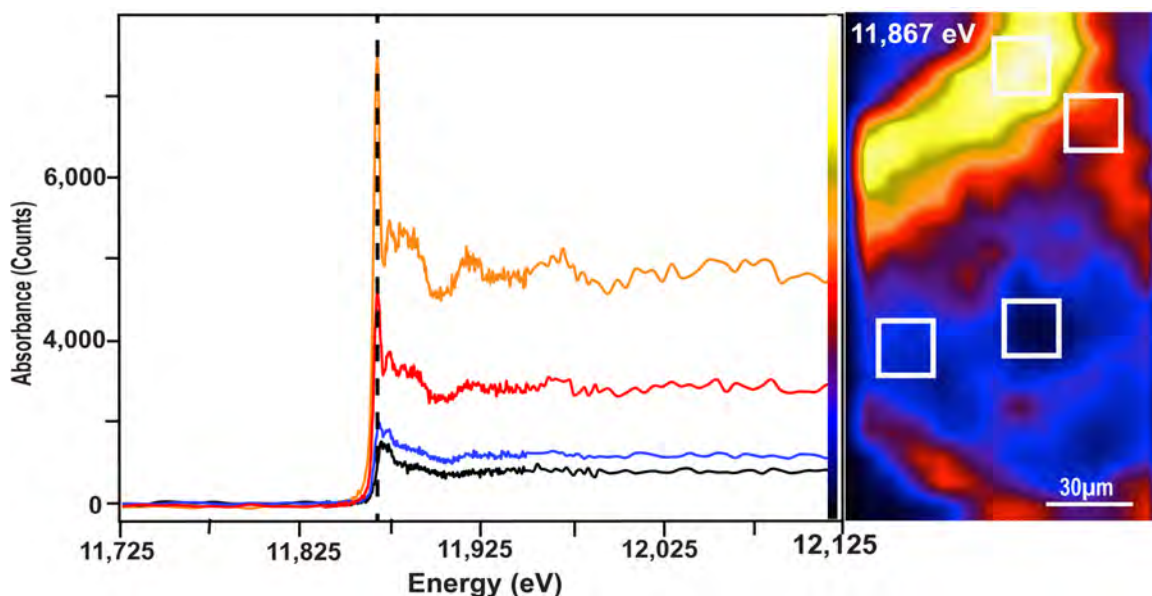


Figure 4-12. XANES As stack of C408779. XANES spectra from a haloed pyrite grain in the auriferous clast, and a map at 11.867 keV (spectra extracted from regions outlined in map, and corresponding colors).

A transect of point SR-XRF analysis across the pyrite grain from the rim to the core in Figure 11 E, shows while there is variability in the As and trace metal contents (Cu, Ni, Zn) across the grain there is no detectable gold (Figure 4-11B). The core of the grain is enriched in Zn while the rim is enriched in Ni and As (Figure 14-11 A,B). XANES analyses were taken from the same locations and reveals variability in the speciation of As across the grain. The XANES spectra from the As rich rim of the grain are characteristic of As^{1-} with an edge position of 11,867 eV (Figure 4-11 C,D). The As-K edge of the XANES spectra from the As poor inner region of the grain is at a higher energy than the rim spectra (Figure 4-11D). The feature at 11.871 eV is characteristic of a more oxidized form of As, likely As^{3+} . SR-XRF map stacks were collected and confirm the presence of As^{1-} as the dominant As species in the pyrite grain, with an edge position of 11,867 eV (Figure 4-12). However, it is apparent that in the central regions of the pyrite grain that the edge shifts to slightly higher energy with a change in edge shape that reflects what is observed in the point spectra. There are no issues with As signal from the

glass slide in this SR-XRF stack because the mapping region is entirely sulfide of sufficient thickness and density to attenuate the incident X-rays.

4.4.6 Whole Rock Mapping of Uncharacterized Samples

The capability of whole rock mapping to provide meaningful geochemical information for previously uncharacterized samples was investigated with 20 μm resolution SR-XRF mapping (Figure 4-13). Whole sample mapping of ankerite vein samples from two different deposits identifies distinct differences in the associations between gold and trace elements (Figure 4-14,15). This also highlights that while processing of multiple maps together is a good first set (Figure 4-13), it is necessary to create sample specific matrices to reveal meaningful trace element associations in each sample (e.g., Figure 4-15,16). Sample specific maps reveal variability in the geochemistry of vein material, which can be related to macro scale observations of banding in the vein (Figure 4-16 Fe, Mn maps) and the relationship with ultramafic host rock (Figure 4-15 Ni content). Gold is identified in multiple contexts. In the Buffalo-Ankerite vein sample, gold occurs in a seam of sericite rich vein material and in the Dome ankerite vein sample, gold is concentrated in sulfide rich vein margins as well in overprinting quartz veining.

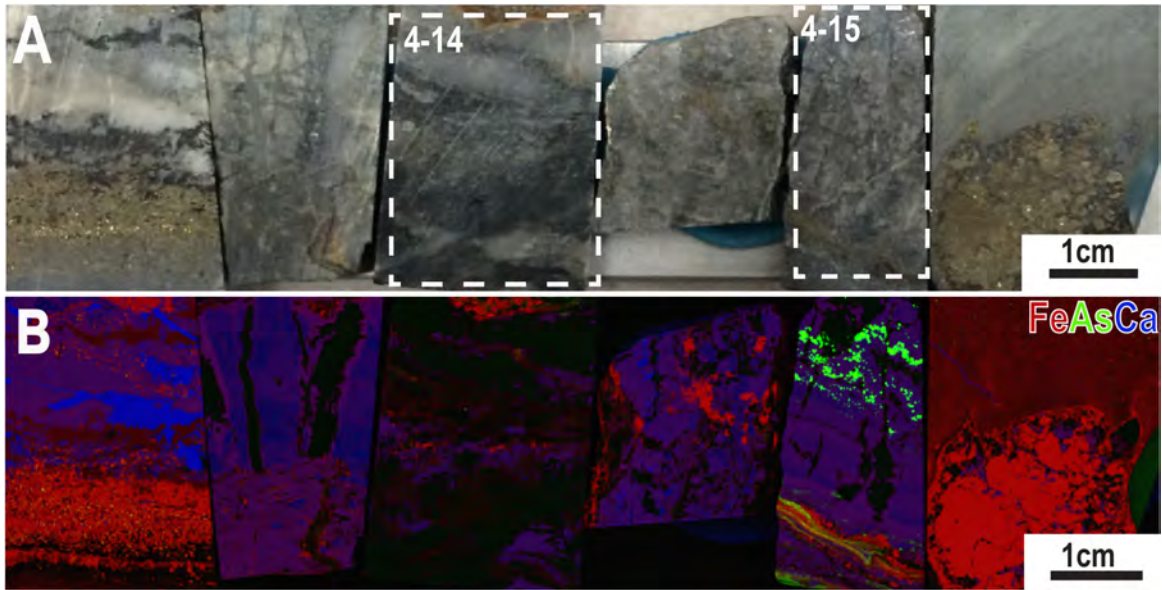


Figure 4-13. Whole rock SR-XRF RGB maps A. Mapping unpolished whole rock samples (left to right - C409401, C410910, BA, C410300, C410280, C408779) significantly cuts down sample preparation time. B. SR-XRF maps (20µm resolution) of the above 6 samples (red – Fe, green – As, blue – Ca) shows variability in the sulfide content of the samples (pyrite, arsenopyrite) as well as carbonate chemistry (Fe and Ca content). Gold can also be identified at this resolution (Appendix D2). The maps from the two boxed samples are features in Figure 4-14 and 4-15.

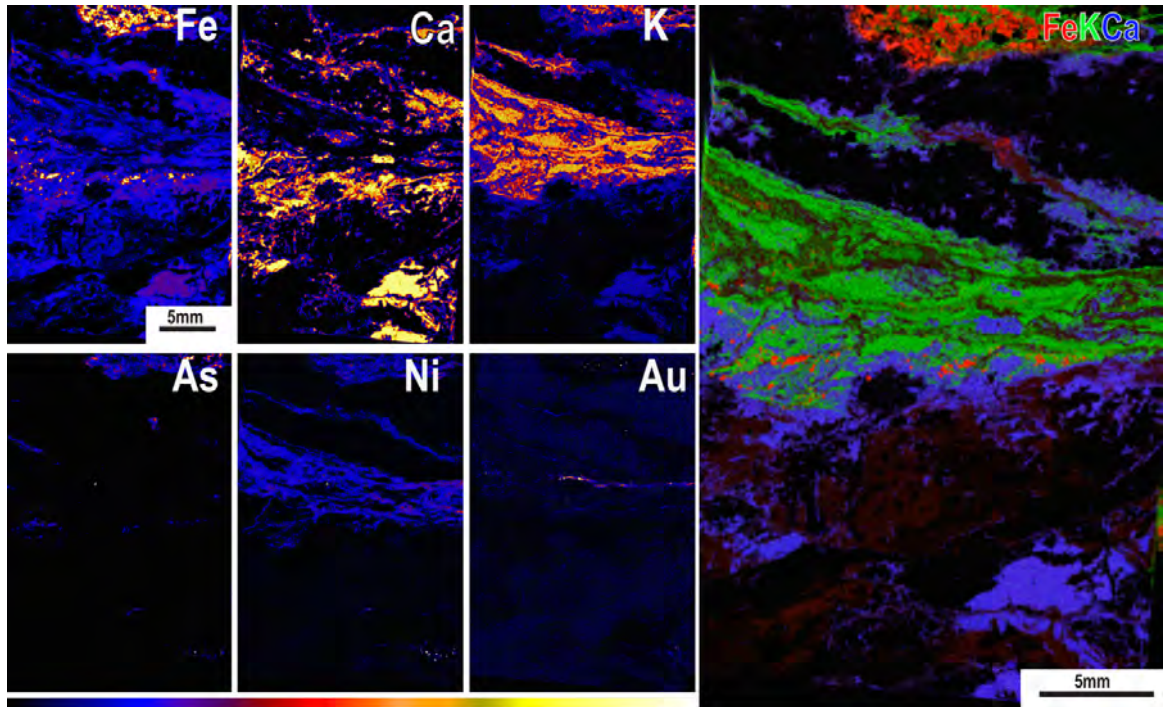


Figure 4-14. Whole rock SR-XRF maps for sample BA (Buffalo Ankerite). This is a previously uncharacterized raw cut sample from the Buffalo-Ankerite mine which reveals differences in the vein geochemistry of these ankerite veins from the Dome ankerite veins (Ni enrichment). It also provides context for gold mineralization in the potassium (sericite) rich regions of the vein, as well as trace element information with mineralogical context samples (As and Ni rich pyrite) which can be used to guide further analysis.

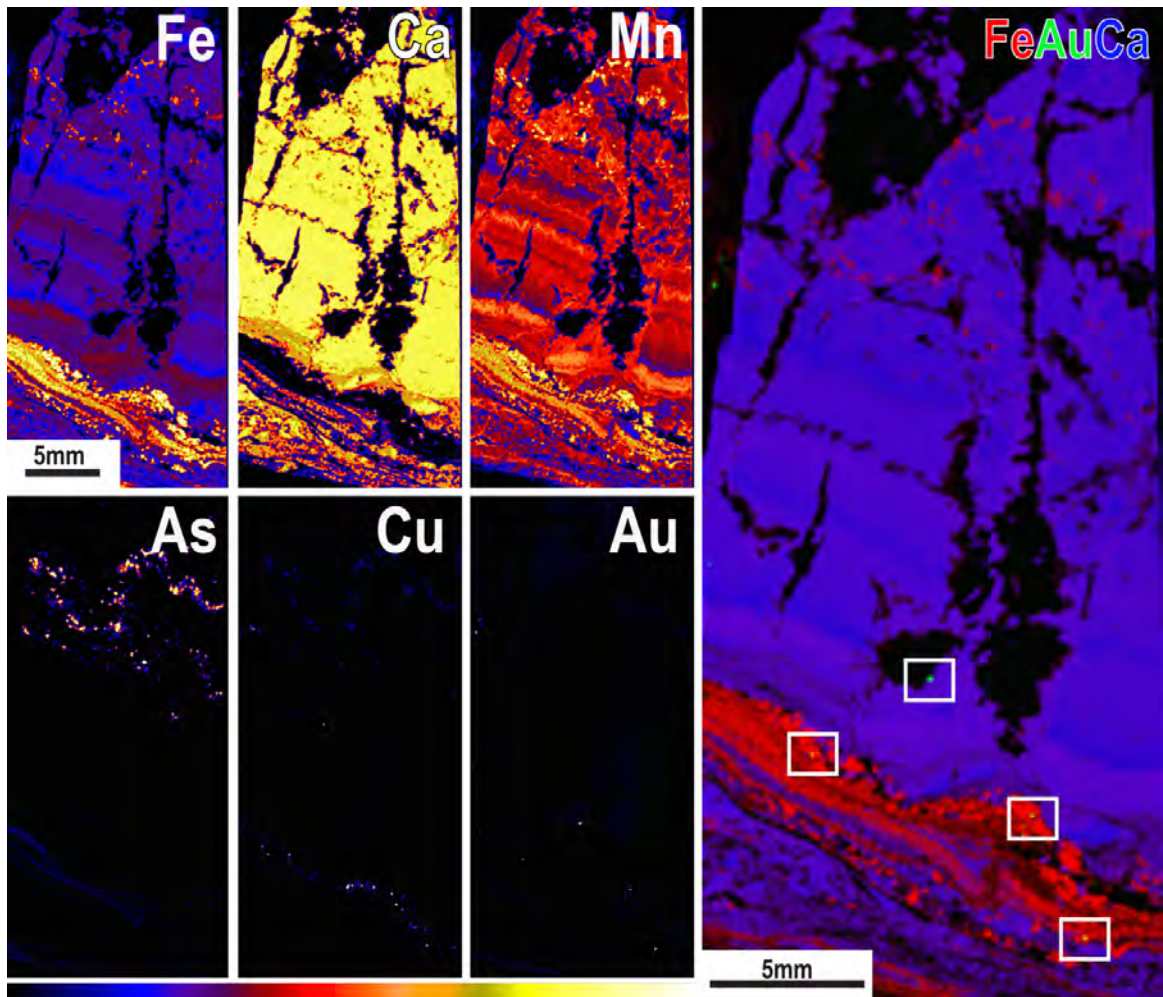


Figure 4-15. SR-XRF maps C410280. This is a previously uncharacterized raw cut sample and provides comparable resolution to thin section mapping at 20 μ m resolution revealing variations in the geochemistry of vein mineralogy (carbonate Fe and Mn content), trace metal content of sulfide phases (As, Cu) and identifies micron scale gold mineralization throughout the sample. This information can be used to guide further analysis.

4.5.0 Discussion

Large scale SR-XRF mapping of samples from orogenic gold deposits is an effective method for quickly and effectively identifying the presence of gold in multiple types of complex samples, for characterizing gold associations with various mineral phases, and for identification of trace element associations with gold (e.g., Figure 4-15,16). This is an inherently time consuming task by conventional petrographic methods as gold in orogenic deposits is commonly nuggety on the sample and micron scale. We show that it is possible to quickly and efficiently detect and characterize gold in a number of different geologic contexts and scales. The integration of trace element associations within the mineralogical and textural context of a sample is incredibly powerful. If this information is available early in the mining cycle it could be used to guide exploration in complex systems where bulk rock geochemistry does not provide satisfying answers.

In addition to quickly identifying ore phases and trace element associations with them, the ability to produce large-scale maps improves the efficiency of grain selection for higher resolution studies (e.g., Figure 4-3,4). While other micro-analytical mapping techniques such as LA-ICP-MS and EMPA are broadly used in the mining industry for grain-scale studies, they rely on extensive sample characterization by traditional methods (petrography, BSE-SEM) for grain selection (e.g., Figure 4-2). This is due to limitations in the scale of the mappable area by EMPA, SIMS and LA-ICP-MS, as well as sample preparation requirements. While traditional grain selection techniques may provide better textural resolution (depending on the resolution of your SR-XRF mapping), they are much more time consuming and provide limited to no geochemical information. Sample selection by SR-XRF mapping reveals heterogeneity in texture, geochemistry, and mineralogical context, which helps minimize bias. On the grain-scale, SR-XRF provides comparable spatial resolution and detection limits to other conventional techniques (e.g., LA-ICP-MS, EMPA, Figure 4-1, 2). Additionally, SR-XRF is non-destructive which makes it very complementary to higher resolution analysis (e.g., TEM) and allows for multi-scale mapping of the same region. Not only does SR-XRF mapping aide in mitigating sample bias by multi-scale mapping, the dataset is not constrained to a small number of preselected elements of interest. Each pixel contains a full spectrum, which

allows for further interrogation of the data and can provide insights in new and sometimes unexpected results.

Examples of this are seen in samples C406934 (Figure 4-6) and E885276 (Figure 4-3). With the arsenopyrite rich sample (E885276) the relationship between gold and arsenopyrite was constrained by multi-scale mapping and a suspected component of refractory gold was ruled out. Conversely, refractory gold was identified in sample C406934 in one stage of pyrite growth. The identification of refractory gold has important exploration and geometallurgy implications. The ability to distinguish whether refractory gold is nano-particulate metallic gold or lattice bound Au^{1+} has significant implications for ore processing and improving recoveries. If there is a significant component of lattice bound gold, then high-pressure oxidation of the pyrite for gold liberation may be required, a process which is more involved and expensive than conventional cyanide leaching. The distribution and nature of refractory gold also influences the fineness of the grind required for economic recoveries. Understanding the relationship between Au and As is also relevant for exploration and remediation. It can provide insights into fluid chemistry, metal endowments and mineralizing mechanisms. Additionally, characterizing the speciation of As reveals the redox conditions of the fluid, and the conditions of As uptake into pyrite which also plays a role in the concentration of deleterious elements. Under more oxidizing conditions, pyrite will incorporate As^{3+} into its structure which allows for the incorporation of higher concentrations of gold as well as deleterious elements such as Se and Pb, but also higher concentrations of refractory gold. Traditionally, these sorts of speciation studies have only been applied late in the mining cycle to address environmental and remediation questions. However, with advances in the application of SR-XRF stacks, it is possible to investigate trace element speciation on the sample scale.

4.6.0 Conclusions

This work highlights the potential for improving the speed and workflow for high-resolution studies of ore deposits while providing simultaneous geochemical and textural datasets which exceeds conventional methods. Integrating bulk rock with *in situ* multi-

scale synchrotron analysis provides a very powerful dataset in which the micron scale geochemical observations are well constrained and can be more confidently extrapolated to the sample or deposit scale. The value of moving beyond simple bulk rock geochemistry early in the mine cycle is being addressed by the scientific community (e.g., QEMSCAN, Terraspec, table top XRF systems). However, none of the techniques presently available provide the same spatially resolvable, multi-scale, and quantitative geochemical information as SR-XRF mapping does. The integration of large scale SR-XRF mapping datasets at the beginning of a workflow (on whole rock samples) followed by higher resolution mapping, point SR-XRF, XANES analysis, and complementary submicron scale analysis has not been previously described. The lack of a need for sample preparation required for these techniques makes them ideal for integration into standard exploration and metallurgical studies early in the mining cycle. This is integral to avoiding mineral liberation issues in the future of a deposit, and for exploring in a climate in which lower grade and more complex deposit types are being exploited. This workflow is not just relevant for orogenic deposits but can be applied to any deposit type in which ore minerals and elements are dilute.

4.7.0 References

- Blanchard, P.E., Van Loon, L.L., Reid, J.W., Cutler, J.N., Rowson, J., Hughes, K.A., Brown, C.B., Mahoney, J.J., Xu, L., Bohan, M. and Demopoulos, G.P., 2017. Investigating arsenic speciation in the JEB Tailings Management Facility at McClean Lake, Saskatchewan using X-ray absorption spectroscopy. *Chemical Geology*, 466(4), pp. 617-626.
- Brugger, J., Pring, A., Reith, F., Ryan, C., Etschmann, B., Liu, W., O'Neill, B. and Ngothai, Y., 2010. Probing ore deposits formation: New insights and challenges from synchrotron and neutron studies. *Radiation Physics and Chemistry*, 79(2), pp.151-161.
- Cabri, L.J., Newville, M., Gordon, R.A., Crozier, E.D., Sutton, S.R., McMahon, G. and Jiang, D.T., 2000. Chemical speciation of gold in arsenopyrite. *The Canadian Mineralogist*, 38(5), pp.1265-1281.
- Cook, N.J. and Chryssoulis, S.L., 1990. Concentrations of invisible gold in the common sulfides. *The Canadian Mineralogist*, 28(1), pp.1-16.

- Cook, N.J., Ciobanu, C.L., Meria, D., Silcock, D. and Wade, B., 2013. Arsenopyrite-pyrite association in an orogenic gold ore: Tracing mineralization history from textures and trace elements. *Economic Geology*, 108(6), pp.1273-1283.
- Deditius, A.P., Utsunomiya, S., Renock, D., Ewing, R.C., Ramana, C.V., Becker, U. and Kesler, S.E., 2008. A proposed new type of arsenian pyrite: Composition, nanostructure and geological significance. *Geochimica et Cosmochimica Acta*, 72(12), pp.2919-2933.
- Deditius, A.P., Utsunomiya, S., Reich, M., Kesler, S.E., Ewing, R.C., Hough, R. and Walshe, J., 2011. Trace metal nanoparticles in pyrite. *Ore Geology Reviews*, 42(1), pp.32-46.
- Deditius, A.P., Reich, M., Kesler, S.E., Utsunomiya, S., Chryssoulis, S.L., Walshe, J. and Ewing, R.C., 2014. The coupled geochemistry of Au and As in pyrite from hydrothermal ore deposits. *Geochimica et Cosmochimica Acta*, 140, pp.644-670.
- Dimov, S.S., and Hart, B.R., 2011, Applications of Microbeam Analytical Techniques in Gold Department Studies, Proceedings of the 50th Annual Conference of Metallurgists of CIM, World Gold 2011, Edited by Deschenes, G., Dimatrikapoulis, R., Bouvhard, J., p. 17-26.
- Dyar, M.D., Delaney, J.S. and Sutton, S.R., 2001. Fe XANES spectra of iron-rich micas. *European Journal of Mineralogy*, 13(6), pp.1079-1098.
- Etschmann, B.E., Ryan, C.G., Brugger, J., Kirkham, R., Hough, R.M., Moorhead, G., Siddons, D.P., De Geronimo, G., Kuczewski, A., Dunn, P. and Paterson, D., 2010. Reduced As components in highly oxidized environments: Evidence from full spectral XANES imaging using the Maia massively parallel detector. *American Mineralogist*, 95(5-6), pp.884-887.
- Etschmann, B.E., Donner, E., Brugger, J., Howard, D.L., de Jonge, M.D., Paterson, D., Naidu, R., Scheckel, K.G., Ryan, C.G. and Lombi, E., 2014. Speciation mapping of environmental samples using XANES imaging. *Environmental Chemistry*, 11(3), pp.341-350.
- Etschmann, B., Liu, W., Li, K., Dai, S., Reith, F., Falconer, D., Kerr, G., Paterson, D., Howard, D., Kappen, P. and Wykes, J., 2017. Enrichment of germanium and associated arsenic and tungsten in coal and roll-front uranium deposits. *Chemical Geology*, 463, pp.29-49.
- Fawcett, S.E. and Jamieson, H.E., 2011. The distinction between ore processing and post-depositional transformation on the speciation of arsenic and antimony in mine waste and sediment. *Chemical Geology*, 283(3), pp.109-118.
- Fawcett, S.E., Jamieson, H.E., Nordstron, D.K., McCleskey, R.B., 2015. Arsenic and antimony geochemistry of mine wastes, associated waters and sediments at the Giant Mine, Yellowknife, Northwest Territories, Canada. *Applied Geochemistry*, 62, pp.3-17.

- Feick, K., Bertelli M., Banerjee, N., McCormack, D., 2015. An evaluation of regional geochemistry in the Kirkland Lake area: Towards a new gold exploration model. PDAC-SEG Student Minerals Colloquium. Abstract #23.
- Feng, R., Gerson, A., Ice, G., Reininger, R., Yates, B. and McIntyre, S., 2007, January. VESPERs: a beamline for combined XRF and XRD measurements. In AIP Conference Proceedings (Vol. 879, No. 1, pp. 872-874). AIP.
- Fisher, L.A., Fougrouse, D., Cleverley, J.S., Ryan, C.G., Micklethwaite, S., Halfpenny, A., Hough, R.M., Gee, M., Paterson, D., Howard, D.L. and Spiers, K., 2015. Quantified, multi-scale X-ray fluorescence element mapping using the Maia detector array: Application to mineral deposit studies. *Mineralium Deposita*, 50(6), pp.665-674.
- Fougrouse, D., Micklethwaite, S., Tomkins, A.G., Mei, Y., Kilburn, M., Guagliardo, P., Fisher, L.A., Halfpenny, A., Gee, M., Paterson, D. and Howard, D.L., 2016. Gold remobilisation and formation of high grade ore shoots driven by dissolution-reprecipitation replacement and Ni substitution into auriferous arsenopyrite. *Geochimica et Cosmochimica Acta*, 178, pp.143-159.
- Gray, M.D. and Hutchinson, R.W., 2001. New evidence for multiple periods of gold emplacement in the Porcupine mining district, Timmins area, Ontario, Canada. *Economic Geology*, 96(3), pp.453-475.
- Gregory, M.J., Lang, J.R., Gilbert, S. and Hoal, K.O., 2013. Geometallurgy of the Pebble porphyry copper-gold-molybdenum deposit, Alaska: Implications for gold distribution and paragenesis. *Economic Geology*, 108(3), pp.463-482.
- Jamieson, H.E., 2014. The legacy of arsenic contamination from mining and processing refractory gold ore at Giant Mine, Yellowknife, Northwest Territories, Canada. *Reviews in Mineralogy and Geochemistry*, 79(1), pp.533-551.
- Jones, M.P., 1987. *Applied mineralogy: a quantitative approach*. Graham & Trotman.
- Kirkham, R., Dunn, P.A., Kuczewski, A.J., Siddons, D.P., Dodanwala, R., Moorhead, G.F., Ryan, C.G., De Geronimo, G., Beuttenmuller, R., Pinelli, D. and Pfeffer, M., 2010, June. The Maia Spectroscopy Detector System: Engineering for Integrated Pulse Capture, Low-Latency Scanning and Real-Time Processing. In AIP Conference Proceedings (Vol. 1234, No. 1, pp. 240-243). AIP.
- Large, R.R., Danyushevsky, L., Hollit, C., Maslennikov, V., Meffre, S., Gilbert, S., Bull, S., Scott, R., Emsbo, P., Thomas, H. and Singh, B., 2009. Gold and trace element zonation in pyrite using a laser imaging technique: implications for the timing of gold in orogenic and Carlin-style sediment-hosted deposits. *Economic Geology*, 104(5), pp.635-668.

- Large, R.R., Bull, S.W. and Maslennikov, V.V., 2011. A carbonaceous sedimentary source-rock model for Carlin-type and orogenic gold deposits. *Economic Geology*, 106(3), pp.331-358.
- Large, R.R., Halpin, J.A., Danyushevsky, L.V., Maslennikov, V.V., Bull, S.W., Long, J.A., Gregory, D.D., Lounejeva, E., Lyons, T.W., Sack, P.J. and McGoldrick, P.J., 2014. Trace element content of sedimentary pyrite as a new proxy for deep-time ocean-atmosphere evolution. *Earth and Planetary Science Letters*, 389, pp.209-220.
- Large, R.R., Mukherjee, I., Gregory, D.D., Steadman, J.A., Maslennikov, V.V. and Meffre, S., 2017. Ocean and Atmosphere Geochemical Proxies Derived from Trace Elements in Marine Pyrite: Implications for Ore Genesis in Sedimentary Basins. *Economic Geology*, 112(2), pp.423-450.
- Li, K., Etschmann, B., Rae, N., Reith, F., Ryan, C.G., Kirkham, R., Howard, D., Rosa, D.R., Zammit, C., Pring, A. and Ngothai, Y., 2016. Ore petrography using megapixel X-ray imaging: rapid insights into element distribution and mobilization in complex Pt and U-Ge-Cu ores. *Economic Geology*, 111(2), pp.487-501.
- Li, X-H and Li, Q-L, 2016. Major advanced in microbeam analytical techniques and their applications in Earth Science. *Sci. Bull.* 61:23, 1785-1787.
- Lintern, M., Anand, R., Ryan, C. and Paterson, D., 2013. Natural gold particles in Eucalyptus leaves and their relevance to exploration for buried gold deposits. *Nature communications*, 4, p.2274.
- Lombi, E. and Susini, J., 2009. Synchrotron-based techniques for plant and soil science: opportunities, challenges and future perspectives. *Plant and Soil*, 320(1-2), pp.1-35.
- Mavrogenes, J.A., Berry, A.J., Newville, M. and Sutton, S.R., 2002. Copper speciation in vapor-phase fluid inclusions from the Mole Granite, Australia. *American Mineralogist*, 87(10), pp.1360-1364.
- McIntyre, N.S., Sherry, N., Fuller, M.S., Feng, R. and Kotzer, T., 2010. X-Ray fluorescence spectroscopy and mapping using excitation from white and broad bandpass synchrotron radiation. *Journal of Analytical Atomic Spectrometry*, 25(9), pp.1381-1389.
- Mukherjee, I. and Large, R., 2017. Application of pyrite trace element chemistry to exploration for SEDEX style Zn-Pb deposits: McArthur Basin, Northern Territory, Australia. *Ore Geology Reviews*, 81, pp.1249-1270.
- Pearce, M.A., Godel, B.M., Fisher, L.A., Schoneveld, L.E., Cleverley, J.S., Oliver, N.H. and Nugus, M., 2017. Microscale data to macroscale processes: a review of microcharacterization applied to mineral systems. Geological Society, London, Special Publications, 453, pp.SP453-3.
- Petruk, W., 2000. Applied mineralogy in the mining industry. Elsevier.

- Ravel, B. and Newville, M.A.T.H.E.N.A., 2005. ATHENA, ARTEMIS, HEPHAESTUS: data analysis for X-ray absorption spectroscopy using IFEFFIT. *Journal of synchrotron radiation*, 12(4), pp.537-541.
- Reich, M., Kesler, S.E., Utsunomiya, S., Palenik, C.S., Chryssoulis, S.L. and Ewing, R.C., 2005. Solubility of gold in arsenian pyrite. *Geochimica et Cosmochimica Acta*, 69(11), pp.2781-2796.
- Reich, M., Large, R. and Deditius, A.P., 2017. New advances in trace element geochemistry of ore minerals and accessory phases. *Ore Geology Reviews*, 81, pp. 1215-1217.
- Ryan, C.G., Kirkham, R., Hough, R.M., Moorhead, G., Siddons, D.P., De Jonge, M.D., Paterson, D.J., De Geronimo, G., Howard, D.L. and Cleverley, J.S., 2010a. Elemental X-ray imaging using the Maia detector array: The benefits and challenges of large solid-angle. *Nuclear Instruments and Methods in Physics Research Section A: Accelerators, Spectrometers, Detectors and Associated Equipment*, 619(1), pp.37-43.
- Ryan, C.G., Siddons, D.P., Kirkham, R., Dunn, P.A., Kuczewski, A., Moorhead, G., De Geronimo, G., Paterson, D.J., De Jonge, M.D., Hough, R.M. and Lintern, M.J., 2010b, April. The new Maia detector system: methods for high definition trace element imaging of natural material. In *AIP Conference Proceedings* (Vol. 1221, No. 1, pp. 9-17). AIP.
- Ryan, C., Siddons, D., Kirkham, R., Li, Z., De Jonge, M., Paterson, D., Cleverley, J., Kuczewski, A., Dunn, P., Jensen, M. and De Geronimo, G., 2013. The Maia detector array and X-ray fluorescence imaging system: locating rare precious metal phases in complex samples. In *Proceedings of SPIE-The International Society for Optical Engineering* (Vol. 8851). SPIE.
- Ryan, C.G., Siddons, D.P., Kirkham, R., Li, Z.Y., de Jonge, M.D., Paterson, D.J., Kuczewski, A., Howard, D.L., Dunn, P.A., Falkenberg, G. and Boesenberg, U., 2014. Maia X-ray fluorescence imaging: Capturing detail in complex natural samples. In *Journal of Physics: Conference Series* (Vol. 499, No. 1, p. 012002). IOP Publishing.
- Schumann, D., Fuchs, S., Stromberg, J., Laquerre, A., Mayer, D., Phaneuf, M.W., Vali, H. and Banerjee, N., 2014. Combining Terapixel-Scale SEM Imaging and High-Resolution TEM Studies for Mineral Exploration. *Microscopy and Microanalysis*, 20(S3), pp.1008-1009.
- Simon, G., Huang, H., Penner-Hahn, J.E., Kesler, S.E. and Kao, L.S., 1999. Oxidation state of gold and arsenic in gold-bearing arsenian pyrite. *American Mineralogist*, 84(7-8), pp.1071-1079.
- Stromberg, J.M., Feick, K., Stammers, L., VanLoon, L.L., Banerjee, N.R., 2016. *Synchrotron Spectroscopy for Ore Systems: Tying Trace Element Geochemistry to Mineralogical Context in the Abitibi Greenstone Belt*. Whitehorse 2016, Geological

Association of Canada and Mineralogical Association of Canada Joint Meeting,
Whitehorse

Stromberg, J.M., Vanloon, L.L., Banerjee, N.R., 2016. Trace Element and Gold Content and Speciation in Pyrites: Insights into Metal Mobility and Gold Mineralization at the Dome Mine. 26th V.M. Goldschmidt Conference, Yokohama. Abstract # 2963.

Sutton, S.R., Rivers, M.L., Bajt, S., Jones, K. and Smith, J.V., 1994. Synchrotron X-ray fluorescence microprobe: A microanalytical instrument for trace element studies in geochemistry, cosmochemistry, and the soil and environmental sciences. Nuclear Instruments and Methods in Physics Research Section A: Accelerators, Spectrometers, Detectors and Associated Equipment, 347(1-3), pp.412-416.

Tardani, D., Reich, M., Deditius, A.P., Chryssoulis, S., Sánchez-Alfaro, P., Wrage, J. and Roberts, M.P., 2017. Copper–arsenic decoupling in an active geothermal system: A link between pyrite and fluid composition. *Geochimica et Cosmochimica Acta*, 204, pp.179-204.

VanLoon, L.L., Banerjee, N.R., Stromberg, J.M., Feick, K., Stammers, L., Kope, E., 2016. Probing Mining Industry Questions using Synchrotron Radiation. 26th V.M. Goldschmidt Conference. Abstract #3260.

Walker, S.R., Jamieson, H.E., Lanzirrotti, A., Andrade, C.F. and Hall, G.E., 2005. The speciation of arsenic in iron oxides in mine wastes from the Giant gold mine, NWT: Application of synchrotron micro-XRD and micro-XANES at the grain scale. *The Canadian Mineralogist*, 43(4), pp.1205-1224.

Wang, P., Liu, Y., Menzies, N.W., Wehr, J.B., de Jonge, M.D., Howard, D.L., Kopittke, P.M. and Huang, L., 2016. Ferric minerals and organic matter change arsenic speciation in copper mine tailings. *Environmental Pollution*, 218, pp.835-843.

Chapter 5

Summary and Conclusion

5.1.0 Summary

Orogenic gold deposits represent almost 30% of the world's gold endowment, yet key questions remain regarding the controls on the formation of world-class deposits and camps. With its 108-year mining history and well-constrained geology, the Dome mine provides a unique opportunity to investigate the multi-stage formation of a world-class deposit and the applications of novel analytical techniques to ore deposit studies.

5.1.1 Mine Scale Geochemistry

The Dome ankerite veins are the earliest stage of veining at the Dome mine and have contributed close to 20% of the 16 Moz of gold mined to date. Despite this, their role in the history of the deposit and their depositional context has remained poorly understood. It is clear from new and historic mapping, as well as a deposit wide study of the geochemistry, that these veins were deposited syn-tectonically through successive pulses from a uniform fluid source. The concentration of the ankerite veins in the Vipond formation is the result of both the ideal host rock chemistry of the Vipond formation (Fe-tholeiitic) and the exploitation of regions of rheological weakness (flow boundaries). Gold in the ankerite veins is associated with pyrite mineralization, but grade is unpredictable and there are no correlations between trace and major elements and gold. This is due to later auriferous fluid events which exploited the same structures as the ankerite veins, as well as the competency contrast which they created in the volcanic pile. The result is a wide range of Au:Ag ratios, REE contents, and trace metal contents, all of which have no spatial trends across the over 5,000 meter strike length of the ankerite veins.

Ankerite oxygen isotope values reveal a trend of increasing $\delta^{18}\text{O}_{\text{VSMOW}}$ values downdip of the ankerite veins and to the northwest, away from the Dome Fault Deformation Zone (DFDZ) region of the mine. This is likely a result of decreasing fluid temperatures away

from the DFDZ, indicating that the DFDZ acted as a conduit for the ankerite forming metamorphic fluids. This resulted in the intense carbonate alteration which overprints the DFDZ, as well as a region locally called the “dacite flows”. These two regions of the mine host the two richest ore bodies (quartz-fuchsite vein, dacite ore) and the early carbonate alteration they experienced during the ankerite vein forming event was key for creating optimal rheological and geochemical conditions for subsequent vein formation. The importance of long-lived major structures in the formation of world-class ore deposits is recognized worldwide. At the Dome mine, the DFDZ and an early stage of carbonate alteration and veining played an integral role in its multi-stage gold endowment.

5.1.2 Fingerprinting Fluids and Gold

The bulk rock geochemistry of the Dome ankerite veins provides evidence for an input of gold into the system by more than one auriferous event. Given the intimate relationship between pyrite and gold in the veins and the refractory nature of pyrite, the trace element geochemistry of pyrite and gold was investigated. This investigation revealed that the Dome ankerite veins have been subject to three separate fluid events, each with a distinct stage of pyrite growth (Py_{1,2,3}) and a unique gold and trace element fingerprint correlating deposit wide mineralization events. Early ankerite vein forming fluids were auriferous, enriched in metals and metalloids, and are related to inclusion-rich Py₁ formation. Their slightly reduced and lower temperature nature (~250 °C) facilitated the enhanced uptake of As, Ni, Au and Cu into the pyrite lattice. The As and Cu content of Py₁ is also reflected in the geochemistry of the gold inclusions it hosts. The occurrence of gold as inclusions in Py₁ growth and as refractory gold in the pyrite lattice provides unequivocal evidence for the auriferous nature of the ankerite forming fluids, which is a historical point of contention. Gold in these fluids was likely carried as a bisulfide complex and deposited during pyrite growth facilitated by the Fe-rich nature of the host rock.

The second stage of pyrite growth (Py₂) is related to overprinting tourmaline veining and quartz-fuchsite vein formation based on trace element geochemistry, Au:Ag ratios, and associated mineral assemblages. Py₂ growth is characterized by a Ni enrichment, telluride

mineralization, and free gold with high Au:Ag ratios. The Ni enrichment in Py₂ growth is also reflected in the trace element geochemistry of gold associated with this fluid event. These fluids were more oxidized in nature, mobilizing Te, Ni, Pb, Cr, Ti from the komatiites and porphyries of the DFDZ. There is also evidence for remobilization of gold and other trace elements (As, Cu) from Py₁ growth during this event which are not enriched in Py₂ growth and have been remobilized to a distal location. The final stage of gold endowment and pyrite growth (Py₃) in the ankerite veins is related to deposit wide quartz veining. Py₃ growth is trace element and Au-poor when compared to Py₁ and Py₂; however, this fluid event contributed the bulk of the ankerite vein gold endowment. Gold occurs as large inclusions in Py₃, at grain boundaries and in fractures and has an Au:Ag ratio close to the bulk rock average value.

These results demonstrate the insights that can be gained by undertaking detailed studies of a complex system and underpin the necessity of having well-constrained sample context to bring those micron scale observations to the deposit scale. They also reveal that the system was fertile for a period of over 20 Ma, which is a key component for the formation of a world-class deposit.

5.1.3 Mine to Micron Studies on the Time-scale of Mining

The results of the pyrite trace element mapping highlight the power of high resolution *in situ* trace element studies for improving our understanding of ore systems. However, the timescale for which the mineral industry requires information regarding improvements to exploration, remediation, and geometallurgy is not conducive to the traditional workflow by which these studies are undertaken. The difficulty is that sample context is key to any meaningful interpretations and sample characterization by conventional petrographic methods is time consuming. The power of *in situ* mapping is the ability to combine geochemistry with mineralogical context. Advances in detector technologies and the ability to do multi-scale mapping has made it possible to push trace element mapping to the front of the workflow. To evaluate this, the application of synchrotron X-ray techniques for ore deposit studies was developed and tested on a number of different types of auriferous samples from across the Timmins camp.

SR-XRF mapping of large areas is shown to be very effective for quickly identifying and characterizing gold and trace element associations with gold even in low grade samples. This is an inherently difficult task in orogenic gold deposits as gold is nuggety. Multi-scale mapping was applied to improve the efficiency of grain selection for higher resolution analysis and aided in mitigating sample bias. Even without undertaking grain scale analysis, it is possible to identify multiple styles of gold mineralization and trace element associations in whole rock samples. This is integral to improving exploration efficiency by untangling complicated ore systems and the development new trace element vectors for exploration. SR-XRF mapping on the individual mineral grain scale is shown to be comparable to EMPA and other conventional mapping techniques, but is non-destructive and provides full spectrum datasets. Additionally, the non-destructive and complementary nature of these techniques is highlighted.

The ability to collect data on the speciation of trace metals by XANES is unique to synchrotron X-ray analysis. The application of XANES is well established in the environmental and remediation sectors of the mining industry, but has not been widely applied early in the mining cycle. An early understanding of the redox state of trace metals, gold and deleterious elements has implications for mitigating issues within geometallurgy and remediation in the future, resulting in greater mining efficiency. The combination of SR-XRF and XANES for the identification, and characterisation of refractory gold and its distribution has direct implications for recovery methods efficient gold liberation. An early understanding of this is integral to decreasing the time between discovery and production as well as improving recoveries.

5.2.0 Future Work

The research has brought forward several areas for future work, such as further investigation of some results and the application of synchrotron techniques to the mineral industry. With the development of large scale SR-XRF mapping (and stacking) and quantitative analysis by GeoPIXE, it is possible to quickly and non-destructively produce an immense dataset. An SR-XRF and XANES dataset, when applied early in the

exploration stage, has the potential to inform and guide exploration, as well as identify possible later stage geometallurgical and remediation issues which may impact production costs. With the increasing complexity, depth and lower grades of new deposit discoveries, it is integral to explore and mine more efficiently. The cornerstone of this is developing and adopting new technologies for better ore characterization.

There are also larger implications of the XANES results, presented in Chapter 4, for local changes in fluid redox and gold mineralizing mechanisms at the Dome mine, which are being explored by applying more involved data processing to a larger dataset not included in this work. Beyond local redox, there are larger scale insights into metal mobility, source and budget, which can be gained from further investigation of whole rock datasets from across the Timmins camp. The application of quantitative analysis to the large-scale mapping datasets, as well as re-examination of grain scale mapping with GeoPIXE may provide insights into the camp scale mineralization history with potential implications for exploration in the region.

5.3.0 Conclusion

This body of work provides insights into the processes and conditions which lead to the formation of world-class gold endowments, such as the 16 million ounces at the Dome mine. These insights emphasize the importance of a long-lived auriferous fluid system, which can be tapped throughout the deformation history of a region by major faults. This has improved our genetic model for the Dome mine and identified the integral role of early carbonate veining and alteration for creating new traps for later mineralizing fluids has been identified. Another common feature identified is the evolution of metamorphic auriferous fluids in terms of gold tenor, trace element content and redox throughout the history of a deposit. These are all characteristics which can be used to improve exploration models for orogenic gold. Finally, the applications of synchrotron studies early in the mine cycle has been described, providing a new framework for undertaking mine to micron ore deposits studies to address the global challenges facing the mineral industry.

Appendix A Sample Information

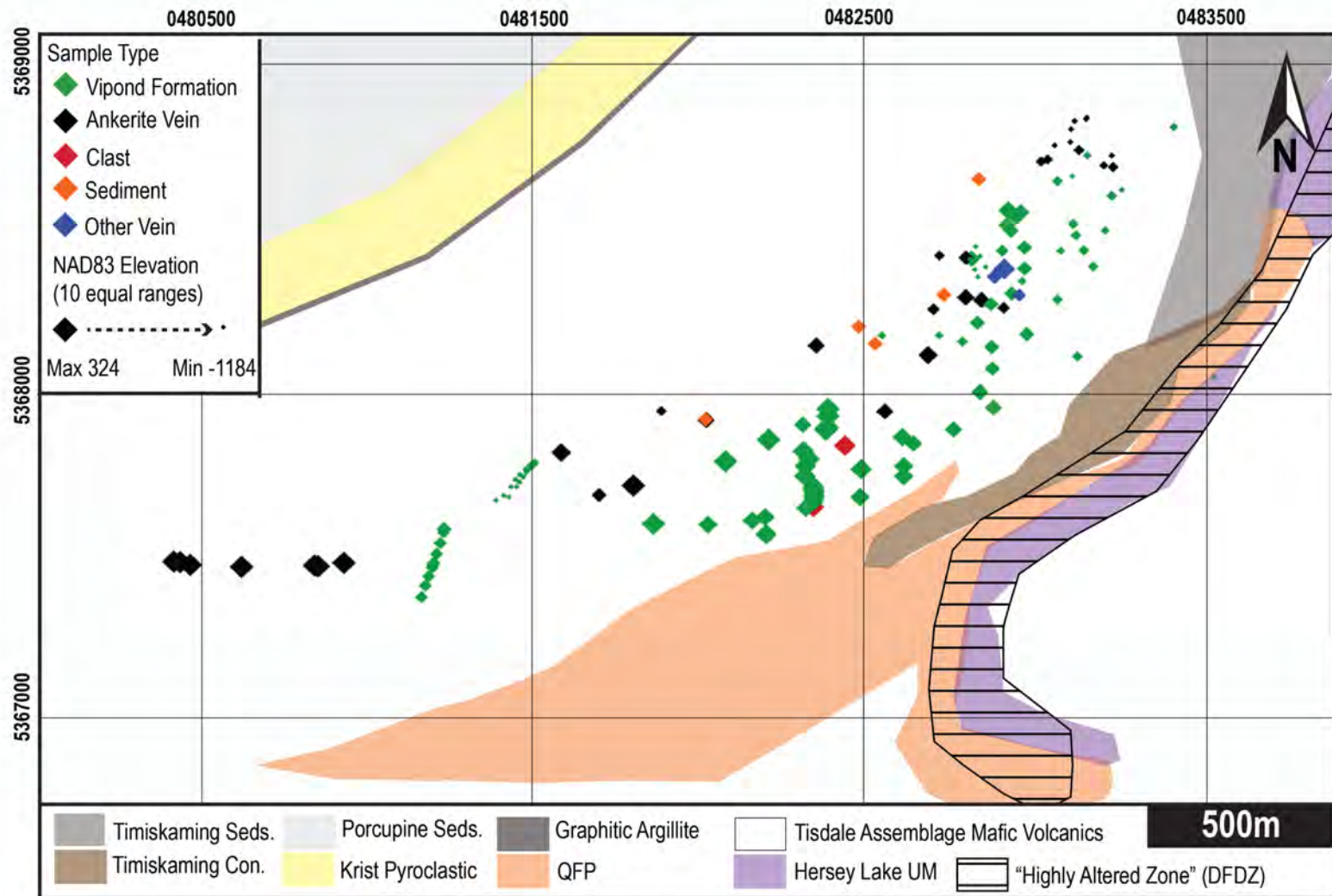
A.1 Sample List

Sample #	Type	Drift	Vein #/Host rock	Dome E	Dome N	Dome Elev.	NAD83 E	NAD83 N	NAD 83 Elev.
C406946	Centre Ankerite	950#4 DR	AND	3104	4266	5014	481787	5367707	5
C406942	East Ankerite	1639#17 X/C	A1	5969	5625	3981	482661	5368118	-310
C406945	West Ankerite	1608#5 DR	AND	2400	4605	3973	481573	5367811	-312
C407894	West Ankerite	1608#5 DR	AND	2400	4605	3973	481573	5367811	-312
C406943	Centre Ankerite	1605 X/C	A1N	3805	4948	3961	482001	5367914	-316
C407893	Centre Ankerite	1605 X/C	A1N	3805	4948	3961	482001	5367914	-316
C406937	East Ankerite	1907 DR	A6	6483	6202	3540	482819	5368293	-444
C406938	East Ankerite discordant	1904 DR	DISC	6328	6228	3540	482771	5368301	-444
C407884	East Ankerite discordant	1904 DR	DISC	6328	6228	3540	482771	5368301	-444
C406940	Centre Ankerite	1939#10 DR	AND	4873	5725	3547	482328	5368149	-442
C407886	West Ankerite	215450AS	P18?	5544	5048	3245	482531	5367942	-534
C411517	East Ankerite	2125DR		6615	6437	3237	482859	5368364	-536
C407891	East Ankerite discordant	2223#6 DRW	DISC	6334	6632	3090	482774	5368424	-581
C406935	West Ankerite	2345 DR	A12	2773	4166	2963	481686	5367677	-620
C410843	East Ankerite	236661AT		6700	6127	2935	482884	5368269	-629
C409401	Center Ankerite	2439 up sub		6015	6102	2889	482675	5368263	-643
C409459	East Ankerite	246862BS		6850	6256	2798	482931	5368309	-670
C407899	East Ankerite discordant	267775BS	DISC	7760	7575	2580	483209	5368710	-737
C406931	West Ankerite	2950 DR	A1	3375	5037	2130	481871	5367941	-874
C406932	Centre Ankerite	2903#10 DR	A6	6073	6657	2110	482694	5368432	-880
C406933	East Ankerite discordant	2909#4W DR	DISC A16	7431	7751	2110	483109	5368764	-880
C407888	East Ankerite discordant	2909#4W DR	DISC A16	7431	7751	2110	483109	5368764	-880


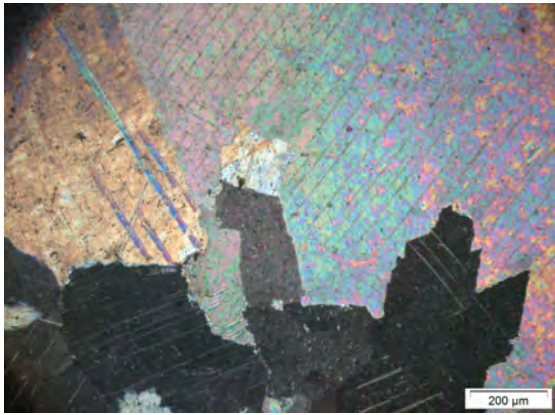
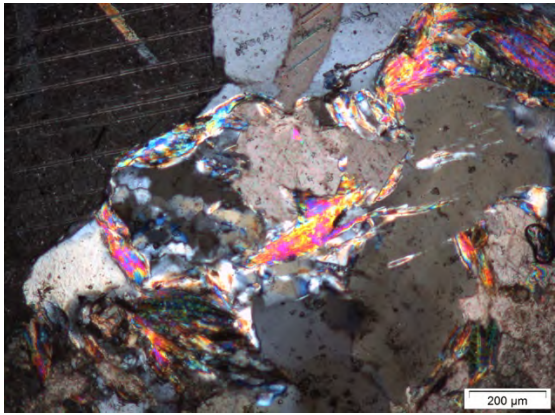
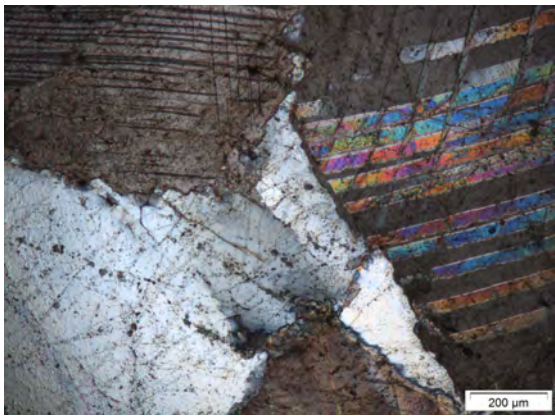
Sample #	Type	Drift	Vein #/Host rock	Dome E	Dome N	Dome Elev.	NAD83 E	NAD83 N	NAD 83 Elev.
C410280	East Ankerite discordant	2909#4W DR	DISC A16	7058	7633	2111	482995	5368728	-880
C406934	East Ankerite	2909#2E DR	A12	7668	7600	2105	483181	5368718	-881
C407890	East Ankerite	2909#2E DR	A12	7668	7600	2105	483181	5368718	-881
C409402	East Ankerite	3409 Ramp	A12	7747	7693	1368	483205	5368746	-1106
C410295	East Ankerite	3409E AS		7353	7967	1328	483086	5368830	-1118
C411098	East Ankerite	3509E AS	A12	7504	8082	1266	483132	5368865	-1137
C411096	East Ankerite	3509 W AS	A12	7345	7831	1262	483083	5368788	-1138
C410097	East Ankerite	3509W AS	A12	7497	8074	1264	483130	5368862	-1138
C410300	East Ankerite	3509E Bypass	A12	7195	7800	1261	483037	5368779	-1139
C406930	East Ankerite	3509E DR		7383	8053	1198	483095	5368856	-1158
C408783	Curts Ankerite Vein Boulder	Paymaster Property	Tisdale (Gold Center)	-1200	3428	6028	480475	5367456	314
C410289	Curts Ankerite Vein Transect	Paymaster Property	Tisdale (Gold Center)	293.6	3453.2	5994.4	480930	5367462	304
C410290	Curts Ankerite Vein Transect	Paymaster Property	Tisdale (Gold Center)	41	3416.2	5974.7	480853	5367451	298
C410291	Curts Ankerite Vein Transect	Paymaster Property	Tisdale (Gold Center)	4.8	3429.2	5978	480842	5367455	299
C410292	Curts Ankerite Vein Transect	Paymaster Property	Tisdale (Gold Center)	-704	3410.4	6033.8	480626	5367450	316
C410293	Curts Ankerite Vein Transect	Paymaster Property	Tisdale (Gold Center)	-1298.3	3457.6	6043.6	480445	5367465	319
C410294	Curts Ankerite Vein Transect	Paymaster Property	Tisdale (Gold Center)	-1360.6	3460.7	6060	480426	5367466	324
C409523	Carbonate vein in Boulder	Hollinger Pit	Tisdale						
C410901	Carbonate vein in Outcrop	Pearl Lake	Tisdale				478277	5369336	
BA	Ankerite Vein Boulder	Buffalo Ankerite Pit	Tisdale (Hersey Lake)				480221	5369333	
C408778	Sulfide Clast	11L (125245BS)	Timiskaming Conglomerate	5158	4692	4665	482413	5367834	-101
C408779	Sulfide Clast	11L (125245BS)	Timiskaming Conglomerate	5158	4692	4665	482413	5367834	-101

Sample #	Type	Drift	Vein #/Host rock	Dome E	Dome N	Dome Elev.	NAD83 E	NAD83 N	NAD 83 Elev.
C408781	Sulfide Rich Interflow Sediment	125446 Scram	Tisdale	5456	5742	4689	482505	5368154	-94
C408777	"Carbonate" Clast	124941BS	Timiskaming Conglomerate	4852	4055	4602	482319	5367640	-120
C408776	Quartz Fuchsite Vein	12L	Tisdale (Ultramafics)	6700	6526	4581	482885	5368392	-127
C406944	Interflow Sediment	1605 X/C	Tisdale	3805	4950	3961	482001	5367914	-316
186567	Cherty Interflow	186567	Tisdale						
C408780	Sulfide rich interflow sediment	1939#10DR	Tisdale	5292	5914	3545	482455	5368207	-443
C406939	Interflow sediment	1904 DR	Tisdale	6121	6250	3541	482708	5368308	-444
C407885	Interflow sediment	1904 DR	Tisdale	6121	6250	3541	482708	5368308	-444
C406941	Basal graphitic argillite	196671AT	Basal Graphitic Argillite	6454	7449	3544	482811	5368673	-443
C411520	Quartz Tourmaline Ladder Vein	2125DR	Tisdale	6615	6437	3237	482859	5368364	-536
C406936	Hyaloclastite	2301#5 DR	Tisdale	6683	6715	2938	482880	5368449	-628
C411519	Quartz Ankerite Vein	246862BS	Tisdale	6850	6256	2798	482931	5368309	-670
C411518	Quartz Tourmaline Ladder Vein	246862BS	Tisdale	6850	6256	2798	482931	5368309	-670
C407887	Massive Mafic Volcanic	2710 DRW	Tisdale	7377	6982	2349	483092	5368530	-807
C407889	Interpillow breccias	2909#1 X/C	Tisdale	7505	7703	2108	483132	5368749	-881
E863294	Greywacke	Hoyle Pond	Porpcupine						
E885276	Greywacke	Hoyle Pond	Porpcupine						

A.2 Dome Mine Sample Location Map



A.3 Sample Descriptions

C406946	
Sample Description: Center Ankerite, 950#4 DR	
	<p>~ 0.5 m wide ankerite vein scaled from the drift wall. Vein was iron stained but fresh surfaces are light grey, coarse-grained ankerite with ~5 cm wide milky quartz tourmaline veins. Tourmaline occurs as clots of dravite in the quartz vein. <1% disseminated pyrite, mild sericitization associated with the quartz-tourmaline vein. The ankerite vein margin crumbly from the weathering of sulfides and sericite.</p>
Petrography:	
	
Coarse-grained ankerite vein material (5X PPL)	Margin of quartz veinlet with sericite alteration (5X XPL)
	
Coarse-grained ankerite and quartz (5X XPL)	

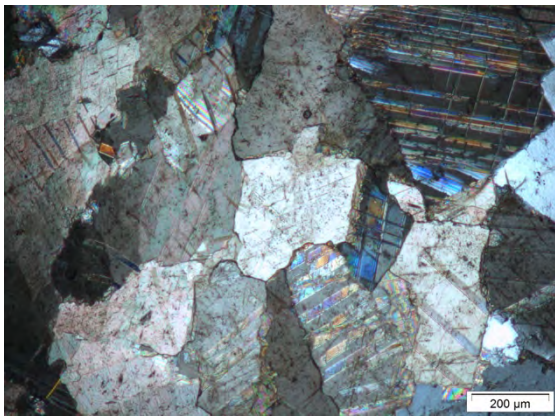
C406942

Sample Description: East Ankerite, 1639#17 X/C

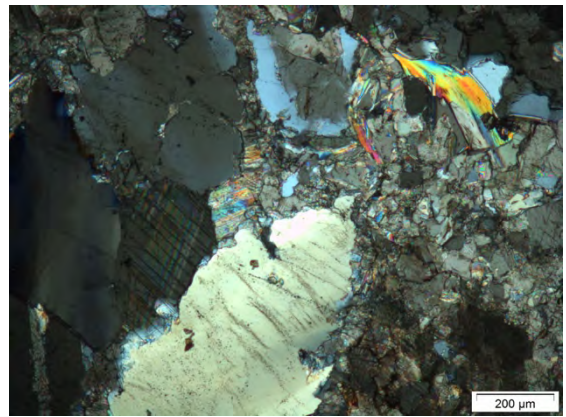


~ 1 m wide ankerite vein scaled from the drift back. Fresh surface is light to medium grey ankerite with ~30% cm scale milky quartz veining and mild sericitization associated with quartz. Sulfide rich vein margin was not sampled. Black tourmaline occurs as mm scale stringers near the vein margin. <1% fine-grained disseminated pyrite.

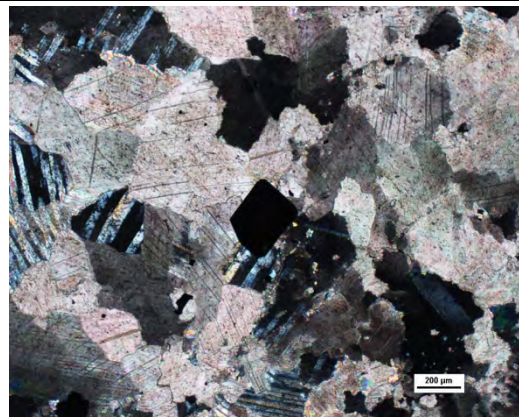
Petrography:



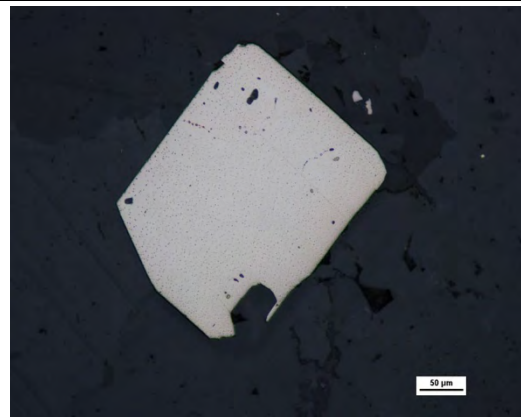
Coarse-grained ankerite vein material (5X PPL)



Margin of quartz veinlet with sericite alteration (5X XPL)



Euhedral pyrite grain in ankerite ground mass (5X XPL)



Euhedral pyrite grain with carbonate inclusions in an ankerite groundmass (20X RFL)

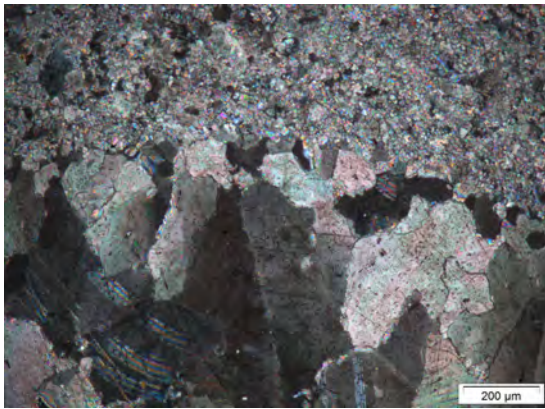
C406945

Sample Description: West Ankerite, 1608#5 DR

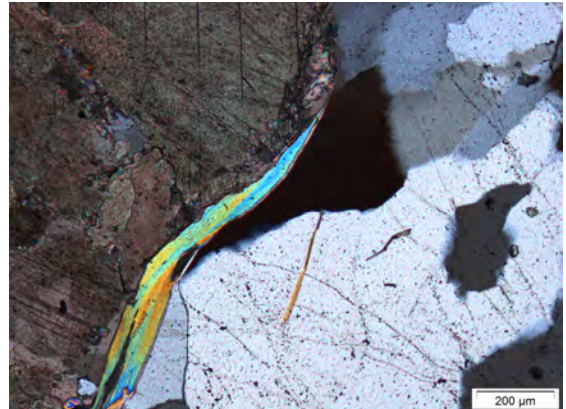


Scaled from a ~1m wide boudinaged ankerite vein in the drift back. Dark grey coarse-grained ankerite with <1% fine-grained disseminated pyrite, 15% cm scale quartz stringers with some quartz flooding. Moderate sericite alteration at the quartz vein margins.

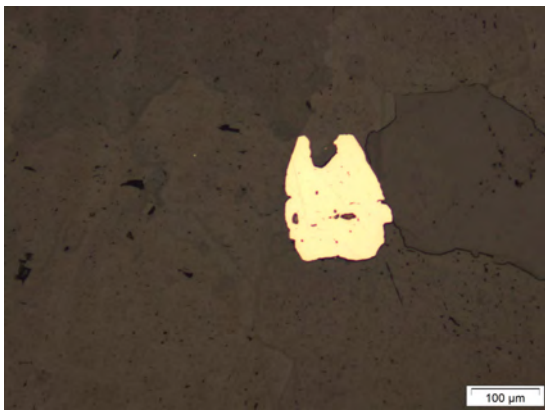
Petrography:



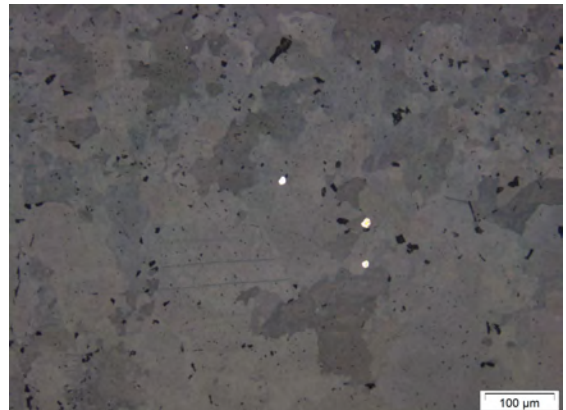
Coarse-grained ankerite vein material grading into fine-grained ankerite near a quartz veinlet (5X PPL)



Recrystallized fine-grained carbonate at the margin of a quartz veinlet with sericite (5X XPL)



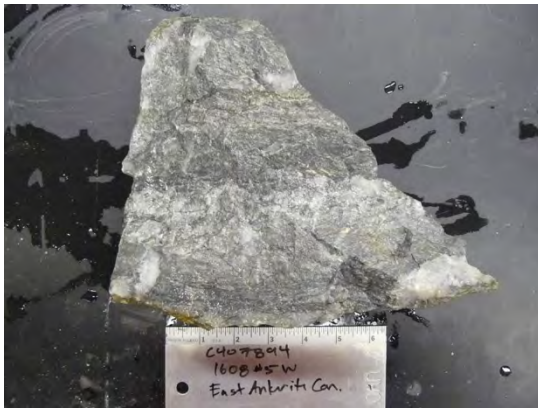
Anhedronal ankerite inclusion bearing pyrite in ankerite groundmass (5X RFL)



Fine-grained, anhedronal disseminated pyrite in an ankerite groundmass (10X RFL)

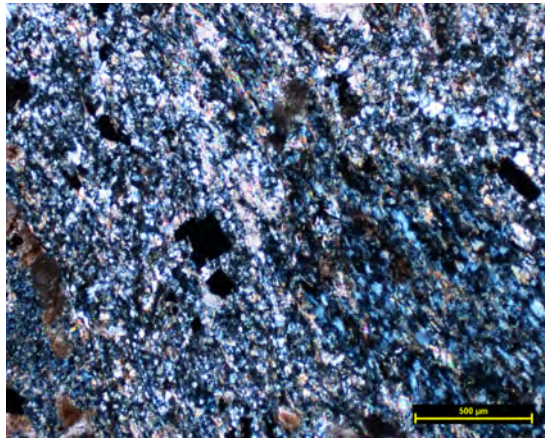
C407894

Sample Description: West Ankerite, 1608#5 DR

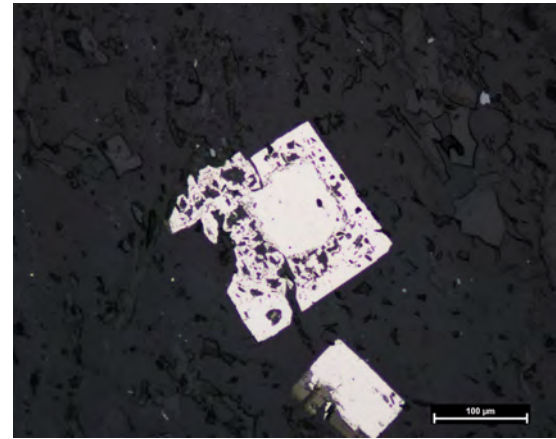


Scaled from a 0.3 m wide boundinaged ankerite vein in the drift back. Sample is medium to coarse-grained light to medium grey banded ankerite with 10% quartz veining. The bottom of the sample is the vein margin and is sericite rich with ~20% fine-grained pyrite. The vein material contains ~1% disseminate pyrite with moderate sericite.

Petrography:



Highly foliated rich vein margin dominated by fine-grained sericite and quartz with some euhedral to anhedral pyrite (5X XPL)



Euhedral pyrite grain with a sieve textured, silicate inclusion rich rim (20X RFL)

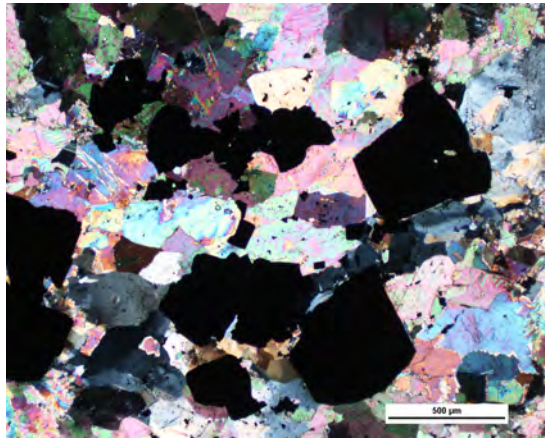
C406943

Sample Description: Center Ankerite, 1605 X/C

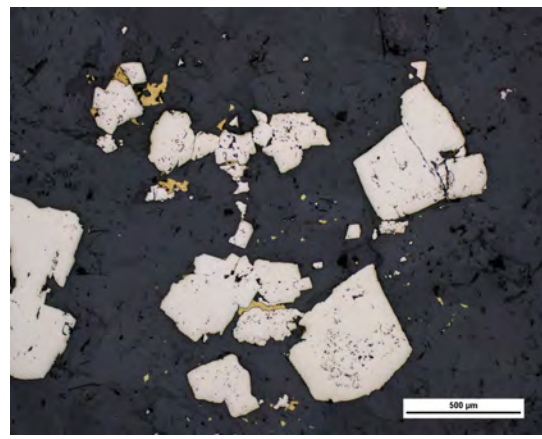


Scaled from a ~1 m wide ankerite vein in the drift wall. Dark grey, coarse-grained ankerite with some compositional banding and 15% 2-3 cm quartz veins with small clots of black tourmaline. The vein material contains ~1% disseminate pyrite. The vein margin (right side of sample photo) is sericite rich and contains ~20% fine-grained pyrite.

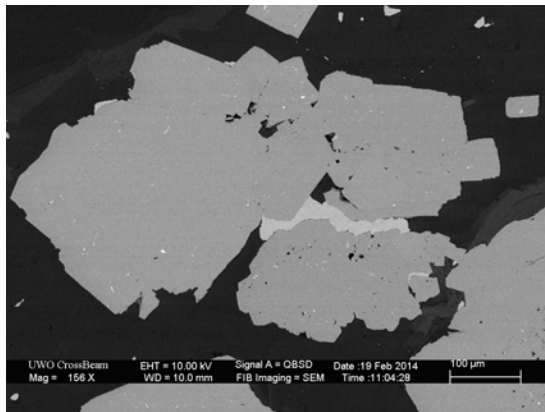
Petrography:



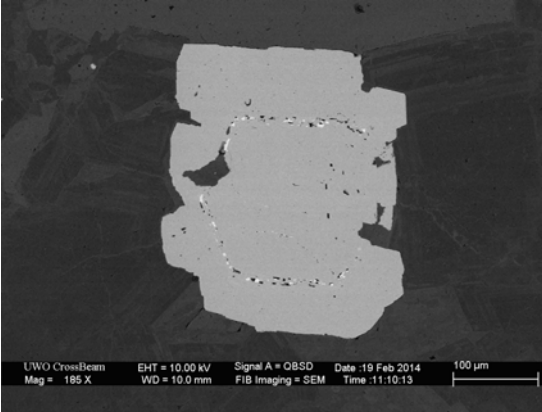
Subhedral pyrite grains in a groundmass of ankerite (5X XPL)



Subhedral sieve-textured pyrite grains and chalcopyrite in ankerite groundmass (5X RFL)



Subhedral pyrite grains with interstitial chalcopyrite and inclusions of galena (bright white) and arsenopyrite (light grey)



Ragged pyrite grain with an inclusion rich halo with arsenopyrite inclusions (BSE-SEM)

C407893

Sample Description: Center Ankerite, 1605 X/C



Duplicate sample from the same vein as C406943 the following year. Scaled from a ~1 m wide ankerite vein in the drift wall. Medium grey, coarse-grained ankerite with 10 % 2-3 cm quartz veins and intense sericitic alteration. The vein material contains ~1% disseminate pyrite.

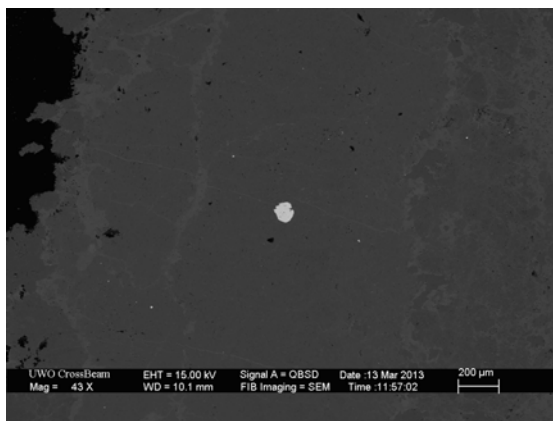
C406937

Sample Description: East Ankerite, 1907 DR

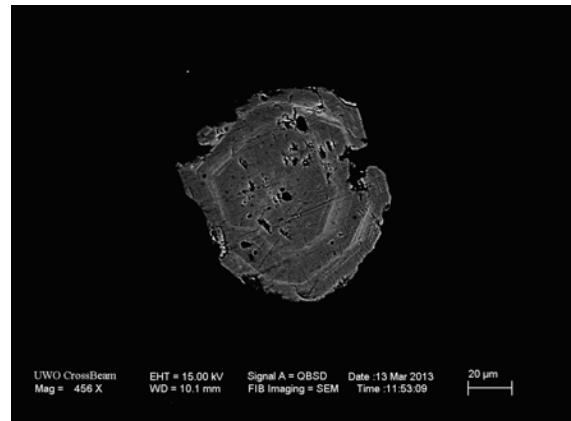


Scaled from a ~0.5 m wide ankerite vein in the back of the drift. The sample is dark grey, coarse-grained ankerite with ~5% mm scale black tourmaline stringers, 3% quartz stringers and 1% disseminated pyrite. Strong sericite alteration proximal to quartz and tourmaline.

Petrography:



Pyrite grain in ankerite groundmass with variability in carbonate chemistry (BSE-SEM)



Ragged, anhedral, inclusion rich pyrite grain with As rich compositional zoning (BSE-SEM)

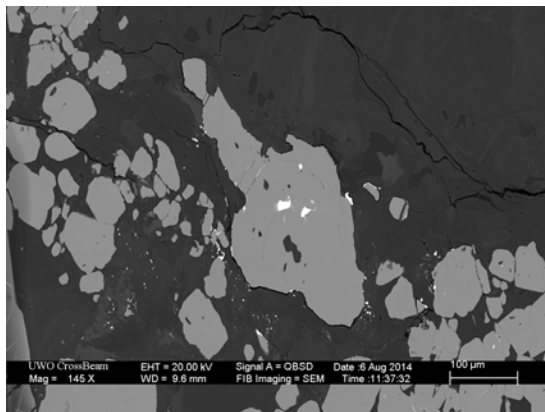
C406938

Sample Description: East Ankerite Discordant, 1904 DR

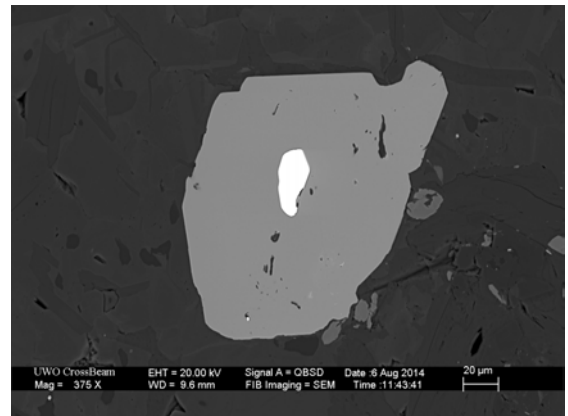


Scaled down from a ~0.5 m wide ankerite vein in the drift back. The sample is coarse-grained, dark grey ankerite with iron staining and ~50% quartz extension vein array. The central vein has ~ 10% black tourmaline as clots and stringers. Coarse-grained pyrite occurs at the quartz vein margins and the ankerite vein material contains ~1% fine-grained disseminated pyrite.

Petrography:



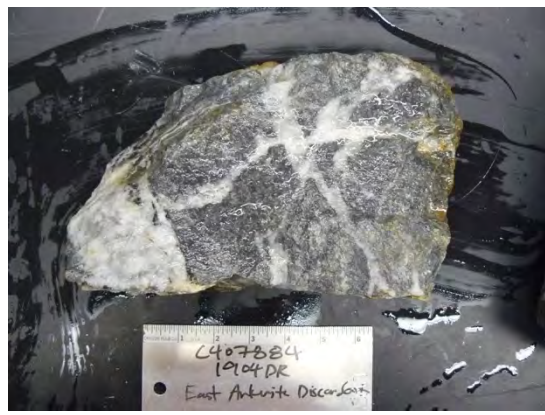
Anhedral pyrite with inclusions of gold at the margin of a quartz vein. (BSE-SEM)



Anhedral pyrite with gold inclusion in a groundmass of sericite and carbonate. (BSE-SEM)

C407884

Sample Description: East Ankerite Discordant, 1904 DR



Duplicate sample of same vein as C406838. Coarse-grained dark grey ankerite with ~20% quartz veining. Minor (2%) tourmaline and pyrite is associated with margin of the large quartz vein. Ankerite material contains ~1% fine-grained disseminated pyrite.

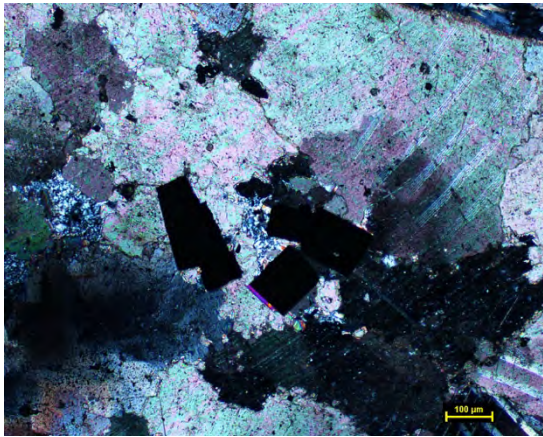
C406940

Sample Description: Center Ankerite, 1939#10 DR

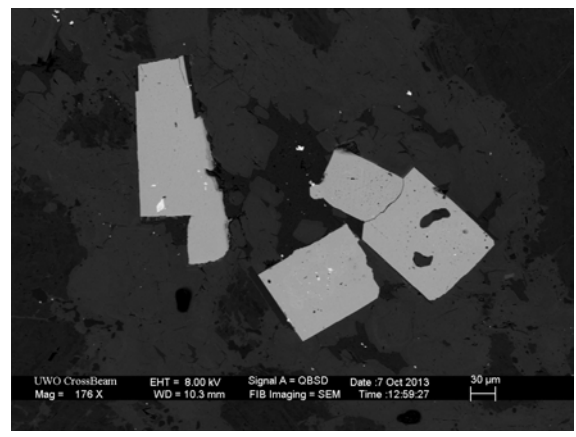


Scaled from a ~1 m wide boudinaged ankerite vein at the drift back. The vein material is dark grey, medium-grained ankerite with ~3% disseminated pyrite and ~1% pyrite stringers. The vein margins contain coarse-grained light grey and milky quartz veining and moderate sericite alteration.

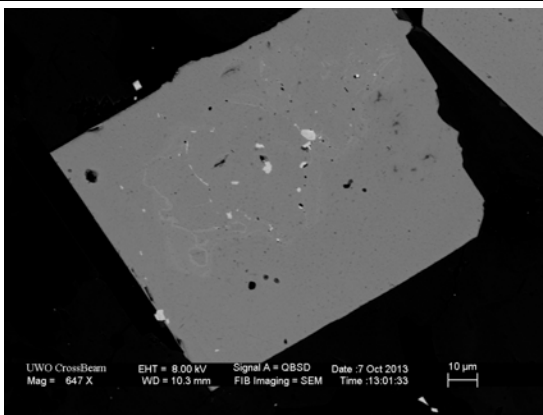
Petrography:



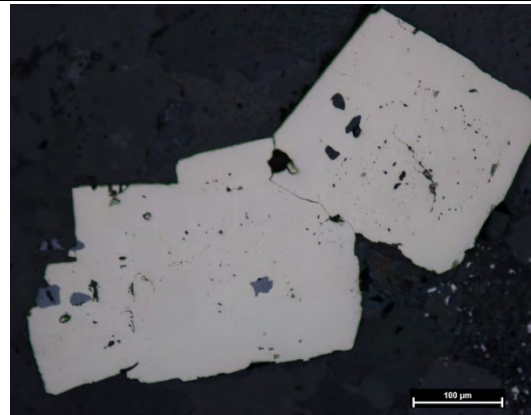
Euhedral pyrite in a coarse-grained ankerite groundmass with a sericite lath and minor quartz (10X XPL)



Euhedral, inclusion rich pyrite. The bright inclusion is galena (BSE-SEM)



Euhedral pyrite with As and arsenopyrite rich core (BSE-SEM)



Euhedral inclusion rich pyrite grains associated with rutile in a carbonate groundmass (10X RFL)

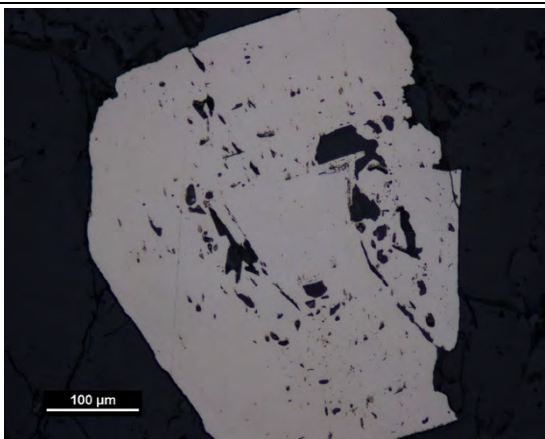
C407886

Sample Description: West Ankerite, 215450AS

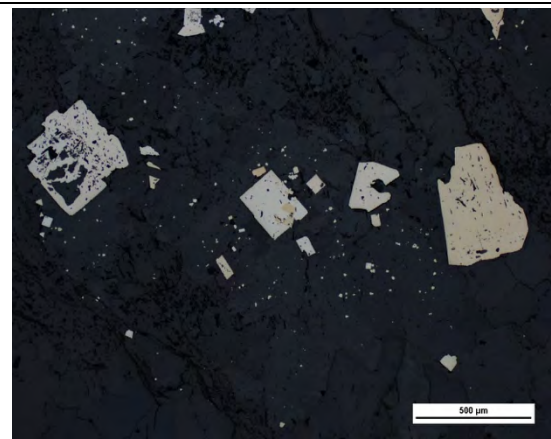


Samples from a ~0.5 m wide ankerite vein next to a ~1.5 m wide milky quartz-tourmaline vein in the drift back. The sample is highly sericitized, medium-grained ankerite with ~15% milky quartz veining. The ankerite material contains ~1% disseminate pyrite and regions of quartz veining have seams of coarse-grained, massive pyrite.

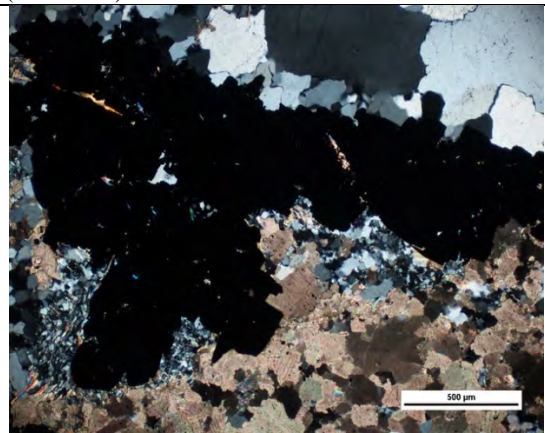
Petrography:



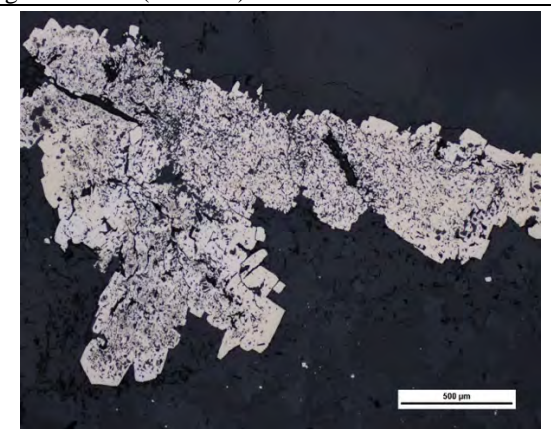
Ragged, sieve textured, inclusion-rich pyrite grain (20X RFL)



Subhedral to euhedral pyrite grains in the ankerite groundmass (5X RFL)



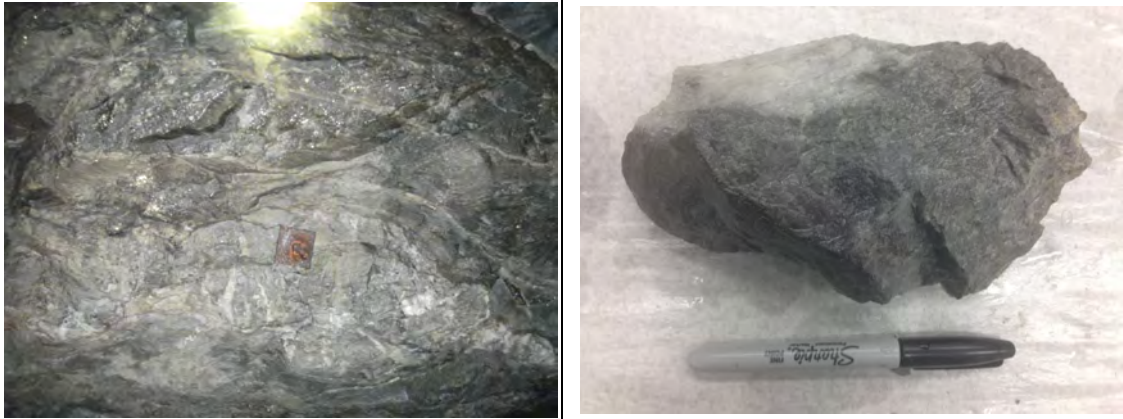
Massive pyrite at the margin of a quartz veinlet and the ankerite vein material (5X XPL)



Massive sieved texture pyrite at the quartz vein margin (5X RFL)

C411517

Sample Description: East Ankerite, 2125DR



Sample was scaled down from a ~1 m wide boudinaged ankerite vein in the drift back. The sample is coarse-grained, medium grey ankerite with ~5% quartz veining and 1% disseminate pyrite. The sample is weakly sericitized and contains no vein margin material. A subsample of the quartz-tourmaline vein material was also scaled down (C411520)

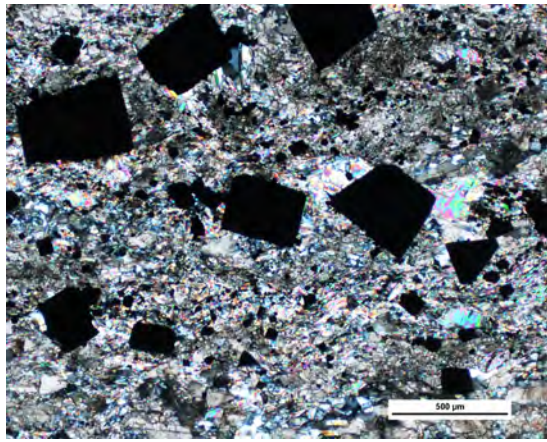
C407891

Sample Description: East Ankerite Discordant, 2223#6 DRW

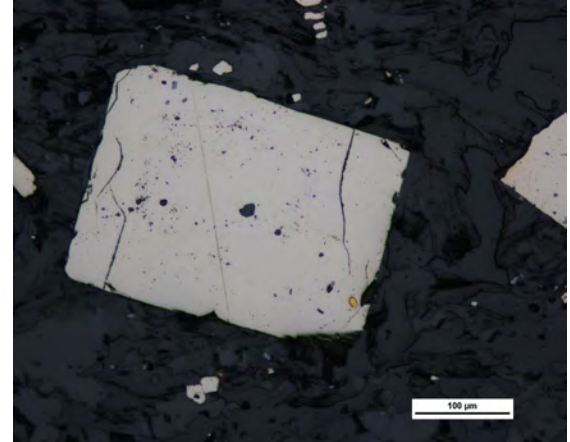


Sample of two small ~5 cm wide boundinaged ankerite veins including the vein margins. The vein material is coarse-grained light grey ankerite with ~1% disseminated pyrite, 5% quartz, and 2% tourmaline stringers. The vein margins are highly foliated, sericite rich, with ~5% pyrite and <1% chalcopyrite.

Petrography:



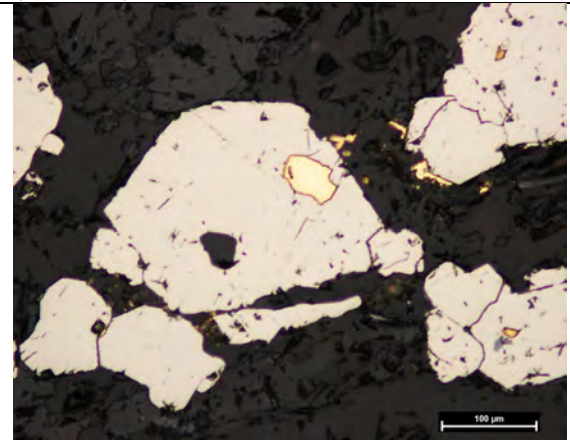
Euhedral coarse-grained pyrite in the sericite rich vein margin (5X XPL)



Euhedral pyrite grain with a gold inclusion at its margin and a sieve textured, inclusion rich core (10X RFL)



Subhedral, inclusion rich pyrite grain with chalcopyrite and rutile (50X RFL)



Anhedral pyrite grains in the vein margin with inclusions of gold and gold at the grain margins (20X RFL)

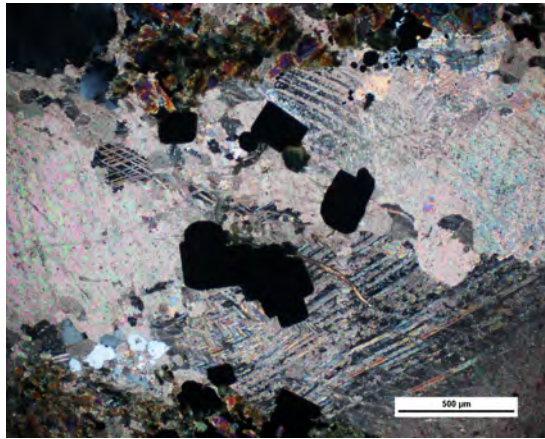
C406935

Sample Description: West Ankerite, 2345 DR

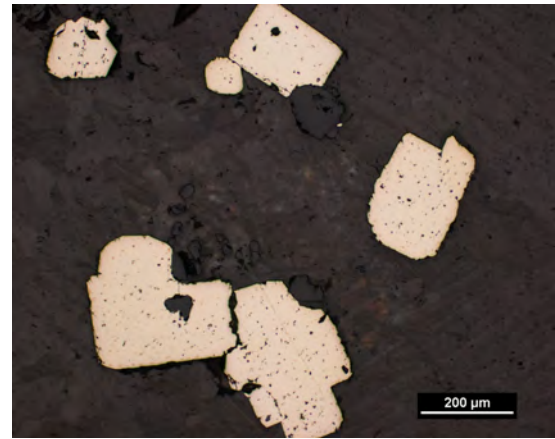


Scaled from ~2 m wide ankerite vein in the drift back. The sample is coarse-grained dark grey ankerite with 2 stages of overprinting veining. There are 20% ~2 cm tourmaline-quartz veins and also ~10% grey to milky white quartz veins which cut them. Both stages have medium-grained pyrite at their margins. The ankerite vein material is strongly sericitized and contains ~2% disseminated pyrite.

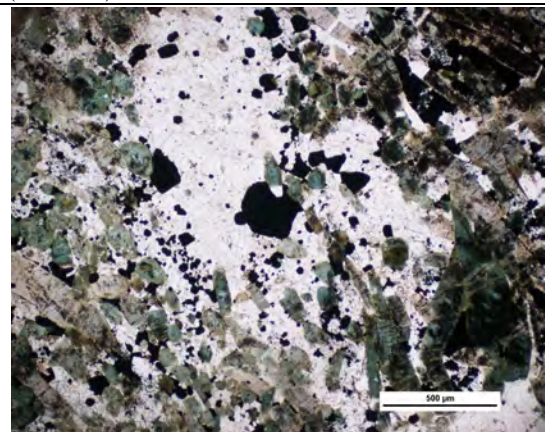
Petrography:



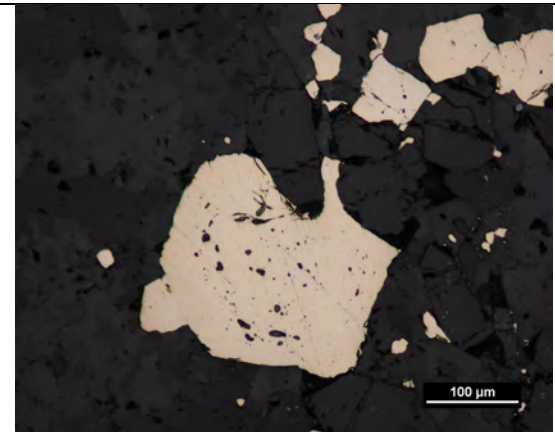
Anhedronal to euhedral pyrite grains in a coarse grained primary ankerite groundmass which is cut by two tourmaline veinlets at the top and bottom (5X XPL)



Sieve textured, anhedronal to euhedral pyrite grains in a carbonate groundmass (5X RFL)



Fine to medium grained pyrite grains in a groundmass dominated by coarse-grained tourmaline and fine-grained carbonate (5X PPL)



Anhedronal sieve texture pyrite grain associated with tourmaline and carbonate (5X RFL)

C410843

Sample Description: East Ankerite, 236661AT



Sampled from a ~0.5m wide boundinaged ankerite vein in the wall of the drift. The vein is crosscut by tourmaline stringers, quartz-tourmaline veins and quartz veining. The ankerite vein material is coarse-grained ankerite ~10% milky quartz veinlets and 2% disseminated pyrite. Black tourmaline occurs as stringers (2%) and as clots in quartz-tourmaline veining. Fine-grained pyrite is associated with tourmaline stringers.

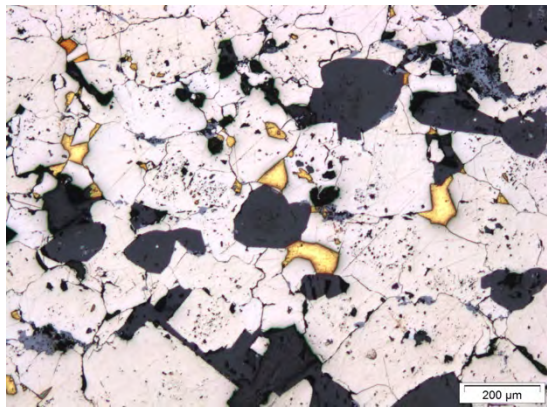
C409401

Sample Description: Center Ankerite, 2439 Upper Sub

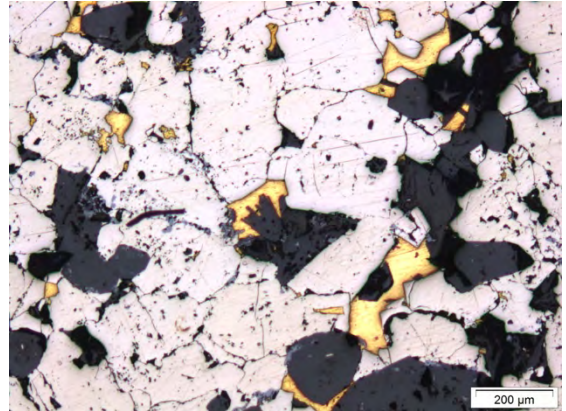


Sample was scaled ~0.5 m thick brecciated ankerite vein in the back of the drift. The main ankerite vein looks brecciated by black tourmaline veining. The ankerite clasts(?) are banded with coarse to medium-grained greyish brown ankerite with 10% cherty(?) quartz and 1% fine-grained disseminated pyrite. The groundmass(?) is fine-grained black tourmaline. The brecciation appears to occur within the original ankerite vein margins. The vein margins are pyrite rich (90%) and contain a seam of visible gold.

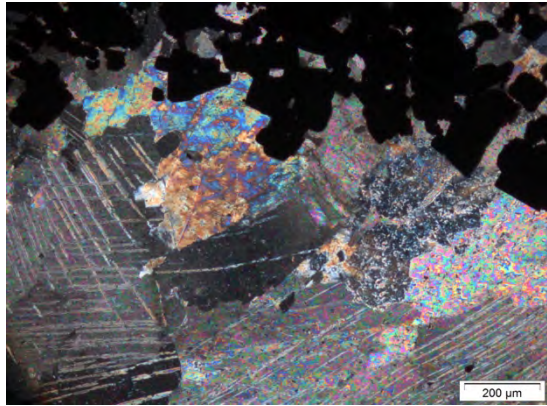
Petrography:



Pyrite rich vein margin with tourmaline and interstitial gold (5X RFL)



Pyrite rich vein margin with tourmaline, sericite with rutile inclusions and interstitial gold (5X RFL)



Coarse-grained ankerite at the vein margin with euhedral pyrite grains (5X XPL)	Contact between a tourmaline stringer and coarse-grained ankerite(10X PPL)
---	--

C409459

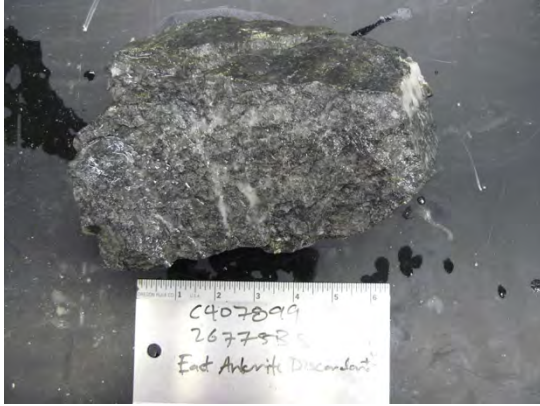
Sample Description: East Ankerite, 246862BS



Sample collected from a ~1 wide ankerite vein in the development face while mapping. The sample is dark grey coarse-grained ankerite with 2% fine-grained disseminate pyrite and 5% quartz. The margin contains ~5% pyrite and is highly sericitized. The ankerite vein was parallel to a quartz-ankerite vein (C411519), and the quartz tourmaline region was subsampled (C411518).

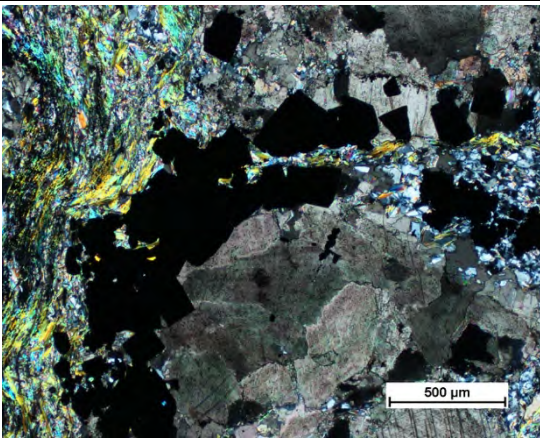
C407899

Sample Description: East Ankerite Discordant, 268875BS

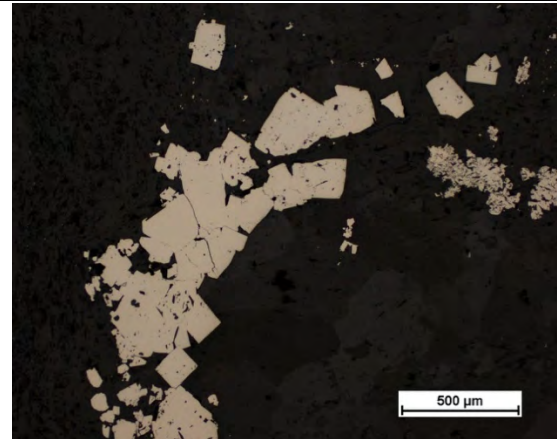


Sample collected while mapping a quartz vein development. The sample is dark to medium grey, coarse-grained ankerite with 5% cm scale quartz stringer and 2% disseminated pyrite. The vein margin region (top of sample) is highly foliated/schistose with 5% pyrite.

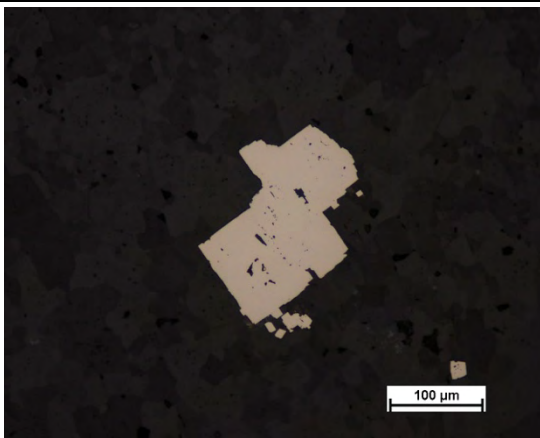
Petrography:



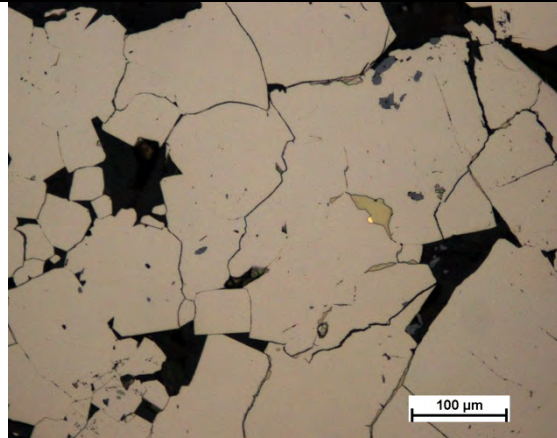
Contact of the highly-foliated sericite and quartz rich vein margin with coarse grained ankerite (5X XPL)



Fine to coarse-grained euhedral, inclusion rich pyrite at the margin of the ankerite vein (5X RFL)



Euhedral, inclusion rich, puppy shaped pyrite grain in a fine grained ankerite groundmass (5X XPL)



Small gold inclusion associated with chalcopyrite and coarse-grained pyrite (20X RFL)

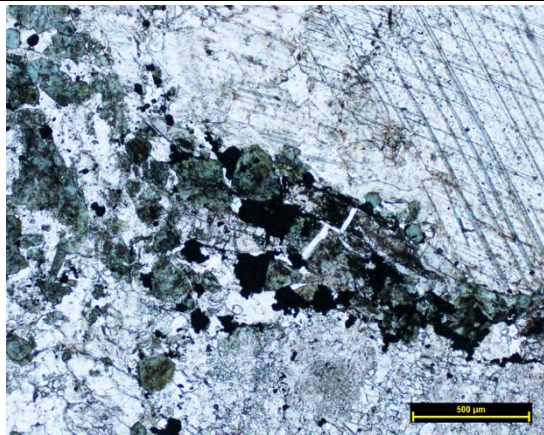
C406931

Sample Description: West Ankerite, 2950DR

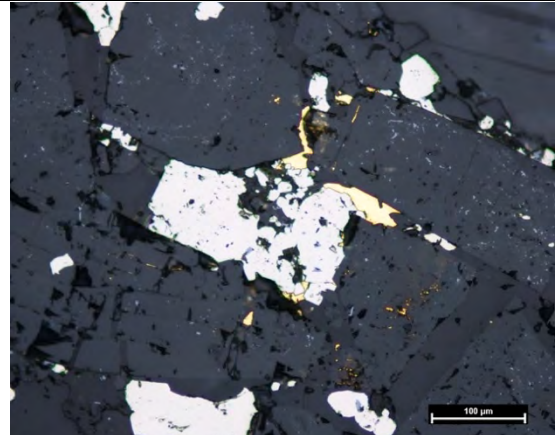


Sample was scaled off from ~0.5 m thick ankerite vein with tourmaline and quartz-tourmaline veining. The sample is coarse-grained light grey ankerite with ~5% mm to cm scale black tourmaline stringers concentrated near the vein margins. These tourmaline stringers are related to pyrite and visible gold that is observable with a hand lens. The ankerite material contains ~3% quartz stringers and 1% disseminated pyrite. The vein margins are highly sericitized with 5-10% fine-grained pyrite and fine-grained carbonate and quartz.

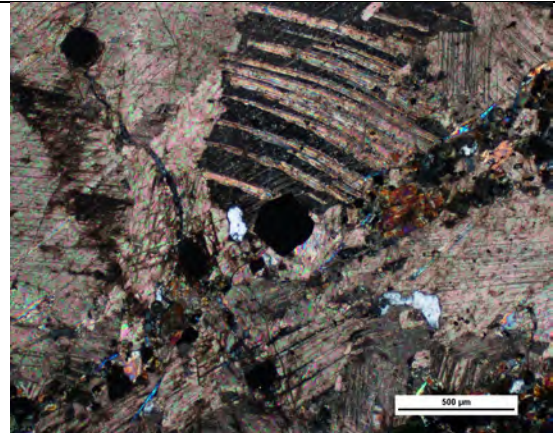
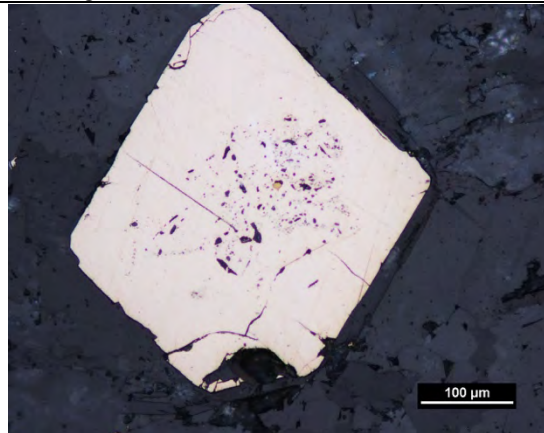
Petrography:



A tourmaline stringer with euhedral pyrite in coarse-grained ankerite (5X PPL)



Ragged pyrite grains with free gold interstitial to and as inclusions in tourmaline. (20X RFL)



Euhedral pyrite grain with anhedral sieve textured core containing a gold inclusion (10X RFL)	Seam of tourmaline and sericite in coarse-grained ankerite with fine to medium-grained euhedral pyrite grain (5X XPL)
---	---

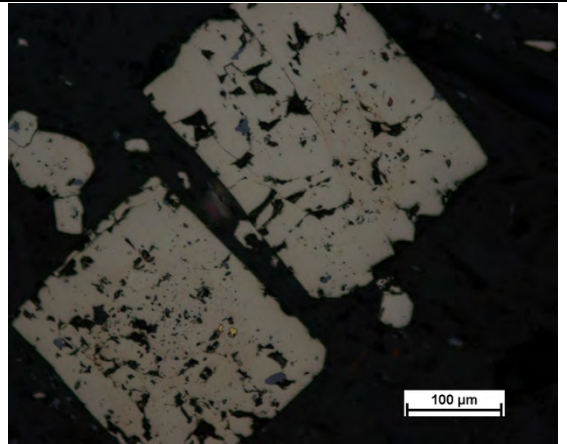
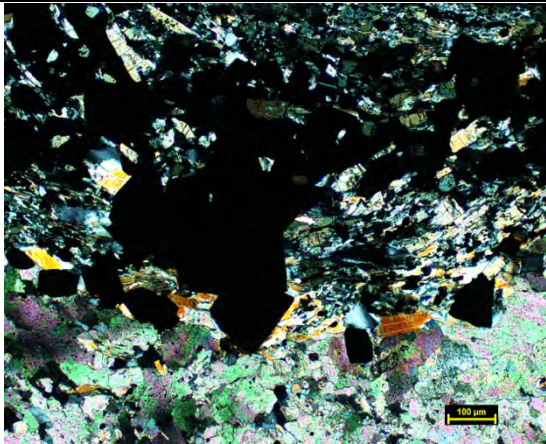
C406932

Sample Description: Center Ankerite, 2903#10 DR



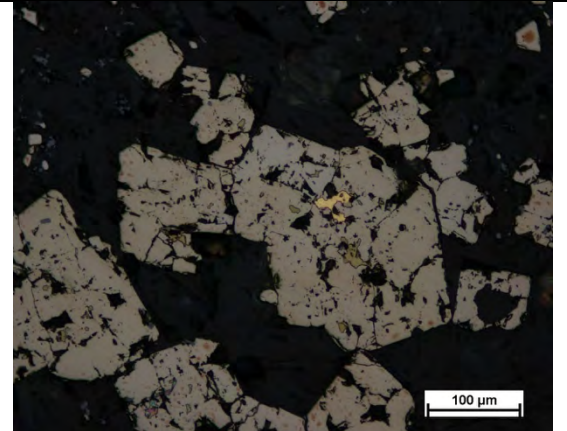
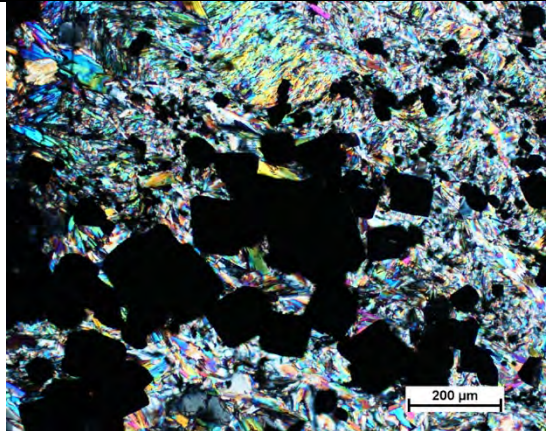
~ 10 cm ankerite vein with vein margins intact. Scaled down from the back of the drift. The vein is light to medium grained ankerite with a large ~5cm quartz vein and minor (2%) black tourmaline stringers concentrated at the vein margins, and 1% disseminate pyrite. The vein margins are highly sericitized, tourmaline rich and contain ~5% pyrite.

Petrography:



Ankerite vein margin where medium-grained ankerite grades to sericite and anhedral pyrite (10X PPL)

Fractured and inclusion rich euhedral pyrite grains in the vein margin with rutile and gold inclusions (20X RFL)



The foliated and sericite rich vein margin contains euhedral pyrite grains (see next panel) (5X XPL)

Fractured and inclusion rich pyrite grain with large gold inclusion and chalcopyrite inclusions (20X RFL)

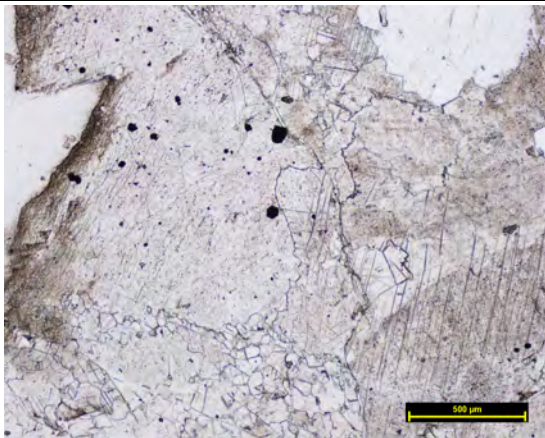
C406933

Sample Description: East Ankerite Discordant, 2909#4W

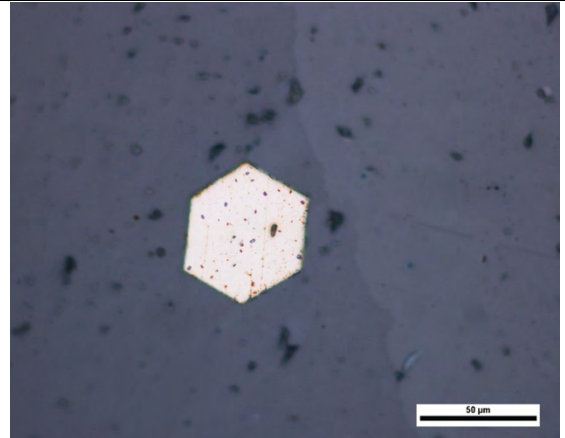


Sample was scaled from a 0.5 m boudinaged ankerite vein in the back of the drift. The sample is coarse-grained light to medium grey ankerite with moderate sericite and 1% fine-grained disseminated pyrite. It contains ~2% black tourmaline stringers and ~20% quartz flooding. The vein margin is highly sericitized and weathered with iron staining and sulfide oxidation.

Petrography:



Fine-grained disseminated pyrite in coarse grained ankerite groundmass (5X PPL)



Fine-grained euhedral pyrite in ankerite groundmass (50X XPL)

C407888

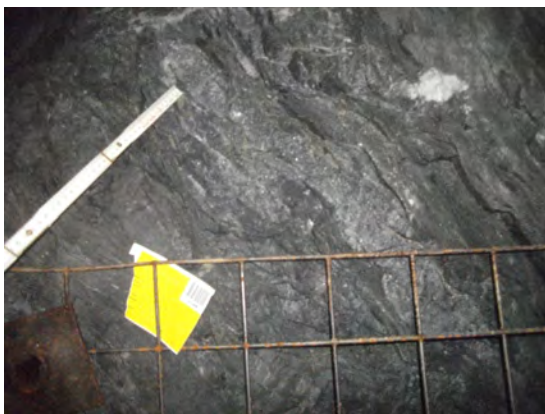
Sample Description: East Ankerite Discordant, 2909#4W



Sample was scaled from a ~30 cm wide ankerite vein from the back of the drift. The sample is medium to dark grey, coarse-grained ankerite with some banding on the cm scale. It contains ~5% quartz but no quartz veining, mild sericite concentrated at the vein margins and ~1% disseminated pyrite.

C409403

Sample Description: East Ankerite Discordant, 2909#4W



Sampled from a 10 cm wide ankerite vein in the back next to an exploration raise along the ankerite veins. The main vein has no major crosscutting quartz or quartz tourmaline veining, but has a sulfide rich alteration halo. The sample is coarse-grained dark grey ankerite with 10% quartz veining and 1% disseminated pyrite. The piece including the vein margins is highly sericitized and contains laminations of fine-grained pyrite.

C410280

Sample Description: East Ankerite Discordant, 2909#4W



Sample was taken from a ~10 cm ankerite vein in the development face. The vein is coarse to medium-grained ankerite and has banding on the mm to cm scale which appears to be related to ankerite grain size and composition. There are cross cutting mm scale quartz veinlets (~5%) and fine-grained disseminated pyrite. The margins are fine-grained, foliated and sericite rich with 2-5% pyrite.

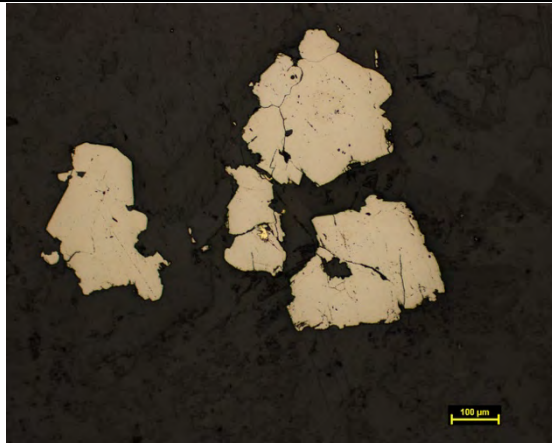
C406934

Sample Description: East Ankerite, 2909#2E DR

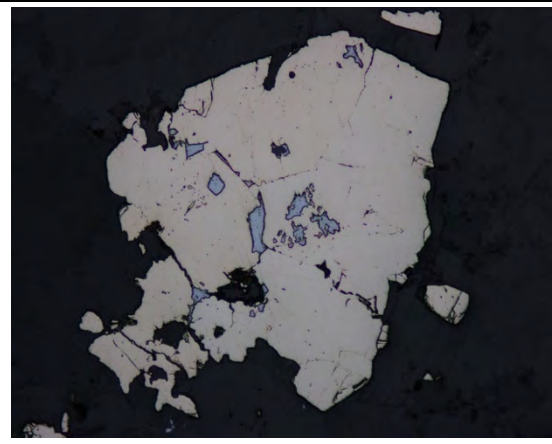


Scaled from a ~ 0.5m boudinaged ankerite vein in the drift back. The sample contain the vein margins and is overprinted by two stages of veining, quartz veining and tourmaline stringers. The ankerite vein material is coarse-grained ankerite with ~2% disseminated pyrite, 5% tourmaline, and is sericitized. The vein margins are schistose, sericite and tourmaline rich with laminations of fine-grained pyrite.

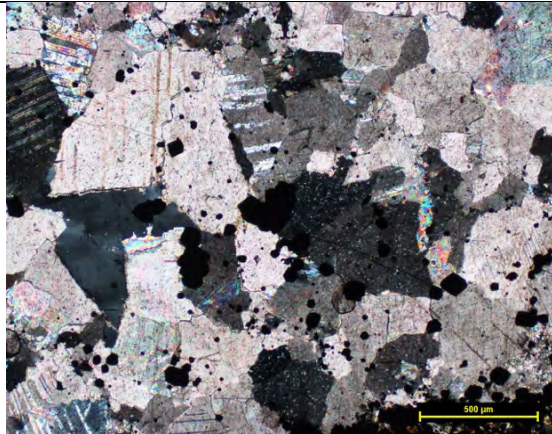
Petrography:



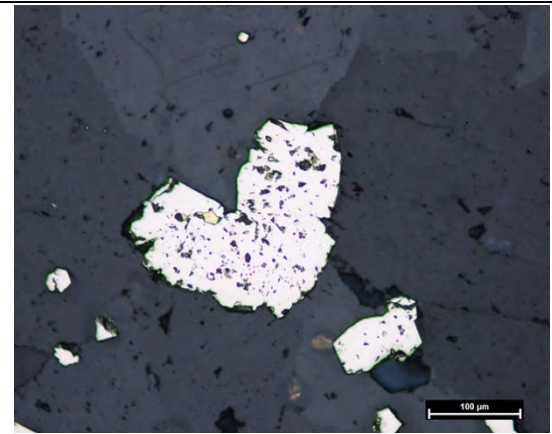
Anhedronal pyrite grains in an ankerite-sericite groundmass. The top pyrite grain contains visible euhedral growth haloes which are inclusion rich. Gold occurs at vein margin and in fractures. (10X RFL)



An anhedronal pyrite grain with irregular galena inclusions (20X RFL)



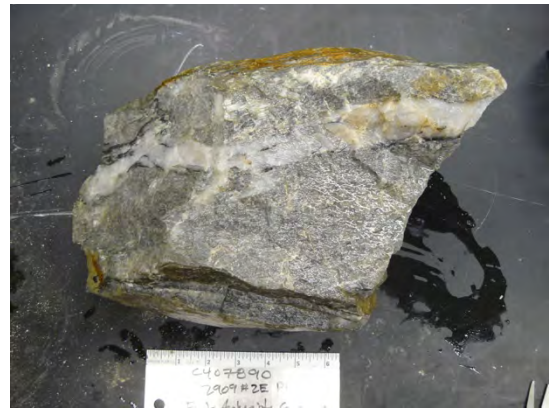
Disseminated, anhedronal pyrite in a coarse-grained ankerite groundmass (5X XPL)



An anhedronal, ragged, inclusion rich pyrite heart with a chalcopyrite inclusion in an ankerite groundmass (20X RFL)

C407890

Sample Description: East Ankerite, 2909#2E DR



A sample was scaled down from a ~1m wide ankerite vein at the back of the drift. The same region of the vein as C406834 (resample). The sample is light grey, coarse-grained ankerite with a ~2 cm milky quartz vein with black tourmaline at its margins. The ankerite material contains ~1% disseminated pyrite and ~3% sericite.

C409402

Sample Description: 3409 Ramp



Sample was taken from a ~0.5 m boundinaged ankerite vein in the wall of the ramp to the 3409 ankerite development.

The sample is coarse-grained, medium to dark grey ankerite with ~15% milky quartz. There is coarse grained pyrite and pyrrhotite (~2%) near the vein margin associated with a mm scale tourmaline stringer.

C410295

Sample Description: East Ankerite, 3409E AS



Samples were collected from the muck pile in the access drift to the 3409 ankerite development. The blast exposed two 0.5-1 m wide boundinaged ankerite veins. The veins contain quartz extension veins and have ~20 cm wide intensely foliated and sulfide rich alteration haloes. The samples are light to medium grey, coarse-grained ankerite with some visible mm to cm scale banding. They contain ~10% milky quartz which is associated with sericite. The ankerite material contains fine-grained disseminated pyrite (<1%).

C411098

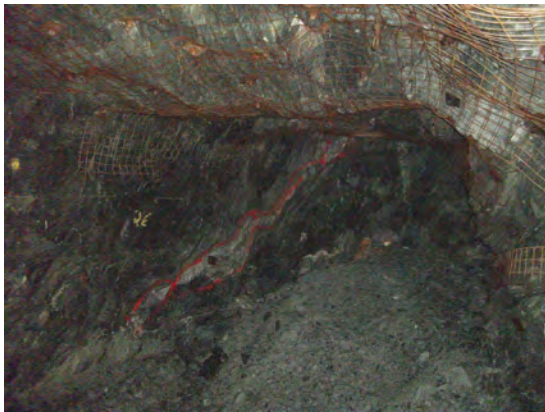
Sample Description: East Ankerite, 3509E AS



Collected from a freshly blasted muck pile. Sample contains vein material and vein margin. Vein material is light to medium grey coarse-grained ankerite with 20% quartz veining associated with sericite. The vein margin is foliated and contains ~20% sulfide banding. The sulfides are fine to medium-grained pyrite with minor chalcopyrite (<1%)

C411096

Sample Description: East Ankerite, 3509W AS



Sampled from a freshly blasted muck pile. The vein is a <0.5 m wide boudinaged ankerite vein in the back and face of the drift. The sample is medium grey, coarse-grained ankerite with ~1% disseminated pyrite and ~20% milky with extension veining associated with sericite.

C410097

Sample Description: East Ankerite, 3509W AS

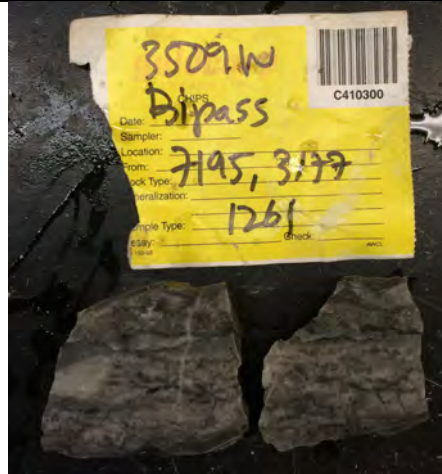


Sample was collected from a freshly blasted muck pile. The veining in the wall of the drift was a set of 3 to 4, 5-10 cm wide ankerite veins in a 2 m wide alteration halo. The sample is a 2-5 cm wide ankerite vein with mm scale light grey and dark grey banding preserved. Visible gold occurs at the vein margins where it is overprinted by quartz extension veins with sericite and minor (<1%) fuchsite. The ankerite vein contains ~50% quartz extension veins with sericite and minor (<1%) fuchsite. The vein margin is highly schistose and sericite rich with laminated pyrite. It also contains several <1cm wide quartz-ankerite stringers.



C410300

Sample Description: East Ankerite, 3509E Bypass



Samples were collected from a freshly blasted muck pile. The ankerite vein in the face was a ~0.5 m wide, boudinaged vein in the wall of the bypass drift. The sample is coarse-grained, light grey ankerite with mm to cm scale banding and 1% disseminated pyrite. It is cut by ~10%, cm scale quartz veinlets which are associated with sericite. Banding is prominent in the fresh cut surface as are mm scale black tourmaline veinlets (2%) which are associated with fine-grained pyrite.

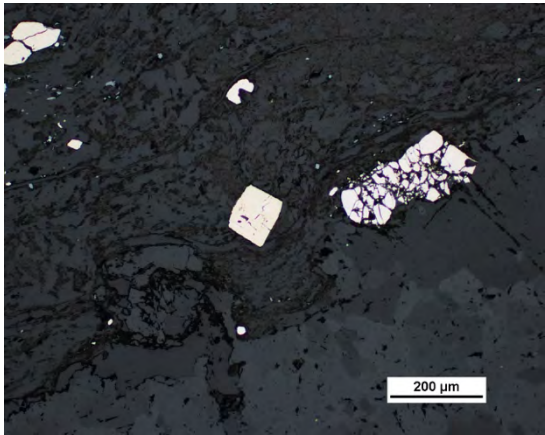
C406930

Sample Description: East Ankerite, 3509E DR

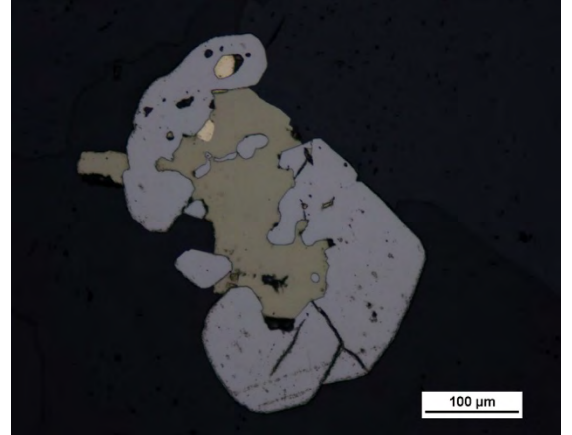


Sample was scaled from the back of a heavily weathered drift where veining was not visible, but was identified from historic mapping. The fresh surface of the sample is medium to dark grey, coarse-grained ankerite with cm scale quartz stringers (~10%). The vein margin is very weathered and iron stained with visible oxidization of sulfides. The vein material contains ~1% disseminated pyrite.

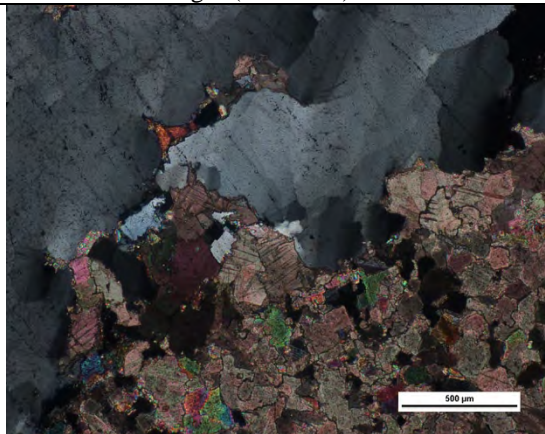
Petrography:



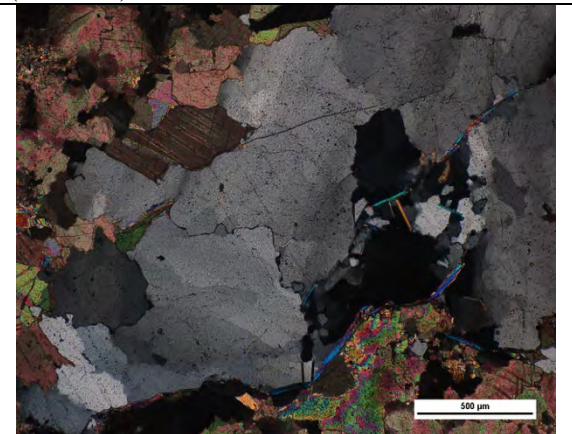
Euhedral and fractured pyrite grains at the ankerite vein margin (10X RFL)



Anhedronal pyrite grain with chalcopyrite and gold (20X RFL)



Fine-grained ankerite at the margin of a quartz veinlet (5X XPL)



Coarse-grained Quartz veinlet with sericite at its margins (5X XPL)

C408783

Sample Description: Curts Ankerite Vein Boulder



Heavily weathered boulder of ankerite vein. The fresh surface is coarse-grained light grey ankerite with ~10% milky quartz veining with sericite alteration, 2% tourmaline stringers and 1% fine-grained pyrite and pyrrhotite.

C410289

Sample Description: Curts Ankerite Vein Transect



Broken off a ~1 m wide ankerite vein with minimal milky quartz veining in outcrop to expose unweathered surface. Coarse-grained light to medium grey ankerite cut by ~15 %, cm scale wide grey quartz veins/stringers. Strong sericite alteration associated with quartz veining. Disseminated fine-grained pyrite <1%,

C410290

Sample Description: Curts Ankerite Vein Transect



Sample was broken off a in test pit of a ~3 m wide ankerite vein with extensive milky quartz veining. The vein material is light grey, coarse-grained ankerite with little to no quartz veining.

C410291

Sample Description: Curts Ankerite Vein Transect



Ankerite boulder found near a ~4 m wide ankerite vein. Boulder was heavily weathered and contained two stages of quartz veining (cm scale) which are orthogonal to one another. The fresh surface reveals that the vein material is 80% coarse-grained light grey ankerite with <1% disseminated fine-grained pyrite, ~20% quartz stringers associated with minor sericitization.

C410292

Sample Description: Curts Ankerite Vein Transect



1-2 cm ankerite veinlet broken off an outcrop in the highly schistose envelope a ~1 m wide ankerite vein with cm scale milky quartz extension veining. The veinlet was mostly weathered out of the vein envelope, is iron stained, and contains a small mm scale quartz extension vein. The vein material is light grey fine-grained ankerite with <1% pyrite and 10% quartz.

C410293

Sample Description: Curts Ankerite Vein Transect



Broken off a ~1 m ankerite vein where a trench sample had been taken. The vein material is coarse-grained, light grey/whitish ankerite and has a mm scale black tourmaline stringer and ~5%, <1cm quartz stringers. There is moderate sericite alteration associated with quartz stringers.

C410294

Sample Description: Curts Ankerite Vein Transect



Broken off ~1m ankerite vein with <5% quartz veining. Weathering has accentuated the crustiform texture in the ankerite material. Fresh surface is white to light grey coarse-grained ankerite with crustiform texture on the mm to cm scale, ~5% quartz and <1% disseminated pyrite.

C409623

Sample Description: Carbonate Vein, Hollinger



Boulder from the Hollinger pit with a ~5 cm wide boudinaged carbonate vein. The vein is weathered to a brownish red and contains 10% mm-cm scale quartz ladder veins and minor sericite. The vein margins are highly foliated and sericite rich with 10% fine-grained pyrite. The host rock is a carbonate and sericite altered metabasalt (Tisdale?).

C410901

Sample Description: Carbonate Vein



Small ~2 cm carbonate vein in an outcrop across from Pearl Lake. The weathered surface is red with iron staining and has a prominent quartz stringer from preferential weathering. The fresh surface reveals a crustiform texture of light to medium grey coarse-grained ankerite with 1% small stringers of tourmaline, and 5% grey quartz veining orthogonal to the main vein.

B-A

Sample Description: Ankertote Boulder, Buffalo-Ankerite Pit



Heavily weathered boulder of ankerite vein with quartz and quartz tourmaline veining. The fresh surface reveals a laminated internal structure to the vein dominated by 45% milky quartz, 40% coarse-grained light grey ankerite, with 10% tourmaline stringers and minor pyrite and fuchsite associated with the tourmaline.

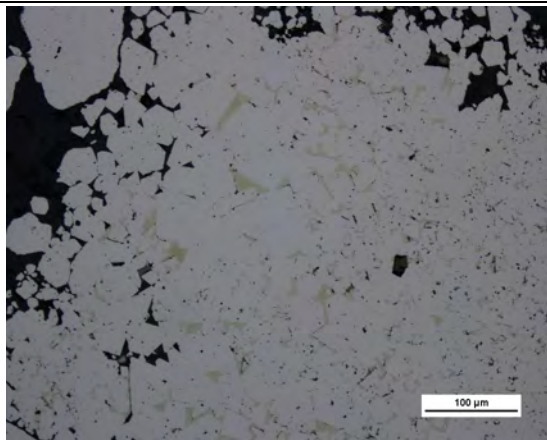
C408778

Sample Description: Sulfide clast, 125245BS

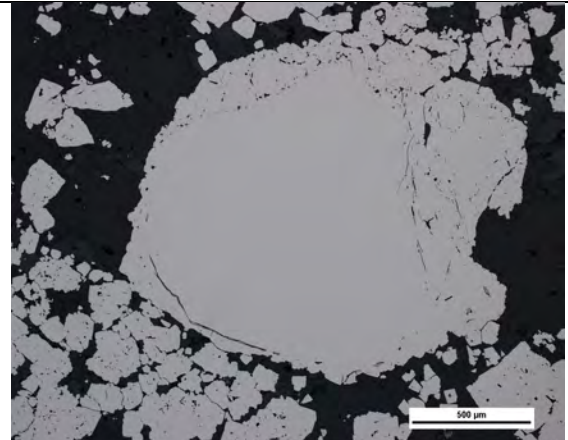


Large ~1 m long sulfide clast in the back of the drift. A small piece was scaled down. 40% coarse-grained euhedral pyrite with interstitial chalcopyrite (<1%). Clast groundmass is medium-grained quartz and carbonate, sericite. The conglomerate groundmass is fine-grained highly foliated and sericitized greywacke.

Petrography:



Anhedral to euhedral pyrite intergrown with interstitial chalcopyrite (20X RFL)



Coarse anhedral pyrite grain with sieve textured rim (5X RFL)

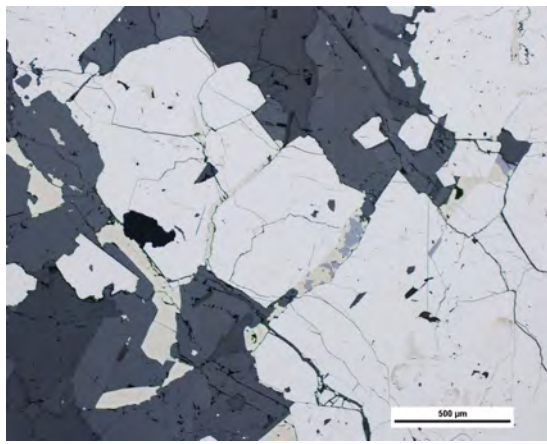
C408779

Sample Description: Sulfide clast, 125245BS

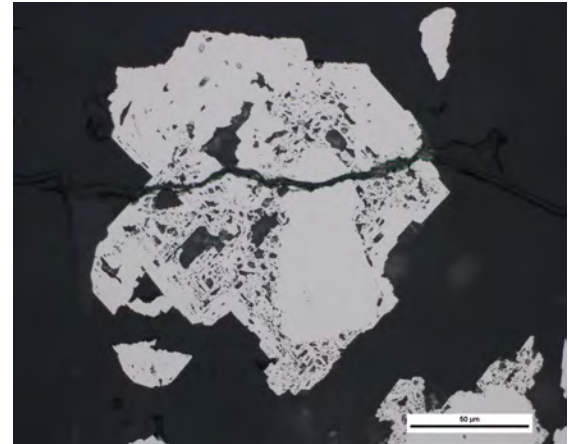


Elongated clast of ~90% coarse-grained euhedral pyrite with interstitial chalcopyrite (~1%). Clast groundmass is medium-grained quartz and carbonate. The conglomerate groundmass is fine-grained highly foliated and sericitized greywacke.

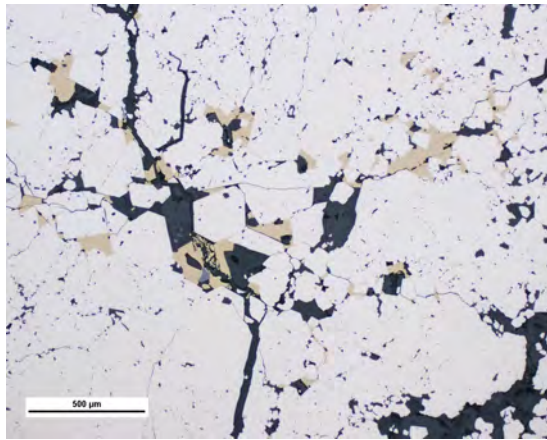
Petrography:



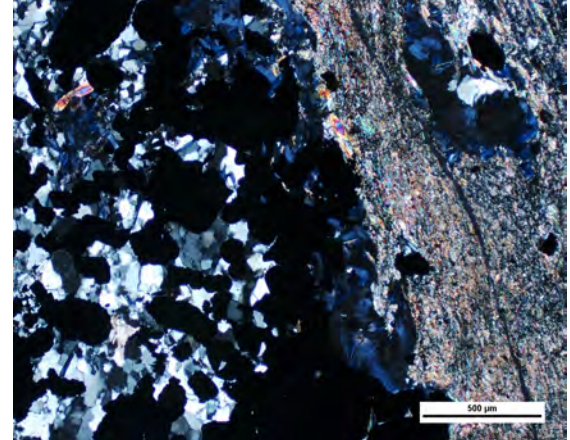
Fractured pyrite with interstitial chalcopyrite and sphalerite (5X RFL)



Pyrite grain with a euhedral core and sieve texture rim. (50X RFL)



Massive fractured and euhedral pyrite with interstitial chalcopyrite (5X RFL)



Margin of the clast. The conglomerate groundmass is fine-grained sericite, quartz and carbonate and the clast groundmass is medium-grained quartz and sericite (5X XPL)

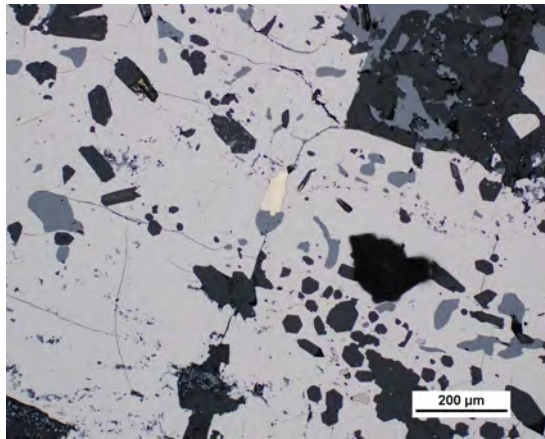
C408781

Sample Description: Sulfide Rich Interflow Sediment, 155446 Scram

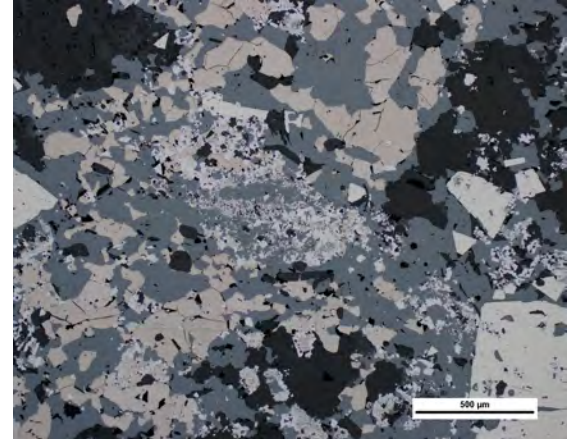


Interflow sediment with cm scale ankerite vein crosscutting it. Fine-grained chlorite, with strong sericite and carbonate alteration and laminations of massive sulfide (~10%). Contains lenses and stringers which are mostly massive sphalerite (2%), 4% coarse to fine-grained pyrite, 4% pyrrhotite.

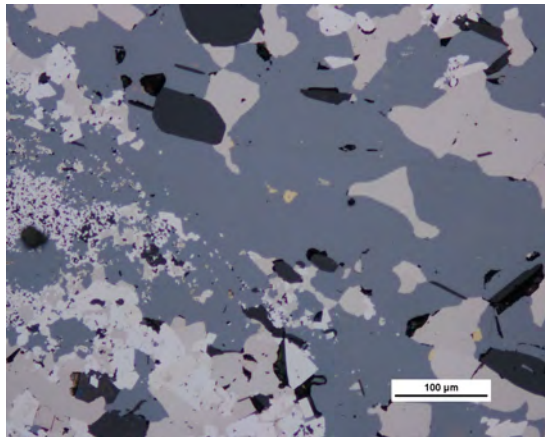
Petrography:



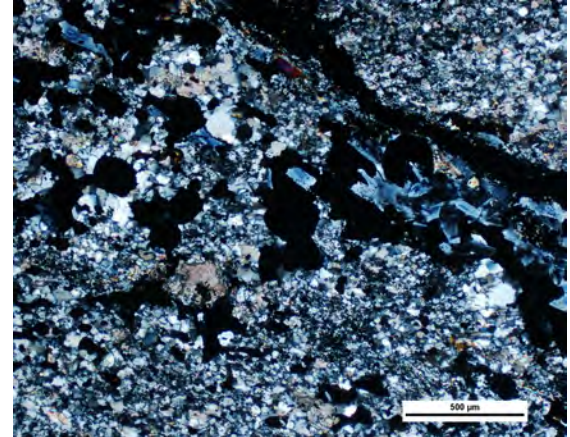
Fracture hosted gold association with sieve texture pyrite with sphalerite (10X RFL)



Massive sphalerite and pyrrhotite overgrowing fine and coarse-grained pyrite (5X RFL)



Massive sphalerite and pyrrhotite with inclusions of chalcopyrite and fine-grained euhedral pyrite (20X RFL)



Stringer of fine-grained pyrite and clots of sulfide (pyr, sph) in a groundmass of fine-grained quartz, carbonate and sericite (5X XPL)

C408777

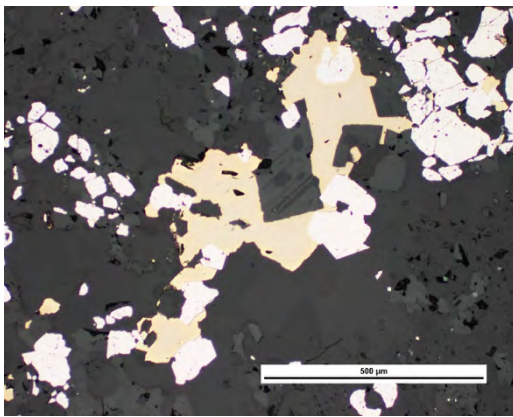
Sample Description: Clast in conglomerate, 124941BS



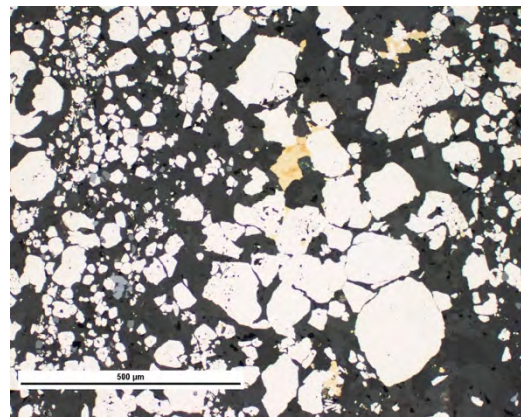
Clast was scaled from the back of a drift in the greenstone nose region of the mine (Timiskaming conglomerate).

Sample is dark grey to green, fine-grained chlorite with intense fuchsite and carbonate alteration and 3-4% fine-grained pyrite laminations.

Petrography:



Anhedral pyrite and chalcopyrite (10X RFL)




Coarse to fine-grained anhedral rounded pyrite grains with minor sphalerite and chalcopyrite (10X RFL)

C408776

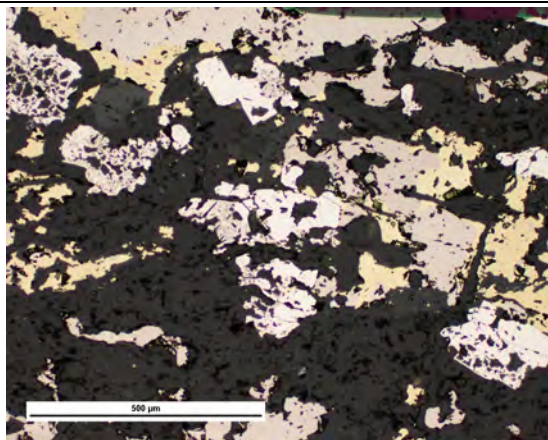
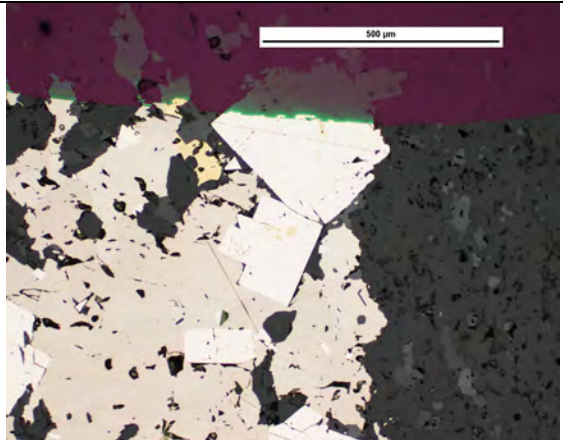
Sample Description: Quartz-Fuchsite Vein, 12L



Small piece of the massive quartz fuchsite vein. The sample is milky quartz with ~30% fine-grained green fuchsite and sericite, and minor (<1%) fine-grained pyrite.

C406944	
Sample Description: Interflow Sediment, 1605XC	
	<p>Iron stained and weathered carbonaceous sediment. Dark grey to greenish, fine-grained chlorite-carbonate-sericite. 1-2% disseminated fine-grained pyrite throughout and 3% mm scale calcite stringers</p>

186567	
Sample Description: Cherty Interflow, 186567	
	<p>Greyish brown microcrystalline quartz (chert) with 20% dark black laminations which contain fine to medium-grained pyrite (1%), pyrrhotite (2%), chalcopyrite (1%)</p>

Petrography:	
	
<p>Ragged, sieve textured pyrite with massive pyrrhotite and chalcopyrite in a groundmass of quartz (10X RFL)</p>	<p>Coarse euhedral pyrite with chalcopyrite inclusion overgrown by pyrrhotite in a quartz groundmass (10X XPL)</p>

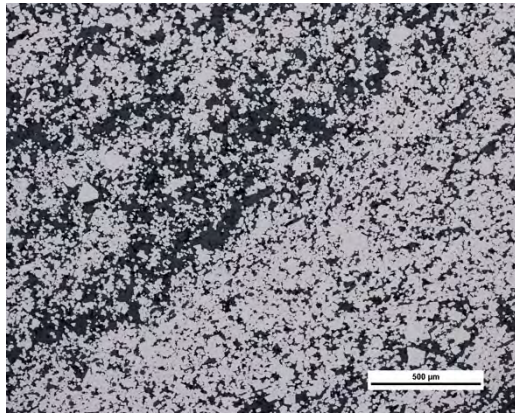
C408780

Sample Description: Sulfide Rich Interflow Sediment, 1939#10DR

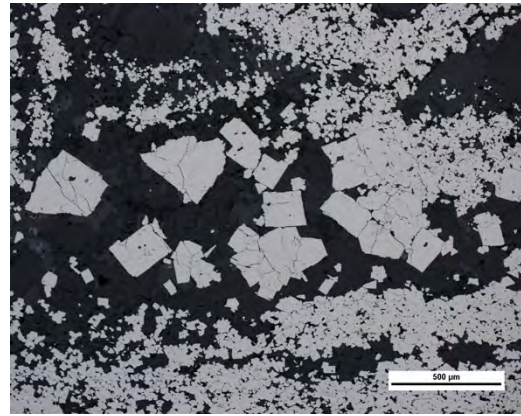


Sample of "massive sulfide" interflow sediment from Eriks collection. ~80% laminated to medium fine-grained pyrite, 5% pyrrhotite, 1% chalcopyrite.

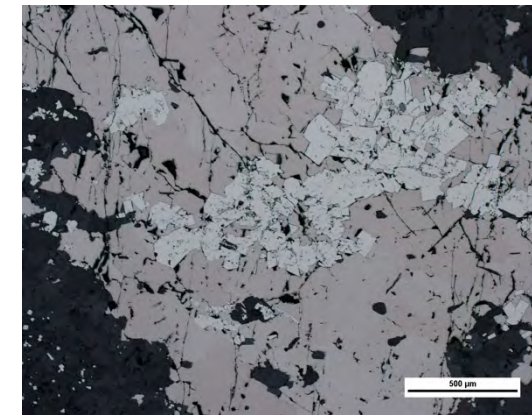
Petrography:



Fine-grained massive pyrite lamination (5X RFL)



Coarse euhedral pyrite and fine-grained euhedral pyrite in quartz and carbonate groundmass(5X RFL)



Euhedral pyrite overgrown by massive pyrrhotite (5X RFL)

C406939

Sample Description: Interflow Sediment, 1904 DR



~1 m thick interflow sediment in the drift wall next to ~0.5 m wide ankerite vein (above in the stratigraphy). Black/grey highly foliated interflow sediment with red iron staining. Coarse-grained carbonate with graphite and chlorite, and minor quartz stringers (2-3%) and disseminated pyrite (1%)

C407885

Sample Description: Interflow Sediment, 1904 DR



Resampled the ~1 m thick interflow sediment in the drift wall next to ~0.5 m ankerite vein (above in the stratigraphy). Dark grey to green coarse-grained chlorite, carbonate, quartz. Highly sericite altered, ~2% disseminated fine-grained pyrite.

C406941

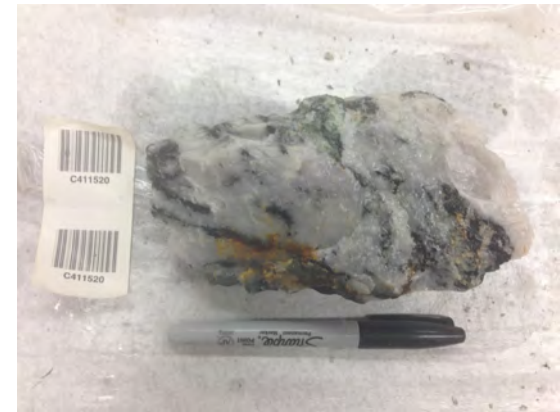
Sample Description: Graphitic Argillite, 196671AT



Highly foliated, carbonaceous (graphitic) sediment with minor ~2% quartz stringers and ~1 % medium-grained pyrite

C411520

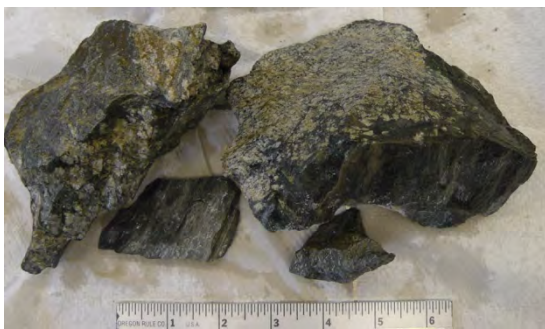
Sample Description: Quartz-Tourmaline Ladder Vein, 2125DR



Sampled from the back of 2125 DR. The quartz-tourmaline ladder vein from a ~1.5 m wide boudinaged ankerite vein. Quartz with stringers and clots of dravite (~10%). Sericite and possibly fuchsite at the margin of the quartz and ankerite. Coarse-grained pyrite associated with tourmaline (~1%)

C406936

Sample Description: Hyaloclastite, 2301#5 DR



Glassy, chlorite rich hyaloclastite, moderate carbonate (calcite) alteration.

C401519

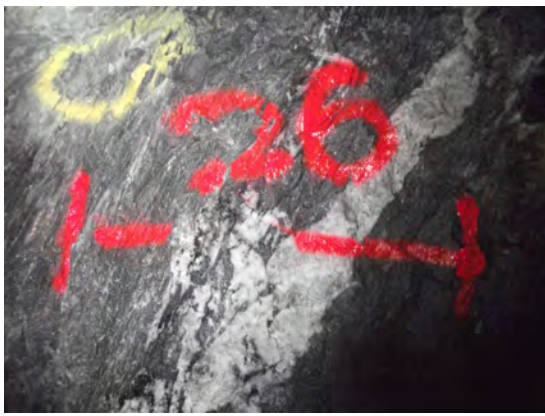
Sample Description: Quartz-Ankerite Vein, 246862BS



~15 cm wide quartz-ankerite vein in the face of an ankerite development drift. The vein was smoky quartz with dog toothed ankerite at the vein margins. ~1% coarse-grained pyrite stringers with <1% brown tourmaline (schorl). The vein was parallel to the main ankerite vein in the drift.

C411518

Sample Description: Quartz Tourmaline Veining, 246862BS



Quartz tourmaline veining was subsampled from a 0.5 m wide ankerite vein in the face of the drift. The sample is milky quartz with ~20% black tourmaline clots.

C407887

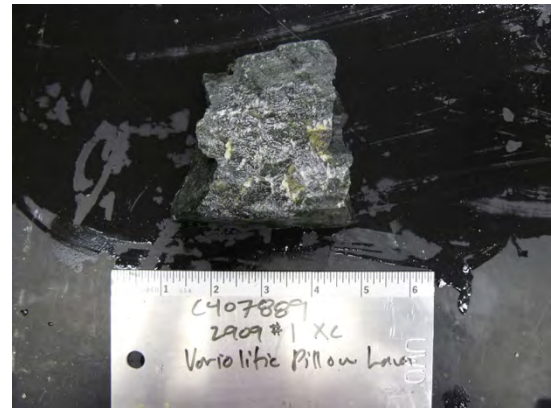
Sample Description: Massive Mafic Volcanic, 2710 DRW



Sampled from the wall of the drift in a region with no veining. The sample is dark green, medium-grained chlorite rich metabasalt. Moderate carbonate and sericite alteration,

C407889

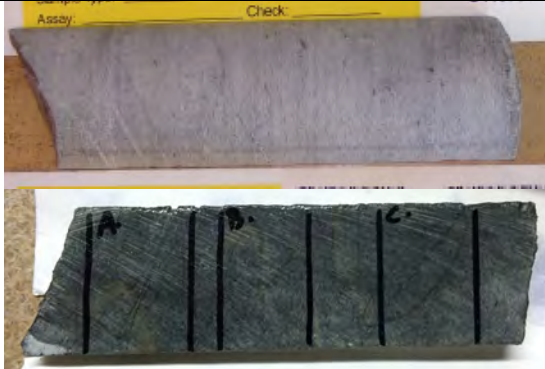
Sample Description: Interpillow Breccia. 2909#1 X/C



Sample was scaled from the back of a drift of highly deformed pillow basalt. The sample is a glassy, chlorite rich variolitic interpillow breccia region with moderate carbonate alteration and silicification.

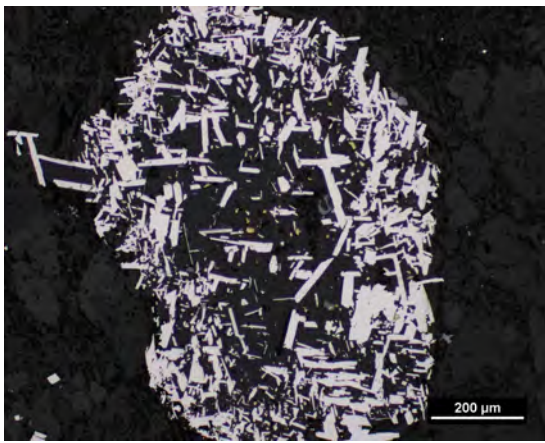
E863294

Sample Description: Greywacke, Hoyle Pond Mine

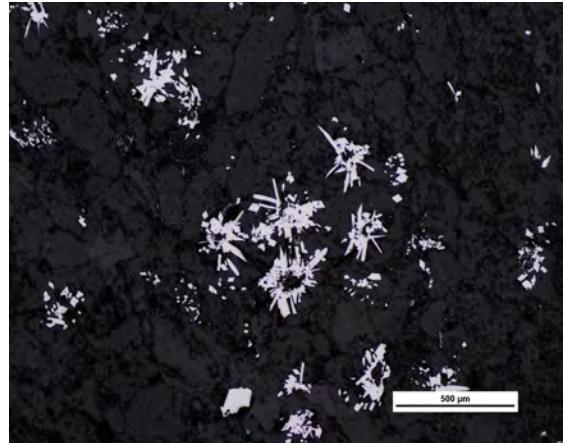


Grey fine to medium-grained greywacke with weak carbon and sericite alteration. 10% quartz-carbonate stringers, 2% arsenopyrite clots and needles associated with stringers, 1% disseminated pyrite.

Petrography:



Clot of arsenopyrite needles with small chalcopyrite grains in the core.(10X RFL)



Clusters of arsenopyrite needles (5X RFL)

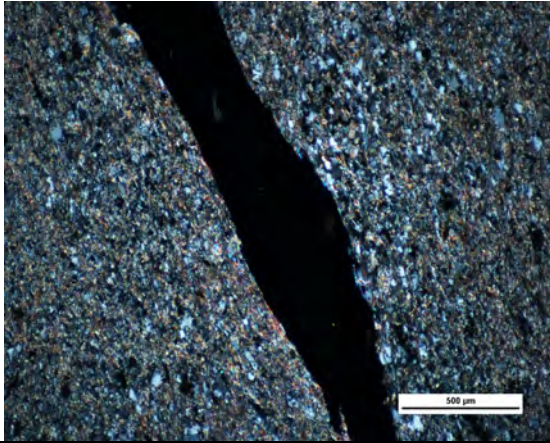
E885276

Sample Description: Greywacke, Hoyle Pond Mine

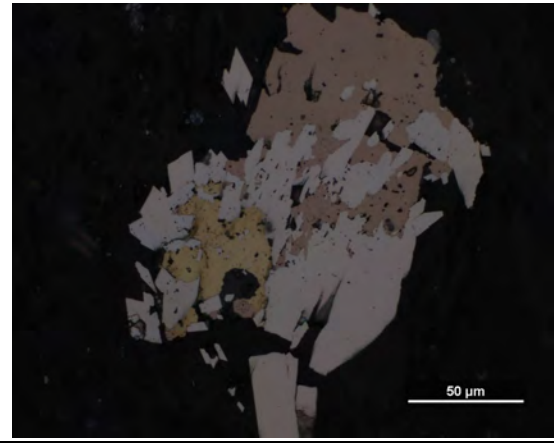


Fine-grained dark grey argillite and fine to medium grained sericite altered greywacke. 25% quartz stringers, some flooding textures, 3% arsenopyrite, <1% pyrite

Petrography:

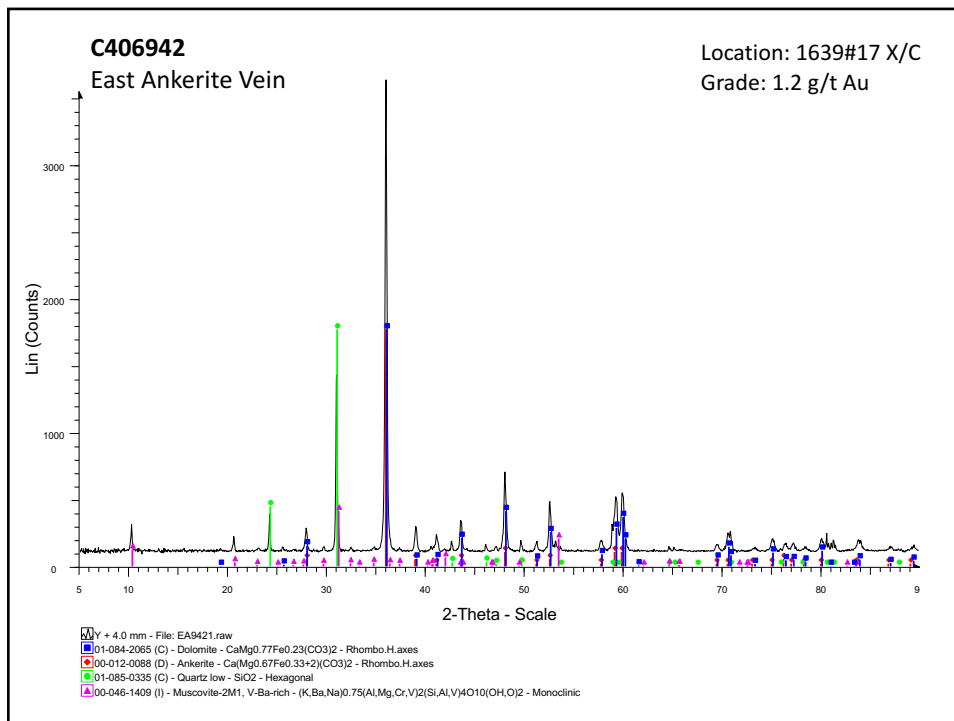
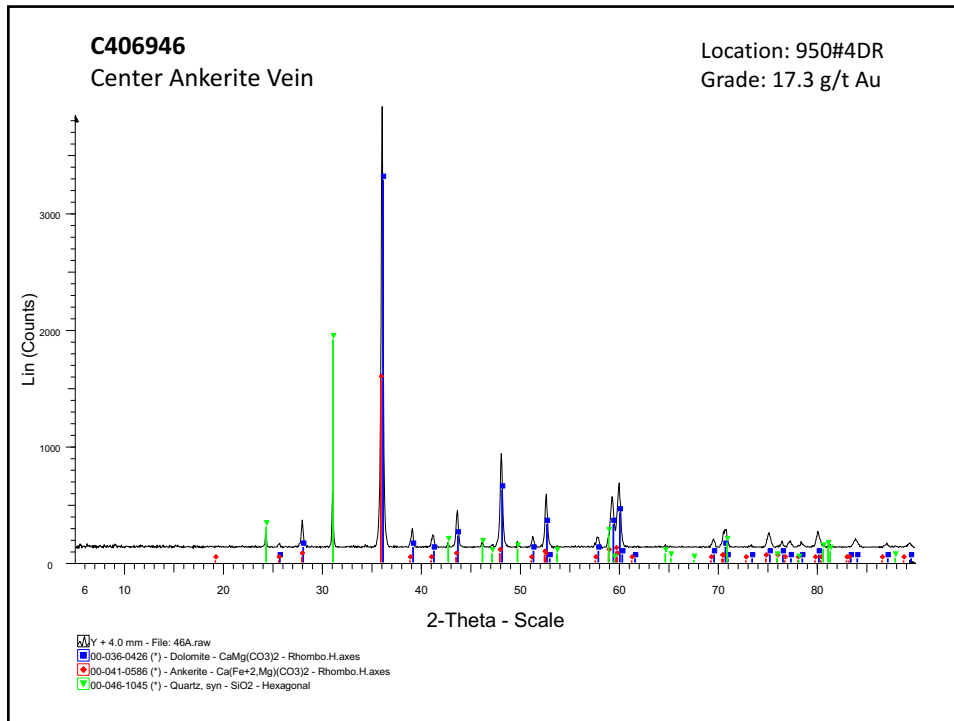


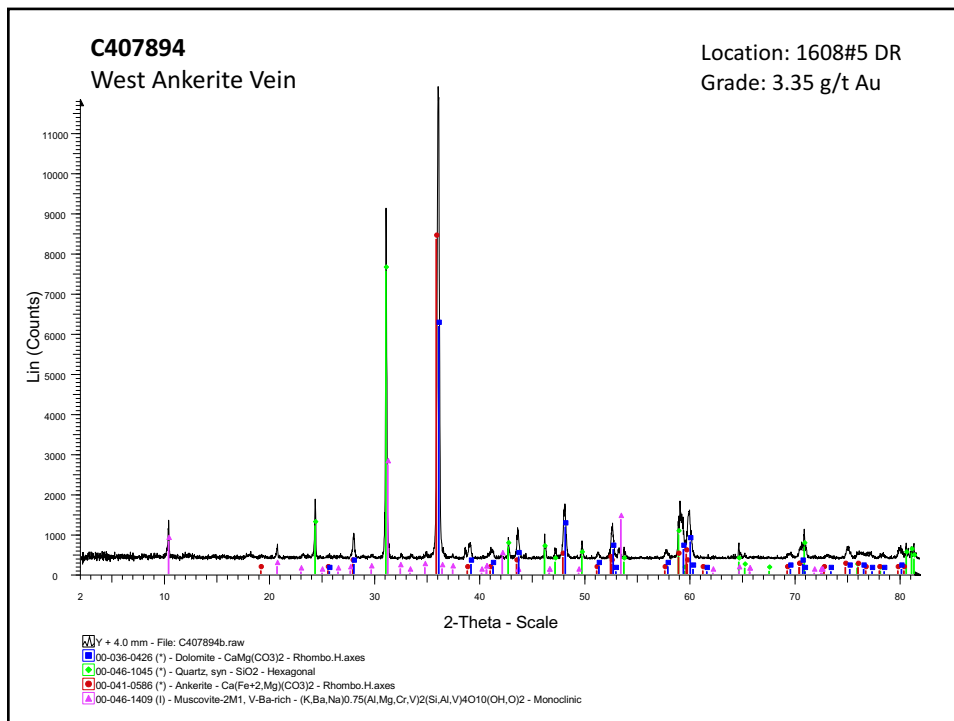
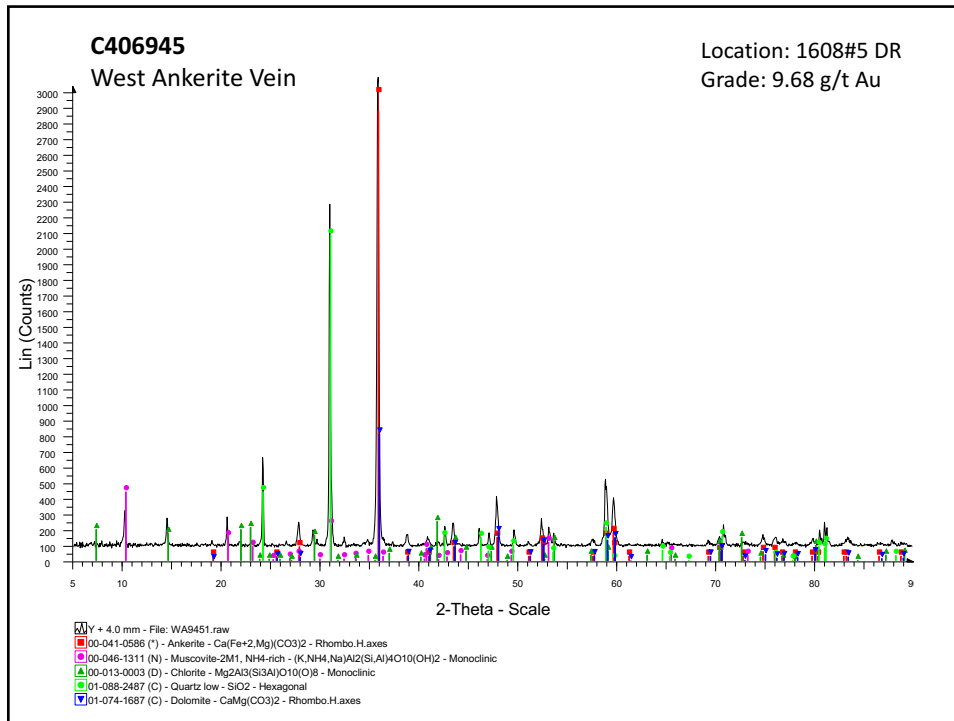
Large arsenopyrite needle in a groundmass of fine-grained quartz, sericite and carbonate (5X XPL)

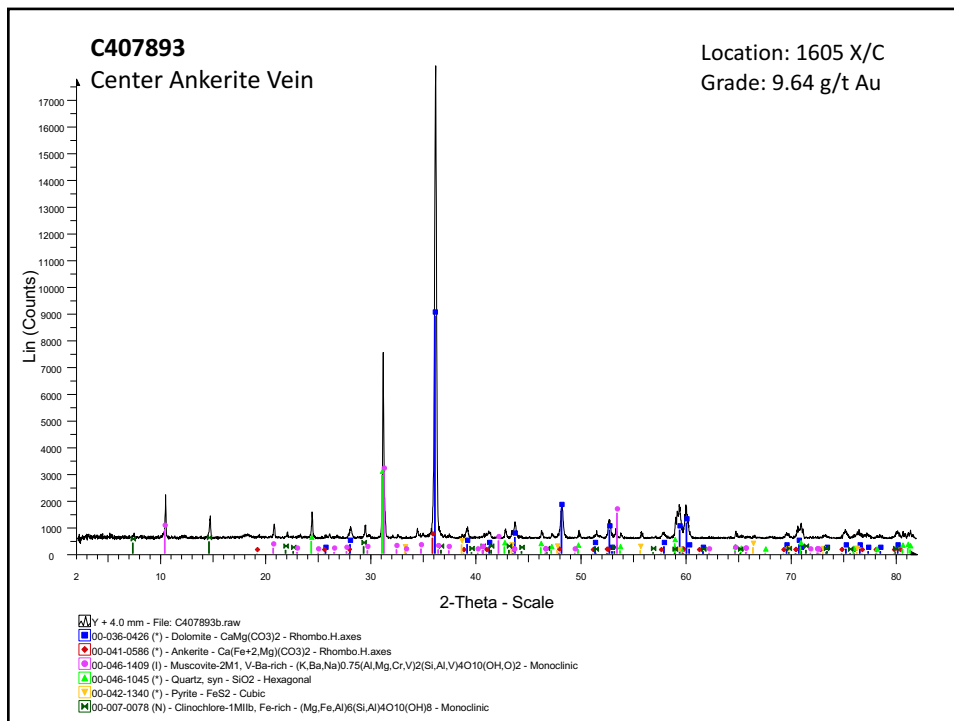
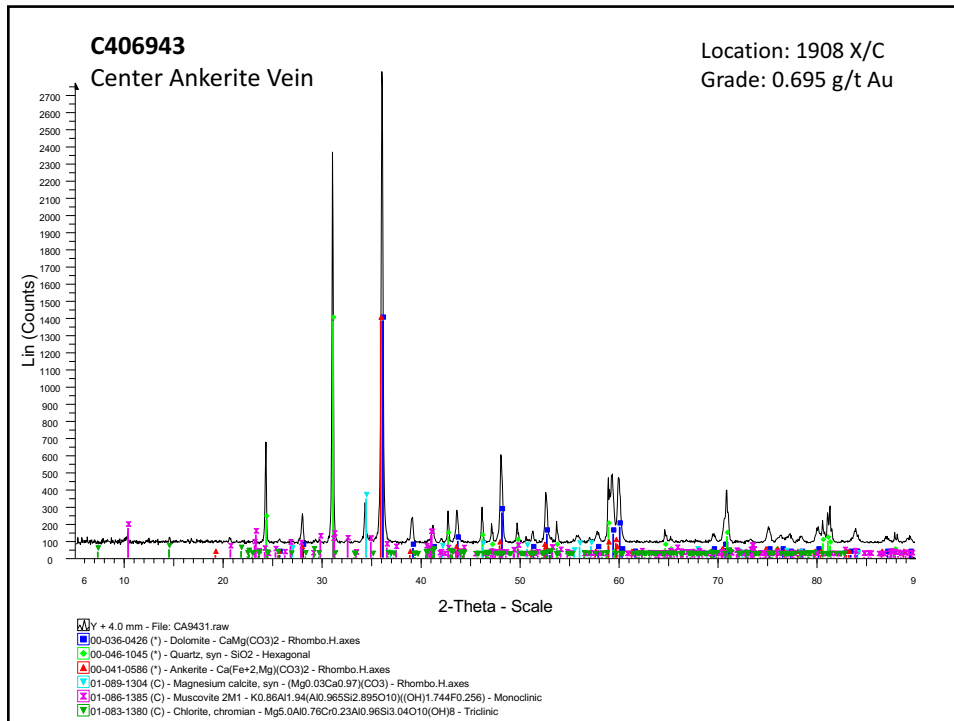


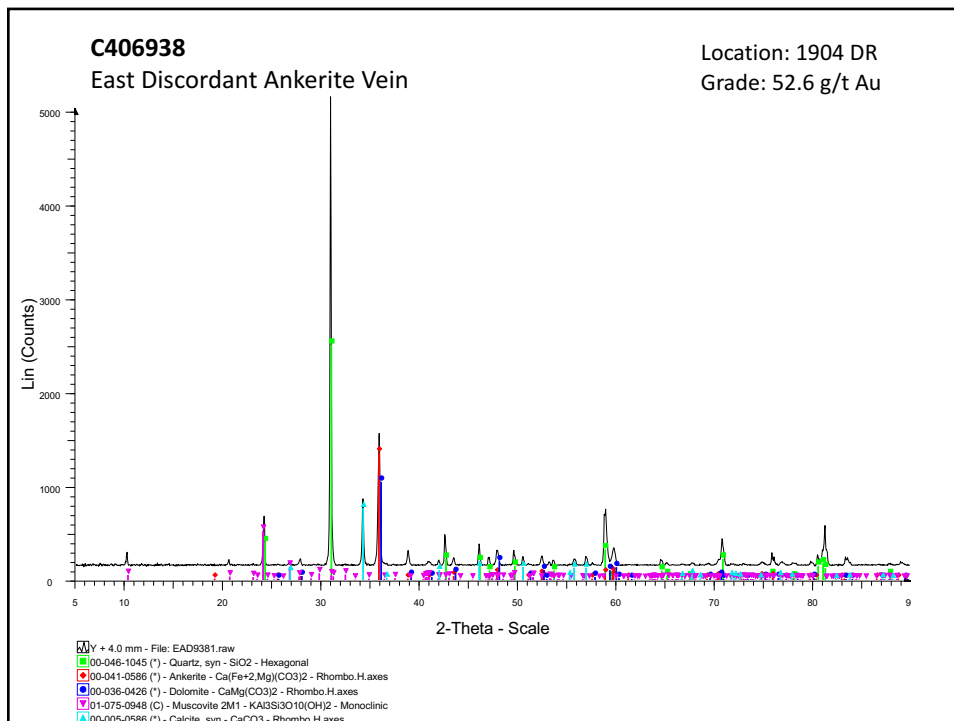
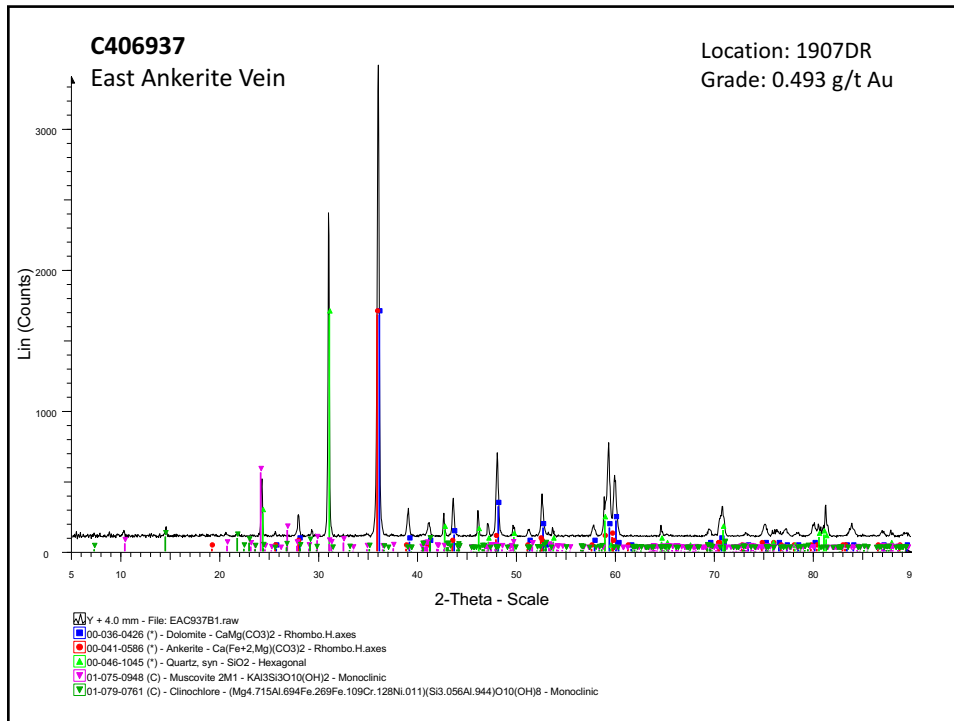
Gold associated with euhedral arsenopyrite and pyrrhotite (50X RFL)

A.4 X-Ray Diffraction



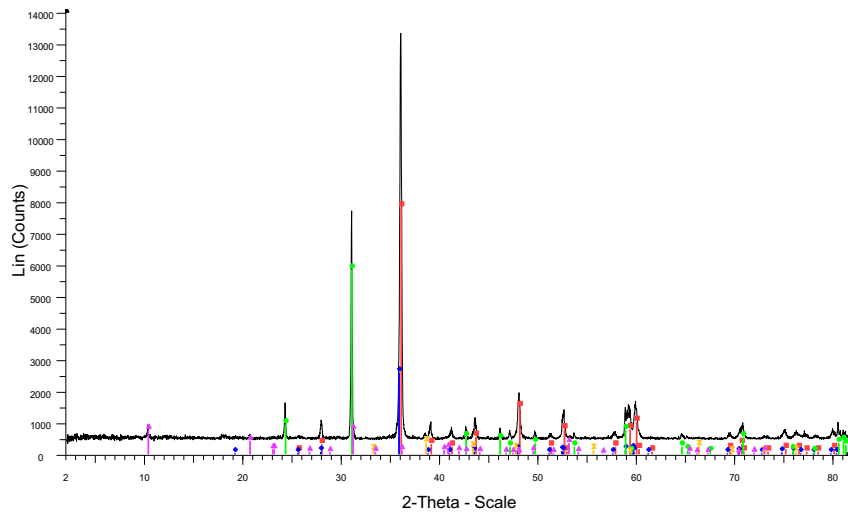






C407884
East Discordant Ankerite Vein

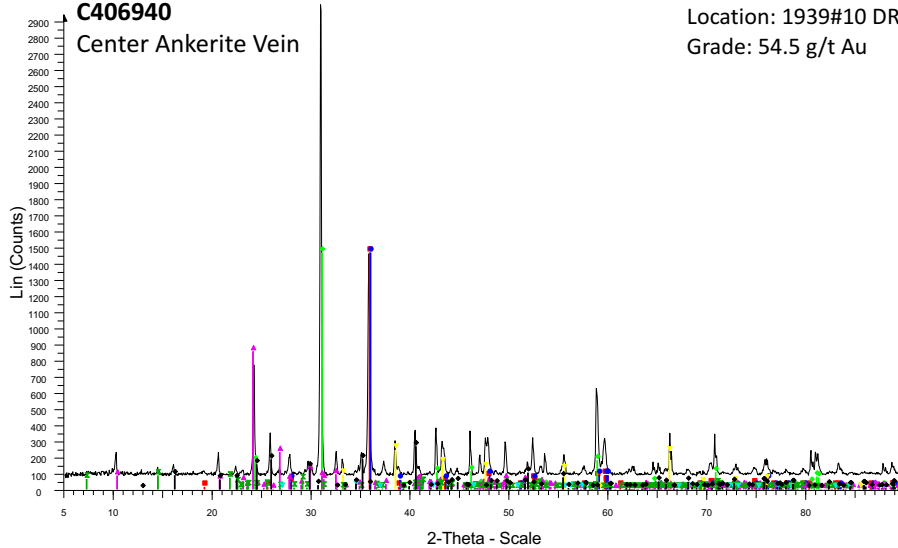
Location: 1904 DR
Grade: 9.66 g/t Au



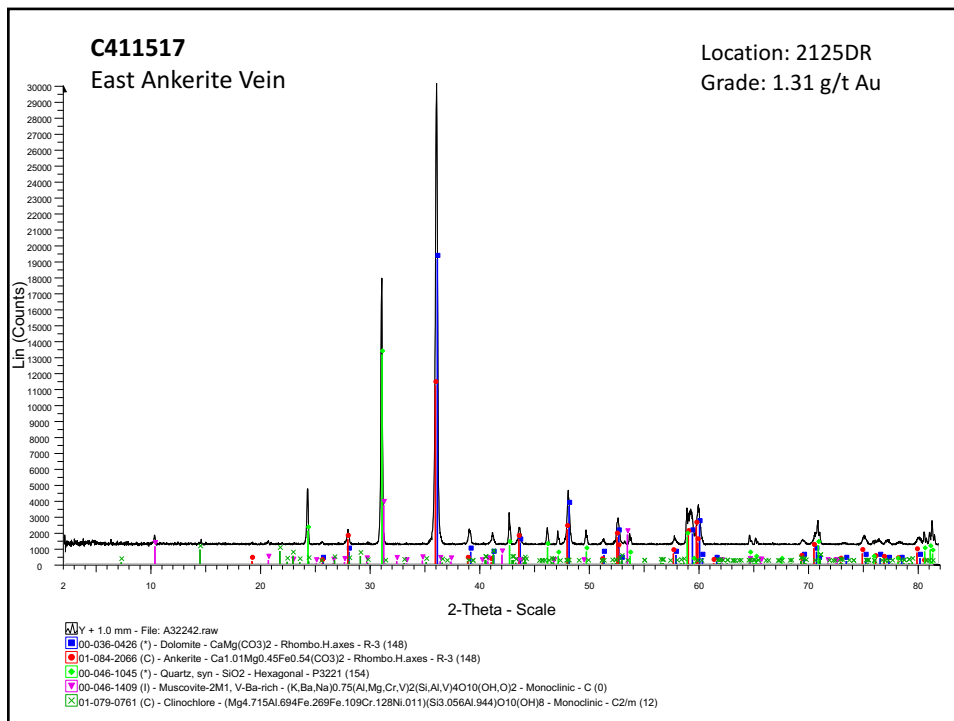
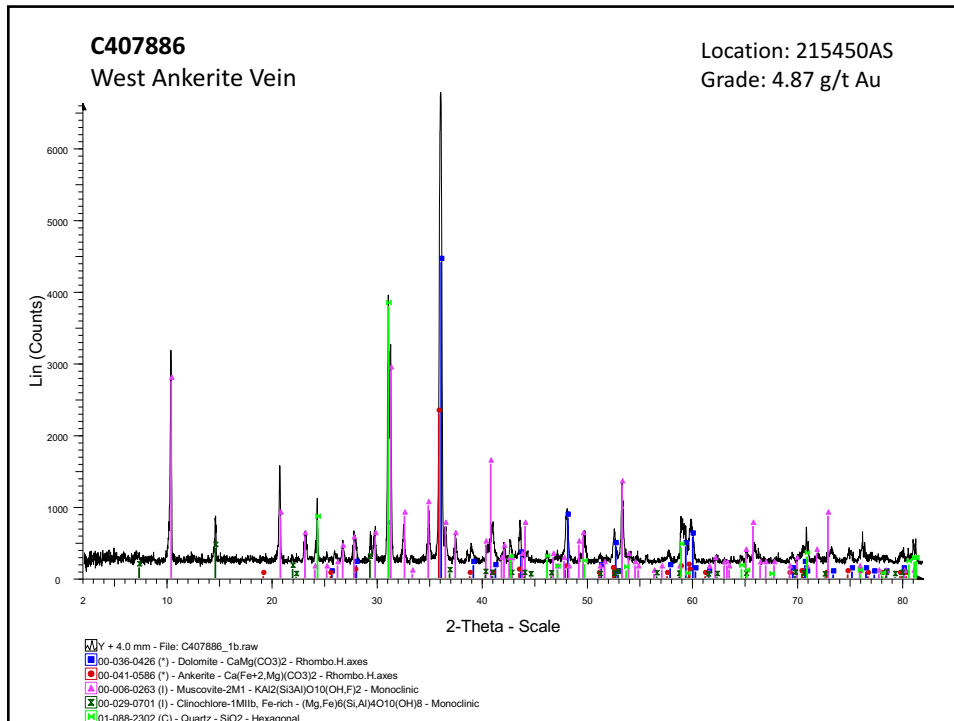
- Cu + 4.0 mm - File: C407884b.raw
■ 00-036-0426 (*) - Dolomite - $\text{CaMg}(\text{CO}_3)_2$ - Rhombo.H.axes
■ 00-041-0586 (*) - Ankerite - $\text{Ca}(\text{Fe}+2\text{Mg})(\text{CO}_3)_2$ - Rhombo.H.axes
■ 00-046-1045 (*) - Quartz, syn - SiO_2 - Hexagonal
■ 00-007-0042 (I) - Muscovite-3T - $(\text{K},\text{Na})(\text{Al},\text{Mg},\text{Fe})_2(\text{Si}_3.1\text{Al}_0.9)\text{O}_{10}(\text{OH})_2$ - Hexagonal
■ 00-042-1340 (*) - Pyrite - FeS_2 - Cubic

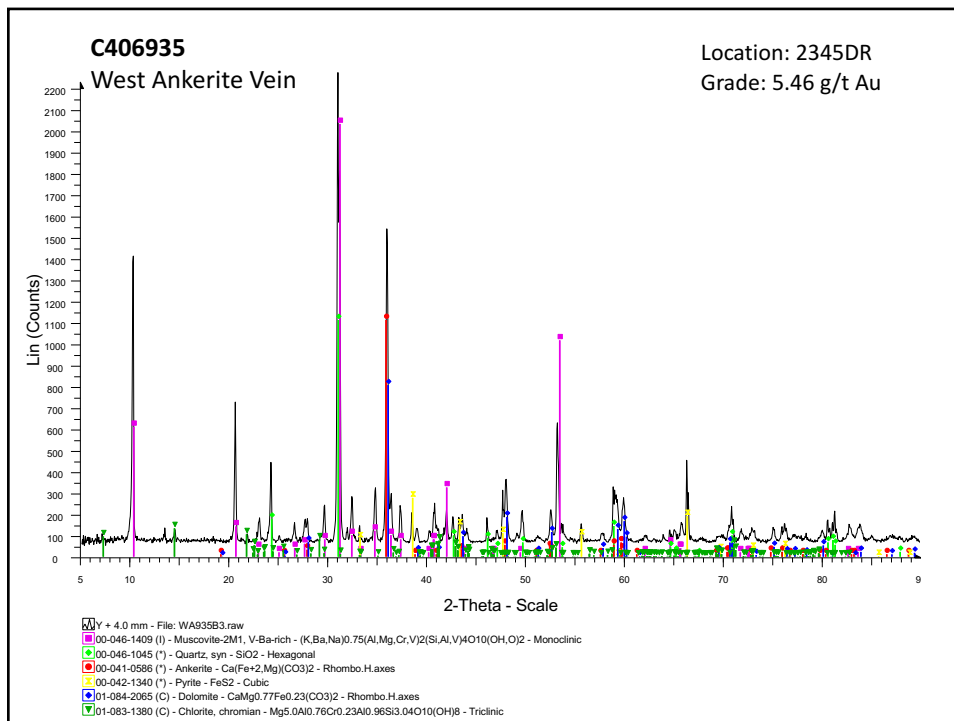
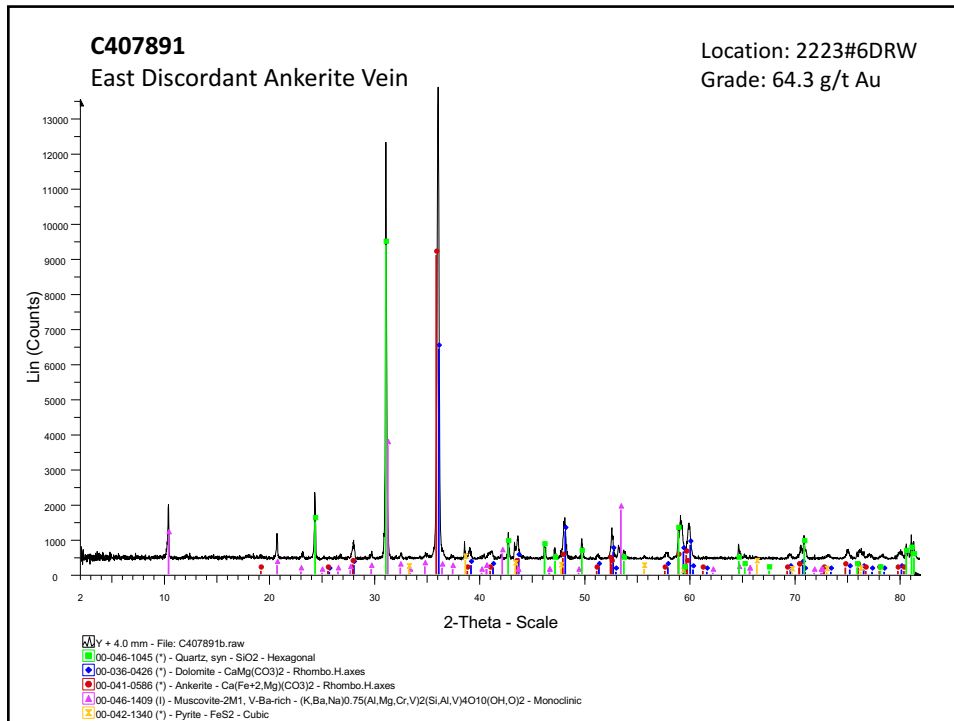
C406940
Center Ankerite Vein

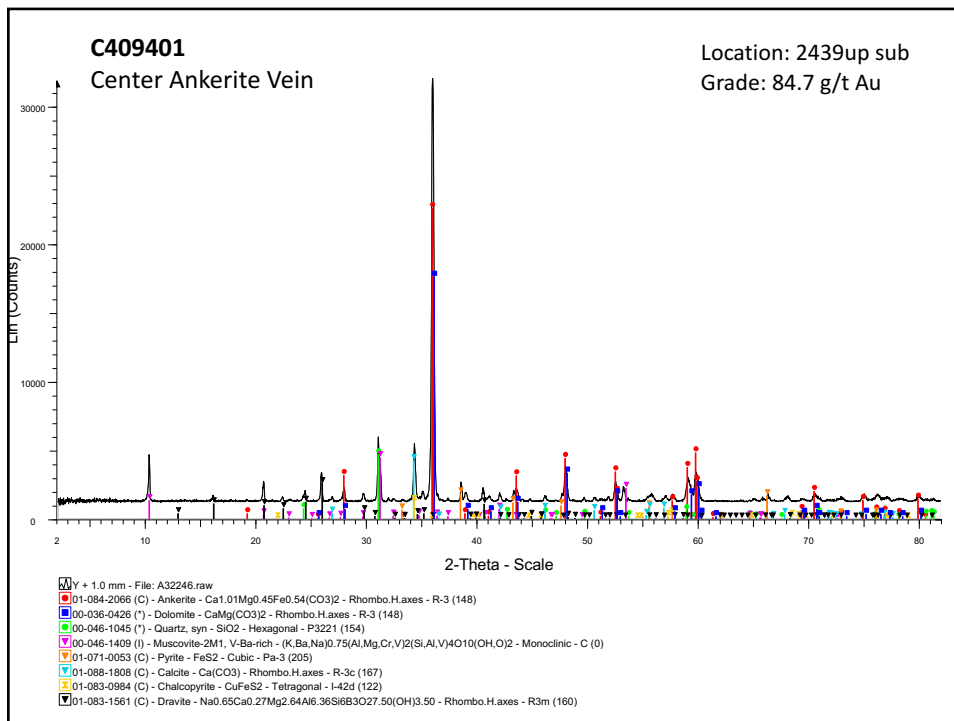
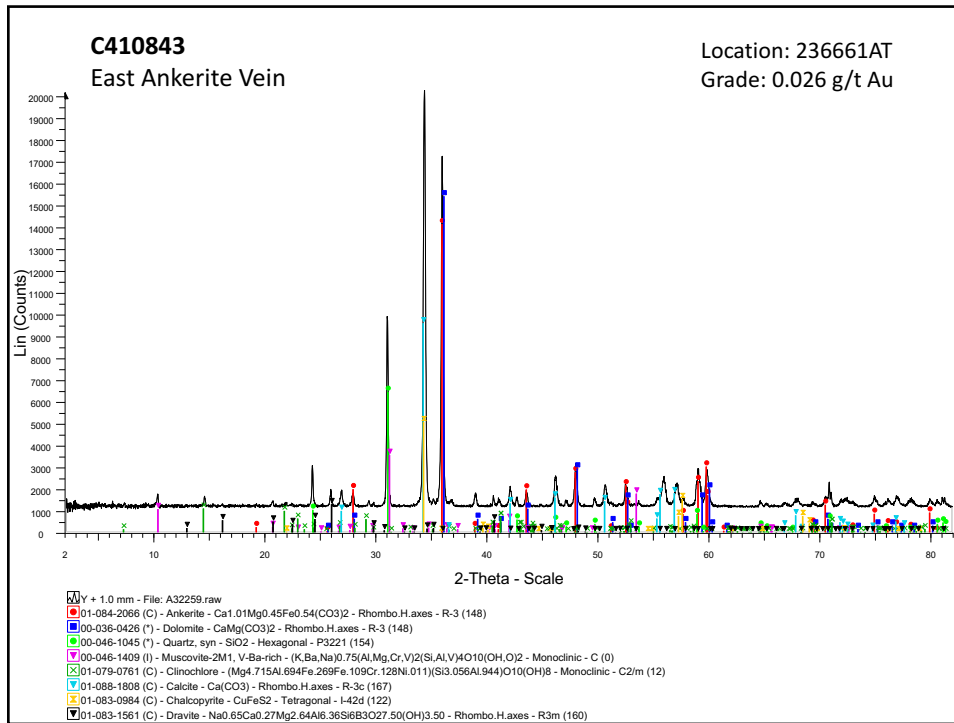
Location: 1939#10 DR
Grade: 54.5 g/t Au

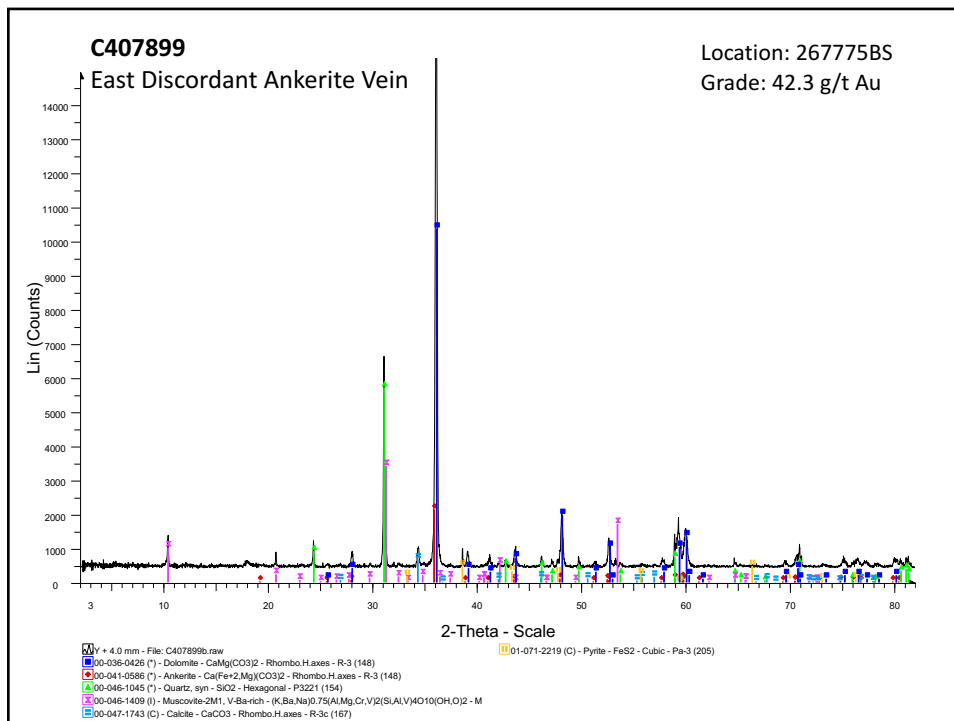
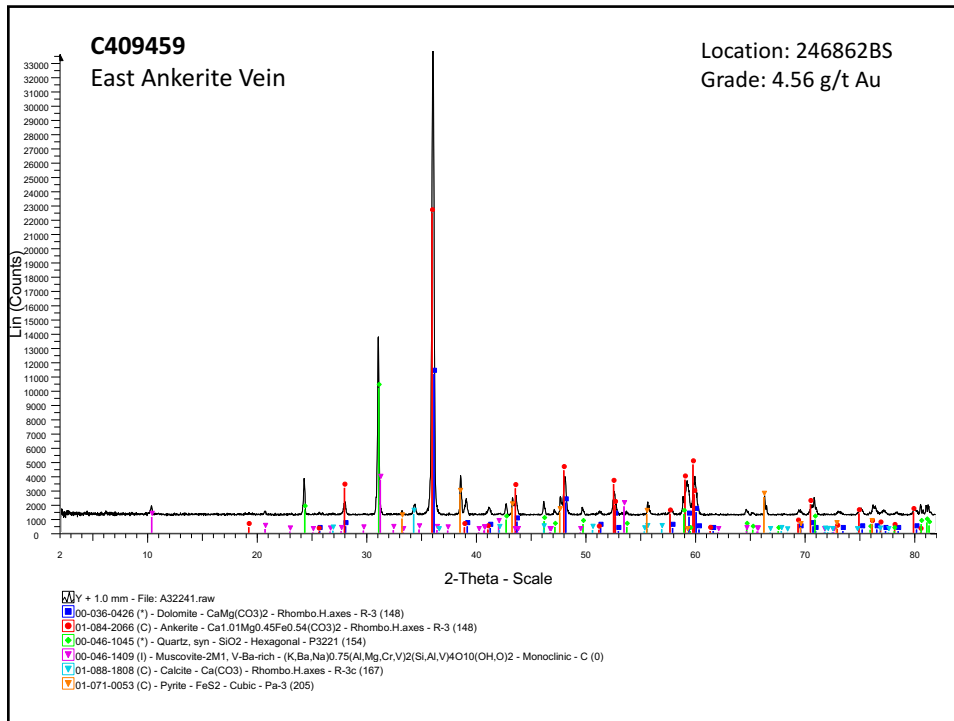


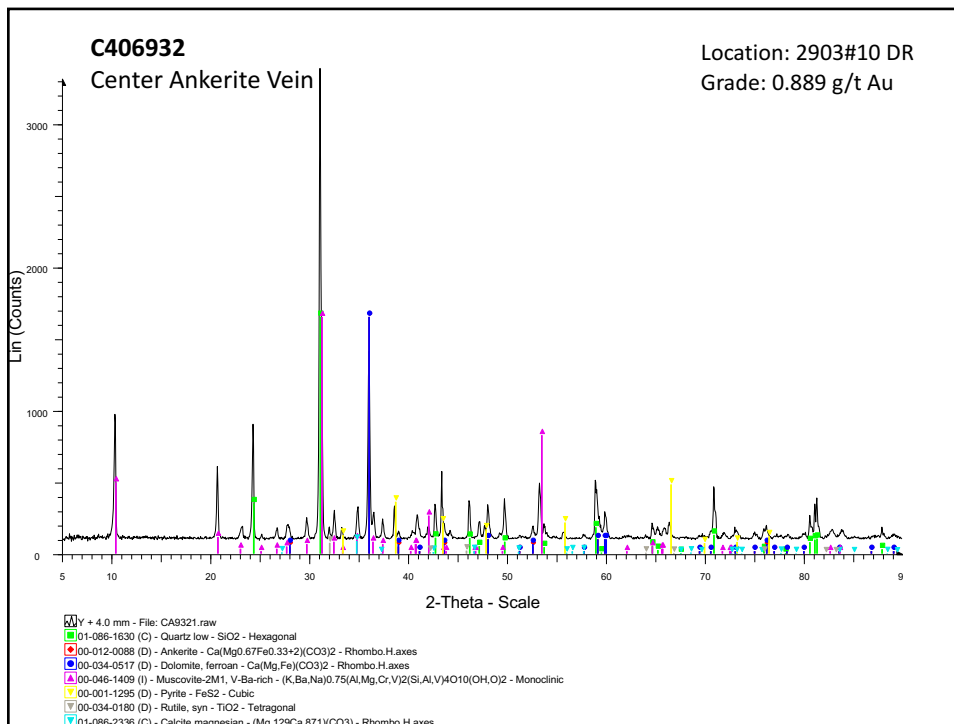
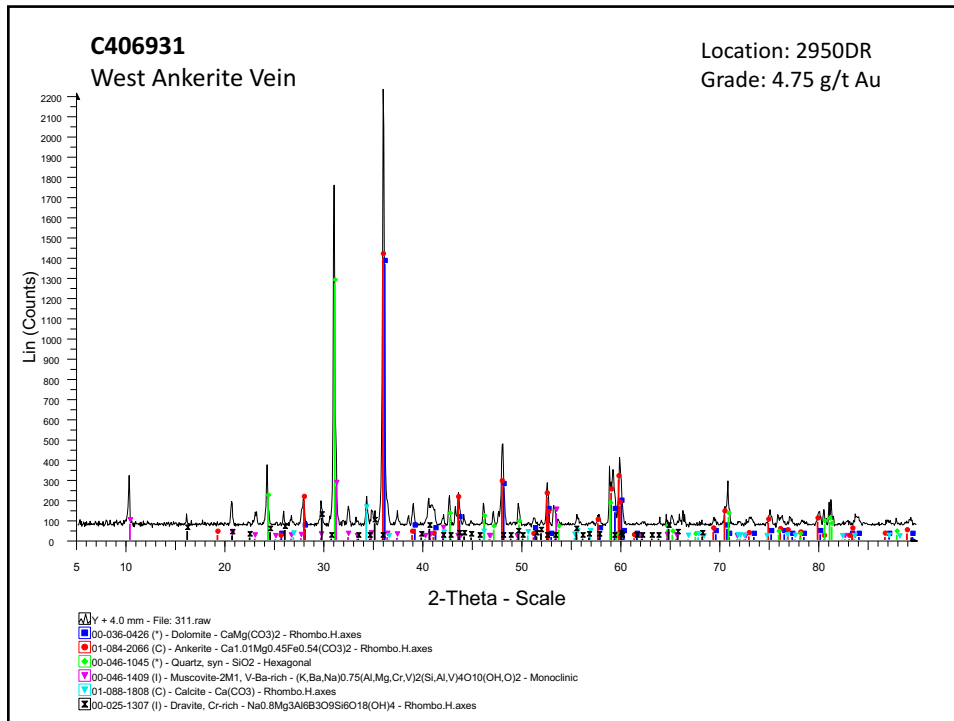
- Cu + 4.0 mm - File: C406940a2.raw
■ 00-041-0586 (*) - Ankerite - $\text{Ca}(\text{Fe}+2\text{Mg})(\text{CO}_3)_2$ - Rhombo.H.axes
■ 01-085-0798 (C) - Quartz - SiO_2 - Hexagonal
■ 00-034-0517 (D) - Dolomite, ferroan - $\text{Ca}(\text{Mg},\text{Fe})(\text{CO}_3)_2$ - Rhombo.H.axes
■ 01-075-0948 (C) - Muscovite 2M1 - $\text{KAl}_3\text{Si}_3\text{O}_{10}(\text{OH})_2$ - Monoclinic
■ 01-071-0053 (C) - Pyrite - FeS_2 - Cubic
■ 01-086-1572 (C) - Tourmaline - $(\text{Na},\text{Ca},\text{Mg})(\text{Mg},\text{V},\text{Cr},\text{Fe})_3(\text{Al},\text{V},\text{Ti})_6(\text{Si},\text{Al})_6\text{B}_3\text{O}_{28}(\text{OH})$
■ 01-083-1381 (C) - Chlorite, chromian - $\text{Mg}_5.0\text{Al}_0.75\text{Cr}_0.25\text{Al}_1.00\text{Si}_3.00\text{O}_{10}(\text{OH})_8$ - Tri
■ 01-089-1305 (C) - Magnesium calcite - synthetic - $(\text{Mg}_0.06\text{Ca}_0.94)(\text{CO}_3)$ - Rhombo.H.

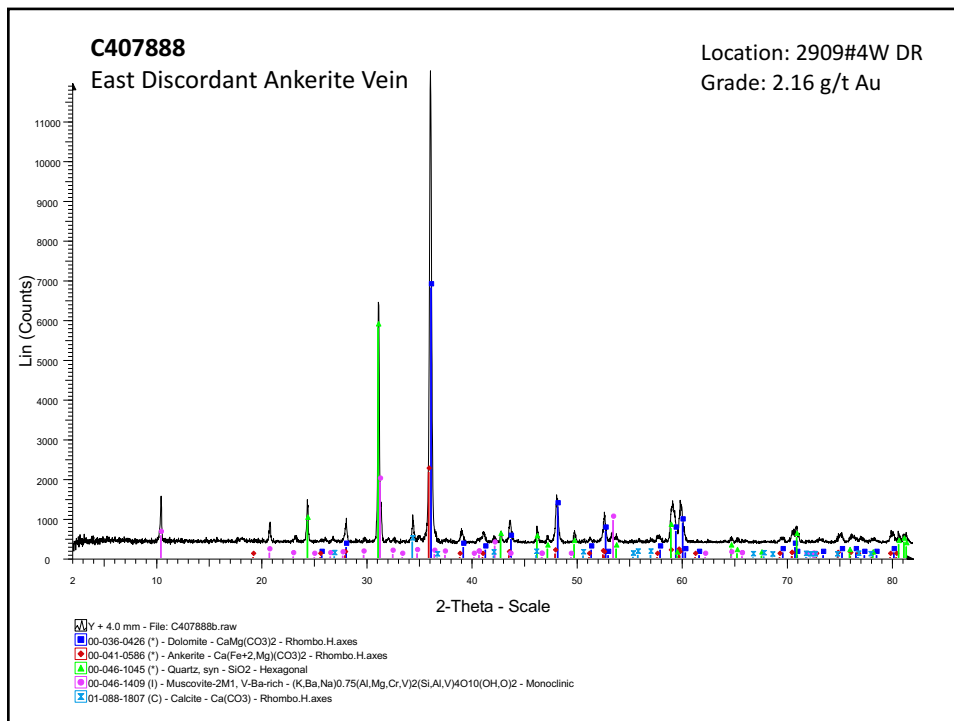
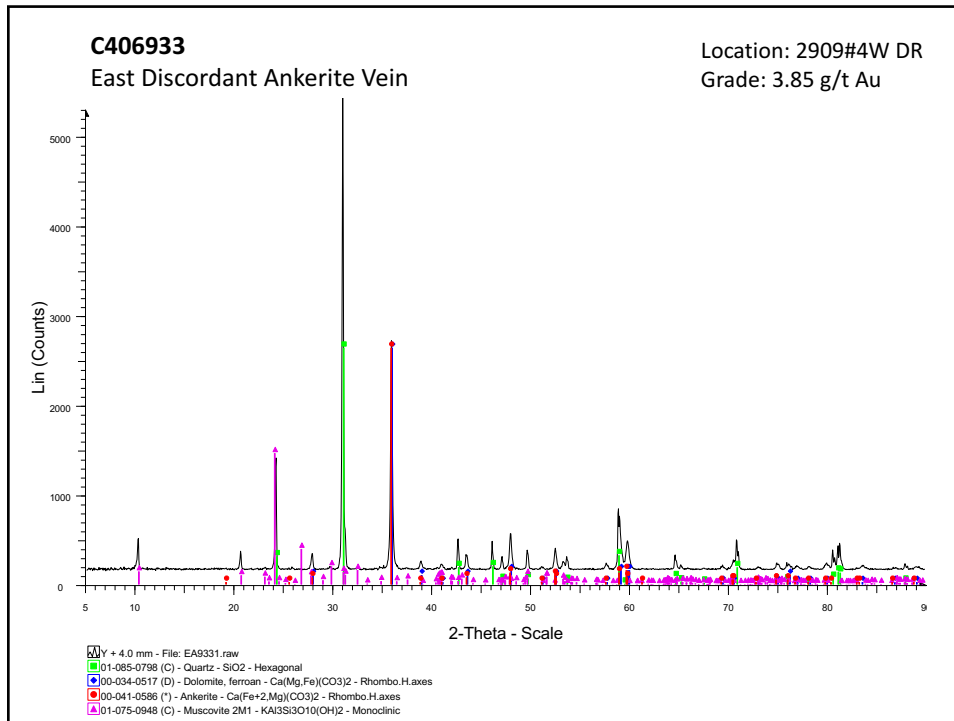


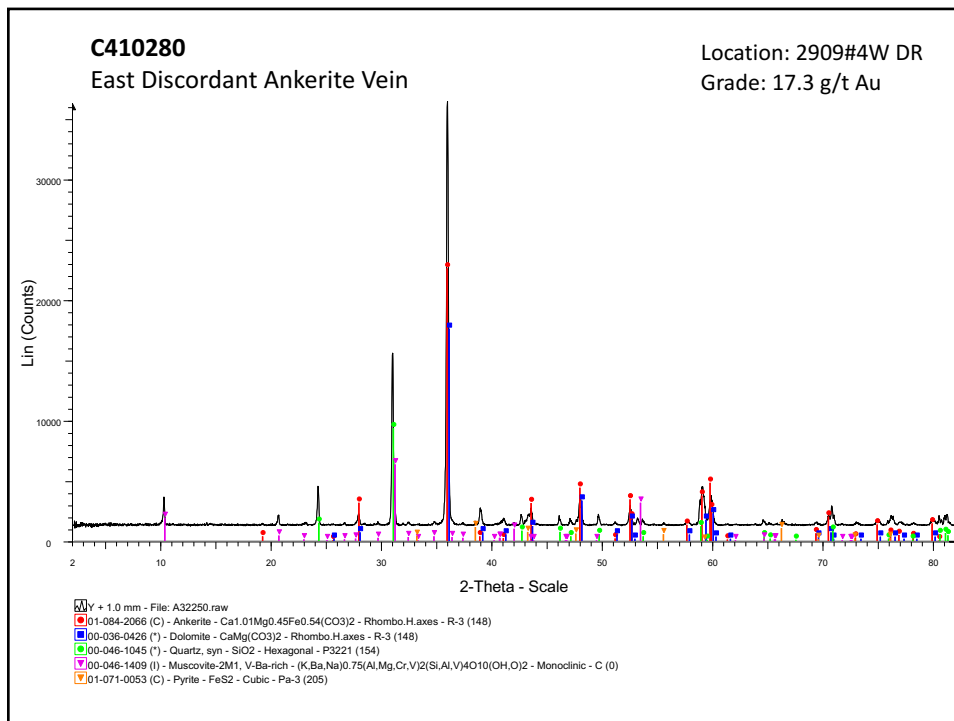
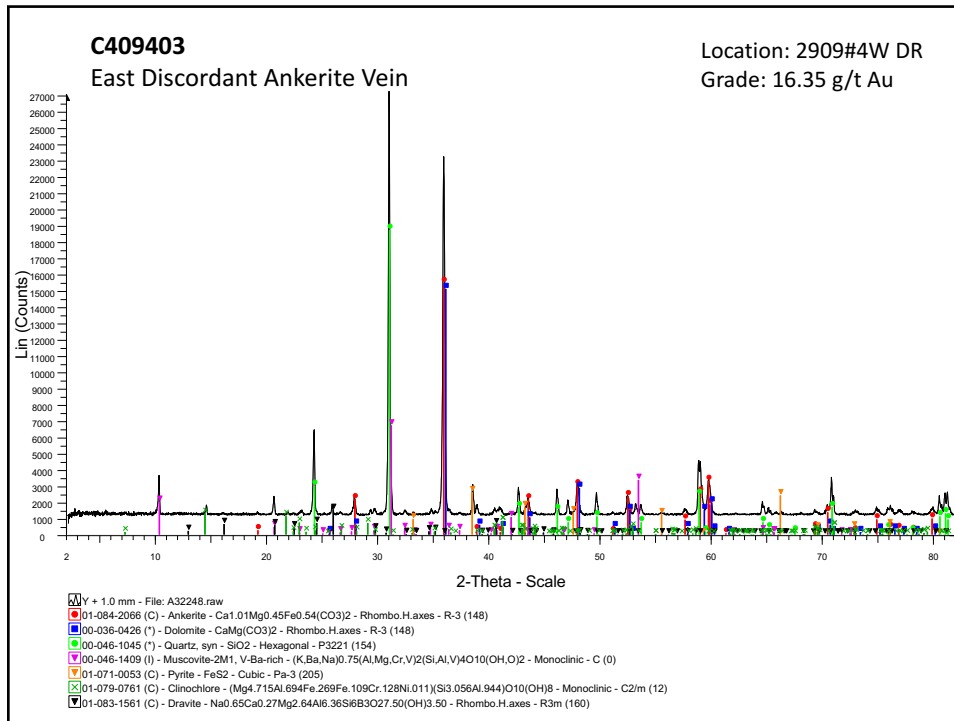


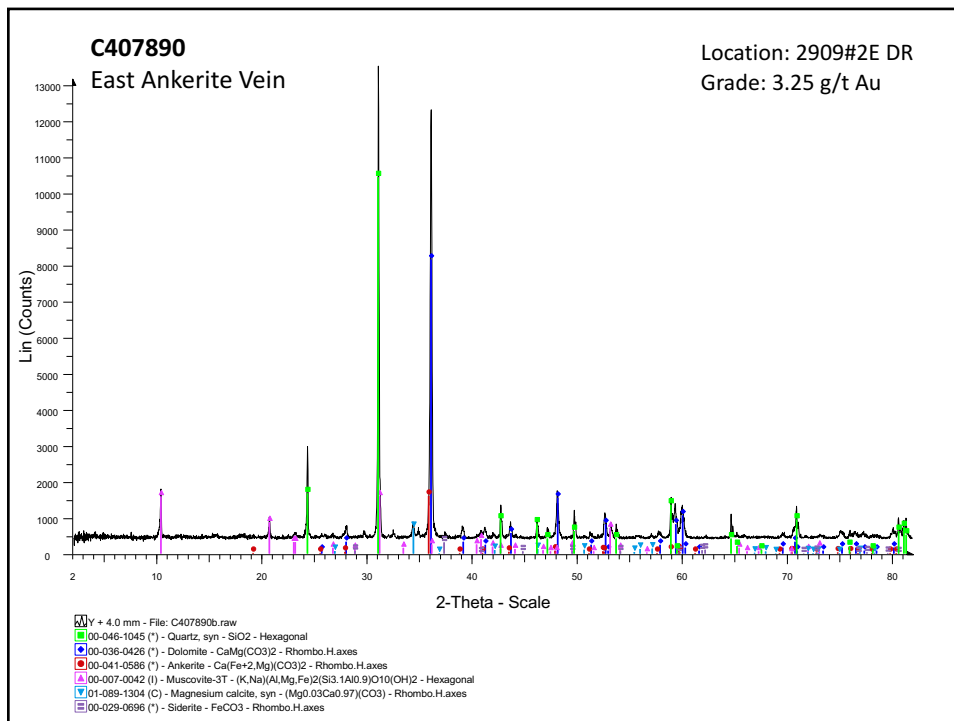
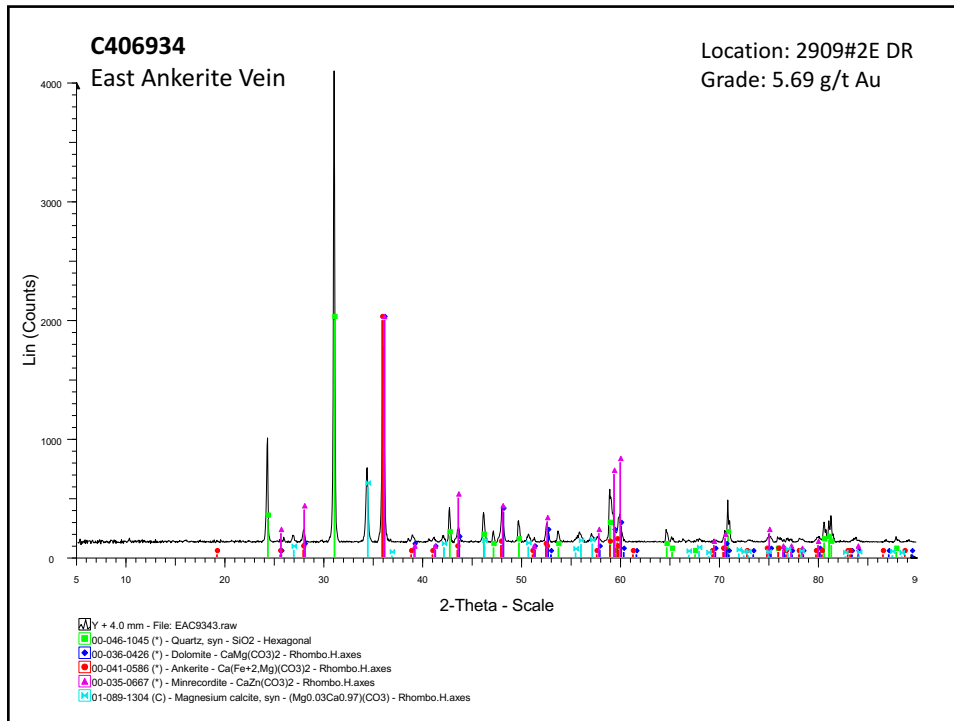






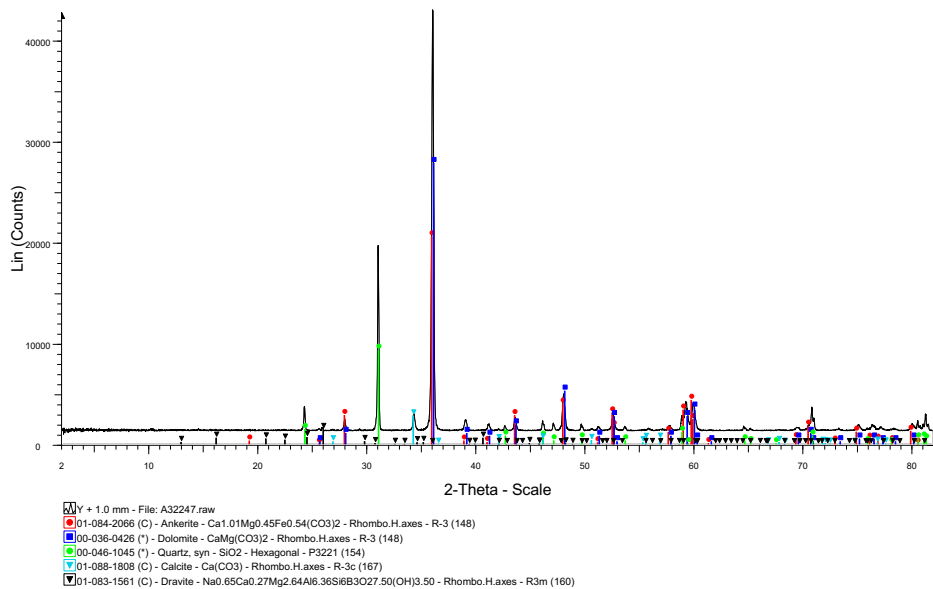






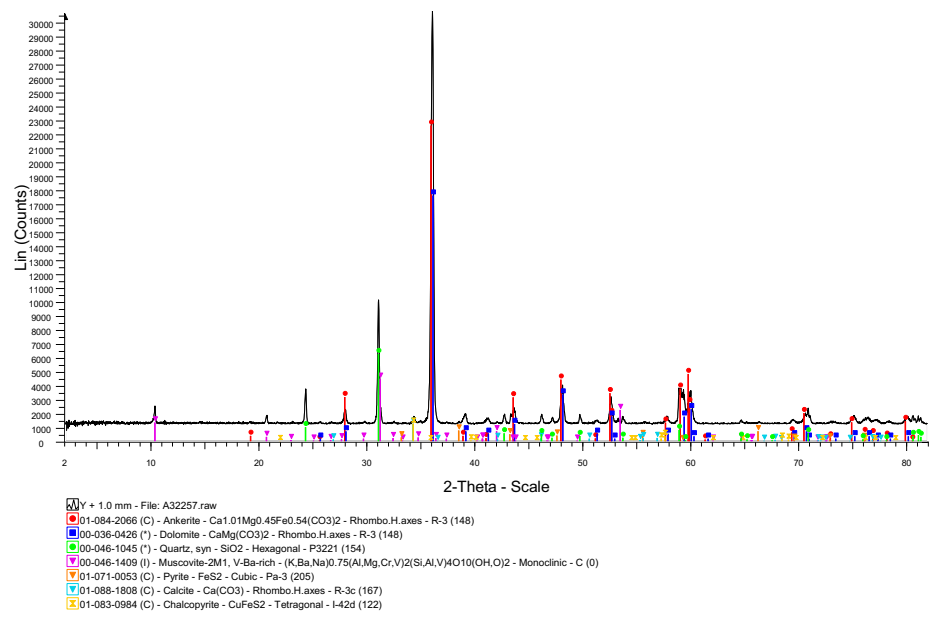
C409402
East Ankerite Vein

Location: 3409 Ramp
Grade: 0.97 g/t Au



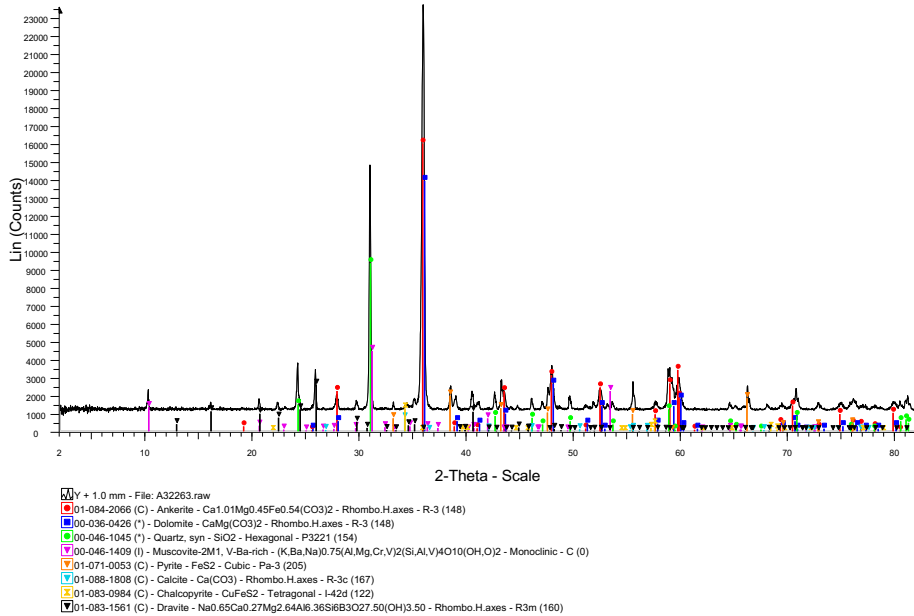
C410295
East Ankerite Vein

Location: 3409E AS
Grade: 3.87 g/t Au



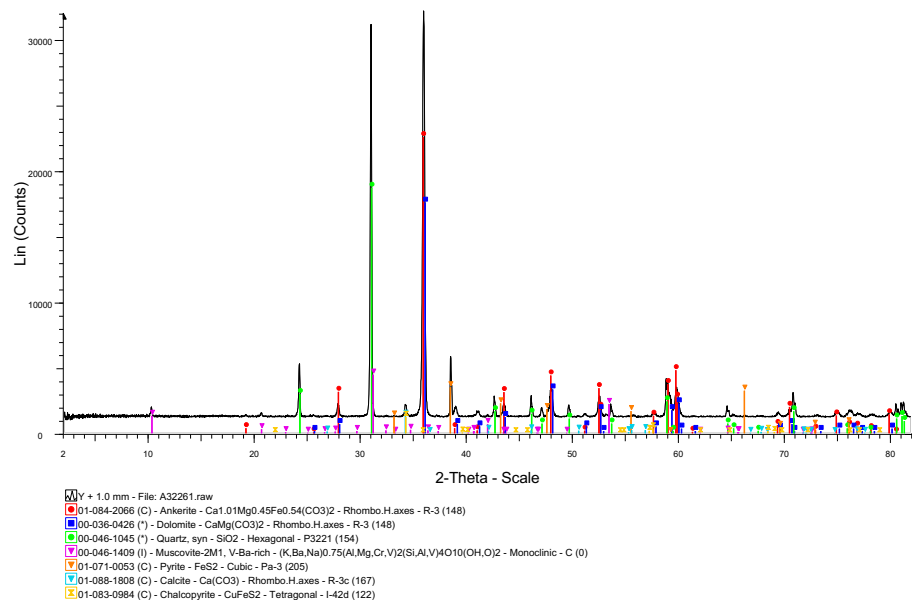
C411098
East Ankerite Vein

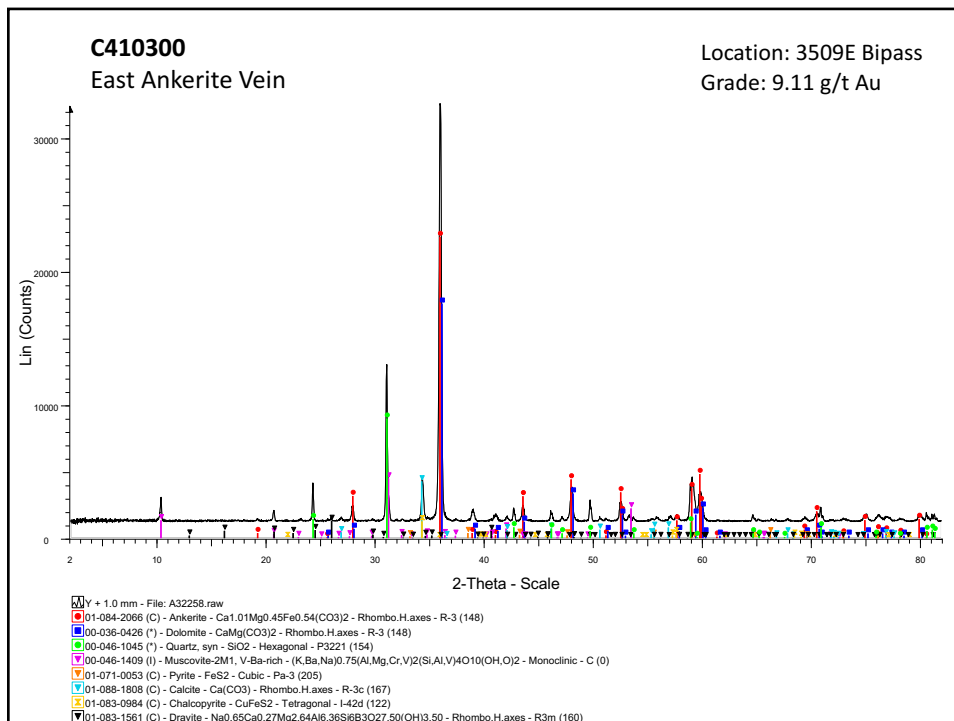
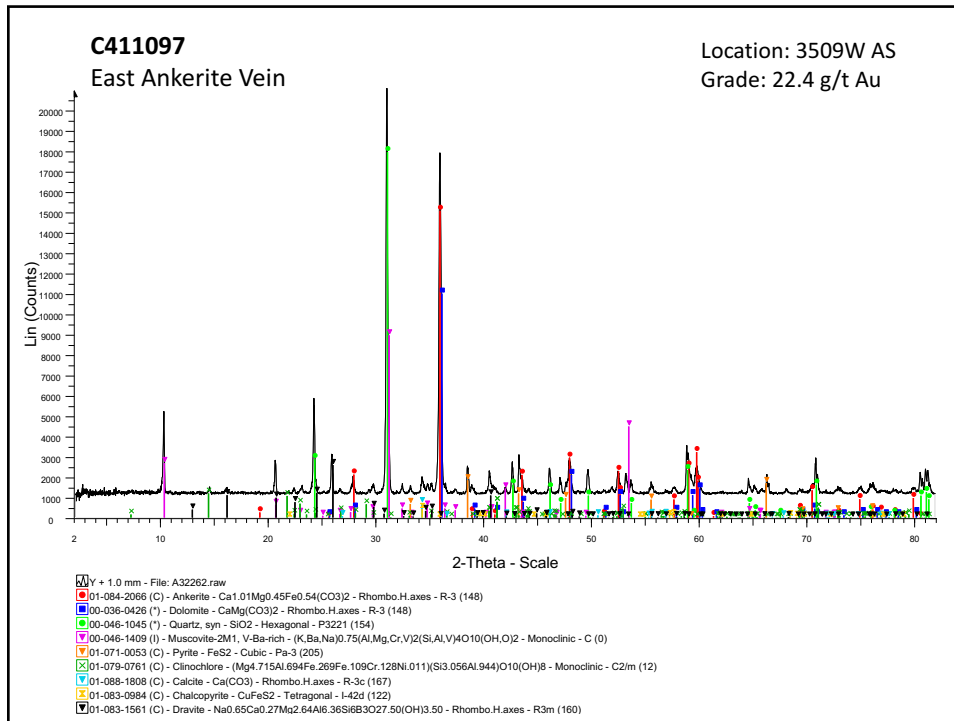
Location: 3509E AS
Grade: 7.55 g/t Au

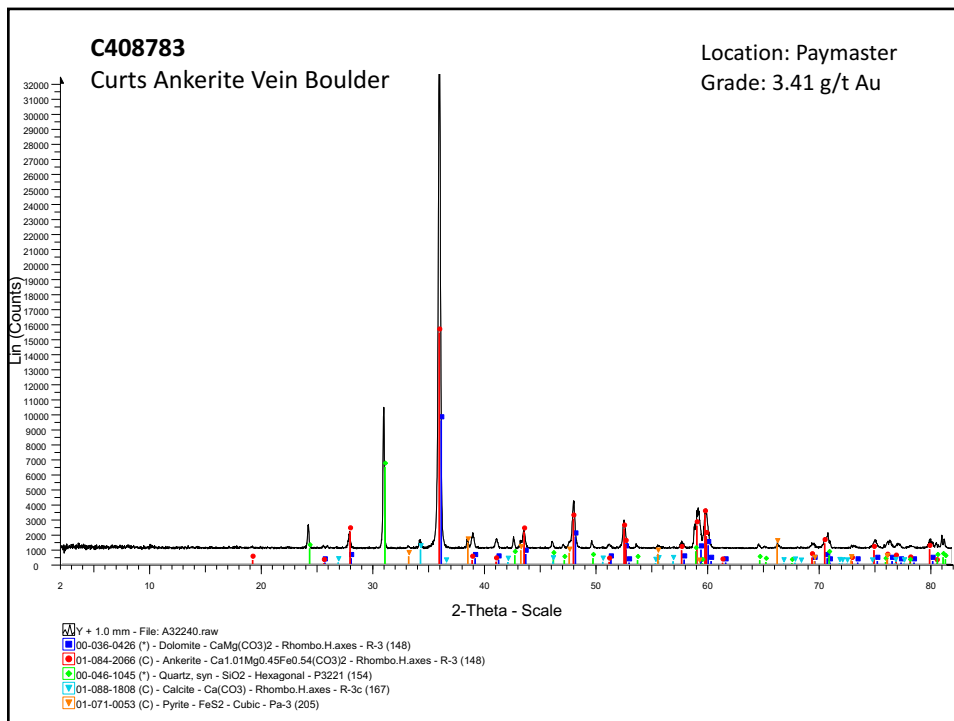
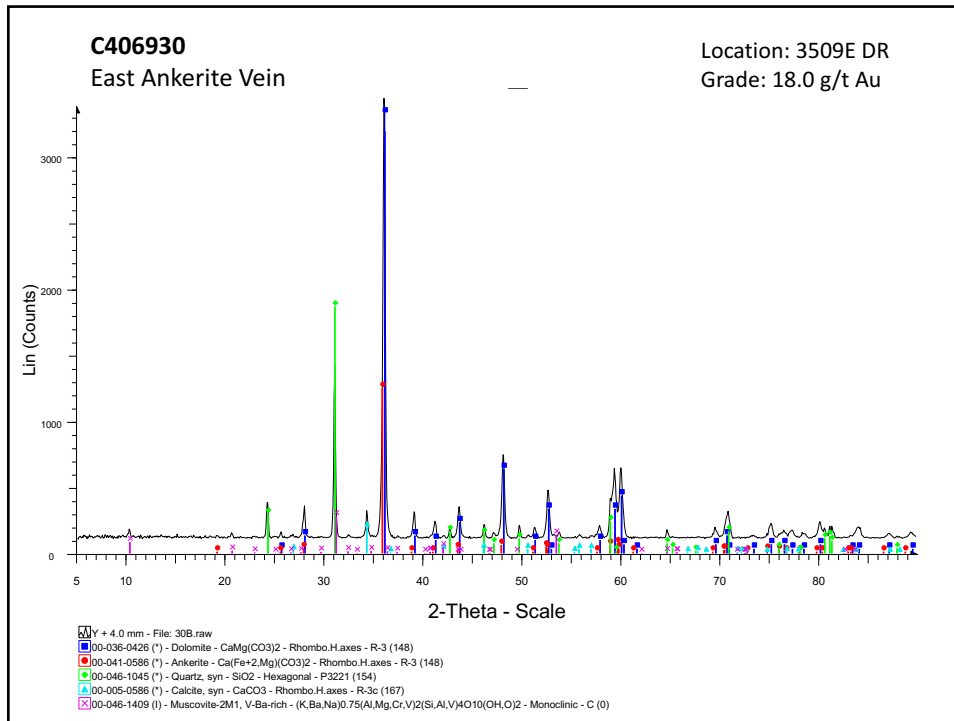


C411096
East Ankerite Vein

Location: 3509W AS
Grade: 2.60 g/t Au

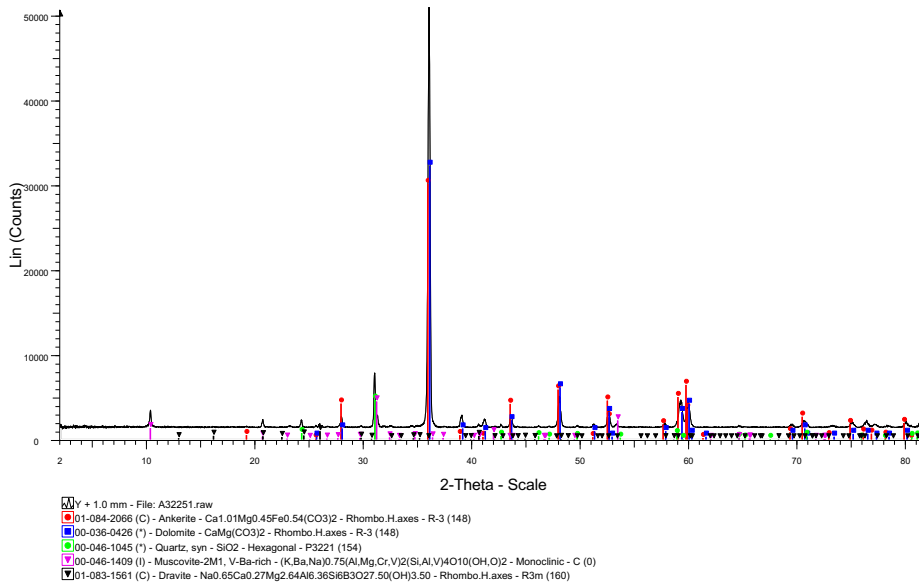






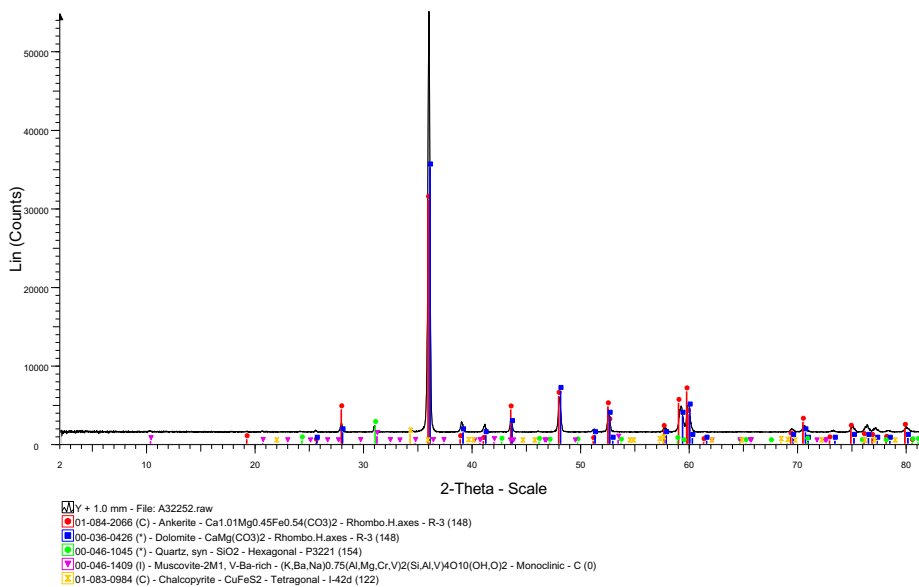
C410289
Curts Ankerite Vein

Location: Paymaster
Grade: 0.207 g/t Au



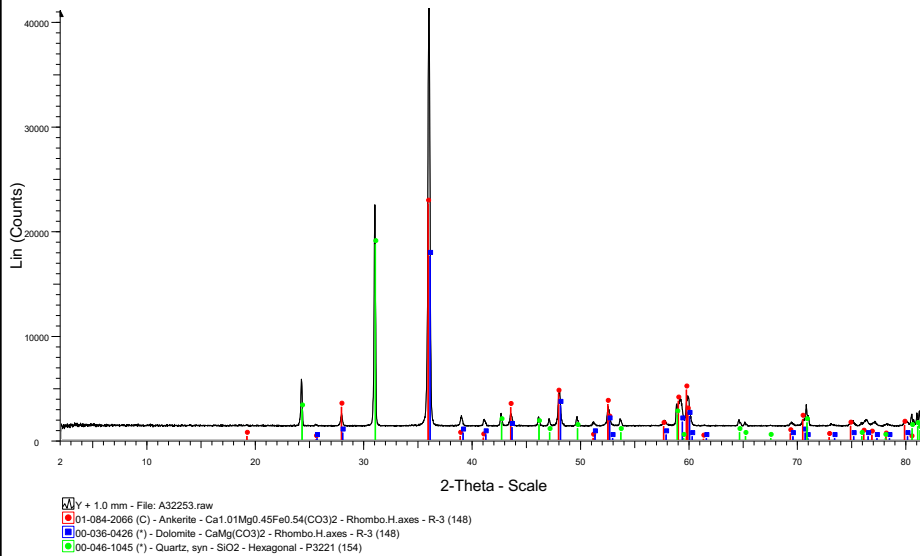
C410290
Curts Ankerite Vein

Location: Paymaster
Grade: 0.259 g/t Au



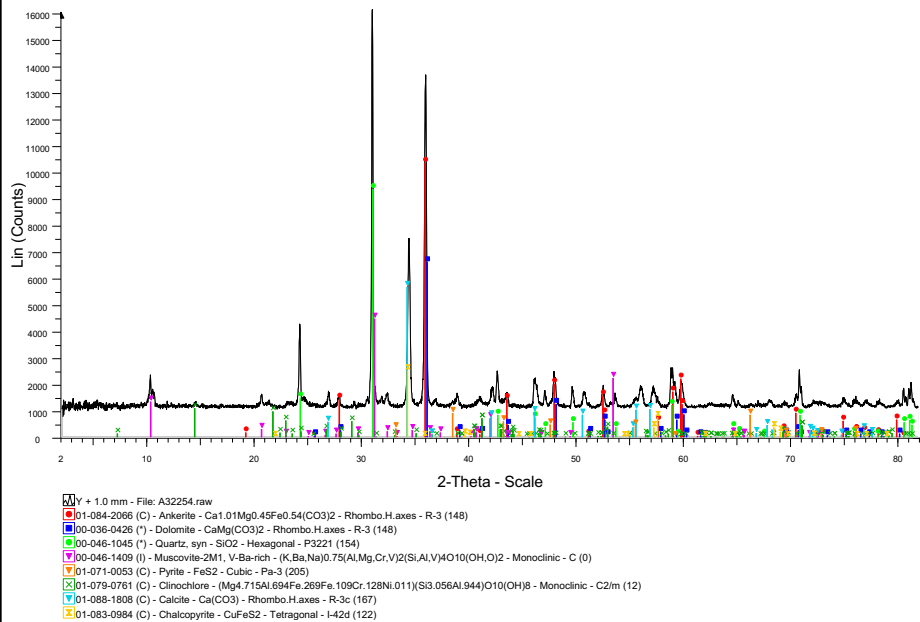
C410291
 Curts Ankerite Vein

Location: Paymaster
 Grade: 2.23 g/t Au



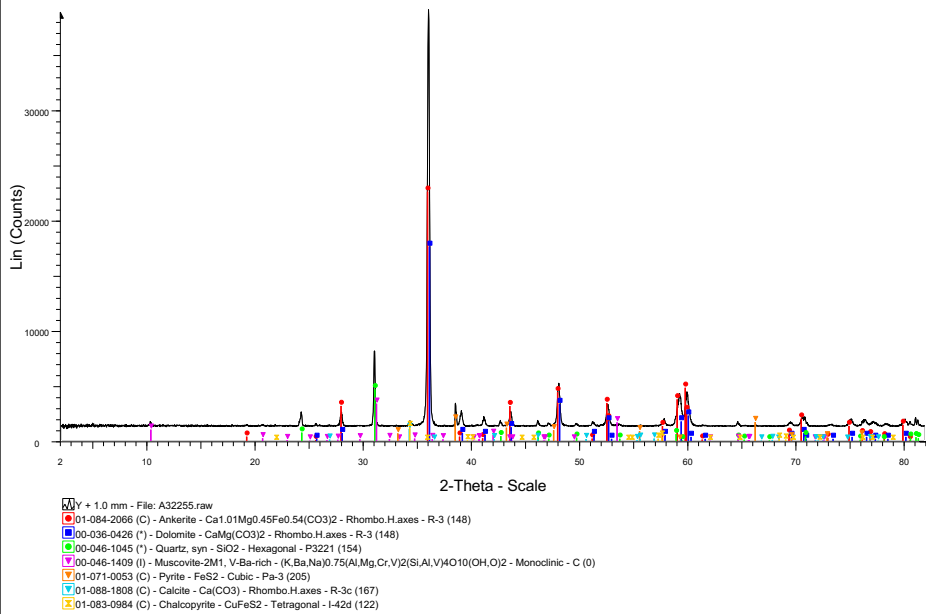
C410292
 Curts Ankerite Vein

Location: Paymaster
 Grade: 2.06 g/t Au



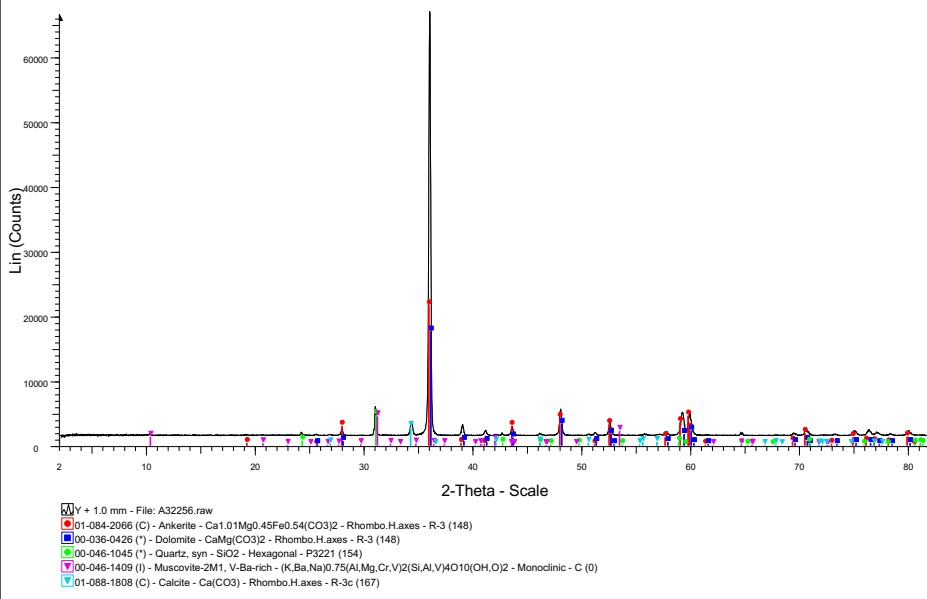
C410293
Curts Ankerite Vein

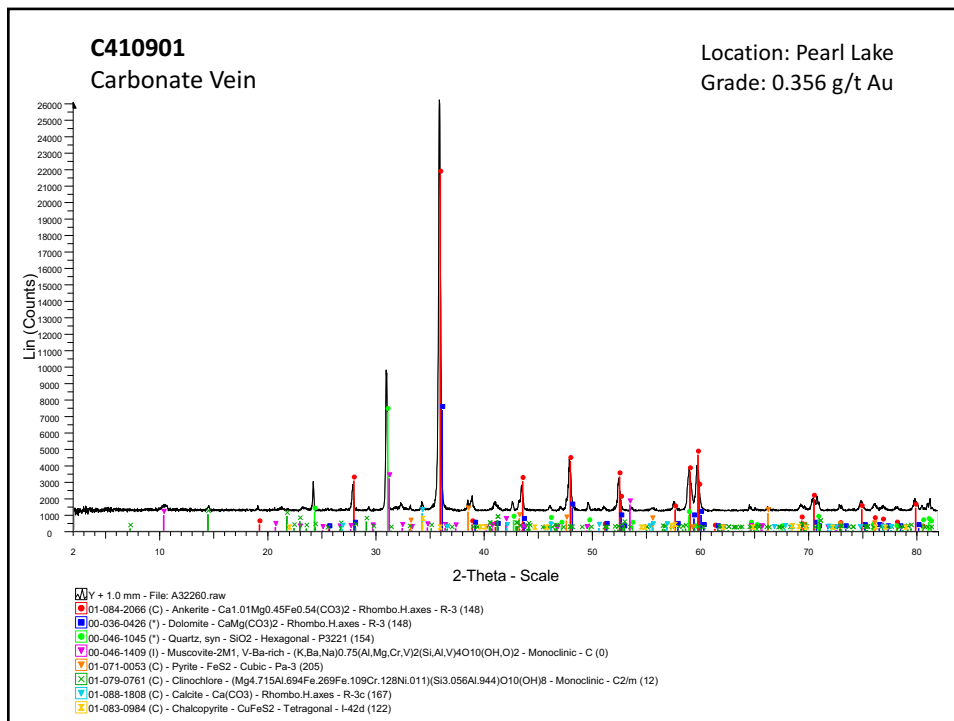
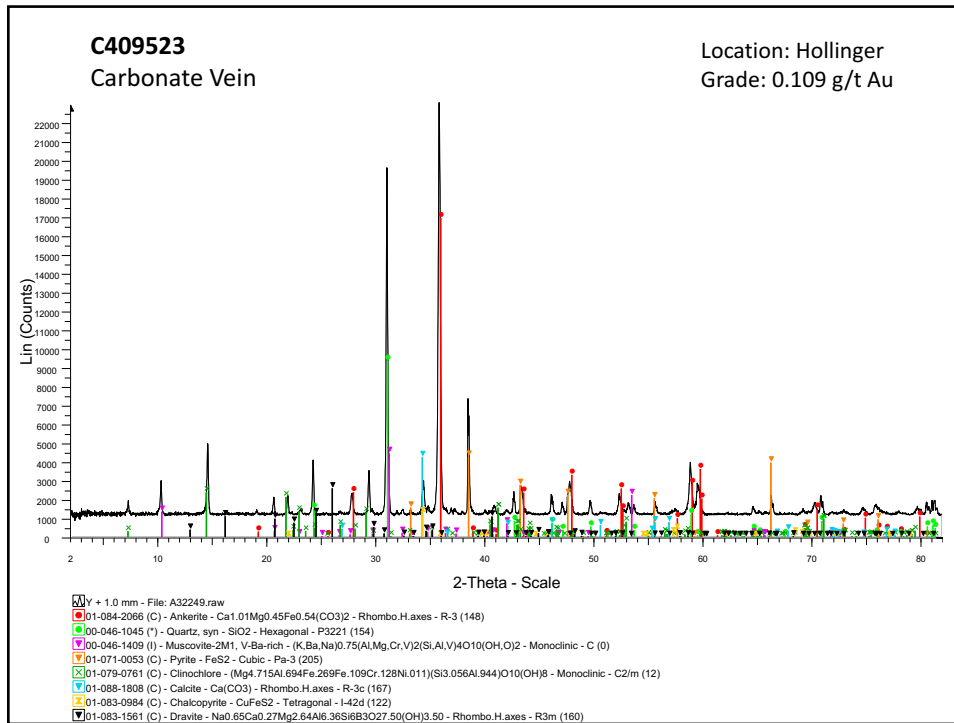
Location: Paymaster
Grade: 0.129 g/t Au

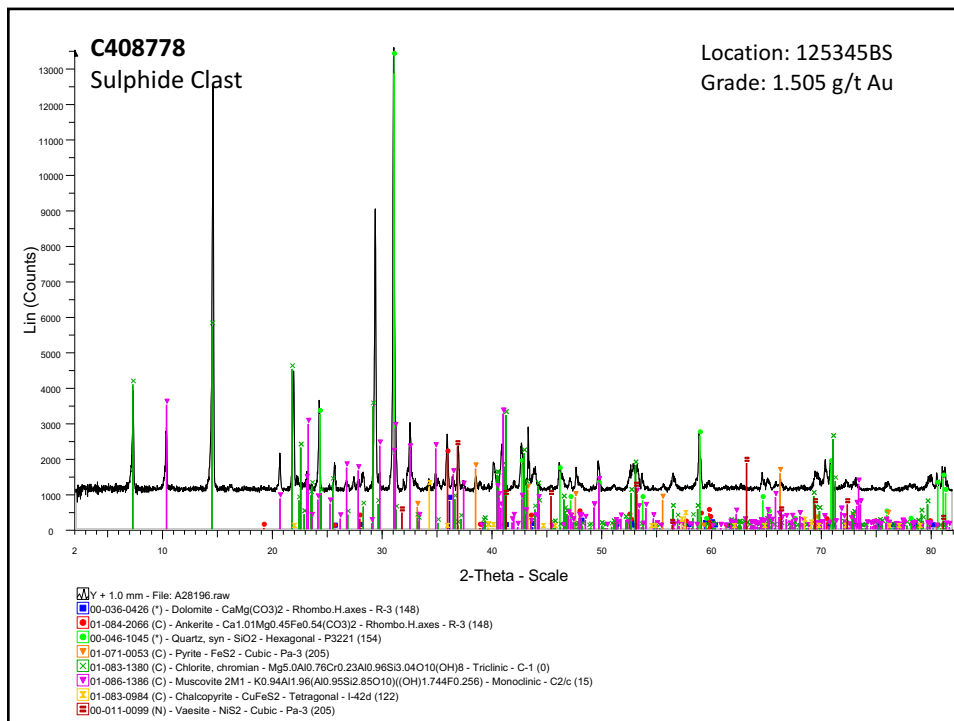
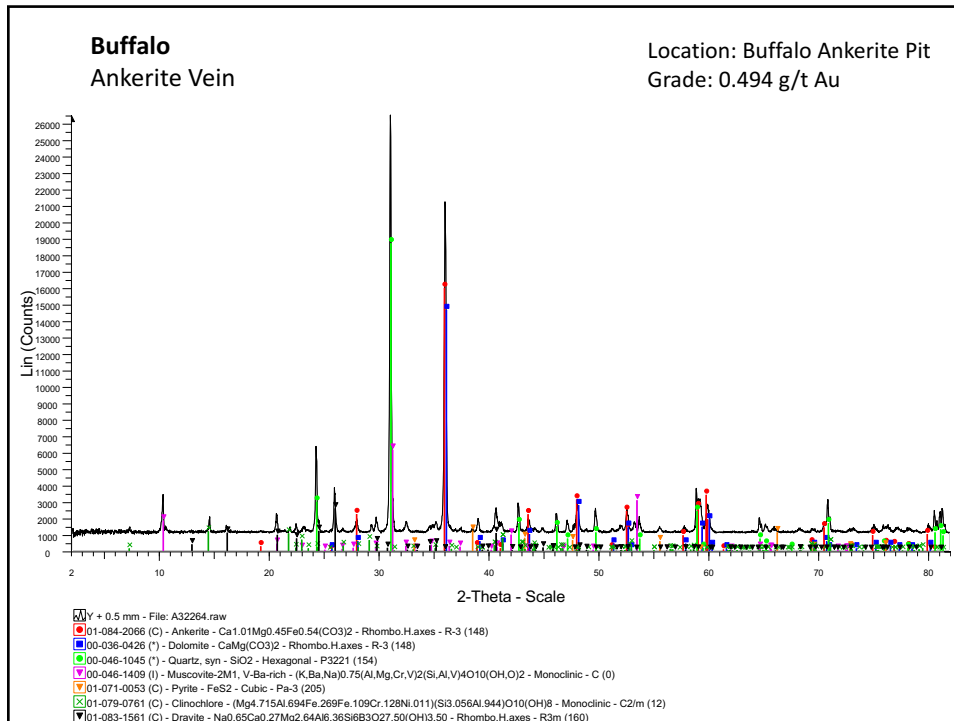


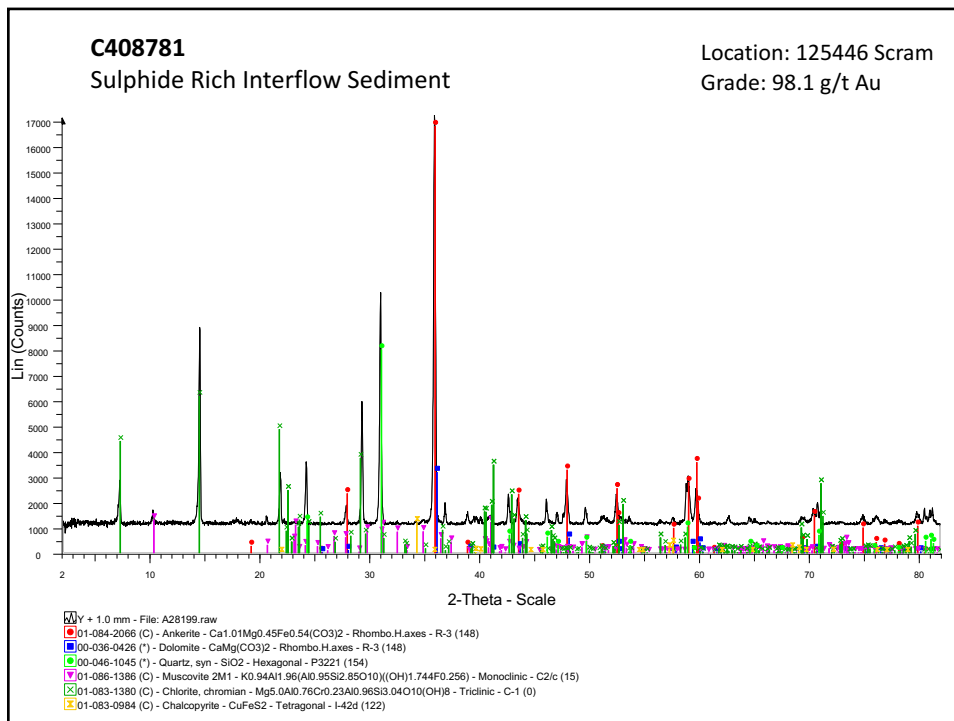
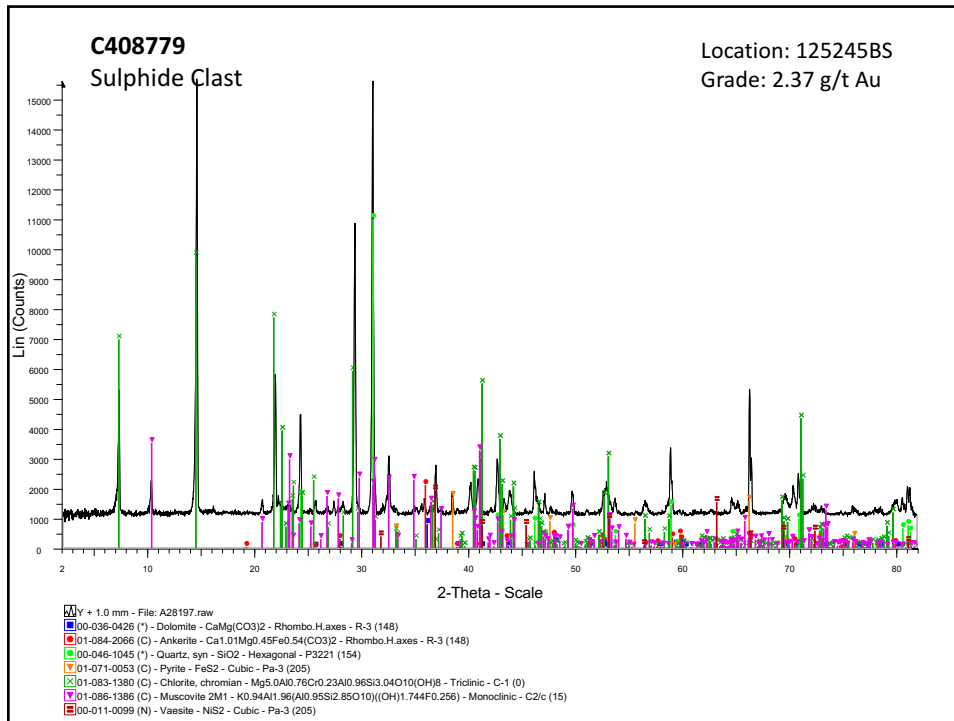
C410294
Curts Ankerite Vein

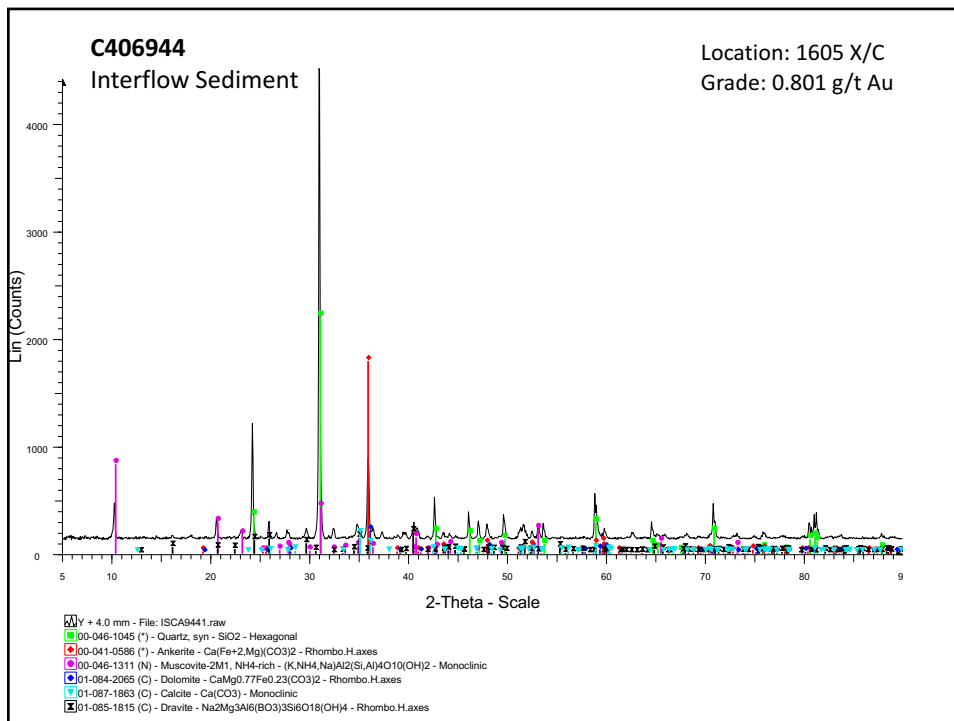
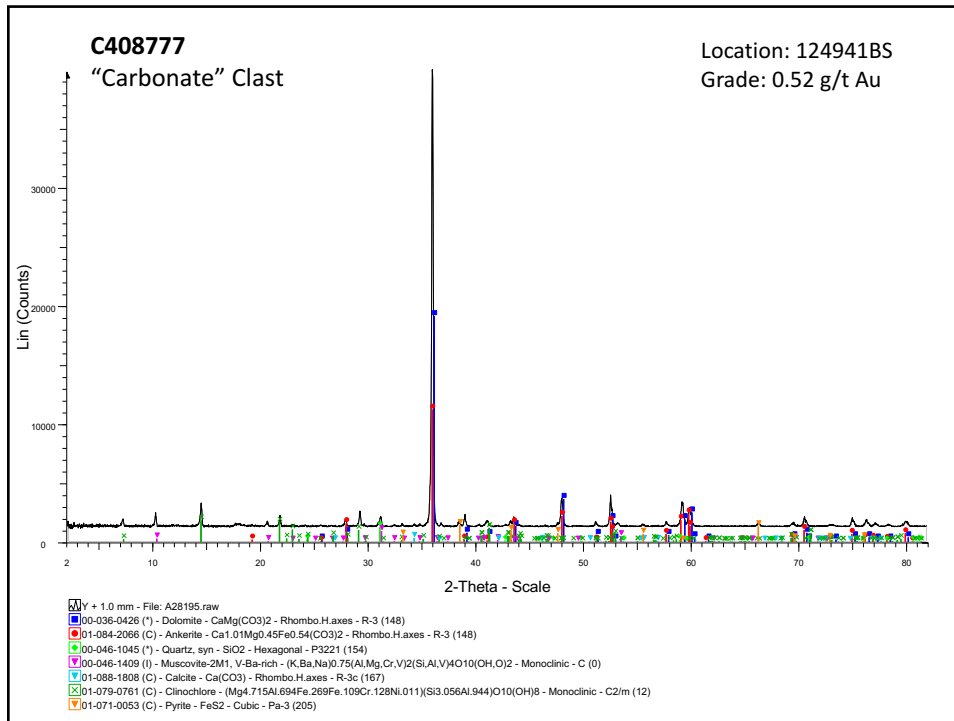
Location: Paymaster
Grade: 0.04 g/t Au

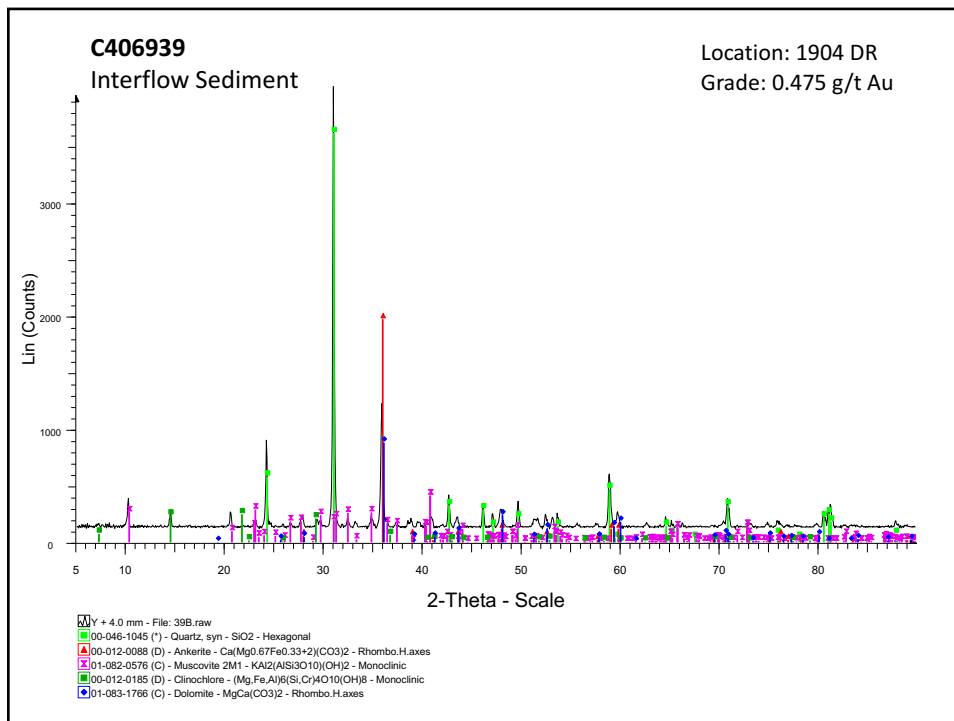
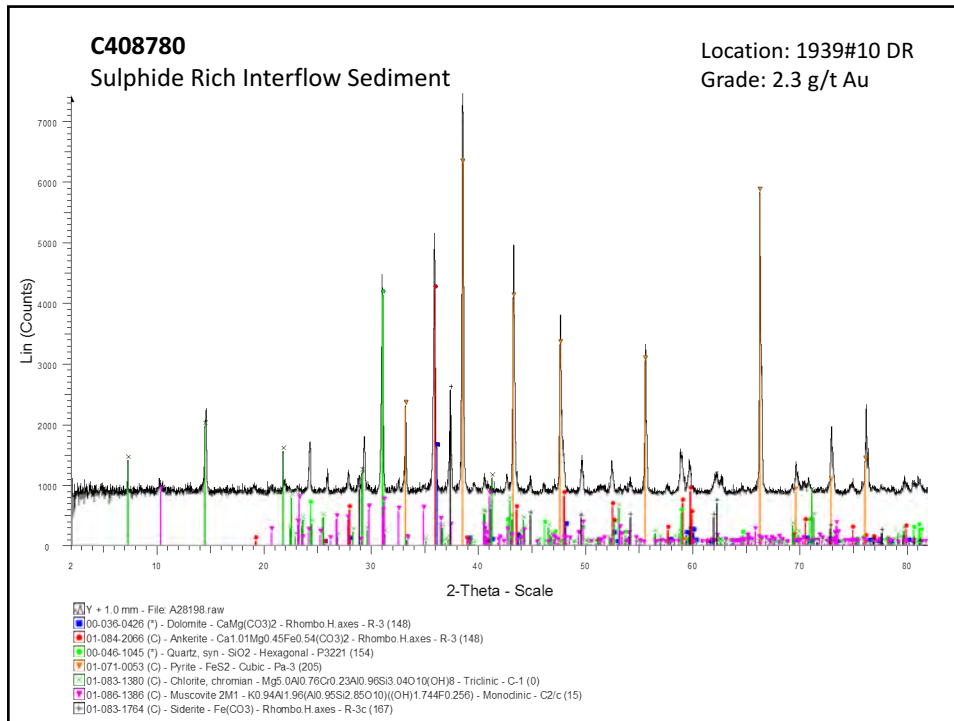


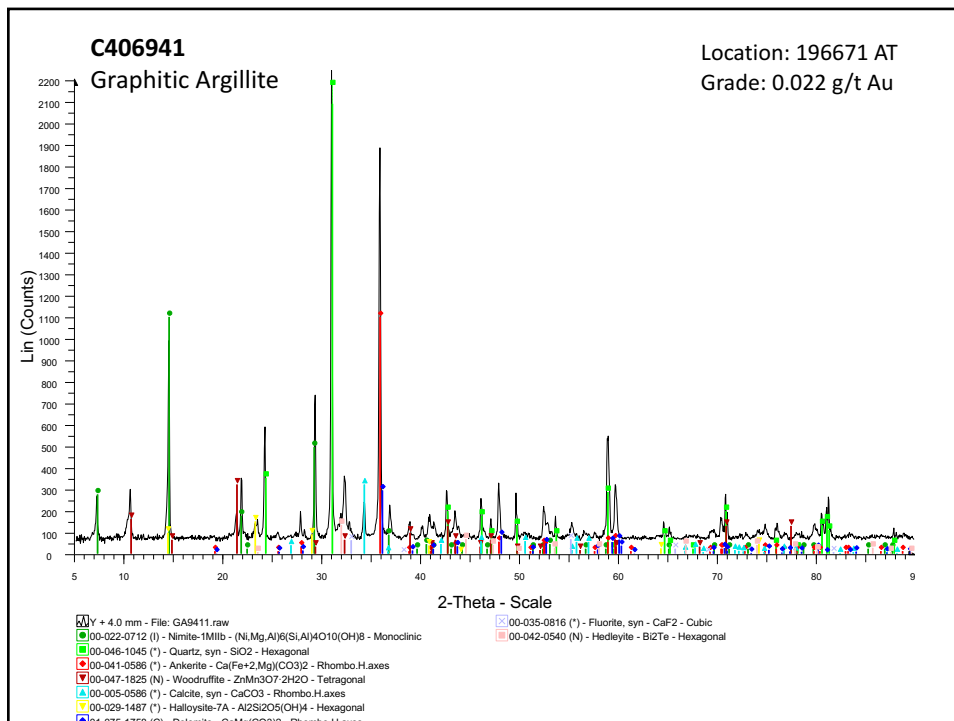
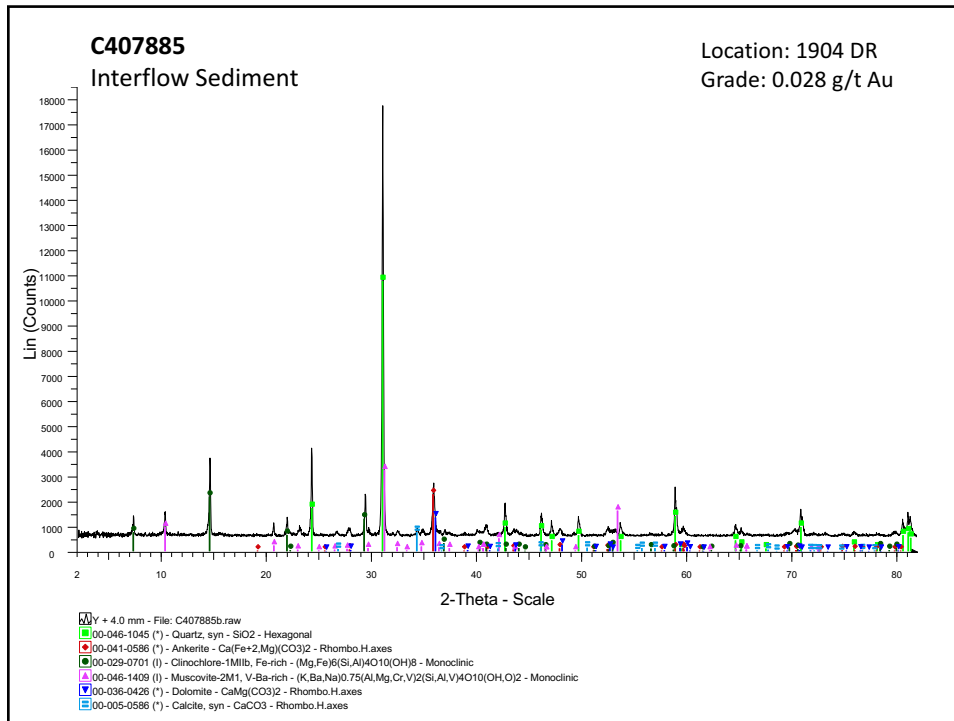


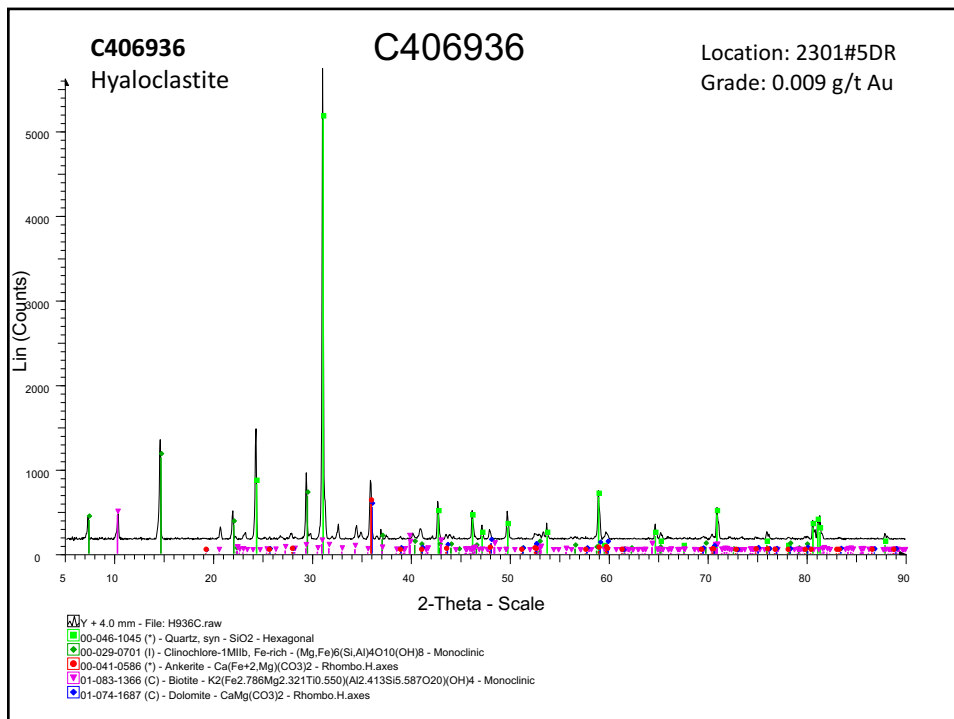
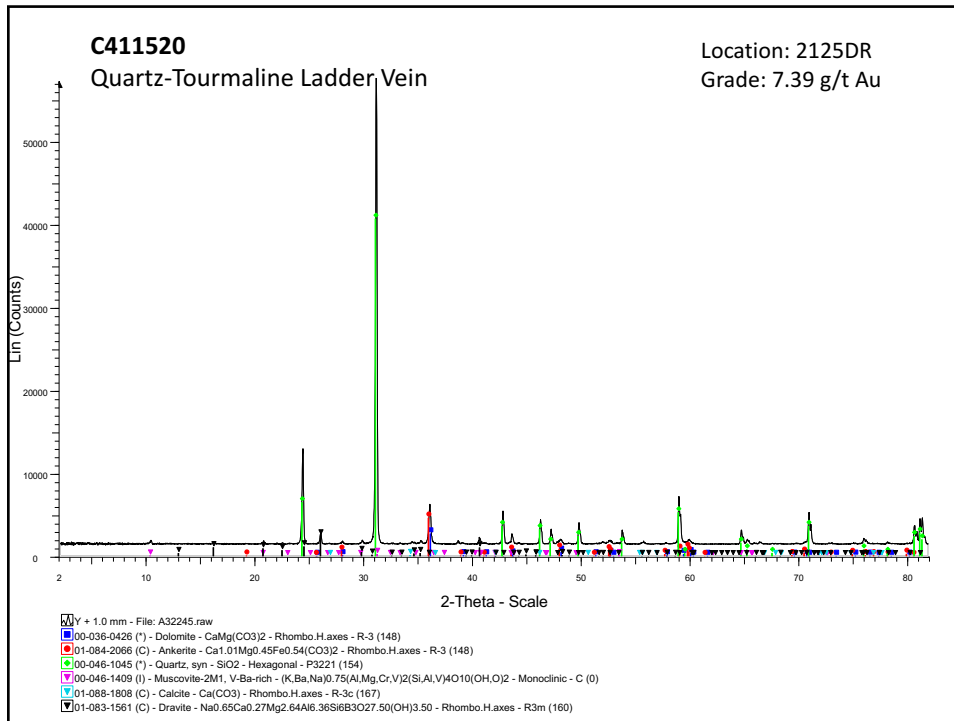






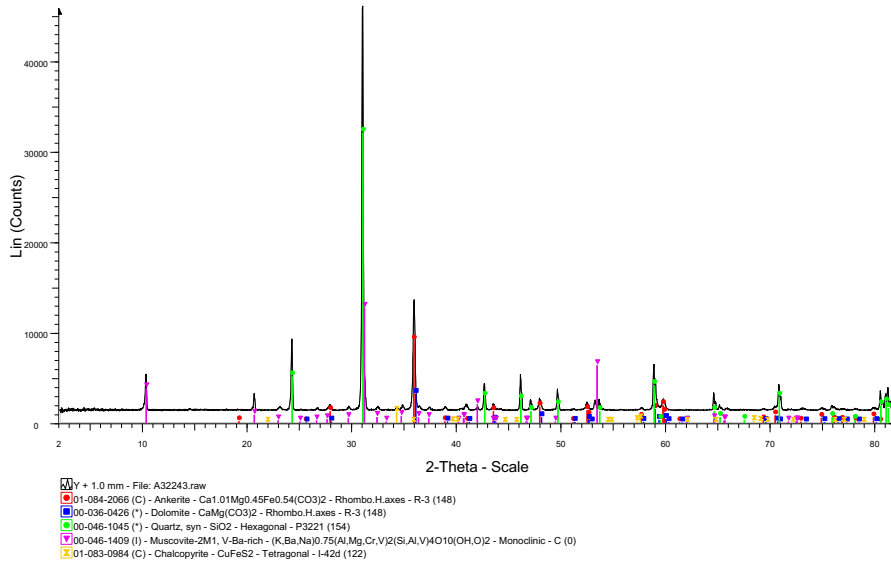






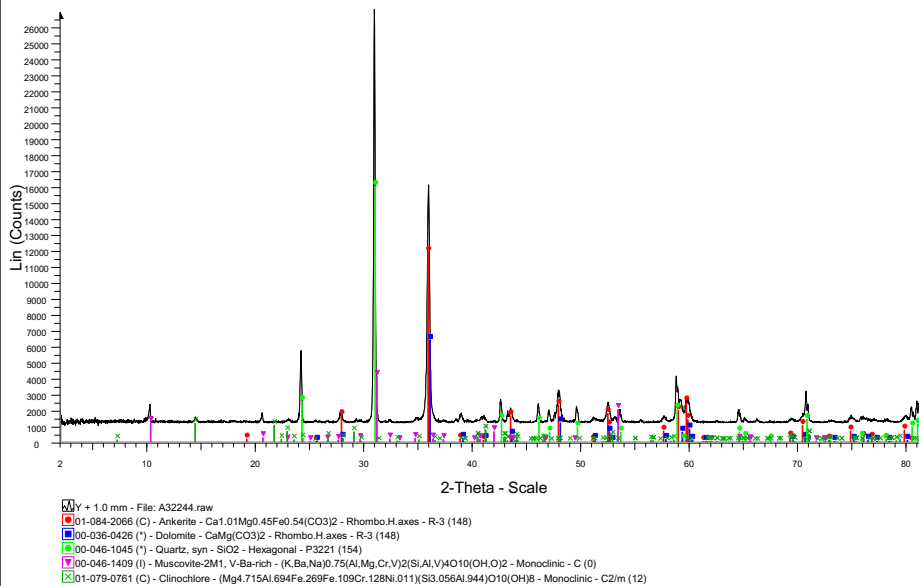
C411518
Quartz-Tourmaline Ladder Vein

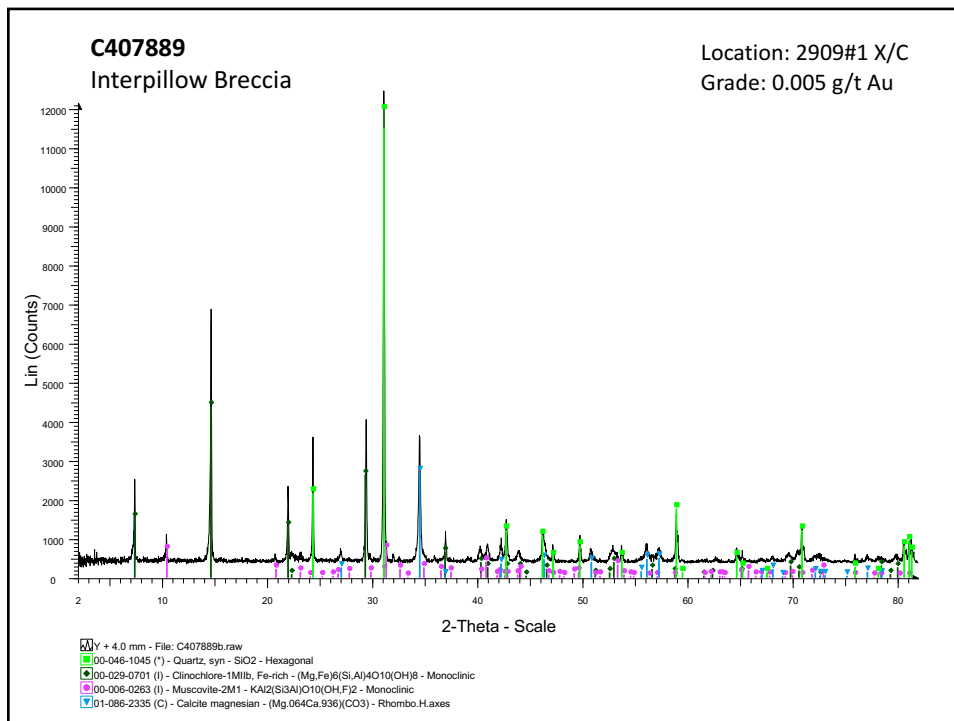
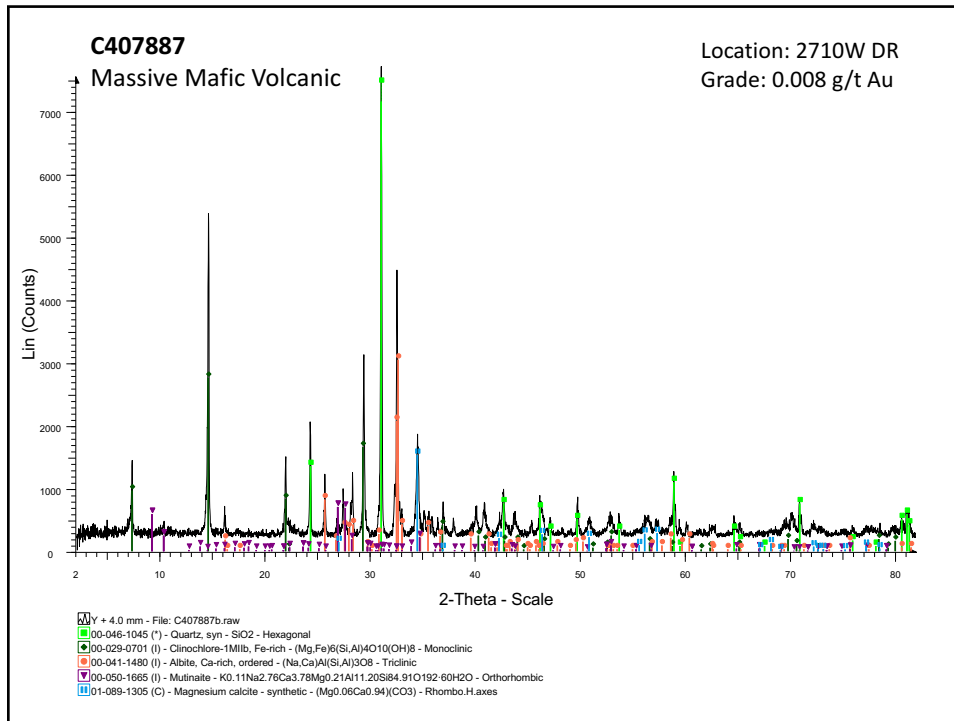
Location: 246862BS
 Grade: 5.04 g/t Au



C411519
Quartz-Ankerite Vein

Location: 246962BS
 Grade: 2.26 g/t Au





Appendix B

Bulk Rock Geochemistry

B.1 Major and Trace Elements

B.1.1 Ankerite Samples

Sample #	Au_ppm	Au_ppm	Ag_ppm	As_ppm	Ba_ppm	Ce_ppm
Method	Au-AA23	Au- GRA21	ME- 4ACD81	ME- 4ACD81	ME-MS81	ME-MS81
Detection Limit	0.005	0.05	0.5	5	0.5	0.5
C406946	>10	17.3	4	88	94.4	22.6
C406942	1.155		0.5	45	20	15.7
C406945	9.68		4.4	17	27.4	17
C407894	3.35		1	<5	16.7	11.2
C406943	0.695		<0.5	12	19.4	3.7
C407893	9.64		17.1	51	33.6	7.6
C406937	0.493		0.5	<5	47.7	2.2
C406938	>10	52.6	91.8	21	12	2.2
C407884	9.66		8.3	57	9.8	6.4
C406940	54.5		9.9	4080	29.3	24.5
C407886	4.87		0.8	19	489	18.4
C411517	1.31		0.7	16	11.4	2.2
C407891	>10	64.3	22.8	98	24.3	5.6
C406935	5.46		4.8	35	115	9.9
C410843	0.026		<0.5	6	10.1	3.9
C409401	>10	84.7	29	233	55.7	7.5
C409459	4.56		16.9	61	21.8	2.9
C407899	>10	42.3	6.7	12	21.8	3.2
C406931	4.75		<0.5	24	22.5	10.4
C406932	0.889		<0.5	177	85.7	13.5
C406933	3.85		0.5	91	28	5.5
C407888	2.16		0.6	68	30.1	6.4
C409403	>10	16.35	4.4	856	30.4	11.9
C410280	>10	17.3	4	>10000	14.9	6.4
C406934	5.69		4.7	90	3.9	5.8
C407890	3.25		1.3	75	27.3	11.3
C409402	0.97		2.1	11	1.9	2.1
C410295	3.87		3.9	40	15.2	3.8
C411098	7.55		3.1	241	14.8	17.9
C411096	2.6		3.2	36	8.2	2.2
C410097	>10	22.4	5.6	144	42.3	21.2
C410300	9.11		5.2	31	27.4	5.2
C406930	>10	18	46.5	68	9.2	2.9

Cd_ppm	Co_ppm	Cr_ppm	Cs_ppm	Cu_ppm	Dy_ppm	Er_ppm
ME-4ACD81	ME-4ACD81	ME-MS81	ME-MS81	ME-4ACD81	ME-MS81	ME-MS81
0.5	1	10	0.01	1	0.05	0.03
<0.5	13.6	30	2.21	25	8.12	5.36
<0.5	5.5	40	0.9	6	6.77	4.52
<0.5	4.2	20	1.18	2	7.21	4.3
<0.5	2.6	30	0.9	2	5.19	3.12
<0.5	9.4	30	0.61	78	1.47	0.83
<0.5	14.5	30	1.09	218	1.98	1.22
<0.5	1.1	<10	0.08	1	0.79	0.43
<0.5	3.6	20	0.15	7	0.95	0.59
<0.5	11.6	50	0.64	144	3.47	2.14
1.7	24.6	50	0.89	106	7.31	4.21
<0.5	10.2	80	1.37	99	1.18	0.62
<0.5	3	10	0.2	4	0.89	0.57
<0.5	17.3	50	1.79	410	2.29	1.44
<0.5	32.5	110	3.76	27	4.76	3.12
0.6	6	20	0.09	7	1.88	1.12
1	34	60	0.73	71	3.49	2.11
0.7	6	20	0.03	133	0.88	0.48
<0.5	5	40	0.31	68	1.18	0.73
<0.5	9.3	10	0.41	1	1.51	0.75
<0.5	41	100	5.01	79	5.26	3.44
1.6	15.4	20	1.53	25	2.31	1.5
0.5	22.3	40	2.06	2	3.33	2.12
0.6	20	20	2.48	145	3.31	2.07
0.8	12	20	2.16	46	2.43	1.35
<0.5	2.9	10	0.1	44	0.75	0.36
<0.5	10.9	100	0.83	41	0.91	0.46
0.6	1	20	0.04	3	0.79	0.37
0.7	6	20	0.64	12	1.52	0.84
1.1	7	20	0.51	134	1.56	0.87
0.5	2	10	0.51	65	1.27	0.66
0.6	15	40	1.53	107	1.79	1.01
0.7	4	20	1.09	53	2.2	1.22
0.8	4.1	40	0.54	686	0.83	0.43

Eu_ppm	Ga_pmm	Gd_ppm	Hf_ppm	Ho_ppm	La_ppm	Lu_ppm	Mo_ppm
ME-MS81	ME-MS81	ME-MS81	ME-MS81	ME-MS81	ME-MS81	ME-MS81	ME-4ACD81
0.03	0.1	0.05	0.2	0.01	0.5	0.01	1
1.5	14.3	6.7	4.5	1.85	8.7	0.83	4
1.37	11.7	5.52	3.5	1.54	6	0.67	3
1.82	7.5	6.68	2.8	1.56	6.3	0.65	23
1.61	5.6	4.75	2.2	1.11	4.2	0.49	15
0.76	4	1.51	0.5	0.3	1.4	0.12	7
0.8	7.3	1.98	0.9	0.41	3.1	0.17	163
0.56	0.7	0.82	<0.2	0.16	0.9	0.05	3
0.39	1.2	0.9	0.2	0.22	0.8	0.08	6
0.84	2.7	2.95	0.5	0.74	2.4	0.28	7
2.25	21.5	7.78	2.9	1.53	9.8	0.59	14
0.89	22.8	1.66	2.5	0.22	9	0.08	44
0.41	2.2	0.82	0.2	0.18	1.1	0.06	<1
0.79	7	2.09	0.9	0.49	2.3	0.21	83
1.24	16	4.07	2.4	1.08	4	0.47	5
0.95	2.3	1.91	<0.2	0.42	1.5	0.14	<1
1.39	9	3.13	1.3	0.72	2.6	0.31	25
0.51	1.8	0.97	<0.2	0.21	1.3	0.06	4
0.58	4.5	1.08	0.4	0.24	1.4	0.1	11
1.02	2.2	2.14	0.3	0.29	4.5	0.09	45
1.22	17.6	4.57	2.7	1.15	4.9	0.52	<1
0.91	6.5	2.14	1.2	0.5	2.1	0.23	10
1.2	7.1	2.98	1.5	0.73	2.5	0.31	4
0.88	6.6	2.96	1	0.7	4.7	0.27	11
0.78	6.2	2.4	0.6	0.48	2.4	0.18	18
0.6	1.2	0.96	<0.2	0.13	2.8	0.04	8
0.62	6.7	1.13	0.9	0.16	5.1	0.06	2
0.55	0.9	0.85	<0.2	0.14	0.9	0.04	30
0.6	3	1.55	<0.2	0.33	1.5	0.13	11
0.75	7	1.68	1.3	0.3	7.8	0.1	7
0.53	1.7	1.23	<0.2	0.25	0.9	0.08	2
0.9	10.3	2.21	1.8	0.38	9	0.18	8
0.73	3.6	2.11	0.2	0.47	2.1	0.17	9
0.38	2.9	0.79	0.2	0.15	1.2	0.06	93

Nb_ppm	Nd_ppm	Ni_ppm	Pb_ppm	Pr_ppm	Rb_ppm	Sc_ppm
ME-MS81	ME-MS81	ME-4ACD81	ME-4ACD81	ME-MS81	ME-MS81	ME-4ACD81
0.2	0.1	1	2	0.03	0.2	1
5.6	17.3	15	12	3.49	59.8	13
4.5	12.5	10	<2	2.45	34.2	10
3.6	14.2	6	5	2.75	22.5	6
2.6	9.6	1	5	1.82	16.8	5
0.7	3.1	15	8	0.61	13.8	5
1.2	5.6	23	16	1.15	24	9
<0.2	1.6	5	5	0.34	1.4	1
0.2	1.7	5	32	0.34	3.8	4
0.5	5.9	26	5	1.07	8.5	9
2.4	19.6	28	91	3.78	17.3	13
2	9.1	31	7	2.29	87.4	5
<0.2	1.7	5	8	0.33	5.4	5
1.2	4.4	28	7	0.89	31.7	11
3.2	7.7	34	7	1.51	69.9	24
0.3	3.5	8	16	0.64	3.2	9
2.2	6.5	33	23	1.16	18.7	19
<0.2	2.3	9	13	0.45	4.8	4
0.5	2.4	10	8	0.47	13.8	5
0.3	7	9	8	1.51	8	3
3.8	10.4	45	11	2.13	100	32
1.6	4.1	20	14	0.83	22.3	14
1.6	5.7	32	16	1.06	30.3	14
1.5	8.6	42	10	1.79	20.8	14
1	5.3	19	22	1.03	20.3	14
<0.2	3.2	7	50	0.77	1.6	3
1.1	6.3	38	41	1.49	26.7	5
<0.2	1.7	2	3	0.3	0.3	2
1	3.1	6	7	0.61	12	5
2.3	9.1	25	10	2.33	8.4	4
0.2	1.7	9	9	0.33	5.6	3
3	11.4	42	9	2.72	29.9	7
0.5	4.1	6	9	0.79	13.5	6
0.2	2.2	12	9	0.44	7.7	2

Sm_ppm	Sn_ppm	Sr_ppm	Ta_ppm	Tb_ppm	Th_ppm	Tl_ppm
ME-MS81	ME-MS81	ME-MS81	ME-MS81	ME-MS81	ME-MS81	ME-MS81, 0.5, 10 (4AD)
0.03	1	0.1	0.1	0.01	0.05	
5.27	1	65.8	0.3	1.2	0.82	0.5
3.92	1	151	0.2	1.01	0.65	<0.5
4.91	1	81.6	0.1	1.14	0.48	<0.5
3.47	1	85.5	0.1	0.83	0.42	<0.5
1.13	1	70.6	<0.1	0.25	0.1	<0.5
1.6	1	79.5	<0.1	0.31	0.19	<0.5
0.64	<1	169.5	<0.1	0.14	<0.05	<0.5
0.65	<1	111.5	<0.1	0.16	<0.05	<0.5
2.09	<1	152	<0.1	0.52	0.1	<0.5
6.68	2	139	0.1	1.22	0.76	<0.5
1.82	1	128.5	<0.1	0.24	1.48	<0.5
0.59	<1	153	<0.1	0.13	0.06	<10
1.49	<1	98.9	<0.1	0.35	0.15	<0.5
2.62	1	87.8	0.1	0.73	0.6	<0.5
1.55	<1	308	<0.1	0.29	<0.05	<10
2.42	1	272	0.5	0.52	0.2	<10
0.84	<1	80.4	<0.1	0.15	<0.05	<10
0.78	<1	149.5	<0.1	0.18	0.14	<0.5
2.17	<1	137.5	<0.1	0.29	0.14	<0.5
3.57	1	75.6	0.3	0.82	0.52	0.6
1.51	<1	96	0.1	0.37	0.21	<0.5
2.05	<1	112.5	<0.1	0.51	0.21	<0.5
2.48	<1	89.8	0.1	0.51	0.17	<10
1.83	<1	71.6	<0.1	0.37	0.1	<10
0.83	<1	112.5	<0.1	0.14	0.09	<0.5
1.24	1	106.5	<0.1	0.15	0.71	<0.5
0.63	<1	49.7	<0.1	0.13	<0.05	<10
1.17	<1	113	<0.1	0.26	0.07	10
1.84	1	124	0.1	0.26	1.08	10
0.73	<1	87.4	<0.1	0.2	<0.05	10
2.5	2	106	0.1	0.34	1.31	10
1.56	<1	138.5	<0.1	0.38	<0.05	<10
0.65	<1	85.1	<0.1	0.13	<0.05	<0.5

Tm_ppm	U_ppm	V_ppm	W_ppm	Y_ppm	Yb_ppm	Zn_ppm
ME-MS81	ME-MS81	ME-MS81	ME-MS81	ME-MS81	ME-MS81	ME-4ACD81
0.01	0.05	5	1	0.1	0.03	2
0.81	0.24	176	14	47.4	5.35	16
0.68	0.44	336	15	41.4	4.28	38
0.63	0.13	49	116	41.8	4.08	37
0.46	0.19	63	1445	28.6	3.1	37
0.12	0.05	123	5	8.3	0.78	42
0.17	0.08	589	16	11.6	1.17	39
0.06	<0.05	202	1	4.8	0.37	31
0.08	<0.05	137	2	6.4	0.57	22
0.3	0.07	210	10	20.8	1.92	24
0.59	0.23	125	22	37.9	3.86	402
0.09	0.62	520	17	6.3	0.56	54
0.07	<0.05	167	181	5.5	0.53	35
0.21	0.09	405	16	13.6	1.41	30
0.47	0.18	454	15	27.2	3.01	41
0.15	<0.05	44	3	12	1.08	21
0.31	0.12	284	52	18.2	2.2	48
0.06	<0.05	99	4	5.3	0.37	34
0.1	0.15	479	15	7.5	0.64	33
0.11	<0.05	160	3	8.3	0.73	16
0.51	0.14	271	30	31.3	3.58	39
0.22	0.07	260	31	13.9	1.54	662
0.31	0.09	224	28	19.4	2.04	59
0.29	0.06	220	25	18.8	1.77	54
0.19	0.08	518	264	13.1	1.23	42
0.04	0.05	144	1	4.7	0.31	86
0.06	0.25	258	8	4.7	0.42	151
0.06	<0.05	36	2	4	0.39	21
0.12	0.05	125	178	8.5	0.84	26
0.11	0.44	289	7	8.3	0.84	105
0.09	<0.05	76	7	6.7	0.55	57
0.15	0.51	286	11	9.8	0.99	92
0.18	<0.05	111	8	13.6	1.09	57
0.06	0.05	403	5	4.4	0.39	105

Zr_ppm	SiO2_pct	Al2O3_pct	Fe2O3_pct	CaO_pct	MgO_pct	Na2O_pct
ME-MS81	ME-ICP06	ME-ICP06	ME-ICP06	ME-ICP06	ME-ICP06	ME-ICP06
2 (20)	0.01	0.01	0.01	0.01	0.01	0.01
152	48.2	7.31	8.96	12.4	6.15	0.17
123	41.4	4.65	5.45	14.9	8.43	0.16
95	24.5	3.03	9.32	21.8	10.65	0.06
71	26.8	2.22	8.2	21.1	10.7	0.05
19	32	1.8	5.96	21.3	10.75	0.04
33	22.5	3.58	9.51	21	11.2	0.07
<20	17.7	0.38	4.34	24.2	14.9	0.15
<20	46	0.72	4.83	15.55	8.99	0.05
16	22.2	1.22	6.64	22.6	12.75	0.09
99	36.9	10.05	18.05	8.18	3.42	0.61
83	33	15.6	7.21	12.2	6.68	0.5
5	25.7	0.81	5.08	21.4	12.5	0.02
31	33.9	3.49	8.27	17.4	8.87	0.06
79	50.7	9.52	11.55	8.93	3.22	0.17
8	16	1.58	5.7	34.6	6.53	0.11
47	11.75	5.98	13.2	22.8	9.23	0.34
4	22	0.88	10.3	23.2	12.35	0.04
14	21.3	1.93	5.93	24.2	13.05	0.05
<20	20.8	1.35	6.1	25.1	12.25	0.07
100	47.3	11.65	9.42	7.11	3.09	0.34
50	24.8	4.21	8.78	20.4	10.5	0.2
50	26.3	3.98	7.24	20.2	9.13	0.2
37	46.6	3.84	9.7	12.3	5.43	0.11
21	27.5	2.57	11.55	17.85	8.71	0.06
<20	28.6	0.88	7.15	23.9	8.46	0.18
31	40.4	4.16	3.61	16.8	9.57	0.09
<2	25.1	0.32	4.3	23.6	12.7	0.03
9	22	1.51	8.05	22.4	11.15	0.04
53	24.7	4.39	11.9	17.95	9.52	0.26
2	36.3	0.74	6.78	19	9.06	0.07
71	41.5	6.54	10.8	11.5	5.64	0.26
11	20.4	1.8	9.76	25.6	9.22	0.09
7	39.5	0.88	6.75	18.4	9.28	0.03

K2O_pct	Cr2O3_pct	TiO2_pct	MnO_pct	P2O5_pct	SrO_pct	BaO_pct
ME-ICP06	ME-ICP06	ME-ICP06	ME-ICP06	ME-ICP06	ME-ICP06	ME-ICP06
0.01	0.01	0.01	0.01	0.01	0.01	0.01
1.92	0.01	0.53	0.2	0.11	0.01	0.01
1.24	<0.01	0.39	0.23	0.15	0.02	<0.01
0.86	<0.01	0.2	0.51	0.03	0.01	<0.01
0.65	<0.01	0.15	0.42	0.03	0.01	<0.01
0.51	<0.01	0.17	0.29	0.02	0.01	<0.01
0.84	<0.01	0.3	0.35	0.02	0.01	<0.01
0.12	<0.01	0.01	0.24	0.01	0.02	<0.01
0.15	<0.01	0.04	0.22	0.03	0.01	<0.01
0.28	0.01	0.15	0.31	0.23	0.02	<0.01
0.61	0.01	0.28	0.22	0.48	0.01	<0.01
3.86	0.01	0.29	0.41	0.09	0.02	0.06
0.23	<0.01	0.07	0.35	0.01	0.02	<0.01
1.09	<0.01	0.31	0.33	0.02	0.01	<0.01
2.59	0.01	1.04	0.25	0.14	0.01	0.01
0.12	<0.01	0.12	0.4	0.01	0.04	<0.01
0.71	0.01	0.74	0.41	0.09	0.03	0.01
0.21	<0.01	0.05	0.48	0.01	0.01	<0.01
0.57	<0.01	0.2	0.31	0.02	0.02	<0.01
0.31	<0.01	0.06	0.25	0.01	0.02	<0.01
3.41	0.01	1.23	0.24	0.14	0.01	0.01
0.79	<0.01	0.39	0.38	0.02	0.01	<0.01
0.99	0.01	0.42	0.35	0.08	0.02	<0.01
0.81	<0.01	0.35	0.22	0.02	0.01	<0.01
0.74	<0.01	0.22	0.34	0.01	0.01	<0.01
0.12	<0.01	0.02	0.29	0.05	0.01	<0.01
1.16	0.01	0.22	0.17	0.05	0.01	<0.01
0.01	<0.01	0.01	0.39	<0.01	<0.01	<0.01
0.43	<0.01	0.23	0.36	0.02	0.01	<0.01
0.33	<0.01	0.19	0.38	0.04	0.01	<0.01
0.23	<0.01	0.05	0.3	0.05	0.01	<0.01
1.11	0.01	0.31	0.24	0.08	0.01	<0.01
0.47	<0.01	0.16	0.51	0.01	0.02	<0.01
0.28	0.01	0.07	0.36	0.01	0.01	<0.01

<u>LOI_pct</u>	<u>Total_pct</u>
ME-ICP06	ME-ICP06
0.01	0.01
14.35	100.33
21.8	98.82
30.8	101.77
30.7	101.03
27.8	100.65
28.7	98.08
37.6	99.67
23	99.59
32.1	98.6
11.8	90.62
18.1	98.03
32.2	98.39
24.5	98.25
5.71	93.85
35	100.21
24.4	89.7
26.8	96.33
33.4	100.98
32.4	98.72
11.9	95.86
29.3	99.78
29.4	98.32
15.55	94.94
22.1	91.66
27.2	96.86
24.4	100.65
33.1	99.56
31.2	97.4
20.5	90.17
25.7	98.29
12.5	90.5
31.8	99.84
23.7	99.28

*Tl ME-4ACD81 10ppm detection limit

*Zr 20ppm detection limit (2011 analysis)

*Inductively coupled plasma atomic-emission spectrometry (ME-ICP06 -Whole Rock Package ICP-AES)

*Inductively coupled plasma – mass spectrometry (ME-MS81 – Lithium Borate Fusion ICP-MS)

*4ACD-81 – 4 acid digestion of sample

*GRA21 - gravimetric assay

*AA23 – gold by fire assay

B.1.2 Other Samples

Sample	Type	Drift	Au_ppm	Au_ppm	Ag_ppm	As_ppm	Ba_ppm	Ce_ppm
Method			Au- AA23	Au- GRA21	ME- 4ACD81	ME- 4ACD81	ME- MS81	ME- MS81
Detection Limit			0.005	0.05	0.5	5	0.5	0.5
C408783	Curts Ankerite Vein Boulder	Paymaster Property	3.41		<0.5	54	8.1	3
C410289	Curts Ankerite Vein Transect	Paymaster Property	0.207		<0.5	97	58.5	3
C410290	Curts Ankerite Vein Transect	Paymaster Property	0.259		<0.5	21	5.3	2.8
C410291	Curts Ankerite Vein Transect	Paymaster Property	2.23		<0.5	11	4	2.3
C410292	Curts Ankerite Vein Transect	Paymaster Property	2.06		0.8	85	61.2	3.7
C410293	Curts Ankerite Vein Transect	Paymaster Property	0.129		<0.5	17	7.9	1.9
C410294	Curts Ankerite Vein Transect	Paymaster Property	0.04		<0.5	6	7.1	1.5
C409523	Carbonate vein in Boulder	Hollinger Pit	0.109		1.1	110	60.3	21.6
C410901	Carbonate vein in Outcrop	Pearl Lake	0.356		<0.5	87	33.9	6
Buffalo	Ankerite Vein Boulder	Buffalo Ankerite Pit	0.494		<0.5	45	91	1.1
C408778	Sulphide Clast	11L (125245BS)	1.505		8.6	416	11.1	6.2
C408779	Sulphide Clast	11L (125245BS)	2.37		22.5	468	13	17.3
C408781	Sulphide Rich Interflow Sediment	125446 Scram	>10	98.1	16.4	>10000	88.2	26.6
C408777	"Carbonate" Clast	124941BS	0.52		6.7	942	138	3.6
C408776	Quartz Fuchsite Vein	12L	>10	28.1	1.3	89	54.5	<0.5
C406944	Interflow Sediment	1605 X/C	0.801		5.2	40	73.2	24.4
C408780	Sulphide rich interflow sediment	1939#10DR	2.3		4.1	208	13	9.1
C406939	Interflow sediment	1904 DR	0.475		2.3	420	44.4	15.2
C407885	Interflow sediment	1904 DR	0.028		<0.5	<5	44.2	27.4
C406941	Basal graphitic argillite	196671AT	0.022		<0.5	50	85.4	5.6
C411520	Quartz Tourmaline Ladder Vein	2125DR	7.39		14.4	2100	14.8	3.6
C406936	Hyaloclastite	2301#5 DR	0.009		<0.5	12	29.5	34.8
C411518	Quartz Tourmaline Ladder Vein	246862BS	5.04		2.1	9	81.8	7.4
C411519	Quartz Ankerite Vein	246862BS	2.26		4	13	44.7	2.8
C407887	Massive Mafic Volcanic	2710 DRW	0.008		<0.5	18	21	19.3
C407889	Interpillow breccias	2909#1 X/C	0.005		<0.5	7	37.7	27.8

Cd_ppm	Co_ppm	Cr_ppm	Cs_ppm	Cu_ppm	Dy_ppm	Er_ppm	Eu_ppm	Ga_pmm	Gd_ppm	Hf_ppm
ME-4ACD81	ME-4ACD81	ME-MS81	ME-MS81	ME-4ACD81	ME-MS81	ME-MS81	ME-MS81	ME-MS81	ME-MS81	ME-MS81
0.5	1	10	0.01	1	0.05	0.03	0.03	0.1	0.05	0.2
0.8	9	10	0.13	8	0.96	0.6	0.43	0.9	0.91	<0.2
0.5	4	20	0.89	1	1.17	0.85	0.47	6.4	1.19	1.1
1	<1	<10	0.15	<1	1.34	0.72	0.48	1	1.25	<0.2
0.6	1	10	0.1	<1	0.9	0.47	0.38	0.7	0.88	<0.2
1.3	23	30	1.08	58	2.14	1.34	0.67	5.1	2.01	0.2
0.9	4	10	0.24	3	0.94	0.57	0.34	1.2	0.84	<0.2
0.6	<1	10	0.16	2	0.48	0.24	0.27	0.7	0.54	<0.2
0.8	7	10	0.6	9	7.87	4.52	2.99	10.2	7.48	1.7
1.1	11	50	0.24	22	2.41	1.47	1.2	5.1	2.75	0.4
<0.5	20	170	0.32	58	0.93	0.84	0.23	6.6	0.47	<0.2
1.7	967	20	0.06	1230	1.11	0.62	0.63	1.2	1.24	<0.2
7.5	716	30	0.07	>10000	3.26	1.72	1.44	3.6	3.2	0.4
175	37	130	1.23	218	6.82	4.48	1.64	23.4	5.08	3.4
0.7	47	2180	0.27	221	1.05	0.62	0.29	8.8	1.02	0.5
<0.5	3	110	0.13	1	<0.05	0.03	<0.03	1.3	<0.05	<0.2
5.9	31.4	60	2.54	636	4.24	2.92	1.25	16	4.41	2.7
2.4	216	20	0.48	196	1.23	0.75	0.56	4.6	1.27	0.7
7	59.1	50	1.39	672	3.2	2.21	0.81	11.3	3.17	1.7
0.6	2.3	30	1.95	<1	12.2	8.08	2.26	21.1	9.92	7.7
<0.5	35.2	340	0.68	43	1.63	1.07	0.54	14.3	1.46	1
<0.5	28	40	0.23	59	1.05	0.56	0.33	4.3	0.96	0.2
<0.5	14.8	40	0.81	34	14.65	9.73	2.29	18.7	11.85	8.2
<0.5	6	20	0.29	49	1.33	0.67	0.46	6.7	1.33	0.8
0.5	26	20	0.18	71	1.1	0.76	0.49	4.6	0.95	0.2
<0.5	33.6	40	0.24	40	7.61	4.85	1.77	20	6.25	3.5
0.5	19.5	50	1.14	34	11.95	7.81	1.98	16.4	9.76	6

Ho_ppm	La_ppm	Lu_ppm	Mo_ppm	Nb_ppm	Nd_ppm	Ni_ppm	Pb_ppm	Pr_ppm	Rb_ppm	Sc_ppm
ME-MS81	ME-MS81	ME-MS81	ME-4ACD81	ME-MS81	ME-MS81	ME-4ACD81	ME-4ACD81	ME-MS81	ME-MS81	ME-4ACD81
0.01	0.5	0.01	1	0.2	0.1	1	2	0.03	0.2	1
0.18	1.3	0.09	1	<0.2	2.4	25	3	0.44	0.9	3
0.28	1.2	0.14	4	1.7	2.7	11	3	0.49	16.3	6
0.27	0.9	0.09	1	<0.2	2.6	2	4	0.48	1.3	3
0.17	0.9	0.06	<1	0.2	2	1	4	0.36	0.5	2
0.44	1.4	0.18	2	0.6	3.5	39	2	0.62	11.6	15
0.2	0.7	0.08	<1	<0.2	1.8	12	3	0.31	1.8	2
0.09	0.6	0.04	4	<0.2	1.1	2	2	0.23	0.9	1
1.63	8.8	0.64	<1	3.2	17.2	1	30	3.36	25.5	17
0.52	2.3	0.22	<1	0.9	5.3	14	4	0.97	5.3	14
0.25	0.5	0.18	1	0.3	0.9	85	<2	0.16	19.5	23
0.24	3.2	0.08	19	<0.2	3.6	96	51	0.77	2.5	4
0.62	8.5	0.22	22	0.5	10.3	88	43	2.32	3	15
1.53	12.2	0.65	10	5.2	17.3	53	49	3.75	37.1	20
0.23	1.7	0.08	<1	0.5	2.2	1350	152	0.5	21.4	18
0.01	<0.5	<0.01	<1	<0.2	0.1	50	22	0.03	5.4	<1
0.95	10.4	0.47	5	4.1	14.7	35	16	3.51	58.8	11
0.28	3.9	0.11	2	1.1	5.3	39	88	1.2	6.5	3
0.76	6.6	0.37	3	2.5	9.6	73	57	2.22	37.6	11
2.79	9.6	1.33	1	10.2	23	<1	101	4.48	39.6	16
0.35	2.5	0.17	1	1.4	3.7	154	<5	0.78	16.2	23
0.2	1.5	0.06	3	<0.2	2.4	10	6	0.5	5.4	5
3.33	13.1	1.47	<2	9.7	26.7	15	4	5.4	20.7	15
0.23	3.1	0.09	<1	0.3	5.1	10	10	1.04	28.3	10
0.21	1.2	0.08	8	<0.2	2.3	22	5	0.37	15.4	10
1.67	7.1	0.72	1	4.9	15.9	21	5	3.07	5.4	32
2.73	10.5	1.2	<1	7.3	21.7	26	3	4.35	16.2	20

Sm_ppm	Sn_ppm	Sr_ppm	Ta_ppm	Tb_ppm	Th_ppm	Tl_ppm	Tm_ppm	U_ppm	V_ppm	W_ppm
ME-MS81	ME-MS81	ME-MS81	ME-MS81	ME-MS81	ME-MS81	ME-MS81	ME-MS81	ME-MS81	ME-MS81	ME-MS81
0.03	1	0.1	0.1	0.01	0.05	0.5, 10 (4AD)	0.01	0.05	5	1
0.73	<1	73	<0.1	0.16	0.21	<10	0.08	<0.05	23	100
0.95	1	79.5	0.1	0.21	0.23	<10	0.13	0.1	170	26
1.05	<1	63.7	<0.1	0.21	<0.05	<10	0.1	<0.05	39	2
0.88	<1	41	<0.1	0.14	0.12	10	0.06	<0.05	13	2
1.47	<1	40.8	<0.1	0.34	0.07	<10	0.18	<0.05	104	18
0.7	<1	57.8	<0.1	0.14	<0.05	<10	0.09	<0.05	27	19
0.44	<1	55.5	<0.1	0.08	<0.05	<10	0.03	<0.05	22	28
5.67	1	114.5	0.2	1.22	0.29	<10	0.64	0.08	7	35
2.54	<1	84.3	<0.1	0.42	0.12	<10	0.23	<0.05	69	3
0.39	<1	58.2	<0.1	0.11	0.06	<10	0.14	<0.05	92	10
1.13	<1	48.2	<0.1	0.19	0.08	10	0.08	1.65	15	1
2.97	2	79.5	<0.1	0.57	0.23	<10	0.27	2.16	56	3
4.41	1	83.3	0.2	1	0.59	<10	0.68	0.18	111	38
0.77	1	164.5	<0.1	0.19	0.21	<10	0.09	0.27	87	6
0.06	<1	14.7	<0.1	<0.01	0.07	<10	<0.01	<0.05	9	1
3.71	15	46.3	0.3	0.7	1.3	0.5	0.44	0.37	87	9
1.17	1	53	<0.1	0.21	0.47	<10	0.11	0.12	15	6
2.52	10	64.1	0.2	0.5	0.95	<0.5	0.34	0.27	85	10
7.25	1	51.9	0.6	1.83	1.3	<0.5	1.25	0.36	<5	35
1.08	1	195	<0.1	0.26	0.22	<0.5	0.15	0.19	171	2
0.93	1	57.4	<0.1	0.15	0.06	<10	0.07	<0.05	173	7
8.26	2	57.7	0.6	2.17	1.39	<0.5	1.44	0.36	74	3
1.39	1	79.3	0.1	0.2	0.37	<10	0.09	0.13	101	19
0.69	1	86.1	0.1	0.16	<0.05	<10	0.07	0.05	210	20
4.94	1	126	0.2	1.14	0.66	<0.5	0.72	0.17	134	1
6.93	1	117.5	0.4	1.76	1.03	<0.5	1.16	0.26	120	4

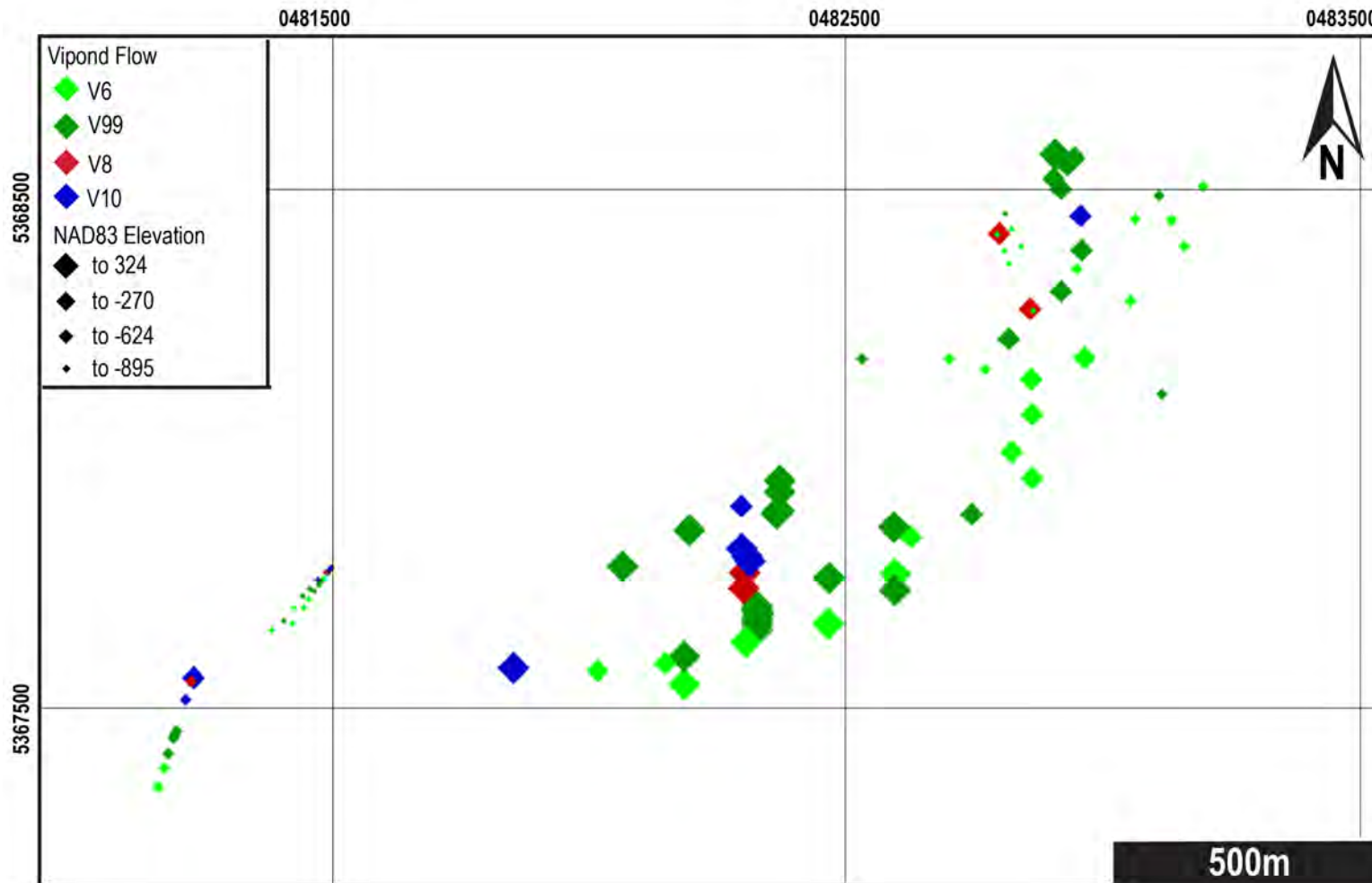
Y_ppm	Yb_ppm	Zn_ppm	Zr_ppm	SiO2_pct	Al2O3_pct	Fe2O3_pct	CaO_pct	MgO_pct	Na2O_pct	K2O_pct
ME-MS81	ME-MS81	ME-4ACD81	ME-MS81	ME-ICP06	ME-ICP06	ME-ICP06	ME-ICP06	ME-ICP06	ME-ICP06	ME-ICP06
0.1	0.03	2	2 (20)	0.01	0.01	0.01	0.01	0.01	0.01	0.01
5.7	0.56	39	2	14.65	0.4	9.41	24.7	13.35	0.04	0.02
7.3	0.88	34	41	10.6	3.48	6.14	26.2	14.9	0.21	0.64
7.3	0.68	34	<2	1.9	0.27	6.99	30.1	17.15	0.03	0.05
4.7	0.39	27	<2	32.4	0.11	6.87	20.2	10.65	0.02	0.02
12	1.21	43	11	30.4	3.37	13.4	21.4	4.7	0.36	0.49
5.9	0.43	29	<2	11.55	0.53	7.36	27.1	14.75	0.06	0.07
2.8	0.25	48	<2	3.59	0.19	6.72	31.2	16.05	0.04	0.04
45.7	4.06	61	64	31.6	4.48	18.9	14.55	3.72	0.07	0.92
14.4	1.35	42	18	18.35	3.46	11.8	21.9	9.45	0.47	0.24
7.1	1.06	38	5	45.6	9.72	5.87	11.1	6.9	0.64	1.02
6.6	0.56	<2	<2	30.3	0.76	42.3	2.48	0.72	0.02	0.1
17.6	1.63	8	8	33.7	3.43	34.3	3.71	1.2	1.07	0.13
38.8	4.59	>10000	19	33.7	7.35	14	10.15	5.38	0.14	1.58
6.2	0.49	18	119	15.3	5.57	13.75	17	12.15	0.05	0.76
<0.5	<0.03	2	2	97.4	0.83	0.67	0.48	0.47	0.04	0.2
30.4	2.76	2100	101	51.2	8.14	9.83	7.56	3.74	0.18	2.08
7.7	0.73	19	8	18.05	1.95	43	4.84	2.05	0.07	0.21
23.3	2.12	2150	69	49.7	6	16.35	6.86	2.84	0.11	1.34
68.8	8.39	190	256	63.4	8.99	10.5	5.28	2.38	0.09	1.58
8.8	1.03	100	33	44.6	11.6	8.93	11.15	4.2	1.45	0.57
5.7	0.5	7	7	80.3	2.77	4.61	3.5	1.8	0.18	0.24
80.5	9.47	47	259	64.7	10.4	7.59	5.33	1.94	2.17	0.78
7.4	0.68	25	25	61.6	4.95	5.01	8.42	3.76	0.14	1.38
5.8	0.55	7	7	42.5	2.83	7.02	16.15	9.23	0.07	0.71
41.9	4.71	148	114	49.8	12.35	14.7	7.88	2.15	3.16	0.22
66.5	7.7	76	194	47.8	9.5	11.7	12.95	4.3	0.05	0.53

Cr2O3_pct	TiO2_pct	MnO_pct	P2O5_pct	SrO_pct	BaO_pct	LOI_pct	Total_pct
ME-ICP06	ME-ICP06	ME-ICP06	ME-ICP06	ME-ICP06	ME-ICP06	ME-ICP06	ME-ICP06
0.01	0.01	0.01	0.01	0.01	0.01	0.01	0.01
<0.01	0.01	0.21	0.01	0.01	<0.01	33.6	96.41
<0.01	0.32	0.2	0.05	0.01	0.01	37.2	99.96
<0.01	<0.01	0.22	0.04	0.01	<0.01	43.8	100.56
<0.01	<0.01	0.21	<0.01	0.01	<0.01	29.5	99.99
<0.01	0.27	0.39	0.01	<0.01	0.01	23.5	98.3
<0.01	0.01	0.24	<0.01	0.01	<0.01	38.7	100.38
<0.01	0.02	0.18	0.01	0.01	<0.01	42.8	100.85
<0.01	0.56	1.17	0.25	0.01	0.01	13	89.24
0.01	0.29	0.59	0.05	0.01	<0.01	29.5	96.12
0.02	0.1	0.15	0.04	0.01	0.01	16.9	98.08
<0.01	0.02	0.22	0.6	<0.01	<0.01	22	99.52
<0.01	0.18	0.19	1.48	0.01	<0.01	17.25	96.65
0.02	0.87	0.21	0.13	0.01	0.01	7.97	82.36
0.29	0.26	0.5	0.03	0.02	0.02	20.9	86.6
0.02	0.01	0.01	<0.01	<0.01	0.01	1.22	101.36
0.01	0.42	0.33	0.11	<0.01	0.01	8.82	92.43
<0.01	0.09	0.31	0.02	0.01	<0.01	23.4	94
0.01	0.31	0.32	0.09	<0.01	<0.01	6.78	90.71
<0.01	0.59	0.28	0.13	0.01	0.01	8.74	101.98
0.04	0.52	0.23	0.04	0.03	0.01	15.9	99.27
0.01	0.12	0.08	0.06	0.01	<0.01	4.5	98.18
0.01	0.7	0.11	0.12	0.01	<0.01	6.74	100.6
<0.01	0.16	0.27	0.07	0.01	0.01	12.3	98.08
<0.01	0.12	0.4	0.02	0.01	<0.01	21.7	100.76
0.01	1.54	0.2	0.28	0.02	<0.01	8.18	100.49
0.01	0.69	0.25	0.09	0.02	0.01	13.7	101.6

*Inductively coupled plasma atomic-emission spectrometry (ME-ICP06 -Whole Rock Package ICP-AES)

*Inductively coupled plasma – mass spectrometry (ME-MS81 – Lithium Borate Fusion ICP-MS)

B.2 Map of Geochemically Distinguished Vipond Formation Flows



B.3 Carbonate Isotopes

B-3.1 Raw Data

Sample	¹³ C VPDB	¹⁸ O VSMOW
C406930.b	-0.56	15.07
C406931.1	-0.81	12.58
C406932.2	-0.67	15.07
C406933.1	-1.01	14.87
C406946a.1	-0.95	13.90
C406931.1DUP	-0.82	12.54
C406930_1	0.30	13.66
C406931_1	-2.32	8.65
C406931_2	-0.63	11.36
C406932-2	-0.60	13.45
C406933_1	-1.91	12.99
C406933_2	-0.60	13.69
C406934_1	-0.38	13.13
C406934_2	-0.81	12.93
C406930_1DUP	-0.80	13.44
C406935_1	-1.38	10.69
C406932_1	0.02	13.58
C406937_1	10.72	12.75
C406937_2	-1.28	12.04
C406938_1	-0.19	12.86
C406938_2	-1.59	12.65
C406940_1	0.06	13.39
C406940_2	0.04	13.56
C406942_1	24.12	14.13
C406935_1 DUP	0.34	10.88
C406943_1	-0.65	12.86
C406943_2	-0.59	12.69
C406945_1	-0.19	13.13
C406945_2	-0.71	13.01
C406946_1	-1.38	12.60
C406946_2	-1.61	12.71
C407884_1	-0.58	13.25
C407884_2	-0.68	13.00
C407888_1 DUP	-0.66	13.71
C407886_1	-2.17	10.77
C407886_2	-5.70	4.28
C407888_1	-0.74	13.50

Sample	13C VPDB	18O VSMOW
C407890_1	-0.76	13.09
C407890_2	-0.57	12.83
C407891_1	-0.62	13.39
C407891_2	-0.65	13.50
C407893_1	-1.20	12.58
C407893_2	-0.90	12.66
C407899_1 DUP	-0.90	11.82
C407894_1	-0.64	12.95
C407894_2	-1.21	14.21
C407899_1	-1.49	10.58
BA	-3.55	12.55
C409402	-1.84	11.73
C409401	-2.21	12.66
C409403	-1.68	12.90
C409523	-1.53	13.11
C410280	-0.51	14.91
C410289	-0.72	13.82
C410290	0.17	14.07
C410901	-1.86	12.34
C410292	-0.63	14.44
C410293	0.89	14.17
C410293 DUP	0.86	14.13
C410295	-0.43	14.26
C410300	-0.55	14.29
C410300 DUP	-0.58	14.32
C411097	-0.97	14.12
C411098	-0.82	14.22
C410294	0.97	14.84
C411096	-0.20	14.07
C410291	-0.26	13.67
C410843	-0.76	11.77

*Samples in red were omitted as outliers

*Samples were analyzed in 3 runs separated by black lines (May 2012, August 2013, June 2016)

B.3.2 Standards

Standard	13C VPDB	18O VSMOW	Expected Value
WS-1	0.64	25.69	0.76/26.23
DOL	5.71	28.87	6.67/30.76
NBS-19	1.95	28.60	1.95/28.6
NBS-18	-5.08	7.20	-5.0/7.2
SUP	-35.28	13.10	-35.28/13.20
WS-1	0.69	26.16	0.76/26.23
DOL	6.52	30.91	6.67/30.76
NBS-19	1.58	27.44	1.95/28.6
NBS-18	-5.51	5.75	-5.0/7.2
LSVEC	-47.09	3.32	-46.60
WS-1	0.32	24.99	0.76/26.23
DOL-368	6.38	30.13	6.67/30.76
NBS-19	2.06	28.07	1.95/28.6
NBS-18	-5.10	6.66	-5.0/7.2
NBS-19	1.93	26.76	1.95/28.6
NBS-18	-5.00	6.82	-5.0/7.2
LSVEC	-47.29	3.17	-46.60
DOL-368	6.66	30.24	6.67/30.76
LSVEC	-46.36	3.84	-46.60
WS-1	1.42	25.58	0.76/26.23
DOL	6.61	30.47	6.67/30.76
SUP	-36.16	12.55	-35.28/13.20
NBS-19	1.69	27.43	1.95/28.6
NBS-18	-5.24	6.21	-5.0/7.2
LSVEC	-47.91	2.43	-46.60
WS-1	0.68	25.37	0.76/26.23
DOL-368	6.49	30.15	6.67/30.76
SUP	-36.07	12.46	-35.28/13.20
WS-1	-0.87	22.84	0.76/26.23
WS-1	0.86	26.39	0.76/26.23
SUP	-35.62	13.32	-35.55/13.30
LSVEC	-46.54	4.17	-46.6
DOL-368	5.68	29.40	6.67/30.76
NBS-19	1.96	28.65	1.95/28.65
NBS-18	-5.05	7.23	-5.0/7.2
SUP	-35.65	13.25	-35.55/13.30
WS-1	0.71	26.26	0.76/26.23
DOL-368	6.13	30.76	6.67/30.76

Standard	13C VPDB	18O VSMOW	Expected Value
DOL-368	6.43	30.76	6.67/30.76
DOL-368	6.46	30.91	6.67/30.76
WS-1	0.75	26.32	0.76/26.23
NBS-19	1.94	28.55	1.95/28.65
NBS-18	-5.04	7.17	-5.0/7.2
SUP	-35.62	13.21	-35.55/13.30
LSVEC	-46.66	4.05	-46.6

B-3.3 Average Plotted Values

Sample #	VDPB	VSMOW
C406946	-1.32	13.07
C406945	-0.45	13.07
C407894	-0.93	13.58
C406943	-0.62	12.78
C407893	-1.05	12.62
C406937	-1.28	12.04
C406938	-0.89	12.76
C407884	-0.63	13.12
C406940	0.05	13.47
C407886	-2.17	10.77
C407891	-0.64	13.45
C406935	-0.52	10.79
C410843	-0.76	11.77
C409401	-2.21	12.66
C407899	-1.19	11.20
C406931	-0.75	12.16
C406932	-0.42	14.03
C406933	-1.17	13.85
C407888	-0.70	13.61
C409403	-1.68	12.90
C410280	-0.51	14.91
C406934	-0.60	13.03
C407890	-0.67	12.96
C409402	-1.84	11.73
C410295	-0.43	14.26
C411098	-0.82	14.22
C411096	-0.20	14.07
C410097	-0.97	14.12
C410300	-0.56	14.30
C406930	-0.35	13.23
C410289	-0.72	13.82
C410290	0.17	14.07
C410291	-0.26	13.67
C410292	-0.63	14.44
C410293	0.87	14.15
C410294	0.97	14.84
C409523	-1.53	13.11
C410901	-1.86	12.34
BA	-3.55	12.55

*Average values for each sample

Appendix C

Trace Element Geochemistry

C.1 Electron Dispersive Spectroscopy

C.1.1 Electrum

Type	Sample	Au:Ag
Free Gold I	C406932b	3.05
Free Gold I	C406932b	3.18
Free Gold I	C406932t	2.57
Free Gold I	C406932t	2.36
Free Gold I	C406934	4.03
Free Gold I	C406934	2.64
Free Gold I	C406934	2.83
Free Gold I	C406934	2.65
Free Gold I	C406938A	5.15
Free Gold I	C406940B	3.81
Free Gold I	C406940B	3.95
Free Gold I	C406940B	3.99
Free Gold I	C406940B	3.88
Free Gold I	C407899A	3.70
Free Gold I	C406932t	4.20
Free Gold I	C406934	2.80
Free Gold I	C406934	2.64
Free Gold I	C406934	2.68
Free Gold I	C406934	3.27
Free Gold I	C406934	2.46
Free Gold I	C406938A	4.28
Free Gold I	C407899A	3.34
Free Gold I	C406934	4.01
Free Gold II	C406931	6.90
Free Gold II	C406931	9.86
Free Gold II	C406931	8.63
Free Gold II	C406931	6.84
Inclusion I	C406931	6.64
Inclusion I	C406931	12.19
Inclusion I	C406932b	6.59
Inclusion I	C406932b	5.40
Inclusion I	C406932b	3.65
Inclusion I	C406932b	4.53
Inclusion I	C406932b	7.74
Inclusion I	C406932b	5.01
Inclusion I	C406932b	6.32
Inclusion I	C406932b	7.33
Inclusion I	C406932t	4.83
Inclusion I	C406932t	4.99
Inclusion I	C406932t	4.99
Inclusion I	C406932t	5.93

Type	Sample	Au:Ag
Inclusion I	C406932t	7.32
Inclusion I	C406932t	4.84
Inclusion I	C406932t	6.15
Inclusion I	C406932t	5.30
Inclusion I	C406934	12.38
Inclusion I	C406934	10.73
Inclusion I	C406934	12.82
Inclusion I	C406934	3.15
Inclusion I	C406938A	10.27
Inclusion I	C406938A	5.19
Inclusion I	C407891	9.61
Inclusion I	C407899A	4.17
Inclusion I	C407899A	4.93
Inclusion I	C408781	4.43
Inclusion I	C406932t	4.37
Inclusion II	C407891	4.58
Inclusion II	C406934	3.00

*Data is in weight percent.

C.1.2 Tellurides

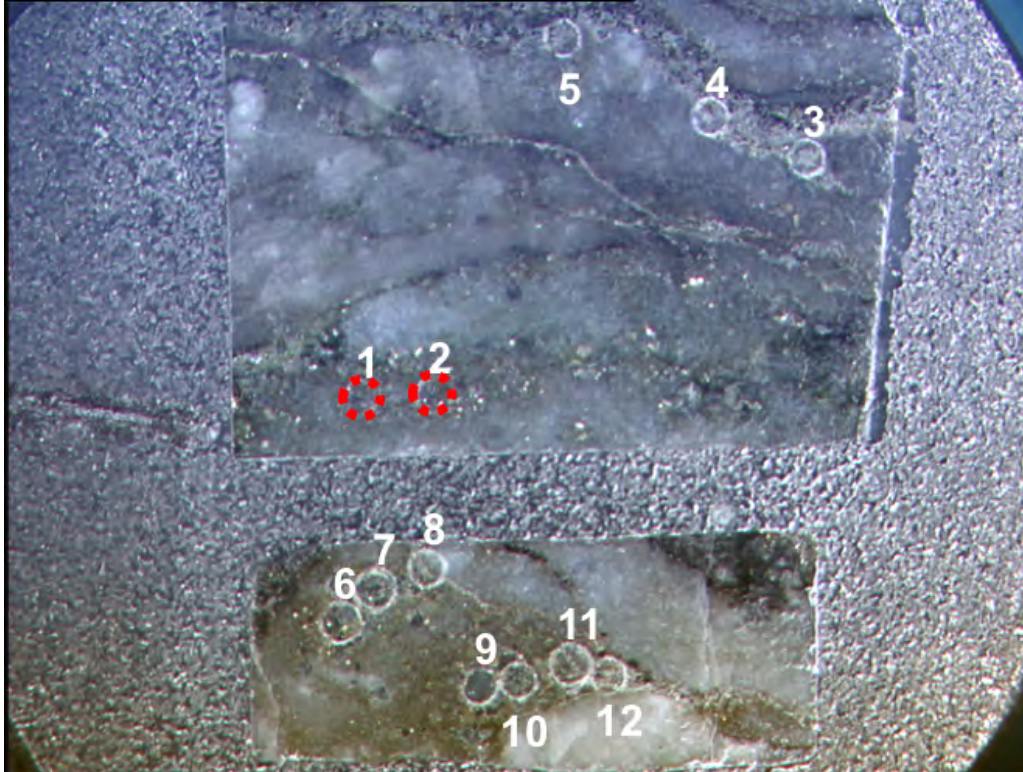
Sample	Au	Ag	Te	
Fracture	C406930A	58.24	36.01	
Inclusion	C406932t	48.6	27.87	
Inclusion	C406932t	60.49	35.8	
Inclusion	C406934	9.52	39.95	28.42
Inclusion	C406934	14.08	25.87	19.29
Inclusion	C406934	17.36	25.46	21.41
Inclusion*	C406540	10.79	6.07	
Fracture*	C406540	0.89	18.03	8.47

* Data from Harris, 2013

* Data is in weight percent

C.2 Dynamic - Secondary Ion Mass Spectrometry

C.2.1 Samples for D-SIMS

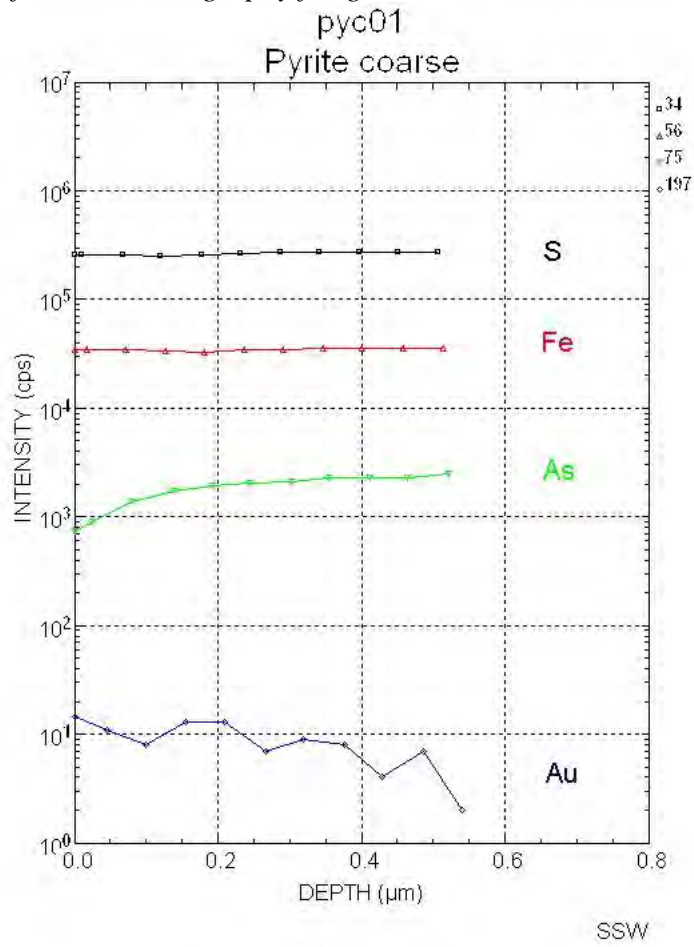


Mounted samples with analysed grains (Top C407890, Bottom C406931)

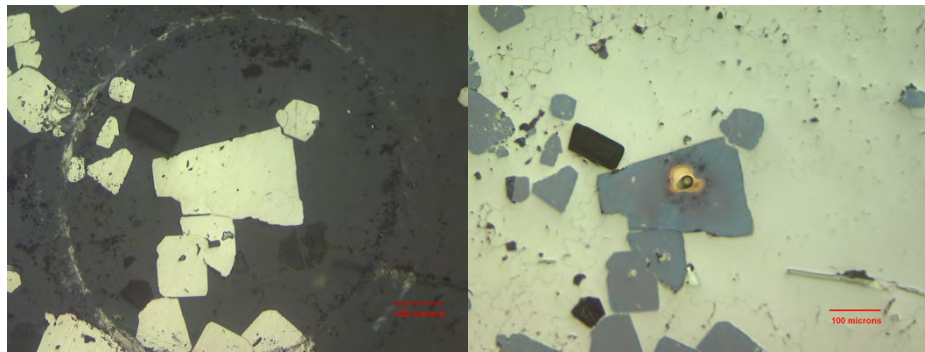
C.2.2 Raw Data Table for Analysis of locations in C.2.1

Texture	Grain I.D.	/	Au, ppm	/	As, ppm
Py3	py01	2.52E-04	1.44	5.97E-02	843.14
	py02	1.22E-03	6.95	4.08E-02	576.99
	py06	1.84E-04	1.05	1.70E-03	24.01
	py07	4.12E-04	2.35	2.82E-03	39.81
	py09	8.81E-05	0.5	2.38E-03	33.6
	pu08	5.78E-03	33	1.35E-01	1914.27
Py2	py10	1.39E-03	7.92	3.23E-02	455.92
	py11	1.07E-03	6.11	4.55E-02	643.57
Py1	pyfd03	8.57E-04	4.89	1.14E-01	1613.83
	py04	2.61E-03	14.91	1.76E-01	2480.92
	py05a	2.67E-03	15.23	3.11E-01	4399.81
	py05b	3.32E-03	18.94	8.01E-02	1132.42
	py12	2.47E-03	14.12	6.00E-02	847.61
Average			9.8		1154.3

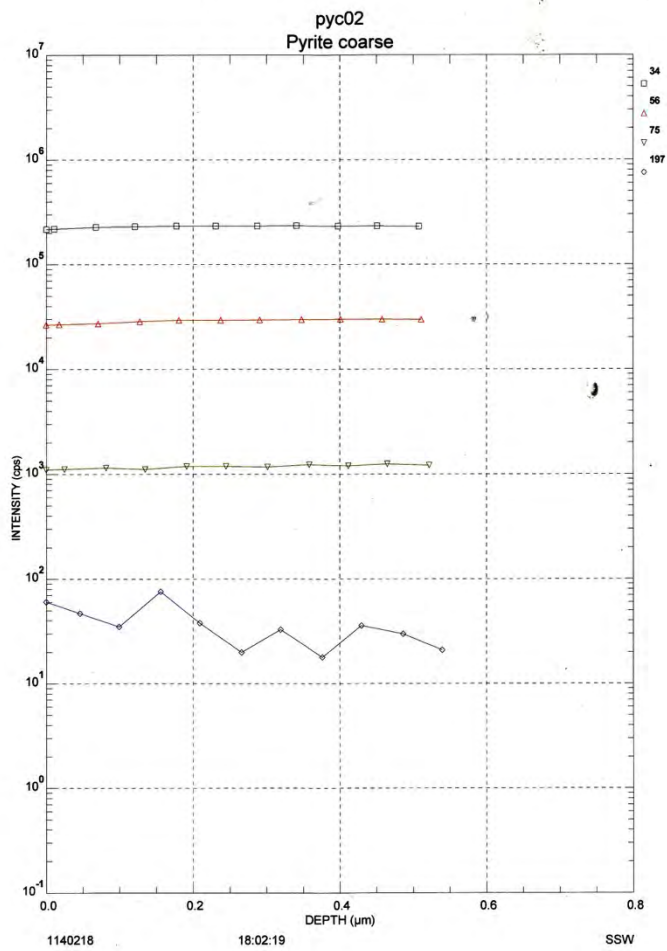
C.2.3 Depth Profiles and Petrography for grains in C.2.1



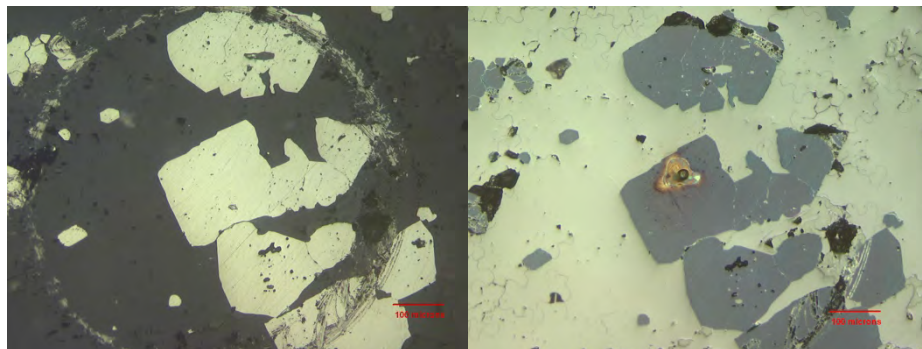
D-SIMS depth profile.



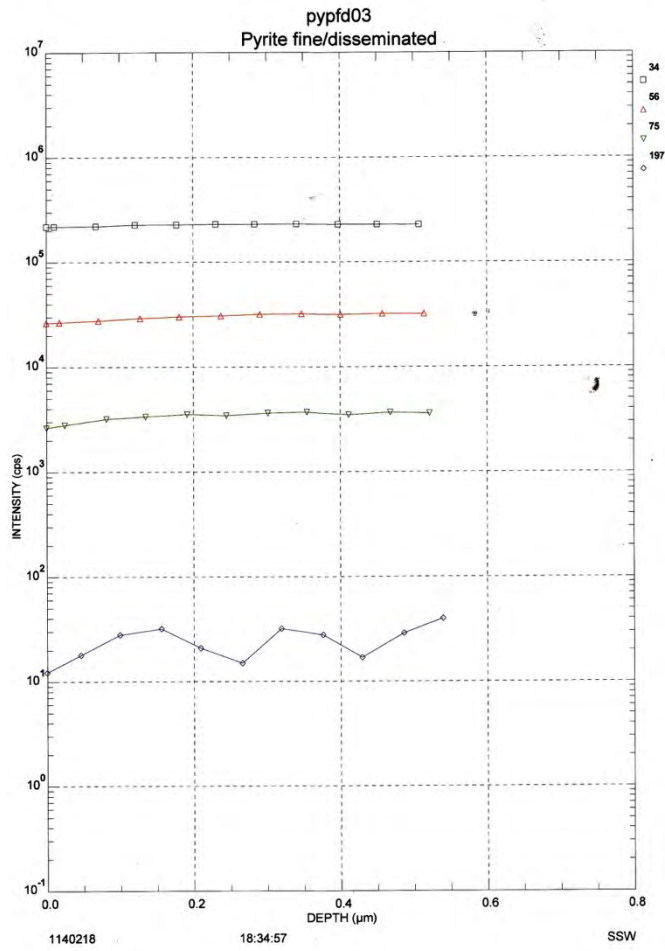
Reflected light images pre-and post-analysis



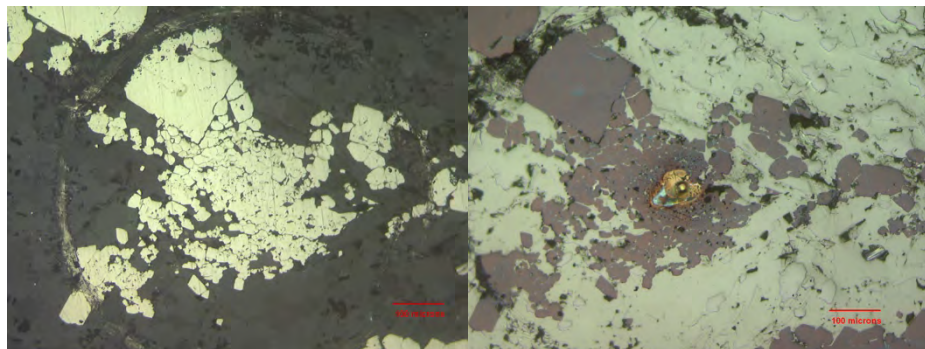
D-SIMS depth profile.



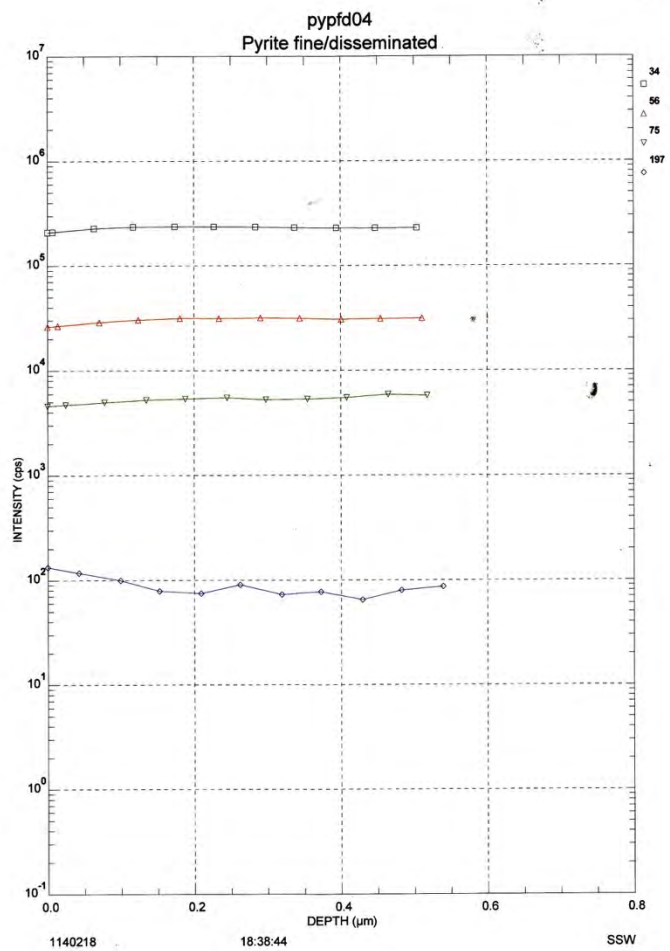
Reflected light images pre-and post-analysis



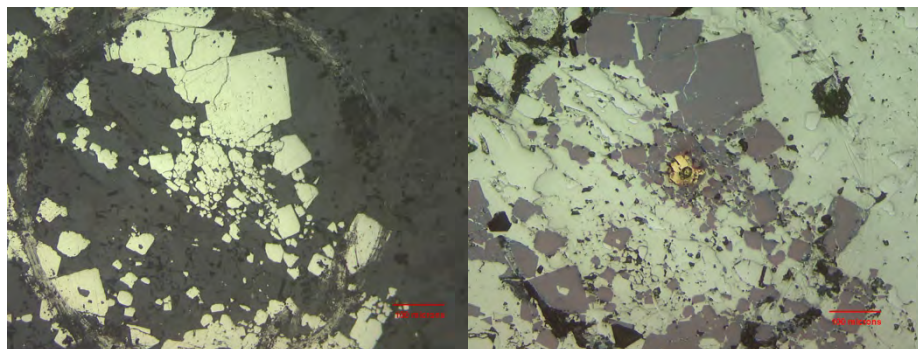
D-SIMS depth profile.



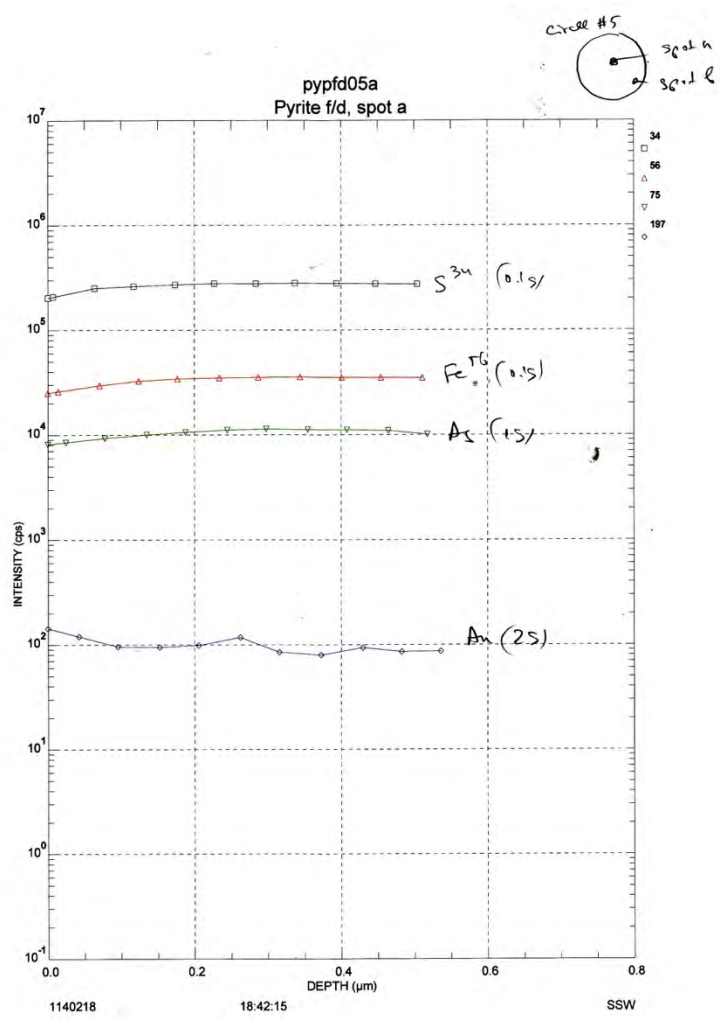
Reflected light images pre-and post-analysis



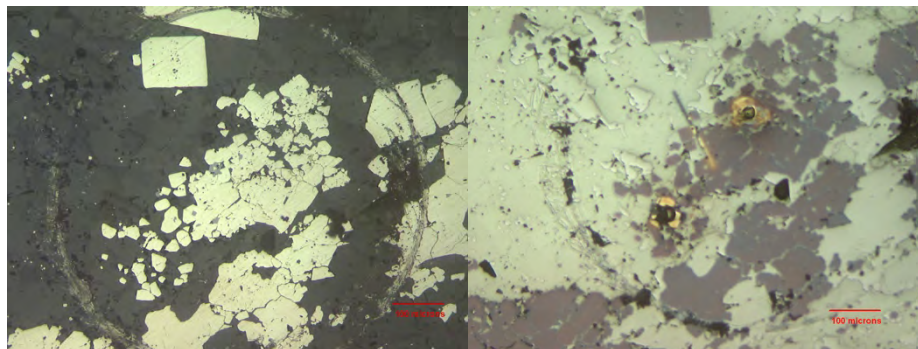
D-SIMS depth profile.



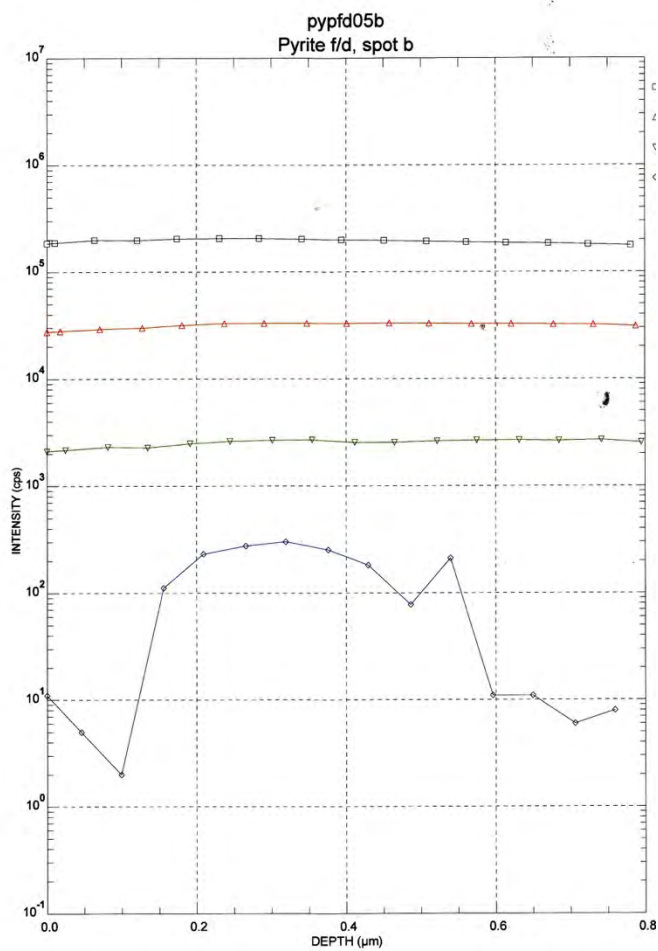
Reflected light images pre-and post-analysis



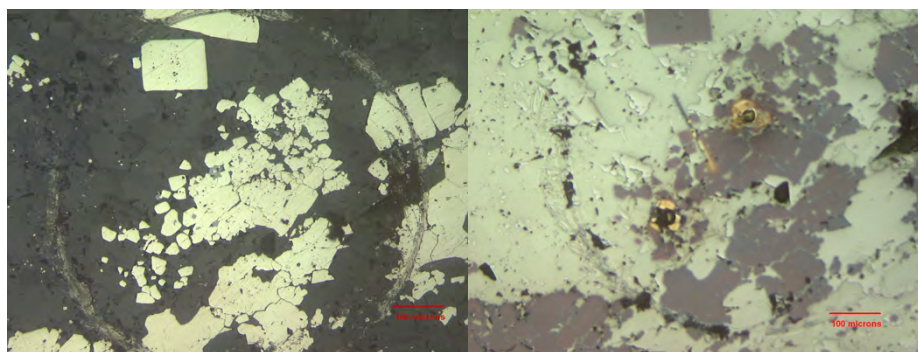
D-SIMS depth profile.



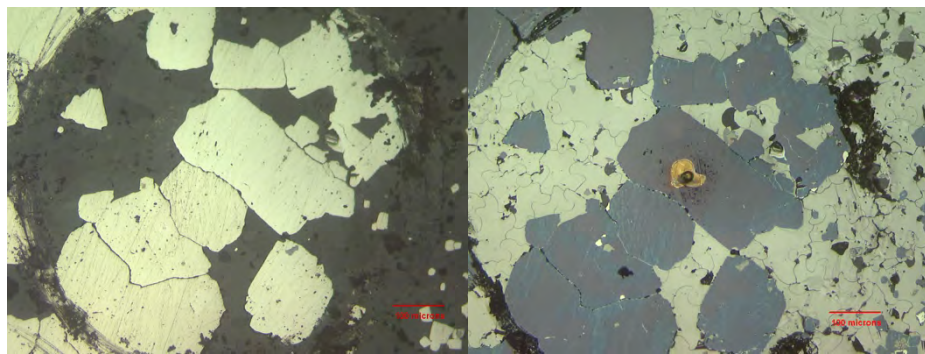
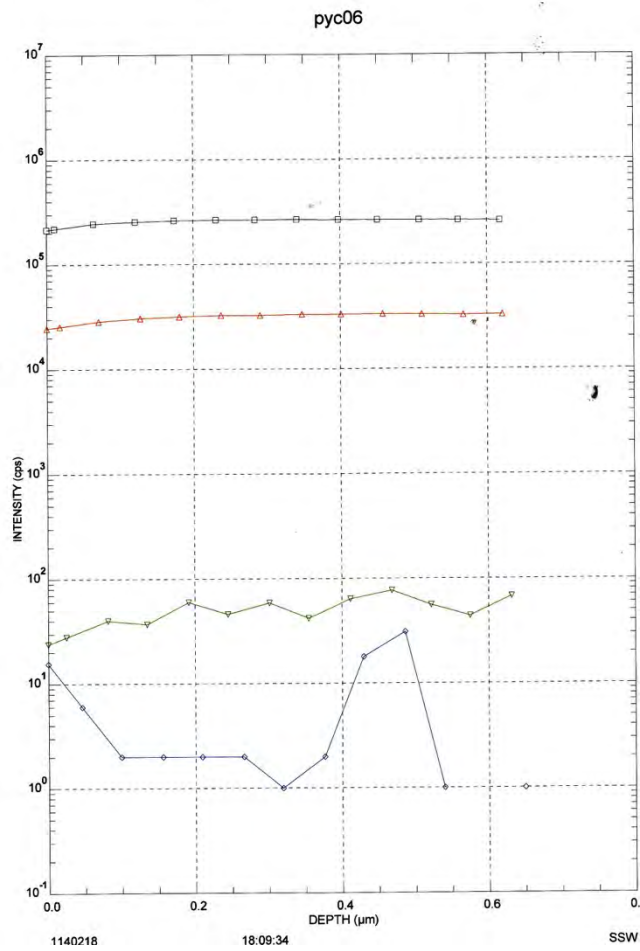
Reflected light images pre-and post-analysis



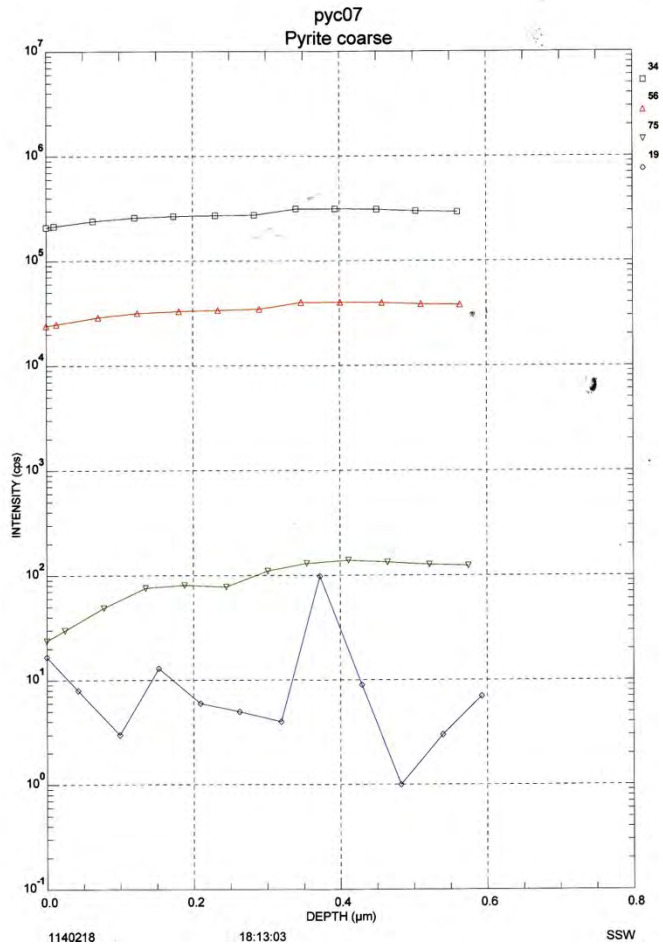
D-SIMS depth profile.



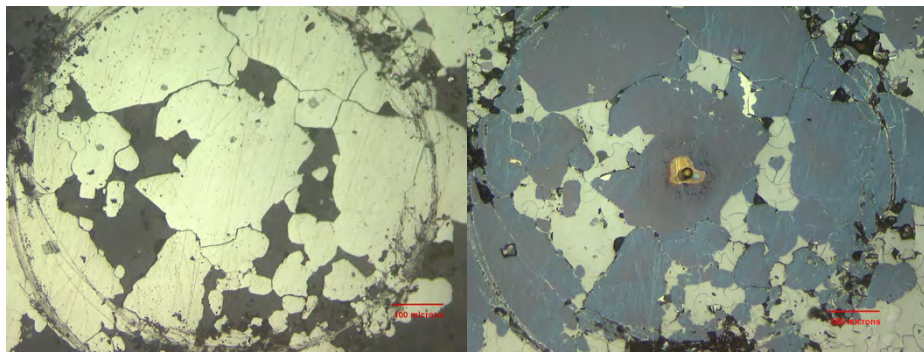
Reflected light images pre-and post-analysis



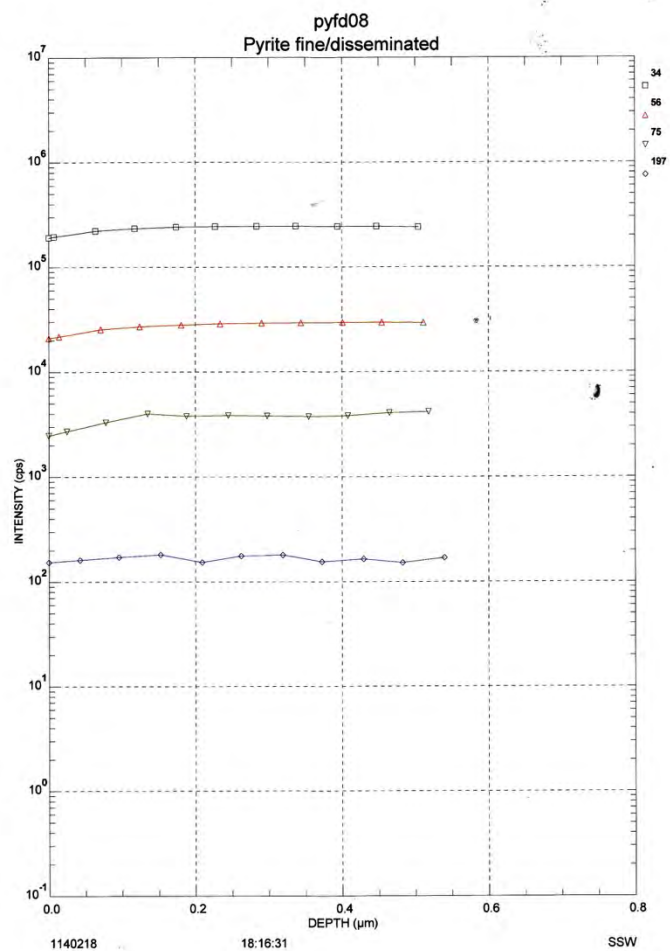
Reflected light images pre-and post-analysis



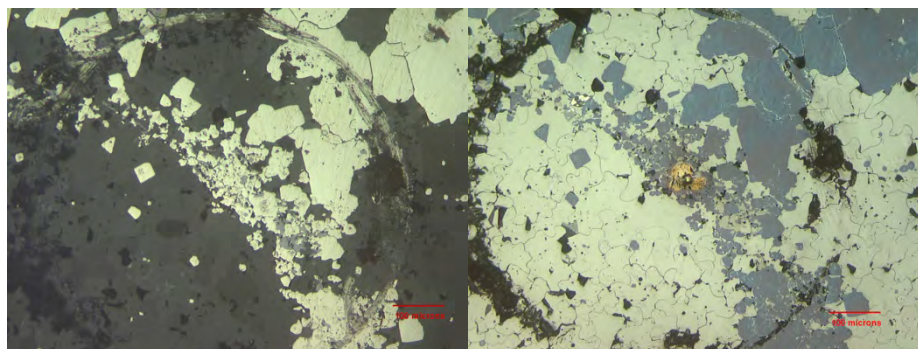
D-SIMS depth profile.



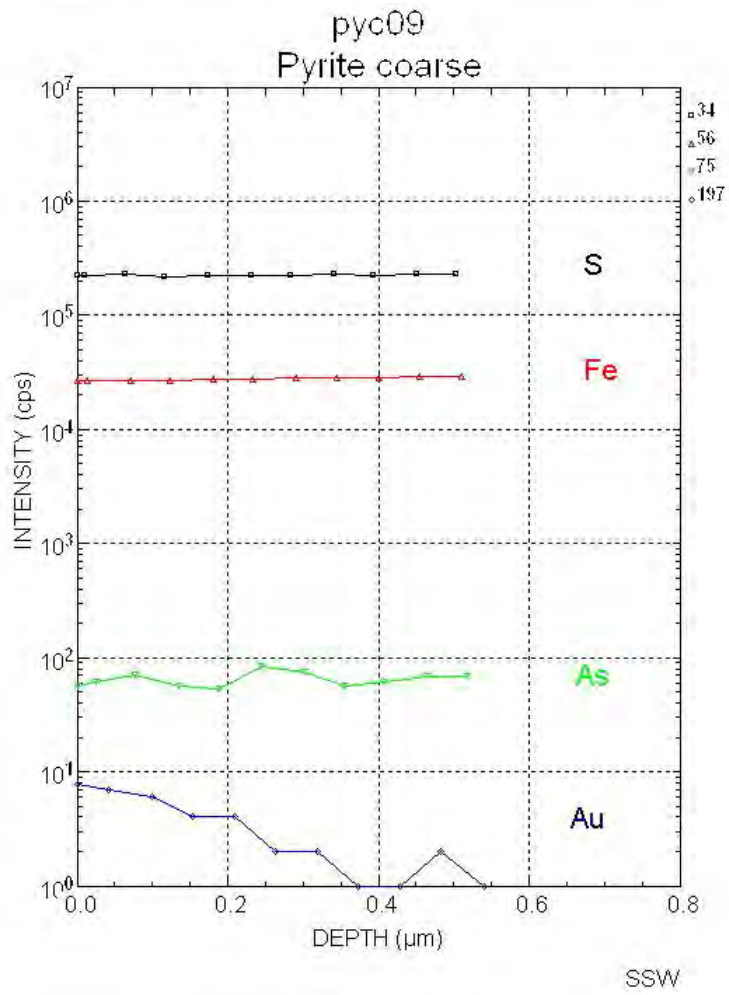
Reflected light images pre-and post-analysis



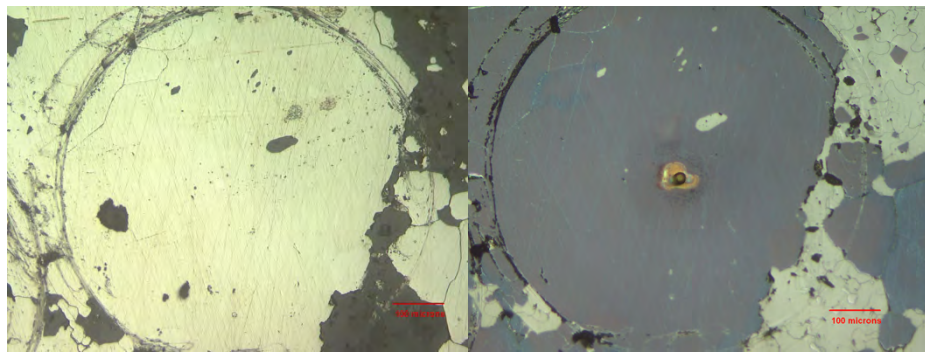
D-SIMS depth profile.



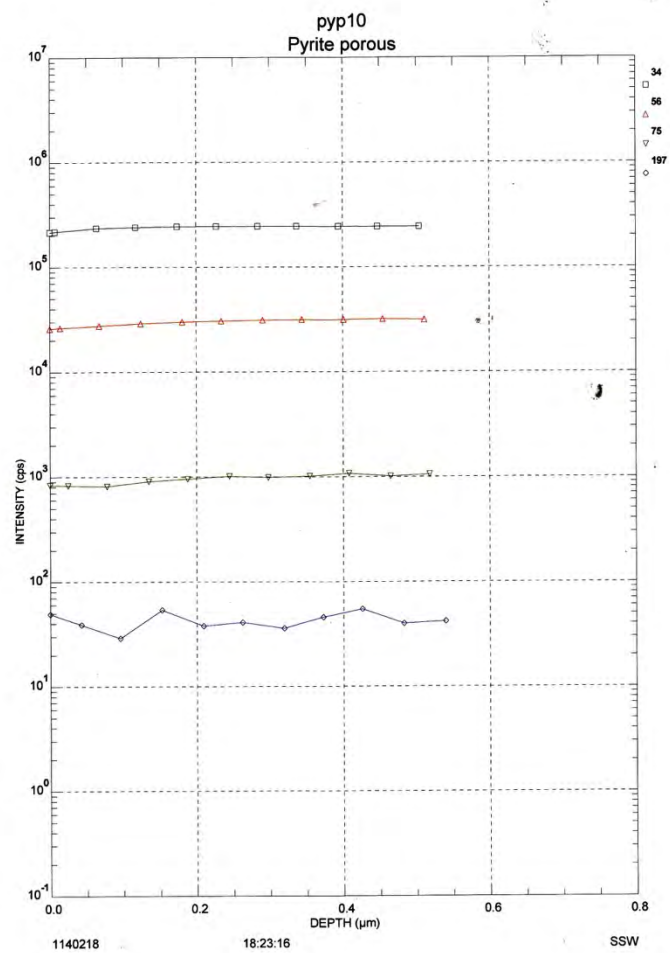
Reflected light images pre-and post-analysis



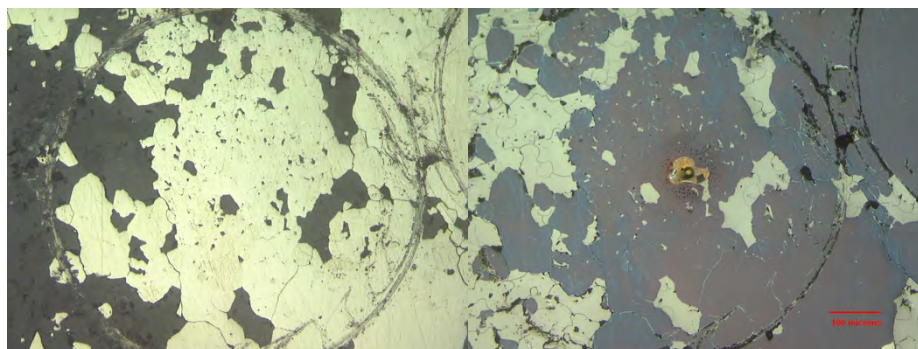
D-SIMS depth profile.



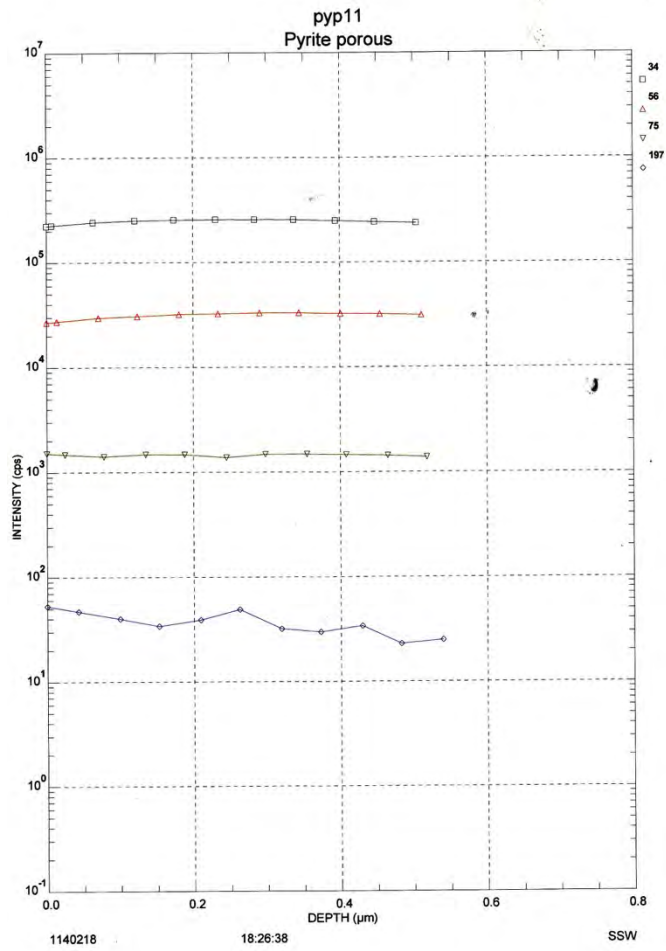
Reflected light images pre-and post-analysis



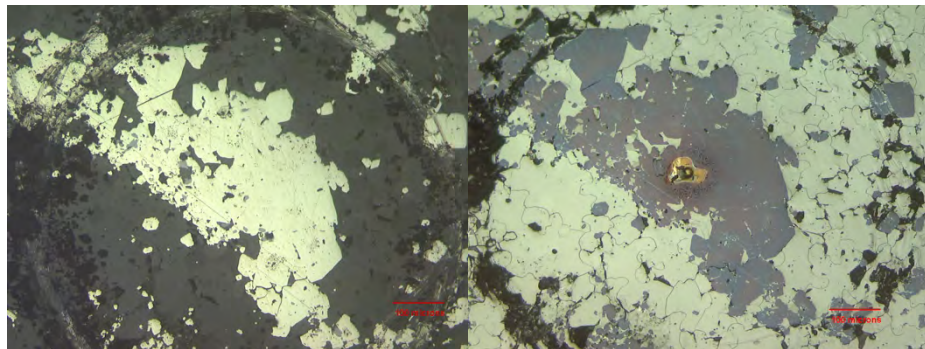
D-SIMS depth profile.



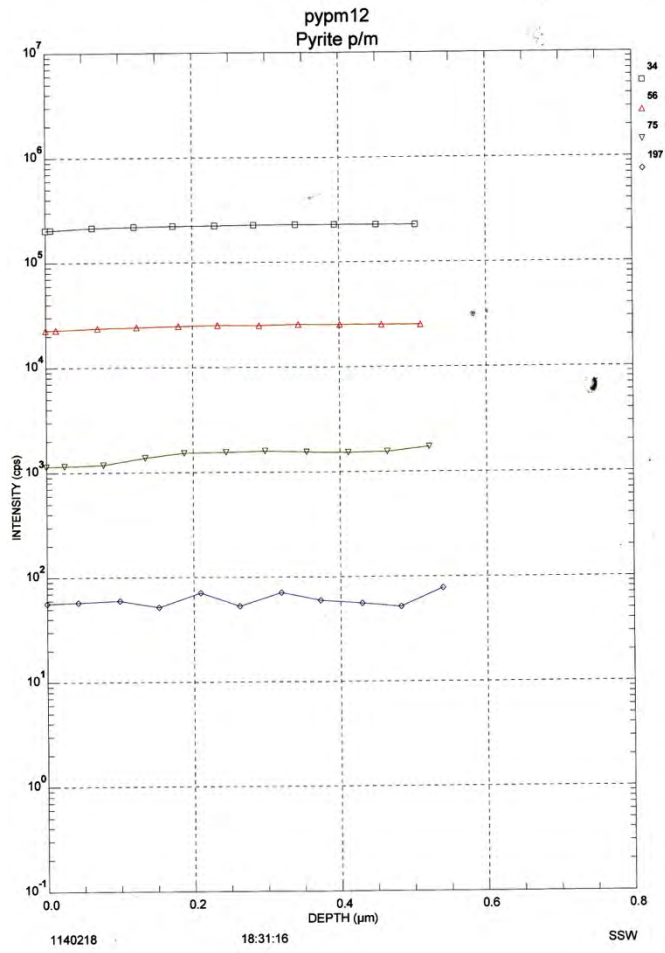
Reflected light images pre-and post-analysis



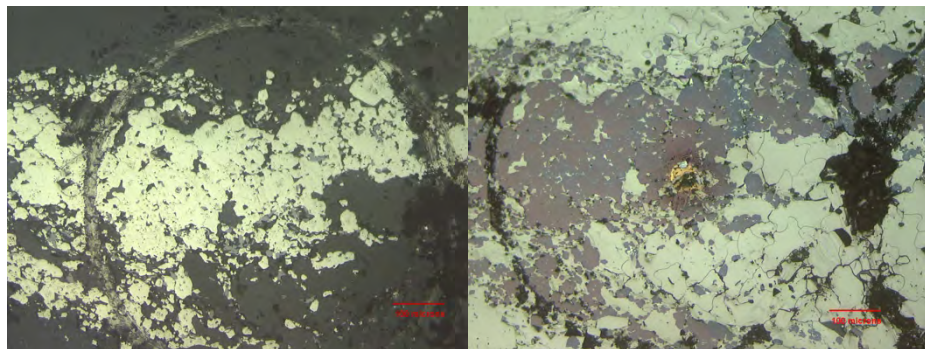
D-SIMS depth profile.



Reflected light images pre-and post-analysis



D-SIMS depth profile.



Reflected light images pre-and post-analysis

Appendix D

Trace Element Mapping

D.1 XRF Parameters

D.1.1 Beamline Specs

	APS 20-ID	CLS VESPERS	CHESSE F3
Source	3.3 Undulator	Bending Magnet	Bending Magnet
Monochromator Type	Si(111)	Si(111)	Si(111)
Energy Range	4.3-27 keV	6-30 keV	7-30 keV
Resolution ($\Delta E/E$)	1.4×10^{-4}	10^{-4}	10^{-4}
Flux (photons/sec)	1×10^{12} @ 10 keV	1×10^9 @ 15 keV	10^9 @ 17 keV
Focused Beam Size (HxV)	$2\mu\text{m} \times 2\mu\text{m}$	$(2-4)\mu\text{m} \times (2-4)\mu\text{m}$	$20\mu\text{m} \times 20\mu\text{m}$
Focus Method	KB Mirrors	KB Mirrors	Monocapillary

D.1.2 Regions of Interest for the APS 20-ID Mapping

Element	Start Bin	End Bin	Start Energy (eV)	End Energy (eV)
Ca $K\alpha$	115	138	3450	4140
Ti $K\alpha$	159	170	4770	5100
Mn $K\alpha$	191	202	5730	6060
Fe $K\alpha$	213	223	6390	6690
Co $K\alpha$	226	236	6780	7080
Ni $K\alpha$	244	254	7320	7620
Co $K\beta$	249	259	7470	7770
Cu $K\alpha$	263	273	7890	8190
W $L\alpha$	274	284	8220	8520
Zn $K\alpha$	282	292	8460	8760
Au $L\alpha$	318	328	9540	9840
As $K\alpha$	346	256	10380	7680
Pb $L\beta_2$	346	356	10380	10680
Bi $L\alpha$	356	366	10680	10980
Se $K\alpha$	369	379	11070	11370
Au $L\beta$	376	386	11280	11580
As $K\beta$	385	395	11550	11850
Pb $L\alpha$	415	445	12450	13350

D.1.3. Mapping Parameters

Figure	Sample Number	Sample Type	Beamline	Energy (keV)	Beam Size (μm)	Step (μm)	Dwell	Filters	Detector	Processing
3-5	C410280	Slab	CHESS F3	13.1	20	20	4 ms	-	Maia	GeoPIXE
3-11	C406934	Stub	APS 20-ID	13.1	2	5	500 ms	5x	Vortex ME-4	2D-Qscanplot
3-12	C306932	Thin Section	APS 20-ID	12.7	2	2	1 s	5x and foil	1-E Vortex	2D-ScanPlot
3-13	C407891A	Thin Section	APS 20-ID	13.1	2	3	100 ms	5x	Vortex ME-4	2D-Qscanplot
3-14A	C407891A	Thin Section	APS 20-ID	13.1	2	5	100 ms	5x	Vortex ME-4	2D-Qscanplot
3-14B	C407891A	Thin Section	CLS VESPERS	Pink	3	3	3 s	250 μm	1-E Vortex	Peakaboo
3-15	C406934	Thin Section	APS 20-ID	13.1	3	2	500 ms	5x and foil	Vortex ME-4	1D-Scanplot
3-16	C407891A (Py1)	Thin Section	APS 20-ID	13.1	2	-	30 s	5x	Vortex ME-4	1D-Scanplot
3-16	C407891A (Py2)	Thin Section	APS 20-ID	13.1	2	-	30 s	5x	Vortex ME-4	1D-Scanplot
3-16	C406934 (Py3)	Thin Section	APS 20-ID	13.1	2	-	30 s	5x and foil	1-E Vortex	1D-Scanplot
3-17	C406932 (Inclusion i)	Thin Section	APS 20-ID	12.7	2	-	30 s	5x and foil	Vortex ME-4	1D-Scanplot
3-17	C406931 (FGII)	Thin Section	APS 20-ID	13.1	2	-	30 s	5x and foil	Vortex ME-4	1D-Scanplot
3-17	C406934 (FGI)	Thin Section	APS 20-ID	13.1	2	-	30 s	5x and foil	1-E Vortex	1D-Scanplot

Figure	Sample Number	Sample Type	Beamline	Energy (keV)	Beam Size (um)	Step (um)	Dwell	Filters	Detector	Processing
4-2	C306932	Thin Section	APS 20-ID	13.1	2	2	200ms	2x	Vortex ME-4	2D-Qscanplot
4-3A	E885276	Thin Section	CHESS F3	13.1	20	20	4msec	-	Maia	GeoPIXE
4-3B	E885276	Thin Section	CLS VESPERS	Pink	5	8	1s	650um	1-E Vortex	Peakaboo
4-3C	E885276	Thin Section	APS 20-ID	13.1	2	2	300ms	2X	Vortex ME-4	2D-Qscanplot
4-4A	C408781	Thin Section	CHESS F3	13.1	20	20	4msec	-	Maia	GeoPIXE
4-4B	C408781	Thin Section	CLS VESPERS	Pink	5	8	1s	450um	1-E Vortex	Peakaboo
4-4C	C408781	Thin Section	APS 20-ID	13.1	2	2	400ms	7X	Vortex ME-4	2D-Qscanplot
4-5A	C406934	Thin Section	CHESS F3	13.3	20	20	4msec	-	Maia	GeoPIXE
4-5B	C406934	Thin Section	APS 20-ID	12.7	2	2	1s	5x and foil	1-E Vortex	2D-ScanPlot
4-6A	C406934	Thin Section	APS 20-ID	13.3	2	2	30s	5x and foil	1-E Vortex	2D-ScanPlot
4-10A	C408779	Thin Section	CHESS F3	13.3	20	20	4msec	-	Maia	GeoPIXE
4-10B	C408779	Thin Section	CLS VESPERS	Pink	3	8	0.5s	800um	4-E Vortex	Peakaboo
4-10C	C408779	Thin Section	APS 20-ID	13.3	3	3	300ms	5x	4-E Vortex	2D-Qscanplot
4-10D	C408779	Slab	CHESS F3	13.3	20	20	4msec	-	Maia	GeoPIXE

Figure	Sample Number	Sample Type	Beamline	Energy (keV)	Beam Size (um)	Step (um)	Dwell	Filters	Detector	Processing
4-10E	C408779	Slab	APS 20-ID	13.3	20	20	300ms	-	4-E Vortex	2D-Qscanplot
4-10F	C408779	Slab	APS 20-ID	13.3	2	2	300ms	-	4-E Vortex	2D-Qscanplot
4-11B	C408779	Thin Section	APS 20-ID	13.3	2	-	30s	5x	4-E Vortex	2D-Qscanplot
4-13	C409401, C410910, BA, C410300, C410280 , C408779	Slabs	CHESS F3	13.3	20	20	4msec	-	Maia	GeoPIXE
4-14	BA	Slab	CHESS F3	13.3	20	20	4msec	-	Maia	GeoPIXE
4-15	C410280	Slab	CHESS F3	13.3	20	20	4msec	-	Maia	GeoPIXE
	C408779	Thin Section	CLS VESPERS	Pink	3	5	500ms	800um	4-E Vortex	Peakaboo
	C408779	Thin Section	APS 20-ID	13	3	2	300ms	4x	4-E Vortex	2D-Qscanplot
	C407899A	Thin Section	APS 20-ID	13	2	2	200msec	6X	4-E Vortex	2D-Qscanplot
	C407891B	Thin Section	APS 20-ID	12.7	3	2	1s	4X	1-E Vortex	2D-ScanPlot

D.1.4 XANES Parameters

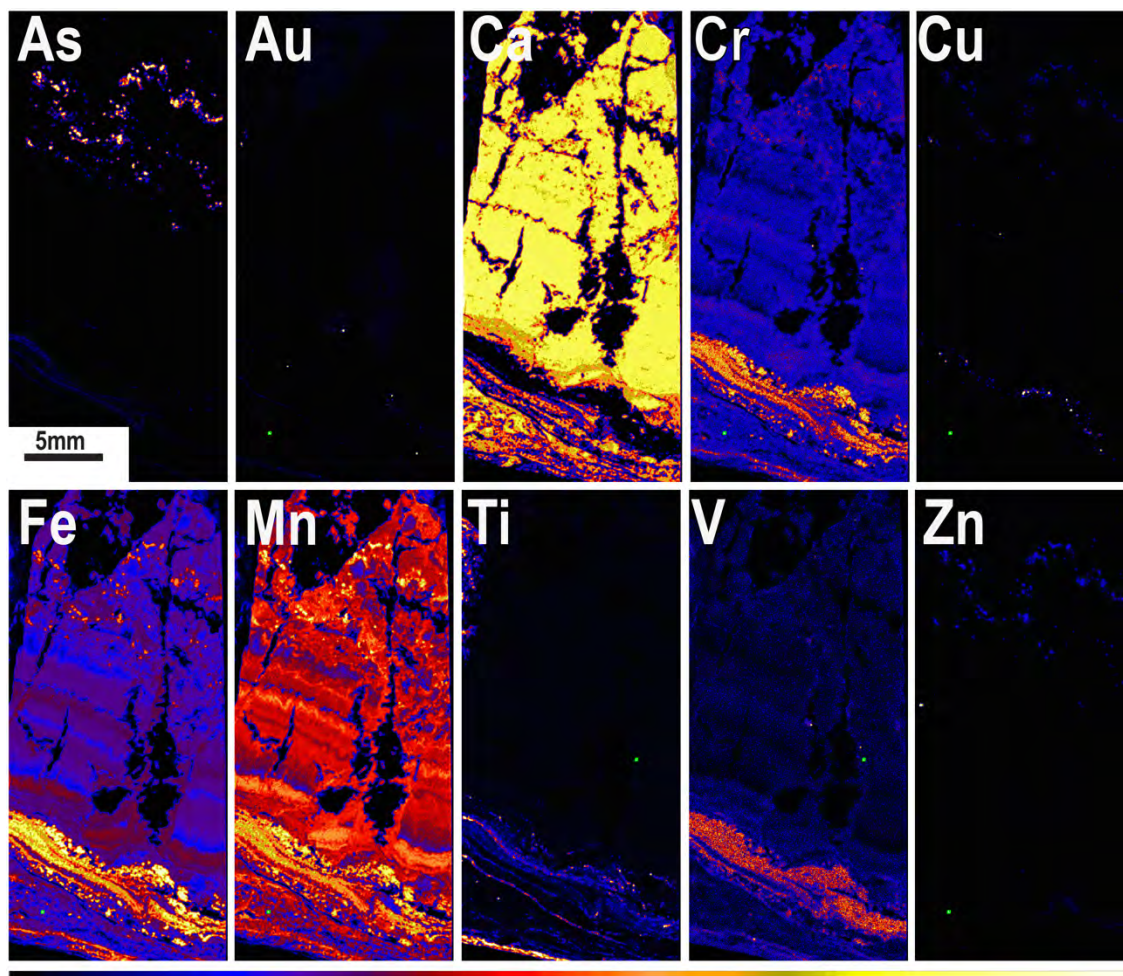
Figure	Sample	Edge	E0	# scans	Scan Bounds	Scan Step	IT	Filters	Detector
4-6C	C406934 (black)	As-K	11868	3	-150, -20, 20, 9k	5eV, 0.5 eV, 0.05K	1	4x	Vortex ME-4
	C406934 (red)	As-K	11868	5	-150, -20, 20, 9k	5eV, 0.5 eV, 0.05K	1	4x	Vortex ME-4
	C406934 (blue)	As-K	11868	5	-150, -20, 20, 9k	5eV, 0.5 eV, 0.05K	1	4x	Vortex ME-4
4-6D	C406934	Au-L3	11919	7	-150, -20, 20, 9k	5eV, 0.5 eV, 0.05K	1	4x	Vortex ME-4
4-11C	C408779 (black)	As-K	11867	5	-150, -30, 20, 9k	5eV, 0.5 eV, 0.05K	1	6x	Vortex ME-4
	C408779 (red)	As-K	11867	3	-150, -30, 20, 9k	5eV, 0.5 eV, 0.05K	1	6x	Vortex ME-4
	C408779 (blue)	As-K	11867	3	-150, -30, 20, 9k	5eV, 0.5 eV, 0.05K	1	6x	Vortex ME-4

*Scan bounds are relative to E0

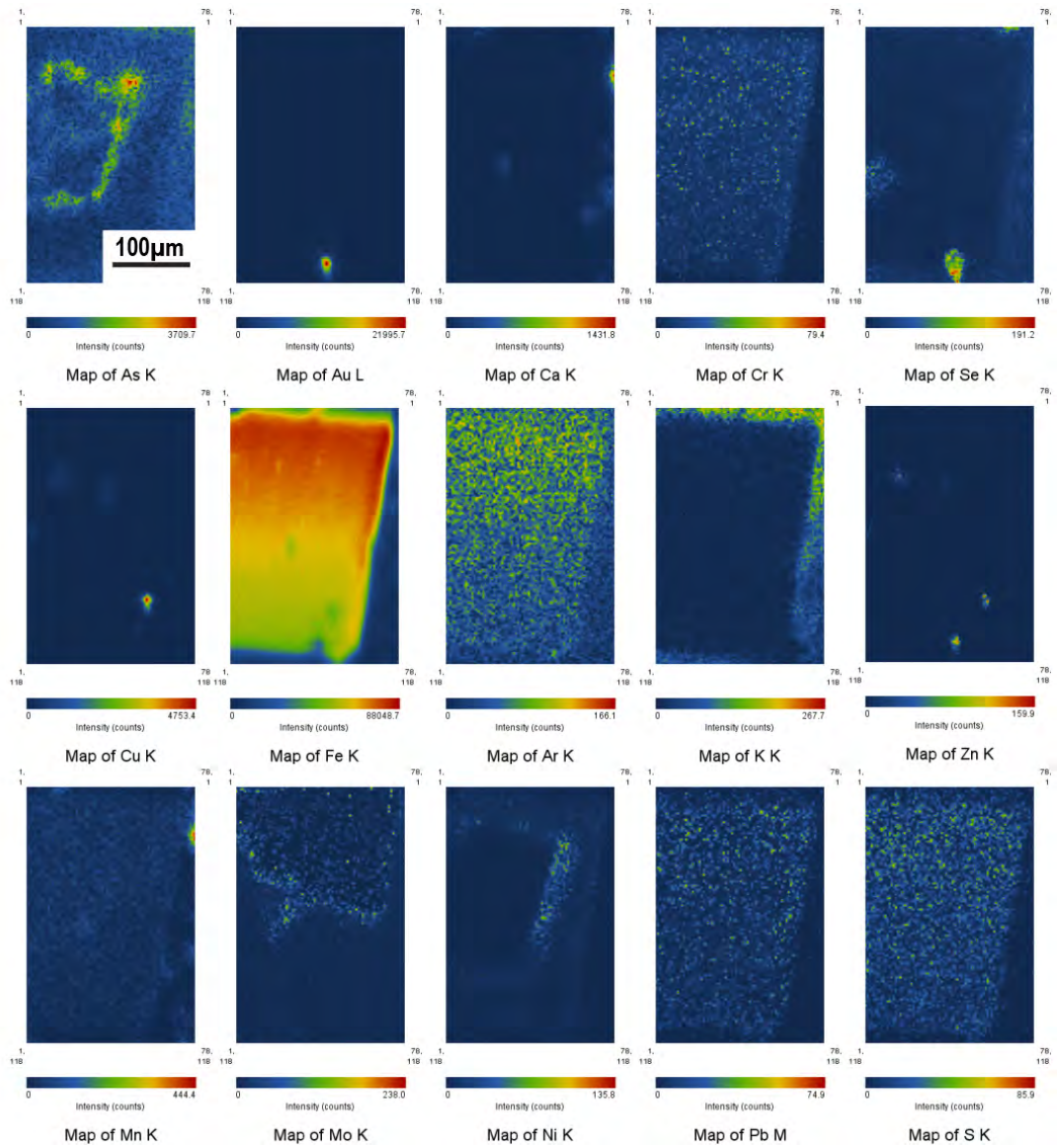
*IT – Integration time

D.2 SR-XRF Maps

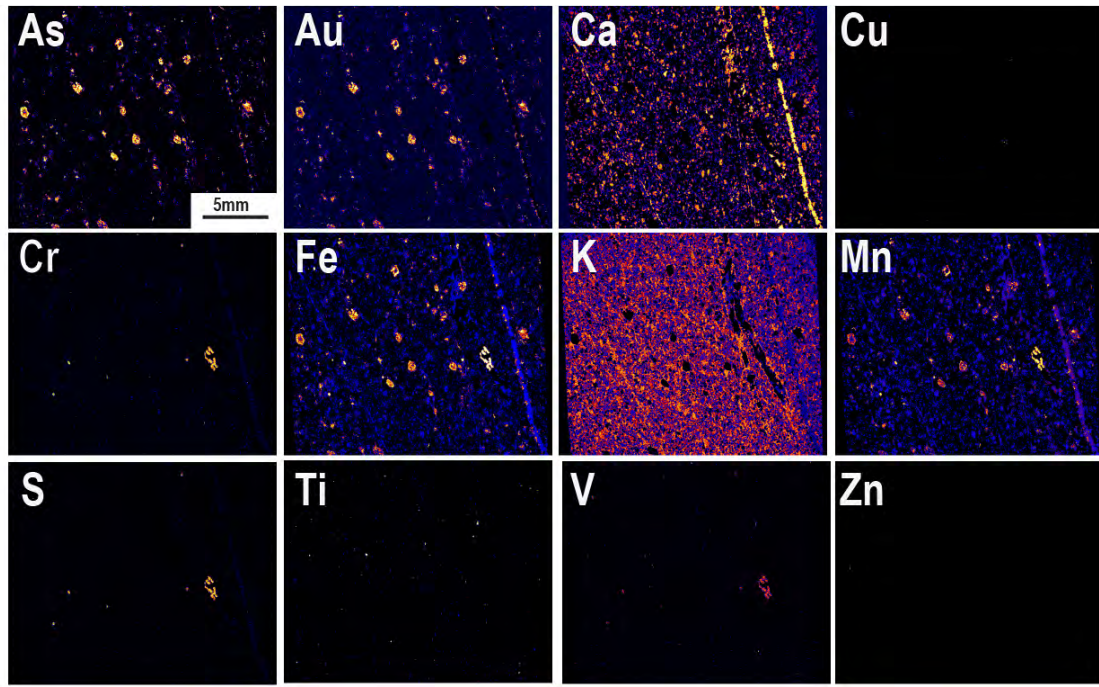
SR-XRF maps from figures in text for which not all confirmed elemental maps were shown (CHESS and Peakaboo), and complementary maps to D.3 EMPA mapping. All mapping parameters are in Appendix D.1.3.



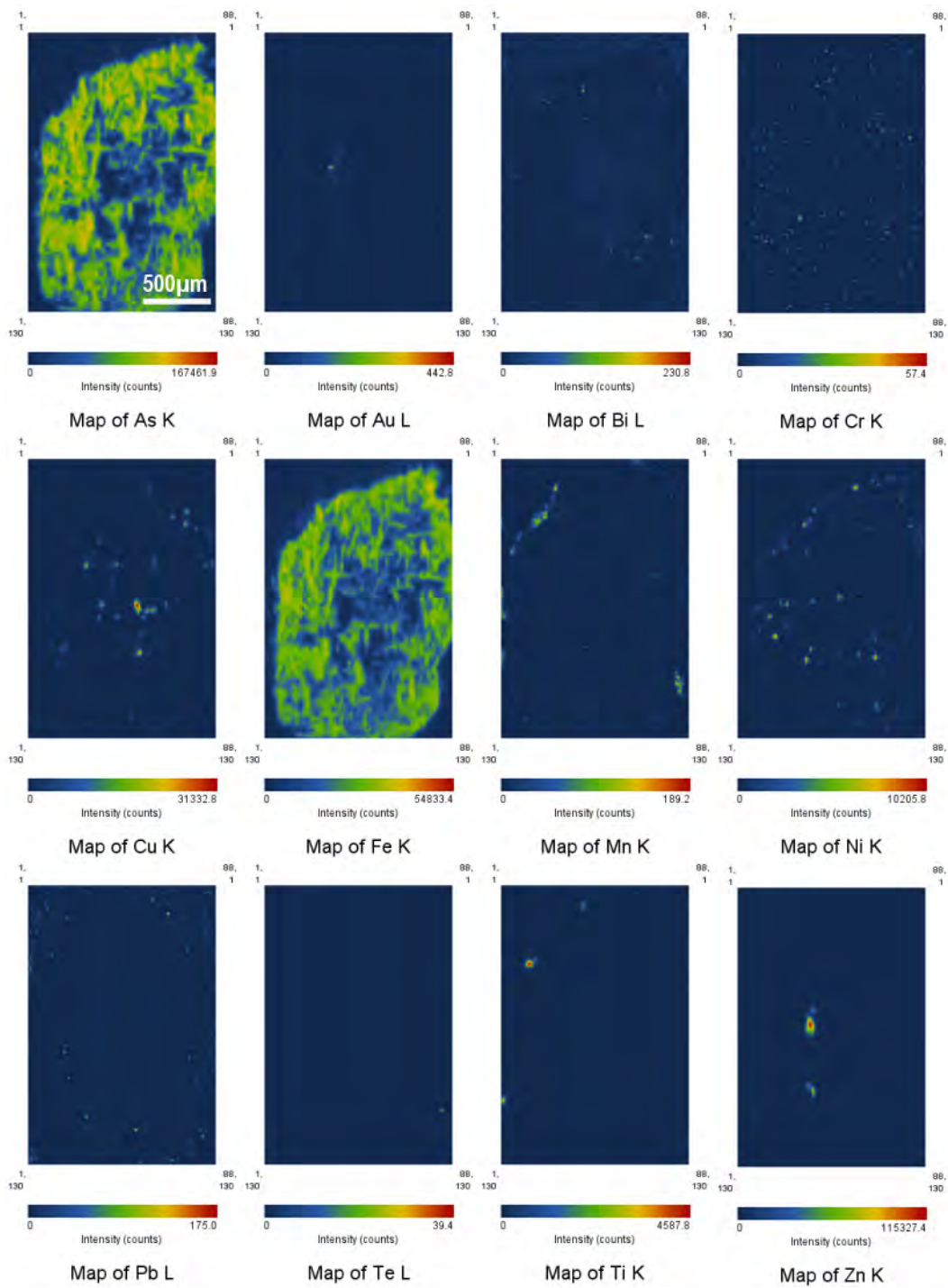
SR-XRF maps of sample C410280 (Figure 3-5, 4-13, 4-15)



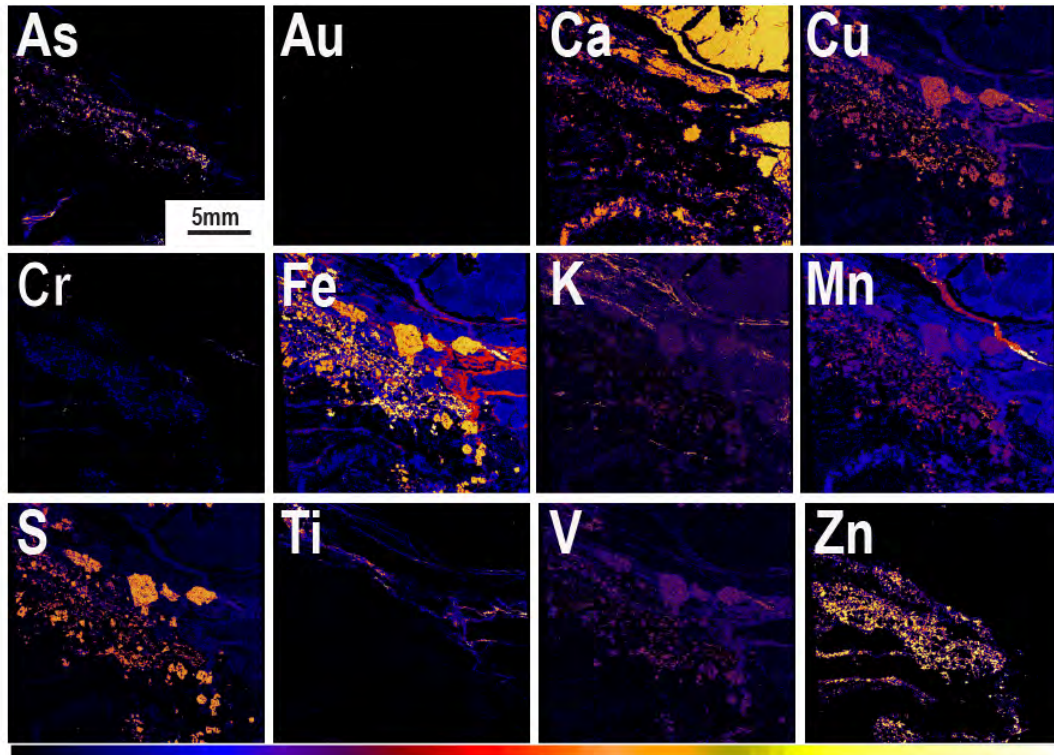
SR-XRF maps of C4078991A (Figure 3-14B)



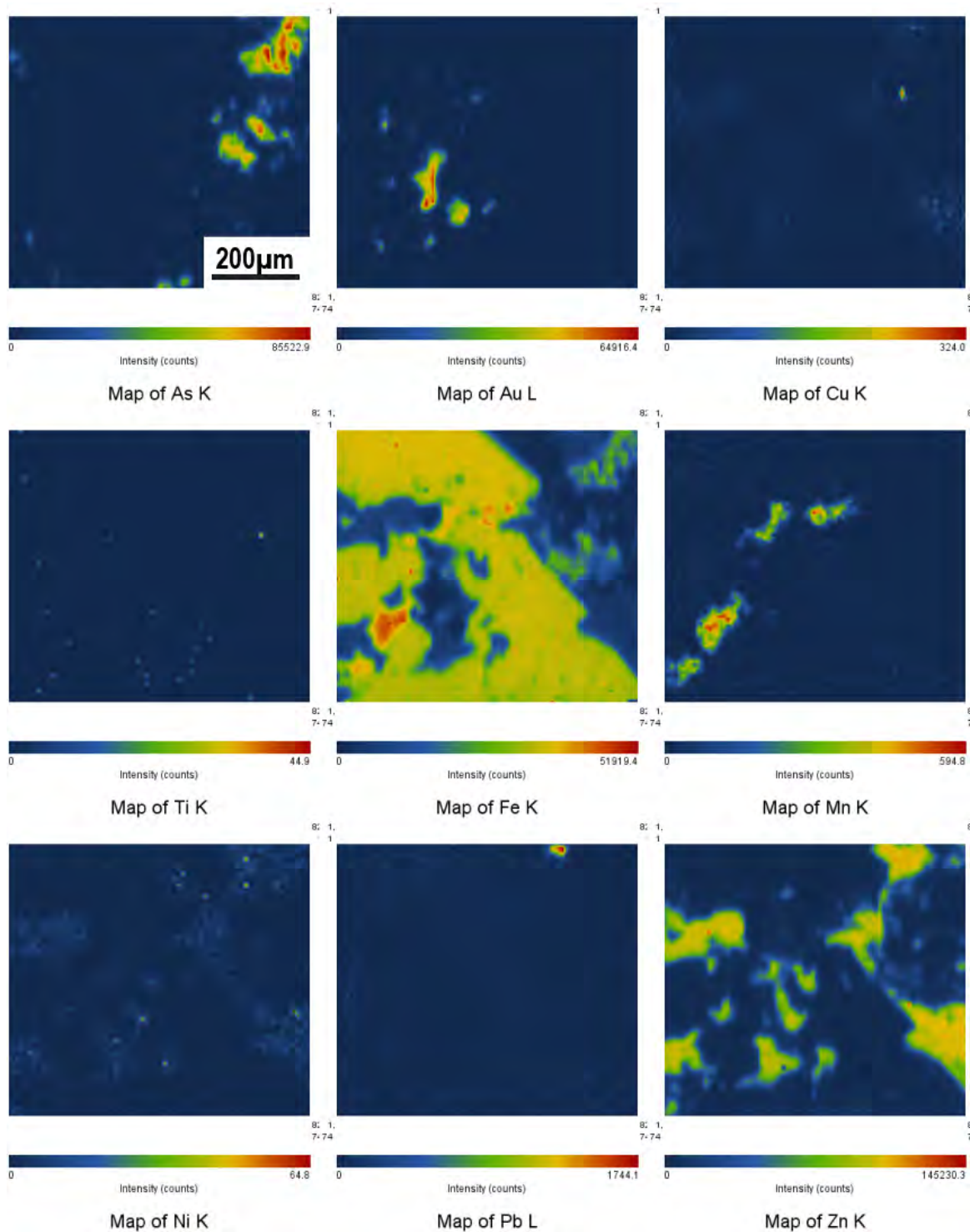
SR-XRF maps of E885276 (Figure 4-3A)



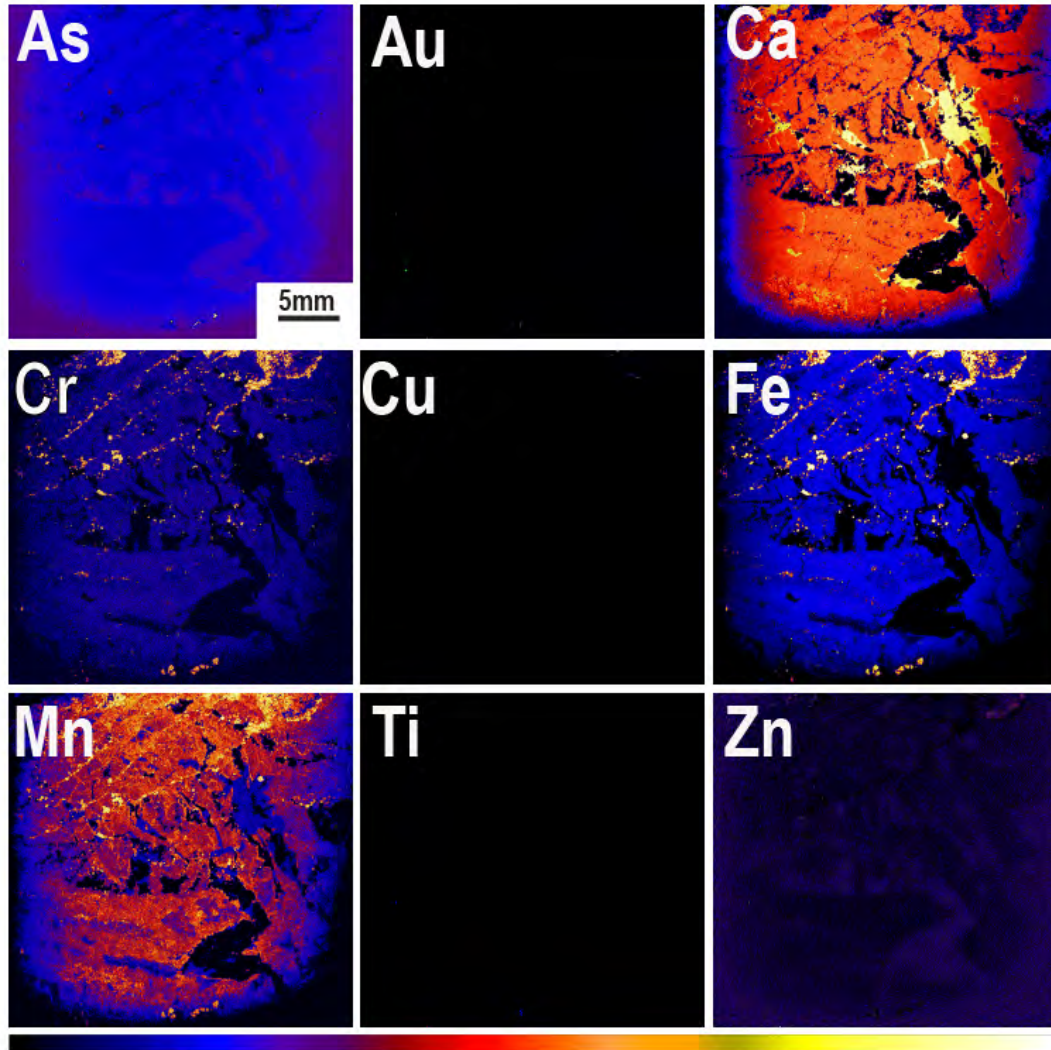
SR-XRF maps of E885276 (Figure 4-3B)



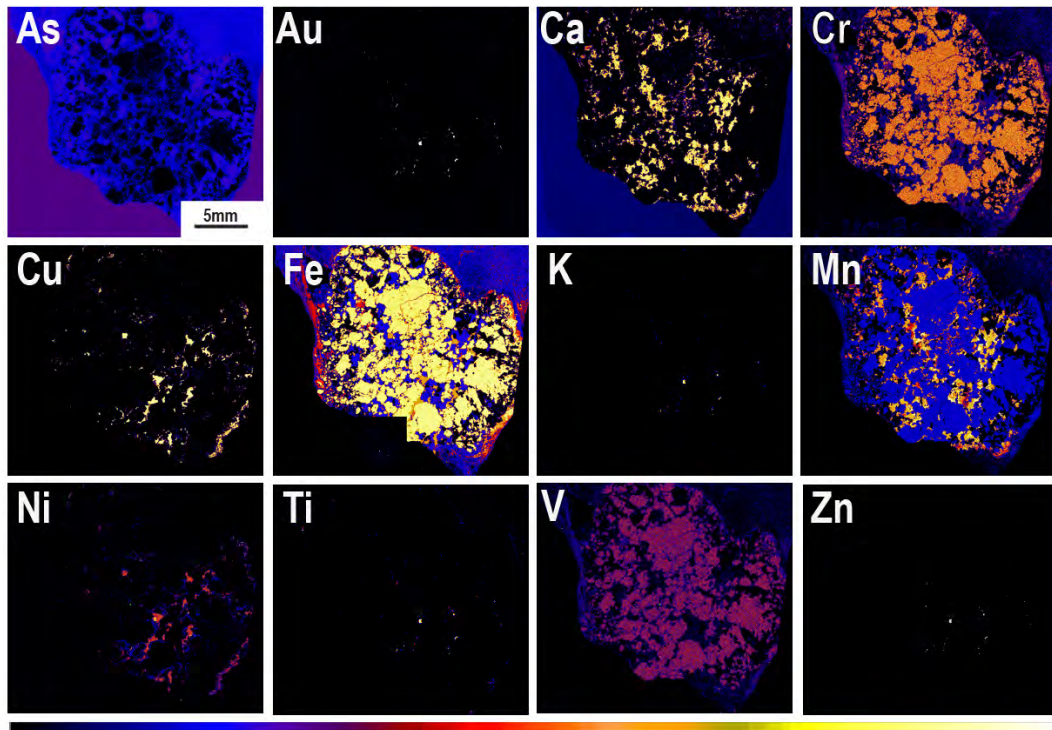
SR-XRF maps of C408781 (Figure 4-4A)



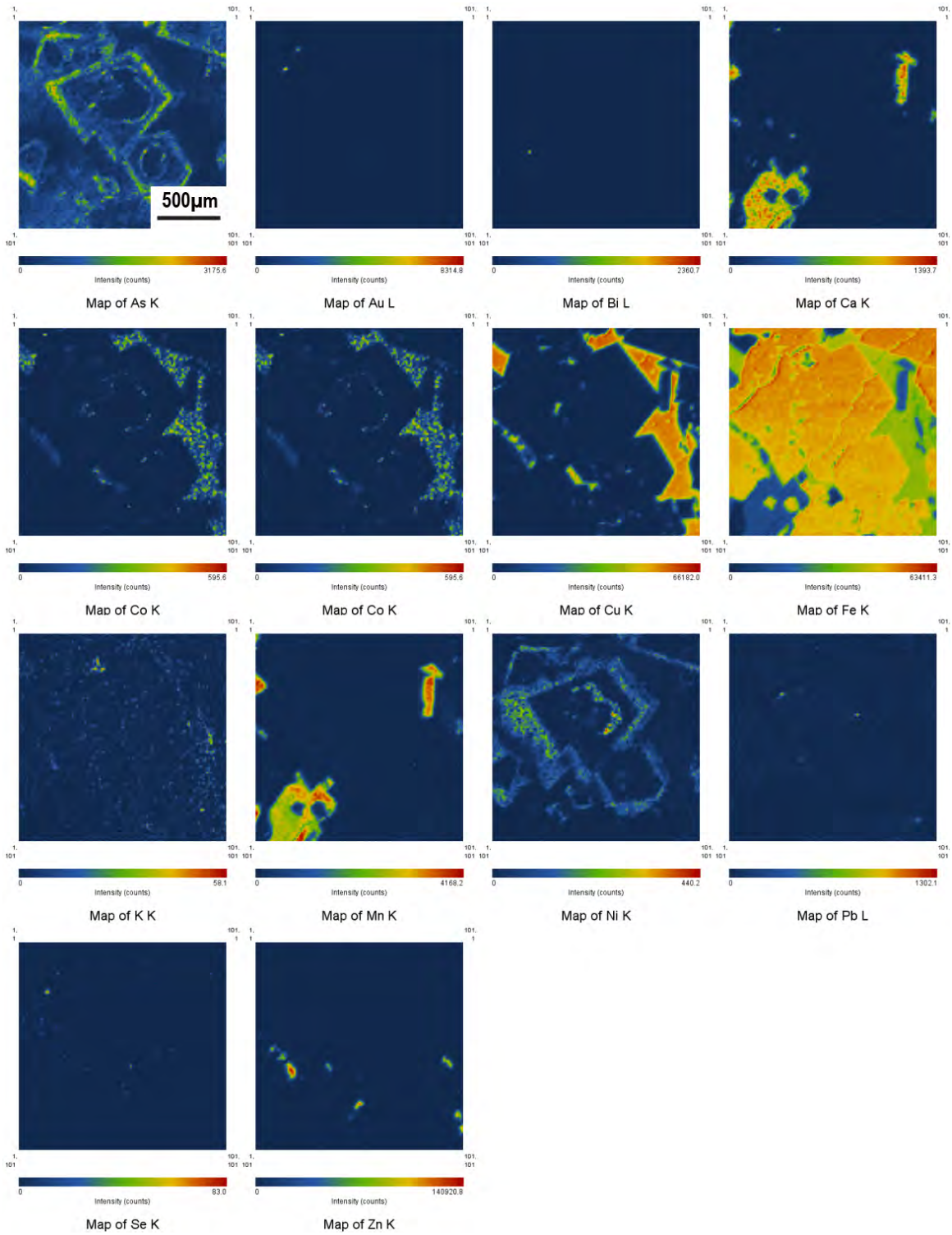
SR-XRF maps of C408781 (Figure 4-4B)



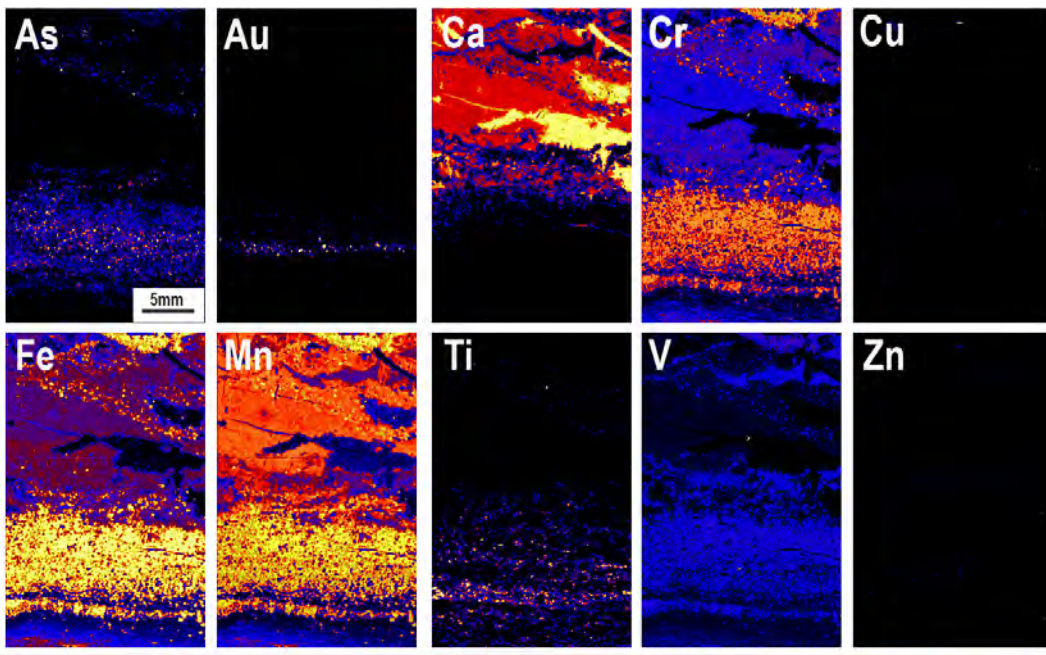
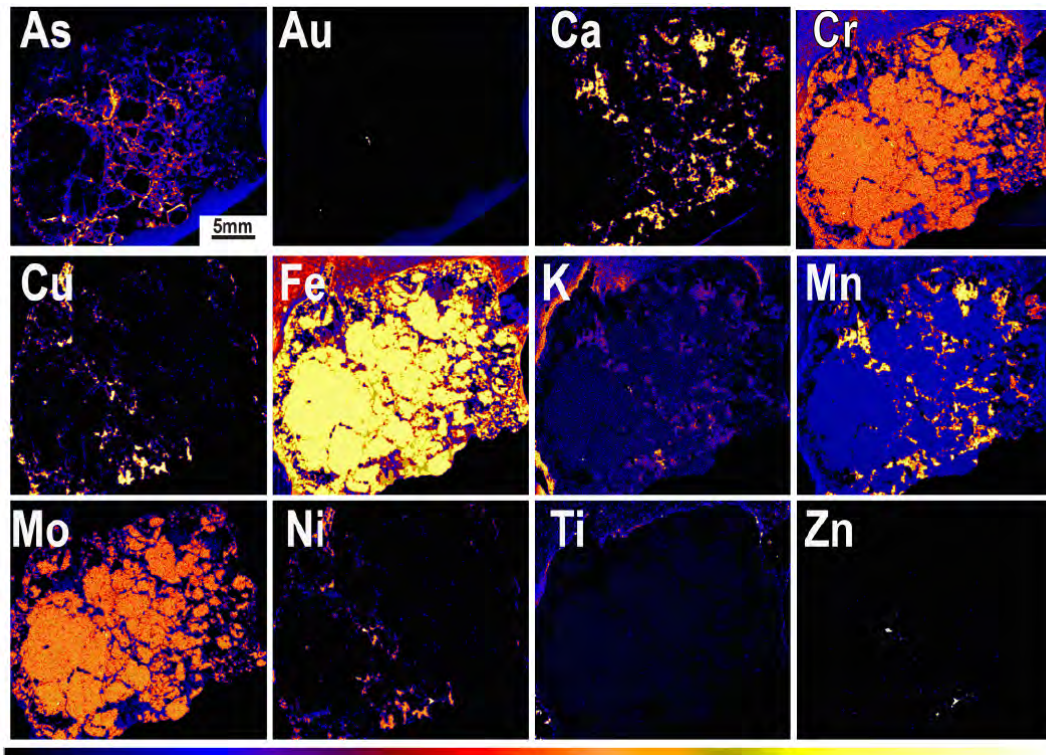
SR-XRF maps of C406934 (Figure 4-5A)

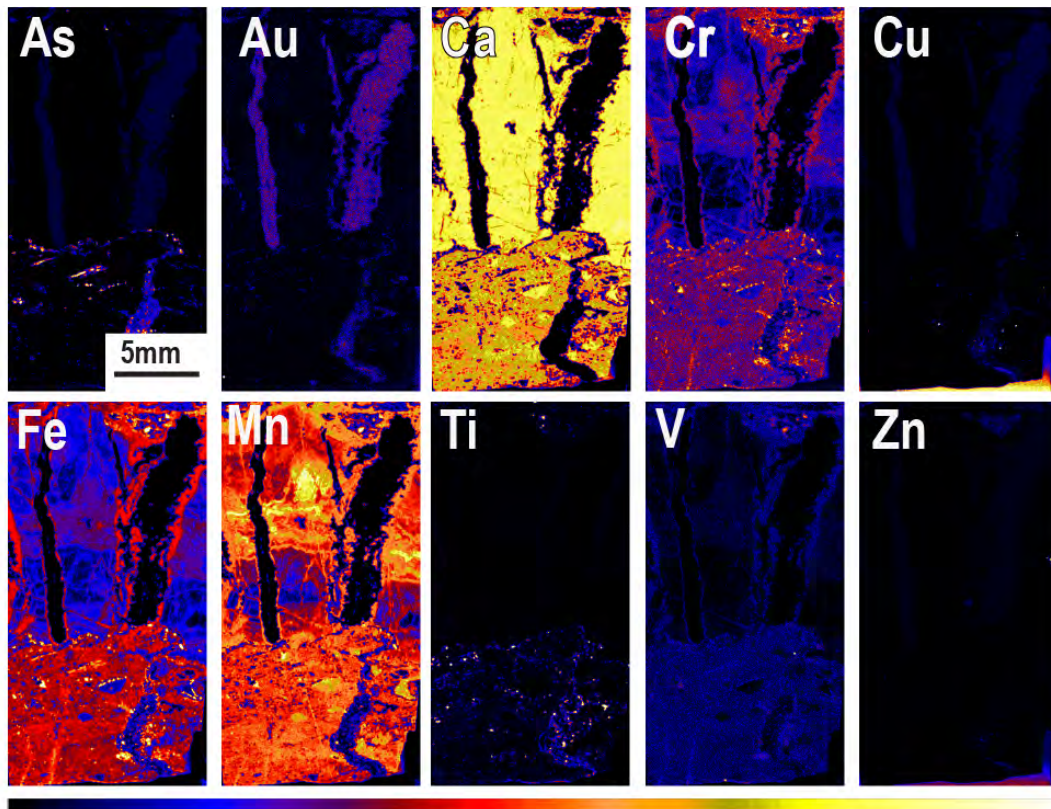


SR-XRF maps of C408779 (Figure 4-10A)

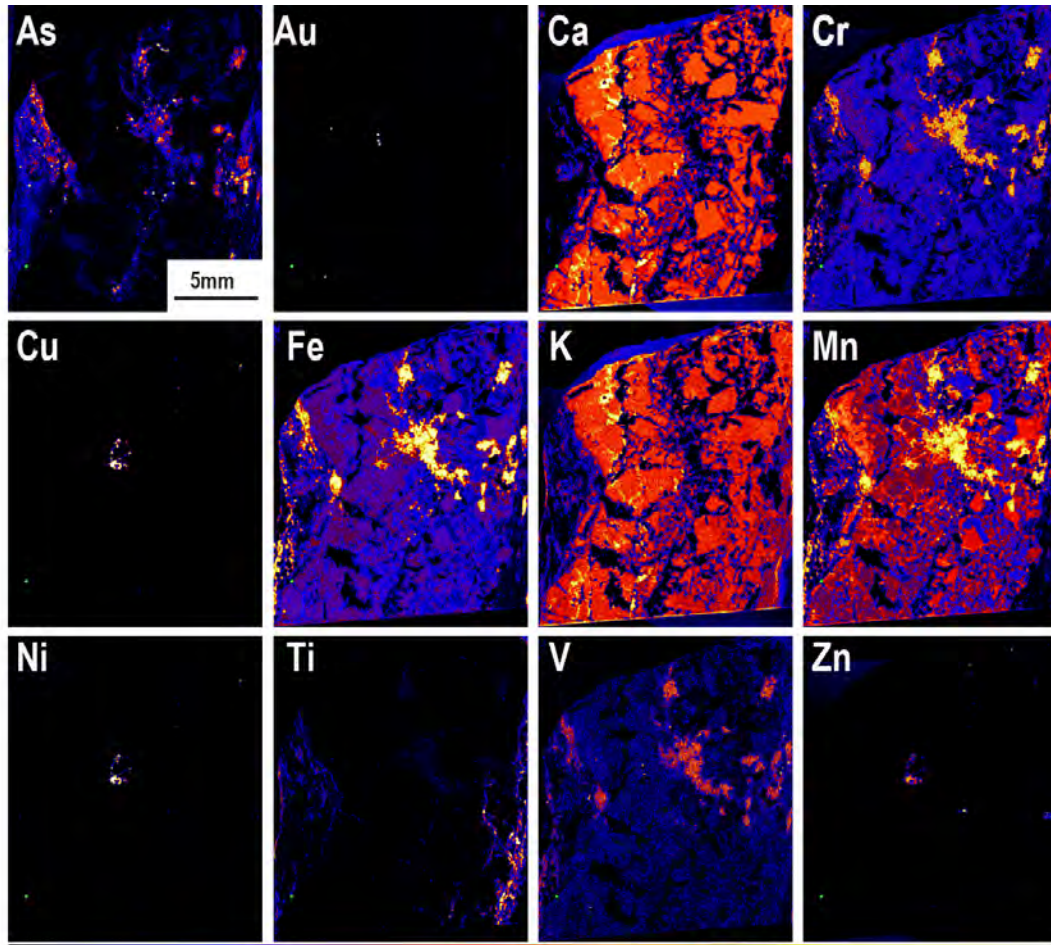


SR-XRF maps of C408779 (Figure 4-10B)

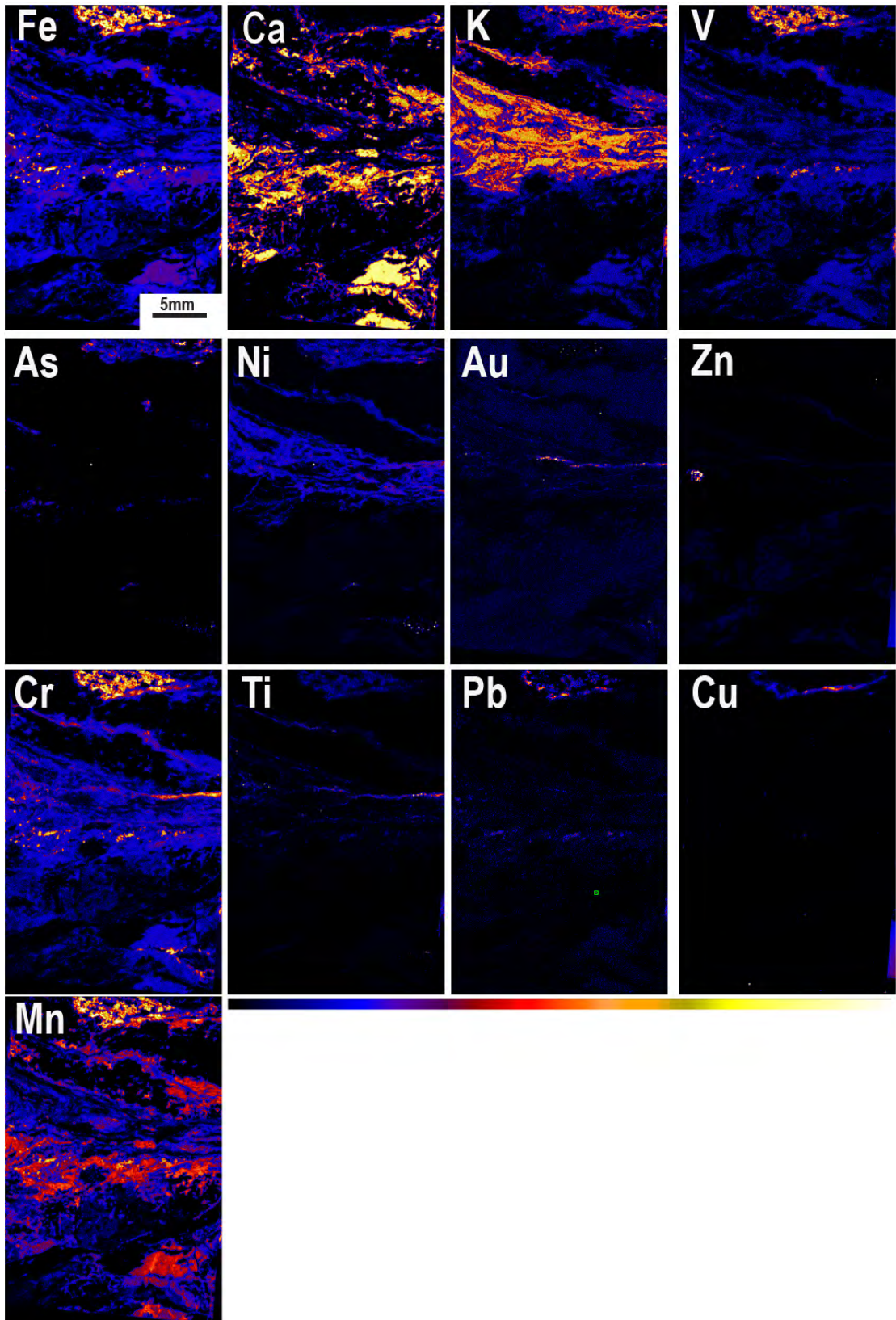




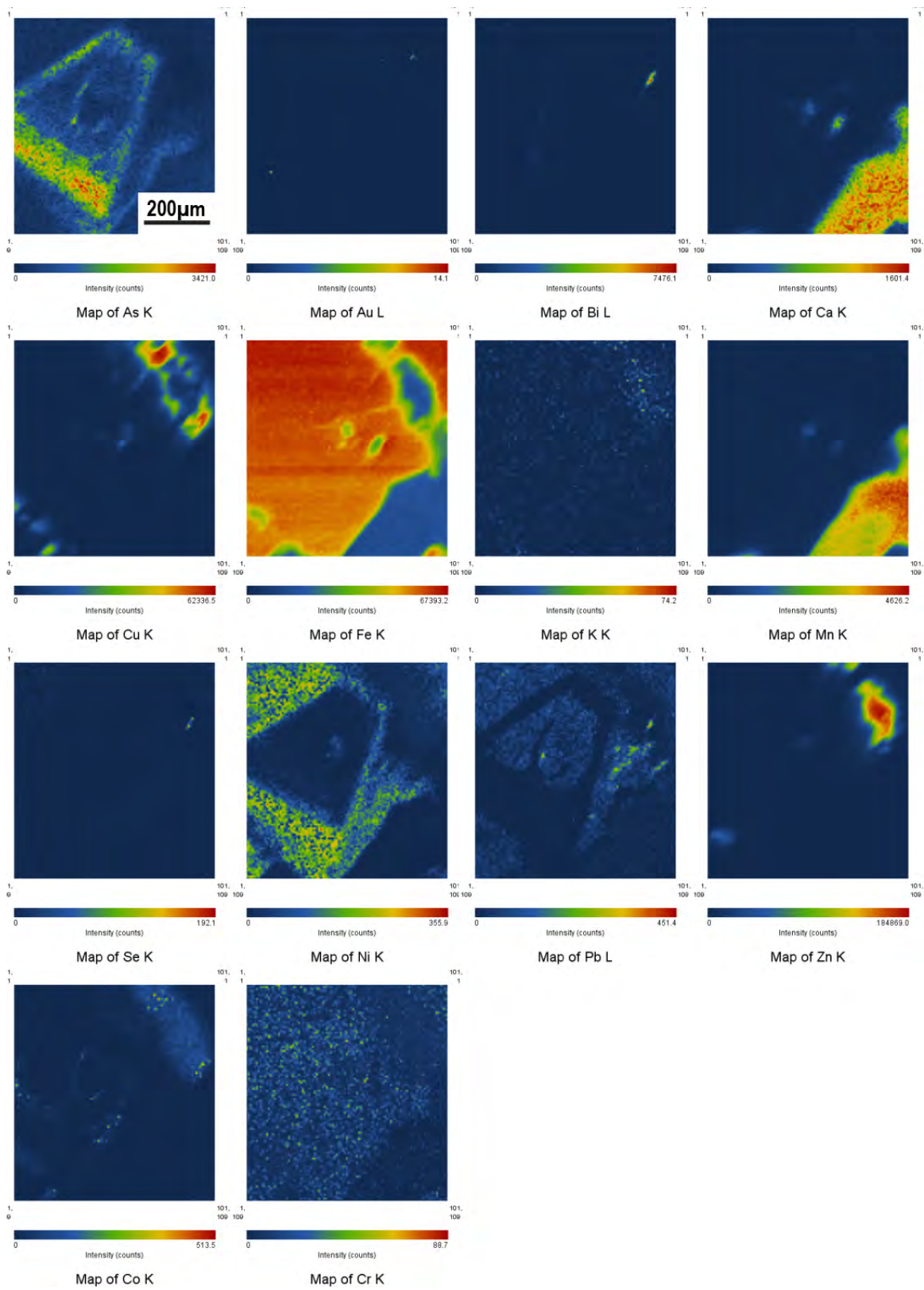
SR-XRF maps of C410910 (Figure 4-13)



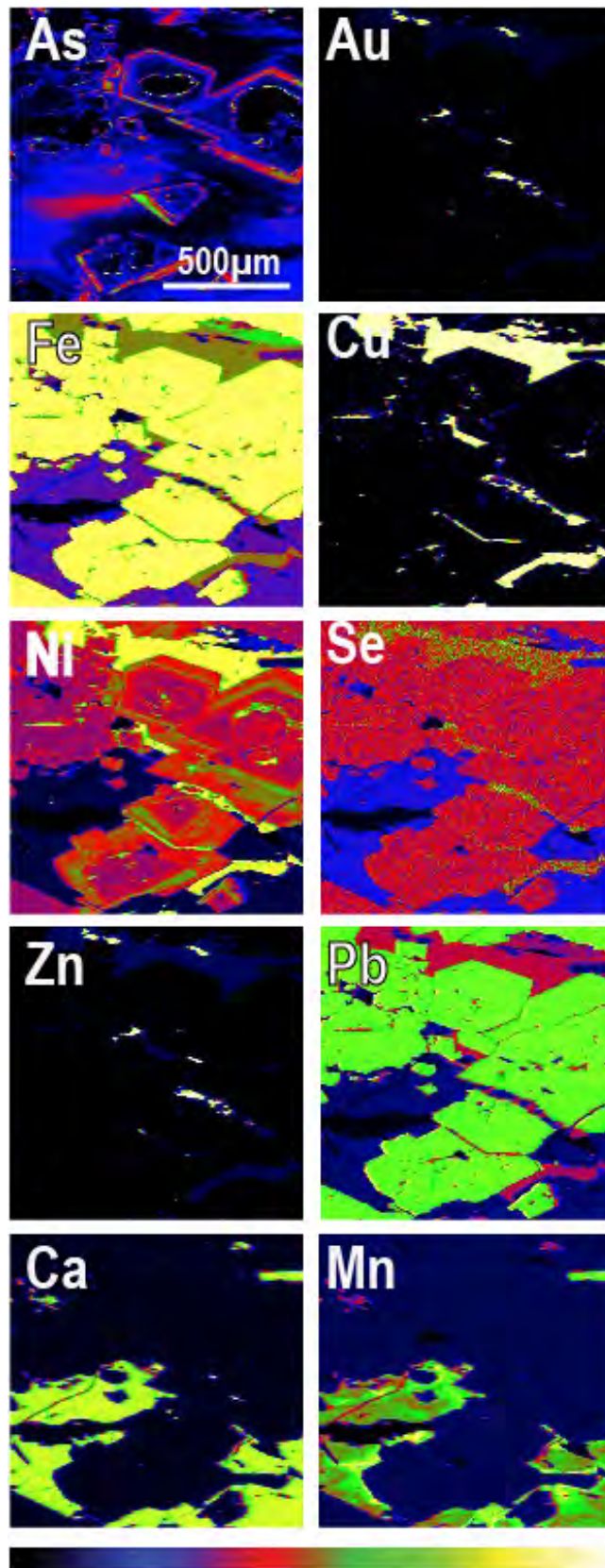
SR-XRF maps of C410300 (Figure 4-13)



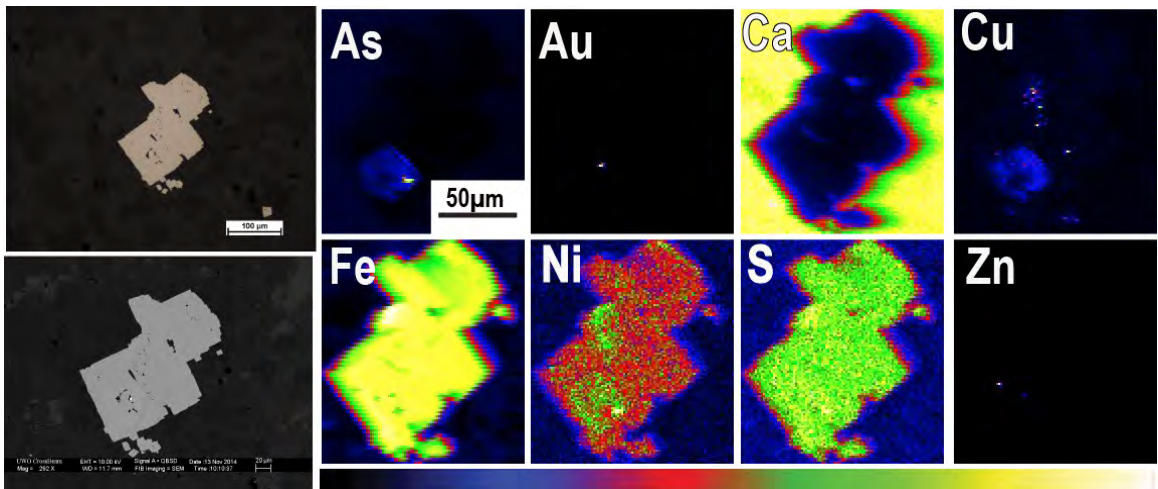
SR-XRF maps of BA (Figure 4-13, 4-14)



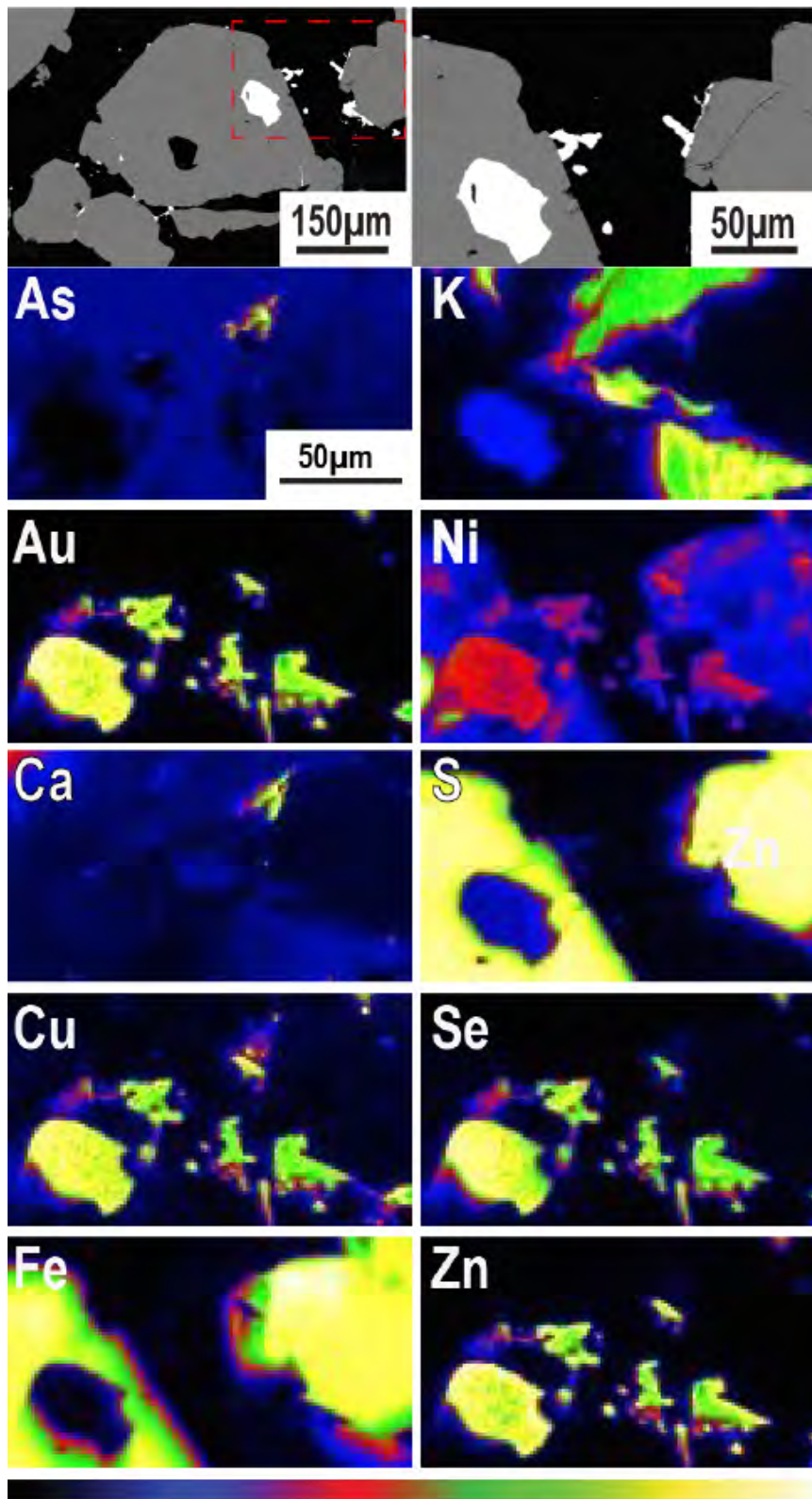
SR-XRF maps C408779 (complements Figure 4-10)



SR-XRF maps of C408779 (complements Figure 4-10)

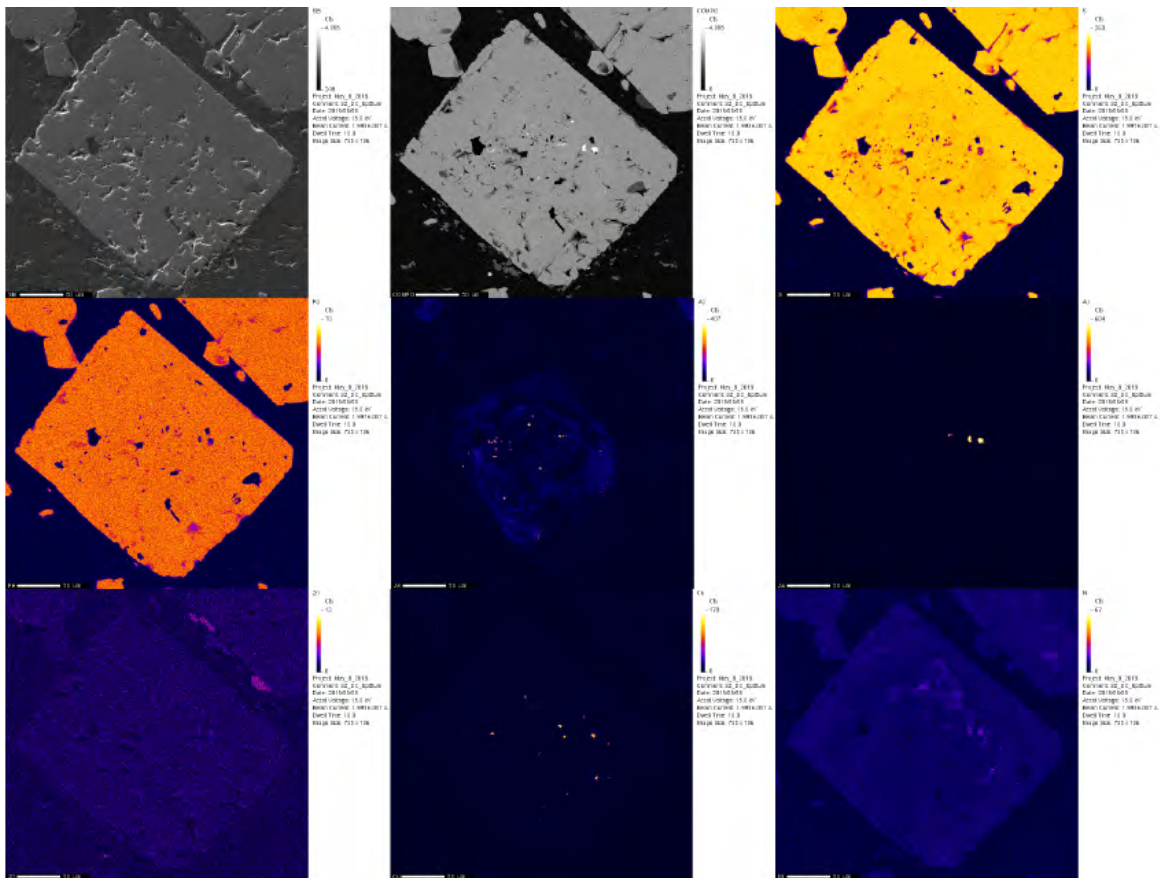


SR-XRF maps of C407899A (complements D.3 EMPA map)

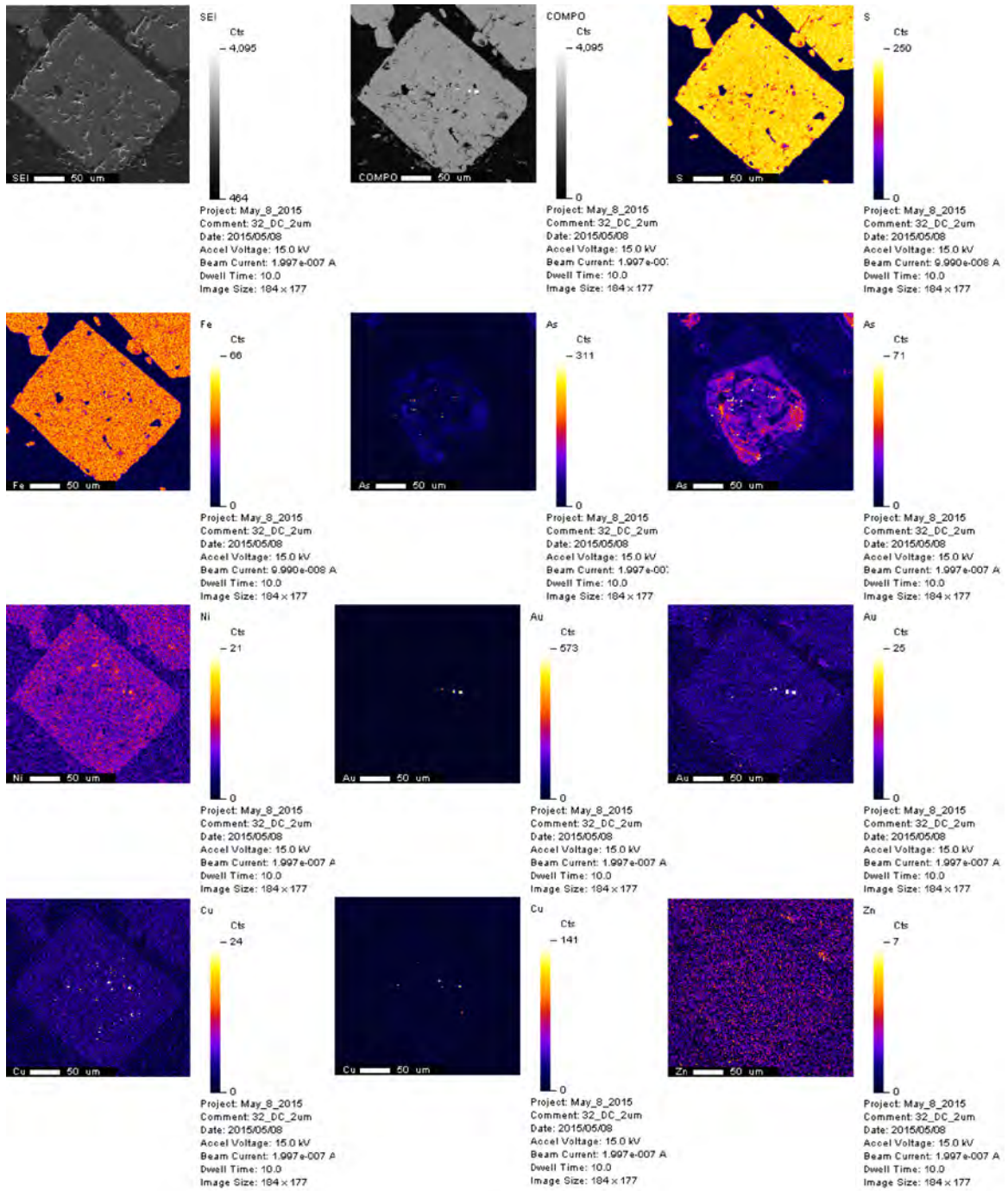


SR-XRF maps of C407891B (complements D.3 EMPA map)

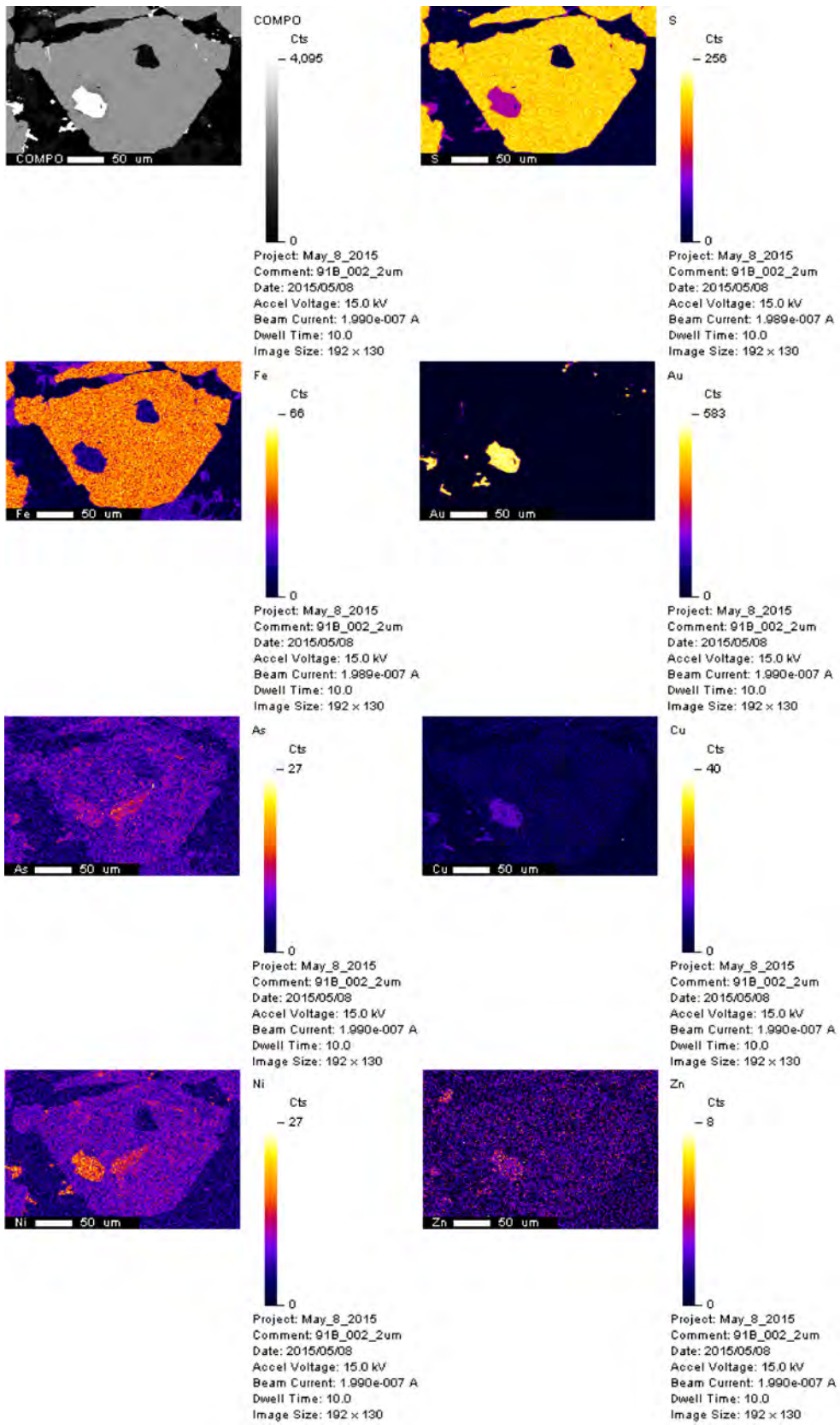
D.3 Electron Microprobe Maps



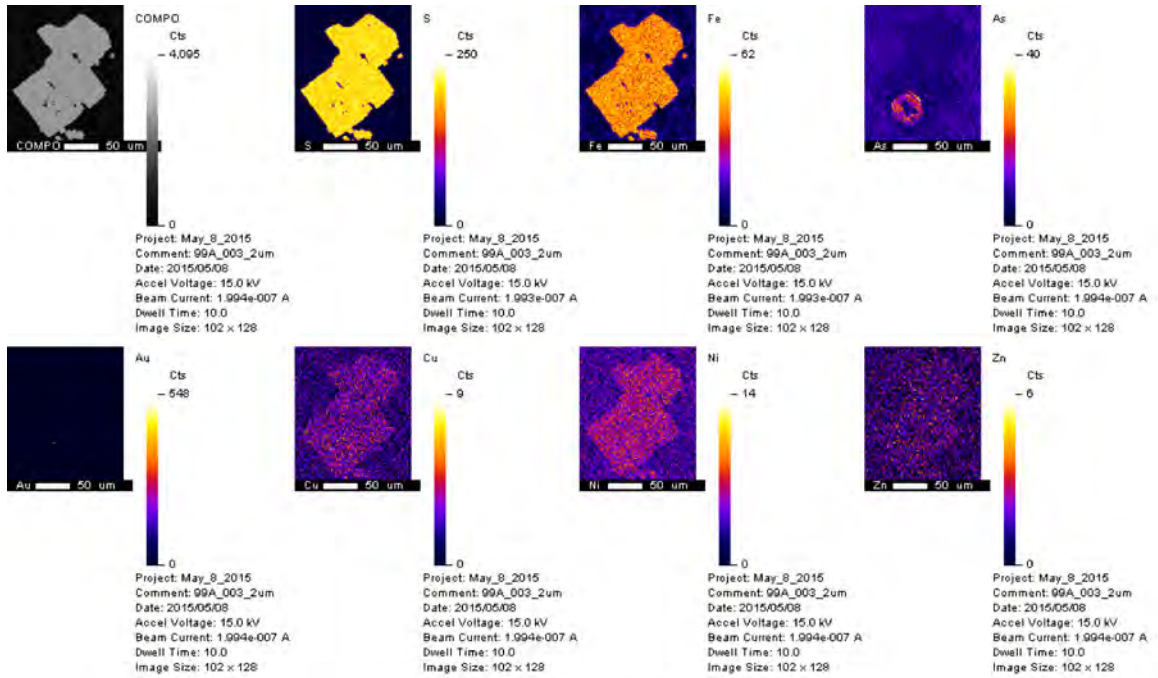
0.5 µm resolution maps of C406932 (Figure 4-2)



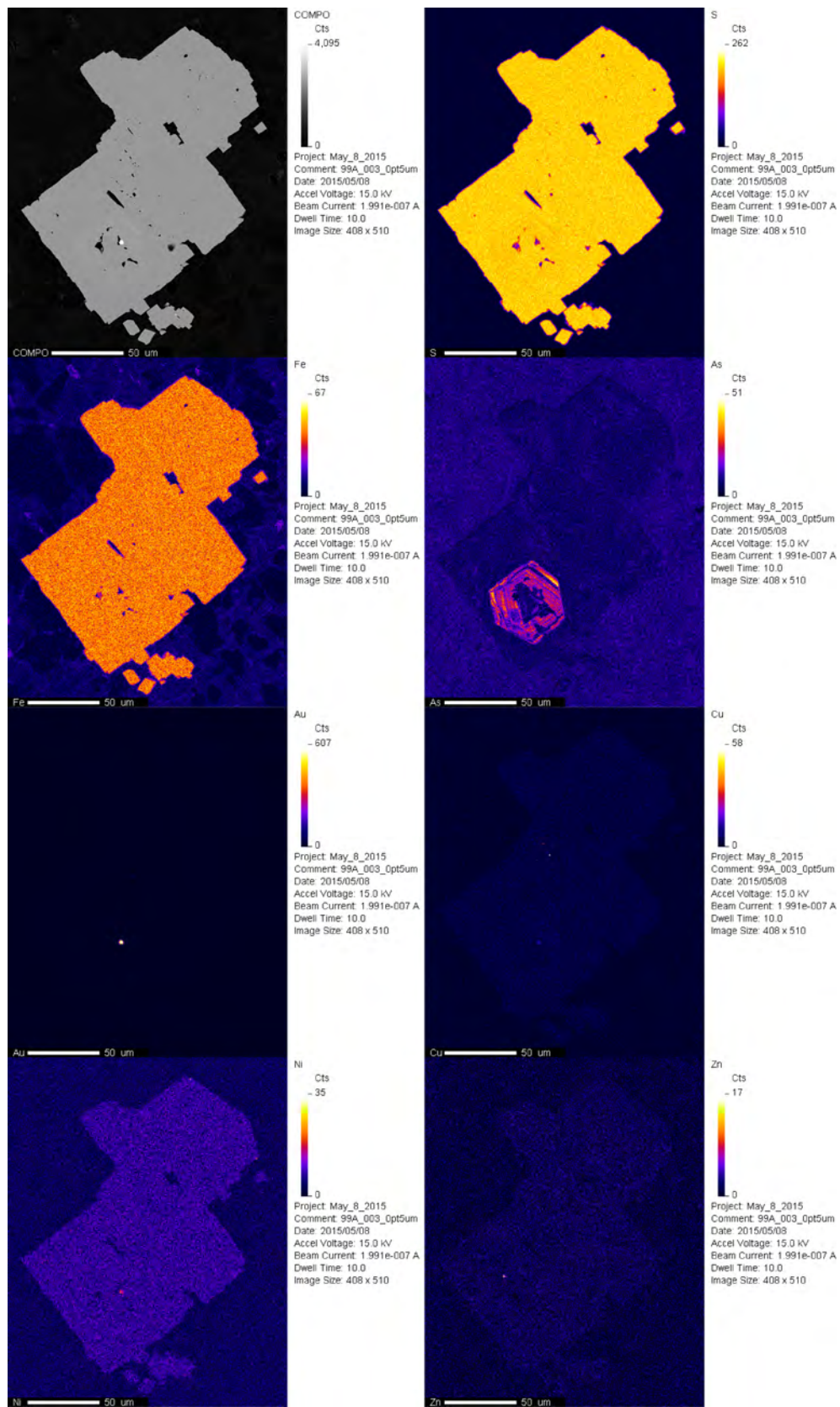
2 μm resolution maps of C406932 (Figure 4-2)



2 μm resolution maps of C407891B (complements D.2 SR-XRF maps)



2 μm resolution maps of C407899A (complements D.2 SR-XRF maps)



0.5 μm resolution maps of C407899A (complements D.2 SR-XRF maps)

Curriculum Vitae

Jessica Maarit Stromberg

EDUCATION

PhD. Candidate, Geology and Planetary Science University of Western Ontario London, Ontario	2011-present
B.Sc. (Hons), Biochemistry University of Winnipeg Winnipeg, Manitoba	2011

POSITIONS HELD

University of Winnipeg Geography Department Post-Doctoral Fellow	September 2017 – present
Instructor	September 2017 – present
Athletics Department Assistant Coach, Varsity Women's Basketball	December 2017 – present
University of Western Ontario Earth Science Department Graduate Research Assistant	September 2011- August 2017
Graduate Teaching Assistant	September 2011 - April 2016
Goldcorp Inc. Porcupine Gold Mines, Dome Mine Student Production Geologist	April - September 2014, 2015
University of Winnipeg Geography Department Research Assistant	May 2010 - August 2011
Biology Department Teaching Assistant	September 2010 - April 2011

TEACHING EXPERIENCE

<i>University of Winnipeg</i> GEOG2215 Mineralogy and Petrology	Instructor, 2017
--	------------------

University of Western Ontario

ES3310 Structure and Chemistry of Minerals and Materials	Guest Lecturer, 2017
ES4452Z International Geoscience Field Experience	Co-Instructor, 2016
ES2230 Introduction to Geochemistry	Guest Lecturer, 2015
ES1022A Earth Rocks	Teaching Assistant, 2015
ES1086F Origin and Geology of the Solar System	Teaching Assistant, 2014
ES4452 Geophysical Field Techniques	Teaching Assistant, 2013
ES2250Y Introductory Field Mapping Techniques	Teaching Assistant, 2013
ES2240F Catastrophic Events in Earth's History	Teaching Assistant, 2012
ES1086F Origin and Geology of the Solar System	Teaching Assistant, 2012
ES220A Plate Tectonic Theory, Environments and Products	Teaching Assistant, 2011

University of Winnipeg

BIOL3901 Microorganisms and Disease	Teaching Assistant 2011
BIOL2902 Prokaryotes and Viruses	Teaching Assistant 2010

FELLOWSHIPS AND AWARDS

PhD. Research Poster Award (1 st place), PDAC Convention	2017
Postgraduate Scholarship (PGS-D), NSERC	2015-2017
Science Poster Award (1 st place), CHESS User Meeting	2016
Research Poster Award (2 nd place), Mineral Exploration Roundup	2016
Ontario Graduate Scholarship, Government of Ontario	2014-2015
Student Poster Award (3 rd place), SEG Geoscience for Discovery	2013
PhD. Fellowship, NSERC CREATE	2013-2014
Graduate Research Scholarship, Western University	2011-2013
MSc. Fellowship, NSERC CREATE	2011-2013
Major Scholarship Incentive, Western University	2011
Undergraduate Fellowship, NSERC CREATE	2010
Tracy McLeod Nominee, CWUAA	2008, 2010
Academic All-Canadian, CWUAA	2007-2010
Women's Basketball Scholarship, University of Winnipeg	2005-2007
Academic Entrance Scholarship, University of Winnipeg	2005
BEST Scholarship, Basketball Manitoba	2005

RESEARCH AND TRAVEL GRANTS

Graduate Student Travel Grant, Canadian Light Source	2017
Graduate Student Travel Grant, Canadian Light Source	2016
Student Travel Grant, GAC MDD	2016
R.W. Hodder Travel Award, Western University	2016
Graduate Student Research Grant, ASTRO-CSA	2015
Graduate Student Travel Grant, Society of Economic Geologists	2015
R.W. Hodder Travel Award, Western University	2015

Graduate Student Travel Grant, Canadian Light Source	2015
Graduate Student Research Grant, SEG Canada Foundation	2014
Graduate Student Travel Grant, Canadian Light Source	2014
Graduate Research Fund, Western Science	2013
Graduate Student Travel Grant, NAI	2012
R.W. Hodder Travel Award, Western University	2012
Student Travel Grant, CIFAR	2011
Student Travel Grant, Canadian Space Agency	2010
Student Travel Grant, University of Winnipeg	2010

PROFESSIONAL AND VOLUNTEER ACTIVITIES

Committee and Society Memberships

Member, Western Faculty of Science National Scholarship Committee	2017
Vice-President, Society of Economic Geologists London Student Chapter	2015-2016
Member, Western Grad Club Committee	2013-2017
Treasurer, Western Graduate Geoscience Society	2015-2016
Secretary, Society of Economic Geologists London Student Chapter	2014-2015
President, Western Graduate Geoscience Society	2013-2015
Member, Conference Organizing Committee (AESRC 2013, Western)	2012-2013
Member, Conference Organizing Committee (Abgradcon 2013, McGill)	2012-2013

Public Education and Outreach

Participant, Three Minute Thesis, Western Faculty of Science	2015
Participant, Three Minute Thesis, CPSX (1 st place)	2014
Volunteer, Earth Science Open House, Western University	2012-2014
Organizer, Astrobiology Speaks, Astrobiology Graduate Conference	2013
Organizer, Science by the Pint, Astrobiology Graduate Conference	2013

Colloquia and Seminars

Australian National University, Research School of Earth Science	2016
Argonne National Laboratory, Advanced Photon Source	2015
Astrobiology Graduate Conference	2013

Field Trips (Organized and/or Lead)

Co-Organizer, Kirkland Lake Gold Camp, SEG Student Chapter	2016
Co-Leader and Organizer, Fennoscandian Shield Finland, ES4452Z	2016
Leader and Co-Organizer, Detachment Fault Settings of the Southwestern US, SEG Student Chapter	2016
Leader and Co-Organizer, Geology of the Timmins Gold Camp, SEG Student Chapter (Leader and Organizer)	2015
Co-Organizer, Geology and Ore Deposits of the Southwestern US	2015

Media Interviews

Canadian Light Source News, Western SGPS	2016
The Star Phoenix, Canadian Light Source News, CPSX Spotlight	2014

Winnipeg Free Press	2011
Winnipeg Free Press, Wesmen News	2010
The Uniter	2009
CBC News, Winnipeg Free Press, CWUAA News	2008

PUBLICATIONS IN REVIEW

1. **Stromberg, J.M.**, Barr, E., Banerjee, N.R., 2017. Early Carbonate Veining and Gold Mineralization in the Timmins Camp: Depositional Context of the Dome Ankerite Veins. *Ore Geology Reviews*. In Review.
2. **Stromberg, J.M.**, Barr, E., Gordon, R., VanLoon, L.L., Banerjee, N.R., 2017. Fingerprinting Multiple Gold Mineralization Events at the Dome Mine: Trace Element and Gold Content of Pyrite. *Economic Geology*. In Revision.

REFEREED PUBLICATIONS

1. Qadi, A., Cloutis, E.A., Whyte, L., Ellery, A., Bell III, J.F., Berard, G., Boivin, A., Haddad, E., Lavoie, J., Jamroz, W., Kruzelecky, R., Mack, A., Mann, P., Olsen, K., Perrot, M., Popa, D., Rhind, T., Samson, C., Sharma, R., **Stromberg, J.M.**, Strong, K., Tremblay, A., Wilhelm, R., Wing, B., Wong B. 2015. Mars Methane Analogue Mission: Mission simulation and rover operations at Jeffrey Mine and Norbestos Mine. *Advances in Space Research*, 55. 2414-2426
2. Schumann, D., Fuchs, S., **Stromberg, J.**, Laquerre, A., Mayer, D., Phaneuf, M.W., Vali, H., Neil Banerjee N.R., 2014. Combining Terapixel-Scale SEM Imaging and High-Resolution TEM Studies for Mineral Exploration. *Microscopy and Microanalysis*, 20, pp 1008-1009.
3. Rhind, T., Ronholm, J., Berg, B., Mann, P., **Stromberg, J.**, Sharma, R., Whyte, L.G., Cloutis, E.A., 2014. Gypsum-hosted endolithic communities of the Lake St. Martin impact structure, Manitoba, Canada: spectroscopic detectability and implications for Mars. *International Journal of Astrobiology*, 4: 366–377
4. **Stromberg, J.**, Applin, D., Cloutis, E.A., Berard, G., Rice, M., 2014 The Persistence of a Chlorophyll Spectral Biosignature from Martian Analogue Sites Following Desiccation under Mars-like Conditions. *International Journal of Astrobiology*. 13: 3, 202-223
5. Berard, G., Applin, D., Cloutis, E., **Stromberg, J.**, Sharma, R., Mann, P., Grasby, S., Bezys, R., Horgan, B., Londry, K., Rice, M., Last, B., Last, F., Badiou, P., Goldsborough, G., Bell III, J., 2013. A Hypersaline Spring Analogue in Manitoba, Canada for Potential Ancient Spring Deposits on Mars. *Icarus* 224: 399-412.

CONFERENCE CONTRIBUTIONS

1. **Stromberg, J.M.**, Barr, E., VanLoon, L.L., Banerjee, N.R., 2017. Geochemistry of the Dome Mine Ankerite Veins; Insights into Fluid Flow Pathways and the Multi-

- Stage Enrichment of a World-Class Orogenic Gold Deposit. Geologic Society of America Annual Meeting, Seattle.
2. Banerjee, N.R., VanLoon, L.L., **Stromberg, J.M.** 2017. Answers at the speed of light: Synchrotron solutions for mineral exploration, production, and remediation. Society of Economic Geologists Annual Meeting, Beijing.
 3. **Stromberg, J.M.**, Barr, E., Banerjee, N.R., VanLoon, L.L., 2017. Fingerprinting gold mineralization using sXRF at the world-class Dome Mine, Timmins, Ontario. Society for Geology Applied to Ore Deposits, Mineral Resources to Discovery, Quebec City.
 4. **Stromberg, J.M.**, Barr, E., VanLoon, L.L., Banerjee, N.R., 2017. Fingerprinting Multi-Stage Gold Mineralization at the Dome Mine, Timmins, Ontario. Prospector and Developers Association of Canada – Society of Economic Geologists Student Mineral Colloquium, Toronto.
 5. Cavellin, H.E., Bajwa, C., **Stromberg, J.M.**, Twomey, T., Kuntz, G., Venturi, C., O’Shea, C., VanLoon, L.L., Banerjee, N.R., 2017. Gold Mineralization at the Monument Bay project, Stull Lake greenstone belt, Manitoba. Prospector and Developers Association of Canada – Society of Economic Geologists Student Mineral Colloquium, Toronto.
 6. **Stromberg, J.M.**, Barr, E., VanLoon, L.L., Banerjee, N.R., 2017. Fingerprinting Early Gold Mineralization in the Timmins Gold Camp: Trace Element and Isotope Geochemistry of the Dome Mine Ankerite Veins. Mineral Exploration Roundup, Vancouver.
 7. Cavellin, H.E., Bajwa, C., Metcalfe, M., **Stromberg, J.M.**, Banerjee, N.R., Twomey, T., Kuntz, G., Venturi, C., O’Shea, C., VanLoon, L.L., 2017. Insights into Gold Mineralization at the Monument Bay Project, Northeastern Manitoba. Manitoba Minerals Convention, Winnipeg.
 8. **Stromberg, J.M.**, VanLoon, L.L., Banerjee, N.R., 2016. Trace Element and Gold Content and Speciation in Pyrites: Insights into Metal Mobility and Gold Mineralization at the Dome Mine. 26th V.M. Goldschmidt Conference, Yokohama.
 9. VanLoon, L.L., Banerjee, N.R., **Stromberg, J.M.**, Feick, K., Stammers, L., Kope, E., 2016. Probing Mining Industry Questions using Synchrotron Radiation. 26th V.M. Goldschmidt Conference, Yokohama.
 10. **Stromberg, J.M.**, Feick, K., Stammers, L., VanLoon, L.L., Banerjee, N.R., 2016. Synchrotron Spectroscopy for Ore Systems: Tying Trace Element Geochemistry to Mineralogical Context in the Abitibi Greenstone Belt. Whitehorse 2016, Geological Association of Canada and Mineralogical Association of Canada Joint Meeting, Whitehorse.
 11. **Stromberg, J.M.**, VanLoon, L.L., Banerjee, N.R., Barr, E., 2016. Mapping Speciation and Trace Metal Content of Gold-Bearing Pyrites at the Dome Mine: Mine to Micron Characterization of Whole Rock Samples Using Synchrotron X-ray Spectroscopy. Prospector and Developers Association of Canada – Society of Economic Geologists Student Mineral Colloquium, Toronto.
 12. **Stromberg, J.M.**, VanLoon, L.L., Banerjee, N.R., Barr, E., 2016. Mine to Micron Characterization of Gold and Arsenic in the Dome Mine Ankerite Veins: Synchrotron X-ray Spectroscopy of Whole Rock Samples. Mineral Exploration Roundup, Vancouver, and Cornell High Energy Synchrotron Source Annual User Meeting, Ithaca.

13. Schumann, D., **Stromberg, J.**, Mayer, D., Couillard, M., VanLoon, L., Barr, E., Phaneuf, M.W., Banerjee, N.R., 2016. Combining large area SEM imaging and nano-scale HRTEM studies for the in-situ characterization of arsenopyrite and arsenian pyrite. An example from the Timmins-Porcupine camp. Mineral Exploration Roundup, Vancouver.
14. **Stromberg, J.M.** Barr, E., VanLoon, L.L., Schumann, D., Banerjee, N.R., 2015. Fingerprinting Gold Mineralization in the Timmins Gold Camp: Synchrotron Trace Element Analysis of Gold and Pyrites from the Dome Mine Ankerite Veins. Society of Economic Geologists, World Class Ore Deposits: Discovery to Recovery, Hobart.
15. VanLoon, L.L., Banerjee, N.R., **Stromberg, J.M.**, Feick, K.E., Stammers, L., Blanchard, P., 2015. Mine to Micron: Synchrotron Science for Mineral Exploration, Production, and Remediation. Yellowknife Geoscience Forum, Yellowknife.
16. Schumann, D., **Stromberg, J.M.**, Laquerre, A., Mayer, D., Phaneuf, M., Banerjee, N.R., 2015. In situ characterization of gold in arsenopyrite combining large area SEM imaging and nano-scale HRTEM studies: an example from the Timmins-Porcupine gold camp. AGU-GAC-MAC-CGU Joint Assembly, Montreal
17. **Stromberg, J.M.**, Barr, E., VanLoon, L.L., Banerjee, N.R., 2015. Trace Element Content and Speciation in Gold-bearing Pyrite Grains: Characterizing “Invisible” Gold and Redox Conditions in the Dome Mine Ankerite Veins, Timmins, Ontario. Prospector and Developers Association of Canada – Society of Economic Geologists Student Mineral Colloquium, Toronto.
18. Schumann, D., **Stromberg, J.**, Feick, K., Laquerre, A., Mayer, D., Collins, R., Phaneuf, M.W., Banerjee, N.R., 2015. Application of novel large area SEM imaging modile “Atlas 5” in combination with nano-scale HRTEM studies to enhance mineral exploration and mining efficiency. Prospector and Developers Association of Canada – Society of Economic Geologists Student Mineral Colloquium, Toronto.
19. Schumann, D., **Stromberg, J.**, Feick, K., Laquerre, A., Mayer, D., Collins, R., Phaneuf, M.W., Banerjee, N.R., 2015. Using high-resolution large area SEM imaging and nano-scale HRTEM investigations for the study of ore deposits. Mineral Exploration Roundup. Mineral Exploration Roundup, Vancouver.
20. **Stromberg, J.M.**, Banerjee, N.R., Van Loon, L.L., Stammers, L., Feick, K., 2015. Mine to Micron: Synchrotron Science for Mineral Exploration. Mineral Exploration Roundup, Vancouver.
21. **Stromberg, J.M.**, Banerjee, N.R., Van Loon, L.L., Barr, E., 2015. Fingerprinting Early Gold Mineralization in the Porcupine Gold Camp: Synchrotron uXRF Mapping and Trace Element Speciation of Gold Bearing Pyrites from the Dome Mine Ankerite Veins. Mineral Exploration Roundup, Vancouver.
22. **Stromberg, J.**, Banerjee, N.R., Barr, E., 2014. Synchrotron-based uXRF analysis of early gold-bearing pyrites at the Dome mine, Timmins. Geological Association of Canada-Mineralogical Association of Canada Joint Meeting, Fredericton
23. Schumann, D., Fuchs, S., **Stromberg, J.**, Laquerre, A., Mayer, D., Phaneuf, M., Banerjee, N., 2014. Unlocking big opportunities in small packages: Application of Novel SEM imaging techniques and nano-scale HRTEM studies to enhance mineral exploration and mining efficiency. Geological Association of Canada-Mineralogical Association of Canada Joint Meeting, Fredericton
24. **Stromberg, J.M.**, Barr, E. Banerjee, N.R., 2014. Synchrotron-based μ XRF Analysis of Early Gold-Bearing Pyrites at the Dome Mine, Timmins. Prospector and

- Developers Association of Canada – Society of Economic Geologists Student Mineral Colloquium, Toronto.
25. Craig, M.A., Osinski, G.R., Flemming, R.L., Cloutis, E.A., Horgan, B., Tornebene, L.L., Izawa, M.R.M., Sapers, H.M., Marion, C.L., Applin, D.M., Mann, P., **Stromberg, J.**, 2014. Near-infrared Spectra of Glassy Impactite from Terrestrial Impact Structures. Lunar and Planetary Science Conference, Houston.
 26. **Stromberg, J.M.**, Banerjee, N.R., Abbott, L., Slater, G., Cloutis, E.A., Barr, E., 2013. Geologic and Astrobiological Context of Gold Bearing Archean Carbonate at the Dome Mine. Canadian Astrobiology Training Program Annual Meeting, Montreal.
 27. **Stromberg, J.M.**, Banerjee, N.R., Harris, R., Barr, E., Flemming, R., Slater, G., Cloutis, E.A., 2013. Exploring Carbonate Organic Content as a Potential Vector for Gold Mineralization in the Ankerite Horizon at the Dome Mine, Timmins, Ontario, Canada. Society of Economic Geologists Geoscience for Discovery Conference, Whistler.
 28. **Stromberg, J.M.**, 2013. Geochemistry of Archean Seafloor Hydrothermal Fluids at the Dome Mine, Timmins, Ontario, Canada. Astrobiology Graduate Conference, Montreal
 29. Cloutis, E., Whyte, L., Qadi, A., Anderson-Trocme, L., Bell III, J.F., Berard, G., Boivin, A., Ellery, A., Greenberger, R., Haddad, E., Jamroz, W., Kruzelecky, R., Mann, P., Mustard, J., Olsen, K., Perrot, M., Popa, D., Ralchenko, D., Rhind, T., Samson, C., Sharma, R., **Stromberg, J.**, Strong, K., Tremblay, A., Wing, B. 2013. How to search for methane on Mars: Results of rover field trials at Mars analogue sites. Geological Association of Canada – Mineralogical Association of Canada Joint Annual Meeting, Winnipeg.
 30. **Stromberg, J.M.**, Barr, E., Slater, G., Cloutis, E.A., Flemming, R., Harris, R., Banerjee, N.R. 2013. Characterization of the ~2.7 Ga ankerite at the Dome Mine, Timmins, Ontario: Implications for understanding Martian paleoenvironments and biomarker preservation. Geological Association of Canada – Mineralogical Association of Canada Joint Annual Meeting, Winnipeg.
 31. **Stromberg, J.M.**, Applin, D.M., Cloutis, E.A., Berard, G., Rice, M., Mann, P. 2013. The Persistence of a Chlorophyll Spectral Biosignature from Martian Evaporite and Spring Analogues Following Desiccation under Mars-like Conditions. UK Astrobiology Conference, Edinburgh
 32. **Stromberg, J.M.**, Cloutis, E.A., Flemming, R., Barr, E., Banerjee, N.R., 2013. Characterization of an Archean Sub Seafloor Hydrothermal System at the Dome Mine, Timmins, Ontario, Canada. UK Astrobiology Conference, Edinburgh
 33. **Stromberg, J.**, Banerjee, N.R., Harris, R., Barr, E., Flemming, R., Slater, G., Cloutis, E.A., 2013. Characterization of the Association between Organic Biomarkers and Gold Mineralization in the Ankerite at the Dome Mine, Timmins, Ontario, Canada. Prospector and Developers Association of Canada – Society of Economic Geologists Student Mineral Colloquium, Toronto.
 34. Horgan, B., Smith, R., Mann, P., **Stromberg, J.M.**, Cloutis, E.A., Christensen, P.R., Bell III, J., 2013. New Evidence for a Weathering Origin for the High-Silica Component of TES Surface Type 2 on Mars. Lunar and Planetary Science Conference, Houston.

35. Cloutis, E.A., Whyte, L., Qadi, A., Anderson-Trocme, L., Bell III, J.F., Berard, G., Boivin, A., Ellery, A., Greenberger, R., Haddad, E., Jamroz, W., Kruzelecky, R., Mann, P., Mustard, J., Olsen, K., Perrot, M., Popa, D., Ralchenko, M., Rhind, T., Samson, C., Sharma, R., **Stromberg, J.**, Strong, K., Tremblay, A. and Wing, B., 2013. How to search for methane on Mars: Results of rover field trials at Mars analogue sites. Lunar and Planetary Science Conference, Houston.
36. Harris, R., Barr, E., **Stromberg, J.**, Banerjee, N., Telluride associations with Gold Mineralization Goldcorp's Dome Mine; Timmins, ON. 2013. Mineral Exploration Roundup, Vancouver.
37. **Stromberg, J.**, Banerjee, N., Cloutis, E.A., Flemming, R. 2012. Characterization of ~2.7 Ga volcanic hosted hydrothermal carbonate: Implications for understanding Martian Paleoenvironments. Canadian Space Summit, London.
38. **Stromberg, J.**, Banerjee, N., Cloutis, E.A., Flemming, R., Barr, E., Slater G., 2012 Biogeochemical Characterization of a Late Archean Sub-Seafloor Hydrothermal System, Dome Mine, Timmins, Ontario, Canada. Astrobiology Graduate Conference, Pasadena and the 22nd V.M. Goldschmidt Conference, Montreal.
39. **Stromberg, J.**, Mann, P., Cloutis, E., 2012. The Effects of Desiccation Under Mars Like Conditions on the Spectral Detectability of Gypsum Associated Endolithic Communities. 43rd Lunar and Planetary Science Conference, Houston
40. Cloutis, E., Whyte, L., Qadi, A., Bell III, J.F., Berard, G., Boivin, A., Ellery, A., Haddad, E., Jamroz, W., Kruzelecky, R., Mann, P., Olsen, K., Perrot, M., Popa, D., Rhind, T., Samson, C., Sharma, R., **Stromberg, J.**, Strong, K., Tremblay, A., Wilhelm, R., Wing, B., Wong, B., 2012. The Mars Methane Mission Analogue Mission (M3): Results of the 2011 Field Deployment. Lunar and Planetary Science Conference, Houston
41. Berard, G., Applin, D., Cloutis, E.A., **Stromberg, J.**, Sharma, R., Mann, P., Grasby, S., Bezys, R., Horgan, B., Londry, K., Rice, M., Last, B., Last, F., Badiou, P., Goldsborough, G., Bell III., J.F., 2012. A Hypersaline Spring Analogue in Manitoba, Canada for Potential Ancient Spring Deposits on Mars. Lunar and Planetary Science Conference, Houston
42. **Stromberg, J.**, Harris, R., Cloutis, E.A., Barr, E., Slater, G.F., Banerjee, N.R. 2012. Characterization of the Depositional Environment of Ankerite and Associated Organic Biomarkers at the Dome Mine, Timmins, Ontario: Implications for Gold Mineralization. Prospector and Developers Association of Canada – Society of Economic Geologists Student Mineral Colloquium, Toronto.
43. Berard G.M., **Stromberg, J.M.**, Cloutis, E.A., Mann, P., Horgan, B., Rice, M. 2011. Desiccation of Algal Mats from Analogue Site When Exposed to Mars-Like Conditions. Lunar and Planetary Science Conference, Houston.
44. Berard, G.M., Cloutis, E.A., **Stromberg, J.M.**, Mann, P., Horgan, B., Rice, M. 2011. A Hypersaline Spring System Analogue in Central Manitoba for Arabia Terra's Potential Ancient Spring Deposits. Lunar and Planetary Science Conference, Houston.
45. Horgan, B., Mann, P., **Stromberg, J.**, Cloutis, E.A. 2011. Acid Alteration of Basalts, Andesites, and Anorthosites: Near-IR Spectra and Implications for Martian Soil Formation. Lunar and Planetary Science Conference, Houston.

46. Cloutis, E.A., Berard, G., Mann, P., **Stromberg, J.**, 2011. The Gypsumville - Lake St.Martin Impact Structure: Shocked Carbonates, Intracrater Evaporites and Cryptoendoliths. Lunar and Planetary Science Conference, Houston.
47. Boivin, A., Samson, A., Vrionis, H., Qadi, A., Scott, A., **Stromberg, J.**, Cloutis, E., Berard, G, Mann, P. 2011. Site Selection for Mars Methane Analogue Mission: Geological, Astrobiological, and Robotic Criteria. Lunar and Planetary Science Conference, Houston.
48. Cloutis, E.A., Hipkin, V.J., Wennberg, P.O., Wolff, M.J., **Stromberg, J.M.**, Berard, G.M., Mann, P., and the MATMOS Team. 2011. Exomars Trace Gas Orbiter MATMOS Instrument: Preliminary Strategy for Development of a Dust Spectral Library. Lunar and Planetary Science Conference, Houston.